Thermomechanical Hot Tool Cutting and Surface Quality in Robotic Foam Sculpting

Joseph Bain

A thesis submitted in fulfilment of the requirements for the degree of Doctor of Philosophy in Mechanical Engineering at the University of Canterbury, Christchurch, New Zealand

May 2011

Abstract

For several years, research work has been carried out at the University of Canterbury aimed at the development of a rapid prototyping and manufacturing process referred to as Robotic Foam Sculpting (RFS). This system uses a six-axis industrial robot and electrically-heated hot-wire and hot-blade tools to sculpt desired parts from blocks of polystyrene foam. The vision for this system is that it will be able to rapidly create large volume foam models at low cost, for a range of potential applications. Parts produced by the RFS system can potentially be used as investment casting patterns, cores for sculptures and architectural details, demonstration and testing models, wind tunnel test models, and many other potential applications.

At the beginning of the work reported in this thesis, there was very little understanding of the nature of the surfaces produced by hot-tool cutting of foam, very little knowledge of the range of input cutting conditions that affected the surface quality, and almost no understanding of the relationships between the cutting strategy and the nature of the surfaces being produced. In addition, there was little evidence of published work on these subjects that was sufficiently robust to be applicable to the RFS system. This research was concerned with rectifying this gap in the existing knowledge.

There were a number of different focal areas for this research. These included the surface texture of surfaces cut with hot tools, the effects of cutting strategy on the surface quality in single-pass cutting of foam, the effects of cutting strategy on the surface quality in multi-pass cutting, and the application of a current-control system to control the surface quality in real time during a cut. In each of the focal areas the goal was to develop a detailed understanding of the nature of the different aspects of surface quality, to map the factor interactions and dependencies that controlled these aspects of surface quality, to develop methods for predicting the expected surface quality based on cutting strategy (and vice versa) and to develop techniques for minimising the surface errors.

The detailed investigation of the surface texture of surfaces produced with hot-tool cutting is presented in Chapter 4. This chapter explores the characteristic nature of foam surfaces, presents the development of a method of measuring the surface texture of foam, and investigates the usefulness of a range of standard texture parameters for assessing foam surface quality. It is concluded in this chapter that common texture parameters based on the relative heights of surface features are not capable of reliably discriminating between different foam surfaces, so a new texture parameter (the 10%-Height Contiguous Diameter) is developed and implemented. Using this parameter, it is possible to reliably predict the surface texture to be expected for a given set of cutting conditions.

Investigations of the cutting strategy in single-pass cutting are presented in Chapter 5. This chapter identifies the two key aspects of surface quality in single-pass cutting, the kerfwidth and the surface barrelling. Experimental work is carried out to investigate the relationships between these errors and the cutting strategy, and the factors that influence each of them are identified. In addition, statistical models are developed for the kerf along the length of a cut so that the kerf can be predicted based on

cutting conditions. This chapter also includes a study of the cutting force in single-pass cutting, and develops models that allow the prediction of the expected cutting force for a given cutting strategy.

A detailed study of the cutting strategy for multi-pass cutting is presented in Chapter 6. This study identifies the most significant surface errors in multi-pass cutting and determines the causes of each of these errors and the factor interactions and dependencies that have to be considered when developing a multi-pass cutting strategy. Once again, statistical models that allow the prediction of these surface errors based on cutting strategy, or the evaluation of cutting strategy parameters to achieve a desired surface quality, are developed. The models for cutting force in single-pass cutting are applied to multi-pass cutting, and it is found that these models can accurately predict the force in multi-pass cutting as well.

The characterisation of the acoustic output in hot-tool cutting forms the subject matter of Chapter 7. This study establishes that the magnitude of the acoustic output is proportional to the cutting force experienced during the cut, and is therefore potentially suitable for use as a trigger signal for feedback current control. This would allow an acoustic signal to be used instead of the current force signal, which has a number of drawbacks that will be discussed in Chapter 2, the Background Material chapter. The specific trigger signal identified as being of most use is the acoustic output in the 4 – 12 kHz band, where the presence of any non-zero acoustic output above background noise is a reliable and repeatable indicator of the presence of thermomechanical cutting.

The work presented in this thesis provides a detailed, quantitative, evidence-based and reliable understanding of the nature of the cutting strategy in hot-tool cutting of foam. The key cutting strategy parameters and the important aspects of surface quality for different cutting types are identified, the relationships between all these parameters are mapped, and quantitative models are developed that allow the output metrics like the surface quality or the cutting force to be predicted with a high degree of accuracy based on the input cutting strategy conditions. Armed with this understanding, it is possible to determine the most suitable cutting strategy for sculpting a given part, and to assess whether a given part can be sculpted with the RFS system. As such, the research problem posed at the start of this thesis has been largely solved, and the stage is set for further research to optimise the cutting strategy for sculpting different parts and to correct the remaining drawbacks of the RFS system to complete the development of a commercially-useful manufacturing system.

Acknowledgements

It is a pleasure to be able to take a few moments to express my appreciation and thanks to all those people whose assistance, support and advice have been of help in the conduct of this research and the writing of this thesis.

Firstly, I would like to thank Scott Amies, Ken Brown, Eric Cox, Rodney Elliot, Mike Flaws, David Read, Paul Southward, Adam Latham and Rebecca Morgan for all their practical help, sound advice and recreational cynicism. Without their assistance, this research would have been impossible.

Secondly, thanks must go to my supervisors, Dr. David Aitchison, Dr. Malcolm Taylor and Dr. Dirk Pons, whose advice, assistance and guidance have been invaluable.

I would also like to thank my friends from the department: Geoff Rodgers, Ross Dawson, Ben Sitzia, Lisa Kauke, Dean Kirk and Andrew Shaw. You have been responsible for most of the fun times since I started working on this project.

Finally, my greatest thanks go to Mum, Sam and Greg, who always manage to balance unconditional support with strongly-expressed criticism when I'm getting carried away and need to be brought up short. I don't tell you often enough how much I depend on you all to keep me on something approximating the right path.

I would like to dedicate this thesis to my mother, Anne Bain. We've all come a long way since 1994, and it's because of you.

Thank you, everybody.

Contents

List of Figures

List of Tables

Glossary of Abbreviations

This section contains definitions for the abbreviations and acronyms used throughout this thesis, for convenient reference.

2D – Two Dimensional

3D – Three Dimensional

EPS – Expanded Polystyrene

FAST – Free-form Automated Sculpting Technology (also see RFS)

FF-TLOM – Free Form Thick Layer Object Manufacturing

PFC – Plastic Foam Cutting

RFS – Robotic Foam Sculpting (also see FAST)

RP – Rapid Prototyping

RP & M – Rapid Prototyping and Manufacturing

STL – Stereolithography (a CAD file format that approximates surfaces as triangular elements)

TCP – Tool Centre Point

TPFC – Thermal Plastic Foam Cutting

VLM – Variable Lamination Manufacturing

XPS – Extruded Polystyrene

Glossary of Nomenclature and Notation

To aid the reader in understanding this thesis, this section provides cross references to the sections in the body of the thesis where each parameter is defined, so that definitions can easily be looked up if required.

10%-Height Contiguous Diameter ($^{\varnothing}S_{10\%}$) – see page 118

Area-Specific Effective Heat Input (Q_{eff}) – see page 43

Cutting strategy – see page 4

Kerf (λ) – see page 60

Lay – see page 63

Path spacing (S_p) – see page 50

Surface Barrelling (ΔH) – see page 60

$R_{max,\ geometric}$ – see pages 60, 183

$R_{max,\ thermomechanical}$ – see pages 60, 198

Thermomechanical balance – see page 50

Tool Temperature Differential, ΔT – see page 50

1 Introduction

1.1 Introduction

Robotic foam sculpting (RFS), also sometimes referred to as FAST (Freeform Automated Sculpting Technologies) is a manufacturing and prototyping system that has been under development at the University of Canterbury for some time. This system uses a Kuka KR6 six-axis industrial robot and electrically-heated cutting tools to sculpt 3D objects from polystyrene foam. Any comparable industrial robot could be used for this application, the novelty of the RFS system lies in the tooling and the detailed study of the thermo-mechanics of hot-tool foam cutting. A general overview of the system is shown in Figure 1.

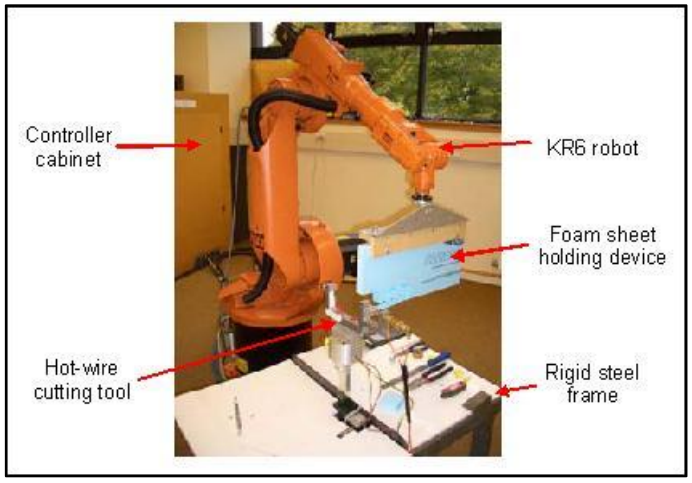

Figure 1: General configuration of the RFS system

The RFS system is intended to be used as a rapid prototyping (RP) and rapid patternmaking system, as well as having potential for application as an industrial manufacturing process in its own right. Examples of possible applications for RFS include:

- Patterns for parts to be made by investment casting
- Prototypes to test the fit and form of products during development
- Architectural detail cores for columns and sculpture to be finished with, for example, plaster
- Fuselage and wing cores for model aircraft and UAVs
- Prototype models for wind-tunnel testing
- Foam cores for surfboards, sailboards, rowing shells and other small watercraft
- Advertising and signage, film industry props, large size concept models
- Sculpture and artwork [2]

The key feature of the robotic foam sculpting system is that it is subtractive in nature. Unlike most rapid prototyping and manufacturing systems, which build up parts using additive, layer-by-layer

processes, RFS starts with a block of polystyrene foam and then cuts this block down to the desired shape and size using a combination of taut hot wire, straight hot blade and curved hot blade tools operated by the Kuka robot. Taut hot wire and straight hot blade tools can be used to sculpt planar surfaces and for profile cutting, while curved hot blades can be used to sculpt 3D and freeform surfaces using multiple tool passes. The subtractive nature of the RFS system is most suitable for the creation of large-size physical models, since subtractive sculpting is much more efficient than additive manufacturing for large build volumes (as the size of a physical model doubles, the surface area increases by 4x and the volume increases by 8x – so clearly it is more economic to produce large models from already solid materials).

As envisaged, the RFS system will be able to sculpt large scale objects with low material costs and rapid build times, and it is this that separates RFS from other Rapid Prototyping and Manufacturing (RP & M) systems. Whereas most RP systems have maximum construction dimensions measured in hundreds of millimetres and use relatively expensive plastic materials, the construction volume of the RFS system can be measured in metres (and can be increased if necessary by using larger industrial robots) and the working material is polystyrene foam, which is readily available in large volumes at relatively low cost throughout the world.

While hot-tool cutting of polystyrene foam has been an extant technology for decades, it has generally been a manual or semi-automated process, or an automated process with limited capability. Examples of existing hot-tool foam cutting systems include:

- Handheld hot-wire or hot-knife tools that allow manual shaping of foam workparts. These are capable of producing very complex parts but obviously require a high level of skill to achieve good results at high levels of part complexity. These tools are also of relatively low cost [3].
- Stationary hot-tool cutting machines that are manually operated and can be used with appropriate jigs to increase the accuracy of cutting. These require less operator skill than handheld tools, but have less capability to produce very complex parts. These machines are also significantly more expensive than handheld tools [4].
- Stationary CNC hot-tool cutting machines. These can achieve higher levels of repeatability than handheld or stationary manual machines, but have similar part-complexity limitations to stationary manual machines. CNC machines of this type are significantly more expensive than stationary manual machines due to the additional expense of the control system [5, 6].

There are some exceptions to this (see section 2.2.1) but these systems use sculpting principles that do not apply to RFS. As a result, there is a potential market opportunity for an automated foam-based sculpting system capable of producing physical models with high levels of complexity with high cutting speed and accuracy, and it is this market opportunity that RFS is intended to satisfy (see Figure 2). Since foam cutting has been primarily a manual or a semi-automated process, only a limited body of knowledge exists concerning the cutting mechanics and the effects of cutting conditions on the quality

of the surfaces produced: in the absence of such knowledge, it is difficult to determine a suitable cutting strategy for sculpting a given part and to properly control the sculpting process.

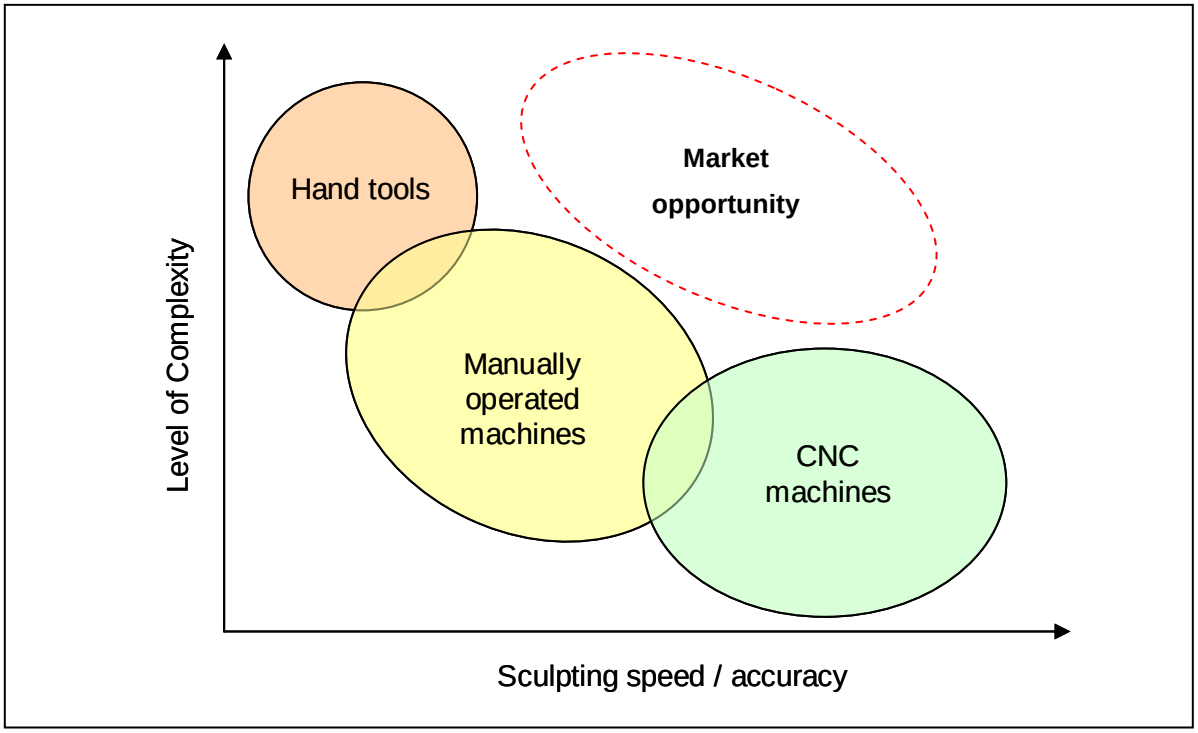

Figure 2: Existing methods of shaping plastic foams, showing the market opportunity the RFS system is intended to satisfy

The RFS system is a work in progress, and as such it had a number of significant limitations at the beginning of the work reported here. These included:

- The lack of any quantitative understanding of the surface texture being produced by thermal plastic foam cutting, the lack of a suitable means of measuring the foam texture, and the lack of detailed understanding of the factors that affected the surface texture.
- The lack of a quantitative understanding of the macroscopic surface form errors present in surfaces that were cut using single-pass and multi-pass tools, and the lack of detailed understanding of the factors that influence these errors of form.
- The lack of a comprehensive model of the inter-relationships between input cutting conditions and the output surface quality (surface texture and errors of form) of the cut surface.

These limitations mean that anyone planning to use RFS to sculpt a given part, or designing a part that will be sculpted, has no knowledge to guide them in the selection of tool feedrate, applied current, tool types, tool sizes, material, path spacing and path orientation. Production planners and design engineers have no idea how to design parts in such a way that they can be easily made with RFS, for example by avoiding surface curvatures that cannot be accurately sculpted. Finally, for a given set of cutting conditions the production planner has no idea what sort of surface quality (surface texture and surface accuracy) can be expected, and no mechanism to select cutting conditions based on desired surface quality. The purpose of the work reported in this thesis is to resolve these limitations, so that

RFS can be developed further and used as a practical RP & M application. The range of input and user-variable parameters that have an effect on the output surface quality of sculpted foam parts are collectively referred to in this thesis as the cutting strategy: this term is defined in more detail below (see Section 1.3).

1.2 Fundamental Research Goals

At the beginning of this work, the most appropriate cutting strategy for robotic foam sculpting was only qualitatively understood. Some limited work had been carried out investigating the surface texture produced by different cutting conditions, and some loose evaluation of different toolpath strategies had been undertaken [7], but no quantitative work had been done to investigate the relationships between cutting strategy and surface finish, geometric form or dimensional accuracy. The full range of potentially relevant factors affecting surface quality had not been determined, and the interrelationships and confounding between these parameters had not been mapped. No work had been done to actually measure the surfaces produced by RFS, to determine the factors that had an effect on the surface texture, geometric form and dimensional accuracy. It was the intention of the work reported here to generate an understanding of the effects of cutting strategy on the models produced, based on quantitative measurement of different aspects of foam surfaces. The fundamental goal of this research was to answer the following questions:

1. What elements of cutting strategy have an effect on the surface quality of parts produced from polystyrene foam using hot tools?
2. What are the most significant surface errors that must be considered when choosing a cutting strategy for a given part?
3. How can the surface errors be measured accurately?
4. Is it possible to develop models that allow the prediction of the value of a given type of surface error based on input cutting strategy conditions?
5. Is there an alternative output metric that can be used as a trigger signal for controlled-current cutting, in place of the cutting force used at present?

Answers to these questions will provide a significantly advanced understanding of the nature of hot-tool cutting of polystyrene foam that allows the selection of a cutting strategy to achieve the desired surface quality and accuracy. In effect, the goal of this thesis is to provide a set of tools that can be used to optimise the cutting strategy for producing a given part with the RFS system, or more generally with hot-tool cutting.

1.3 Cutting Strategy for Robotic Foam Sculpting

‘Cutting strategy’ is a catch-all term for all the controllable factors acting during RFS and exerting an influence on the quality of the final surface produced by the sculpting process. There are a wide range of such factors, values of which can be selected during the production planning process by the designer of the part to be sculpted. When a part is to be produced using the RFS system, the cutting strategy needs to be developed based on the part geometry to achieve the desired surface texture,

geometric and form accuracy, and sculpting time. Alternatively, depending on the application, the process planner may want to know what surface quality can be expected from given values of input cutting conditions.

Cutting strategy has a number of factors and interrelationships, and a map of these interactions can be seen in Figure 3. This map has been developed based on qualitative observation of many hundreds of cutting trials. The major factors that influence cutting strategy can be divided into categories as follows:

- Tool design
- Material
- Surface Condition
- Workholding
- Cutting mechanics
- Toolpath

These factors all influence the cutting strategy, and also mutually affect each other. For instance, the tool design and the tool path influence each other, since the tool path required to sculpt a given surface with a Φ20mm round-nose tool will be different from the tool path required to sculpt the same part with a 15mm square-nose tool. Workholding fixtures and the toolpath are also interdependent, since it may be necessary to hold a workpart in a specific way for a given tool path to be practical. The cutting strategy and the part design also influence each other, since for example a closely-spaced tool path is necessary to produce an accurate part if the surface has a tight curvature. These are only examples of interrelationships between different strategy aspects: the full range of interactions is shown in detail in Figure 3.

Although workholding is a major aspect of cutting strategy, it has been excluded from the scope of this research. The reason for this exclusion is that workholding of parts for robotic foam sculpting is not fundamentally different from the workholding of parts for any other kind of robotic manufacturing process [8]. This area of manufacturing is relatively mature and the further development of the RFS system requires no particular new, novel or innovative workholding system, so attention was focussed on the aspects of RFS cutting strategy that are as yet poorly understood.

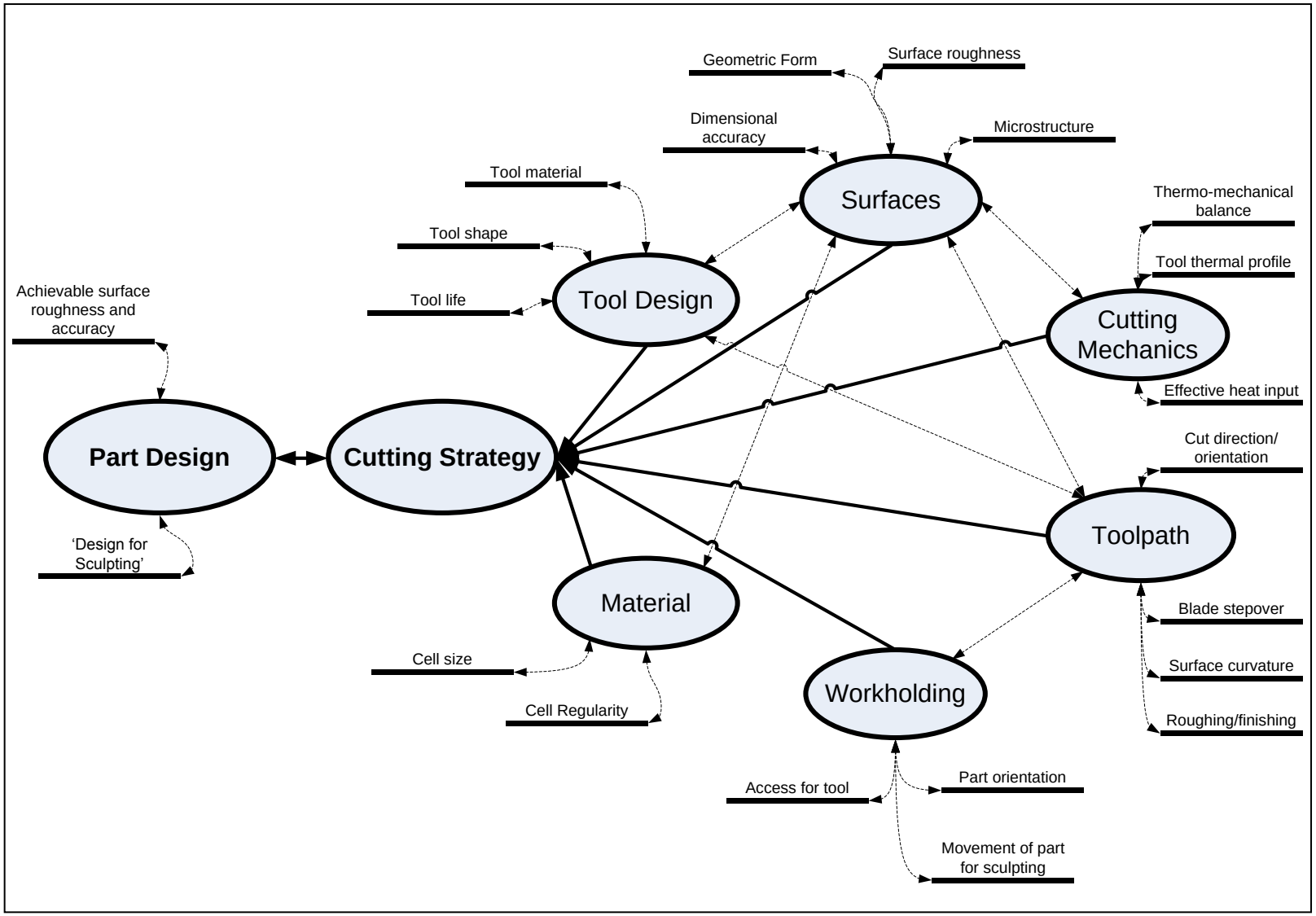

Figure 3: Factors and Interrelationships involved in cutting strategy

The factors that must be considered when developing the cutting strategy for sculpting a given part can be divided into three broad categories: the user-controllable input variables, the output variables used to assess surface quality, and the intermediate variables that affect the values of the output variables but are themselves controlled by the interaction of two or more input variables. The factors of relevance in each of these categories are presented in Table 1. The variables will be defined in more detail in Chapter 3.

Table 1: Cutting Strategy Factors

User-controllable input variables	**Intermediate variables**	**Output surface quality variables**
• Path spacing • Tool shape • Tool size • Surface curvature • Supplied current • Tool feedrate • Material • Cut depth	• Effective heat input, Q_{eff} • Distance along cut • Thermomechanical balance • Tool Temperature Differential, ΔT • Engaged tool length	• R_{max} (geometric) • Peak Spacing (multi-pass) • Multi-pass lay • Surface texture • Kerf width • Surface barrelling ΔH

1.4 Thesis Structure

The structure of this thesis is shown in Figure 4, below. This introduction sets out some of the general background to the research topic, explains the need that this thesis is intended to satisfy, defines what is meant by cutting strategy, defines and explains each of the parameters that are significant for the cutting strategy, explains the factor interrelationships that influence it, and outlines the scope of the research.

The Background Material chapter is next, and serves to present the context of this research in detail. This chapter summarises previous work done as part of the Robotic Foam Sculpting project, and presents a literature review of relevant similar research. This covers rapid prototyping systems based on thermal plastic foam cutting, with particular attention being paid to any consideration of cutting strategy, surface quality, surface texture, geometric form and dimensional accuracy assessment.

Chapter 3 presents the definition of all the relevant cutting strategy factors that have an impact on the quality of surfaces produced using hot-tool cutting of polystyrene foam, and the parameters that are used to measure surface quality. This chapter also summarises the interactions between these parameters and each of the surface quality metrics that will be used in later chapters.

Following the presentation of background material and the factor definitions, there are four thematic chapters. These chapters are not sequential, but rather exist in parallel. Each is concerned with the detailed analysis of an aspect of cutting strategy and surface quality, and each can be considered separately if the reader is interested only in a specific area of this research. The interrelationships of the factors that influence cutting strategy and surface quality are examined in depth in these chapters.

Chapter 4 presents the detailed investigation of the factors influencing the surface texture of surfaces produced by a single-pass of taut hot wires or straight hot blades. This includes the determination of a suitable method of measuring the surface texture of foam, the determination of suitable parameters for expressing information about foam surface texture, and the development of a predictive model for the surface roughness due to different input factors, based on statistical analysis.

Similar analysis techniques are used to investigate the cutting strategy and surface accuracy of single pass cuts in Chapter 5. This chapter covers the development of an understanding of the relationships between the cutting strategy and surface form accuracy when using straight-wire and straight-blade tools making single passes to produce nominally-planar surfaces.

In Chapter 6, the geometric form and dimensional accuracy of multi-pass foam cutting are investigated. This begins with the development of an idealised model for the geometric form accuracy of a surface produced by multi-pass cutting, and then quantifies the discrepancies between geometric and as-measured surface inaccuracy resulting from thermomechanical factors, in order to produce an accurate understanding of the surface accuracy and the factors affecting it.

Chapter 7 is concerned with adaptive current control for RFS: this is used as a means of controlling the power input during cutting, in order to control the tool temperature, based on an objective measure of the state of the cut. The present state of the art for this system is summarised, the drawbacks are explained, and initial results are presented for an innovative and novel method of controlling the supplied current based on the acoustic output of the thermomechanical cutting process.

Finally, Chapter 8 presents a discussion of the results of the thematic chapters, relating them to the goals of the research. The research outcomes will be evaluated against the goals, the limitations of the research will be discussed, and the implications of this work for further research and for practitioners using the RFS system or any other hot-tool foam cutting system will be discussed. The significant novel contributions of this research will be presented, and overall conclusions will be drawn.

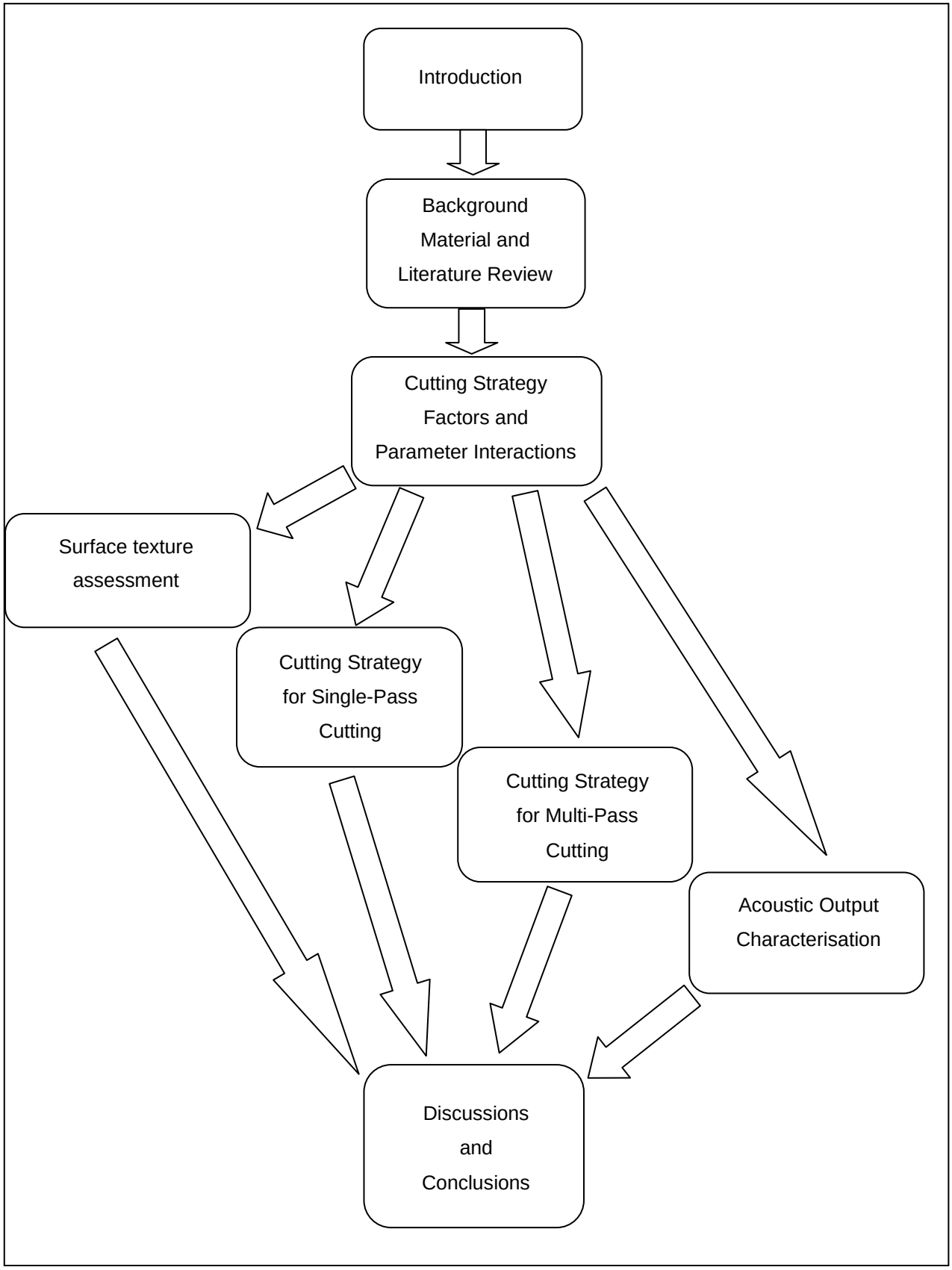

Figure 4: Chapter structure of this thesis

2 Background Material and Literature Review

In order to provide context and background for the research presented in this thesis, this chapter presents a summary and critical review of the existing body of knowledge that is relevant to the control of surface quality in hot-tool cutting of polystyrene foam. This background material is presented in two sections. Section 2.1 presents the research that has previously been carried out as part of the Robotic Foam Sculpting project at Canterbury University, while section 2.2 presents relevant research that has been carried out by other parties and published publically. The entirety of Chapter 2 is summarised and critically reviewed in section 2.3, which discusses the results of the review and identifies the gaps in the body of knowledge that this thesis is intended to fill.

2.1 Previous Robotic Foam Sculpting Work

This section summarises the research that has previously been carried out on the RFS project at Canterbury University. For convenience, three primary themes of research have been identified as organising categories for this review. Section 2.1.1 deals with Cutting Mechanics and Surface Assessment, section 2.1.2 is concerned with Tool Design and Control, and section 2.1.3 presents the results of research into Cutting Strategy and Toolpath Generation.

2.1.1 Cutting Mechanics and Surface Assessment

In the early stages of the RFS project, a wide range of cutting trials were conducted with taut hot-wires to observe the cutting mechanics and make some qualitative conclusions about the mechanism of hot-wire cutting, and to build a body of knowledge about the surface finish that could be expected for a given combination of applied electric current and tool feedrate [9]. This work identified five different cutting modes based on different mechanisms of cutting. These modes were named vapourisation, line contact, stick and slip, solid contact and mechanical cutting.

Vapourisation (Figure 5(a)) occurs as long as the wire has no physical contact with the foam. The wire is hot enough to vapourise the foam with no physical contact between wire and foam. There is no detectable force on the wire, thus extending its operating life. The only problem that occurs with this process is that the wire can be too hot, resulting in bad surface accuracy due the excessive amount of foam being vaporised. The main characteristic of this problem is the formation of a tough outer skin and, in extreme cases, a heavily pitted surface. This mode of cutting is associated with vapourised surfaces, as outlined below.

Line Contact (Figure 5(b)) occurs when the wire has cooled sufficiently to allow contact along a continuous line at the front of the wire. This causes a small amount of sticking and results in small amplitude striations on the surface of the foam. There is small cyclical force on the wire as the foam alternates between contact and non-contact cutting. This phenomenon usually begins after a short period of vaporisation cutting.

Stick and Slip (Figure 5(c)) follows both the previous regimes when the feed rate is further increased. The wire is now in constant contact with the foam and the contact occurs over more of the circumference. The result is a heavily striated surface with a much greater degree of irregularity compared with line contact cutting. The force on the wire is now highly cyclical as the wire cools and sticks to the wire followed by a sudden slip when the temperature increases due to the lack of vaporisation.

Solid Contact (Figure 5(d)) follows the other three, and occurs only at relatively high feed rates. The cyclical nature of the previous two cutting regimes disappears, and is replaced by a constant surface finish. The wire is now surrounded by liquefied foam and, as it moves through the foam, leaves sharp peaks on the surface. Apart from the peaks, the surface is generally very rough and undulating. The force on the wire is constant and the wire is visibly bent throughout the duration of this cutting process.

Mechanical Cutting (see Figure 5 (e)) is the last of the cutting processes and could also be described as carving. The force on the wire is extremely high and, in most cases, the wire breaks very quickly after this process is initiated. The surface finish is extremely rough and flaky, with chunks of foam becoming dislodged as the cut proceeds.

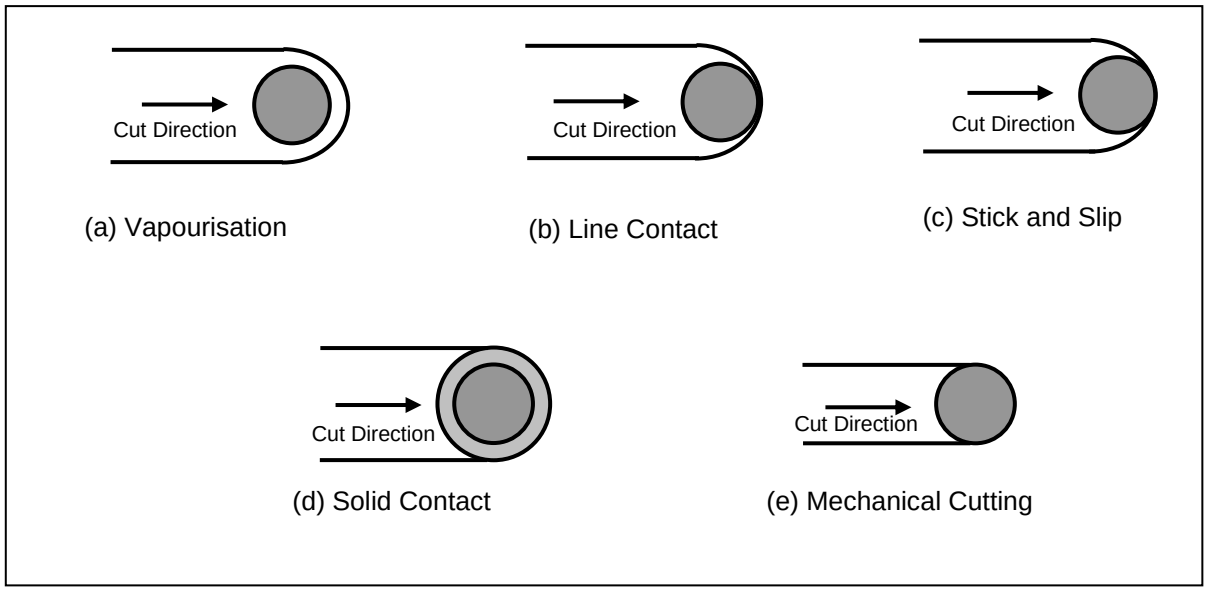

Figure 5: The five different hot-tool cutting modes

These cutting modes exist as a continuum, from vapourisation up to mechanical cutting. Generally speaking, cuts made with a high feedrate and low current (or low effective heat input, in other words) are most likely to have ‘solid contact’ or ‘mechanical’ cutting as the steady-state cutting mode, while cuts with a high effective heat input are more likely to have a steady-state cutting mode closer to the vapourisation end of the continuum. That said, most cuts undergo a sequence of these cutting modes since the wire is usually much hotter than the melting point of the foam when it first enters the material, before cooling to the steady state temperature. At the beginning of the cut vapourisation is

the dominant mode, and the cut progresses along the continuum until it reaches whatever cutting mode is predominant in the steady state for the cutting conditions in question.

It should also be noted that these cutting modes are somewhat subjective, and that no clear and definable boundaries exist between them: one cutting mode simply fades into the next. This concept has been outlined as the concept of ‘thermomechanical balance’ above.

These initial cutting trials also identified a characteristic pattern for cutting force and mid-cut tool temperature. At the beginning of a cut, the temperature of the cutting tool was generally much higher than the melting point of the foam, so the initial cutting mode was vapourisation. As a result, the force was negligible. As the cut progressed, the tool would begin to cool and start to come into physical contact with the foam, which led to an increase in the cutting force. Finally, steady state conditions would be reached where the temperature of the tool and the cutting force levelled off: this state would last until the end of the cut. This characteristic pattern of force and temperature can be seen in Figure 41, above, where it is used to illustrate the concept of thermomechanical balance. It should be noted that while all cuts exhibited this basic pattern, steady-state conditions were not necessarily reached in all cases, due to the limited length of cut being investigated: some cuts ended while the temperature was still declining and the force was still increasing.

Some very basic surface assessment has also taken place during the Robotic Foam Sculpting project. This can be separated into two broad categories: assessment of surface texture and assessment of geometric form.

The surface texture assessment carried out prior to this reported research has been qualitative in nature, and has been based around the identification of basic surface texture categories into which cut surfaces can be grouped. These categories are defined based on the visual appearance of the surfaces and the cutting mechanics that produced them, and have evolved somewhat over time [10]. The different categories were developed based mostly on expanded polystyrene foam (EPS) and were defined and described (as at the start of the research project that led to this thesis) as follows [11]:

Smooth surfaces were the best surface finishes that could be achieved, and did not show any unevenness. These surfaces were categorised by low but non-zero cutting forces, and it was thought that the smoothness was the result of the wire dragging molten material into the recessed cell boundaries, smearing and smoothing the surface during the cut.

Sporadic bubble surfaces were similar to the smooth surfaces, but with occasional material accumulations resulting in sporadic ‘pimples’ on the surface.

Bubble surfaces were distinguished by multiple pits and material accumulations on the surface, and were associated with a wire temperature that was too low relative to the feedrate. These surfaces were thought to be the result of the wire pulling EPS beads out of the parent material, which then

melted and re-attached to the surface as protuberances. This surface type differed from the sporadic bubble surface in that the area of bubbles was larger than the areas of smooth surface between them.

Vapourised surfaces were described as having a 'shot-blast' appearance, and were the result of the feedrate being too low relative to the wire temperature, so that the surfaces were being cut by purely thermal means, with no physical contact between wire and foam. In cuts of this type the surface had a hard 'skin' of relatively high density. It was thought that this surface type would be unsuitable for typical end applications.

Wavy surfaces were characterised by a wavy longitudinal profile. These surfaces occurred in high temperature cuts (free-air wire temperatures greater than 600ºC) where the tension on the wire had been reduced to avoid wire breakages: this led to the wire oscillating up and down as a result of the cutting force.

Finally, **Ripped surfaces** were the worst finishes produced during the conducted cutting trials. These were the result of the hot-wire temperature being too low relative to the feedrate, or the feedrate being too high relative to the wire temperature. Surfaces of this type were the result of primarily mechanical cutting, where cells of foam had been physically torn from the surface, producing an extremely rough final surface.

These surface categories provided a framework within which the performance of hot-wire foam cutting could be evaluated, but suffered from a number of drawbacks. The first was that they are qualitative, and hence subjective: this makes it difficult to reliably categorise different surfaces, especially on the borderlines between categories. It is also very hard to reliably communicate the nature of these surfaces to parties not regularly involved with the RFS project. The second major drawback is that these six categories are comprehensive, describing all the different surfaces that were produced during cutting trials: the range of categories covers surfaces produced by fundamentally different mechanisms, which leads to potential confusion. For example, the wavy surface category is not caused by thermomechanical cutting mechanics, but is a function of tool design, and the difference between a sporadic bubble surface and a bubble surface is a matter of degree, not a fundamental difference in cutting mechanics. The limitations of these categories, and a redefinition of them to make them more useful, will be presented in Chapter 4.

Some basic elements that can be considered to be geometric form have been considered during the FAST project within which this thesis falls. To date, these have mostly been concerned with kerfwidth, but a few qualitative observations have been made that are relevant to the work discussed later.

Some work has been carried out on the use of a coordinate measuring machine (CMM) to assess the surface form of foam surfaces [12-14]. This work was based on the use of 20 touch points of the CMM tip, and the generation of a single surface form measure that was basically the maximum deviation of a measured point from the nominal surface. This work was unsuccessful, due to the nature of the foam material: in order to achieve a good measurement resolution a small CMM tip was needed, but if

the tip was small enough to get a good resolution the surface stress during contact was high enough to deform the foam, rendering the measurement result unreliable. No real conclusions were made based on this research.

It was observed at an early stage that single-pass taut hot wire cuts exhibited a characteristic form, where the kerf width was wide at the beginning of a cut and reduced as the wire cooled, so that a surface had a characteristic longitudinal profile as shown in Figure 6. It was also observed that the surfaces exhibited a transverse profile that was described as 'barrelled.' [1, 15]

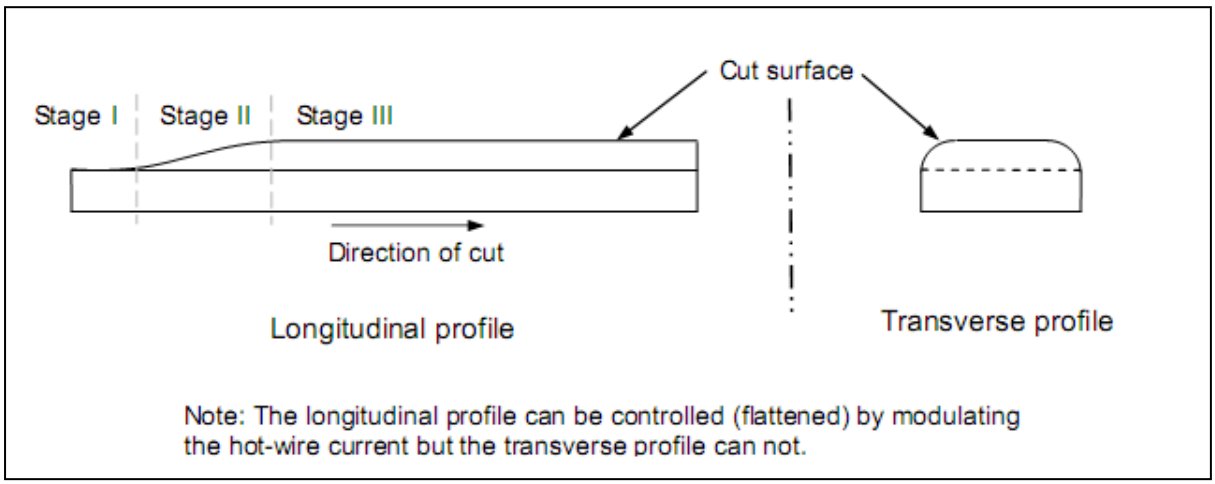

Figure 6: General form of the longitudinal and transverse surface profiles of single-pass cutting [15]

Basic kerfwidth measurements were taken for a range of different cutting conditions [1]. These measurements were made using vernier callipers on foam strips that had been cut with the same cutting conditions at top and bottom and had a known nominal thickness, so that the kerf could be derived from ideal and measured geometry. The kerfwidth measurements taken using this technique confirmed the change in surface height (and reduction in kerfwidth) along a cut, as shown in Figure 7. The 'end of cut' kerf width was measured at 300mm from the start of the cut. It was observed that the kerf width was approximately constant after the first 100mm of cut, and so the kerf width at the 'end of cut' was considered the steady state value.

When the steady-state force and kerf values were plotted against the area-specific effective heat input (a parameter first developed by Ahn et al [16] and developed further by Brooks [1]), it becomes clear that the kerf is linearly related to Q_{eff} and the force follows an exponential decay pattern across the range of Q_{eff}. This is shown in Figure 8. This force distribution was found to indicate a change from one dominant cutting mode to another: areas of high force on the left indicate that the steady-state cutting mode was thermomechanical, and the near-zero forces on the right indicate purely thermal cutting. It was stated that the 'kink' in the distribution represented 'smooth cutting conditions' where there was a small non-zero cutting force.

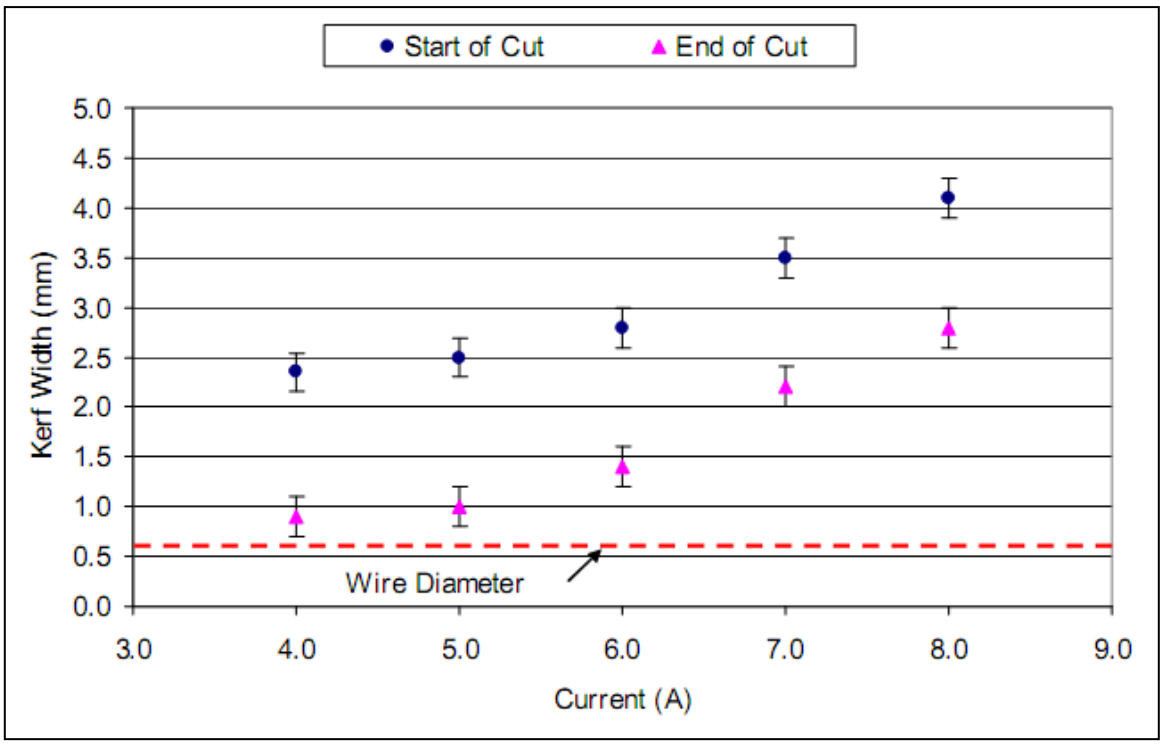

Figure 7: Kerfwidth vs. current for XPS cut at 0.0150m/s at two different positions along the sample length [1]

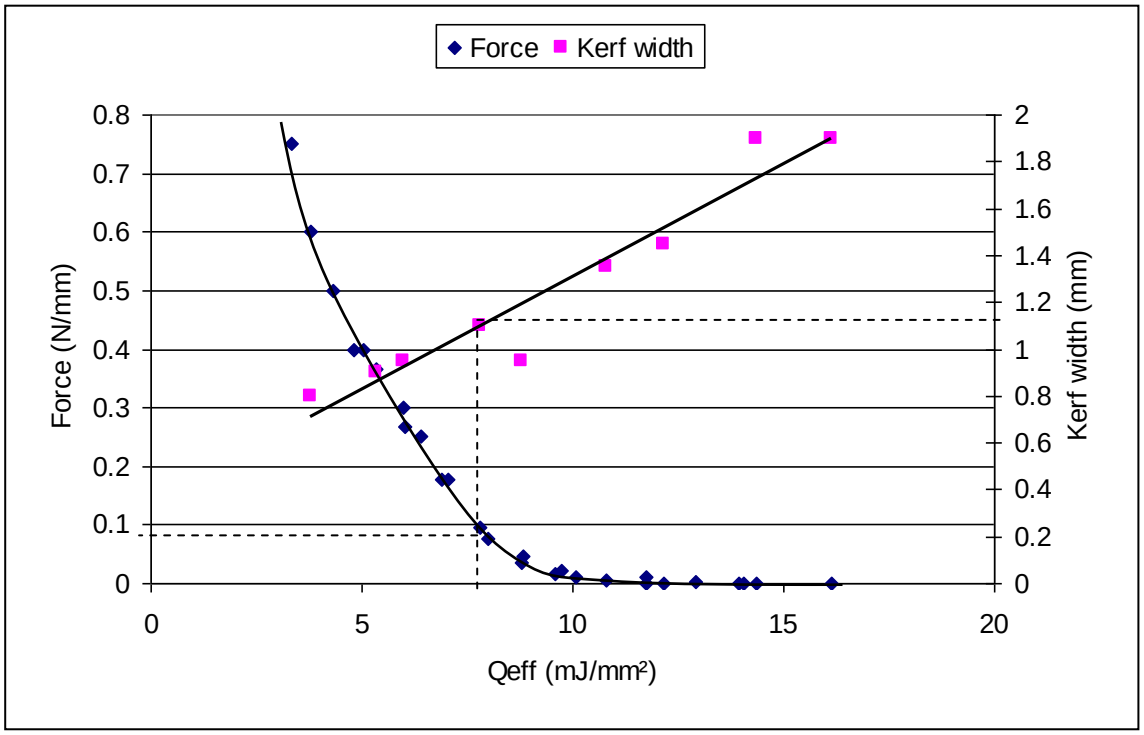

Figure 8: Force and kerfwidth vs. effective heat input for VH Grade EPS [1]

While useful, this data suffers from a number of drawbacks. The first of these was that only steady-state kerf and force values were used. The linear relationship between Q_{eff} and kerf cannot be used to

predict the kerf width along a given cut at a given distance from the start, since the kerf changes with distance. Secondly, the method of measuring the kerf was not very robust, since it was dependent on manual measurements of the thickness of a sample using vernier calipers. This had significant potential for parallax error and error resulting from the physical contact between the soft foam sample and the instrument. Finally, this experimental work was restricted to only a limited range of foams, engaged lengths and cutting conditions, so is only of restricted use. Without further work, it is difficult to apply these results more generally. Overcoming these drawbacks is one of the desired outcomes form this research (see Chapter 5).

Some assessment of surface accuracy and quality has also taken place for multi-pass surfaces. This was primarily qualitative assessment based on visual inspection [7], although some temperature profile measurement has taken place [1]. It was observed that when blades were used for multi-pass cutting, a 'weatherboard' effect was produced, as shown by the dimetric view in Figure 9. This effect is thought to be a result of the temperature profile in the blade. Temperature profiles along the cut were measured at points A – E, and it was found that the temperature difference between points B and D was approximately 300ºC after 4s of cutting, and had stabilised at approximately 200ºC by the end of the cut. This supported visual observations that the weatherboard effect was more pronounced at the beginning of the cut than at the end.

This work on multi-pass surface accuracy was interesting, and indicated a relationship between blade thermal profile and weatherboarding, but was not pursued further. The temperature profiles gathered were for a single set of cutting conditions and were not investigated in relation to cut depth, stepover, engaged blade length or any of the other important cutting strategy parameters. The weatherboard effect was considered a major aspect of multi-pass geometric form and is one of the major areas of research for this thesis (see Chapter 6).

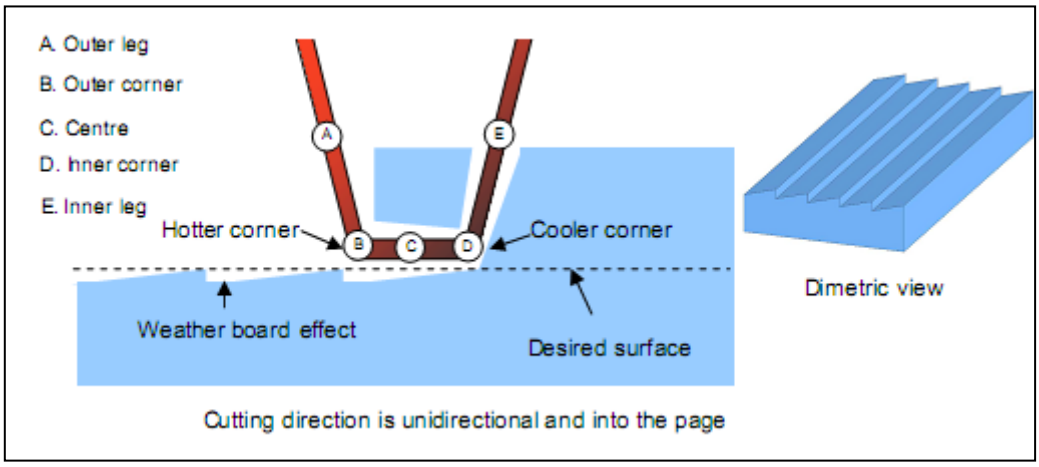

Figure 9: 'Weatherboard' effect created by multi-pass cutting with a square-end blade

2.1.2 Tool Design and Control

Two basic tool types have been developed for use with the RFS system: single-pass and multi-pass tools. Single-pass tools use a straight length of nichrome wire or ribbon held under tension by a pneumatic actuator to cut planar surfaces, while multi-pass tools use a shaped length of ribbon to cut curved surfaces incrementally using multiple tool passes to approximate 3D shapes. Straight-wire tools have been in use since the very beginning of the RFS project [13], while multi-pass tools have been developed over time to facilitate the sculpting of more complex 3D shapes [7, 17, 18].

Since the early stages of the RFS project, it has been apparent that some means of adaptive current control for hot-tool cutting was desirable, so that the tool temperature would increase in the early stages of a cut to offset the cooling of the wire due to the cutting process. The initial attempt to develop a current-control process was based on a measure of the resistivity of the tool, and was not a success [17].

More recently, an adaptive current control system was developed that used the cutting force as the metric to activate the current step [1, 19]. The principle of this control system is simple: when a trigger value of cutting force is reached, the current is stepped up to increase the wire temperature. The centre-cut temperature profiles shown in Figure 10 demonstrate the effectiveness of this system: the blue temperature profile shows the temperature of the wire along a cut for a constant current of 7A, and the pink profile shows the temperature of the wire when force-feedback control is used to implement a step from 3A in free-air to 7A in the cut. As can be seen, the temperature of the wire along the cut varies much less with force-feedback control than it does in the uncontrolled case.

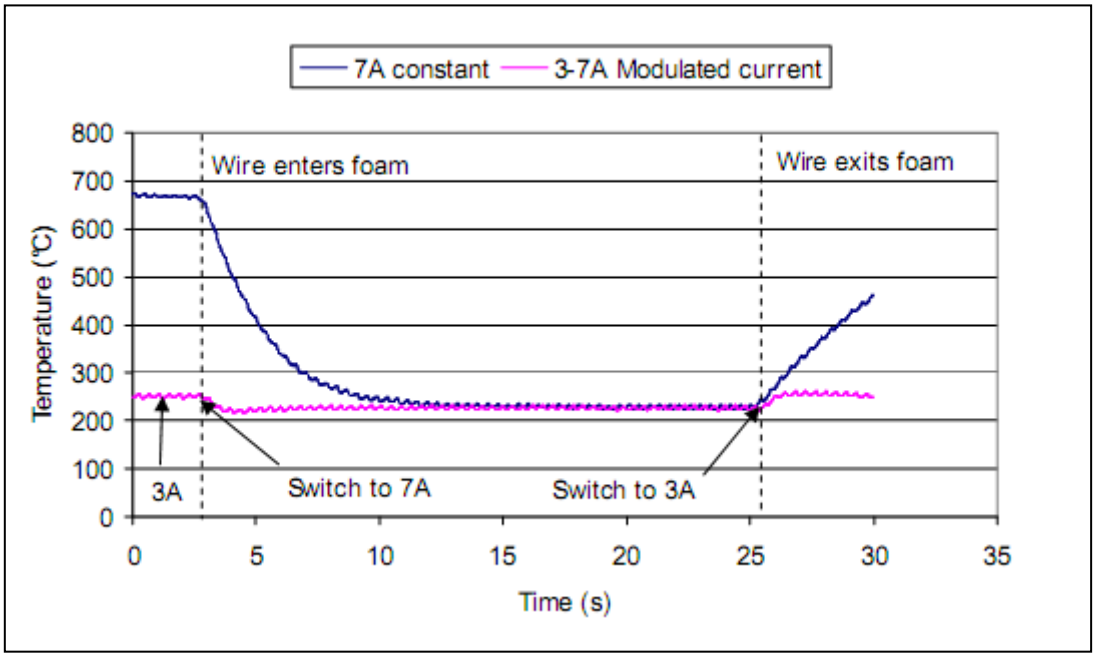

Figure 10: Wire temperature in a cut, with and without temperature control [1]

As a result of this temperature stability, the kerf along the cut was found to be much more regular. Compared to the uncontrolled case, where the kerf could vary by up to 1.5mm along a cut, the controlled-current kerf was found to vary by approximately 0.1mm, as is shown by the example case (XPS, 0.0150m/s, 5A modulated current) in Figure 11.

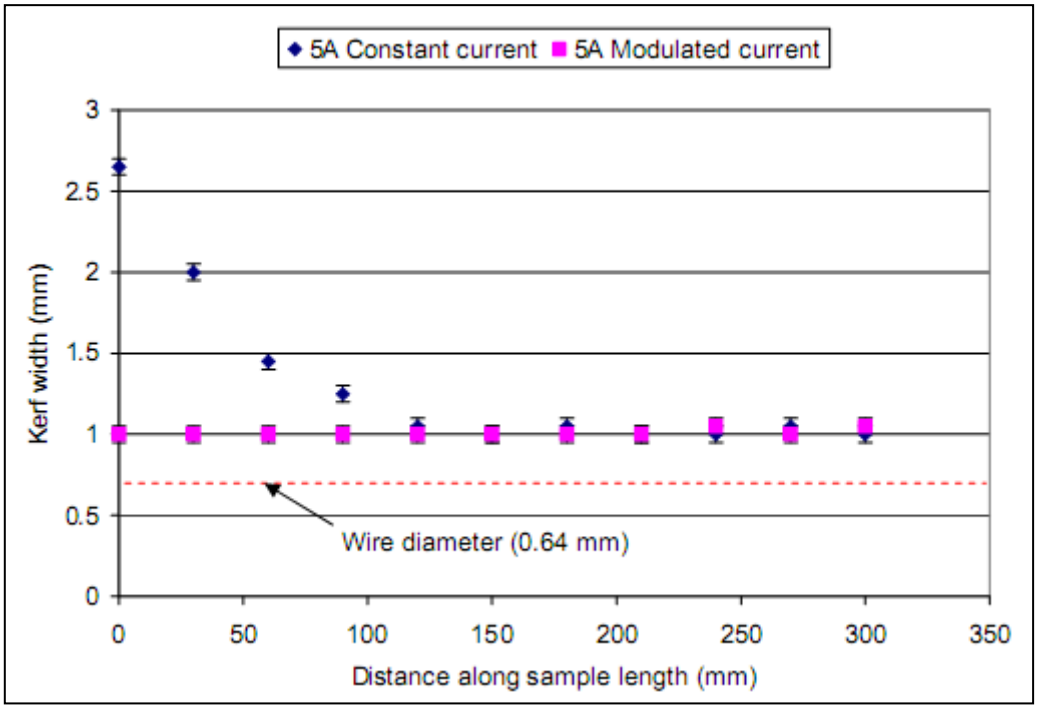

Figure 11: Kerf width of a hot-wire cut with and without force feedback temperature control (XPS, 0.0150m/s) [1]

There are three key problems with this current control system: the limited range of cutting conditions for which it has been implemented, the fact that it has only been implemented for wires and not for blades, and the fact that a cutting force reading is necessary to trigger the current step. The system has been implemented only for two sets of cutting conditions, a 3 – 7A modulated current and a 5A modulated current: this limits the range of feedrates that can be used with current control, and so limits the versatility of the RFS system as a whole and constrains the sculpting speed. Current control implemented over a wider range of cutting conditions is desirable, as is a range of cutting conditions for blades over which current control can be used. Neither of these is currently in place, because development of the current control system has been limited by the third problem, that of reliably and accurately determining when the current step should be triggered.

Since a cutting force reading is necessary, a loadcell has to be incorporated into the RFS system. By extension, this means that the cutting tool has to be mounted on a fixed base with the robot being used to manipulate the foam workpart. The reason for this is that if the loadcell and cutting tool are on the robot then spurious force readings are created by the acceleration of the robot end effector when moving, which makes the force-feedback current control less reliable. This is an undesirable state of affairs, since programming the robot is much easier if the workpart is fixed and the robot moves the

tool, and since moving a large foam block with the robot is difficult for the sculpting of freeform shapes, due to the likelihood of joint limit violations. As a result, although the force-feedback current control system is a step forward for the RFS system, it is not really useful in a practical sense: a new and more practical trigger metric is needed. To help resolve this need, work has been undertaken (see Chapter 7) to characterise the acoustic output of a thermomechanical cut to determine if it can be used as a trigger for current control, and to develop models for the during a cut based on cutting conditions to allow the determination of suitable conditions for controlled-current cutting before cutting begins.

2.1.3 Cutting Strategy and Toolpath Generation

During his Masters degree research, Posthuma conducted a range of multi-pass cutting trials with different cutting conditions to produce arbitrary freeform surfaces, in order to test and assess the robot programming procedure he developed [7]. This required him to assess the quality of the surfaces produced in a qualitative manner, and while doing so he developed a few cutting strategy guidelines to achieve a 'good' surface quality [7], and drew some conclusions about the causes of surface defects. These guidelines and conclusions are summarised here, since they form a starting point for the development of the cutting strategy model presented in this thesis:

- A large portion of the surface defects in the sculpted samples were the result of the overlap between passes, but a certain amount of overlap was necessary to minimise the cusp between successive tool passes.
- Concave surfaces were found to be more prone to defects than convex surfaces: it was postulated that this was a result of the direction of the cutting force (away from or into the foam).
- Bi-directional toolpaths (i.e. paths where the blade made one cut, turned around in space and then made a return cut adjacent to the first but moving in the opposite direction) were found to cause melted holes (which have been referred to as 'surface flaws' in this thesis, seeSection 3.2) at the start of the cut. This was not found to be the case with uni-directional toolpaths. It was concluded that these holes were caused by molten material that built up on the blade during one tool pass being re-deposited onto the foam at the beginning of the next, and melting into the surface. In uni-directional cutting, the molten material had time to burn off the tool while it was moving in space to the start position of the next pass.
- If the tool was too large relative to the local surface curvature, 'gouging' occurred. This was the result of the tool centre point following the path while the corners of the blade gouge into the already-cut surface.
- The best 'surface finish' (assessed subjectively) was found to be the result of the smallest tool used (4mm) applied with a small path spacing (2.5mm).

It should be noted that these cutting trials were conducted solely with square-end tools, and that the cutting parameters being altered for each trial were the current, the tool feedrate, the path spacing and the tool size. It is likely that conclusions drawn from these trials will be applicable to more general

multi-pass cutting using different tools, etc, but this cannot be assumed. It must also be noted that the assessment of surface quality or surface finish for these cutting trials was qualitative and subjective, and essentially consisted of comparing surfaces and deciding which was better and which was worse. In addition, the assessment of surface finish was strongly influenced by the magnitude of the lay on the surface, since this was the predominant feature. As a result, the exact nature of the surfaces evaluated is somewhat difficult to communicate.

During this research a robot programming procedure using RobotWorks™ and Mastercam™ was developed [7, 18]. This procedure will not be summarised in detail here, since the step by step process of generating robot command code is not relevant to the cutting strategy optimisation, but the drawbacks of the current system will be briefly discussed since resolving these drawbacks is an important part of the pathway to commercialisation presented in Chapter 8.

The primary drawback of the programming procedure developed by Posthuma was the number of different software packages needed to generate robot control code, and the largely-manual method of transferring data between them. For example, if a surface was to be sculpted that had been generated with a 3D laser scanner, seven different software packages were needed to process the data. Each time data was transferred from one package to another, this was done manually. At each stage a significant amount of manual processing of data was required. This was inconvenient, not user-friendly, and greatly slowed the process of generating robot control code. A significant amount of the body of remaining work that must be carried out before the RFS system is able to be commercialised is concerned with streamlining the generation of programs for the Kuka robot (See Chapter 8). Refer to [7] for a more detailed discussion of the drawbacks of the current system.

Since the beginning of the RFS project, a significant amount of work has been carried out to develop an understanding of the nature of the cutting process and to allow the selection of cutting conditions to achieve high surface qualities. To date this has mostly been qualitative work, or work of only limited applicability, and it is one of the aims of this thesis to tie together and advance much of the previous work to a point where a body of knowledge exists that can be used as a toolbox for the design of an appropriate cutting strategy for sculpting a given part. However, before this work can be presented it is necessary to consider what analogous or relevant work has been conducted by researchers outside the RFS project. This other work will be summarised in the following section.

2.2 Literature Review

This section summarises research that has been conducted into the hot-tool sculpting of polystyrene foam by researchers from outside the University of Canterbury. The literature review has been broken down into three sections. First, existing foam-based rapid prototyping systems will be outlined, and the differences between them and the RFS system explained. This will be followed by a specific review of research into the surface texture of hot-tool cut polystyrene surfaces, and then a review of research into the geometric form of hot-tool cut surfaces. These surface quality reviews have been treated separately from the summaries of the systems to which they relate so that it is easier for the

reader to find the section of the literature review that is relevant to the thematic chapters concerned with surface quality.

2.2.1 Foam-based Rapid Manufacturing Systems

A number of systems exist that are used to create 3D objects from polystyrene foam. Many of these use straight hot wires held under tension and can only be operated essentially as profile cutting tools, where the tool path is two-dimensional. Due to the limitations of these systems, they cannot easily be used to create 3D freeform objects, and so cannot really be considered to be rapid prototyping tools. For this reason, they will not be considered here. For the same reason, handheld hot-wire or hot-blade tools have also been omitted. Discussion will be concerned solely with systems that have been or are being developed that are designed to readily create 3D shapes. The fact that the foam-based RP systems encountered and summarised in this section, and some of the investigations of surface roughness and geometric form presented in following sections (cross-reference to next and next but one sections) were conducted by the same people presents some organisational difficulties for this Literature Review, so this section will concentrate solely on descriptive overviews of the systems developed, with cross-references to later sections where appropriate. Finally, it must be observed that the systems reviewed here have been restricted solely to those that use heated cutting elements on the foam workparts, since only these are strictly relevant to the cutting strategy optimisation work with which this thesis is concerned. As a result, systems like the True Surface System (Trusurf) that cut layers of foam using water-jet cutters [20, 21] have not been summarised.

2.2.1.1 Variable Lamination Manufacturing (VLM)

Variable Lamination Manufacturing is a foam-based RP system that has been developed at KAIST (the Korean Advanced Institute of Science and Technology) that uses thin sheets of expanded polystyrene foam (EPS) as a construction material and taut-hot wire tools actuated by a four-axis machine tool. The wire is used to cut a planar shape with sloped edges from ‘thick’ sections of foam (<10mm thick), and once multiple planar shapes have been cut they are assembled into 3D objects [22-25]. This process is shown diagrammatically in Figure 12. The process consists of the following basic steps:

1. Material feed and handling: EPS in thicknesses of 3.7mm to 10mm is stored on a roll and fed into the cutting area via rollers that both apply the bonding agent and determine the layer thickness. The stock layer is then held in place from above by controlled suction part holders.

2. Shape generation: The next step is the cutting of the basic shape of each layer. Layers may be composed of either a single EPS shape (a Unit Shape Layer, USL, where the cut part makes up one entire layer of the final model) or several EPS shapes which are assembled together in a manner reminiscent of a jigsaw (a Unit Shape Part, USP). In cases where USP’s are used, the joining edges in the feed direction are cut with opposite 5° angles and are staggered like brickwork in the transverse direction to improve the strength of the final object.

3. Stacking and bonding: The individual pieces (either USP's or USL's) are stacked on a controllable x-y table after cutting. Once each layer has been assembled the table is moved underneath a pressing mechanism that presses the bonded layers together to increases the bond strength of the finished model. Any un-cut material is then manually cut off and removed by gravity, and the steps are repeated until the object is complete.

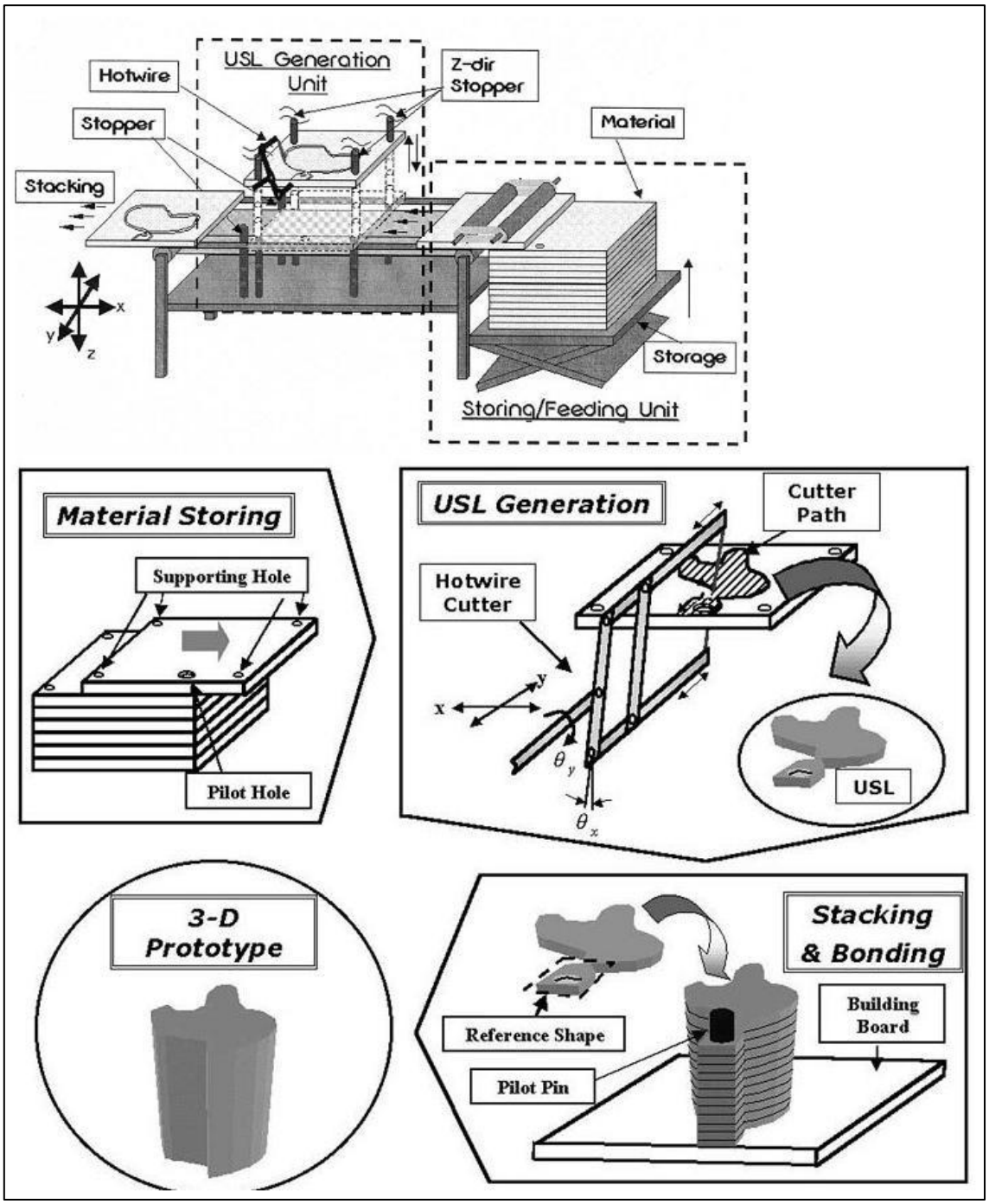

Figure 12: Schematic showing the operating principle of the VLM process [24]

The published work produced by these researchers' deals with a number of aspects of foam cutting mechanics, surface texture and geometric form, the most relevant of which are discussed in sections 2.2.2 and 2.2.3.

Some work was carried out to investigate the anisotropy and material properties of EPS [26]. Based on this, it was found that the maximum attainable cutting speed was in the rolling direction, and that 64% of this speed was the maximum that could be obtained in the transverse direction, due to the greater cutting forces resulting from differences in cellular structure in these directions.

Some work has also been reported on the reconstruction of surfaces and generation of mid-slice profiles for toolpaths [27]. This work is relevant specifically to VLM cutting strategy, and is not relevant to the RFS system, so will not be discussed in detail.

The VLM process developed at KAIST has been commercialised by Menix Engineering Co. Ltd under the product name 'Rapid Shaper' (see Figure 13). The VLM 300 produces parts using 3.7mm thick A4-sized sheets of EPS, while the VLM 400 uses 3.7mm, 5mm and 10mm A3-sized EPS sheets [28].

Figure 13: Menix Engineering Co. Ltd Rapid Shaper Range, based on Variable Lamination Manufacturing

There are a number of drawbacks to this system, including:

- Only a single type of foam (EPS) is used.
- The system is only capable of first-order approximation of surfaces. Some work was carried out to check that a sloped wire would not adversely affect surface quality [16], but the system still faces a fundamental geometric limitation on surface accuracy. The effect of this is limited by the very thin layers of foam used, but the limitation is there nonetheless.
- The researchers made a fundamental assumption that there was no gradient in the temperature distribution along the cutting wire, except at the ends (i.e. where the ends of the tool were clamped) [25]. This was valid for the 2 - 4mm sheets of foam used in this system [16], but RFS work has shown that there are distinct thermal profiles along the wire during cutting, especially when cutting thicker sheets.

- There is evidence that suggests that VLM works only in the vapourised cutting region [25, 29]. This limits the cutting speed and the surface quality that can be achieved.
- The system has relatively small build volumes (250mm x 180mm [24]) and competitive accuracy and build times with other RP systems [24], so the VLM-s system is not really a comparable system to large-volume high-speed prototyping systems like RFS.
- As a result of the thin foam sheets used and the assumptions made for modelling, much of this work can't really be extended to cuts with a tool engaged length much greater than 10mm, so the results achieved here are not really transferable to the RFS system.
- Some analysis of the thermal field around the wire has been conducted analytically and experimentally, but this has dealt with kerfwidth only, and has not considered transverse surface inaccuracies like barrelling. In addition, there appears to be no published information on the method used for kerfwidth measurements [16].

2.2.1.2 Free Form Thick Layer Object Manufacturing (FF-TLOM)

Free Form Thick Layer Object Manufacturing is a layer-based RP&M system developed at Delft University of Technology. The system uses thick layers of Styrofoam (XPS) that are assembled into a physical model of a part after the edge of each layer has been cut with a hot-blade tool: essentially it is a hybrid between additive and subtractive prototyping systems. The blades used were either nickel-chromium or stainless steel, and movement of the blade is achieved through the use of a 6-axis industrial robot. The system is intended for the creation of large-size physical models with relatively low cost.

There are two features of this system that are unique: the use of adaptive slicing to improve surface accuracy, and the use of a controllable blade profile to shape the cut edges of the foam layers.

The concept of adaptive layer thickness is demonstrated in Figure 14. When the local surface curvature is low the layers used to make the physical model can be much thicker than when the local surface curvature is high, without impairing the accuracy of the surface produced. Naturally, if thicker layers can be used then the production time can be substantially reduced, since fewer cuts need to be made for a given volume of the physical model. With FF-TLOM, the layer thickness can be varied to reduce the production time while still maintaining an acceptable level of surface accuracy [30]. A significant amount of work has gone into the development of algorithms to perform adaptive slicing of layers and to divide raw CAD models into segments that can be easily produced by VLM-s [31].

The variable-geometry blade is the other unique feature of the FF-TLOM system, and the development and control of this blade has been a major focus of the reported work on the development of this system [32-37]. The concept is a simple one (although in practice it is somewhat more complex): for layered manufacturing, if the cut sides of each layer can be curved (a higher-order approximation in Figure 14) then the physical model can be made much more accurate than if zero-order approximations (like most additive rapid prototyping systems) of first-order approximations (like VLM-s) are used. In order to achieve cut surfaces with variable geometry a variable-shape hot blade

tool was developed (a concept model of this is presented in Figure 14, and a photograph of the as-built test rig is shown in Figure 15). The details of the control and optimisation of this blade shape will not be summarised here, since this material is not relevant to the work reported here.

A maximum cutting speed has been determined for the FF-TLOM system, of 0.018ms^{-1}. This is relatively slow for a cutting tool that uses hot blades (by comparison, RFS uses a minimum speed of 0.028ms^{-1} when cutting XPS with hot-blade tooling). The reason for this slow speed is the vulnerability of the flexible blade to unintended distortion: if the cutting force gets too high, the blade shape can vary during a cut in an unplanned way and the surface produced will not be the one desired. For this reason, cutting in the FF-TLOM system almost always takes place in the 'vapourised' cutting region, with no thermomechanical cutting taking place and hence very low cutting forces.

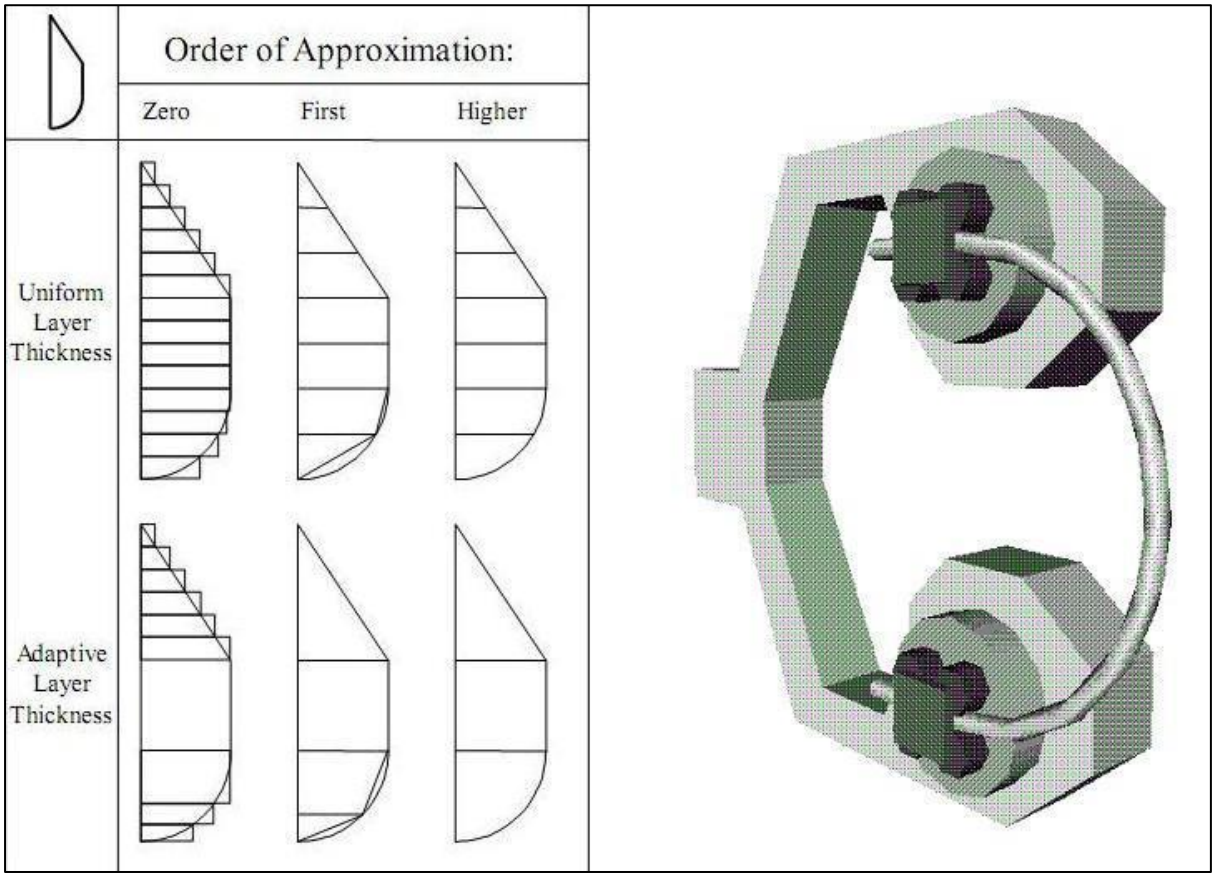

Figure 14: Approximation strategies for layered manufacturing (left) and a CAD model of a variable geometry tool for FF-TLOM

There are a number of other drawbacks to the FF-TLOM system. These include its dependence on as-manufactured sheets of Styrofoam, the investigation of only a single material type, the complexity of the system, and the assumption that cutting condition investigations made for 50mm thick foam sheets will generate results that can be applied directly to sheets up to 100mm in thickness.

The use of as-manufactured sheets of Styrofoam (i.e. sheets that have not had any surface treatment or reprocessing since being extruded) has meant that test parts made with the system have

encountered the edge-melting effects caused by the higher-density skin on the side of the sheet, but the authors do not appear to have been aware of this skin or its effect on surface quality [38, 39]. The centre picture in Figure 16 shows a surface produced by FF-TLOM, and the edge-melting effects are clearly visible as the dark blue lines at either side of the surface. The authors have classed a surface of this type as 'moderate' in their surface quality investigations (see section 2.2.2), and have limited their cutting conditions to a range that avoids such surfaces, but this reduces the versatility of the FF-TLOM system and limits it to sets of cutting conditions that may use more power than necessary or be unable to produce physical models as fast as could actually be possible.

When developing this system, testing and optimisation was restricted to a single material type, Styrofoam, on the assumption that results found for one type of plastic foam could easily be applied to others [39]. As this thesis will show (see Chapters 5 and 6) the surface quality achieved when cutting polystyrene foams with thermomechanical tools varies significantly between extruded and expanded polystyrene foams, let alone between polystyrene foams and foams made from other types of plastic.

Essentially the biggest problem with the FF-TLOM system is its complexity. Quite apart from the six axes of the robot that need to be controlled, there are three tool degrees of freedom that must be controlled: the lateral position of the tool supports, the bending moment applied to the blade to control the curvature, and the winding of the tool mounts to control blade length. The blade shape has been modelled and to some extent controlled using a minimum strain energy criterion [34] but the shape is still subject to instability and cutting forces must be limited to less than about 2N [39] in order to avoid unplanned deformation and inaccurate part sculpting.

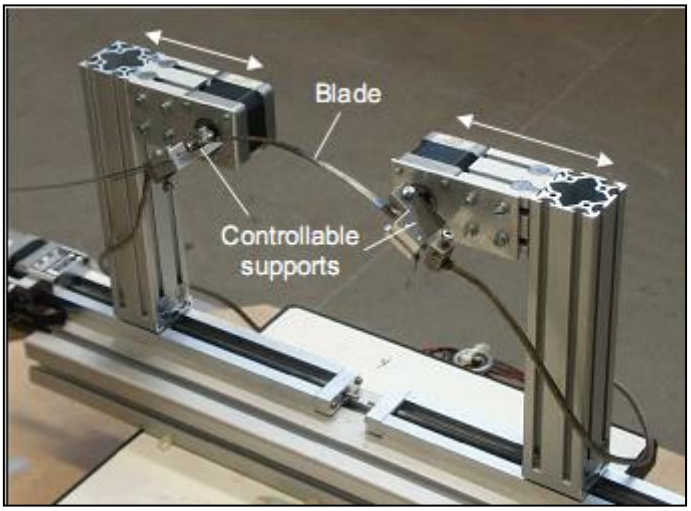

Figure 15: Prototype Tool for FF-TLOM [33]

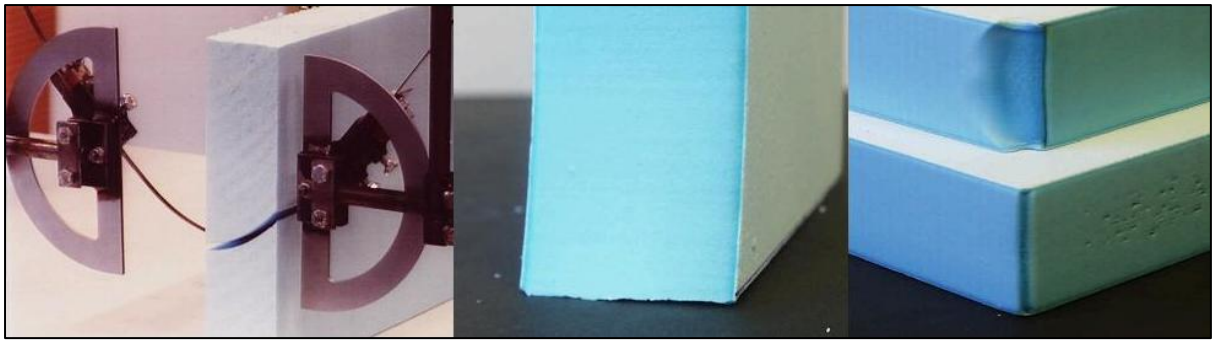

Figure 16: FF-TLOM tool during cutting (left), a cut surface (centre) and the results of a rapid change of cutting direction (right)

Some of the published research into this system deals with examinations of surface quality and dimensional accuracy. [39, 40] This material is considered in sections 2.2.2 and 2.2.3 below, so that the reader can easily compare later chapters with related sections of the literature review.

2.2.1.3 Rapid Heat Ablation (RHA)

In addition to the work on Variable Lamination Manufacturing, researchers at KAIST have published a body of work on a novel process they call Rapid Heat Ablation (RHA), that uses a hot tool similar to a ball end mill to create surfaces by ablation of foam. RHA can be used as a standalone RP process or to create detail on VLM parts that cannot be created using straight wires. This section also covers a process developed by these researchers called Rapid Feature Detailing (RFD) which operates in a very similar fashion at a smaller scale.

The tool used is very similar to a ball-end mill, except that instead of shaping the surface by using rotating cutting edges, it is heated above the melting point of the foam material and is used to vapourise unwanted foam: this can be seen at the top of Figure 17. The processing sequence from initial toolpath through to completed prototyped part can be seen in Figure 18. The published work on the development of this system has dealt with toolpath planning algorithms [41], the optimisation of the tool design to minimise the heat affected zone (HAZ) in the foam material [42], and the nature of the thermal field surrounding the tool and its effect on surface quality [43].

The developers of RHA also determined that toolpath generation procedures used to generate toolpaths for ball-end milling could also be used to generate toolpaths (and hence control code) for the RHA system, since the tool motions necessary to produce a surface were basically the same [44]. As a result it was much easier to produce control code for the RHA system than for more complex or unique cutting systems.

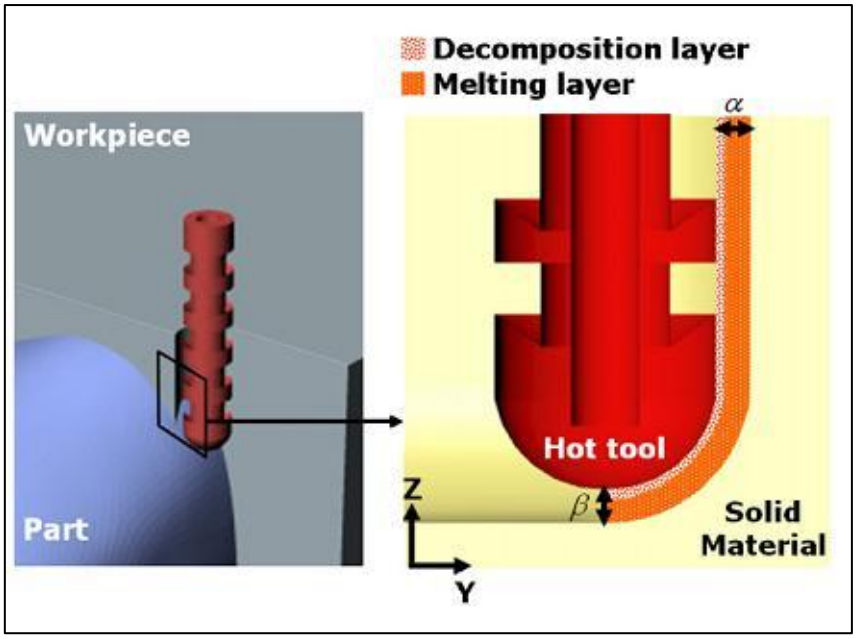

Figure 17: Operating Principle of Rapid Heat Ablation

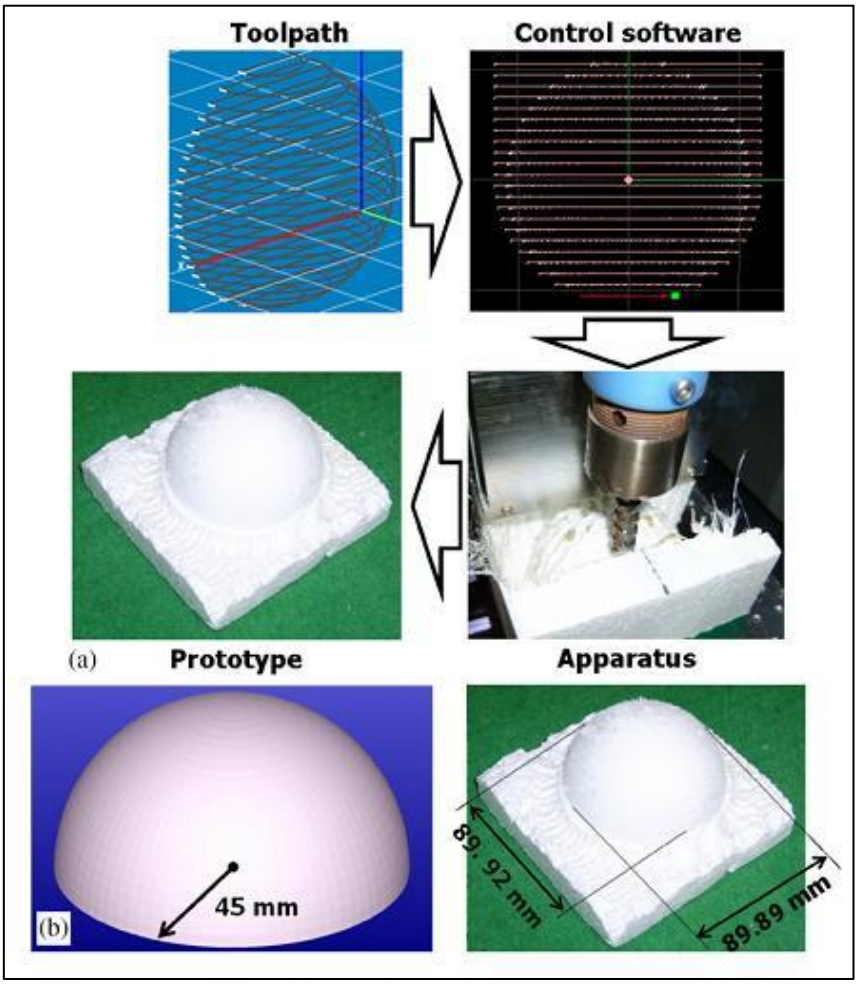

Figure 18: Workflow for the production of a hemispherical foam part using RHA

In order to achieve acceptable surface accuracies with the RHA process, it is necessary to control the heat generated by the tool to minimise the kerf width around the tool. This control needs to be based on an understanding of the relationship between the kerfwidth and the effective power input. Once this relationship is understood the tool can be offset from the desired surface to obtain accurate surface geometry.

The researchers conducted an empirical study and determined that the kerfwidth (η) could be expressed by the equation:

$$\eta = 0.82Q_{eff} + 5.14 \quad (1)$$

This equation had an R^2 value of 0.92, so could be regarded as an accurate predictor of the kerfwidth that would result from a cut with a given effective heat input [44]. Knowledge of the kerfwidth in these terms meant that the kerf could be controlled by means of controlling the effective heat input, and that toolpaths could be accurately planned with the knowledge of both tool size and kerfwidth for a given set of cutting conditions.

RHA has a number of advantages. The most significant are that tool paths can be generated using standard CAM software (since the tool is so similar to a ball end mill, as shown in Figure 17) and that finishing cuts can be made without any prior roughing cuts, since the full length of the tool can be used for 'machining' the foam. Other advantages include the lack of swarf (since the foam is completely vapourised during sculpting) and significantly reduced machining time relative to metal machining (55 minutes compared to 430 minutes on a milling machine for a test part made by the authors).

Some drawbacks of this system include:

- Because RHA works by completely vapourising unwanted material, the energy input required would be substantial, unlike RFS multi-pass cutting where only a relatively small volume of foam actually gets thermomechanically cut [42].
- Since the tool is vapourising the foam, the cutting speed and thermal output must be balanced to keep the operation of the tool in the thermal-only region. This means that cutting speeds are lower than they could be for a given thermal output if thermomechanical cutting could be used. Currently the tool operates at feedrates of 600 – 3600mm/min, but it could cut even faster if it could be used for thermomechanical cutting.

2.2.1.4 Michelangelo

The Michelangelo system was developed by Zhu et al of the Tokyo Institute of Technology [45], and is composed of a six-axis Motoman industrial robot and a two-axis worktable, giving eight functional axes. The system uses taut hot wire tools and is designed to approximate 3D objects by carving simplified representations with planar faces from EPS foam. The tool used is a length of manually-tensioned hot-wire, as shown in Figure 19. The test models created used blocks of 100 x 100 x

100mm foam, although given the nature of the 8-axis system larger blocks could in principle be used as feedstock for this process.

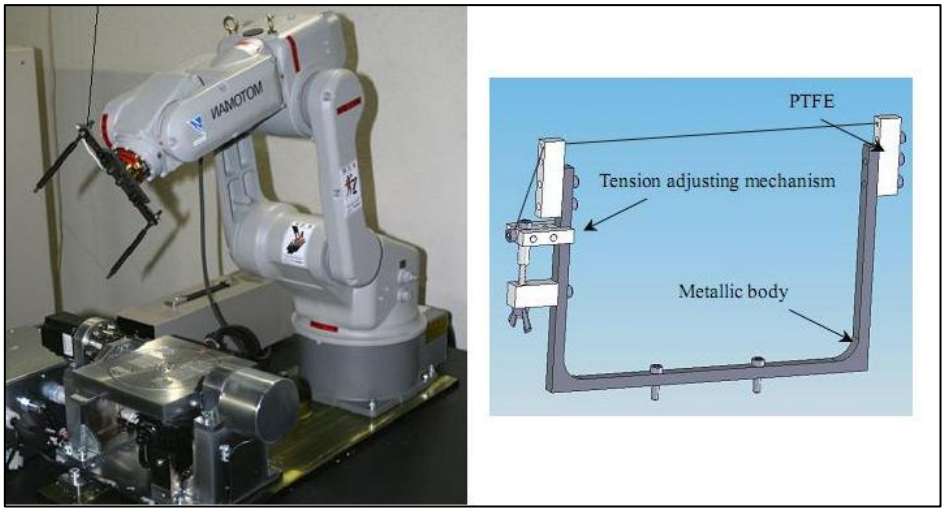

Figure 19: Michelangelo equipment setup, showing 2-axis worktable (left) and hot-wire cutting tool (right)

Much of the published work on the Michelangelo system is concerned with the approximation of CAD data as a set of flat facets that can be cut by the taut-hot-wire tool. The researchers' developed a mesh simplification algorithm that reduces the model complexity by reducing the number of facets that are used to represent the true surface: the principle behind this is shown by Figure 20. Once the shape to be created has been sufficiently simplified another algorithm is used to create the tool path. The shape is then cut from a single large block of foam by the robot.

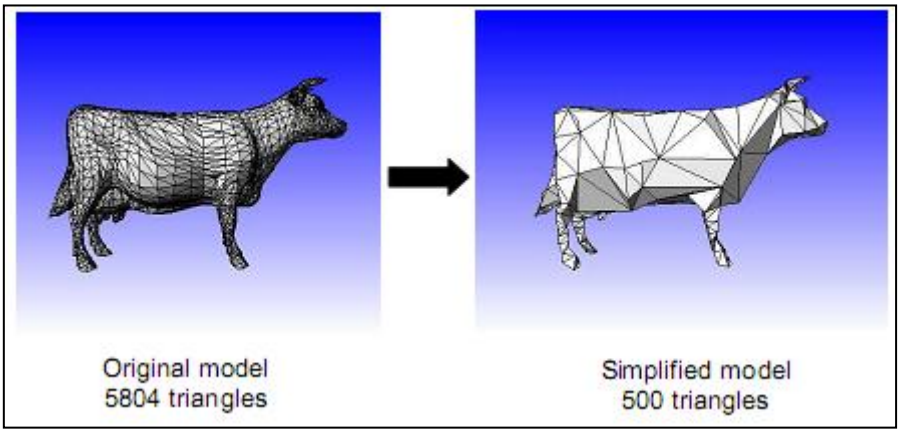

Figure 20: Example of mesh simplification in the Michelangelo system

Examples of parts produced by this system from EPS foam are shown in Figure 21. The icosahedral shape was relatively simple to sculpt accurately, since the desired shape is already faceted, but the same could not be said of the shoe. In this instance, the Michelangelo system was trying to approximate curved surfaces as flat facets, which results in inherent inaccuracy. Since Michelangelo

uses only a single taut-wire tool, it is not really capable of producing parts with curved or freeform shapes: the best that can be expected from the system is a roughed shape that would need finishing by some other process. This is the fundamental limitation of the system from a rapid prototyping point of view

As part of the development of the Michelangelo system, a limited investigation was also carried out into the mechanism of hot wire cutting [46]. The goal of this work was to develop an understanding of the offset that would be required from a given toolpath to allow for the kerfwidth (which the authors referred to as 'passage width' (Figure 21) of the cut, in order to accurately produce desired parts. The method used was a simple thermal conduction model of a stationary wire in foam over time, showing the shape of the melted region. This can be seen on the bottom left of Figure 21, with a distinct teardrop shape due to upward heat flow. Clearly, as time passes the melted region gets larger. Using this situation is valid enough for the Michelangelo process, where the cutting is by purely vapourised means (and therefore slower than it could be for a given thermal input), but of very little relevance to RFS since no thermomechanical cutting takes place. No explicit conclusions are made in this paper regarding the size of offset that should be applied to the toolpath to achieve good surface accuracy. Regardless, the thermomechanical errors in this manufacturing environment are clearly going to be outweighed by the geometrical inaccuracies resulting from shape approximation.

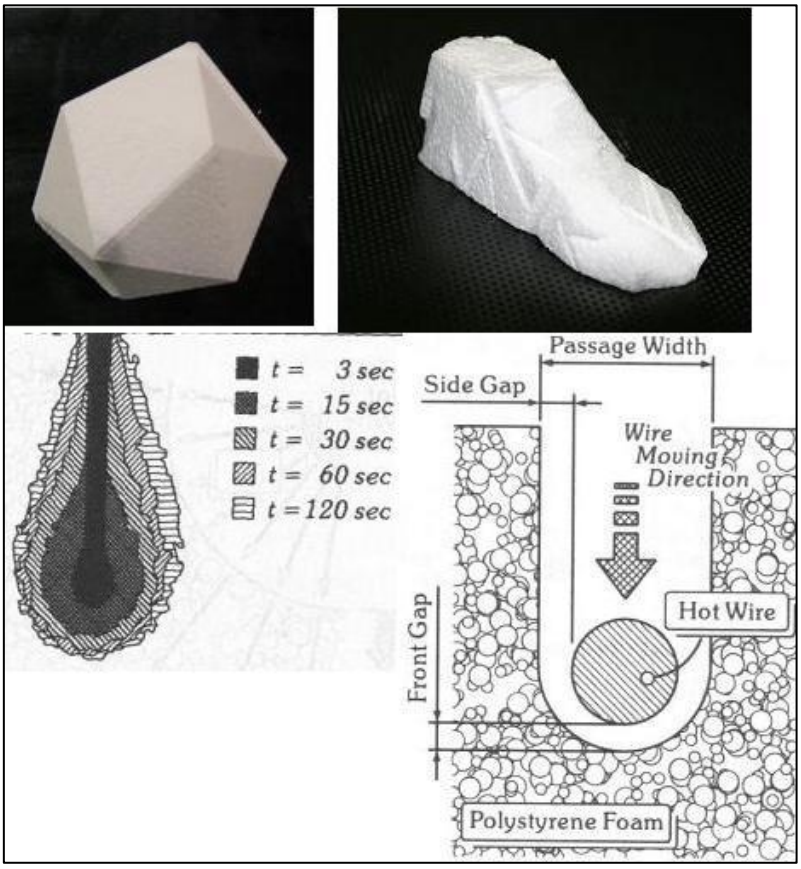

Figure 21: Icosahedral and shoe shapes approximated with the Michelangelo system (top), thermal field around the cutting wire with time (bottom left), and representative geometry of hot-wire cutting (bottom right)

Another drawback of the published research on the Michelangelo system is that the assessment of surface quality only considered the surface errors resulting from approximating curved surfaces as ruled facets. There was no evidence in the published work of research into the influence of the cutting process itself on the surface texture and form accuracy of the surface produced.

2.2.1.5 ModelAngelo

ModelAngelo uses a 5-axis gantry robot to manipulate shaped tools made from heated wires and blades that are used to sculpt 3D parts from a range of foams, including polyurethane and expanded polystyrene [47]. The cutting strategy used for this system is based on breaking a supplied CAD model down into geometric facets that approximate the required surfaces, and then producing this geometrically-approximated shape with a selection of appropriate tools. The working volume of the machine measures 200mm x 200mm x 200mm.

The ModelAngelo system uses a tool turret to facilitate rapid tool changes, and a range of shaped tools that are designed specifically for the part being produced [48]. Examples of these tools can be seen in Figure 22. This aspect of the system means that, for any given part to be manufactured from foam specialised tools will be necessary, especially for the cutting of curved or chamfered surfaces. While this does make the planning of toolpaths substantially simpler, and can avoid geometric or thermomechanical errors (like those present in RFS) by essentially using a single-pass cutting strategy, it does mean that specialised blades will be required quite frequently. This is a substantial drawback of the ModelAngelo system, and reduces the system's ability to be versatile without substantial operator input.

The published work on the ModelAngelo system contains no real discussion of the cutting mechanics, but it can be inferred that primarily-vapourised cutting is the usual cutting mechanism. This inference is based on a statement by the authors that the cutting forces are 'very low' and that the cutting depth can be as deep as the tool clearance height (see Figure 22): as this thesis shows, the cutting force is proportional to the engaged tool length, so for cuts of that depth to be made with non-vapourised cutting would likely result in sufficient cutting force to bend the tool.

One of the novel features of the system is the use of a dual-wire tool, as shown in Figure 23. This is arranged in such a way that there is a heated wire at both the top and bottom of a cut: the lower wire actually does the cutting, while the upper one serves to radiate heat into the swarf and act as a chip-curler, so that the swarf bends away from the cut area. The authors do not discuss in detail the cutting conditions being used for making these cuts, but based on experience derived from the development of the RFS system it seems likely that the cut depths used are relatively large and that the effective heat input into the cut is relatively small, since otherwise the swarf would curl by itself, without needing a secondary chip-curler to be designed into the tool.

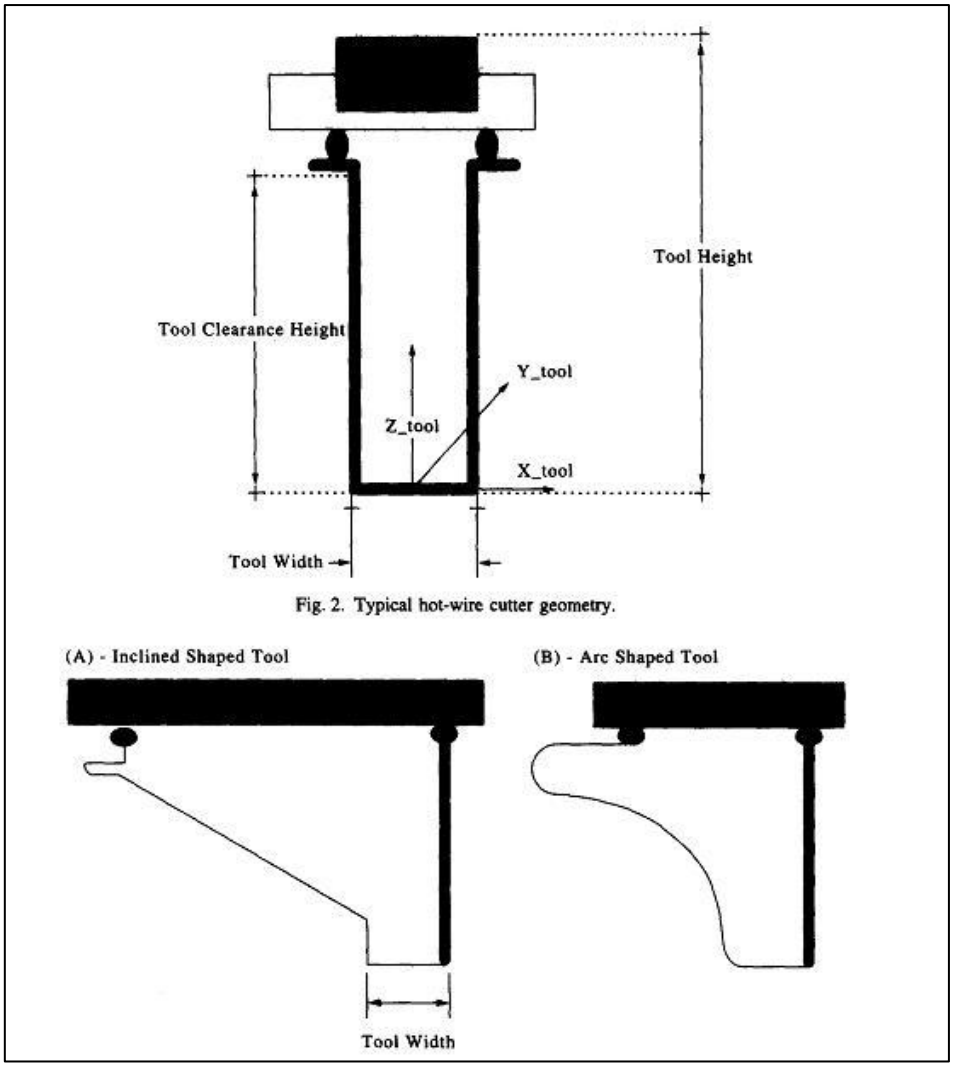

Figure 22: Example Modelangelo tools [48]

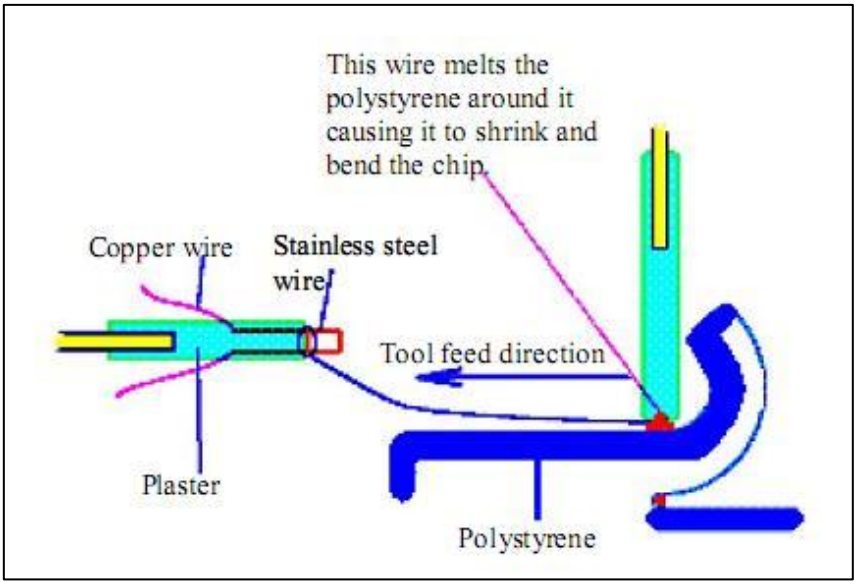

Figure 23: Modelangelo tool concept [48]

There were a number of drawbacks and limitations to the ModelAngelo system. Briefly, there were:

- A small working volume (200 x 200 x 200) compared with RFS, making the ModelAngelo system more comparable with other, additive, rapid prototyping systems
- The tools have a fundamentally specialised nature, in that to sculpt a given shaped surface a tool bent to the same shape is required. This means that a much larger number of tools are required to sculpt a complex 3D shape, which dramatically reduces the versatility of the system and increases to expense of sculpting a given part
- The system operates almost entirely using purely-vapourised cutting, which reduces production speed since thermomechanical cutting cannot be used.
- The reported assessments of surface quality were very qualitative, so the conclusions drawn could not easily be built on and applied to the RFS system.

2.2.1.6 Stratoconcept

The Stratoconcept HW series of foam-cutting RP machines are based on a four-axis taut hot wire cutter that is used to cut quite large sections of parts that are then manually assembled into complete objects [49]. It is thus very similar to the VLM process except that the final assembly of the object is manual instead of automated as in the Rapid Shaper system, and the scale at which it operates is much larger. The system is able to craft both exterior and interior detail on each layer, at high volume and high speed, and can craft lightweight, full scale prototypes. This process is demonstrated for the sculpting of a full scale boat hull in Figure 24.

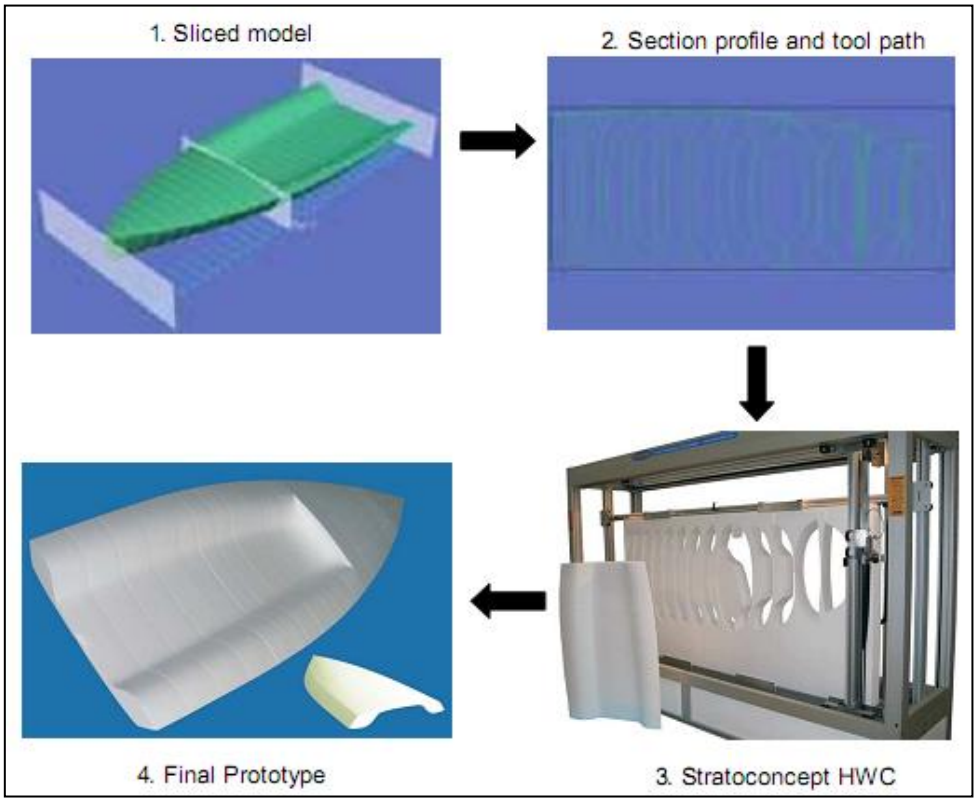

Figure 24: Use of Stratoconcept HW to sculpt a boat hull

The largest machine in the Stratoconcept range is capable of making parts with cross-sections up to 2.5m x 5m, and the length of the object is a simple function of the number of layers. Inserts are used to align the layers and strengthen the prototypes to withstand handling.

There are a few disadvantages to this system: detail in the axial direction must be larger than the thickness of the foam layers (there is a fundamental 'resolution' to the objects that can be created), the surface is only a linear approximation (i.e. first-order) of the desired surface so some post-processing may be required, and some expert knowledge is required to place the inserts and to select the strata orientation to maximise the strength of the prototype.

2.2.1.7 Foam Cutting Systems Summary

This section has presented brief summaries of six existing foam-based RP systems, two of which have been commercialised (VLM and Stratoconcept HW). Most of these systems use layered manufacturing techniques (whether manually or automatically assembled) to progressively build objects. The systems examined here use hot wires, blades or bar-like tools to thermally or thermo-mechanically cut foam, but other systems do exist that use water jets or other cutting techniques to make the layers. These systems have not been considered here because they are not relevant to the RFS system.

Figure 25 [1] shows a comparison of the part size and part complexity that different systems are capable of achieving. Comparisons of the parts size are based on the available published material, while assessment of the possible part complexity for each system is based on a qualitative comparison of the operating principles for each system and a consideration of the type of surface approximation used. As can be seen, the RFS/FAST system is in principle capable of achieving significant part complexity (although this state of development has not yet been reached) and is in the middle of the range for part size.

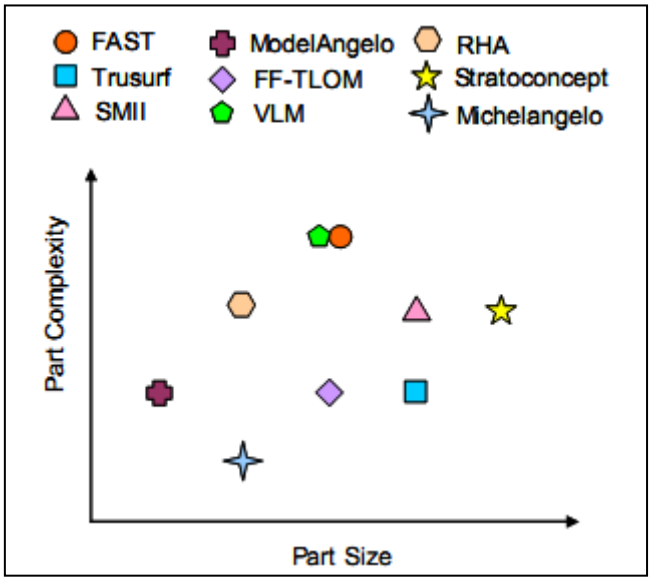

Figure 25: Qualitative comparison of part size and complexity for nine foam-cutting RP machines [1]

The majority of the systems reviewed are intended to sculpt large-size objects (concept models and prototypes) for a wide range of purposes, including concept verification, architectural details and sculptures, composite cores for aerospace applications, patterns for investment casting, and medical body-part supports.

Although it also uses heated tools to cut foam, the RFS system is fundamentally different from these other foam-based rapid manufacturing systems. The VLM-s and FFTLOM systems both use single passes of hot-wires or hot-blades, as the RFS system can when appropriate, but they are used to shape individual layers of foam which are then assembled to make a 3D shape. By contrast, the RFS system makes use of a small range of tools (straight hot wires, straight hot blades, and shaped hot blades) which can be used to subtractively sculpt a complex part from a starting block of foam: this means the system can sculpt relatively complex parts with no need to post-process the cut parts to assemble the layers.

The Modelangelo system uses customised blades for generating curved profiles, which produces surfaces with a high level of accuracy (with no lay errors, for example) but requires a large number of specialised blades to produce a complex shape. RFS uses a small range of general purpose blades, which increases the versatility of the system and reduces the number of tools that are required. Instead of using tool design to achieve a high level of surface quality, the sculpting paradigm of the RFS system depends on optimising the cutting strategy for good surface quality.

The most fundamental difference between RFS and the other reviewed foam-based rapid manufacturing systems is the sculpting paradigm. RFS is entirely subtractive, uses a combination of different tool types, and uses both purely-thermal and thermomechanical cutting to cut foam. As such, very little of the work undertaken by other researchers to understand the hot-tool cutting process is particularly relevant to RFS, since it applies to only a specific tool type, or a limited range of foams, or is fundamentally qualitative.

2.2.2 Investigations of Polystyrene Foam Surface Texture

Despite the relatively wide selection of research work conducted into the hot-wire cutting of polystyrene foam for rapid prototyping and manufacturing purposes, very little published work exists investigating the relationship between the surface texture of foam and the cutting conditions used to generate the surface. Furthermore, the work that does exist tends to deal with surface texture in a very qualitative fashion. Two studies were encountered during this research which had a quantitative approach to the measurement of surface texture, and are briefly summarised here.

Ahn et al conducted an investigation of the factors affecting surface roughness as part of their development of Variable Lamination Manufacturing using expanded polystyrene foam (VLM) [29]. The process parameters considered as possible influences on surface roughness were effective heat input (Q_{eff}) and cutting angle.

An experiment was conducted with three levels of Q_{eff} (0.0081, 0.011 and 0.016 W.sec/mm^2) and cutting angles from 0 – 50° (in 10° increments). The surfaces produced by these cuts were investigated using a Scanning Electron Microscope (SEM) and measured using a Surftest SJ-401 stylus-based surface measurement instrument. The output roughness parameters used were R_{max} and R_a (for brief explanations of these parameters see section 4.2, below). The key results of this investigation are reproduced as Figure 26. The meaning and significance of the property Q_{eff} is described in detail below (section 2.2.4).

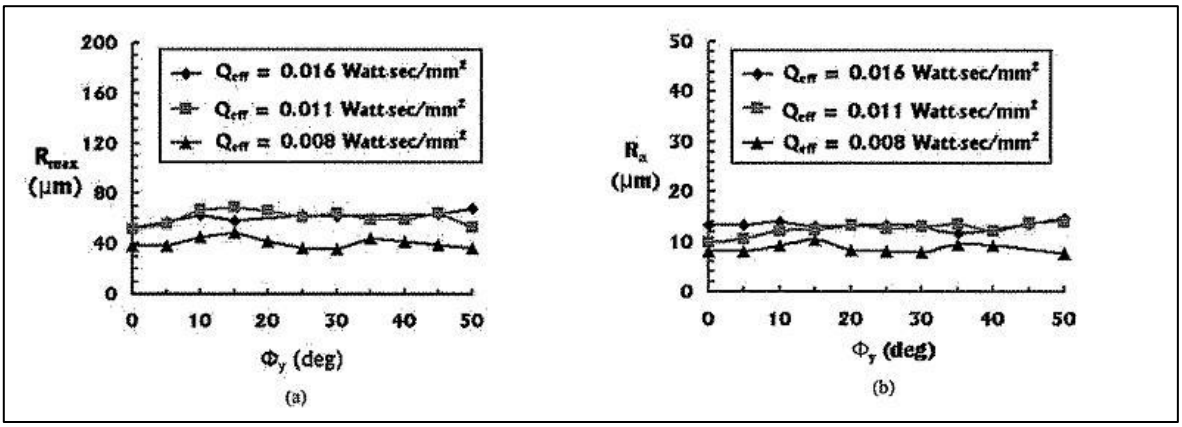

Figure 26: Relationships between Texture, Effective Heat Input and Cutting Angle [29]

Using experimental and theoretical results, the authors investigated the loss of stiffness in the wire due to low effective heat input (and hence high cutting forces). From this investigation, it was concluded that the critical value of Q_{eff} (i.e. the value of Q_{eff} at which the wire came into physical contact with the foam) was approximately 0.011 W.sec/mm^2. If the effective heat input was lower than this value, purely thermal cutting was not the primary cutting mechanism (see section 2.1.1) and the mechanical component of cutting could cause a loss of wire stiffness: in other words, if the effective heat input was above the critical value, the cutting mechanism is purely thermal, and the surface finish would be categorised as 'vapourised' in RFS terms.

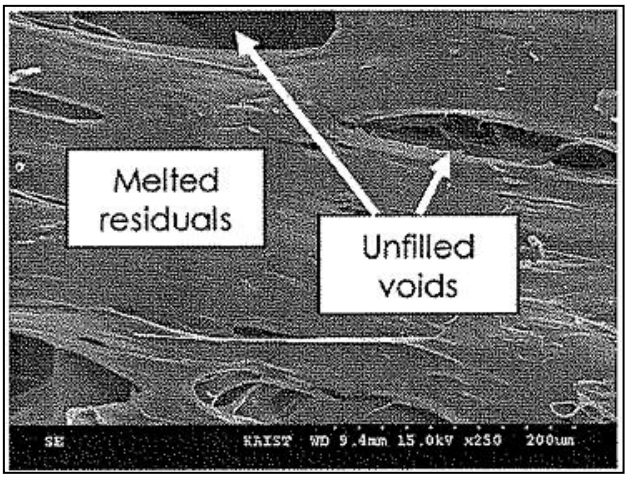

Figure 27: EPS Foam Surface cut with Qeff below the critical value [29]

SEM investigation of the foam surfaces found that cuts with Q_{eff} below the critical value (i.e. thermomechanical cutting) produced surfaces where the voids in the EPS foam would be filled by melted plastic as the wire passed through and so a smoother surface would be produced than if Q_{eff} was above the critical value. A surface of this type is reproduced here as Figure 27. In cases where the effective heat input was above the critical value (purely thermal cutting), the EPS material was completely decomposed by the input energy and remaining voids are not filled in, resulting in surfaces with a roughness R_{max} approximately equal to half the grain size.

The conclusions of this study were that the surface roughness of hot-wire cut polystyrene foam was not significantly affected by the cutting angle, and that Q_{eff} had a much more significant influence. The authors also determined that the roughness R_{max} was equal to approximately half the grain size of the foam in cases where the effective heat input was greater than the critical value, and that a smoother surface was produced if Q_{eff} was below the critical value.

This study has limited applicability to surface texture assessment for RFS. Since the work reported was concerned purely with EPS foam, no conclusions can be drawn about the surface texture when XPS is cut with thermomechanical tools. Additionally, this study measured surface texture using a stylus-based instrument: the authors found that this was a suitable measurement method. This is not what was found during the surface texture investigation conducted for RFS: it was found that the foam surface was scratched and deformed when a stylus was dragged across it, which would render roughness measurements unreliable (see section 4.3.1). Finally, and most significantly, the study reported here was quite simple in nature: the authors were mostly concerned with determining a range of cutting conditions in which they could expect purely-thermal cutting, and were not conducting a detailed investigation of the factors and interactions responsible for the surface texture across a wider range of cutting conditions. As a result, this work cannot be applied to surfaces cut using thermomechanical cutting. Additionally, during the research conducted for this thesis, it was found that surface texture parameters based solely on the relative heights of surface features were not really appropriate for the measurement of foam surfaces, even those produced by purely-vapourised cutting, due to the cellular nature of the material (see Chapter 4).

Sun et al [50] published a study on the influence of process parameters on surface roughness in EPS-based rapid prototyping. Since this study appears to be standalone (no other similar work by the same authors could be found) this manufacturing system has not been summarised in section 2.2.1, above.

The system was an EPS-based rapid patternmaking system intended to create patterns for use in the lost-foam casting process. The tool was a point heat source kept sufficiently hot that foam would always be sculpted by vapourisation: that is, no physical contact would ever occur between the tool and the foam (in this respect the system is quite similar to Rapid Heat Ablation and Rapid Feature Detailing, as outlined above). STL format CAD models were used to generate sectional layers of the object to be manufactured, and the tool used to melt a thin layer (0.1mm) of EPS foam from above so that only the material making up the first layer was left. The tool was then indexed down the thickness

of one layer, and the process was repeated. This was done until the final object was manufactured (naturally this system has a number of limitations, the most significant of which is that undercuts could not be manufactured and would have to be added later using a different process). The authors observed that the tool created a cone shaped gasification zone around it, as shown in Figure 28. H and W were the depth and width of the gasification zone, respectively, while Φ is the 'heat influence angle.'

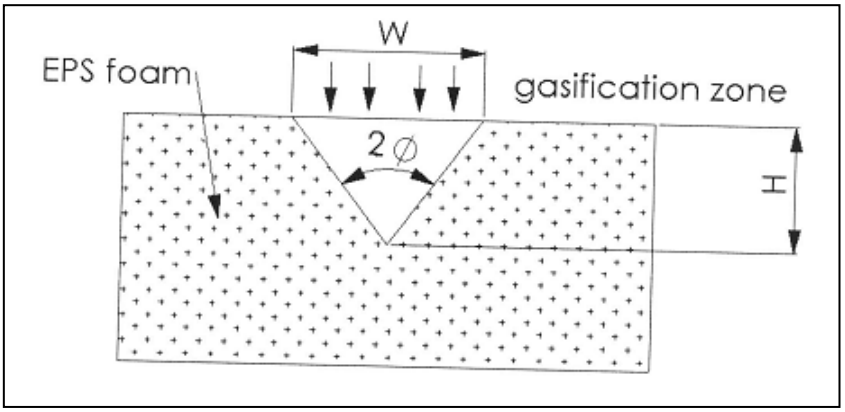

Figure 28: Gasification zone around point heat source [50]

Figure 29 shows the idealised surface resulting from sequential layers produced using the cutting tool (the angled sides are one half of the gasification zone shown in Figure 28). θ is the overall profile angle, and the dotted line represents the nominal surface of the part. The solid line represents the true surface produced.

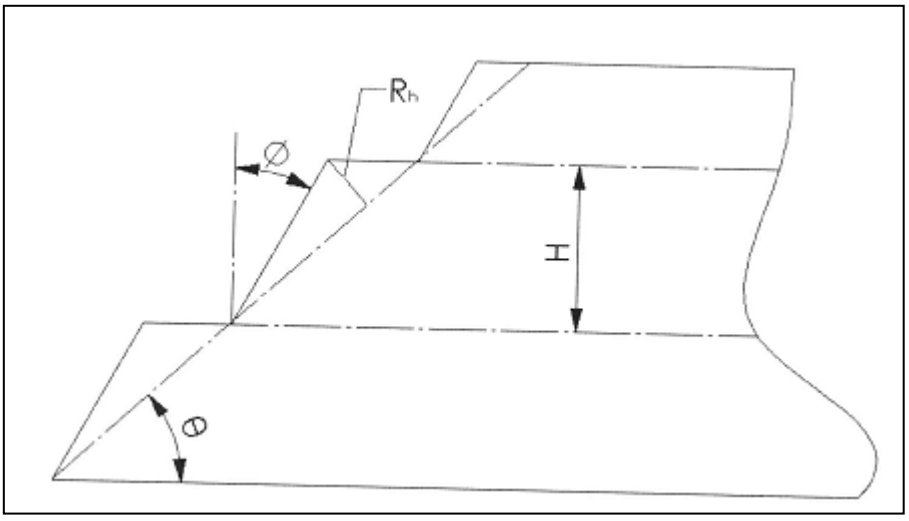

Figure 29: Stair-stepping surface resulting from layered cuts [50]

Based on this, a formula was developed to enable the calculation of R_a based on easily-measured parameters. This formula was:

$$R_a = \frac{R_h}{2} = \frac{H}{2\cos\phi}\cos(\theta + \phi) \quad (2)$$

An experimental study was carried out to determine the factors that influenced the roughness of surfaces produced. This study looked at factors like the layer thickness, the cutting tool temperature, and the processing speed. The conclusion of the study was that the layer thickness had the most effect on surface roughness, followed by temperature, and that speed had the least effect. In order to create surfaces with low surface roughness (i.e. smooth surfaces) the optimum conditions were as shown in Table 2, and the roughness obtained could be less than 35µm R_a.

Table 2: Optimum Process Conditions for layered EPS patternmaking

Parameter	**Value**
Tool speed (mm/s)	35
Tool temperature (°C)	400
Layer thickness (mm)	0.1

This study has only limited relevance to the optimisation of surface roughness for RFS, since it is based on a very different manufacturing process, has a very different approach to sculpting freeform objects, is restricted to non-contact vapourised cutting and deals with a definition of roughness that is mostly predicated on the lay of the surface. In other words, the roughness model as considered here is primarily geometric. It is summarised here for completeness but will not be referred to again.

All the work summarised up to this point has been concerned with the surface finish of surfaces cut by a hot wire with a circular cross-section. However, surfaces produced by hot blades (with rectangular cross-sections) are also relevant to this research programme, as the RFS system under development uses blade tools with multiple tool passes as well as single passes of taut hot wires. As far as can be ascertained, even less research work has been carried out on the surface textures produced by hot blades than has been carried out for hot wires. The only work that could be found was carried out as part of the development of FF-TLOM at Delft University of Technology, as outlined above.

The team developing FFTLOM noticed that different surface types were produced by different cutting conditions, and so conducted an experiment to more rigourously evaluate the factors influencing surface texture [40]. For this experiment, 48 cuts were conducted using different levels of heating power and cutting speed. The cuts were made using 50mm thick DOW Styrofoam material (XPS) and were 300mm long. Blade temperature was measured before and after the cut, and the surfaces produced were evaluated visually and separated into categories (the process of qualitative evaluation undertaken here is very similar to that followed by Aitchison et al, as outlined above). Only the last

50mm of each cut were investigated, since it was thought that by this time the cutting conditions had stabilised: this means that the start-of-cut transient conditions were not considered. It also means that, since a blade was being used (which requires a longer cut length to fully stabilise) for cuts of only 300mm, and since the cutting force was still increasing at the end of the cut [39], the 'steady-state' surfaces that were investigated were probably not the result of steady-state cutting (RFS research has established that when cutting with hot-blade tools a minimum cut length of 600mm is required to achieve steady-state cutting conditions).

During the visual inspection process, the surfaces were classified as one of three possible values: good, moderate or bad. These surfaces are shown in Figure 30. Good surfaces were described as being smooth with no visual irregularities, moderate surfaces as being smooth but warped due to high temperature combined with a low speed (causing the surface to melt in an uncontrolled manner) and poor surfaces as having significant irregularities, apparently as a result of there being insufficient blade temperature to make a clean cut (this makes bad surfaces in this case analogous to the 'ripped' surface category identified by Aitchison et al [11]). As far as can be seen, the warping that led the authors to classify some surfaces as 'moderate' (See Figure 16 and Figure 30) was what would be called edge-melting in the concept of RFS. This defect is a function of the denser as-manufactured 'skin' on the sides of Styrofoam sheets, and will be discussed in detail in Chapter 5.

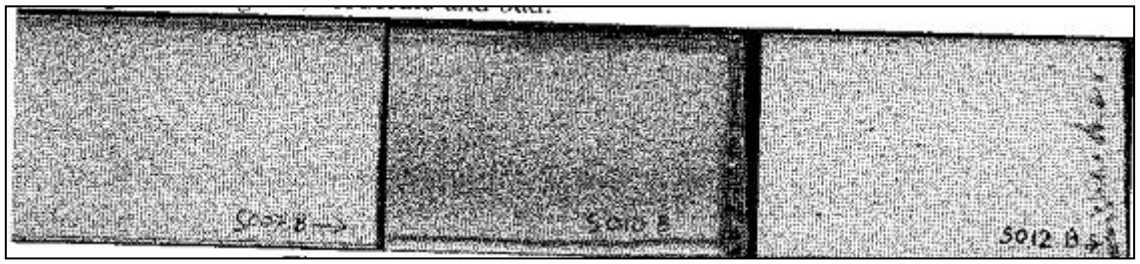

Figure 30: Good, Moderate and Bad Surfaces as defined by de Smit et al [40]

The results of these experiments are summarised by Figure 31. It must be noted at this point that the only available copy of this image was from a poor quality scan, so in the interests of clarity the figure has been re-drawn for presentation here. In this graph, surface quality is given a numerical value where 0 is equal to a bad surface, 1 is a moderate surface and 2 is a good surface. The surface quality results are displayed in terms of dissipated energy per square centimetre, which has units of Joule/cm^2. The key result of this experimental work was that all the surfaces were categorised as good if the dissipated energy per area was between 3 and 7 Joule/cm^2, and so the authors concluded that this was the optimal window within which to operate the tool for FFTLOM.

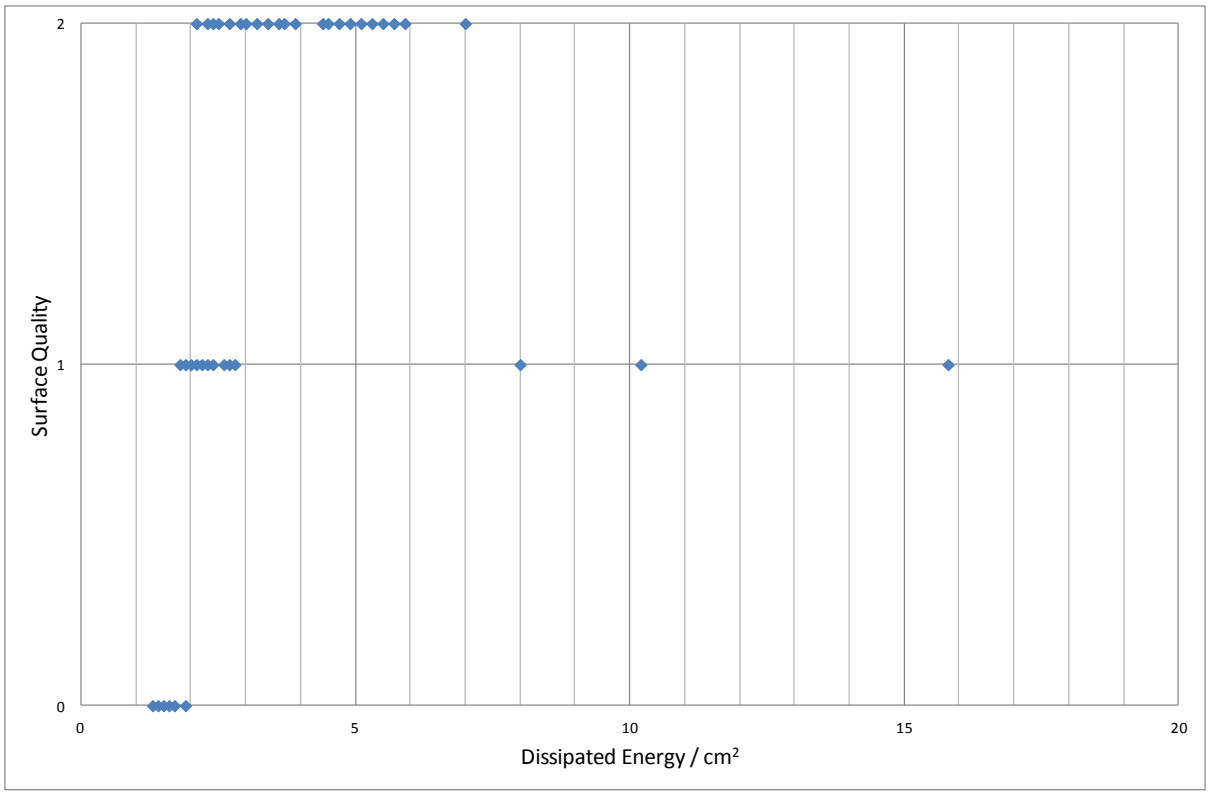

Figure 31: Surface Quality Results for FFTLOM [40]

There were some significant limitations to this research. First, since only three surface quality categories were used, the resolution of the assessment is fundamentally limited. Second, since the assessment of surface quality was qualitative this work suffered from the same limitations to accuracy and repeatability that the qualitative assessment of RFS surface quality experienced. Finally, not all the surface features used to assess the quality of a surface were actually the result of primary surface texture: as has been observed, the edge melting that resulted in many surfaces being categorised as 'moderate' is an error more of geometric form than of surface texture (see Chapter 5).

2.2.3 Investigations of Polystyrene Foam Geometric Form

During the development of the VLM process outlined above, Ahn et al developed a mathematical model for the thermal field around the cutting wire, and from that they were able to establish offsets to use to ensure that the final shape as cut from foam was the size and shape that was desired (in other words, they were able to account for the kerf width resulting from the thermal field). To test the accuracy of the VLM system, they sculpted a human head from a CAD model using both VLM and Laminated Object Manufacturing (LOM), a paper-based layered manufacturing system that creates plywood-like parts. The virtual model and the two physical artefacts are shown in Figure 32.

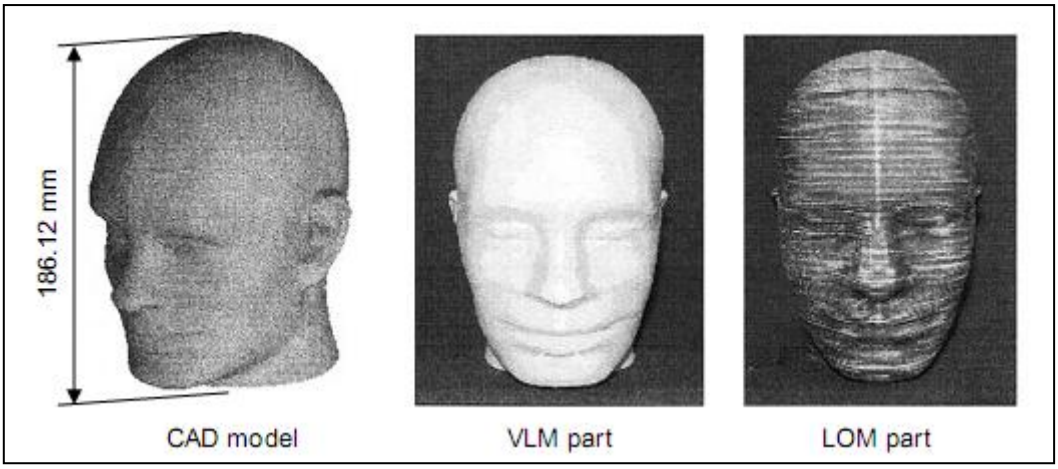

Figure 32: Human head model used to assess surface accuracy of VLM [31]

The two resulting parts were then compared, and the results are summarised in Table 3. As can be seen, the build time and build cost for VLM were significantly less than the corresponding values for LOM, but the most relevant data is the dimensional accuracy information. This shows that VLM is slightly less accurate than LOM in the plane of the layers but significantly more accurate in the z-direction (i.e. along the build axis). This assessment does not strictly speaking deal with the foam accuracy of the parts, but only with the dimensional accuracy along orthogonal axes, but it is included here for convenience. The development of the VLM system did not cover any more detailed assessment of geometric form, other than kerfwidth assessment. Form errors like surface barrelling, etc, that are relevant to RFS were not relevant to VLM due to the thin sheets being cut.

Table 3: Performance Comparison of VLM and LOM when fabricating a human head model

Process	Building time (min)				Build cost (US$)	Dimensional Accuracy (%)	
	Set-up	Build	Decubing	Total		In-plane	z-direction
LOM	80	2125	120	2325	720	0.7	1.8
VLM	-	35	5	40	8	0.8	1.1

Other than this example, there appears to be no published work on the geometric form accuracy achieved by any of the foam-based rapid prototyping systems reviewed in this chapter.

2.2.4 Effective Heat Input

This section of the review deals with a parameter that is used to measure the energy input for hot-tool cutting of polystyrene foam, the effective heat input Q_{eff}. Since this parameter was first postulated by

one group of researchers and then further developed by another, and since it is important to the research presented in this thesis, it has been presented here as a separate section.

2.2.4.1 Area-Specific Effective Heat Input

As part of the development of the Variable Lamination Manufacturing system by Ahn et al at KAIST, a property called the effective heat input (Q_{eff}) was developed. This was developed as follows [25].

When an electric current is passed through a resistive metal, the *Joule heating effect* occurs, and is defined by:

$$Q = i^2 R \tag{3}$$

Where Q is heat produced in Watts, i is the electrical current in Amperes (Amps) and R is resistance, in Ohms. In the case of a hot-wire the generated heat can be defined as a linear volumetric heat flux:

$$Q_L = \frac{Q}{L_e} \tag{4}$$

In this case L_e is the length of wire in the cut. Finally, the effective heat input is developed as a means to consider the influence of both the heat input and the cutting speed:

$$Q_{eff} = \frac{Q_L}{V_C} \tag{5}$$

Where V_c is the tool speed in meters per second (ms^{-1}) and Q_{eff} has units of Joules per square meter (Jm^{-2}). Q_{eff} is thus effectively the same as the 'dissipated energy per square centimetre' measure used by Broek et al, in that it is a measure of energy emitted by the wire per unit area of cut surface. Ahn et al referred to Q_{eff} as the 'Effective Heat Input' and this usage will be followed throughout this thesis, since it is the area-specific effective heat input that is of greatest relevance to the cutting strategy work that follows.

2.2.4.2 Volume–specific and Mass–specific Effective Heat Input

The concept of an effective heat input was developed further by Brooks [1] in his Ph.D. thesis (as part of the RFS project, see section 2.1.1). He divided the area-specific effective heat input Q_{eff} by the corresponding kerfwidth (measured after a cut) to produce the Volume-specific Effective Heat Input:

$$^{Vol}Q_{eff} = \frac{Q_{eff}}{\lambda} \tag{6}$$

In this equation λ is the kerfwidth in meters.

The volume-specific effective heat input, $^{vol}Q_{eff}$, represents the quantity of energy (electrical or thermal) required to 'melt' a unit volume of foam, and has units of Joules per cubic meter, Jm^{-3}. The

term ‘melt’ was used to denote the process by which foam near the wire reduces in volume, without necessarily actually melting. This parameter can also be referred to as the volumetric effective heat input.

Brooks also developed a property he called the mass-specific effective heat input, defined as:

$$^{mass}Q_{eff} = \frac{^{vol}Q_{eff}}{\rho_f} \quad (7)$$

In this case ρ_f is the density of the foam in kgm^{-3}. The mass specific effective heat input can be used for comparing plastic foams that have identical molecular structures but different densities (for instance, the different grades of EPS). The value of $^{mass}Q_{eff}$ is the same for all EPS foams, and was used to develop a mathematical model (for steady-state taut hot wire cuts) linking kerfwidth, power, feedrate, and material.

This work was used to develop a Hot-Cutting Calculator (HCC) that could be used to predict the kerf from input cutting conditions, but this tool was of only restricted use since it applied only to hot-wire cutting with steady-state conditions and took no account of the effect of the engaged tool length.

2.3 Background Material and Literature Review Summary

This chapter has presented a review of the previous research work that has been carried out on the development of the RFS system (section 2.1) and of relevant similar published work carried out by other researchers (section 2.2). This work constituted the starting point for the research reported in this thesis, and as such a thorough critical review was necessary.

Previous research carried out as part of the development of the RFS system fell into three main areas: cutting mechanics and surface assessment, tool design and control, and cutting strategy and toolpath generation. Most of the detailed research prior to this thesis was concentrated on understanding the cutting mechanics, with some (generally qualitative) work on tool design and cutting strategy.

In the area of cutting mechanics and surface assessment, five cutting modes had been identified and five qualitative surface texture categories had been developed to allow some limited assessment of surface quality. In addition, some work had been undertaken to investigate the relationship between the steady-state kerf and the effective heat input when cutting. The main limitation of this work was that it was mostly qualitative. This was a particular problem for the surface assessment work, since the five categories that had been defined were very subjective, and therefore were not reliably repeatable or communicable to parties who did not have access to physical surface samples. This made the work of only limited use as a measure of the performance of the hot-tool cutting process. The research into the relationships between kerf and effective heat input was more useful, in that it was based on quantitative measurements of the surfaces produced, but this work also had

drawbacks. In particular, it was limited to steady-state kerf measurements, taking no account of initial conditions or the kerf throughout transition cutting, and it was restricted to a relatively small range of foam types, engaged lengths and cutting conditions.

The research carried out into tool design and control had produced a system that allowed the control of the kerf along the length of a cut by varying the supplied current based on measurements of the cutting force. This system used a loadcell to identify when vapourised cutting had ended (and thermomechanical cutting was taking place) and then applied a step change to the supplied current to compensate for the cooling experienced by the tool. This system had three main disadvantages: a cutting force reading was necessary (and therefore the cutting tool could not be mounted on the robot), it had only been implemented for hot-wire tools, and it had only been implemented for a limited range of cutting conditions.

Finally, in the area of cutting strategy and toolpath generation, some research had been carried out which identified some rules of thumb that could be used to achieve good surface quality in multi-pass cutting. This research was based on very subjective assessments of the surface quality. As such, while it provided a useful starting point for further investigation of the multi-pass cutting strategy and was of some limited use for selecting a cutting strategy appropriate to the sculpting of a given part, it was not comprehensive or sufficiently quantitative to allow the selection of the most appropriate cutting strategy to sculpt a given part using multi-pass cutting.

Given the limitations of these elements of prior research in the RFS project, one of the purposes of the research reported here was to tie together the existing body of knowledge, and add a significant and detailed quantitative understanding of the factors that affect surface quality and the interactions between them. This understanding could then be embodied in a set of tools to allow a user of the Robotic Foam Sculpting system to develop an appropriate cutting strategy and select appropriate cutting conditions to achieve good surface quality and accuracy when sculpting a given part from polystyrene foam.

In addition to the prior research carried out in the RFS project, there also existed some published research on other foam-based rapid prototyping systems. A review of the similarities and differences between these other systems and the RFS process was necessary to establish gaps and limitations in the published knowledge and to guide the effort to understand the effects of cutting strategy on surface quality in RFS.

There were found to be six foam-based rapid prototyping or rapid manufacturing systems using heated tools that were relevant to the research being carried out for the RFS project. These were Variable Lamination Manufacturing (VLM), Free Form Thick Layer Object Manufacturing (FF-TLOM), Rapid Heat Ablation (RHA), Michelangelo, ModelAngelo and Stratoconcept. All of these used sculpting paradigms that were fundamentally different from that used by RFS, being either based on the assembly of layers that were cut using hot tools or on the vapourisation of excess foam to

produce a desired part surface. However, since in all cases research on these systems considered the effect of cutting strategy on surface quality the published work had to be considered.

The VLM system was a layer-based rapid prototyping system using straight hot wires to shape thin layers of expanded polystyrene foam that were then stacked together to form a finished model. This sculpting paradigm limited the applicability of this work to the RFS system, but there were additional limitations. Since VLM used only a single type of foam, results reported for this system could not necessarily be extrapolated to the behaviour of the cutting process when other types of foam, especially extruded polystyrene, were used. Also, since the VLM system used very thin sheets of foam (2 – 4mm thick) the engaged length of the tool in any cut was also very short: as a result the thermomechanical behaviour of the cutting tool during a cut in VLM would fundamentally differ from that in RFS, where the engaged length is much longer and therefore there is a pronounced thermal gradient along the engaged length. Finally, since VLM operated using purely vapourised cutting, with no physical contact between the cutting tool and the foam, the results reported for experiments using VLM would apply only to a very small area of the operational space used by the RFS system. The researchers who developed VLM also published a single paper on the surface texture and how it was influenced by cutting conditions, but this was also of limited use given its restriction to purely vapourised cutting and the use of a stylus-based measurement instrument to gather the surface roughness data. As will be reported in Chapter 4, stylus-based instruments were found to scratch the surfaces of polystyrene foam, thus distorting the roughness measurements achieved.

The FF-TLOM system was also a layer-based prototyping system that used a heated blade to cut thick layers that were then assembled into a physical model. The key feature of this system was the variable-geometry blade which allowed curved surfaces to be produced on the edges of each layer to improve overall part accuracy. This system was also restricted to a single type of foam, in this case extruded polystyrene, and since it used as-manufactured sheets of this foam the assessment of surface quality undertaken was influenced by the presence of edge-melting effects due to the higher density skin resulting from the manufacturing process (see section 5.6). Even setting aside this distorting influence on the surface quality assessment, surfaces were only assessed qualitatively and categorised as bad, good, or moderate. Since this assessment was qualitative it suffered from the same limitations as the qualitative surface assessment carried out for RFS, with the additional disadvantage that using only three categories did not allow sufficient assessment resolution to accurately assess the influence of different factors on the surface quality. Finally, since the variable-geometry blade was vulnerable to unintended distortions even at very low cutting forces, this system was limited to vapourised or low-force thermomechanical cutting, which meant that results from this research would only apply to a small area of the RFS operational space.

RHA was developed by the same team of researchers who produced the VLM system, but used a tool similar to a ball-end mill to ablate unwanted foam from a workpart to produce a part surface. This system had one significant advantage in that toolpaths could be programmed easily using standard CAM software, but suffered from the disadvantages that large energy inputs were required and that

the cutting speed had to be kept low enough that purely-vapourised cutting remained the cutting mode, which limited the cutting speed to below 3600mm/min.

Michelangelo used an industrial robot to manipulate a taut-hot-wire cutting tool, and as a result was restricted to the production of parts that approximated curved surfaces using planar facets. As such it is clearly not as potentially versatile or accurate as the RFS system. Much of the published work concerning this system deals with the approximation of CAD data as a set of flat facets that can be cut by the tool, and the development of a mesh-simplification algorithm to reduce the model complexity by reducing the number of facets used to approximate a surface. There was a limited investigation into the mechanics of hot-wire cutting, although this was limited to vapourised cutting and no explicit conclusions were drawn regarding offsets that might need to be applied to compensate for kerfwidth. In addition, the only assessment of surface quality undertaken dealt with the inaccuracies resulting from surface approximation, and not with inaccuracies resulting from the cutting process.

The ModelAngelo system uses shaped tools made from heated wires and blades to subtractively sculpt curved shapes, with manipulation of the tools being achieved by a five-axis robot. Since surfaces are produced with curved tools specifically shaped to sculpt the shape sought, this system lacks versatility. Different tools must be produced for every different shape that is desired, unlike in RFS where a limited range of tools are used and complex freeform surfaces are to be produced by choosing an appropriate cutting strategy. While the published work on this system contains no discussion of the cutting mechanics, it can be inferred that cutting takes place purely by vapourisation. There was little evidence of surface quality assessment, and what little had been carried out was qualitative rather than quantitative.

Finally, the Stratoconcept system uses taut hot wires to cut layers of foam that can be assembled to produce a final physical model. This is similar in principle to VLM, except that the Stratoconcept is capable of producing parts that are much larger and the assembly of the layers is manual rather than automated. There was little available published material concerning the surface quality produced using this system.

This literature review has identified a number of gaps in the existing knowledge concerning the cutting strategy and surface quality of thermomechanical cutting of polystyrene foam. The research that forms the content of this thesis will correct these gaps in the knowledge in order to allow the selection of an appropriate cutting strategy for sculpting a given part using the Robotic Foam Sculpting system. In brief, the key gaps in existing knowledge are as follows.

- There is no quantitative understanding of the nature of texture of polystyrene foam surfaces, and no understanding of what input factors influence this texture. What little work does exist is based on qualitative assessment based on visual observation.
- There is very little understanding of the macroscopic surface form errors resulting from single-pass hot-tool cutting of polystyrene foam. What little work does exist has been limited to

studies of the steady-state kerf, with no consideration of the initial or transition kerfs, or of other surface form errors. In addition, there is no detailed understanding of the different factors and interactions that determine the single-pass geometric form errors, and hence no ability to control these errors.

- Apart from some very basic assessment based on qualitative surface assessment, there has been no research conducted into the nature of geometric form errors in multi-pass cutting. There is no detailed understanding of the parameters and parameter interactions that affect the surface form errors in multi-pass cutting, and therefore only a very limited ability to control these errors.
- It is not possible to predict the behaviour of the surface texture or the geometric form errors based on the cutting conditions being used, so it is not possible to select cutting conditions to achieve desired textures or form errors. Therefore, no reliable control of the texture and form errors on a surface produced by hot-tool cutting is possible.
- While some understanding has been achieved of the factors that have an effect on the cutting force, the relevance of these factors has not been rigourously established, and it is not possible to predict the expected cutting force based on the cutting conditions being used. This makes it impossible to select cutting conditions that will not result in tool failure.
- The existing system for controlling the kerf in single-pass cutting, based on the use of a real-time cutting force reading to control the current supplied to the tool, makes it impossible to mount the cutting tool on the robot. There is a need for an alternative trigger signal that is capable of identifying when thermomechanical cutting is taking place so that the current can be controlled without the use of a direct cutting force measurement.

These limitations of the existing body of knowledge present a number of significant drawbacks for the robotic foam sculpting system. In the absence of a thorough and detailed understanding of which input factors influence the different errors in thermomechanically-cut surfaces, and an understanding of how those factors and surface errors interact, it is not possible to develop a cutting strategy to achieve a desired level of surface quality. The purpose of this thesis is to round out these gaps in the existing knowledge and develop a set of tools that can be used to select an appropriate cutting strategy for sculpting a given part using the RFS system.

3 Cutting Strategy Parameters and Factor Interactions

As has already been stated, there are a significant number of parameters that have to be considered when examining the cutting strategy for hot-tool cutting of polystyrene foam. These parameters can be divided into output surface quality parameters, user-controllable input parameters and intermediate parameters that directly influence the output parameters while being influenced by input parameters, without it being possible for the user to directly control their value. These individual factors and the interactions between them must be thoroughly investigated in order to develop a comprehensive model of the cutting strategy and its effects on surface quality in Robotic Foam Sculpting.

The factors of relevance to the cutting strategy for RFS have already been summarised in Table 1, above. In this chapter, each of the factors will be defined in detail, and diagrams will be presented showing the interactions between these parameters. These diagrams will be presented here without showing how they were developed, since the development of the diagrams is considered in the relevant thematic chapters.

3.1 User-controllable and intermediate variables for cutting strategy

As noted, there are a range of input parameters that together constitute the cutting strategy used for RFS. These parameters are divided into parameters that are directly controllable by the system operator (user-controllable input variables) and intermediate variables that directly influence the values of the output metrics but are themselves not directly controllable, although they are generally determined by the user-controllable parameters. These controllable and input parameters are defined in this section.

Path spacing is the distance between adjacent tool passes in multi-pass cutting. Such tool paths can be either bi-directional, where the tool moves through the workpart in one direction, turns around in free space, and re-enters the workpart on the adjacent pass moving in the opposite direction, as shown in Figure 33, or they can be uni-directional, where the tool makes one pass through the material, moves in free space back to the end where the first pass started, and then makes the adjacent cutting pass with the same direction of cut as the previous one. It has already been found qualitatively that uni-directional toolpaths generally result in surfaces with fewer surface flaws (see section 2.1.3).

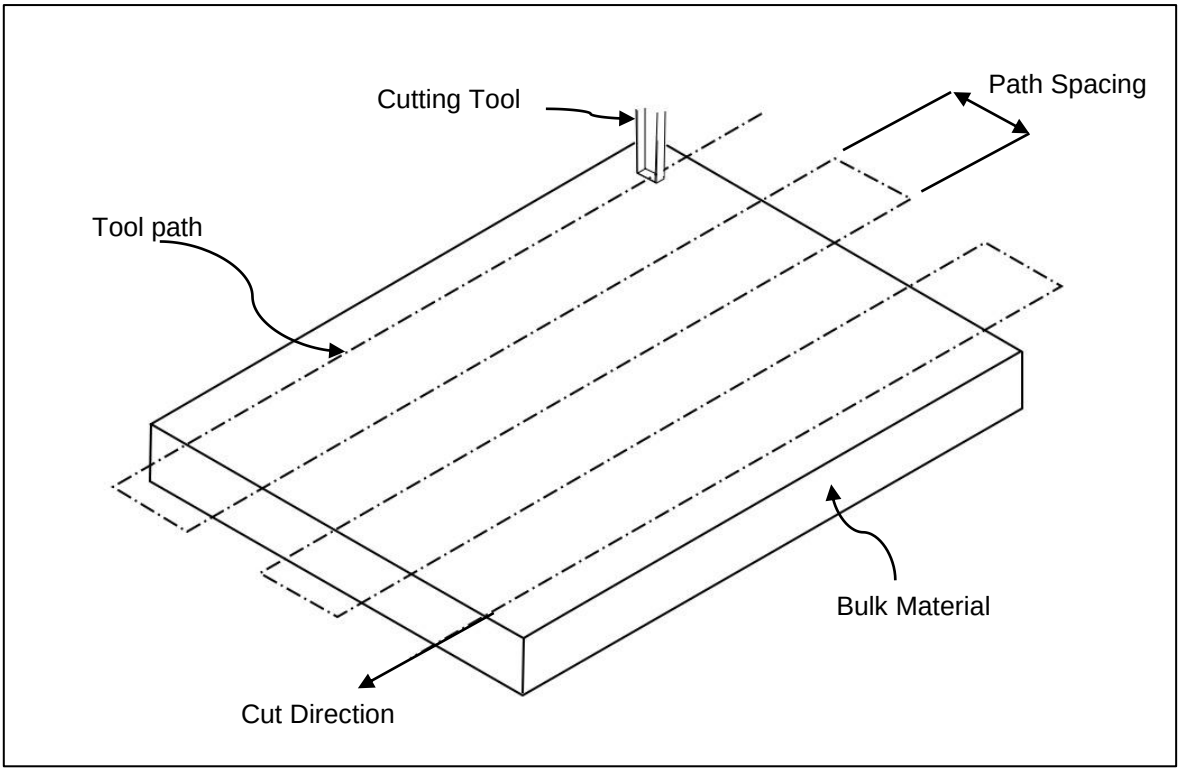

Figure 33: Path spacing for a bi-directional tool path on a nominally-flat surface

Tool shape is a function of the type of tool being used for sculpting a given shape. Four basic tool shapes are used in the RFS system: these are referred to as straight-wire, straight-blade, square-nose and round-nose tools. Straight-wire and straight-blade tools are used for single-pass cutting to produce planar surfaces, while square-nose and round-nose tools are used for multi-pass cutting to produce curved surfaces.

Straight-wire tools are a single length of heated wire with a circular cross-section, kept taut by a pneumatic cylinder at one end. These were the first tools used on the RFS system, and can produce higher-quality surfaces than other tools, but they have limited tool durability and can only cut at relatively low speeds (of $0.0217ms^{-1}$ or less) and current levels. Straight-blade tools are broadly similar, except that they are made of a straight length of 1/8” by 0.018 inch nichrome ribbon with a rectangular cross-section held under tension. Due to the shape and size of these blades, they can cut faster and at higher currents than hot-wires, but the quality of the surface achieved can be less than optimum. These two types of tools are shown in Figure 34. The mixed notation used for specifying the size of the nichrome ribbon is taken from the manufacturer’s notation, and used here for convenience.

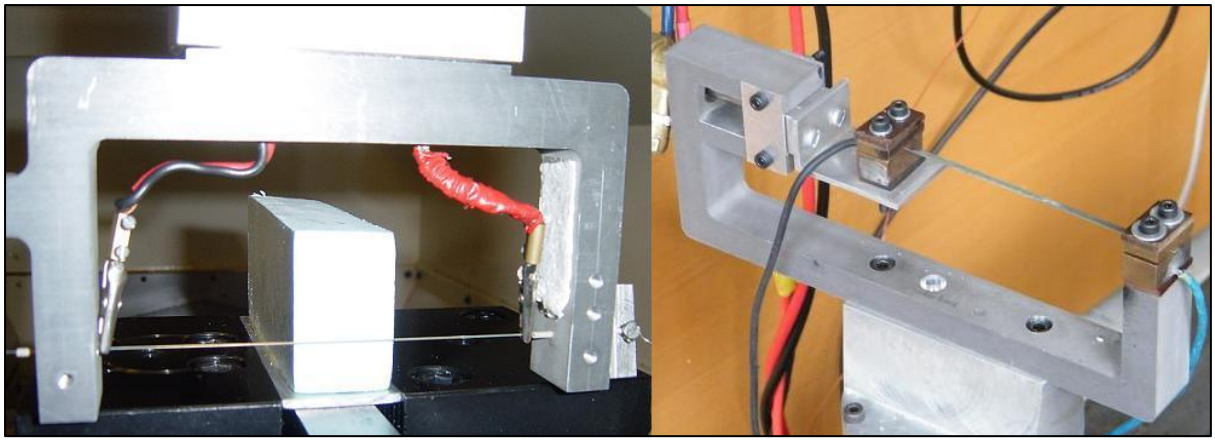

Figure 34: Straight-wire (left) and Straight-blade (right) tools

Square-nose and round-nose tools are made of the same nichrome ribbon used for straight-blade tools, but the ribbon is shaped so it can be used for multi-pass cutting, as shown in Figure 35. These tools are used for multi-pass cutting to shape curved surfaces. It should be noted that the term ‘square-nose’ is used because the end of the tool is a straight length of ribbon that lies parallel to the section of foam being cut, not necessarily because the corners of the bent ribbon have an angle of 90º.

Figure 35: Square-nose (left) and Round-nose tools for multi-pass cutting

The **tool size** is a very important factor for the cutting strategy. Aspects of tool size affect the available values for path spacing and cut depth, as well as influencing the engaged tool length and the cutting force, and hence the tool durability. The important tool dimensions vary depending on

whether the tool is curved-blade or straight-blade: these important dimensions are shown in Figure 36.

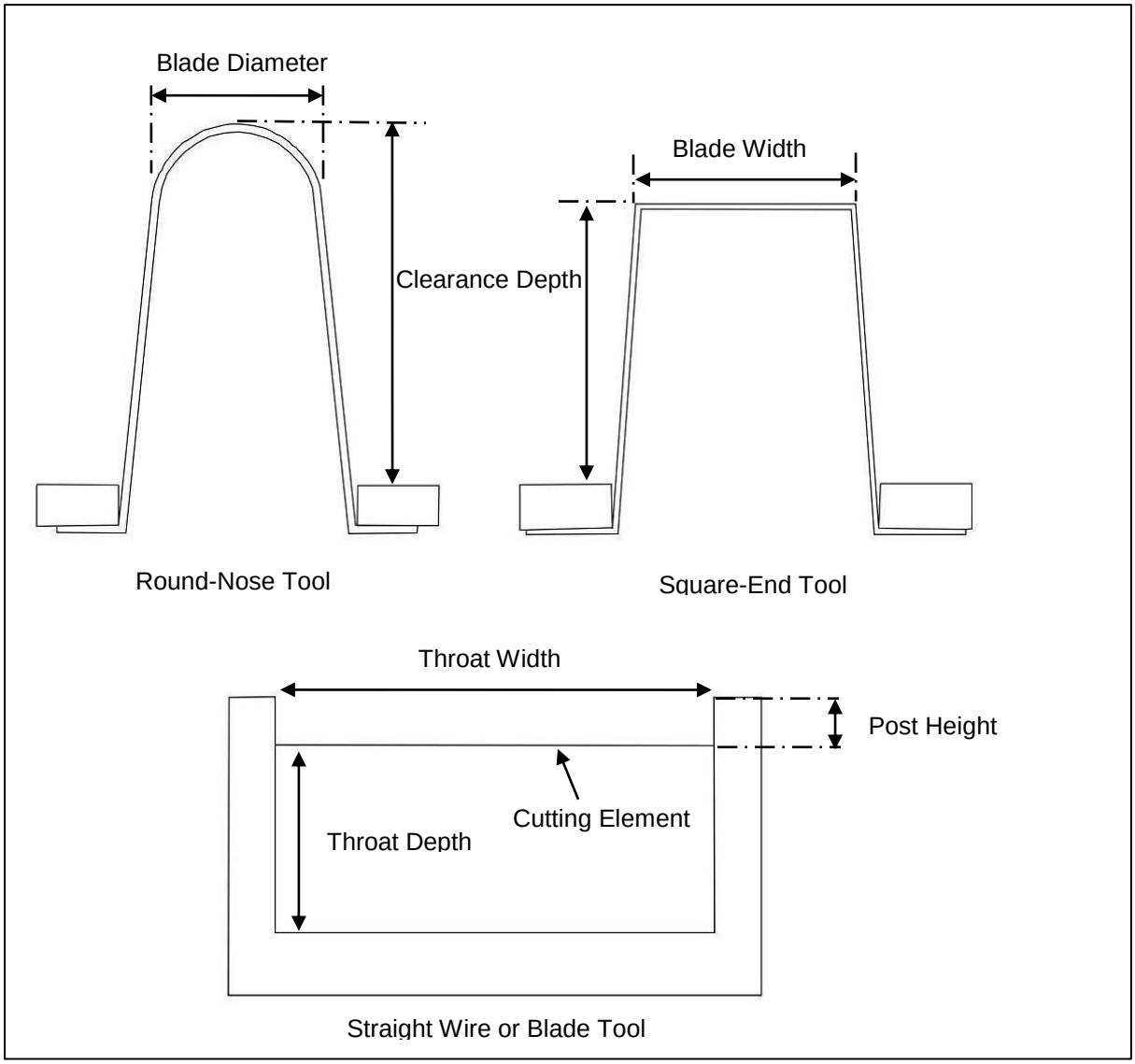

Figure 36: Important tool dimensions

The blade diameter or blade width has an effect on the path spacing, and is in turn influenced by the desired surface accuracy: since curved surfaces are approximated by multiple tool passes, the path spacing helps determine how accurate that approximation is, and so the blade width or diameter is relevant to the surface accuracy. This dimension, along with the clearance depth and the path spacing, also influences the engaged length.

The tool clearance depth or throat depth determines the maximum cut depth that can be achieved at any one time, since cut depths greater than these values result in collisions between the workpart and the tool. The throat width and post height of single-pass tools are important for the same reason. The clearance depth of a multi-pass tool is also important because it influences the durability of the tool:

the longer the clearance depth, the greater the bending moment in the blade for a given cutting force. So, as the clearance length gets longer, the critical bending moment that results in tool failure will occur for a lower cutting force. The cutting force is also proportional to the engaged length during the cut, so longer clearance depths can result in excessively deep cuts, which in turn result in more frequent tool failure.

Surface curvature influences a number of aspects of cutting strategy, including the tool type, tool size and path spacing. There are three basic states of surface curvature that have an influence on cutting strategy: flat, concave from the point of view of the tool, and convex from the point of view of the tool. These are shown in Figure 37. There are also two cases of direction that need to be considered: whether the curvature is perpendicular to the cut path or along the cut path. More complex compound surfaces also occur, but these are made up of some combination of these three basic surface types. Each surface type has a different effect on the cutting strategy necessary to achieve high surface quality, as will be discussed in later chapters.

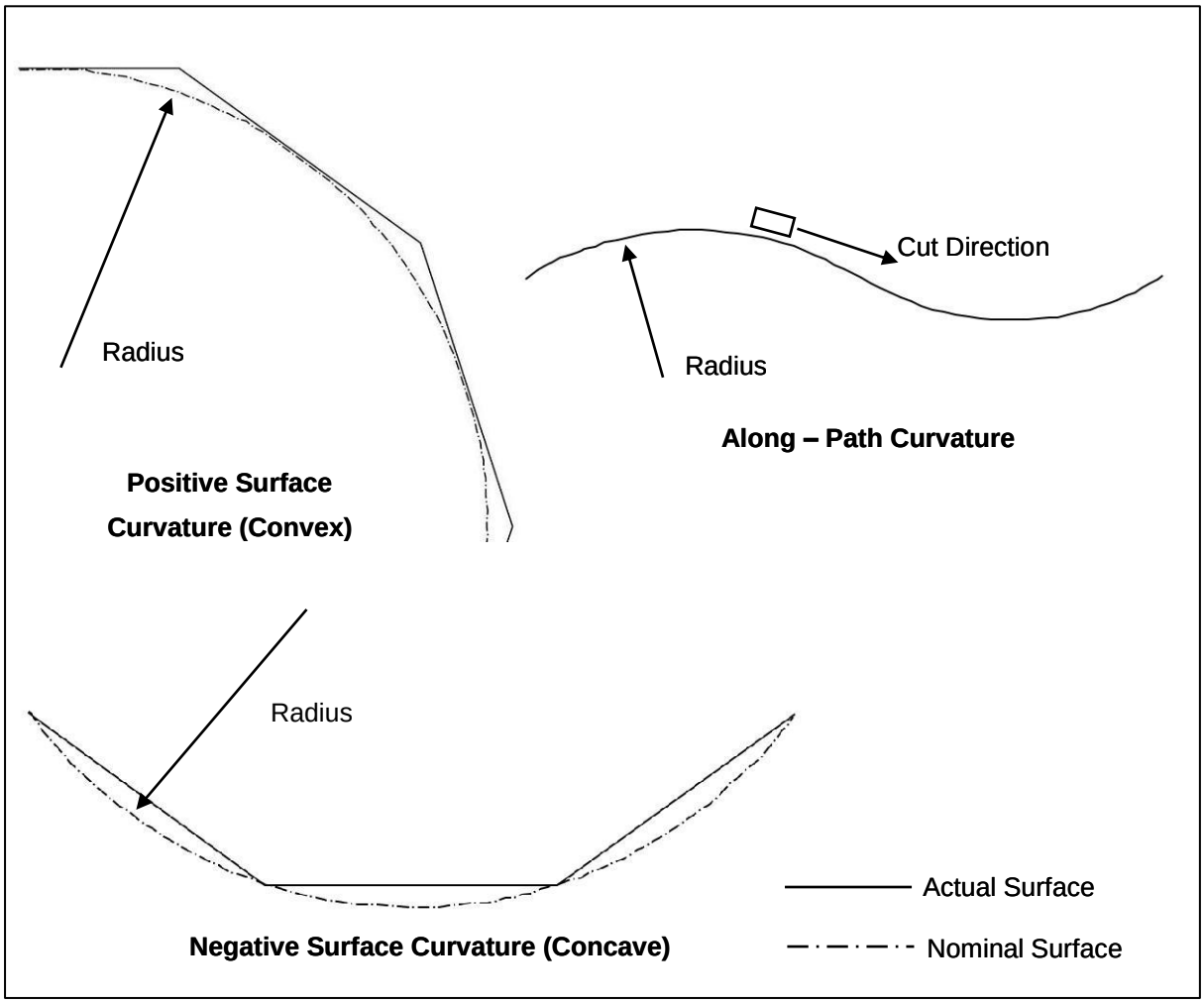

Figure 37: Types of surface curvature of relevance to cutting strategy

Supplied current is the electrical current supplied to the tool, which is proportional to the free-air temperature of the tool. Higher levels of current result in hotter tools, and hence with higher currents higher tool speeds can be used.

Feedrate is the rate of relative motion between the tool centre point (TCP) and the foam workpart, as applied by the Kuka robot. This may be the result of moving the tool through a fixed workpart, or moving the workpart across a fixed tool. The feedrate is measured in either mm/min or m/s. In some situations, there may be local variations in feedrate: for example, if the TCP of a square-end blade is moving along a curved path, the outer corner of the blade will move faster than the TCP around the curve, and the inner corner will move slower. The feedrate is shown diagrammatically for a single-pass cut in Figure 38.

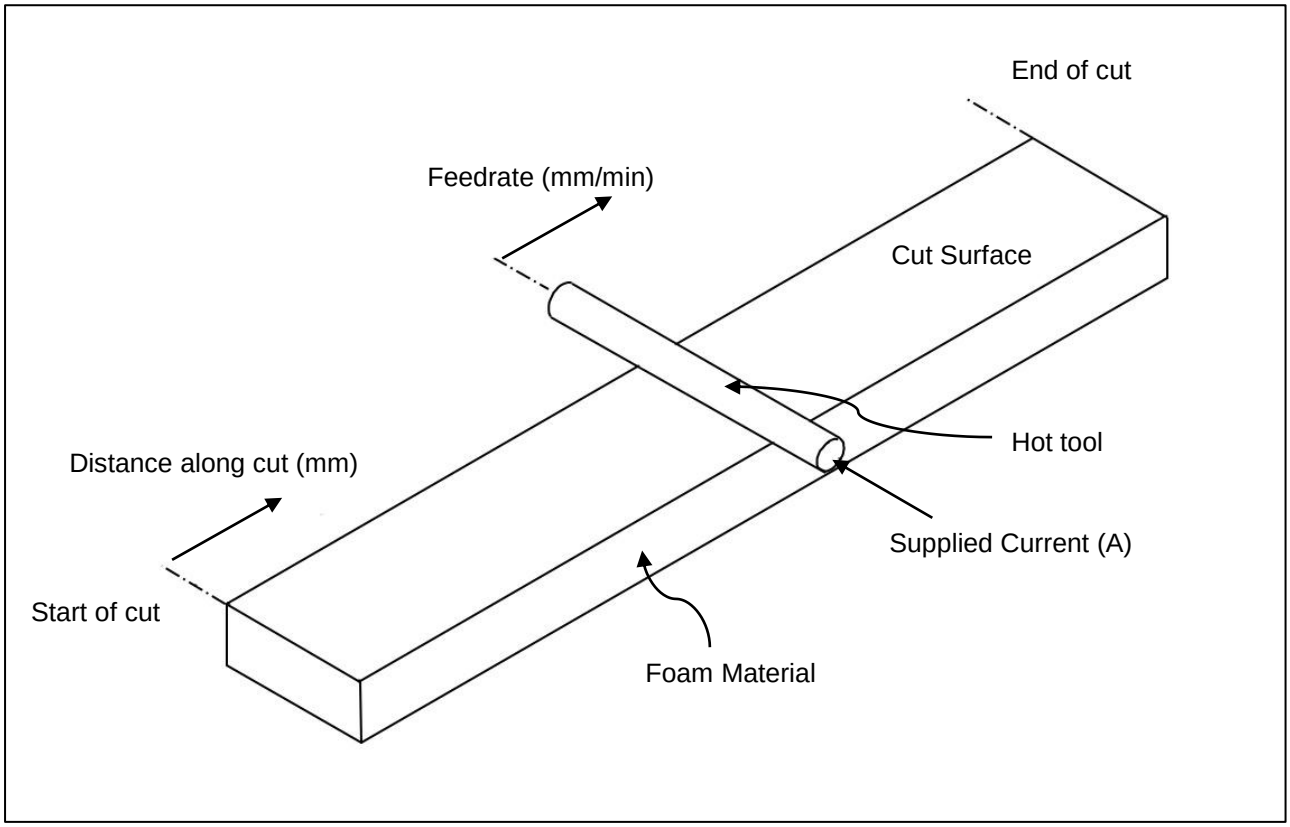

Figure 38: Current, feedrate and distance along the cut for a single-pass cut (not to scale)

The nature of the polystyrene foam **material** has a significant impact on the selection of an appropriate cutting strategy for sculpting a given part. The two materials usually used for RFS are expanded polystyrene foam (EPS) and extruded polystyrene foam (XPS). EPS is made up of relatively large (up to ≈5mm in diameter) beads of polystyrene, with smaller cells within the beads and occasional relatively large open areas in the interstices between the beads. XPS is made up of much smaller (≈150μm in diameter) cells that are much more regularly sized and distributed than the cells in EPS, and with no analogous structure to the beads in EPS. The cellular structures of these two foams are shown in Figure 39. As a result of these differences in structure, EPS foam is significantly softer

than XPS even for foams of the same density. These differences in the cellular structure of the foam are very significant for the selection of an appropriate cutting strategy, in a number of ways. These are summarised below:

1. The softer nature of EPS means that it can be cut with a higher feedrate than XPS for the same level of tool temperature (i.e. for the same applied current).
2. The more regular nature of the cellular structure in XPS means that the measured aspects of surface quality (discussed below) are more predictable and repeatable for XPS.
3. The observed surface finish is of a higher quality for XPS than for EPS. XPS surfaces look significantly smoother than surfaces produced in EPS under the same circumstances.

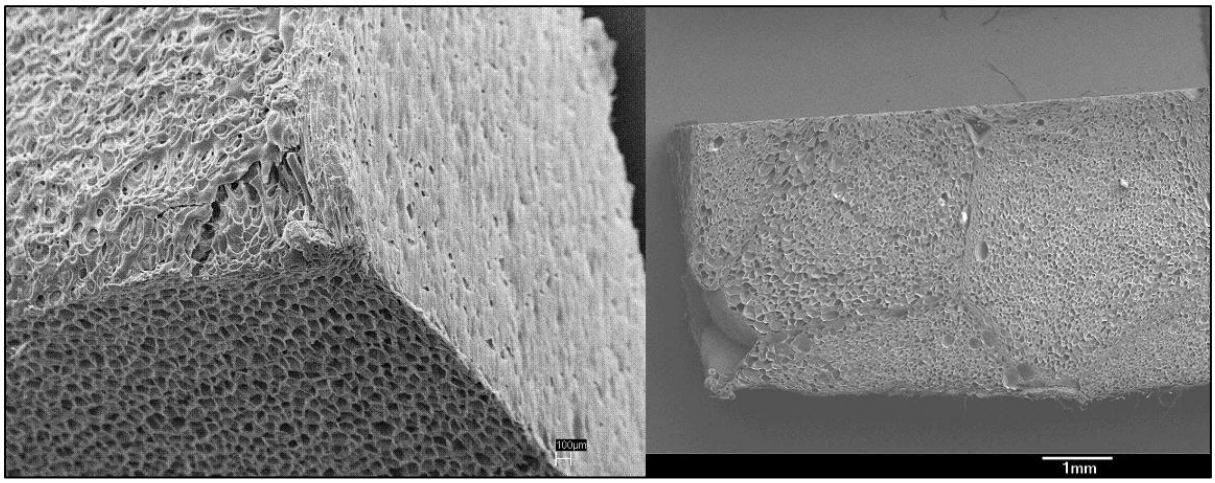

Figure 39: SEM images of polystyrene foam materials: Extruded Polystyrene (XPS) on the left, Expanded Polystyrene (EPS) on the right

The **Cut depth** is the distance between the outer surface of the raw workpart and the surface being cut by RFS, and is an important cutting strategy factor for two reasons. The first is that the designed cut depth must be achievable within the limits of the clearance depth or the throat depth of the tool being used, without interference between the tool and the foam. The second is that the cut depth directly effects the engaged tool length (an intermediate variable that will be defined below) which in turn effects the cutting force, the thermomechanical balance, the tool life and most of the surface quality metrics used to assess RFS. Cut depth is shown diagrammatically, along with engaged length, in Figure 42.

In addition to the user-controllable input variables, there are a range of intermediate variables that directly affect the output surface quality metrics and are controlled by the input variables. While it would be possible to understand the factor interrelationships of importance to cutting strategy without considering the intermediate parameters, and treating the links between the user-controllable variables and the output metrics as a ‘black box’, a much deeper understanding of the cutting process can be gathered by considering these intermediate variables and the relationships between them and

other factors. These intermediate variables are summarised here, and the links between them will be discussed in the next section.

Effective heat input (Q_{eff}) is a parameter first defined by Ahn et al [16] and further developed by Brooks [1]. It is a measure of the power input to the cut as a function of surface area, and is therefore calculated based on tool feedrate and applied current. Q_{eff} is based on the linear volumetric heat flux along the engaged length of the tool, Q_L, which is defined as:

$$Q_L = \frac{i^2 R}{L_e} \tag{8}$$

Where L_e is the engaged length of the tool, i is the applied current and R is the resistance of the tool. Q_L can then be divided by the tool feedrate in m/s (V_c) to give the area-specific effective heat input, Q_{eff}, in units of J/m^2:

$$Q_{eff} = \frac{Q_L}{V_c} \tag{9}$$

Distance along cut is the distance along the toolpath from the point where the tool first encountered the foam to the point of interest. This is an important parameter because the cooling of the tool along a cut has an effect on the surface quality and the surface accuracy, as will be shown later in the thematic chapters. This variable is illustrated in Figure 38.

The **Tool Temperature Differential, ΔT** is the difference in temperature between the tool at the centre of the engaged length (which follows the characteristic power-law decline shown in the graph in Figure 41) and the temperature of the tool in free-air for the relevant level of applied current. The sections of the heated tool outside the engaged length are not cooled by the cutting process, so they remain at the free-air temperature during the cut. This results in a transverse thermal profile along the tool, which has an influence on the transverse surface profile produced. The value of ΔT is dynamic during the transient stage at the beginning of the cut, being effectively zero at the start of the cut and reaching its maximum value when steady-state cutting conditions are achieved. It is this thermal profile that leads to the characteristic barrelling effect found on a single-pass cut and measured by the output parameter ΔH (defined below), and the transient nature of ΔT leads to the characteristic longitudinal surface profile resulting from the change in kerfwidth along a cut as the cutting mode progresses from purely-vapourised cutting (Stage I) to steady-state thermomechanical cutting (Stage III). The concept of Tool Temperature Differential, ΔT, is demonstrated in Figure 40. Values of ΔT are calculated using the formula:

$$\Delta T = T_{Free\text{-}air} - T_{Centre} \tag{10}$$

Where $T_{Free\text{-}air}$ is the temperature of the tool in free-air, where no cutting is taking place (which is a function of the tool type and the applied current), and T_{Centre} is the temperature of the tool at the centre

of the engaged length (the centre of the cut is always where the tool is coolest during a cut). In this thesis ΔT has units of ºC.

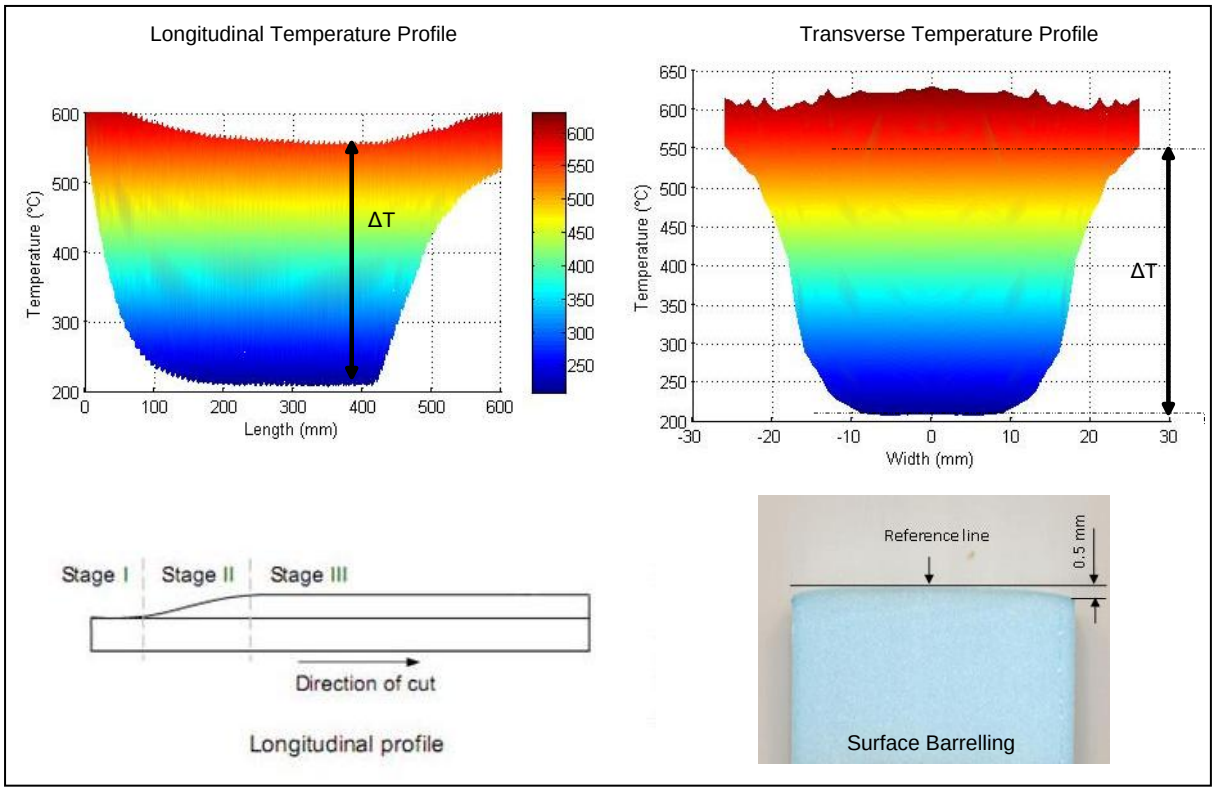

Figure 40: Tool thermal profile ΔT and its relationship to surface form

The **thermomechanical balance** is the balance between the centre-cut temperature and the cutting force. The centre-cut temperature is the temperature of importance since the coolest point on the tool occurs at the centre of the tool's engaged length. At the beginning of the cut the tool temperature is the steady-state temperature for the tool under the given applied current, and as the cut progresses the tool cools until it reaches a steady-state value some distance into the cut. The cutting force follows a similar but inverse pattern: initially the cutting force is zero since the foam is being cut by vapourisation and there is no physical contact between the wire and the foam, and as the degree of physical contact increases the cutting force also increases, until it too reaches a steady-state level. As such, the thermomechanical balance is a function of the effective heat input, the distance along the cut, and the material in question: this concept is expressed in Figure 41. The thermomechanical balance along the cut affects the surface quality, since the surface finish changes depending on the level of cutting force (see Chapter 4), as does the geometric form (Chapters 5 and 6). The thermomechanical balance is not a quantitative input parameter, and has no metric associated with it, but is a very useful concept for understanding the nature of the cutting process and the effects of different cutting modes on surface quality.

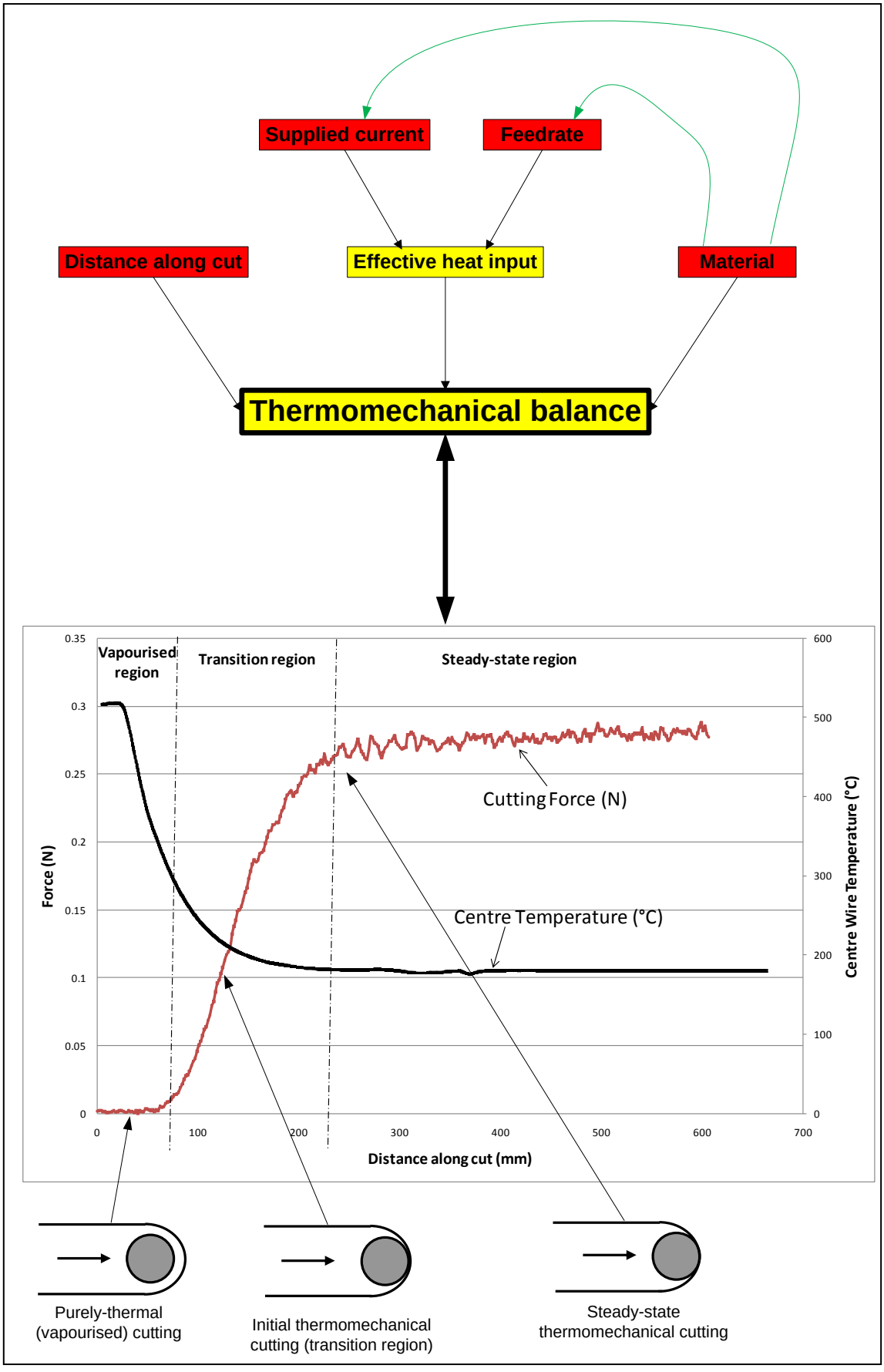

Figure 41: Thermomechanical balance and the factor interrelationships by which it is influenced

Engaged tool length is, logically enough, the length of the tool that is physically within the foam during cutting (Figure 42). In the case of single-pass cutting, the engaged tool length is simply a function of the thickness of the foam being cut measured along the cutting tool. In multi-pass cutting, the engaged tool length is a function of the tool shape, the path spacing and the cut depth. As noted above, the engaged tool length (which is denoted throughout this thesis by l_e) affects the cutting force, tool life, and thermomechanical balance, and so is a significant factor that must be considered when determining the cutting strategy most suitable for sculpting a given part.

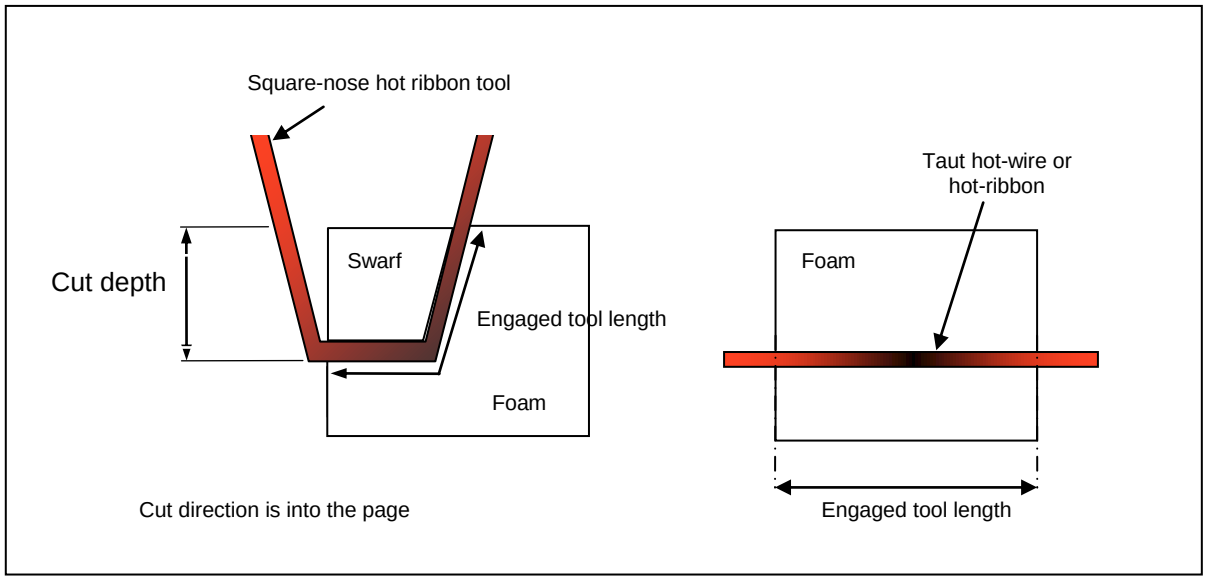

Figure 42: Engaged tool length for multi-pass (left) and single-pass cutting

3.2 Aspects of Surface Quality for Robotic Foam Sculpting

Surfaces produced by any manufacturing process are never perfect: there are always deviations from the nominal surface that is desired. The Robotic Foam Sculpting system is no exception to this rule. When sculpting parts with RFS, the surfaces produced can have a range of different characteristic errors that need to be allowed for when determining how to sculpt parts. In other words, the cutting strategy to be used is dependent on the desired surface quality.

The characteristic errors in foam surfaces can be divided into two broad categories: geometric and thermomechanical errors. The two sources of error both act during sculpting of foam parts, and are superimposed on the final surface, so both must be well understood and accounted for in order to optimise the cutting strategy properly.

3.2.1 Geometric Errors

Geometric errors are generally (but not always) of larger scale than thermomechanical errors, and are produced by the interaction of tool path, tool type and surface geometry. For example, when sculpting a curved surface using multiple passes of a square-nose tool, the shape of the tool will not exactly match the local curvature of the nominal surface on any given path, so the nominal surface is approximated as a series of straight surfaces (this is akin to the triangular surface approximation of an

stl file). The smaller the spacing between adjacent tool passes, the closer the approximated surface is to the nominal surface. Geometric errors are purely a function of the geometry of the tool, tool path and shape to be produced, hence the term used in this thesis. They are also generally much simpler to predict than thermomechanical errors.

The two main geometric errors of relevance to this thesis are the maximum geometric deviation between the nominal surface and the actual surface (the geometric R_{max}, denoted by $R_{max,\ geometric}$) and the spacing between the lay peaks parallel to the nominal surface (the peak spacing, denoted by S_p). These general geometric errors are shown in Figure 43, which shows in cross section the geometric R_{max} and the peak spacing for a flat surface cut by multi-pass cutting with a round-nose tool. It is important to note that these errors are ideal cases: in other words, for a given tool design and tool path the best surface accuracy that can be achieved is given by the geometric errors. It should be noted that a flat surface cut with multiple passes of a square-end tool forms a special case where the geometric R_{max} is zero (unless an angular misalignment exists between the nominal surface and the end of the tool), although all other combinations of surface curvature and tool that have been considered in this thesis have geometric R_{max} errors.

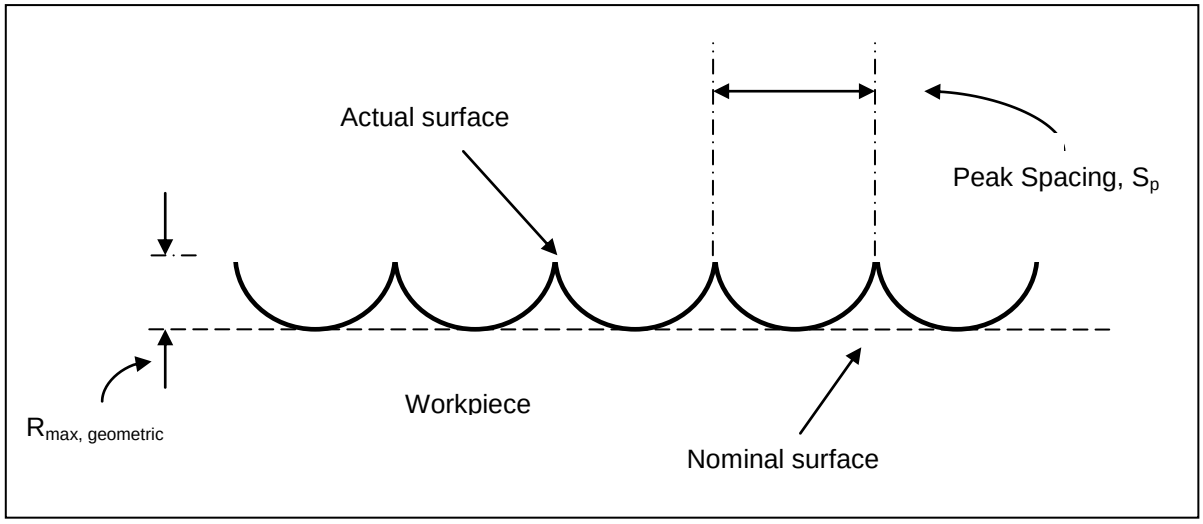

Figure 43: Geometric Surface Errors for a Flat Surface cut with Multiple Passes of a Round-nose tool, viewed in cross section

3.2.2 Thermomechanical Errors

Thermomechanical errors are generally of smaller scale, and are significantly more complicated than geometric errors. The range of input factors is much larger, and more output metrics are needed to fully measure these aspects of the final surface. As the name suggests, these errors are the result of the different thermomechanical factors of hot-tool cutting of foam, such as the tool feedrate, the applied current, the wire temperature, the balance between thermal and thermomechanical cutting, the type of foam material and the tool type being used. Some geometric parameters also influence the thermomechanical errors, such as the distance along the cut.

The complexity of this broad categorisation of surface imperfections is increased by the fact that some errors that result from thermomechanical conditions can in fact be larger than the geometric errors, depending on the exact context, and the fact that both thermomechanical and geometric errors are generally superimposed on surfaces in practice so that, for example, the lay of a surface produced by multiple tool passes is the result of both geometric and thermomechanical error.

There are four main thermomechanical errors that can be used to measure the performance of the robotic foam sculpting system: these are the surface texture, the kerfwidth, the lay R_{max} (for multi-pass cutting), and the surface barrelling ΔH (of most significance for single-pass cutting).

The **surface texture** (sometimes referred to as surface roughness or primary texture, although surface texture is the term that has been used in this thesis) is the primary surface imperfection. It occurs in all foam surfaces cut by hot tools, whether they have been made with single passes of hot-wires or hot-blades, or multiple passes of hot-blades. The surface texture is the small-scale deviations of a surface from the nominal surface, and is labelled in Figure 44. The nature of the surface texture falls into one of a range of qualitative categories that have been previously defined (see section 2.1.1), and these categories tend to occur in sequence along the length of a cut. The size of the surface texture makes it difficult to represent photographically and to measure, and this will be discussed in detail in Chapter 4. The surface texture is the smallest of the thermomechanical surface errors, and is unavoidable in practice. Any foam surface cut by thermomechanical tooling will have surface texture errors, so it is important to be able to measure and quantify these errors.

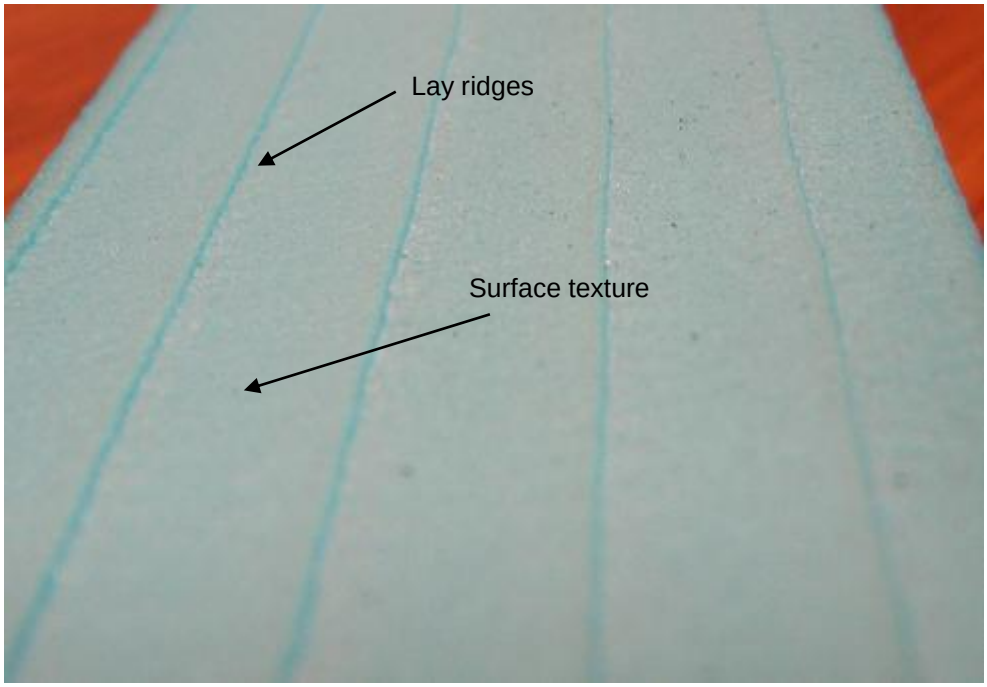

Figure 44: Lay and texture

The **Kerfwidth** is the macroscopic surface deviation resulting from the width of the wire or the wire and the thermal field surrounding it. At the beginning of the cut, when the wire is hot and cutting by

vapourisation, the kerfwidth is quite wide. Later in the cut, when steady-state thermomechanical cutting has been achieved, the kerfwidth is substantially smaller. The concept of kerfwidth is shown in Figure 45. Obviously, in order to achieve a sculpted part that is dimensionally accurate, the kerfwidth must be accounted for when planning the cutting paths, since an offset needs to be applied from the desired surface to compensate for the kerf around the cutting tool.

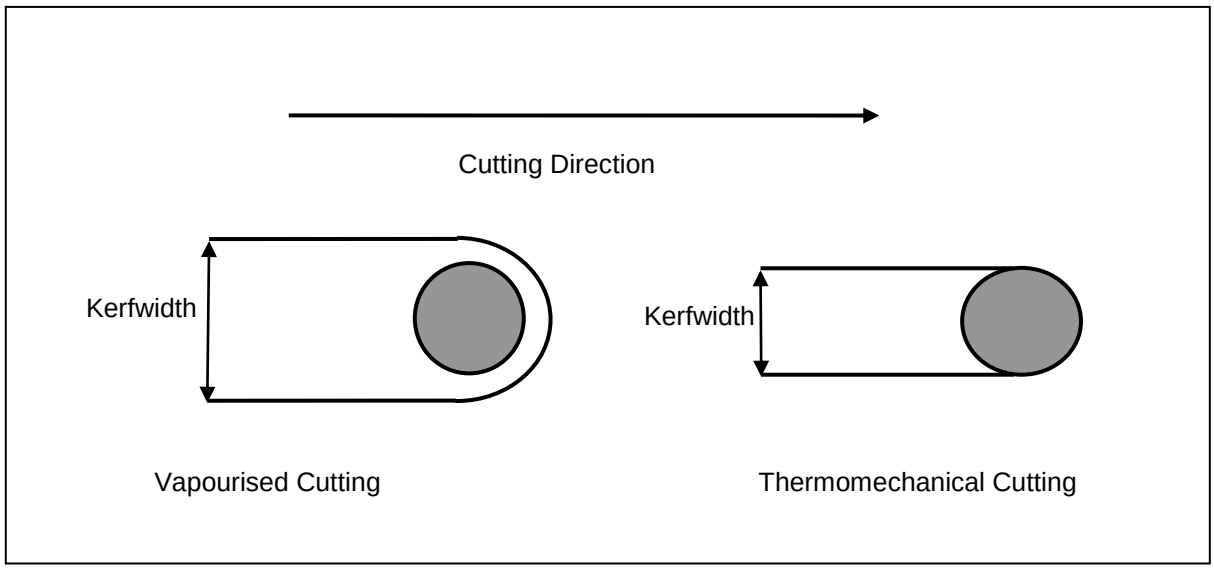

Figure 45: Kerfwidth for Vapourised and Thermomechanical cutting with a hot-wire tool, shown in cross-section

Lay occurs in multi-pass cutting, and is the result of the thermal profile along the engaged length of the cutting tool. As with single-pass cutting, the blade cools the most during cutting at the centre of the engaged length, while the un-engaged length of the tool remains close to the free-air temperature. As a result, there is a thermal gradient along the length of the cutting tool. This results in a surface profile characterised by small ridges parallel to the direction of cut, the spacing of which is largely determined by the path spacing. The nature of the thermomechanical lay is illustrated in Figure 46, and was also annotated in Figure 44. R_{max} is the parameter used to measure this lay, and is the vertical distance between the highest and lowest points on the surface profile.

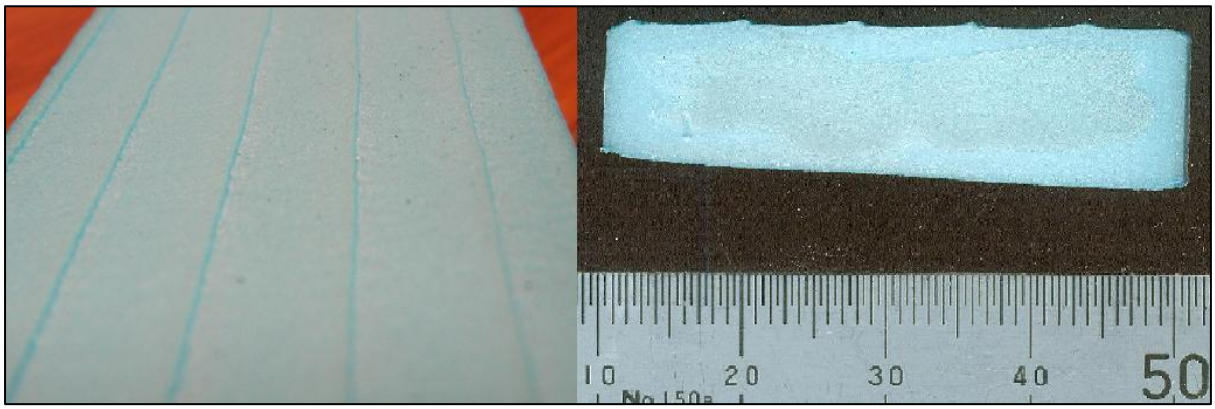

Figure 46: Thermomechanical lay of a surface cut by multi-pass cutting (cross-section on the right)

Surface barrelling, *ΔH* is a major macroscopic deviation present in all surfaces, and caused by the transverse thermal profile of the engaged length of the tool. The centre of the engaged section of the tool is the coldest point, and as you move along the tool from the centre to the end of the engaged section the temperature increases. This results in more ablation of the foam material near the edge of the cut that occurs at the centre, producing surfaces that exhibit a significant degree of convexity, as shown in Figure 47. In steady state cutting this barrelling is of the order of 0.5mm. The exact definition of the measurement parameter *ΔH* is presented in Chapter 5, along with a discussion of its measurement. Surface barrelling is present in all foam surfaces cut by thermomechanical means, but is of most significance in surfaces cut with single tool passes: when the surface in question has been produced by multi-pass cutting the degree of barrelling is much smaller due to the generally shorter engaged tool lengths, and is relatively insignificant compared to the thermomechanical lay and geometric lay, measured by R_{max}.

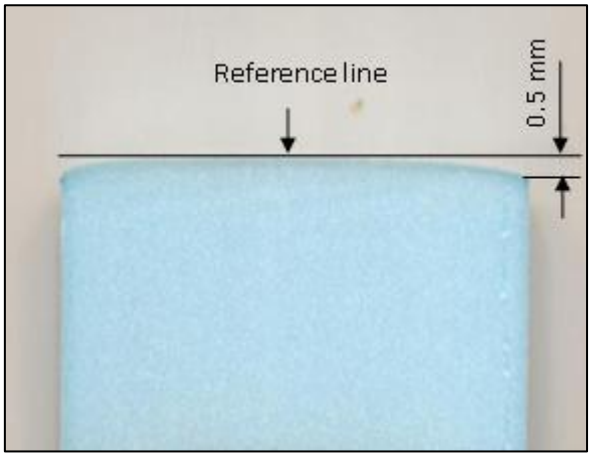

Figure 47: Exaggerated cross section of a surface cut with a single pass of a straight hot wire, to demonstrate surface barrelling ΔH

In addition to these basic errors, under some circumstances surfaces can also exhibit surface flaws. These are melted pockets in the surface, and are the result of molten plastic building up on the wire or blade during a cut: the liquid plastic is carried along with the wire or blade until a sufficient mass is reached, at which point the liquid comes off the blade and melts a pocket into the surface. A representative sample of surface flaws on an arbitrary freeform surface can be seen in Figure 48.

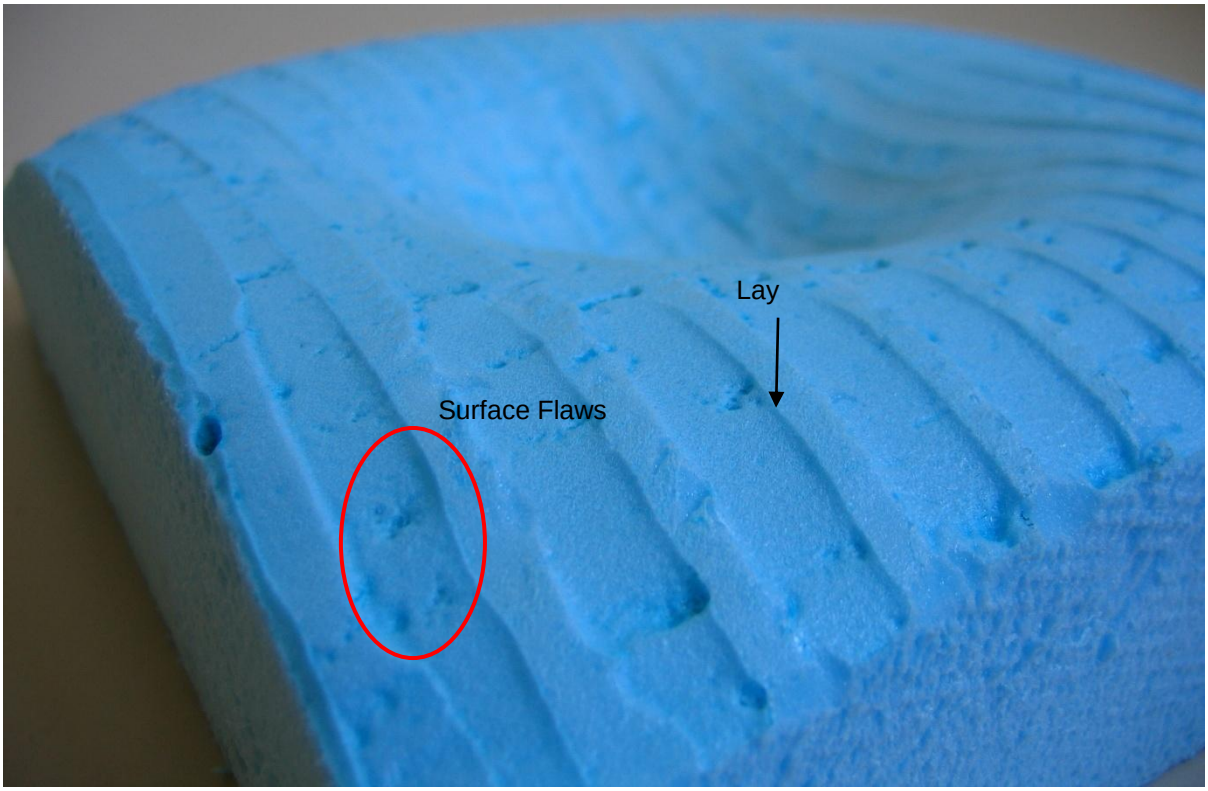

Figure 48: Surface flaws, lay and geometric form

The minimisation of surface flaws in multi-pass cutting was one of the goals of the qualitative cutting strategy work undertaken by Posthuma [7], and it was determined in this case that simply using uni-directional instead of bi-directional tool paths largely eliminated the occurrence of surface flaws, since the molten plastic remaining on the blade was burnt off when the blade was in moving through free air to reposition itself between cutting passes. This toolpath strategy resulted in much neater surfaces, like that shown in Figure 49, where there are no surface flaws. Since a valid method of avoiding these surface flaws already existed, they were not included within the scope of this thesis, but are mentioned here in order to give a full picture of the different aspects of surface quality that are relevant to RFS.

The quality of a surface (i.e. the combination of errors that together constitute the surface) is directly influenced by the cutting strategy used to sculpt the surface. For instance, if the surface being sculpted is planar it may be possible to use a single pass of a taut hot wire or straight hot blade tool, rather than multiple tool passes. This results in a surface with no lay, and therefore no thermomechanical R_{max}, which is clearly of better quality. When sculpting surfaces that have curvature, multiple tool passes are essential and these necessitate a certain amount of overlap between passes: this leads to lay. When deciding on the tool size, tool shape and path spacing to use when making curved surfaces, it is necessary to make a tradeoff between the geometric form (best served by having a large number of passes by a small tool with small path spacing) and the lay (best served by wide tools with large path spacing). Cutting strategy is the term used throughout this work to describe these aspects of part design and manufacturing process that directly affect surface

quality. The variables and interactions that determine the values of each surface quality metric are presented in the following section.

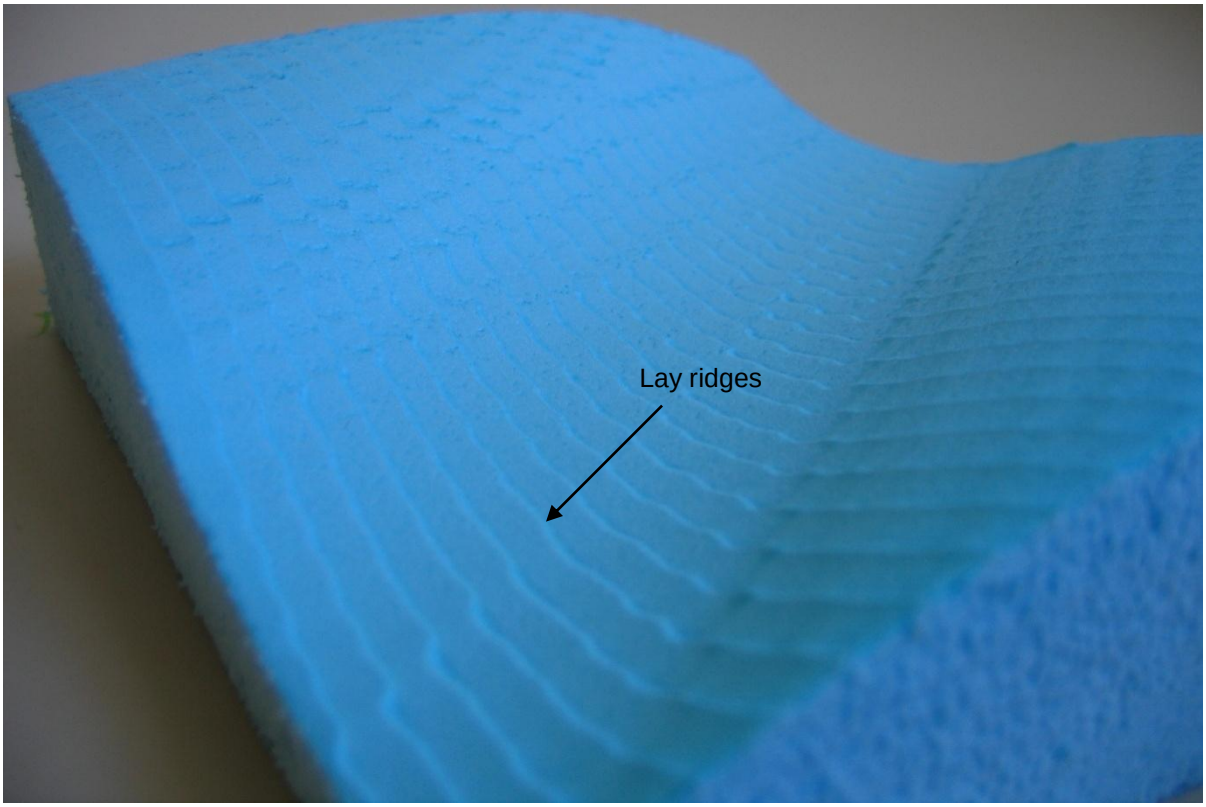

Figure 49: Lay and geometric form

3.3 Factors and Factor Interactions Influencing Surface Quality

The relationships between the different cutting strategy factors and the surface quality output metrics outlined above are complex, and had not been comprehensively mapped before this research. In this section, the factors contributing to the value of each output metric will be documented, and the interactions between these factors will be discussed. The effect of the various factors on other performance criteria for RFS will also be noted, where appropriate. As will quickly become clear, the factors contributing to one aspect of surface quality also contribute to most of the others, but are to some extent in conflict: a combination of factors that produce a smooth and predictable surface texture can, for example, at the same time produce a pronounced degree of surface barrelling ΔH. When developing a cutting strategy for a given part to be produced by RFS, the desired levels of each output metric must be defined and to some extent traded off against each other during the process of choosing input parameter values. It is the necessity for these tradeoffs that really makes the optimisation of cutting strategy for RFS important.

The relationships between factors that have been established and documented here have been developed during this research, based on a combination of detailed investigations of different aspects of surface quality (as documented in the thematic chapters), observation of a large number of

thermomechanical cuts, and systematic analysis of the geometric and physical realities of the cutting process. These dependencies will be simply stated and explained in this section, and evidence for each chain of dependency will be presented in the thematic chapters.

The parameter dependencies of importance to each surface quality metric will be shown in a series of cause-and-effect diagrams (these are essentially modified Ishikawa diagrams). To aid understanding these charts use a standard style convention, as follows. Straight black arrows are used to indicate that the parameter pointed to depends directly on the parameter being pointed from. Curved green arrows demonstrate dependencies between factors. In addition, the factors themselves are colour coded: blue factors indicate measureable output metrics, red factors are controllable input parameters, and yellow factors are dependent intermediate parameters. In the case of the geometric surface errors, surface curvature is shown in red with white diagonal hatching, to indicate that this is controllable by the process planner but only between limits defined by the design and purpose of the part being sculpted. The determination of surface curvature is a design for manufacture (DFM) problem rather than a cutting strategy problem.

The factor dependencies influencing the surface texture are shown by Figure 50: as is shown, the controllable parameters influencing the texture are tool type, material, current and feedrate, while the dependent parameters of importance are the distance along the cut, the effective heat input and the thermomechanical balance.

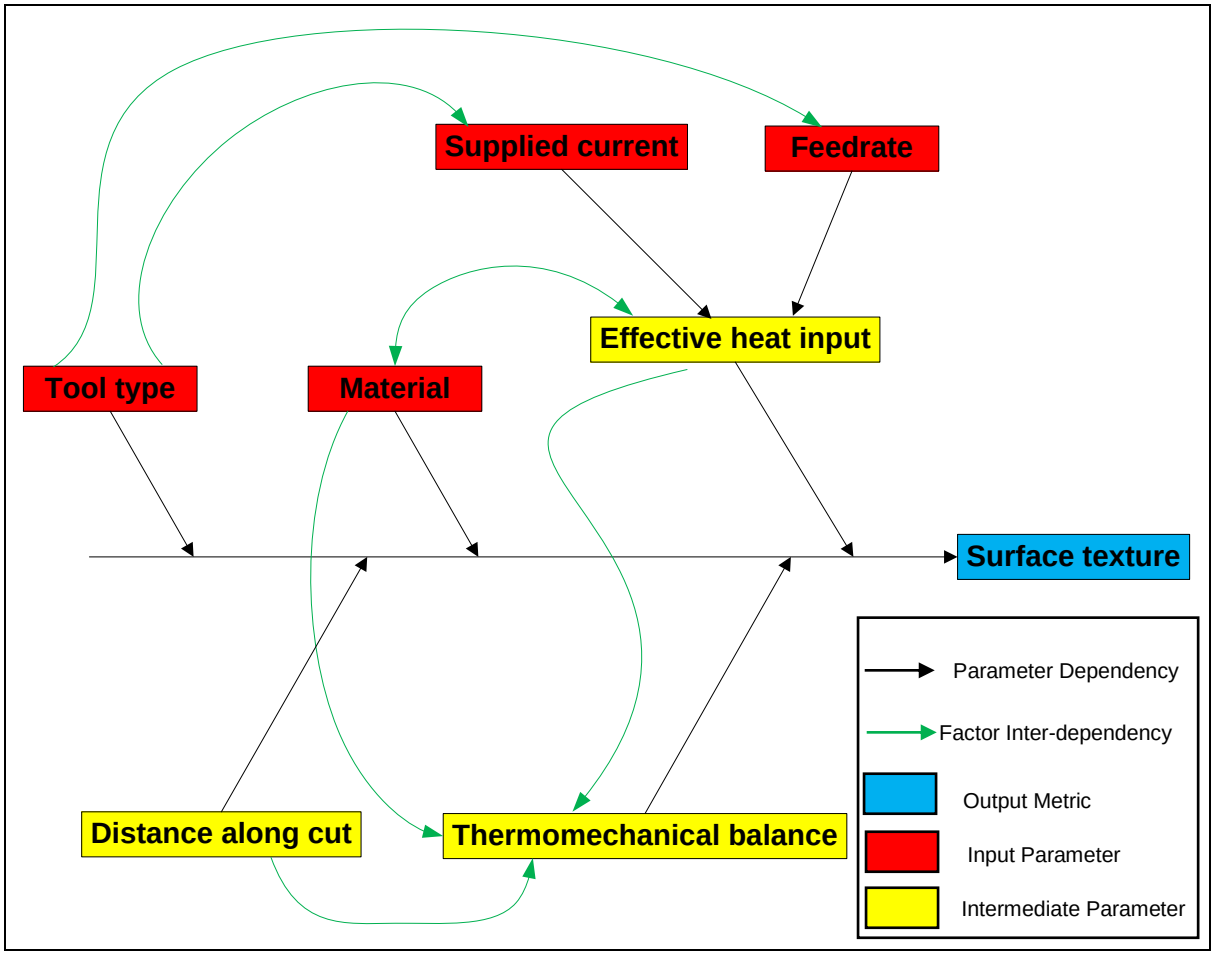

Figure 50: Factor interrelationships contributing to the surface texture

Tool type does not influence the texture through the cutting mechanics, as will be shown in Chapter 4 when the statistically significant parameters are identified by multi-factor regression analysis, but the importance and quantifiable effects of the other parameters vary depending on whether cuts are made with taut hot wires or hot blades. As a result, the tool type has to be considered a factor of importance that must be incorporated into any comprehensive cutting strategy model.

The selection of tool type influences the selection of values for current and feedrate, since the blade tools used for RFS require more current to heat them and can cut much faster without deformation than the wire-based tools. These two factors determine the effective heat input [1, 25], the value of which must be chosen with reference to the exact type of plastic foam being cut, since the heat input required to make a good cut depends on the density and structure of the foam.

Finally, the material, effective heat input and distance along the cut all combine to determine the thermomechanical balance, which influences the exact cutting mode in use at any given point of interest along the cut, whether purely-thermal or thermomechanical. This in turn strongly influences the directionality of the surface texture features, and has a strong effect on the apparent surface texture of the cut surface: this dependency will be described in more detail in Chapter 3.

The factor dependencies influencing the kerfwidth are shown in Figure 51, and are very similar to those that determine the surface texture. For this reason, they will not be summarised in detail: a comprehensive understanding of the interrelationships in questions can be gained from the diagram.

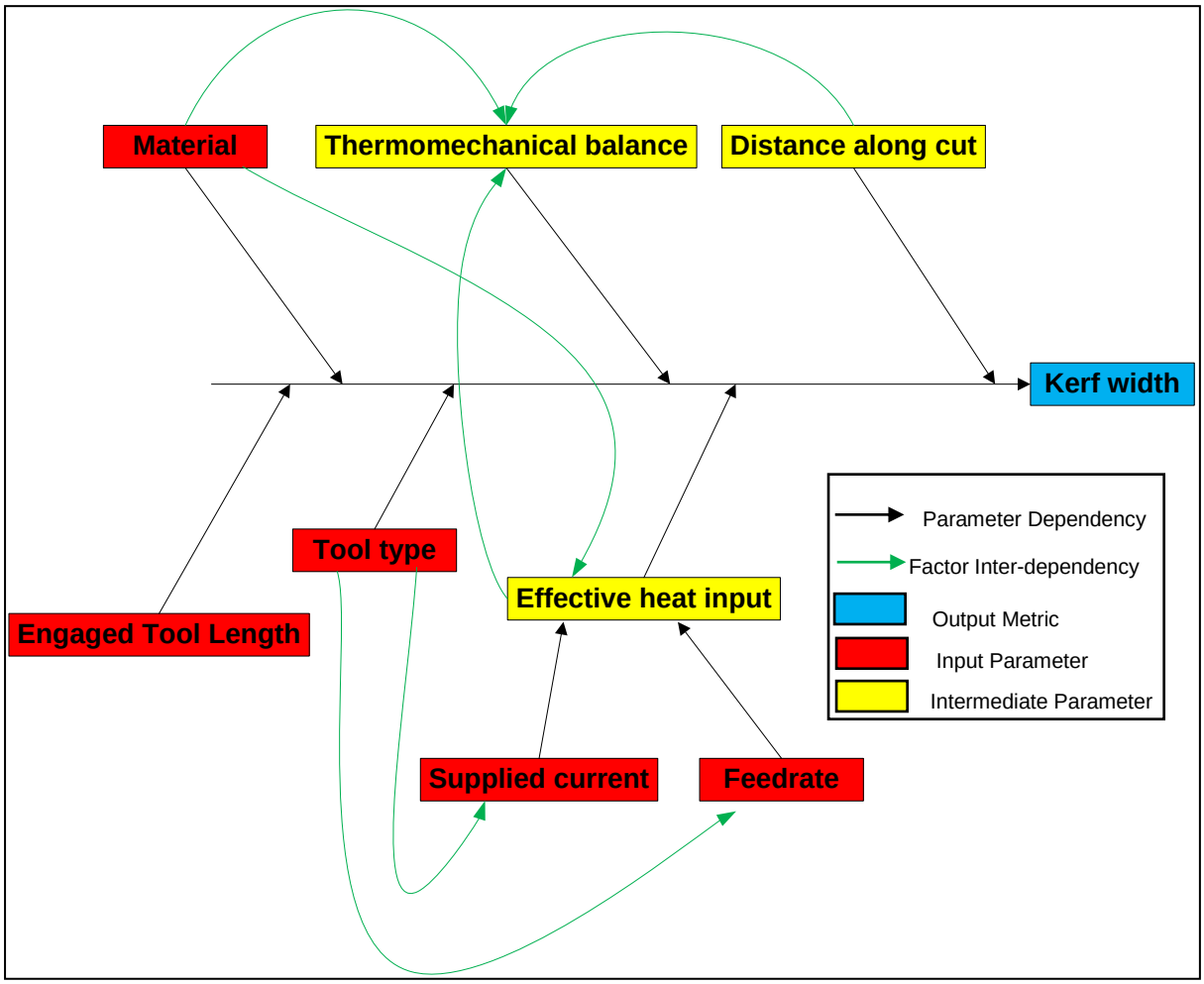

Figure 51: Factor interrelationships contributing to the kerf width

The factor dependencies that control the transverse surface barrelling in a cut are shown in Figure 52. The Tool Temperature Differential ΔT, thermomechanical balance and effective heat input are the most important parameters influencing barrelling, along with the distance along the cut. All of these parameters are also influenced by the material and the tool type.

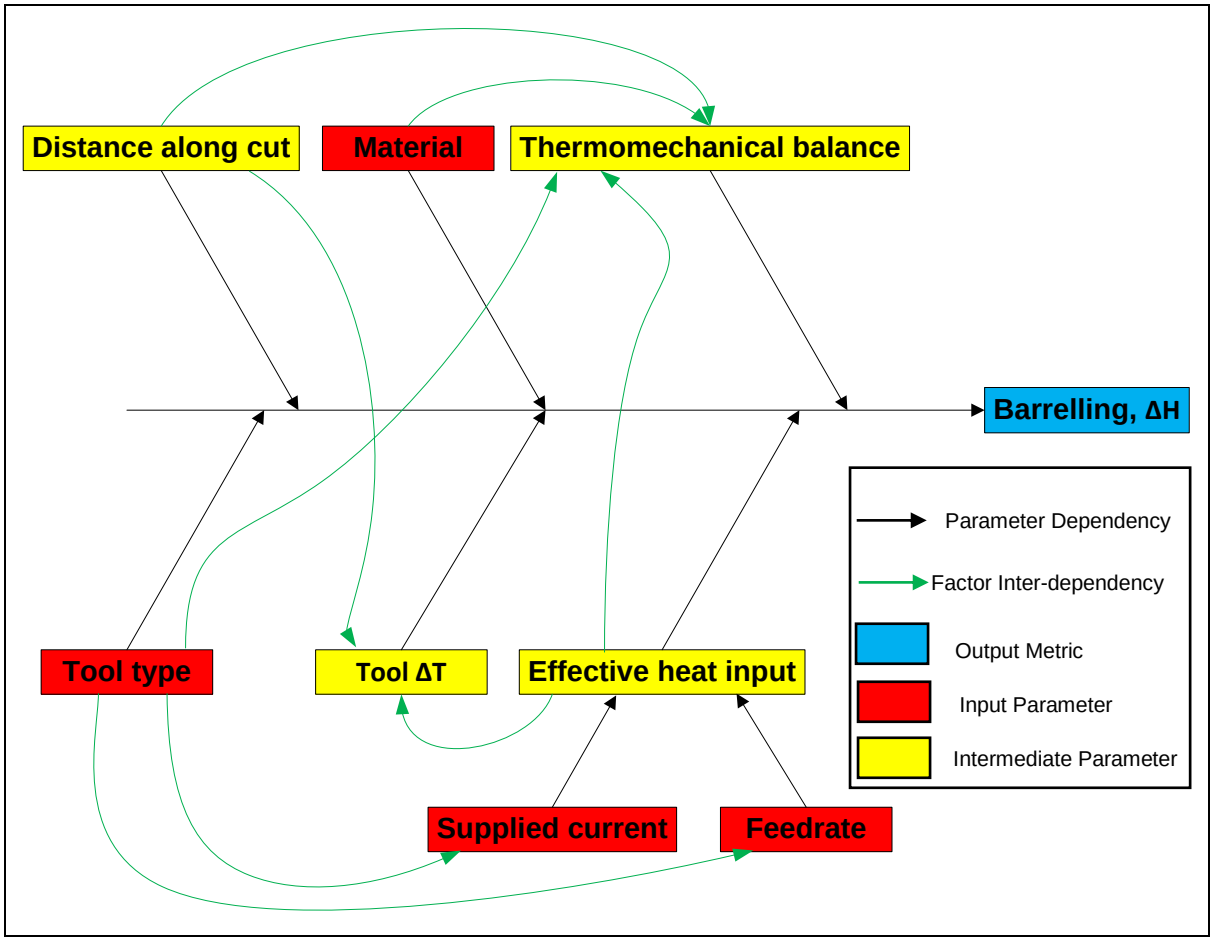

Figure 52: Factor interrelationships contributing to the surface barrelling

Figure 53 shows the factor interrelationships that control the thermomechanical R_{max}, which is only an issue in multi-pass cutting. Most of the factor interactions are generally similar to those controlling the other thermomechanical errors, with the addition of the path spacing, which is mutually dependent on the tool type. That is to say, the value of the path spacing influences the tool sizes that can be used, and the tool sizes available contribute to determining the appropriate path spacing. These are also influenced in turn by the geometric conditions pertaining to the part being sculpted, like the required geometric R_{max} and the curvature of the surface to be produced.

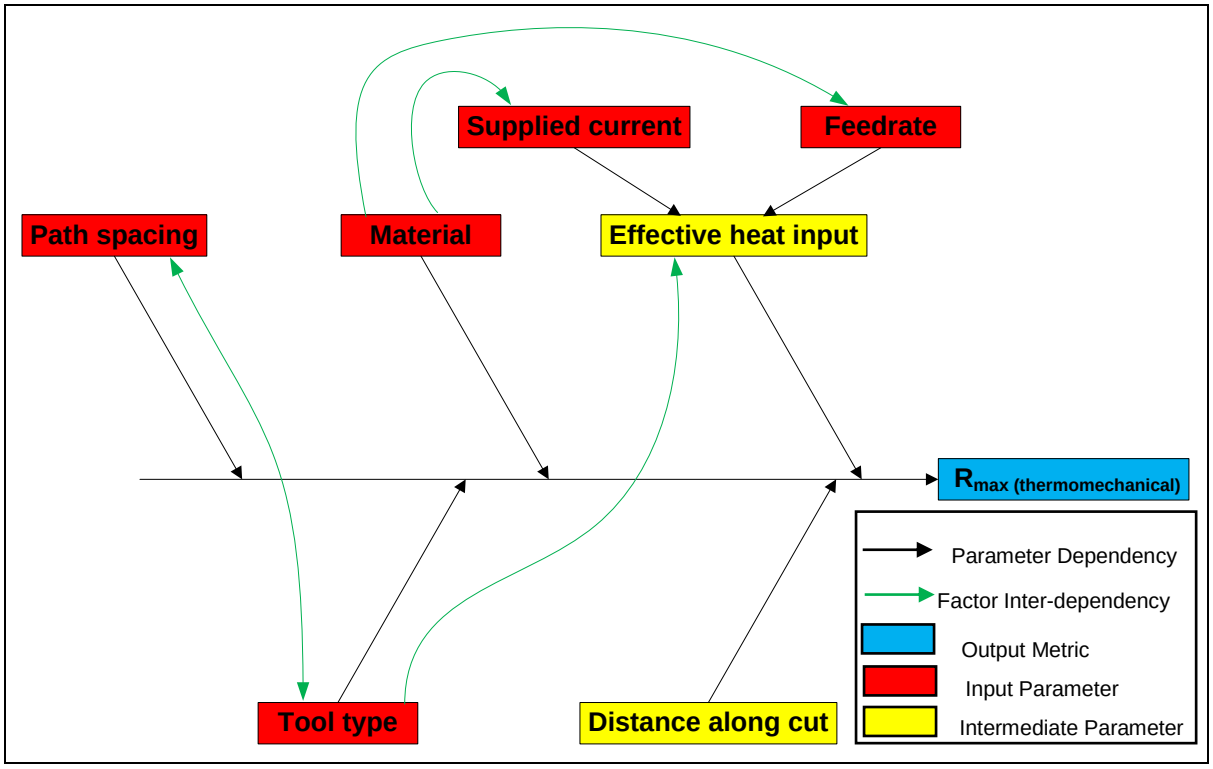

Figure 53: Factor interrelationships contributing to the thermomechanical R_{max} of a foam surface

Figure 54 shows the factor interrelationships that contribute to the geometric R_{max} of a sculpted surface. For the geometric errors, the factor interrelationships that determine the value of the error are generally somewhat simpler than those for thermomechanical errors, since there are fewer input parameters involved and since the geometric errors tend to be determined directly by user-controllable input variables, with no intermediate variables that must be considered. As can be seen, the geometric R_{max} is a function of the surface curvature, tool shape, tool size and path spacing. In addition, the values of these input parameters all mutually affect each other. The interrelationships that determine the peak spacing are the same as those that determine the geometric R_{max}, and are shown in Figure 55.

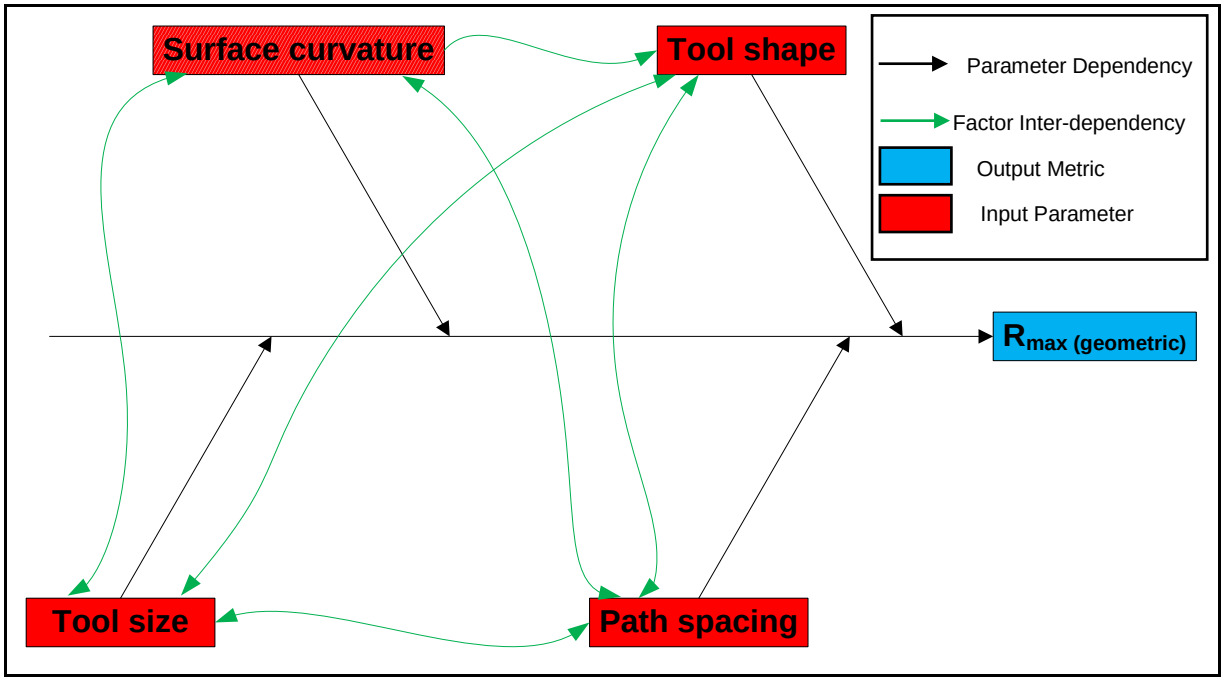

Figure 54: Factor interrelationships contributing to the geometric R_{max}

The factor interactions that contribute to the peak spacing in surfaces cut with multi-pass cutting are shown in Figure 55. As is immediately obvious, the factor interactions for peak spacing are the same as those for the geometric R_{max} in multi-pass surfaces. Despite this, the two metrics must be treated separately because the nature of the surface error is fundamentally different, and because the exact nature of the input factor interactions that control the output metrics are different for each of the two types of surface error. As will be explained in Chapter 6, there is a thermomechanical component to the peak spacing in multi-pass cutting, but the effect of this thermomechanical component is negligible, so in effect the peak spacing is a geometric error and thermomechanical effects can be ignored.

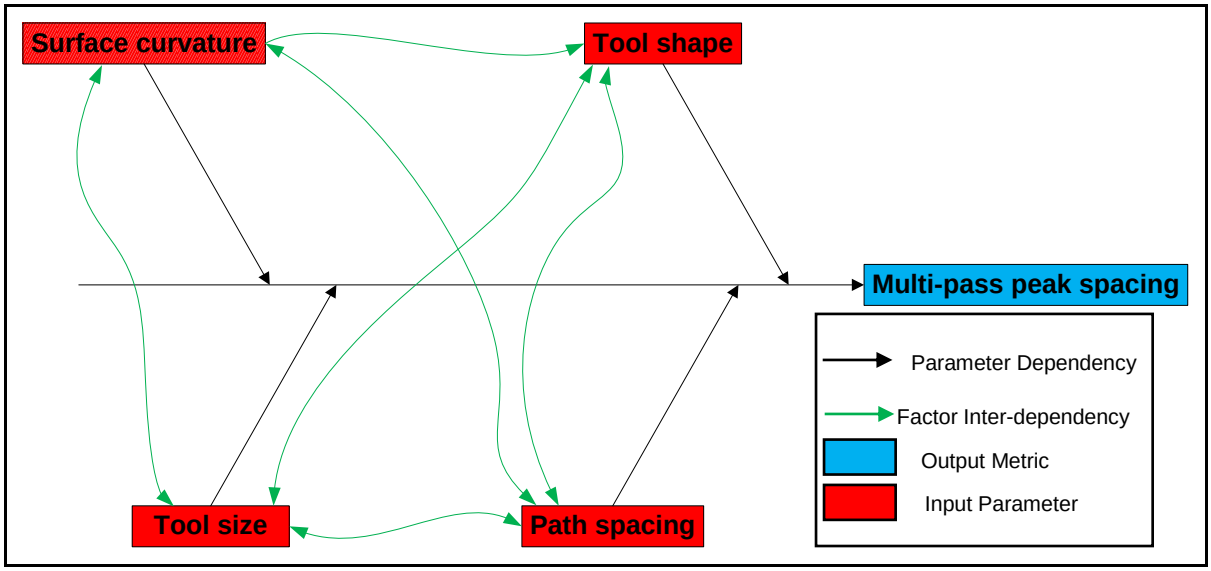

Figure 55: Factor interrelationships contributing to the peak spacing of surfaces produced with multi-pass thermomechanical cutting

3.4 Other Important Cutting Strategy Metrics

When determining a suitable cutting strategy to use when sculpting a given part, the final surface quality is not the only output metric that must be considered. In addition, there are other relevant factors and parameters that must be used to assess the performance of a given strategy. These include, but are not limited to:

- Sculpting time
- Cutting forces
- Tool life

The time taken to sculpt the part must be a factor, since if the production time is longer than necessary then the production cost will be unnecessarily high. Figure 56 shows the factors that control the total production time: from the cutting strategy point of view the production time is most influenced by the tool feedrate and the total toolpath length.

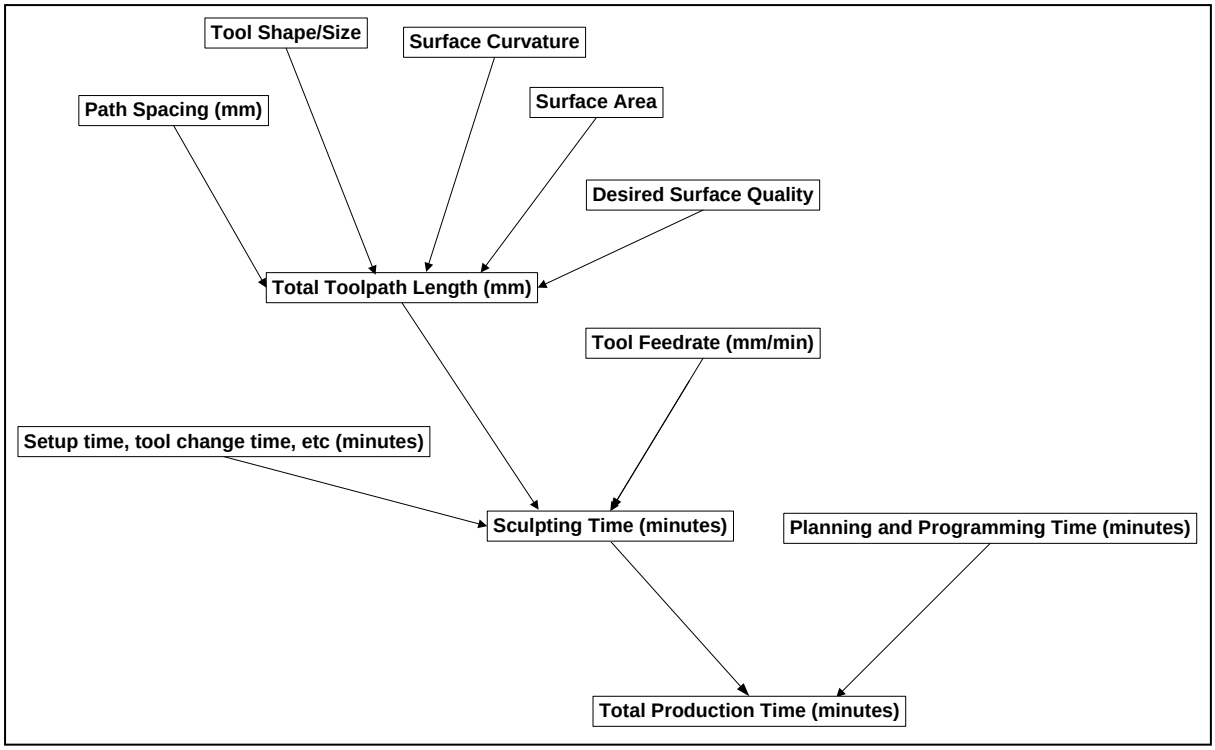

Figure 56: Factors affecting Total Production Time

The cutting force, and in particular the steady-state cutting force, is important because it has a significant effect on the life of the tool, and on the quality of the final surface produced. The force experienced by the tool during cutting changes along the length of the cut: at the beginning of the cut when vapourised cutting is taking place, the cutting force is zero, and as the tool cools down and physical contact begins to occur between the tool and the foam the cutting force starts to increase, until it stabilises at a more-or-less constant steady-state value that depends on the cutting conditions and strategy being used. There is some variation in the cutting force after steady-state conditions have been achieved, but this is mostly due to local variations in the density and structure of the foam the tool is passing through, so does not negate the fundamentally constant nature of steady-state cutting force. Since the cutting force in steady-state conditions is the maximum force that can be experienced for any given set of cutting conditions, attention in this thesis has focused on this value of cutting force, without paying any significant attention to the transient force between initial and steady-state cutting.

The cutting force is an important factor that must be considered when developing a cutting strategy because it has a significant effect on the tool life and tool durability of a given cut. Any tool has a range of different failure modes, and a given critical cutting force above which failure will occur. If the cutting strategy being used can be reasonably expected to produce a force greater than this critical value, then either the strategy or the tool design must be changed to mitigate the risk of tool failure. This is especially important because of the nature of the cutting process: since the tool is dependent on a combination of mechanical slicing and thermal input to cut the foam, tool failure can result in very serious damage to the part being sculpted. This is because tool failure usually results in a break in the

electrical circuit that heats the tool, so if the tool fails during a cut it quickly cools down, leaving the failed tool to be dragged through the foam workpart by the robot. This results in a significant amount of surface ripping and usually results in the workpart being discarded. Having to discard workparts has not been of particular inconvenience to date, since the parts sculpted so far on the RFS system have been relatively small and simple, but if a large, complex part was being sculpted then a single instance of tool-failure could result in the waste of a significant amount of work. This is clearly undesirable for a manufacturing process, so the nature of the cutting force must be well understood and a means found of predicting it before cutting to allow the development of a robust cutting strategy.

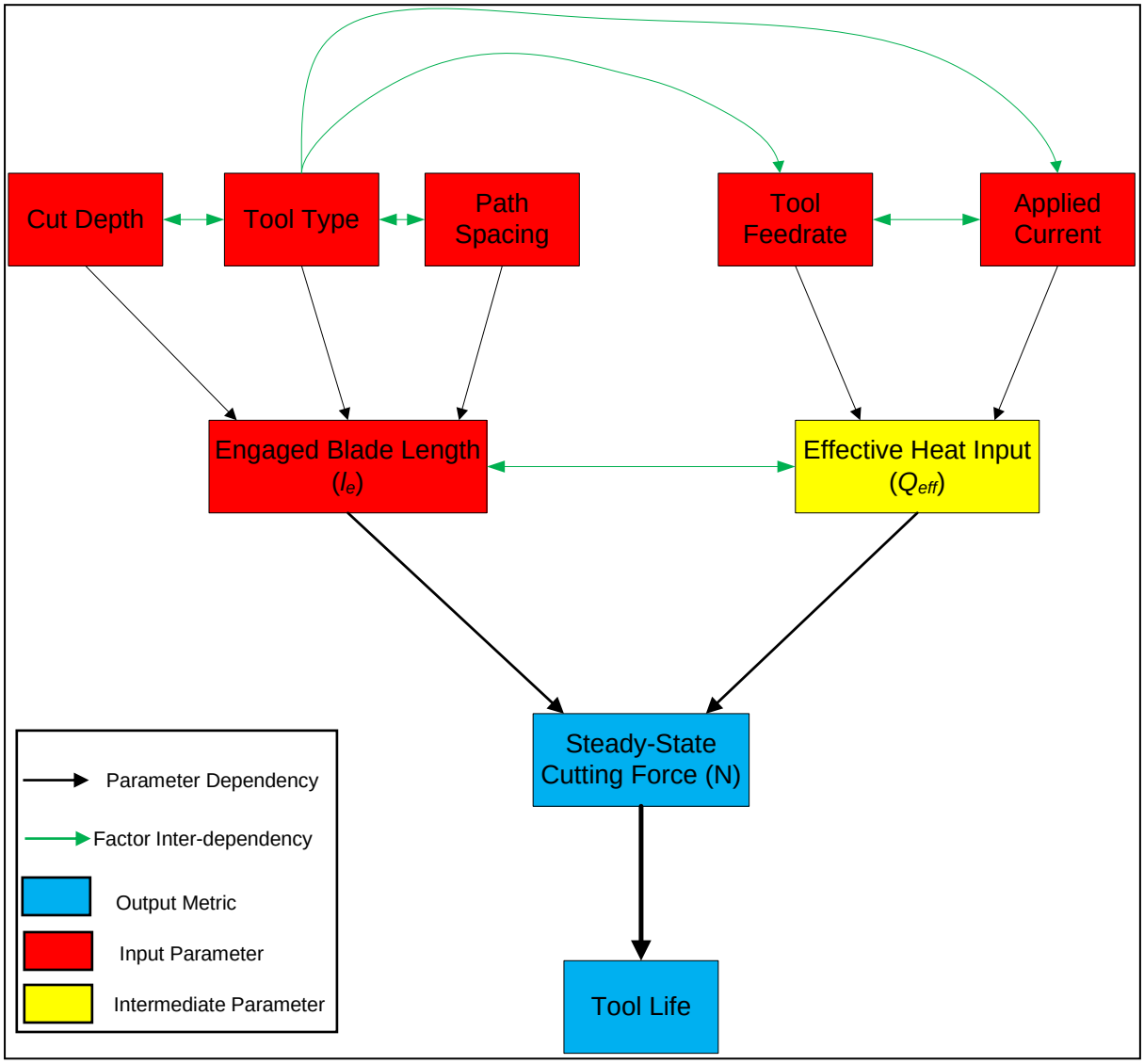

Figure 57: Factors and interactions that influence the steady-state cutting force

In addition to the relationship between cutting force and tool life, there is also a relationship between force and surface quality. As will be shown in the thematic chapters, the thermomechanical balance has a significant effect on all of the output surface quality metrics used, especially the surface texture, with optimum surfaces being produced by a low but non-zero cutting force.

The factor interdependencies that influence the steady-state cutting force are shown in Figure 57. As can be seen, these factors are a combination of thermomechanical and geometric cutting parameters, which must be considered together to analyse the cutting force. The development of this cause-and-effect diagram and predictive models for cutting force will be presented in sections 5.7 and 6.4, below, along with a discussion of the factors influencing the critical cutting force for different tool types.

4 Surface Texture Assessment

The surface texture of polystyrene foam surfaces produced with hot-tool cutting is one of the key metrics by which the quality of the surface can be assessed, and is the most obvious aspect of quality when a surface is inspected visually. In this chapter, the results of a thorough investigation into the nature and causes of foam surface texture are presented. The key conclusion of the investigation was that standard surface texture parameters based on the relative heights of different surface features were not capable of discriminating between different types of foam surface. As a result, a new surface texture parameter, the 10%-Height Contiguous Diameter ($^{\varnothing}S_{10\%}$) is postulated and validated. The use of this parameter to distinguish between different surfaces is also demonstrated.

4.1 Introduction

As outlined in the introduction to this thesis, the texture of surfaces produced by Robotic Foam Sculpting is an important output metric for assessing the performance of the system, and must be considered when developing an optimised cutting strategy for sculpting a given part from foam. Based on qualitative observations of the hot-tool cutting process, it seemed that the surface texture produced by a given cut was a function of the tool type used (wire or blade), the supplied current, the feedrate and the distance along the cut. Apart from the distance along the cut, these are factors that can be directly controlled by the production planner. The distance is partially controllable, since toolpath configurations can be selected to limit the length of any particular cut, but is fundamentally constrained by the nature of the part being sculpted. It was surmised that the controllable input factors act on the surface texture via the intermediate factors of thermomechanical balance and effective heat input. To develop a more complete understanding of these relationships, a detailed quantitative investigation was carried out.

The purposes of this investigation were:

1. To determine a suitable measurement instrument and measurement parameter to express the surface texture of polystyrene foam surfaces cut by a hot tool.
2. To use these quantitative measures to investigate which input factors have an effect on the surface texture produced by the cutting process.
3. To develop models that could be used to predict the expected surface texture for a given set of cutting conditions, so that the cutting strategy could be tailored to the required level of surface quality for a given part to be sculpted.

At the beginning of this research, surface texture assessment for the RFS system had been undertaken at only a very qualitative level, and was dependent on a subjective manual assessment of whether one surface was ‘better’ than another. This presents significant problems for the accuracy and repeatability of results, and makes it very hard to communicate those results easily, and so this investigation was both desirable and necessary. It was first necessary to reconsider the pre-existing surface texture taxonomy developed earlier in the RFS research project, to relate the established

surface texture categories to the nature of the thermomechanical cutting process, and to revise the qualitative categories to separate surfaces produced by different cutting modes.

When a hot wire cuts through polystyrene foam it exhibits consistent thermo-mechanical behaviour. At the initial point of the cut, the wire is at its maximum free-air temperature which is well above the melting point of the foam. As a result, there is a thermal field around the wire that melts the foam without physical contact between the wire and the foam. As the wire cools, it comes into contact with the foam, with increasing degrees of physical contact until the wire cools to such a degree that the foam is no longer being melted but is in fact being mechanically cut by the wire. As the wire temperature reduces and the degree of physical contact between the wire and the foam increases, the cutting force also increases. When the foam is being cut by purely thermal means the cutting force is effectively zero, and starts to increase when physical contact between the wire and the foam begins to occur. These characteristic force and temperature profiles are shown in Figure 58. Eventually the centre temperature and cutting force reach consistent levels in the steady-state cutting region.

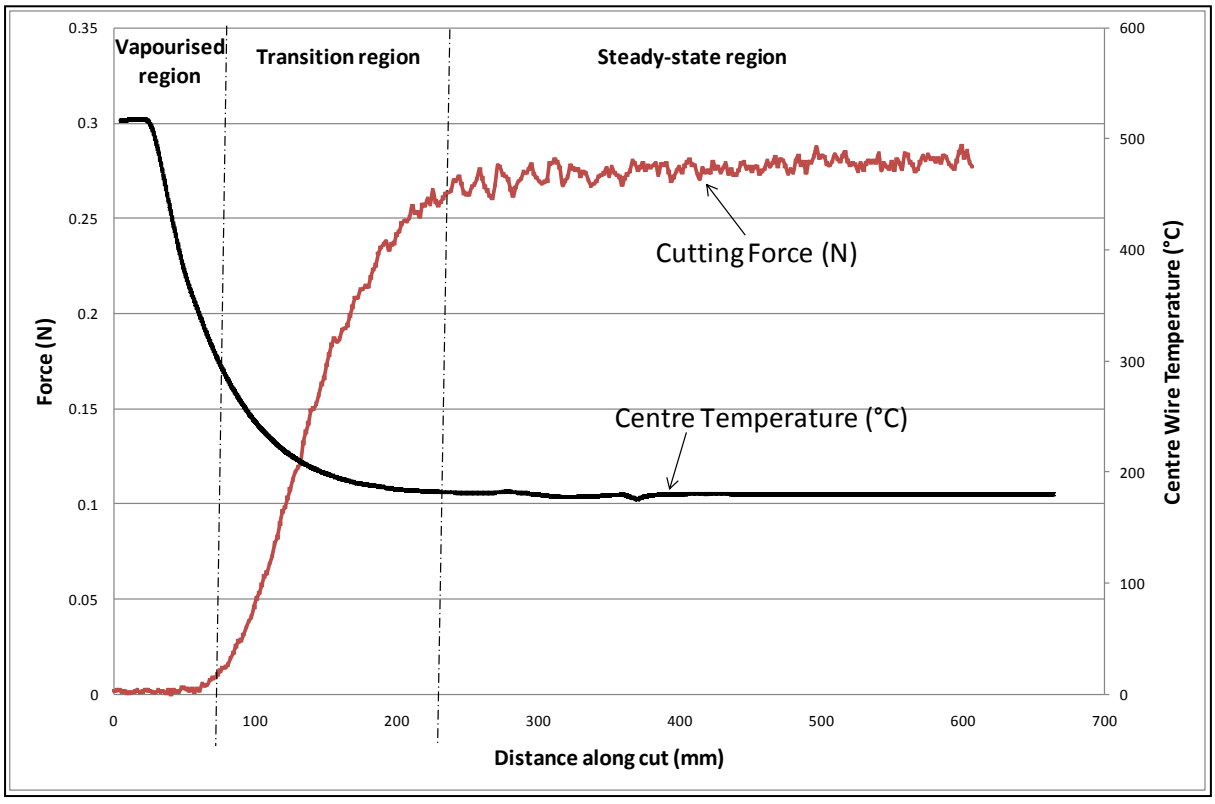

Figure 58: Characteristic centre-cut temperature and force profiles for hot-tool cutting of polystyrene foam

These characteristic cutting force and temperature profiles directly influence the surface finish produced by the cut. When the temperature is high and the cutting force is low (i.e. in the vapourised cutting region) a vapourised surface is produced. When the cutting force begins to increase, the various thermomechanical surface finishes are produced in sequence. Low but non-zero cutting

forces produce smooth surfaces, and as the cutting force increases further visually disturbed and eventually ripped surfaces are produced.

The rate at which the cut progresses through these surface finishes varies depending on the cutting conditions. In cases of low feedrate and high current, each region will last for a longer length of the cut, so depending on the cut length the surface may be vapourised or smooth for most of the cut. Conversely, cuts with low current and high feedrates progress through the different stages of cutting mechanics relatively quickly. The relationship between tool temperature, cutting force, cutting mechanics and surface finish is shown graphically in Figure 59.

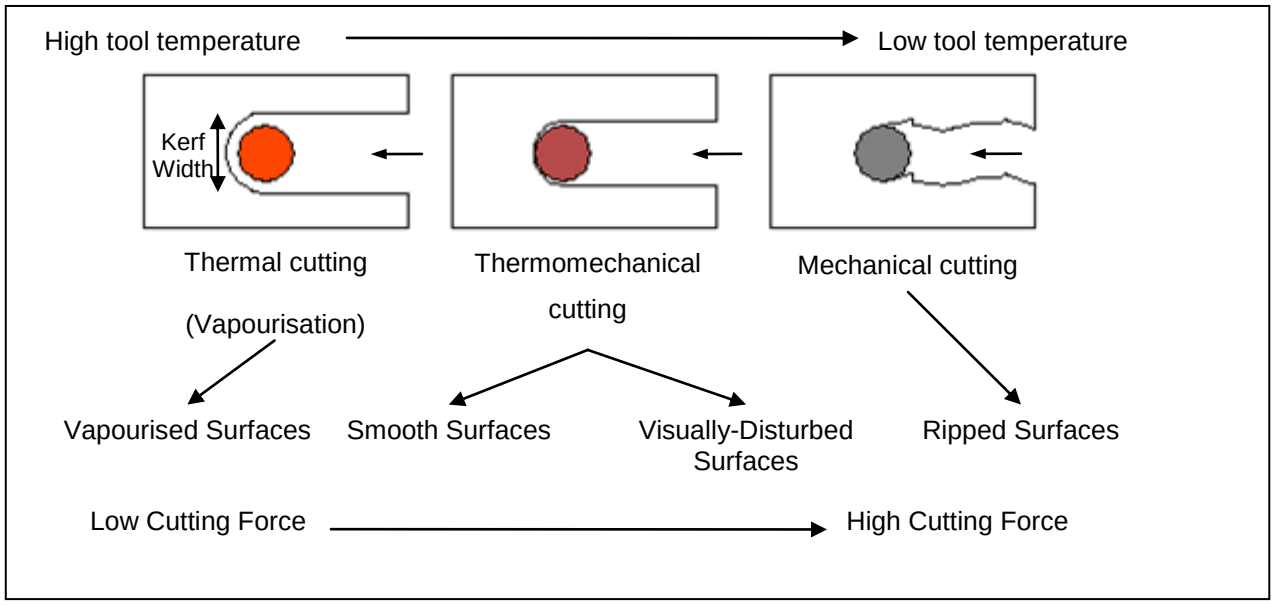

Figure 59: Relationships between tool temperature, cutting force, cutting mechanics and surface finish category

The progression of cutting mechanics along a cut results in a progression of surface types that can be qualitatively distinguished by visual inspection. These surface types form a continuum of their own, as they are directly related to the cutting mechanics continuum described above. Although the changes in the surface are continuous, preliminary surface texture assessment work for the Robotic Foam Sculpting project was based on categorising the surfaces produced into one of four surface categories based on surface features visible to the naked eye. This categorisation work has already been summarised in the literature review, above.

The surface texture taxonomy developed before this research project consisted of six different surface categories: vapourised, smooth, sporadic bubble, bubbled, wavy and ripped surfaces. This system had a number of flaws. The first was that wavy surfaces (which occurred during high-temperature cuts where the tool tension was reduced to prevent wire breakages) were not actually the result of the cutting conditions, but rather the result of tool oscillations, and therefore were not a primary texture category.

The second flaw was that the categories of ‘sporadic bubble’ and ‘bubbled’ were not really very useful. The categories were developed primarily for expanded polystyrene foam, where the ‘bubbles’ resulted from beads of EPS being partially torn out of the surface: when extruded foam was used the surfaces following smooth (associated with higher cutting force) could not reasonably be described as bubbled, although there was a clear difference between these and smooth surfaces and they seemed to be the result of the same local-tearing mechanism.

To rectify these flaws in the surface finish taxonomy, an updated system of categories was developed. This is summarised in Figure 60. Vapourised, smooth and ripped surfaces remain unchanged, while ‘wavy’ has been eliminated as a surface texture category. Sporadic bubble and bubbled surfaces have been consolidated into a single category, called ‘visually disturbed.’ This is more appropriate to both types of foam used in the RFS system, and takes into account the fact that the difference between the two original categories was one of degree rather than of the nature of the surfaces. Smooth and visually disturbed surfaces are both produced by thermomechanical cutting, while vapourised surfaces are cut without any mechanical component.

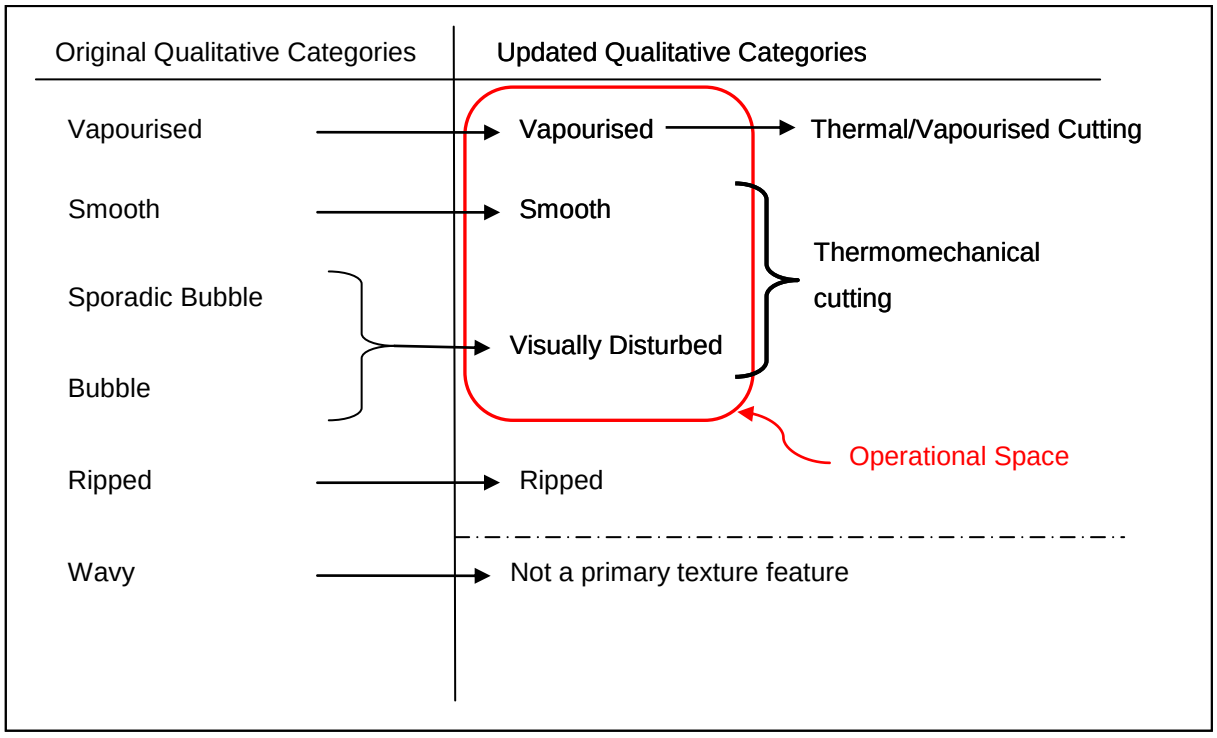

Figure 60: Updated qualitative surface texture categories

It is possible to define an operational space for RFS based on the achieved surface finish. This constitutes the range of surfaces that are produced within the operational space, and includes vapourised, smooth and visually disturbed surfaces. While it might be thought that only ‘smooth’ surfaces would be acceptable, there are other factors than surface finish that must be considered. For example, if surface texture is not the primary consideration for a part being sculpted, but sculpting time is important, it may be desirable to cut visually disturbed surfaces.

Ripped surfaces, which result from very high cutting forces that cause physical tearing of the polystyrene foam on a large scale (as shown in Figure 61, which also demonstrates waviness) are obviously undesirable. Not only are the surfaces extremely rough and unsuitable for any practical application of foam parts, but the high cutting forces that result in these surfaces also substantially reduce the tool life, generally resulting in tool failure within 200mm of the start of purely-mechanical cutting (when cutting with hot-wire tools: the exact tool life under ripped cutting conditions will depend on the tool type, the tool size and the feedrate).

Figure 61: Example 'Ripped' Surfaces, also exhibiting Waviness

The relationship of these surface categories is shown by the morphology diagram in Figure 62 (for a description of the derivation of the Effective Heat Input, Q_{eff}, refer to the literature review). This diagram is based on experimental results for cutting parameters within the operational space with a cut length of 350mm. As can be seen, at the start of a cut a vapourised surface is inevitable for constant-current cuts, and as the cut length increases the surface segues into a ‘smooth’ surface, and then into a ‘visually disturbed’ surface. However, if the effective heat input is sufficiently high, the wire does not cool enough in the cut length to enter the visually disturbed surface zone, and so the smooth zone continues until the end of the cut. It should be noted that, although trendlines have been fitted to this data in Figure 62 to indicate the boundaries between the different surface category zones and to show how the surface categories vary depending on distance along the cut and effective heat input, these boundaries are not reliable (as can be seen by the poor fit between the data points and the trendlines). Therefore this diagram cannot be used to reliably assess the surface texture that will be achieved for a given effective heat input and distance along the cut.

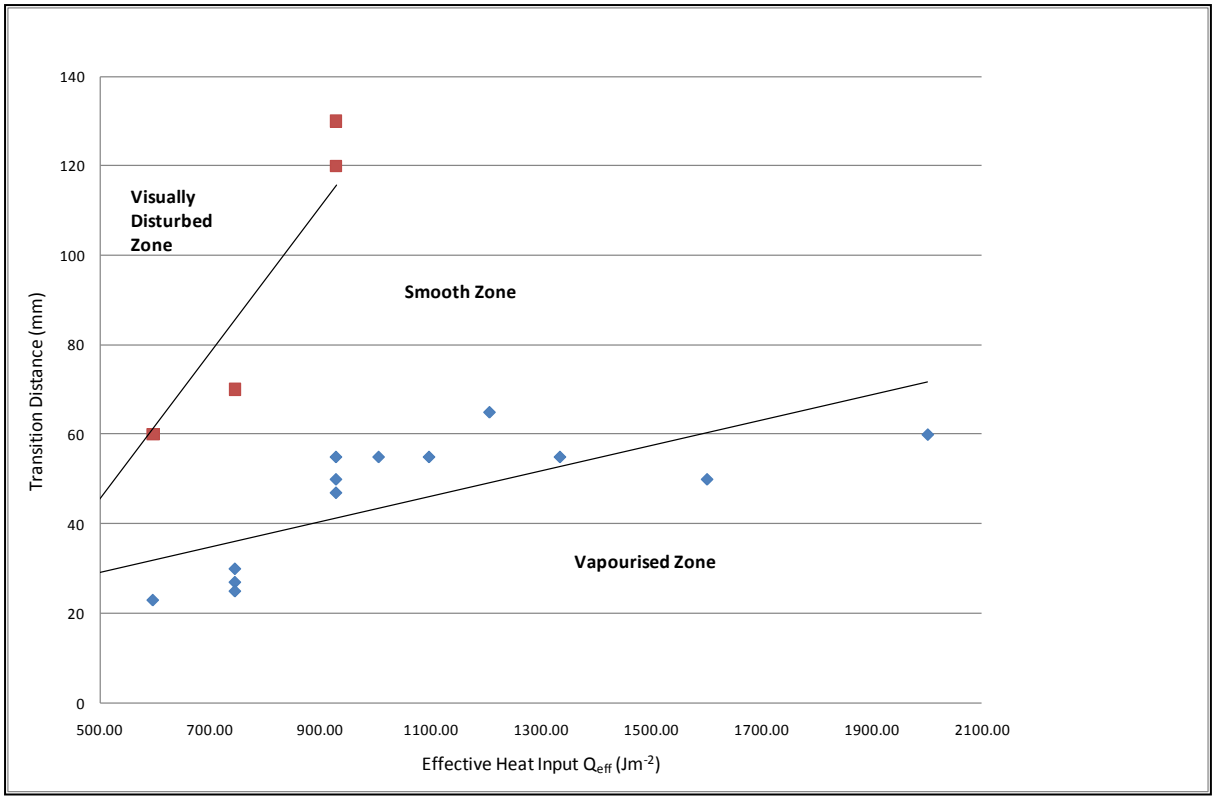

Figure 62: Surface Category Morphology Diagram

These surface categories allowed preliminary assessments of the performance of the Robotic Foam Sculpting system, and allowed the selection of cutting conditions to achieve a desired surface type, but the qualitative nature of these measures imposed some major limitations. Most importantly, the classification of surfaces into different categories is inherently subjective, open to misinterpretation and dependent on experience. As a result, assessment of the surface finish based on surface categories is not particularly accurate or repeatable. It is also very difficult to communicate meaningful results to anyone who does not have samples of each surface category.

Based on this preliminary and qualitative work, a need was identified for a method of quantitatively and accurately measuring the surface texture of polystyrene foam surfaces that had been cut by hot-wire tools. The desired outcomes were:

- An accurate and quantitative method of gathering surface texture data for polystyrene foam surfaces.
- A better understanding of the features of surface texture that determine the visual nature of these surfaces.
- A useful quantitative measure of the surface texture of foam that was consistent, repeatable and communicable.
- Threshold values of this quantitative parameter for the different surface finish categories that have already been identified.

- A statistical model that could predict the expected surface texture of surfaces cut with hot-wires and hot-blades based on the values of input parameters, so that the texture could be considered along with other output metrics to optimise the cutting strategy used to sculpt a given part.

The first step towards achieving these outcomes was to identify the basic components of a surface and the most appropriate method of measuring them.

4.2 Surface Definition

Any surface is made up of up to four superimposed components (in order of increasing feature size): primary texture (often loosely referred to as surface roughness), waviness, lay and geometric form. Each of these is caused by different factors or combinations of factors, and in sum constitute the definition of the surface. The four components are measured separately because they are due to different causes and are typically of significantly different sizes. Geometric form is generally considered to be in a separate category of surface metrology from primary texture, waviness and lay, and so will be dealt with separately in later chapters of this thesis. Diagrammatic representations of these different surface components can be seen in Figure 63 and Figure 65.

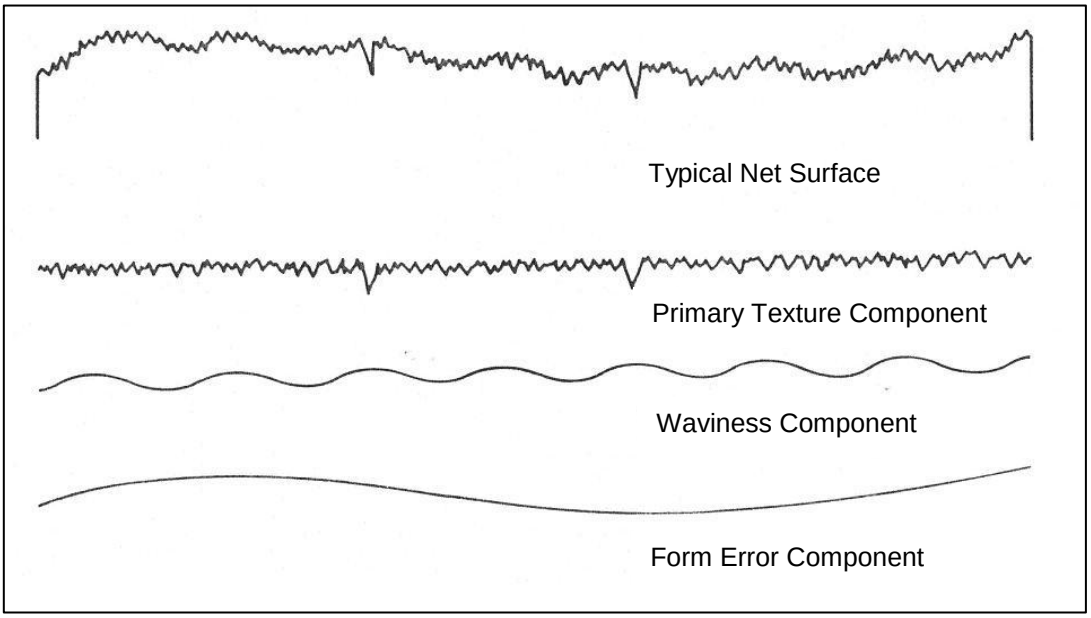

Figure 63: Roughness, Waviness, and Errors of Form [51]

Roughness or primary texture (referred to here as ‘texture’) is the surface component that generally has the smallest feature size. Surface errors in this category are the result of inherent factors in the production process. In the case of hot-tool cutting of polystyrene foam, texture is most influenced by tool feedrate, wire current and the length of the cut: in other words, texture is a thermomechanical error.

Waviness is the result of factors that are unique to the particular tool used for producing the surface: in most cases tool deflections, vibrations or chatter will result in waviness. In the case of polystyrene foam surfaces, waviness occurs only under certain cutting conditions, and seems to be largely influenced by the tension of the hot-wire. Waviness has not to date been observed in hot-blade cutting.

Lay is used to describe the predominant surface pattern, and is a result of the production method used. For instance, a surface which has undergone a facing operation on a lathe will exhibit Circular lay, while a surface that has been milled in multiple tool passes will exhibit parallel lay patterns. In the polystyrene case, lay is not exhibited by surfaces that have undergone a single-pass hot-wire cut, but is found in surfaces that have been cut using multiple passes of a hot-blade tool. A parallel lay pattern can be seen in Figure 64, with a cross-section to the right showing the approximate magnitude that lay can achieve in foam surfaces (the top surface is the multi-pass cut surface in this case). As can be seen, lay errors of ≈0.5mm can be expected in steady-state conditions, but this naturally only happens in multi-pass cutting since single-pass cut surfaces do not exhibit lay.

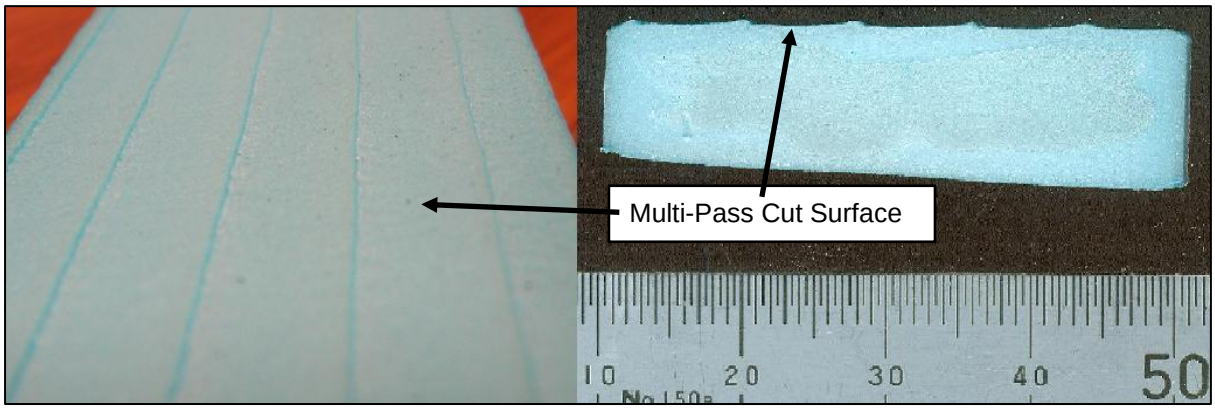

Figure 64: Examples of Lay in a Polystyrene Surface (cross-section to the right)

Figure 65, below, shows how roughness, waviness and lay combine to form a surface (in the absence of any geometric form errors). Because these different components of a surface are the result of different causes, it is necessary to separate them from each other for measurement purposes. In order to separate roughness from waviness, the standard procedure is to measure roughness only along a relatively short length, referred to as the cut-off length. This length is sufficiently short that the long-wavelength effects of waviness are negligible and roughness-type errors predominate.

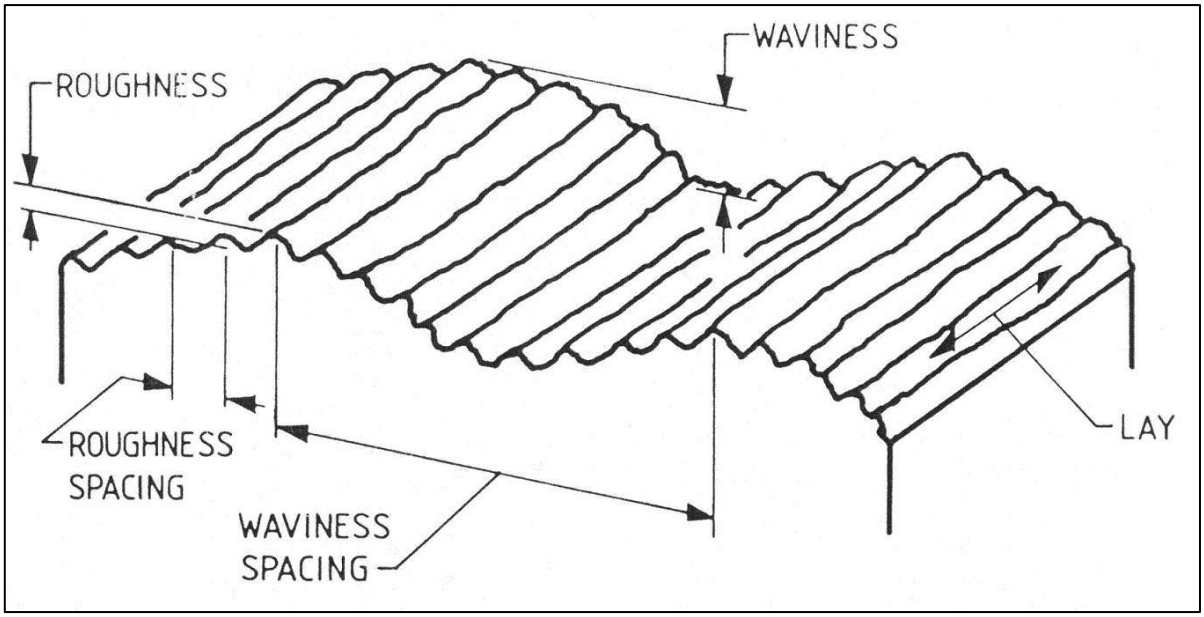

Figure 65: Surface Characteristics and Terminology [51]

For the purposes of this research, most attention has been focused on primary texture (roughness), lay and geometric form errors. Waviness has been largely ignored as it usually only occurs under cutting conditions that result in very rough, ripped surfaces. Since the main goal of this research is to optimise the Robotic Foam Sculpting system for manufacturing purposes, and since the ripped surfaces are inherently inaccurate and undesirable from a manufacturing point of view, these cutting conditions were not investigated since they are most unlikely to be used in practice. Finally, because of the relatively large magnitude of lay in multi-pass hot-blade cutting of foam, lay has been treated as a geometric form error and has been investigated elsewhere (see Chapter 5). Of the different components of a surface, the most important for the performance of RFS are geometric form and lay, since multi-pass cutting with blades is necessary to sculpt complex freeform objects, and since these errors have much greater magnitude than the surface texture. Surface roughness is primarily relevant to single-pass taut hot wire cutting: since this is sometimes useful when sculpting objects, the causes of variation in roughness have been investigated in some detail.

Surface texture of surfaces is expressed in engineering through a wide range of numerical parameters. These have been developed over many years, and are used to express different aspects of the surface texture. Only a few such parameters have been used in this research, and these are summarised in Table 4. Detailed definitions of these parameters will not be given here but readers who wish to know more can refer to the referenced source material.

Table 4: Summary of Surface Texture Parameters

Parameter	Definition
R_a	**Arithmetic Average Roughness** Average deviation of the surface from the mean line. Profile based [52].
R_{max}	**Maximum Surface Deviation** Distance from highest peal to lowest valley of the surface profile within the sampling length. Profile based [51].
R_z	**Ten-Point Height** Average of the five largest peak–to–valley distances within the sampling length. Profile based [53].
S_a	**Arithmetic Mean Surface Height** 3D areal equivalent of R_a. Average value of all the surface departures from the mean plane [54].
S_q	**Root Mean Square (RMS) Deviation** Root mean square of all surface departures from the mean plane within the sampling area [54].
S_{sk}	**Skewness** Measurement of the asymmetry of the surface deviations from the mean plane. Used to indicate the presence of 'spiky' features [55].
S_{ku}	**Kurtosis of topography height distribution** Provides an indication of whether the surface is spiky or flattened. S_{ku} values greater than 3 indicate a spiked surface height distribution; S_{ku} values less than 3 indicate a flatter distribution [55].
S_{tr}	**Surface Texture Aspect Ratio** Provides a measure of surface isotropy based on the areal autocorrelation function. A S_{tr} of 1 indicates a perfectly isotropic surface, and a S_{tr} of 0 indicates a perfectly anisotropic surface [56, 57].

4.3 Measurement of Foam Surface Texture

The technical challenge encountered when seeking to measure the texture of polystyrene foam was not inconsiderable, due to the nature of the material and the size of the surface features that needed to be measured. Both of these are significantly dissimilar to surface texture measurement tasks normally encountered in engineering metrology, since the foam material is soft (and therefore easily damaged) and the surface features are much larger than those found on, for example, machined metal surfaces. This section presents a summary of the measurement challenge that had to be overcome to produce useful surface texture results, an evaluation of the different measurement options identified to solve this problem, and a summary of the operating principles of the chosen method of measuring surface texture, confocal microscopy.

4.3.1 Considerations for the Measurement of Foam Surface Texture

The measurement of the surface texture of polystyrene foam presents a number of challenges that are not encountered when measuring the surfaces of parts made of, for instance, metals. The most crucial difference is that polystyrene foam is a cellular material, and therefore mostly consists of air. Whereas metals have solid grains that (in terms of surface metrology) are significant only on microscopic scales, the cells of polystyrene foam are much larger and have much more influence on the surface properties of the material when it has been cut by a hot-wire. These considerations have significant bearing on the selection of a suitable instrument for measuring the surface roughness, as outlined below.

Figure 66 shows an image of an approximately isometric image of an extruded polystyrene foam sample that has been cut by a hot wire. This image was obtained using a Scanning Electron Microscope (SEM) after the sample had been sputter-coated in gold to give the sample some electrical conductivity. One of the visible surfaces is thermomechanically cut, one is the as-manufactured edge of the XPS sheet, and the third is an internal view of the foam (visible because the foam was physically sectioned with a razor blade during sample preparation). These different surfaces are annotated on the figure. As can be seen on this view, the cells of XPS have a diameter of the order of 100µm, or 0.1mm, and so can be expected to have a significant effect on the texture of a foam surface. Because of this cell size, for a measurement instrument to be suitable for measuring the texture of foam surfaces it had to be able to accommodate a surface height variation of at least 100µm, and probably more given that some surface features exhibited height variations greater than this (particularly in some ‘visually disturbed’ surfaces where the surface height could vary by up to about 2mm). This sort of range in surface feature height is not normally encountered for the primary texture of surfaces produced by conventional manufacturing processes, so the problem of finding a way to measure the surface texture of foam is somewhat more difficult than simply finding an off-the-shelf texture measurement process.

Since the cell size of XPS foam is approximately 0.1mm, and since the surface feature size is likely to be related to the cell size, an instrument needed to have lateral and vertical resolutions of at least 10µm in order to be suitable for the measurement of foam surface texture (based on the rule of thumb that the accuracy and resolution of a measuring instrument should be 10% of the expected feature size).

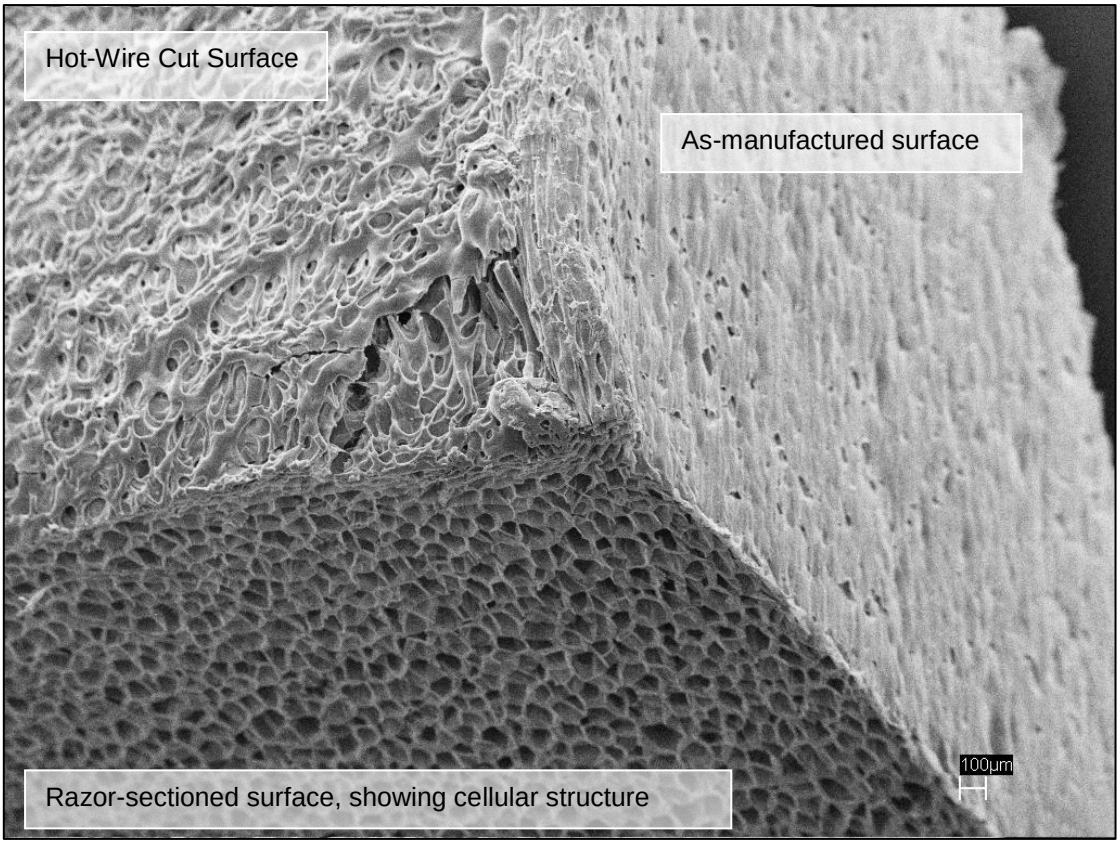

Figure 66: SEM Image Showing Cellular Structure of Extruded Polystyrene Foam

The final consideration for selecting a surface texture measurement device was related to the physical strength of the foam. Since XPS foam is only 2% polystyrene by mass (the remainder being air) and since polystyrene is quite soft, it was necessary to consider the possibility of surface damage occurring during measurement. When a stylus-based surface measuring instrument (Taylor-Hobson Tallysurf) was trialled, it was found to scratch the surface during measurement, and so return a distorted measure of roughness. For this reason, it was desirable for the chosen measuring instrument to either have a stylus that applied a very small load to the surface or to be entirely non-contact.

4.3.2 Evaluation of Alternative Measurement Systems

Once the basic considerations for measuring surface texture of polystyrene foam had been established, it was possible to investigate different measurement techniques and tools, and to eventually select one for use during experimental investigations. A wide range of different tools exist and were considered, but only the final shortlist of options will be discussed in any detail here. The various specifications of the shortlisted instruments are summarised in Table 5.

Due to the easily-damaged nature of the foam, common stylus-based instruments like the Taylor-Hobson Tallysurf were only briefly considered: the only instrument on the shortlist that operates by physical contact is the Ambios XP-2, an instrument that exerts a tip load of only 10mg. This instrument is essentially a micro-scale Coordinate Measuring Machine, and is capable of very high resolution measurement. However, due to the design of the instrument the largest surface area that can be measured is a square patch 3 - 4mm on each side. Since the cells of XPS foam are ≈100µm in diameter, a patch this size would give an insufficient profile length for accurate measurement of roughness, and would be too small to contain some of the surface features expected on a surface, especially surfaces in the 'visually disturbed' category. An example of one of these surface patches (a vapourised surface) can be seen in Figure 67. Finally, the most geographically proximate of these instruments was in the USA, so measurement of samples would be expensive, time consuming and inconvenient.

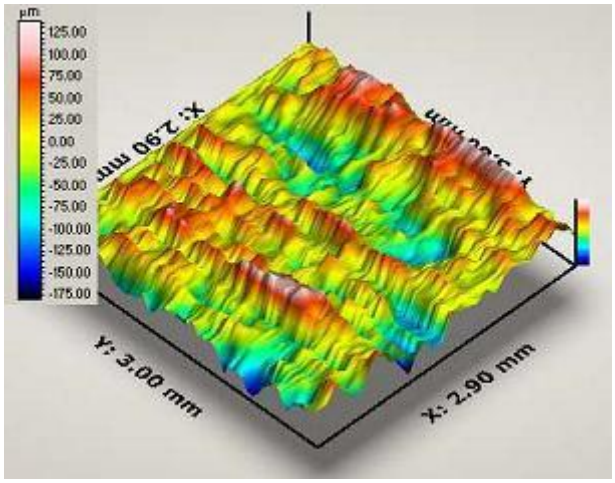

Figure 67: Ambios XP-2 Surface Output

The shortlist of non-contact surface measurement instruments was somewhat longer. The options here included the NewView 600s and 6300, the Proscan 2000 and the Leica TCS-SP5 confocal microscope.

The two NewView instruments both had acceptable resolution and accuracy, but suffered from the same limitations on surface measurement area as the Ambios XP-2, except that in the case of the 6200 the surface patch could have sides up to 14mm long and this could be increased by stitching adjacent surface patches together. However, despite being able to investigate a larger area the

NewView 6200 could only accommodate a vertical range (i.e. peak to valley height, or R_{max}) of 150 µm, which was too small a range to handle the expected 200 – 300 µm feature sizes for XPS surfaces. Finally, the nearest available instrument was in Singapore, and a number of trial samples went missing in transit when attempts were made to test this instrument, so this instrument suffered from the same geographical drawbacks as the Ambios XP-2 with additional reliability concerns.

The Proscan 2000 was a similar instrument, except that it operated on a chromatic spectroscopy principle rather than white light interferometry. This instrument could accommodate a surface height range of up to 10mm, and a surface sample size of 100mm by 150mm. Additionally, the lateral resolution was specified by the manufacturer as 0.3µm, which was the best resolution achievable by any of the shortlisted measurement options. However, for the purpose of measuring polystyrene foam surfaces this resolution was deemed excessive. Since the only available Proscan 2000 was in the United Kingdom, with all the difficulties of inconvenience, expense and danger to samples that entailed, it was decided that the Proscan 2000 was not the best available surface measurement instrument.

The instrument that was finally selected was the Leica TCS SP5 confocal microscope. A confocal microscope is an instrument with the ability to optically section a surface and capture a stack of surface images in the direction normal to the surface, from which a topographic image of the surface can be constructed (See Section Surface Texture Measurement using Confocal Microscopy). This instrument had an effective lateral resolution of 2.95µm (more than adequate for the expected feature sizes on foam surfaces) and a vertical resolution that could be tailored to the requirements of the samples simply by altering the spacing between the different surface slices. The confocal microscope did have the drawback that with a 10x magnification objective lens (the lowest magnification available) it could only capture a surface patch 1.51mm on a side, but this drawback could be overcome by knitting adjacent surface patches together to produce a longer profile length for roughness measurements. Finally, the confocal microscope had the significant advantage that one was available on the University of Canterbury campus, which meant that experimental procedures would be faster, there would be no shipping delays, samples would not go missing in transit and there would be no difficulty if supplementary measurements needed to be made. It was decided that the advantages of the confocal microscope outweighed its one disadvantage, and so the Leica TCS SP5 was selected as the best available instrument for surface texture measurement.

Table 5: Surface Texture Measurement Tools Evaluation Matrix[1]

Instrument	Surface Contact?	Technique	Form Capable?	Lateral Resolution	Vertical Resolution	Field of View	Vertical Range	Availability
NewView 6200	No	White-light interferometry	No	9.5 *μm*	<0.1nm	≤14mm, more with field stitching	150 *μm*	Singapore
NewView 600s	No	White-light interferometry	No	5.18 *μm*	<0.1nm	≤3.5mm	≤150 *μm*	Singapore
Ambios XP-2	Yes	Stylus contact	No	2*μm (stylus radius)*	1Å at 10 *μm*	≤4mm	400 *μm*	USA
Ambios Xi-100	No	Phase-shifting interferometry	No	4*μm*	0.2nm	2.016mm x 2.016mm	49 *μm*	Australia
Proscan 2000	No	Chromatic spectroscopy	Yes	0.3*μm (50 μm spot size)*	0.3 *μm*	Scanning, 150mm x 100mm	10mm	UK
Leica TCS SP5 Confocal	No	Confocal Microscopy	No	2.95 *μm*	Dependent on slice spacing	1.51mm x 1.51mm, more with field stitching	Constrained only by z-stage limits	NZ, UC

[1] Resolutions quoted in this table are those specified by the manufacturer. While achievable under ideal conditions, it is doubtful whether these could be achieved during everyday use.

4.3.3 Surface Texture Measurement using Confocal Microscopy

Once confocal microscopy had been selected as the most appropriate method of measuring surface texture, a significant amount of work was required to implement those measurements. Because the instrument being used was owned by the University of Canterbury Biological Sciences Department, the microscope and its software were optimised for biological imaging tasks. This meant that surface metrology operations were not immediately or natively supported by the system, so methods had to be determined for capturing appropriate surface data and processing it into surface imagery and evaluated roughness parameters. These procedures are briefly outlined below.

The basic principle of using confocal microscopes for surface interrogation is shown diagrammatically in Figure 68. A confocal microscope is an instrument capable of looking at a single focal plane and excluding all others while doing so [58].

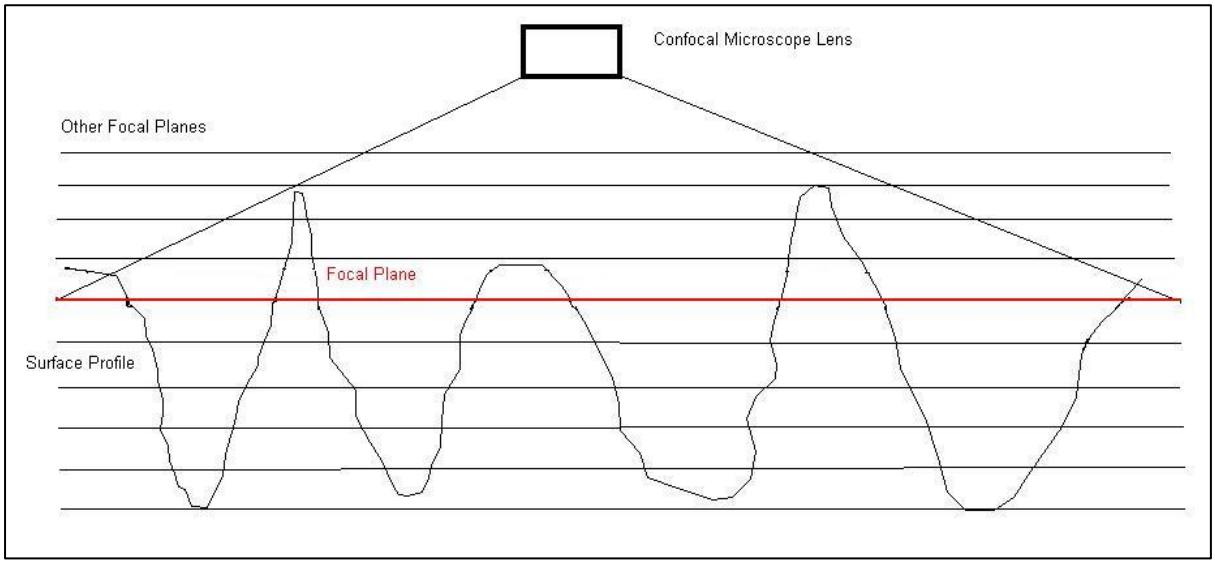

Figure 68: Surface Cross-section Showing Confocal Microscope Optical Sectioning Technique

When in reflection mode, the microscope can be made to return a black and white image where white areas correspond to areas with material in the focal plane, and dark areas correspond to areas with no material in the focal plane [59]. The focal plane can then be moved in the z-direction (i.e. normal to the surface) and another image captured. This process is repeated until the entire surface has been optically sectioned and stored as images. The start and end heights are determined manually by varying the focal plane height until there is evidence of material in the image: these are taken to be the heights of the highest peaks or lowest valleys in the surface. Figure 69 shows an example of one of these optical sections, from approximately the midpoint of a stack capturing a polystyrene foam surface. Even in a single focal plane, the cellular structure of the foam is clearly apparent.

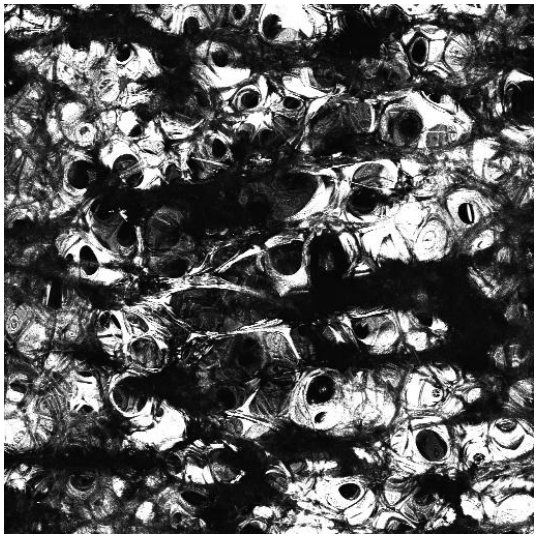

Figure 69: Example optical section of an extruded polystyrene foam sample

Once an image stack has been completely captured, it can be processed into a single image that is effectively a topographic map of the surface within the area of interest, using an extended depth of field plugin for the open-source image-editing software ImageJ [60]. This image is generally referred to as a surface topology image, and an example can be seen in Figure 70, which shows the topology image of the stack from which Figure 69 was taken.

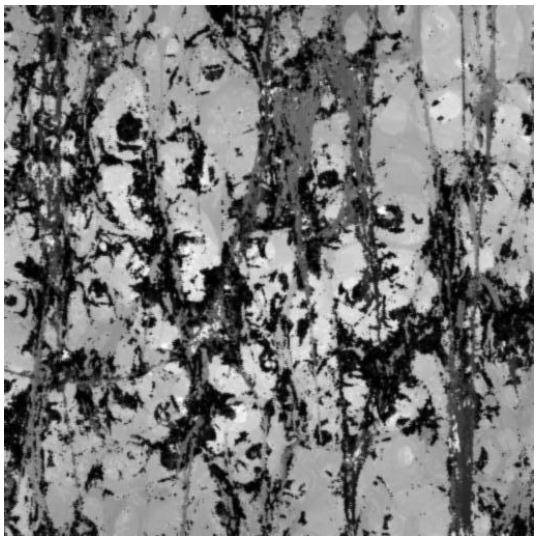

Figure 70: Example topology image of an extruded foam surface

This topology image is a greyscale image, where the grey value of each pixel ranges from 0 (black pixels) to 255 (white pixels). These correspond to the deepest valleys and highest peaks, respectively. The grey value of every pixel represents the relative height of the point that pixel represents between the two extremes. Since the physical heights of the maxima and minima are recorded when the microscope is used to capture an image stack, it is possible to calibrate the pixel

values to the physical dimensions of the surface. This calibration takes place in the Matlab program that is used to turn surface profile data into roughness parameters, as discussed below.

Since these square surface patches are only 1.51mm on a side, it is necessary to capture a number of different stacks adjacent to each other (in practice with a small amount of overlap to aid registration). These are taken with the same start and end heights, and the number of stacks to be captured depends on the cut-off length required. If this technique is used for machined metal parts, for instance, then one stack is usually sufficient. In the case of polystyrene foam surfaces, a cut-off length of at least 4mm is necessary, so a minimum of three stacks are usually required. These stacks are knitted together into a surface strip image as shown in Figure 71. The surface strip image can in turn be processed into a 3D representation of the surface, as shown. Once this has been done, the image processing stage of confocal microscope roughness measurement is complete.

This surface strip image can be processed in a number of ways, depending on the surface texture parameters being evaluated. If R_a or other profile-based parameters are required, the image is processed as shown by Figure 72. Lines (usually three in this research) are drawn along the strip and plots of the greyscale pixel values along those lines are exported as x-y coordinates. These profiles are then loaded into Matlab and processed (using the script that can be seen in Appendix A3) to generate values of R_a, R_z and R_{max}.

If areal parameters are required, it is not necessary to capture surface profile data before beginning Matlab processing. The surface topography image is loaded directly into Matlab and processed using the script in Appendix A3. This generates values of S_a, S_q, S_{ku} and so on.

For the evaluated of parameters based on the areal autocorrelation function, like the surface texture aspect ratio S_{tr}, another script is used (Appendix A3). This script loads the image directly, in the same manner as the areal-parameter script.

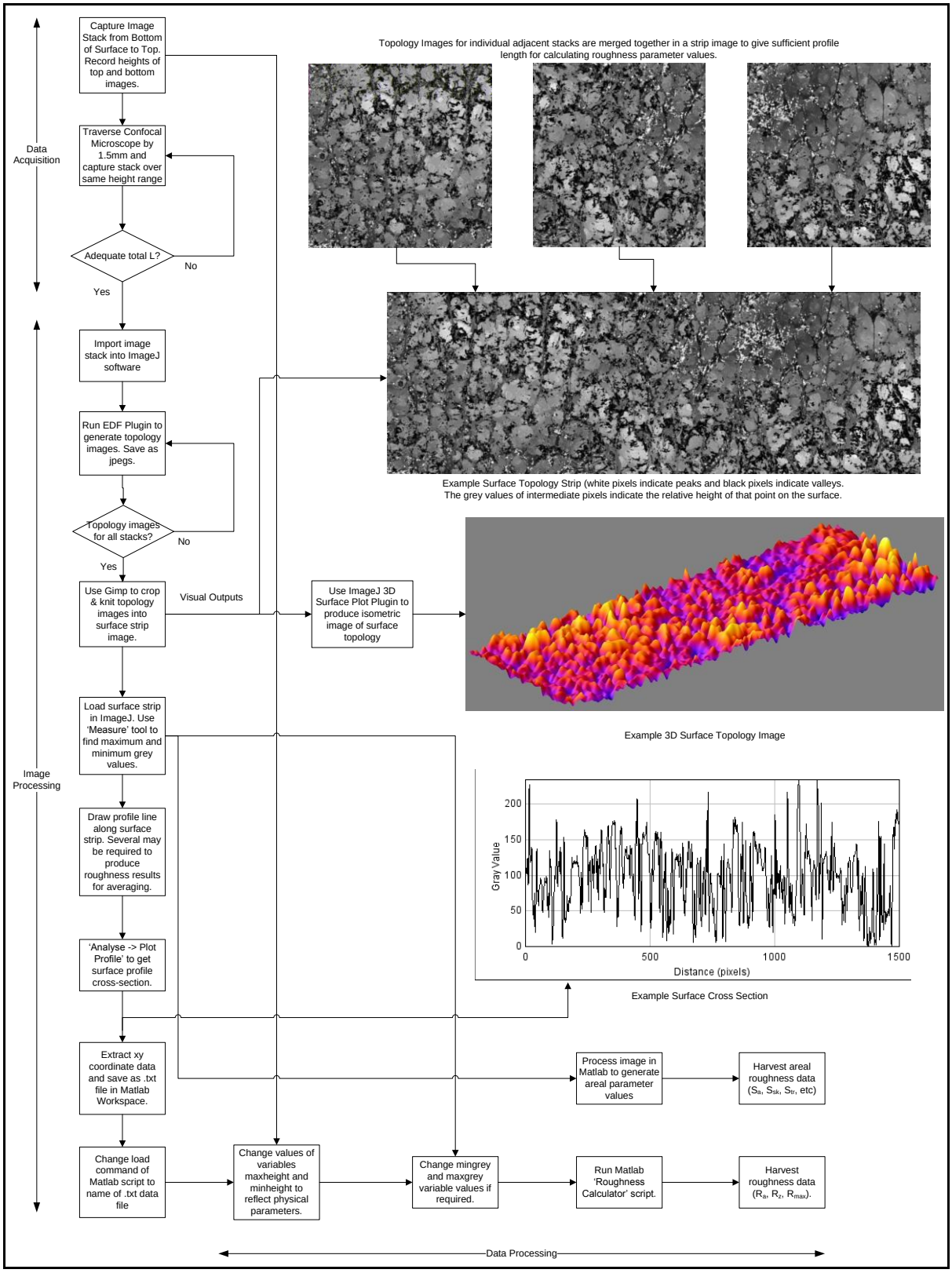

Figure 71: Confocal Microscope Surface Measurement Process

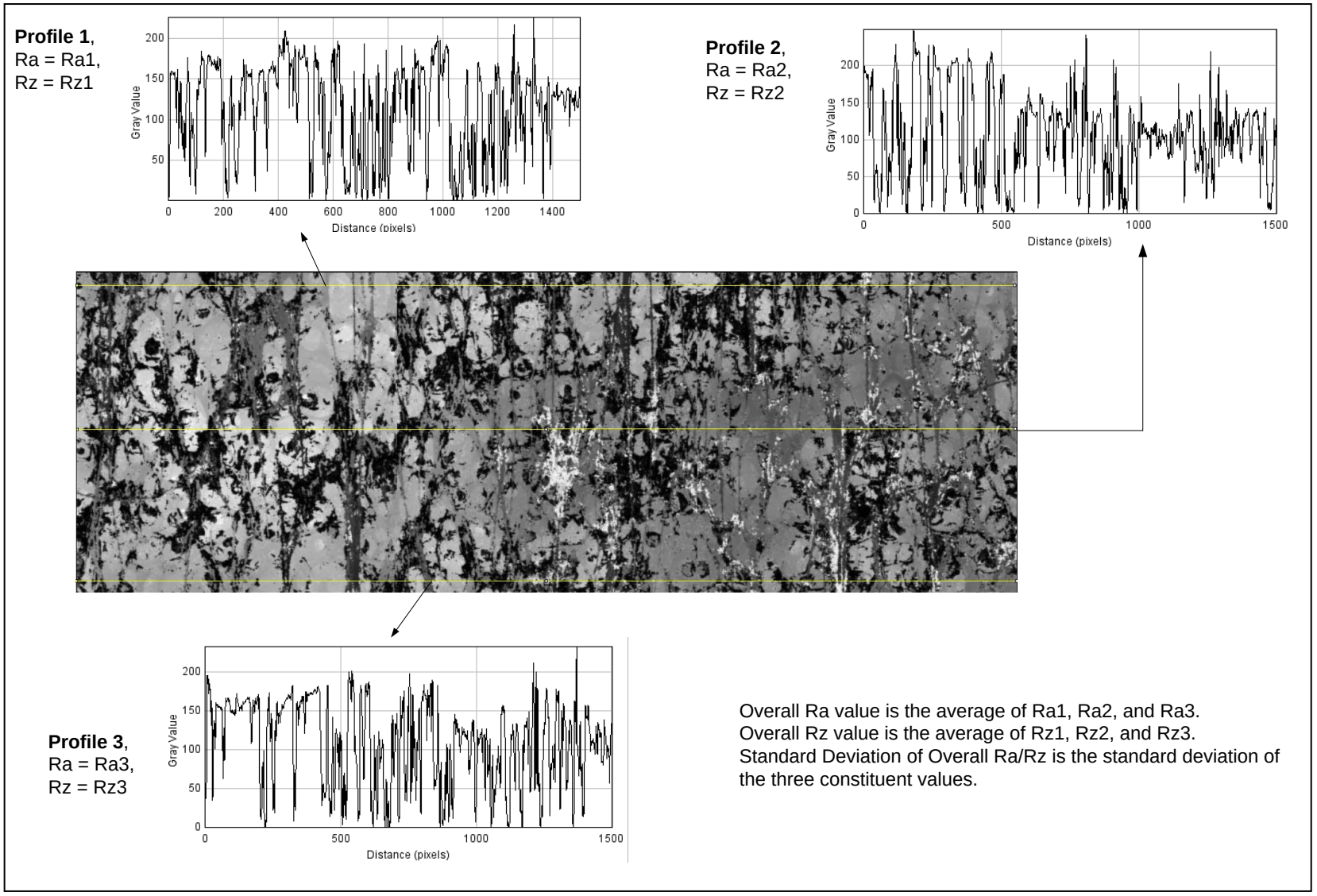

Figure 72: Greyscale Profile Extraction from 2D Topography Images

When the procedure for measuring surface texture with confocal microscopy had been developed, it was necessary to validate the results produced before it could be used for the interrogation of polystyrene foam surfaces. For this reason, a calibrated surface roughness standard (See Figure 73, below) was measured. Only one image stack was captured in this case, since the certified roughness of the standard was 5.88µm R_a, and 1.51mm was an adequate profile length for a roughness of that order [51]. The topography image and 3D surface projection of this stack are shown in Figure 74. These images clearly show the lay of the surface standard, which can also be seen in Figure 73.

Figure 73: Surface Texture Calibration Standard

The standard had a roughness certified as 5.88µm R_a ± 0.173µm. When the profiles extracted from the surface were processed, the roughness value produced using the confocal microscope measurement procedure was 5.9237µm R_a. This is within the tolerance of the standard's roughness, and so the test indicated that the confocal microscope measurement procedure was producing accurate results. This was supported by a qualitative comparison using the foam samples produced for analysis in Section 4.4. For this comparison, foam samples were measured on the confocal microscope to determine their roughness, and then they were compared with metal samples known to have the same roughness. Within the limits of this visual inspection technique, the vertical surface imperfections of the foam surfaces appeared to have approximately the same magnitude as the surface imperfections of the metal samples, indicating that they had approximately the same roughness. Based on the measurement of the texture calibration standard and the qualitative comparative assessment, it was concluded that the confocal microscope was producing reliable results.

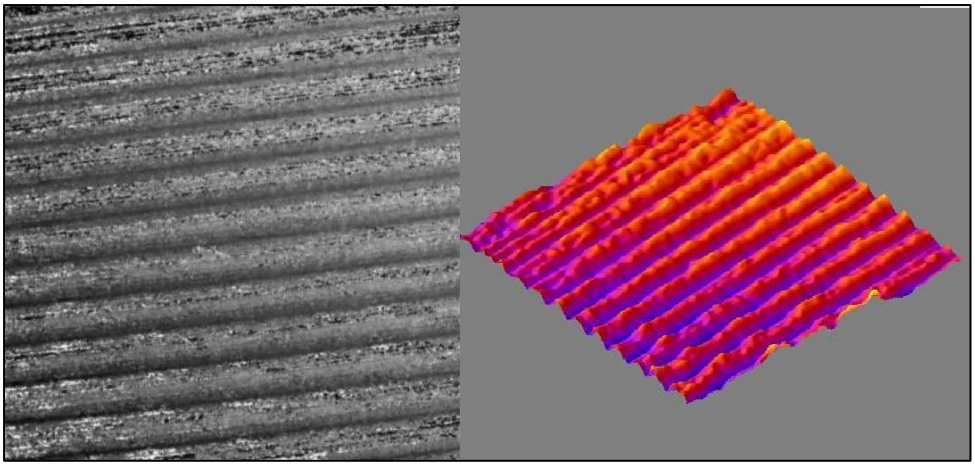

Figure 74: Confocal Microscope Imagery of Surface Texture Standard

4.4 Empirical Investigation of Polystyrene Foam Surface Texture

Armed with the understanding of surface texture and the validated method of measuring the texture of polystyrene foam that has been summarised in the previous sections, it was possible to conduct a thorough investigation of the nature of polystyrene foam surfaces. This investigation was intended to develop a quantitative understanding of the causes of the texture of foam surfaces, to identify which input parameters and parameter interactions were of most significance, and to develop a method of predicting the surface texture that could be achieved under a given set of cutting conditions.

4.4.1 Surface Texture of Surfaces cut with a Hot Wire

Once a method for measuring the surface texture of polystyrene foam had been established and validated, experimental work was undertaken to identify the influence of different process parameters on the roughness of the cut surface. To identify appropriate cutting conditions for the experimental work, the samples produced during early work on characterising foam surfaces were inspected (see Chapter 2.1.1). Cutting conditions that resulted in 'ripped' or 'wavy' surfaces were deliberately avoided since they lie outside the operational space of the RFS system and therefore do not need to be investigated. In order to gather a broad range of surface texture information across the operational space without having to cut an unwieldy number of samples, an experiment was designed [61] that covered the full range of cutting conditions while only incorporating specific levels of each condition. The selected levels of current and feed are shown in Table 6.

Table 6. Cuts with 7A of applied current and feedrates of 0.0183ms^{-1} and 0.0217ms^{-1} were included to allow comparison with samples of these cutting conditions that had been measured with other instruments while selecting an appropriate roughness measurement technique, and to compare with previous research material generated by the RFS project. Based on these chosen cutting conditions, the expected surface categories that would be produced were 'vapourised,' 'smooth,' and 'visually disturbed.' Two sets of conditions were chosen to be duplicated (5A, 0.0133ms^{-1} and 7A, 0.0217ms^{-1}). The purpose of this duplication was to provide a measure of the repeatability of the roughness results

produced, to see if the surfaces had a consistent and predictable roughness for a given set of cutting conditions. These cutting conditions are marked by an 'X' in Table 6.

Table 6: Cutting Conditions for Hot-Wire Surface Texture Investigation

Feed (ms^{-1})	**Current (Amps)**		
	5	**7**	**8**
0.0133	X	+	+
0.0167	+	+	+
0.0183		+	
0.0200	+	+	+
0.0217		X	

The experimental design for surfaces cut by hot-blades was broadly similar, with current levels between 16A and 22A and feedrate levels between 0.028ms^{-1} and 0.075ms^{-1}. The exact cutting condition combinations used are shown in Table 7. One set of conditions, 19A and 0.040ms^{-1} (marked with an 'X' in Table 7) was carried out three times to provide a measure of the repeatability of the surface texture results.

Table 7: Cutting Conditions for Hot-Blade Surface Texture Investigation

Feed (ms^{-1})	**Current (Amps)**		
	16	**19**	**22**
0.028	+		+
0.040		X	
0.052	+		+
0.075			+

Prior experimental work had identified a succession of surface categories as the length of a cut increased, so another process parameter was added to the experimental model. This was cut length,

or the distance the wire had travelled from the start of the cut. Four levels of this were chosen for hot-wire cutting by inspection of existing samples, to capture as much surface information as possible while still keeping the number of samples manageable. These levels were 0mm (at the start of the cut), 34mm, 94mm, and 244mm from the start. For the hot-blade cuts, five levels of cut length were chosen based on the same criteria: 0mm, 50mm, 250mm, 400mm and 550mm. Longer samples were needed for hot-blade cuts because hot-blade tools take much longer to reach steady-state conditions, since the tool is operating at a much higher temperature and has much greater thermal inertia: in effect, it takes longer for a blade to cool down from free-air to steady-state temperatures.

The scope of the experiment was restricted to extruded polystyrene foam (XPS), with no attention being given to expanded foam (EPS). There were a number of reasons for this decision. Firstly, EPS foam generally produces surfaces that look rougher and less regular than those produced by XPS foam, so for any part being produced where surface texture was a primary consideration, it seemed likely that XPS foam would be the material used. Secondly, the measurement process based on confocal microscopy was very time consuming, and therefore expensive. Since it took between 15 and 20 minutes to capture each image stack, and since multiple stacks were needed for each surface sample, the number of stacks required had a significant effect on the total time required to gather data. It would have taken significantly longer to capture data for EPS foam, since the beaded nature of EPS would have required a much longer sample length to get reliable texture parameter values: instead of needing between three and five stacks as was the case for XPS, it was estimated that EPS samples would have needed at least seven stacks each, and possibly as many as twelve. Since time on the confocal microscope was very expensive, resource constraints meant that it was necessary to maximise output for the time available. Therefore, a choice had to be made between a thorough investigation of one foam type and a more superficial examination of both foams. It was decided that a more comprehensive examination of a single type of foam would be of more use, so the experiment was restricted to extruded polystyrene foam.

This experimental plan for hot-wire cuts gave 15 sets of cutting conditions, and four levels of distance, resulting in a total of 60 samples to be measured (in practice, one sample was damaged before it could be measured, but since this was one of the repeatability samples appropriate roughness measurements were still available). The plan for hot-blade surface textures gave 8 sets of cutting conditions with five levels of distance, for a total of 40 samples. Overall this meant that the surface texture investigation was based on a total of 99 samples covering the full range of surface types, cutting conditions and cut lengths of importance for the RFS system.

The surface patches of interest were distributed along the cut surface as shown in Figure 75. Each sample was made up of several confocal microscope surface images as discussed above, spaced along the cut surface at the distances specified above. Each patch was centred on the centreline of the cut.

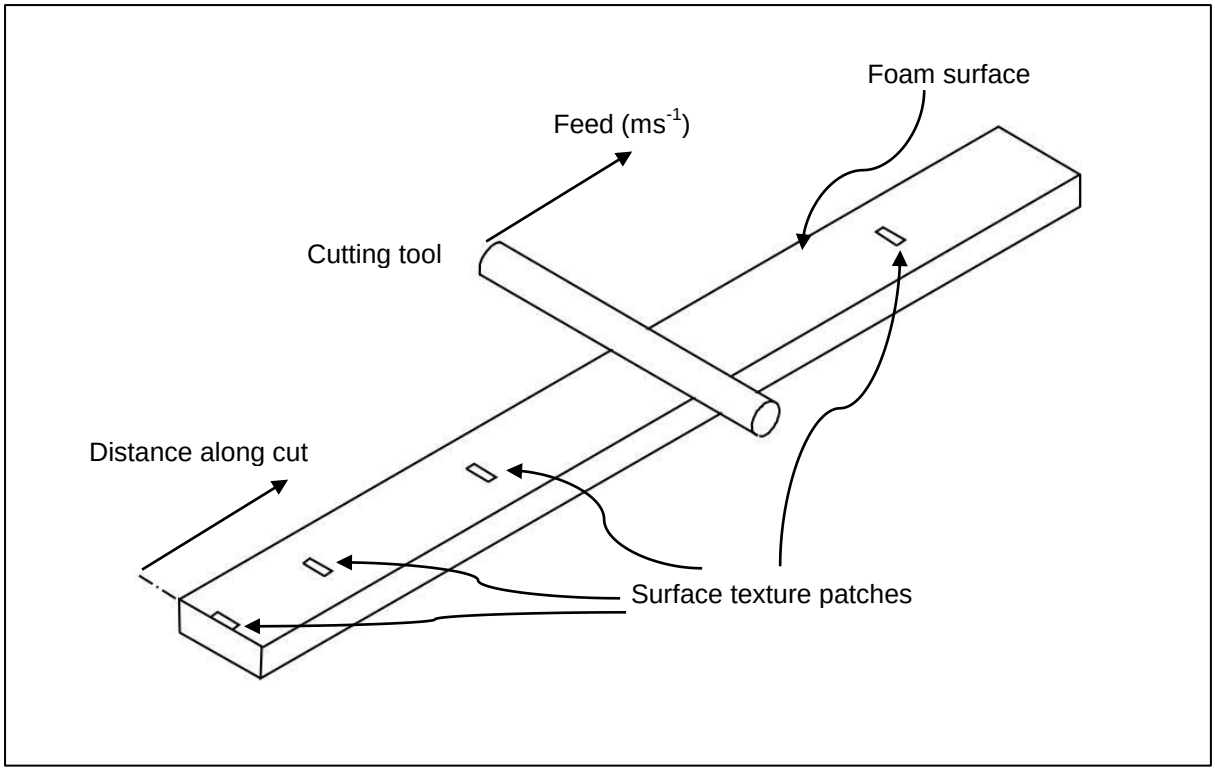

Figure 75: Position of measured surface texture patches on cut surface, and parameters relevant to the surface texture investigation

The 15 cuts were made on the Kuka KR6/2 robot using 0.6mm Nikrothal N80 Nichrome wire. The current was set for each cut on a programmable power supply, and the voltage was allowed to float throughout the cut. Adaptive current control was not implemented during these cuts, in order to provide an accurate baseline of roughness measurements. The order in which the cuts were made was randomised to minimise the effects of errors that built up over time [62]. The wire was kept under the same tension for all cuts. During this process video of the cuts was recorded so that a qualitative assessment of the thermomechanical balance could be made at each level of cut length. Cutting force readings were also taken throughout, using a loadcell mounted on the cutting tool. Once the cuts had been made, small surface samples were carefully cut out of the resulting foam strips using a sharp razor blade and mounted on microscope slides, for measurement with the confocal microscope as described above. The kerfwidth was also measured at the points of interest along the cut, with the technique outlined in the next chapter.

Sequences of surface topology images for two sets of cutting conditions are shown in Figure 76 and Figure 78, with 3D projections of these surfaces in Figure 77 and Figure 79. Figure 76 and Figure 77 show the surfaces produced by an 8A, 0.0133ms^{-1} cut at the different distances from the start. Figure 78 and Figure 79 show the same image sequence for cutting conditions of 5A and 0.0200ms^{-1}. These two sets of cutting conditions were chosen because they are, respectively, the ‘hottest and slowest’ and the ‘coldest and fastest’ of the cutting conditions examined. They therefore represent the extreme

levels of effective heat input and of surface types produced. Surface topology images for the other sets of cutting conditions and distances can be seen in Appendix A2.

Comparing the two images from the start of the cuts (Figure 76(a) and Figure 78(a)), it is clear that they are very similar. Both have a mottled, regular appearance: this appearance is characteristic of surfaces that have a 'vapourised' finish, and therefore is the usual surface type at the beginning of a cut. In the 8A, 0.0133ms^{-1} case, because the applied current is high and the feed is low the wire only cools slowly as it passes through the foam. This means that cutting by thermal vapourisation persists longer, and that the heavy mechanical cutting stage is never really reached. As a result, the surface images retain the characteristic mottled appearance of a vapourised surface throughout the entire length of cut (Figure 76, b – d).

This stands in marked contrast to the 5A, 0.0200ms^{-1} case. In this cut, the wire is never really very hot and it is progressing through the foam quite quickly, so the vapourisation stage at the start of the cut is very brief and the degree of mechanical cutting quickly increases. When the cut length is 34mm (Figure 78 (b)) the surface is taking on a more 'smeared' appearance, with relatively large contiguous areas exhibiting the same grey value (and hence the same surface height). This surface smearing is even more apparent at 94mm and 244mm from the start of the cut (Figure 78, c and d), where the surface is mostly contiguous grey areas with a few large peaks and valleys (white and black areas, respectively).

This difference of surface types is perhaps better demonstrated by the 3D topographic images in Figure 77 and Figure 79. In Figure 77, all the surfaces have a similar morphology, characterised by peaks with regular height and spacing. This morphology can also be seen in Figure 79(a), since this is also a vapourised surface, but when the mechanical contact between the wire and the foam increases, the morphology of the surface changes substantially. These surfaces (Figure 79, c and d) are still regular, but in a different way. Whereas vapourised surfaces have frequent peaks and valleys of consistent height and spacing, mechanically-cut surfaces exhibit large contiguous areas of approximately the same surface height, with other areas of high peaks and low valleys.

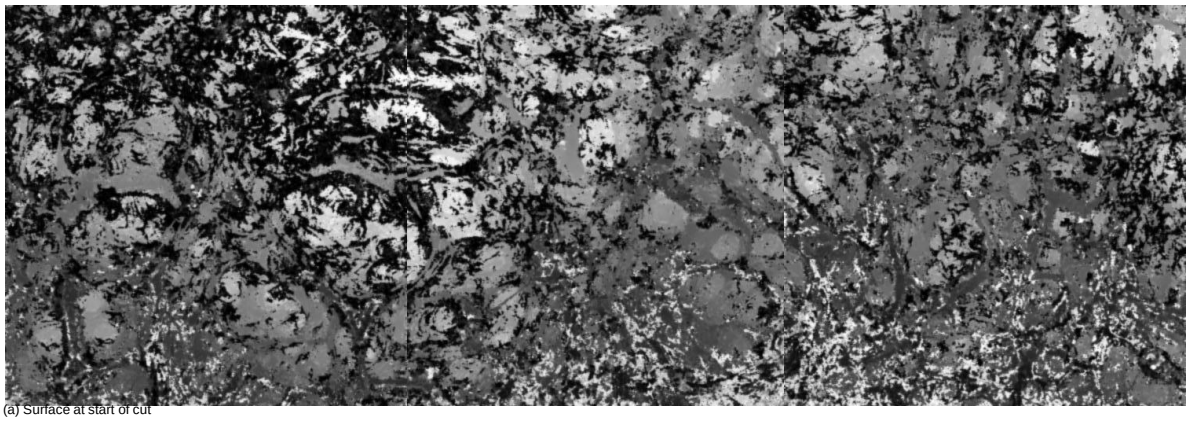

(a) Surface at start of cut

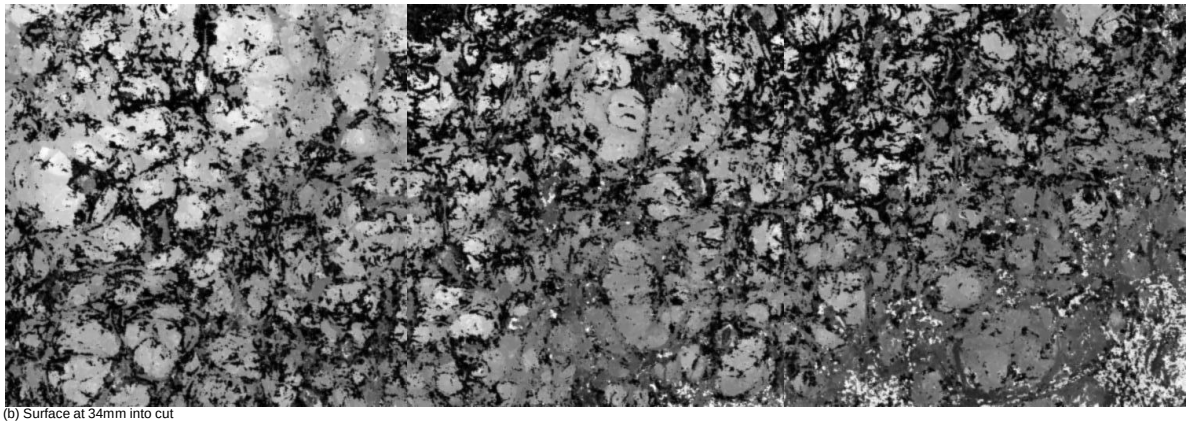

(b) Surface at 34mm into cut

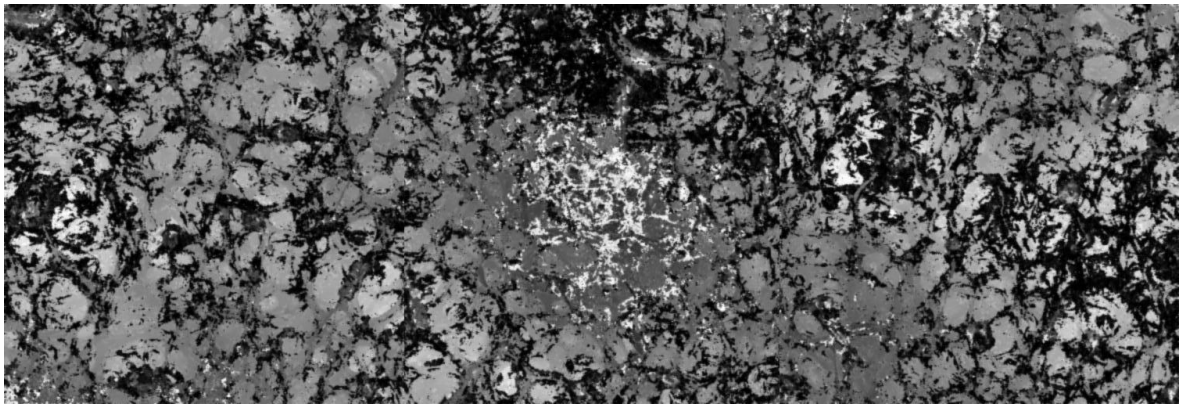

(c) Surface at 94mm into cut

(d) Surface at 244mm into cut

Figure 76: Surface Topology Sequence for 8A, 800mm/min

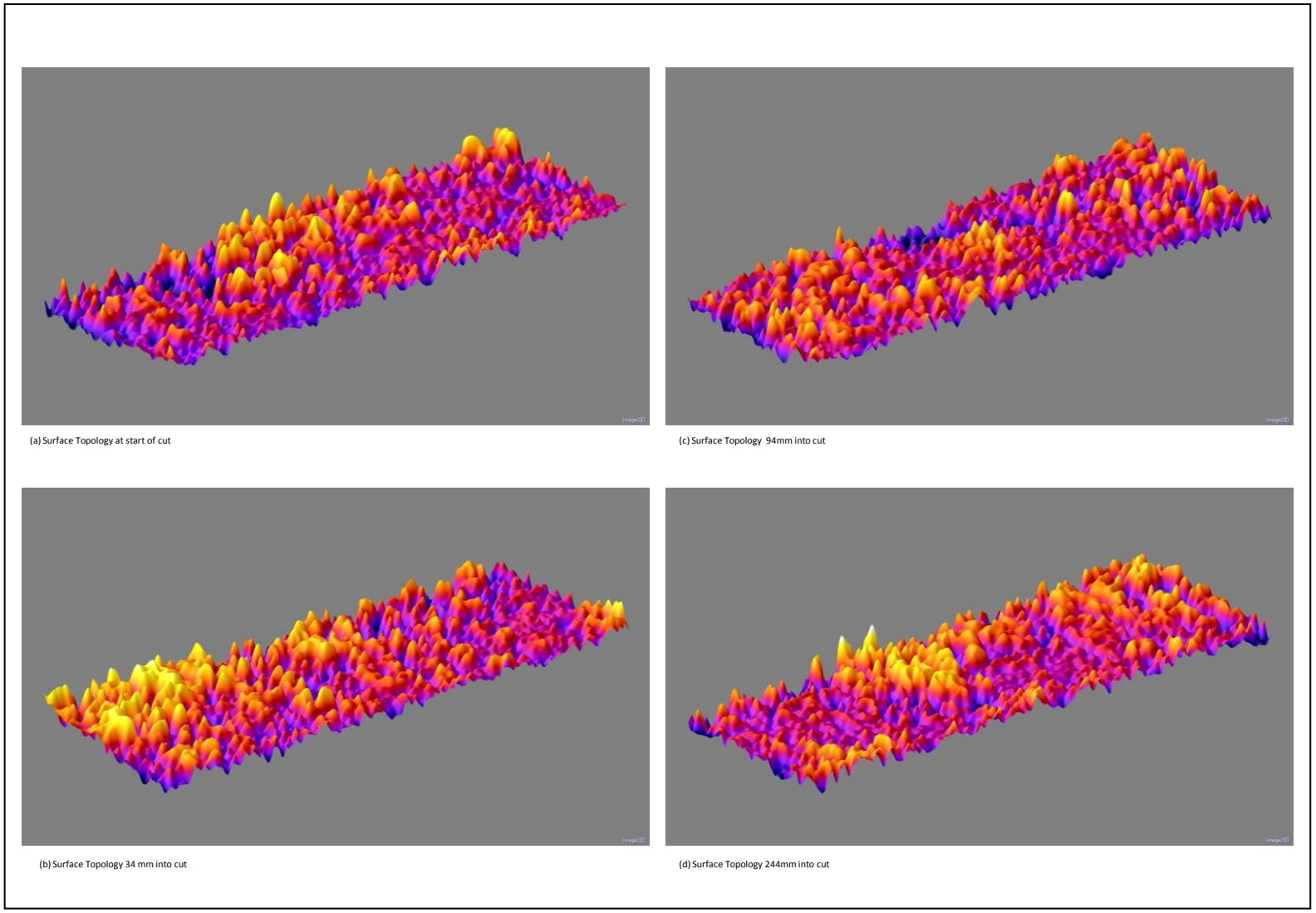

(a) Surface Topology at start of cut

(c) Surface Topology 94mm into cut

(b) Surface Topology 34 mm into cut

(d) Surface Topology 244mm into cut

Figure 77: 3D Surface Topology Images for 8A, 800mm/min

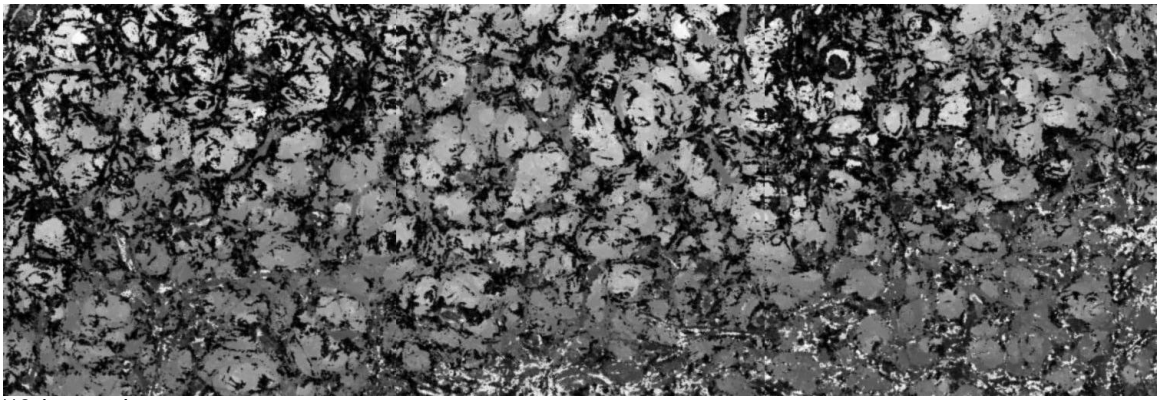

(a) Surface at start of cut

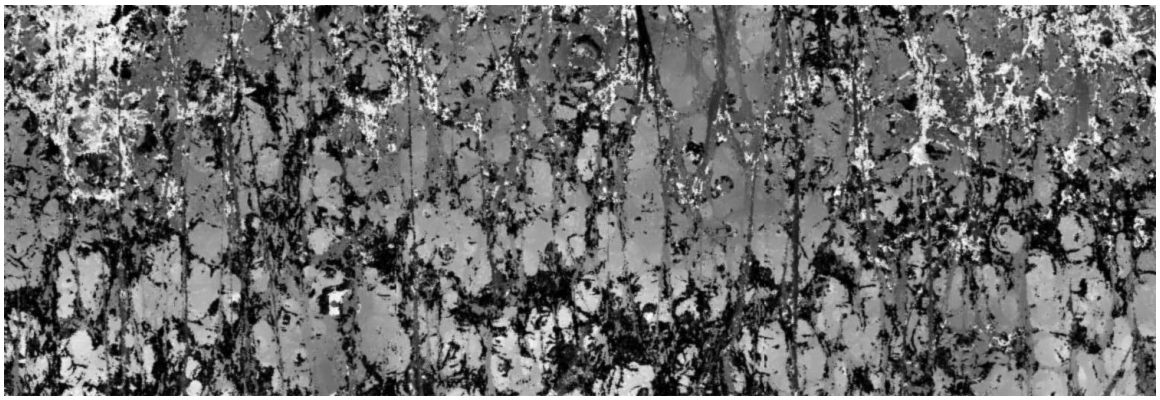

(b) Surface at 34mm into cut

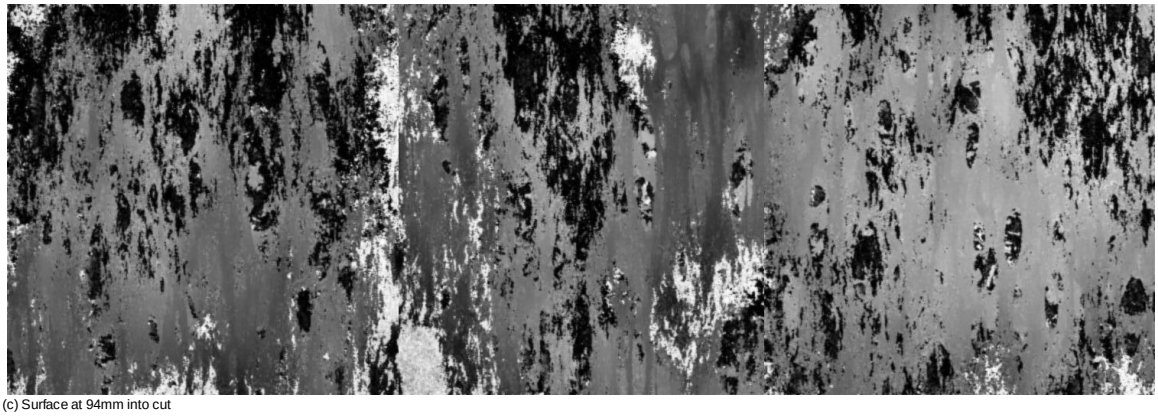

(c) Surface at 94mm into cut

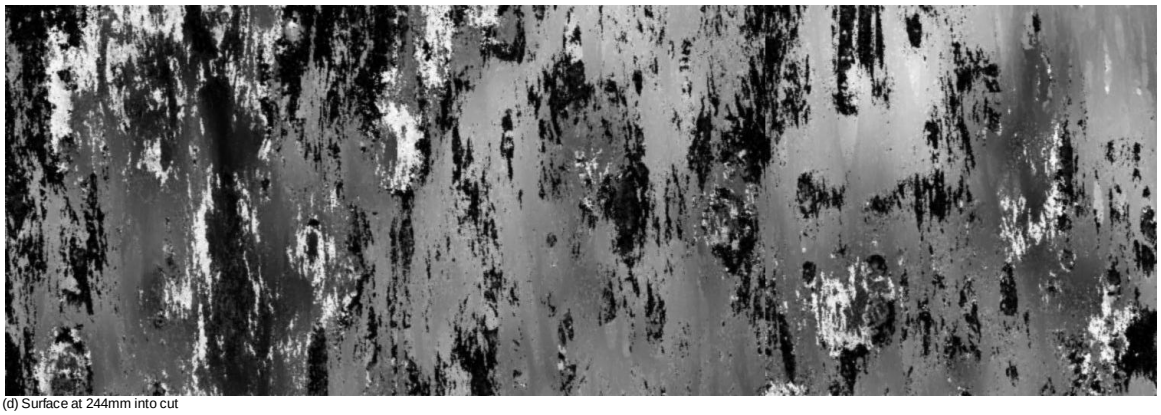

(d) Surface at 244mm into cut

Figure 78: Surface Topology Sequence for 5A, 1200mm/min

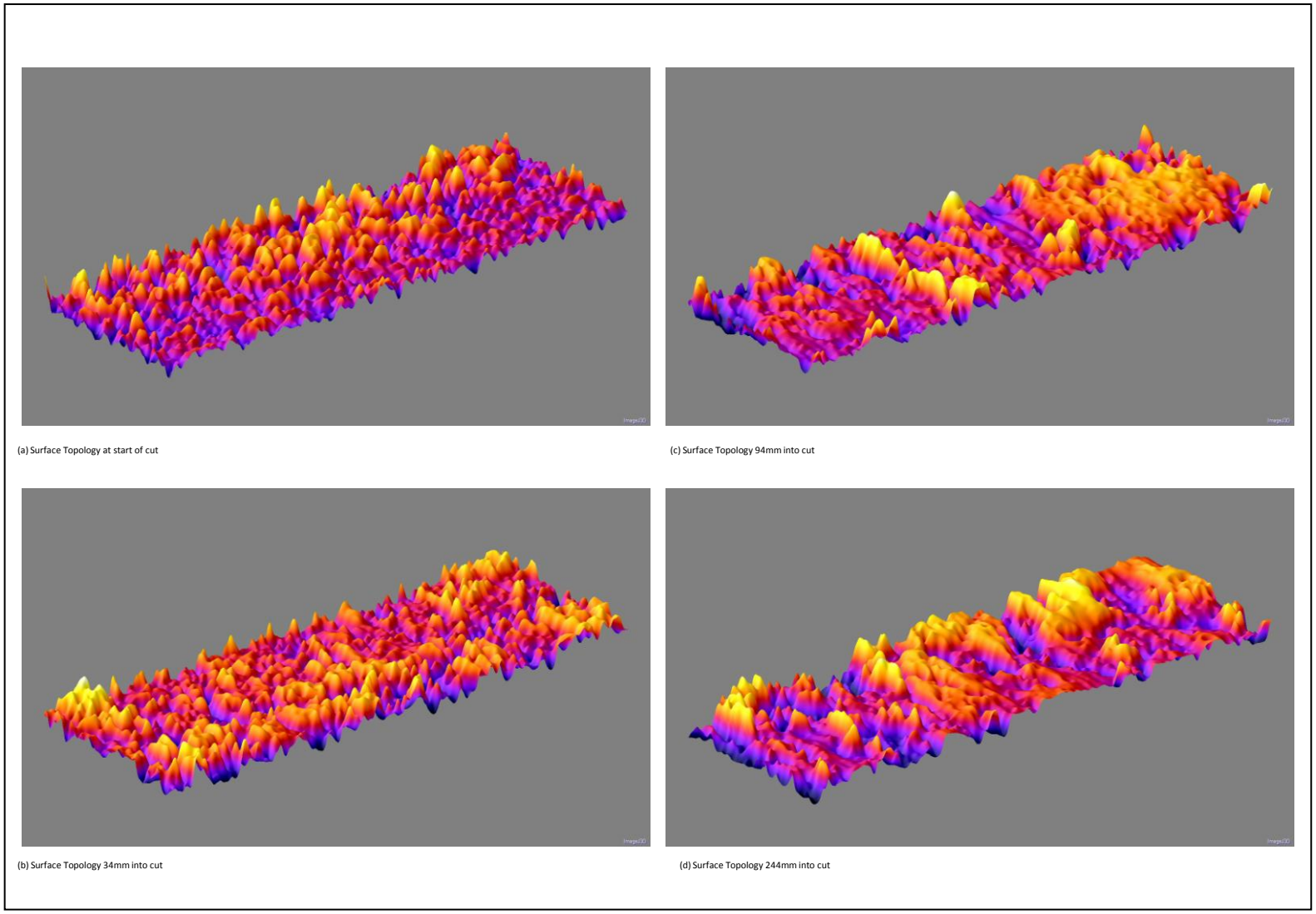

Figure 79: 3D Surface Topology Images for 5A, 1200mm/min

Once topology images of all 59 surfaces in question had been developed, they were processed into roughness values as described in Section 4.3.3, above. The calculated values of the different surface texture parameters can be found in Appendix A1.

As shown in Figure 80 and Figure 81, the three profile-based roughness parameters that were calculated (R_a, R_z and R_{max}) have an approximately linear relationship to one another. This is not surprising since they are all calculated in one way or another from information about surface heights, but it does mean that discussion here can be limited to one type of parameter for conciseness, since broad trends noted for one parameter will hold true for other parameters as well. In this instance, most discussion will be focussed on the arithmetic average roughness, R_a. Some discussion of the results using the parameter S_a will also be included.

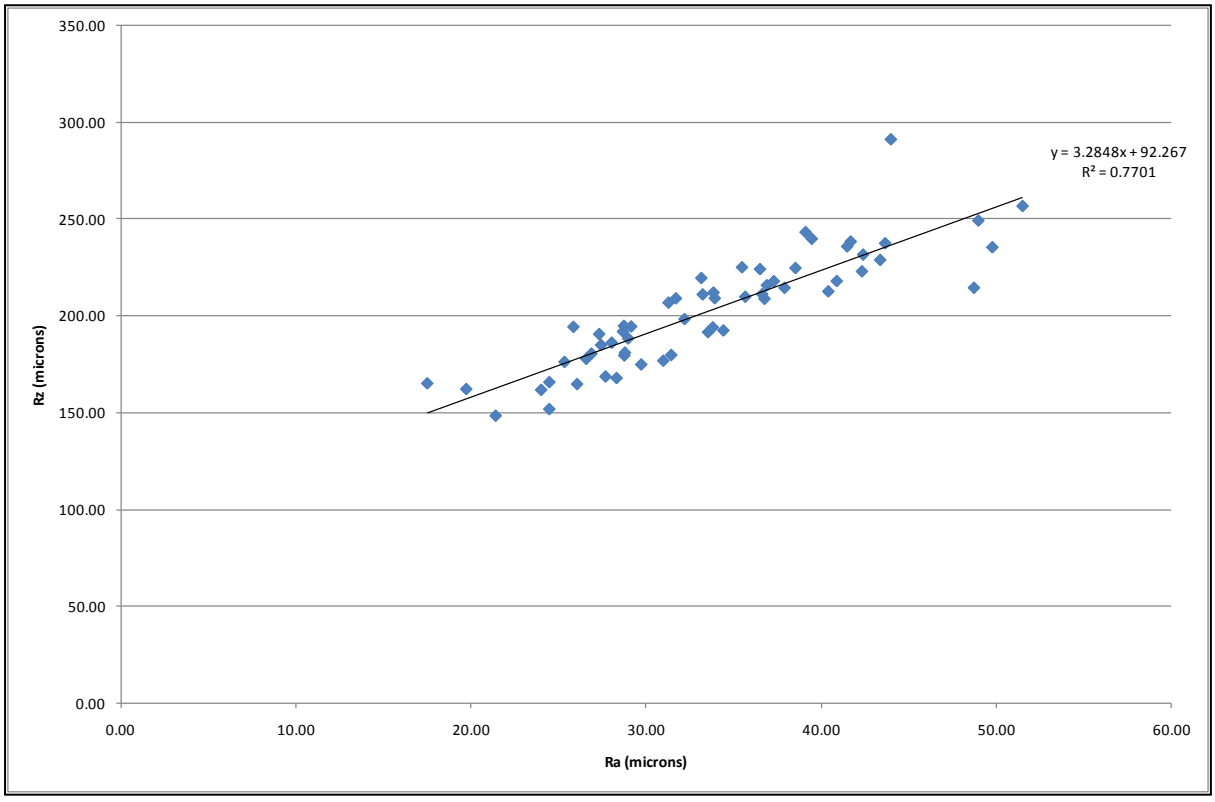

Figure 80: Relationship between R_z and R_a

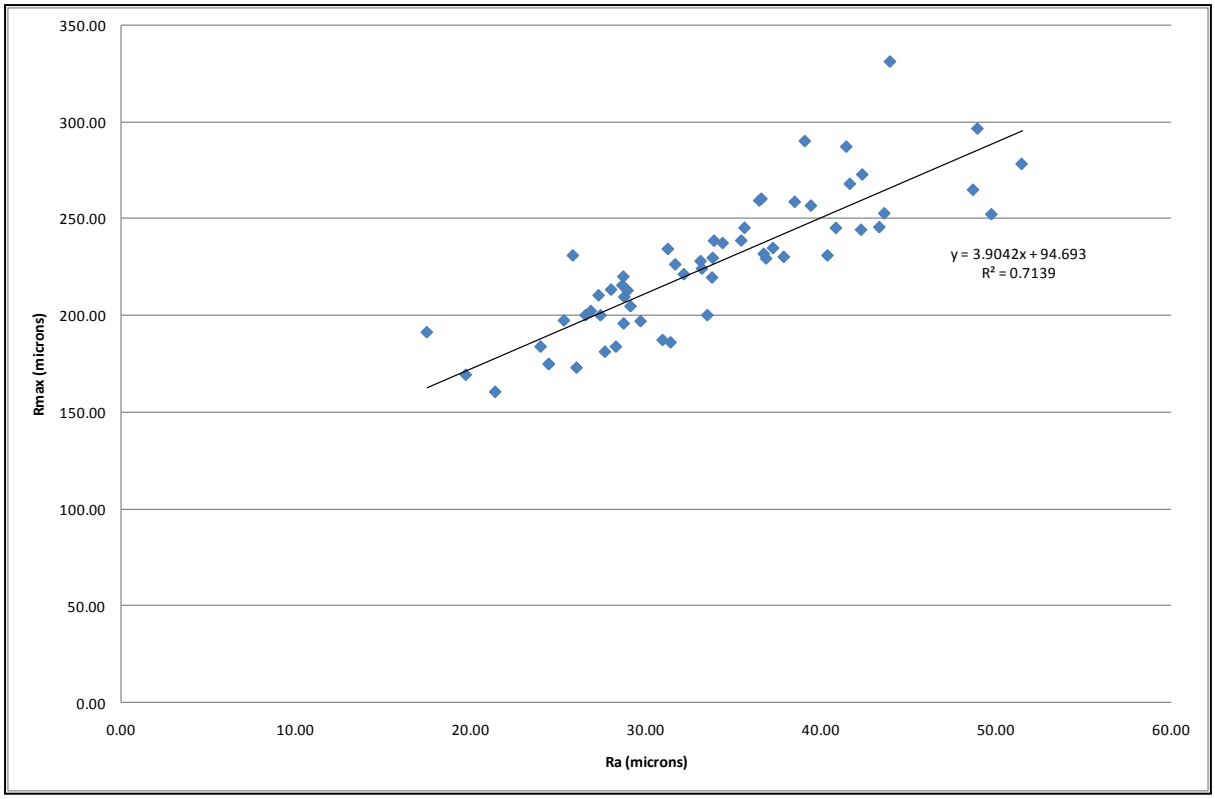

Figure 81: Relationship between R_{max} and R_a

To identify what relationship(s) existed between the texture of a foam surface and the process parameters used to create that surface, multi-factor linear regression was used to analyse the experimental results [63, 64] (the technique used was similar to that used by Lou et al for investigating the roughness of CNC end milling in [65]). This analysis generated numerical models for the texture to be expected based on the input processing parameters (for a range of different surface texture parameters as outlined above), and allowed an assessment of the statistical significance of each input parameter. Each model also had a Coefficient of Determination (R^2), which expressed how well the model fitted the observed data: an R^2 value close to 1 indicated a very good fit, while a value close to 0 indicated a very bad fit. In most circumstances values of less than 0.5 are considered to indicate that the model accuracy is unacceptably low.

The regression analysis identified feedrate, current and distance as the only parameters that had a statistically significant effect on the output R_a, for both hot-wire and hot-blade cutting. However, the best R^2 that could be achieved through the regression analysis for hot-wire cutting was 0.146, which indicates that there is no predictable and consistent relationship between surface texture and input parameters that remains valid for all combinations of cutting conditions. Similar results were found for hot-blade cutting, and the best achieved coefficients of determination using a range of parameters are summarised in Table 8. As can be seen from the values of the coefficients of determination, none of the regression models has an acceptable fit to the observed data.

Table 8: Summary of Coefficients of Determination for regression models

Cutting Tool	Parameter	Best R^2
Hot-wire	R_a	0.146
	S_a	0.1224
	S_q	0.1363
	S_{tr}	0.14
Hot-blade	R_a	0.145
	S_a	0.146

It can also be observed from the texture parameter results that, generally, for higher values of cut length the R_a results exhibit a much greater range of values than is the case at low values of cut length. In other words, as cut length increases the values of texture parameters appear to become more variable.

When this result is considered in conjunction with Figure 82, the apparent trend becomes more nuanced. Figure 82 shows the variation of R_a values with Volumetric Effective Heat Input (refer to section 2.2.4) and shows that at low values of volumetric effective heat input the surface texture values lie across a very large range, while at high values of volumetric effective heat input the surface texture lies across a much narrower range. The nature of the volumetric heat input is such that high values indicate high current, low feedrate and large kerfwidth, while low values indicate low current, high feedrate and small kerfwidth. In other words, high volumetric effective heat input is associated with vapourised cutting, while low volumetric effective heat input is associated with thermomechanical cutting. Therefore, it is clear from Figure 82 that surfaces produced with vapourised cutting exhibit relatively low surface texture variability, while surfaces produced with thermomechanical cutting exhibit much more variability. This is a strong indication that surface texture parameters based on surface heights are more predictable for vapourised cutting than for thermomechanical cutting.

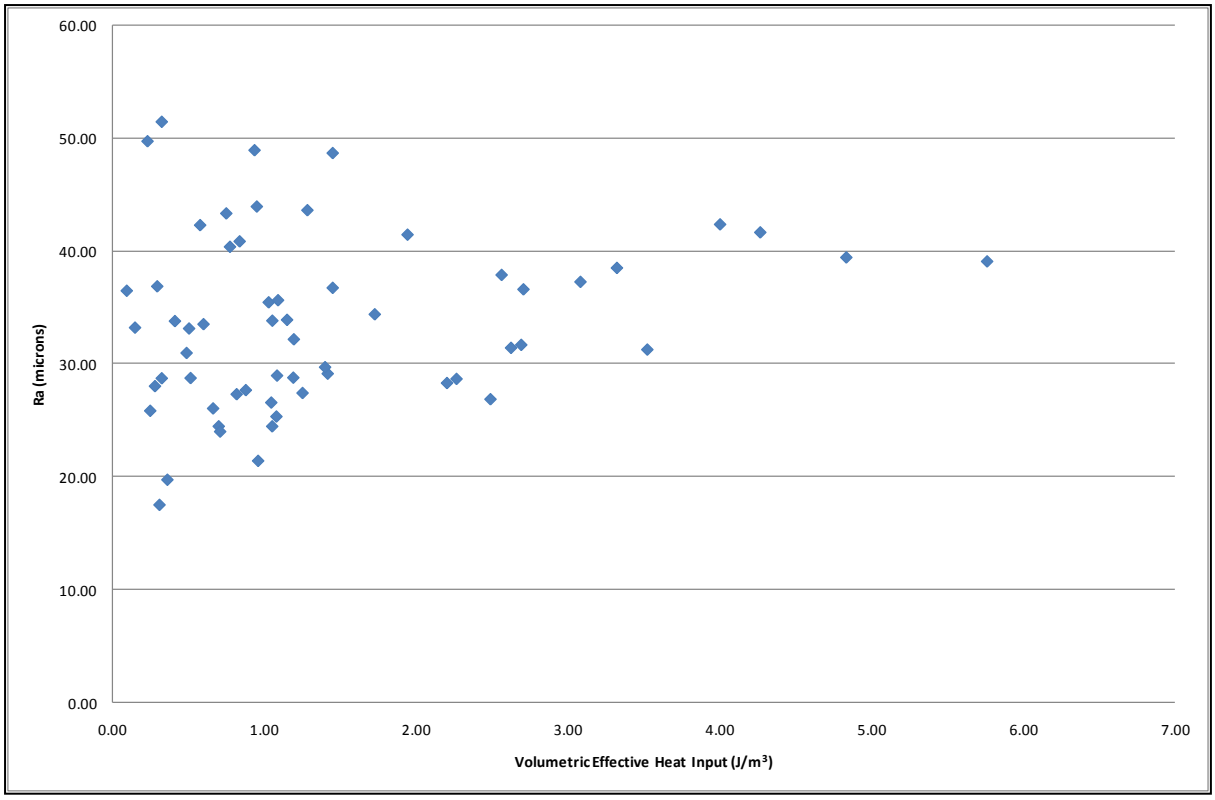

Figure 82: Variation of R_a with Volumetric Effective Heat Input

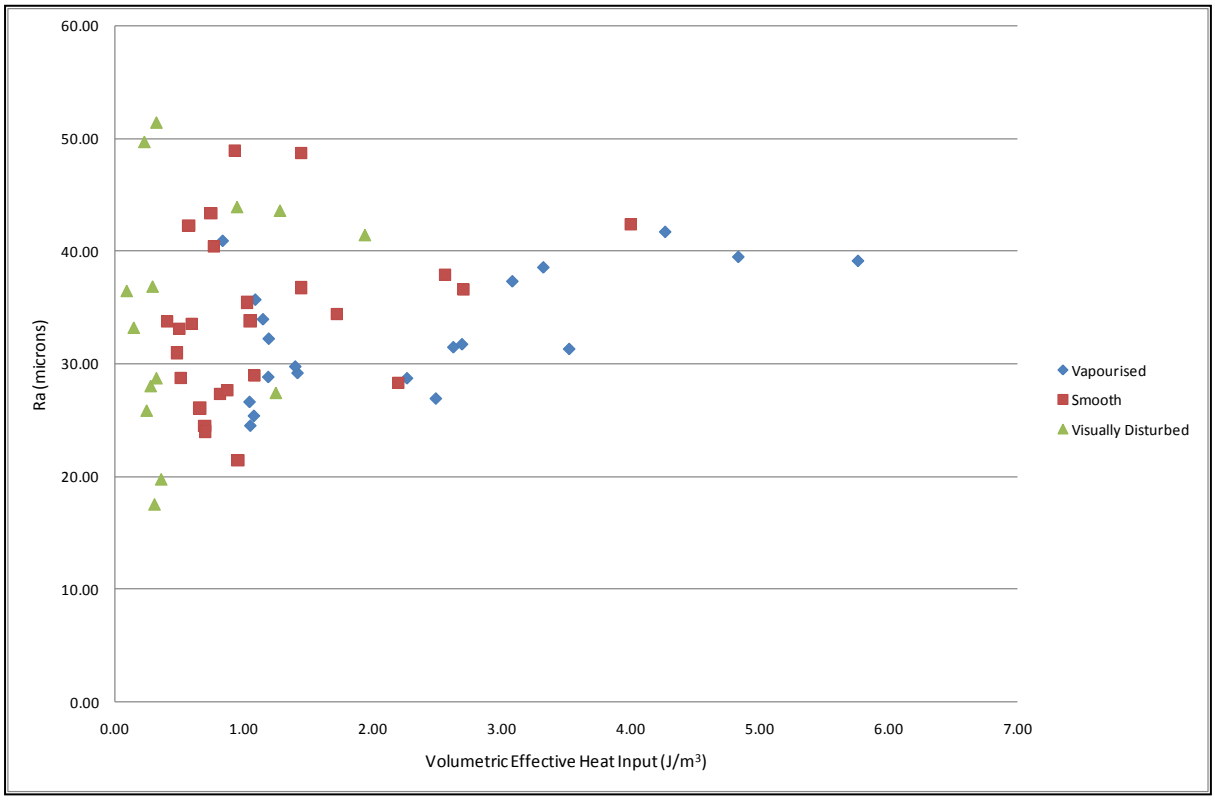

Figure 83: Variation of R_a with Volumetric Effective Heat Input, by Surface Category

In Figure 83, R_a is again plotted against Volumetric Effective Heat Input, but in this case the separate data points have been categorised by the surface category into which those samples fall, based on qualitative assessment. This classification of surface types is subjective and prone to error, but the relevant general trend can still be seen. Surfaces that are classified as 'vapourised' are the product of purely thermal cutting, and the range of the R_a values for surfaces of this type is relatively low. For 'visually disturbed' surfaces (which are the product of a substantial degree of mechanical cutting) the R_a values exist across a much greater range, and thus exhibit greater variability.

This increased variability (and reduced predictability) is also shown by Figure 84, which displays the roughness values against cut length for the three cuts made with cutting conditions of 5A and 0.0133ms^{-1}. As can be seen, at the beginning of the cut (i.e. vapourised cutting) the roughness results are very close together, whereas at 244mm of cut length (a visually disturbed surface) the texture values have a substantial range, from less than 30µm to more than 50µm. This increasing variability is a more or less consistent trend along the cut length. It is also clear from Figure 84 that the value of R_a for different cuts with the same cutting conditions is not in fact that predictable, and no consistent trend along the cut can be observed; this will be discussed further below.

The same general distributions were also observed for the other surface texture parameters evaluated. This can clearly be seen from Figure 85 and Figure 86, which show the parameter value distributions by surface morphology for S_a and S_q: comparing these two figures with Figure 83 it can be seen that S_a and S_q exhibit essentially the same distribution as for R_a.

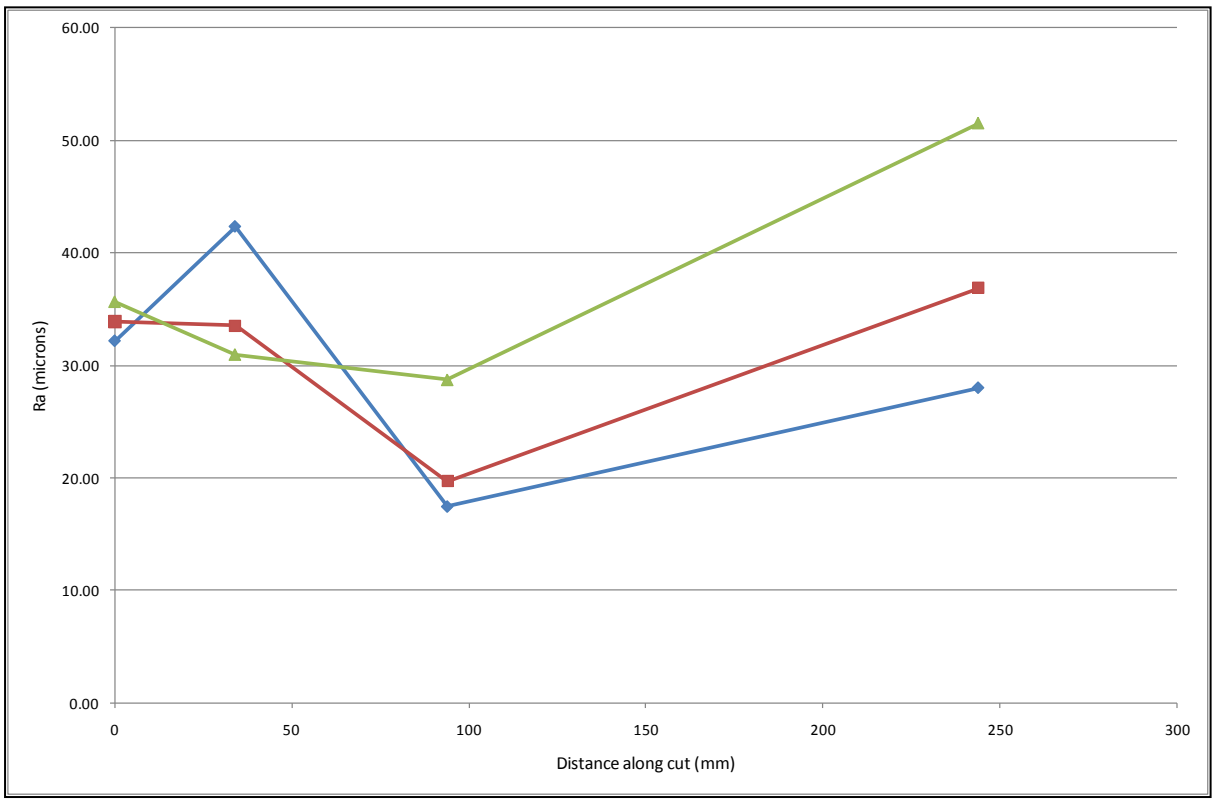

Figure 84: Repeatability Tests (5A, 0.0133ms^{-1})

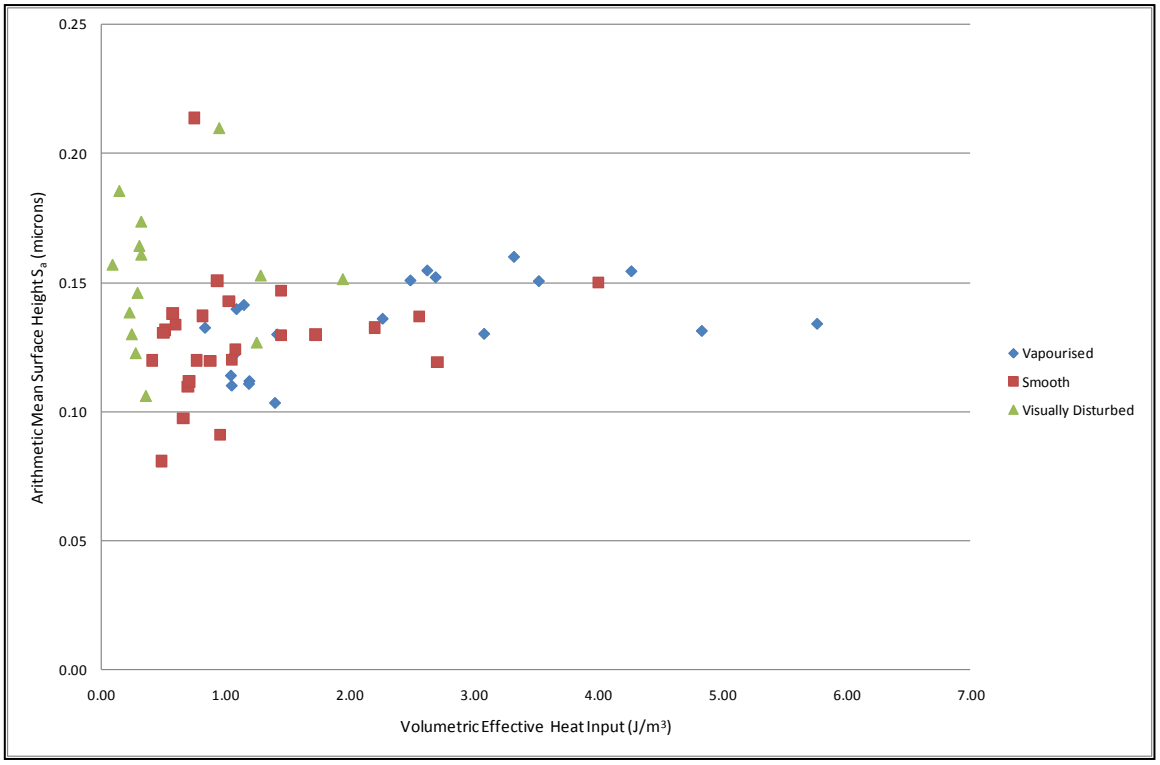

Figure 85: Variation of arithmetic mean surface height S_a with volumetric effective heat input for hot-wire cuts, by surface morphology, showing that S_a exhibits a similar distribution to R_a

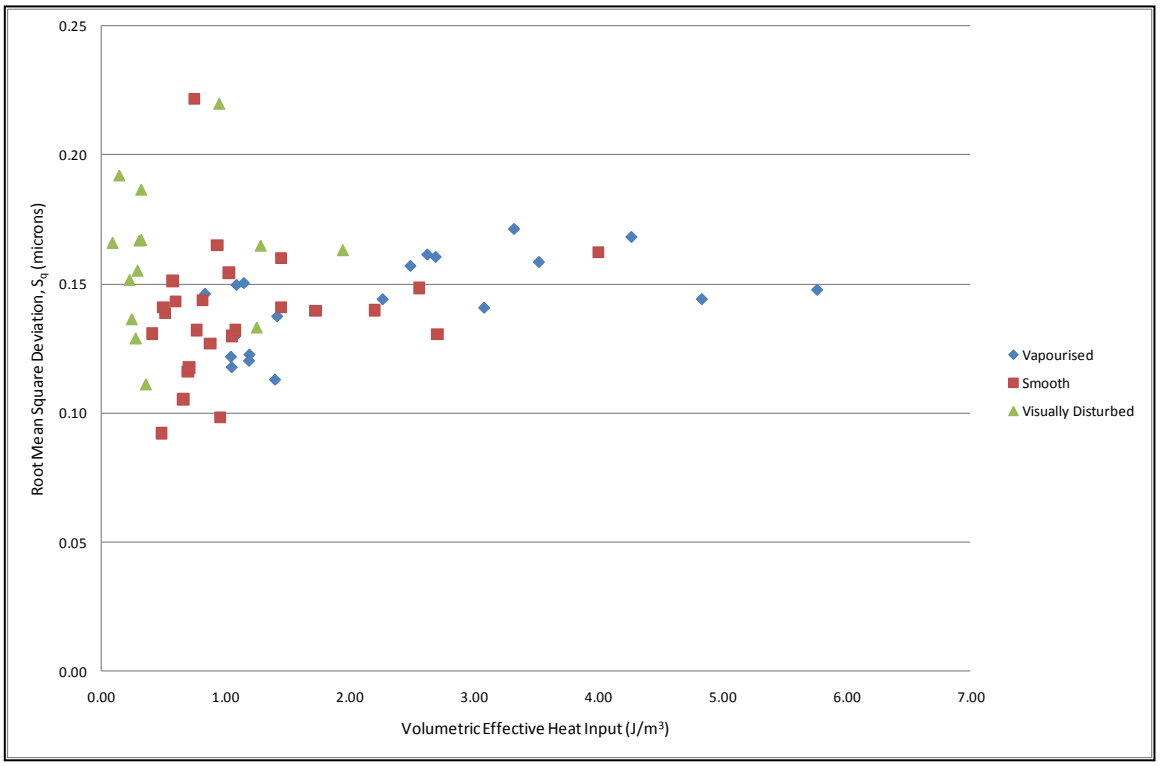

Figure 86: Variation of root mean square deviation S_q with volumetric effective heat input, by surface morphology, showing that S_q exhibits a similar distribution pattern to S_a

Figure 87 shows the distribution of S_a values for surfaces cut by hot blades. As can be clearly seen, the distribution of the surface texture values exhibits the same basic distribution as the surface texture measurements taken for hot-wire cutting. This characteristic distribution was exhibited by all the standard surface texture parameters investigated, which were based on the relative heights of the different surface features. As a result, conclusions drawn from the nature of the surface texture measurements for hot-wire cutting are equally applicable to surfaces produced by hot-blade cutting.

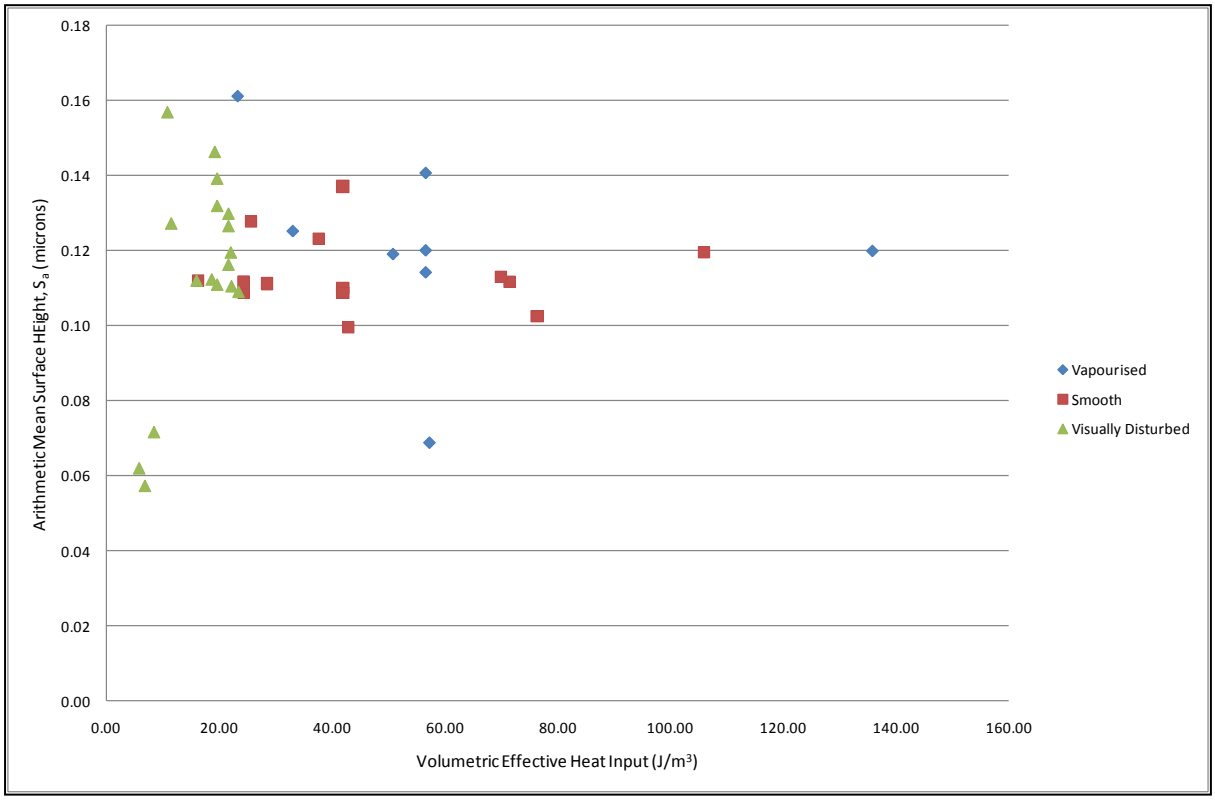

Figure 87: Variation of S_a with volumetric effective heat input for hot-blade cutting, by surface morphology, showing that the pattern of S_a distribution is broadly the same as for wire tools

Upon further consideration, the greater variability of surface texture parameters during thermomechanical cutting seems reasonable. In purely thermal cutting, the plastic material melts and flows as the wire passes, and the resulting surface exhibits a regular and mottled appearance, as in Figure 76. However, in thermo-mechanical cutting (towards the mechanical end of the continuum) the wire is in physical contact with the foam and acts to drag and smear the molten material along the surface. This results in unfilled voids and partially-ripped cells, as seen using confocal microscopy (the large dark and white areas in Figure 78 (d)).

Since the position of the unfilled voids and ripped up cells is inherently unpredictable it is impossible to say beforehand whether or not a void will be present to distort the surface texture measurement, and so the texture is less predictable for thermomechanical cutting. This also makes sense when the next stage of the surface categories continuum is considered: after ‘visually disturbed’ cutting comes ‘ripped’ cutting, where the cutting is almost entirely mechanical. Ripped surfaces were left out of the

experimental model because they were obviously going to be unpredictable, given the size and distribution of the surface features observed. These surfaces were even more unpredictable than visually disturbed surfaces, which in turn are more unpredictable than smooth surfaces, which are more unpredictable than vapourised surfaces.

A simple measure of the predictability of surface roughness within each cutting zone is the correlation coefficient. This is a value between -1 and 1 that indicates how closely correlated two sets of numbers are: a coefficient of 1 indicates a very strong positive correlation, and a coefficient of -1 indicates a very strong negative correlation. 0 would indicate no correlation. The values of the correlation coefficient between Volumetric Effective Heat Input and R_a for hot-wire cutting can be seen in Table 9. When the surface would be categorised as 'vapourised' the correlation is 0.57, which is an indication that there is a significant correlation between the two properties. As the surface zone transitions into 'smooth,' i.e. as some mechanical cutting begins to take place, the correlation coefficient drops precipitously to 0.29. This indicates that there is still a degree of correlation but that it is not very strong. Finally, as the degree of mechanical cutting increases and the surface zone becomes 'visually disturbed' the coefficient drops again, to 0.23, indicating even less relationship between the two parameters for this level of mechanical cutting. A similar pattern was observed for the samples produced by hot-blade cutting.

Table 9: Correlation Coefficients between R_a and Volumetric Q_{eff}

Surface Zone	**Correlation Coefficient**
Vapourised	0.57
Smooth	0.29
Visually Disturbed	0.23

Given the relatively strong correlation between Volumetric Effective Heat Input and texture R_a for vapourised surfaces, multi-factor linear regression was carried out using only the hot-wire samples that had a surface that was qualitatively categorised as vapourised. Surface texture parameters were used as the output variable, and the input variables were applied current, feedrate and distance from the start of the cut, since these had been identified as statistically significant during the regression analysis of all the data. This regression model performed much better than was the case when all the different cutting zones were being considered. The R^2 value that the final hot-wire model exhibited was 0.531. This is still not especially accurate, but is a vast improvement on the R^2 of 0.146 achieved originally.

The hot-wire surface texture model produced by this analysis predicts the expected surface roughness based on input values of current, feedrate and distance from the start of the cut. The

results of the regression model are shown in Table 10, along with the AIC (Akaike Information Criterion) values for each parameter. The AIC is a tool for assessing the significance of the input parameters included in the regression analysis: a value is calculated for each input parameter and one for (none). Any parameter that has a smaller AIC value than (none) is likely to be statistically insignificant and can safely be removed from the model. The (AIC) values for each parameter are all larger than the AIC value for (none), so in this case all three parameters have to be regarded as significant. The column P_r (>|t|) is a measure of the relative significance of each parameter: the closer this value is to 0, the more significant the parameter is. In this case it is clear that distance is actually the most important parameter for determining the surface roughness within the vapourised zone, with current and feed both some distance behind.

Table 10: Coefficients and AIC Values from Vapourised Surface Roughness Model

	Coefficient	Pr(>|t|)	AIC Value
(none)	-	-	59.18
Intercept	32.036035	0.000295	-
Current	1.499783	0.130875	60.12
Feed	-0.006764	0.193431	59.36
Distance	-0.213673	0.003242	68.34

A selection of regression models were produced for the surface texture of vapourised-only cutting, using different texture parameters. The R^2 values for the models generated for each parameter are summarised in Table 11. As is clear from even a brief investigation of these R^2 values, none of the models produced for vapourised cutting are particularly accurate, with R^2 values between 0.38 and 0.64. While these models fit the measured data significantly more accurately than the models for all the cutting modes did, they are still not especially accurate. It should also be noted that the R^2 of 0.64 for S_a in hot-blade cutting is likely to be the result of an over-fitted model, since the data set for this analysis was very small.

Table 11: Summary of Coefficients of Determination for regression models of vapourised-only cutting

Cutting Type	Parameter	Best R^2
Hot-wire	R_a	0.531
	S_a	0.3823
	S_q	0.4103
Hot-blade	R_a	0.5441
	S_a	0.6345

It should be noted that the $^{\text{Vapourised Blade}}S_a$ model does not include the distance along the cut as a significant parameter. This seems odd given that the distance along the cut is one of the most significant parameters for hot-wire cutting models, and given that the surface texture clearly varies along the cut when assessed qualitatively. The absence of cut length from this regression model is not in fact an indication that distance is less significant for hot-blade cutting than it is for hot-wire cutting, but merely a reflection of the experiment design. Since surface texture measurements were taken at discrete distances along the cut, rather than continuously along the full length, the surface texture measurements for hot-blade cutting that were categorised as 'vapourised' (and therefore included in the vapourised-only regression analysis) all had a value for cut length of 0mm. In other words, since all the vapourised surfaces were at the start of the cut and had the same value of cut length, it was not possible to determine a statistical relationship between the cut length and the surface texture.

From these results, it is possible to predict the approximate surface texture based on input cutting conditions for surfaces that have been produced by purely-vapourised cutting. However, it is highly questionable that such texture predictions would be useful to any significant degree. There are a number of very serious problems with the predictive models developed, including:

1) The predictive models have to be restricted to purely-thermal cutting to achieve even a minimally-acceptable level of accuracy. This means that no texture predictions or understanding can be developed for thermomechanical cutting, despite the fact that thermomechanical cutting has qualitatively superior surface finishes and is desirable for high-speed cutting by RFS.
2) The models generated for purely-thermal cutting are not really accurate enough to be useful. It is difficult to accurately predict exactly what length of the cut surface will have been produced by purely thermal cutting, and even when this determination has been made the predictive models produced have very limited conformance with the measured data.

So, while the vapourised-only models generated are able to give an indication of what the expected texture should be, these are no more than a ballpark estimate. As such, surface texture predictions based on these models are of no real use in assessing the performance of the RFS system.

This conclusion raises an important question: why not? Visual inspection of cut surfaces produced clearly shows that the surface texture changes depending on the cut length and the cutting conditions, a valid system of gathering accurate surface topography data has been established and validated, and the surface topography data produced by this system shows clear differences of surface composition between the different qualitative surface zones, so why is it not possible to produce a statistical model that provides an accurate and reliable prediction of the surface texture along the entire cut length and for all cutting modes?

The answer to this question lies in the nature of the surfaces produced by thermomechanical cutting of polystyrene foam, and the distribution of the surface height-based surface texture parameters used to date. When the measured values of S_a for hot-wire cutting are plotted as a histogram (Figure 88), it becomes apparent that this distribution resembles a normal distribution, and that the most common range for the S_a values to lie in is between 0.13 and 0.14 µm S_a. This is very close to half the cell size of XPS foam and appears to indicate that the distribution of heights on the surface is strongly influenced by the cell size of the foam being cut, and the cell size is a much more important factor than the cut length or the cutting conditions. This being the case, with the cell size being the predominant factor in determining the heights of various points on the surface, it makes sense that the attempts to fit statistical models based on cutting conditions and cut length to the measured data were unsatisfactory: in short, a very significant parameter was not being considered in the models. This conclusion conforms to that conclusion by Ahn et al that the value of R_a is equal to about half the cell size (see Section 2.2.2).

There is a broader conclusion that can be drawn from these observations. None of the statistical models developed using standard surface texture parameters produced an acceptable fit to the measured data using statistically significant input parameters, and it was clear that the size of the cells in the foam was a strong determining factor in the values of surface texture measured, with the measured texture values being close to randomly distributed around the mean cell size of the foam. Despite this, there are still clear differences in the textures of cut surfaces: these have been assessed qualitatively and linked to the cutting conditions, cut length and cutting mode. The logical conclusion in this case is that the observed differences between surface types are not due to the relative heights of surface features (as is the case with most machining operations) and therefore it can be concluded that measurements of the foam surface texture using texture parameters based on the heights of surface features will not be suitable for the discrimination of different surface types. Thus far, all of the surface texture parameters used have been height-based, and so the statistical models developed have been very inaccurate. Armed with this new understanding, it is possible to consider the topography of foam surfaces in more detail and to develop a more suitable parameter for the expression of the foam surface texture. This development is the subject of the following section.

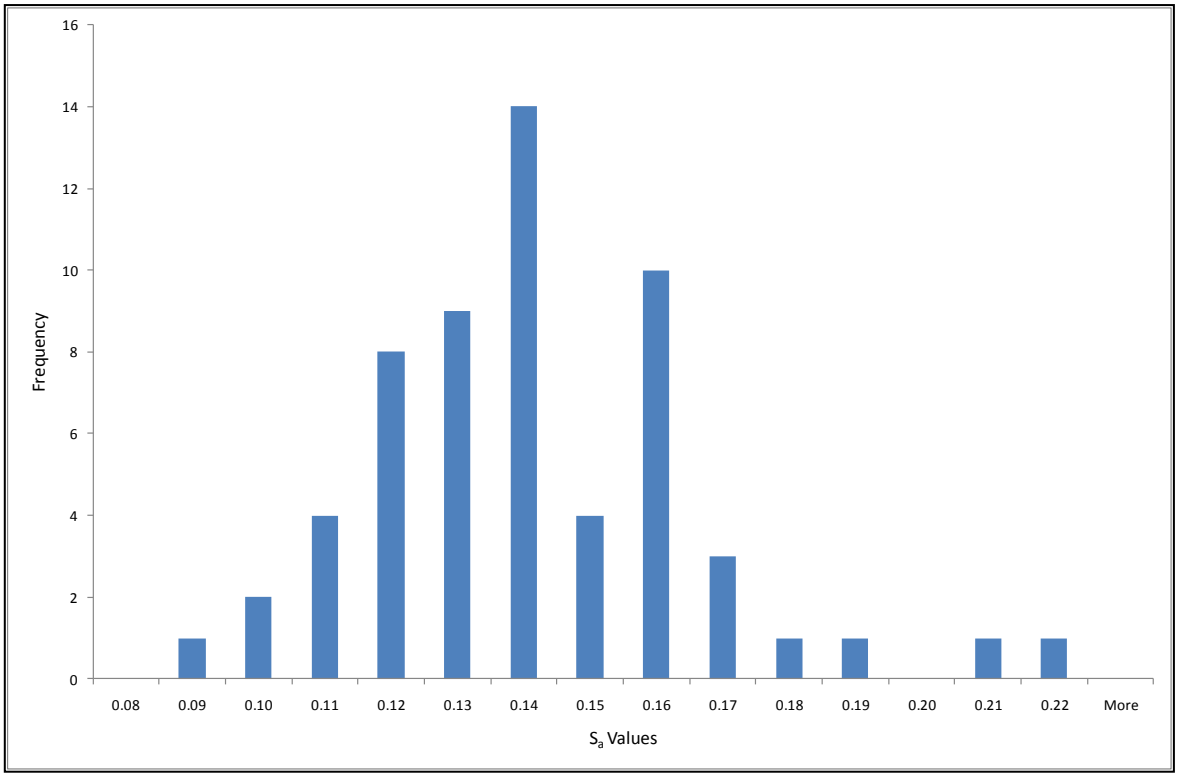

Figure 88: Histogram distribution of S_a values for hot-wire-cut surfaces, demonstrating the approximately normal distribution of S_a values

4.4.2 The 10%-Height Contiguous Diameter

As has been shown above, common surface texture parameters based on the relative heights of surface features are not suitable for the measurement of the surface texture of polystyrene foam. It was found that the range in height from the lowest value to the highest was not in any way consistent with the observed differences in the smoothness of the surfaces: surfaces that are considered smooth when assessed qualitatively can have approximately the same S_a, R_a or R_{max} (for example) values as surfaces that are considered to be 'vapourised' or 'visually disturbed' despite the fact that these surfaces are judged to be sub-optimal. Based on these observations, it was concluded that amplitude-based surface parameters are most influenced by the cell size of the foam rather than by cutting conditions, and are therefore not useful for quantitatively measuring the primary texture of surfaces produced by the RFS system.

Despite this, it was still desirable to have a means of quantitatively assessing the primary texture of the foam, since the qualitative categories used in the past have such significant drawbacks. The surface texture data gathered using confocal microscopy demonstrates clear differences between the different surface categories, so it seemed likely that quantitative measures of the texture were possible if an appropriate parameter could be determined for expressing this data.

Investigation of the surface topography imagery produced by confocal microscopy showed that there were clear differences between surfaces that were categorised as 'vapourised,' 'smooth,' or 'visually disturbed.' These differences are best demonstrated by comparing the topography of a 'vapourised'

surface with the topography of a ‘visually disturbed’ surface. Figure 89 shows a vapourised surface, while Figure 90 shows a visually disturbed surface. As is readily apparent, these surfaces exhibit fundamentally different topographies, despite the lack of difference shown by the use of texture parameters based on surface heights. Vapourised surfaces exhibit considerable isotropy, with a mottled appearance and relatively regular distribution of regions of different pixel shades (recall that the grey value of each pixel is proportional to the relative height of that point on the surface).

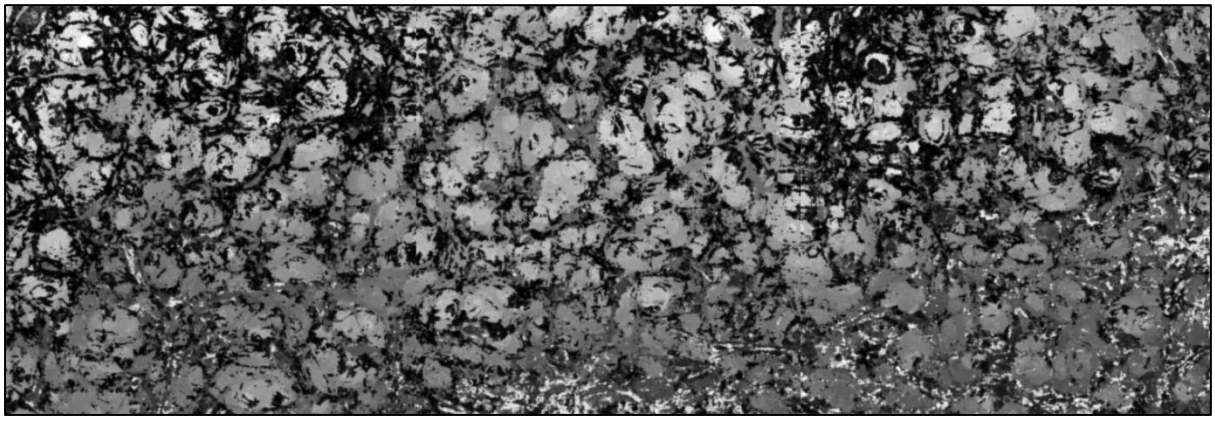

Figure 89: Surface topography of a representative vapourised surface (5A, 0.0200ms^{-1}, 0mm from start of cut)

The topography of a visually disturbed surface is fundamentally different. Here the surface is much less regular, with large black regions indicating open cells in the surface, with large contiguous regions of approximately the same surface height, resulting from the mechanical smearing of foam along the surface by the cutting tool during the cut, and occasional peaks (white areas) resulting from localised mechanical tearing of the foam (it is this tearing that constitutes the main difference between smooth and visually disturbed surfaces.

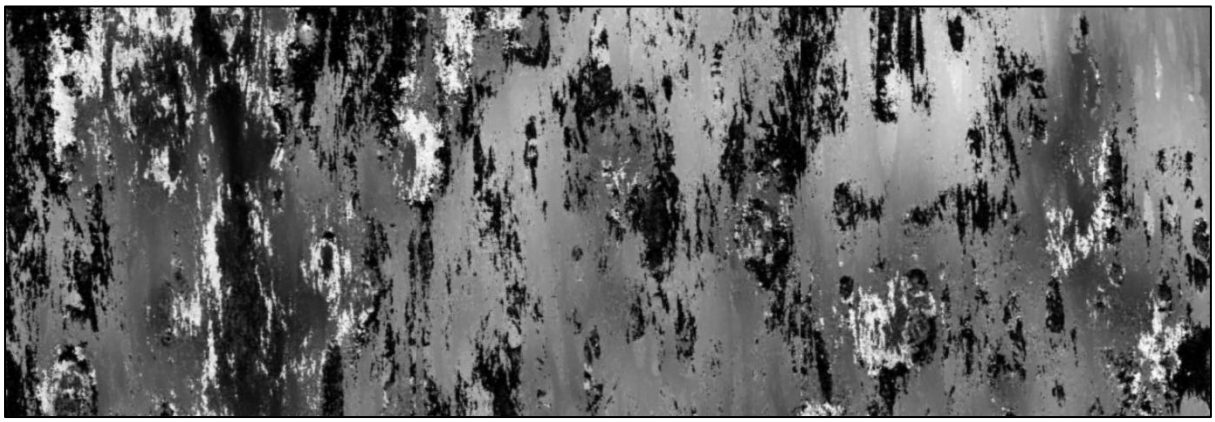

Figure 90: Surface topography of a representative Visually Disturbed Surface (5A, 0.0200ms^{-1}, 244mm from start of cut)

Based on these observations, it was hypothesised that the differences in the observed surface texture between the different qualitatively categories used was not a result of the heights of surface features

(unlike surface textures caused by most machining operations on metal [66]), but was instead a result of the horizontal distributions of the surface heights. It was thought that surfaces cut by thermomechanical means (smooth and visually disturbed surfaces) would have large areas with very little variation in surface height as a result of the mechanical smearing of the surface, while the size of contiguous regions with comparable variation in surface height would be much smaller for vapourised surfaces.

From this hypothesis, a new surface texture parameter was postulated (based on both surface height data and the horizontal distribution of the heights) that would be able to differentiate between the different surface categories and provide a useful measure of the texture of surfaces produced by RFS. This parameter has been called the 10%-Height Contiguous Diameter (for reasons which will become clear) and is denoted by ${}^{\varnothing}S_{10\%}$ (the S-notation was used to conform with the notation conventions for areal surface texture parameters of ISO25178 [67]). The introduction of a new parameter was not undertaken lightly, since the 'parameter rash' for measuring surface texture is already somewhat extreme, but none of the existing parameters trialled was useful for thermomechanical cutting of foam (and an extensive review of existing parameters did not reveal a parameter that seemed to be potentially useful). This is a result of the nature of thermomechanical cutting, which uses both thermal softening of the foam and physical smearing of the surface. As such, the mechanics of the cutting process are very different from the mechanics of metal cutting, where shearing or smearing of the metal is a much less significant factor for determining the surface texture. As a result, it was decided that a new parameter tailored to the requirements of thermomechanical foam cutting was required.

Values of ${}^{\varnothing}S_{10\%}$ were calculated from the surface topography images produced by confocal microscopy, using the Matlab script which can be found in the Appendix A3. Once the grey values indicating relative surface heights had been replaced with actual surface height values, the mean surface height was found, as was the range from maximum to minimum surface heights. The topography image is then processed to identify pixels that lie within a band defined by the Mean Height ± 10% of the Height Range, as shown graphically in Figure 91. This defines a band with a height range equal to 20% of the total height range, centred on the mean height. The value of 10% used here is simply a threshold value that was selected as a starting point for the development of the new parameter, based on the Pareto principle. This range was found to provide useful data for the surface texture of foam. The threshold could be set to higher or lower values, or to some function like the standard deviation of the height distribution, for other materials or types of texture, with appropriate changes to the parameter notation, but in this case the ±10% range was found to provide useful results.

Once pixels with surface heights lying within this ±10% band were identified, a new surface image was produced where pixels lying within the band of interest were set to a value of 0 (making the pixel black) and pixels outside the band of interest were set to 255 (white) to produce a binary image.

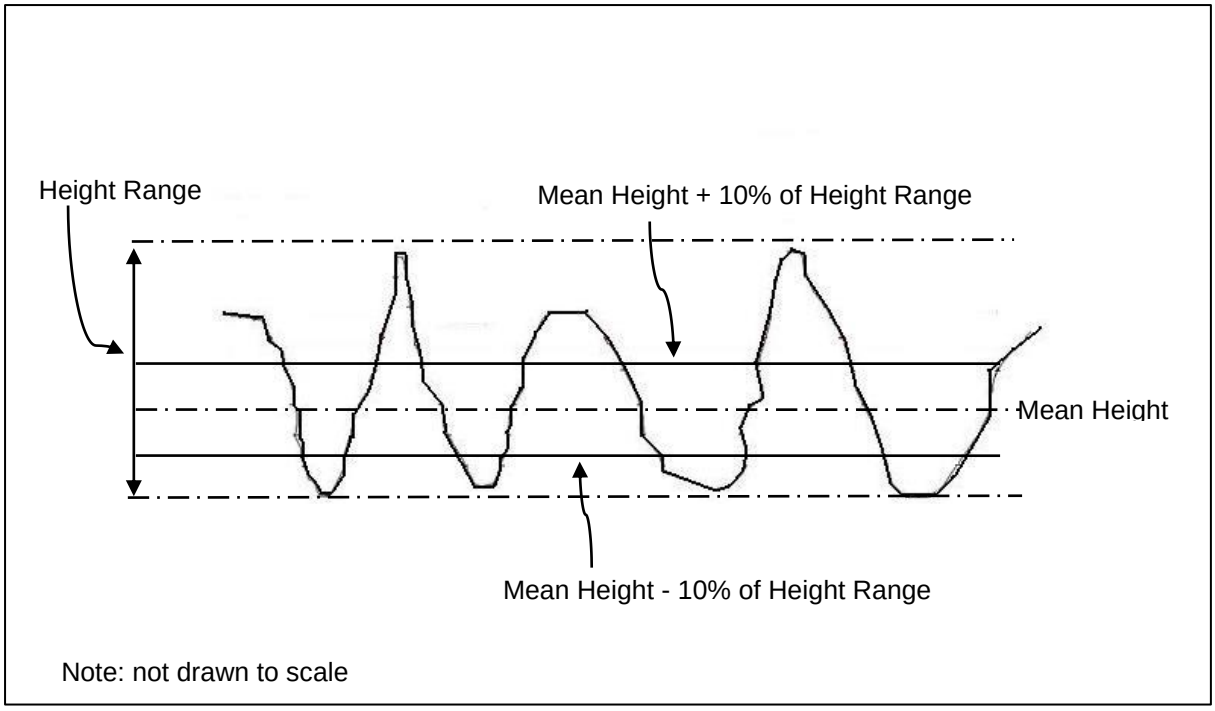

Figure 91: Arbitrary surface profile showing definition of the 10% surface band

This binary image was then processed further. The ten largest circles that could be fitted to contiguous black regions were drawn onto the image (i.e. the largest circles that could be fitted with no internal white regions) and the diameters of these ten circles measured. Again the use of ten circles is somewhat arbitrary: the real value of interest was the largest contiguous diameter that could be found, with multiple measurements being taken to minimise the effects of random error. In practice it was found that the variation in circle diameters for a given surface image was very small, typically of the order of 1 – 2 pixels. This circle-fitting stage of the parameter evaluation was done manually by drawing circles on the image using the open-source image manipulation package GIMP, since there was insufficient time available to write a Matlab script to carry out this operation. Once the ten circle diameters had been recorded, the ${}^{\varnothing}S_{10\%}$ parameter was evaluated by averaging the ten measured diameters.

$$ {}^{\Phi}S_{10\%} = \frac{\Phi_1 + \Phi_2 + ... + \Phi_{10}}{10} \tag{11} $$

${}^{\varnothing}S_{10\%}$ has units of mm throughout this thesis, and in effect defines the diameter of a cylinder centred vertically on the mean height and only containing topography data points within 10% of the mean height. A graphical example of the calculation of this parameter is shown in Figure 92.

1) Take original surface topography image from confocal microscope

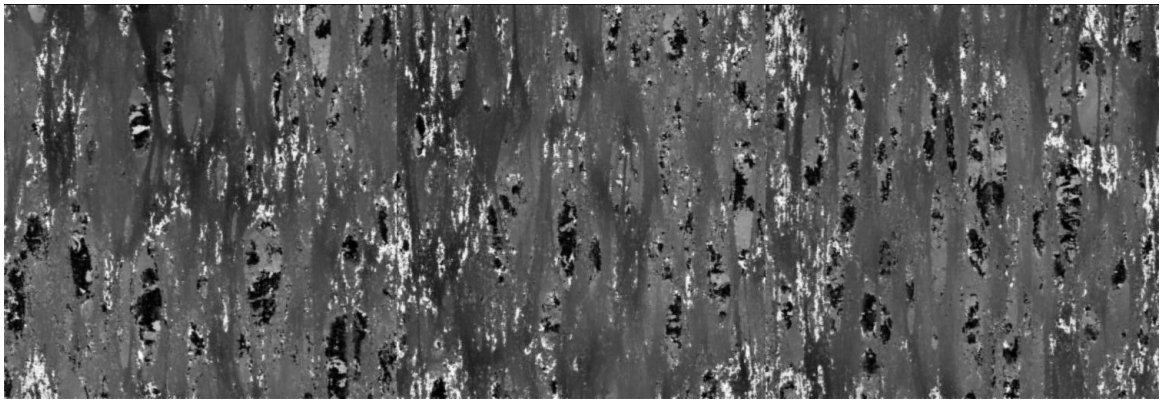

2) Determine 10% of the surface height range and the mean height, and set pixels within ±10% of the range from the mean to black, others to white

3) Fit 10 circles to the largest contiguous black regions and measure diameters $\phi_1 - \phi_{10}$

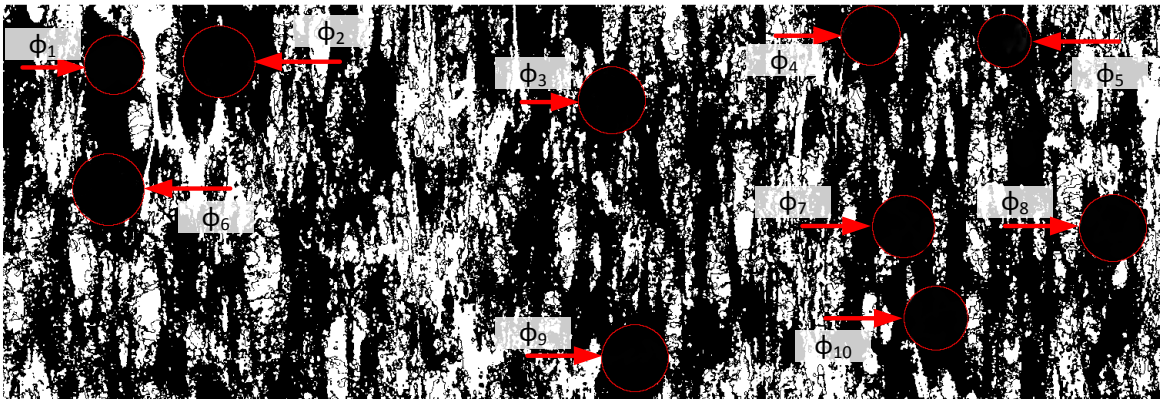

4) Calculate average of diameters $\phi_1 - \phi_{10}$

Figure 92: Processing sequence for determining the 10%-Height Contiguous Diameter

It was thought that the 10%-Height Contiguous Diameter ${}^{\emptyset}S_{10\%}$ would display clear differences between the different qualitative surface categories, would show a predictable trend along the length of a cut, and would be repeatable for a given set of cutting conditions, producing the same results for different cuts made with the same cutting conditions. In practice, the new parameter ${}^{\emptyset}S_{10\%}$ performed extremely well for foam surfaces produced by RFS, as will be shown.

It was found that the value of ${}^{\emptyset}S_{10\%}$ could be modelled accurately as being linearly proportional to the distance along the cut, as shown by Figure 93 to Figure 95 (these examples are for surfaces cut by a hot wire with cutting conditions of 5A and 0.0133ms^{-1}, so as to also demonstrate repeatability). As can be seen, the linear trendlines fitted to the data for each cut all have R^2 values of 0.9254 or greater, indicating that the linear trend has a very good fit to the measured data.

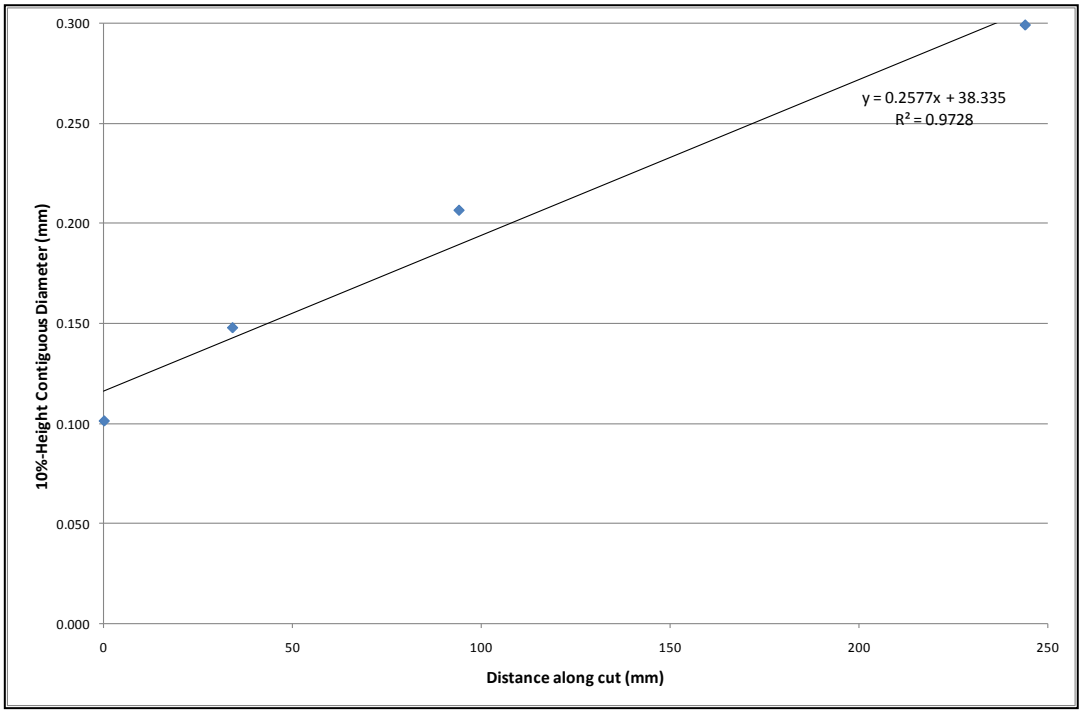

Figure 93: Variation of the 10%-Height Contiguous Diameter along a cut (5A, 0.0133ms^{-1}, Run #1)

It can also be seen that the measured value of ${}^{\emptyset}S_{10\%}$ are very repeatable for a given set of cutting conditions. The measured data points for these three cuts (denoted by the run numbers used for these samples during the experiment planning, 1, 2 and 14) with conditions of 5A and 0.0133ms^{-1} are very similar at each level of distance along the cut, with a maximum deviation of 9.9% and a minimum deviation of 1.5%. These results are summarised in Table 12. It seems likely that this deviation could be reduced by using a computer script to automatically fit the contiguous circles to the binary surface images as discussed above, since fitting these circles manually is likely to be a significant source of what little error was found in practice.

The slope of the linear trendlines for the repeatability tests is also generally consistent across all three cuts, so the rate of change of ${}^{\emptyset}S_{10\%}$ with distance along the cut is also broadly consistent. The same

basic repeatability of the measured data was also observed for the other repeatability test, using conditions of 7A and 0.0217ms^{-1}.

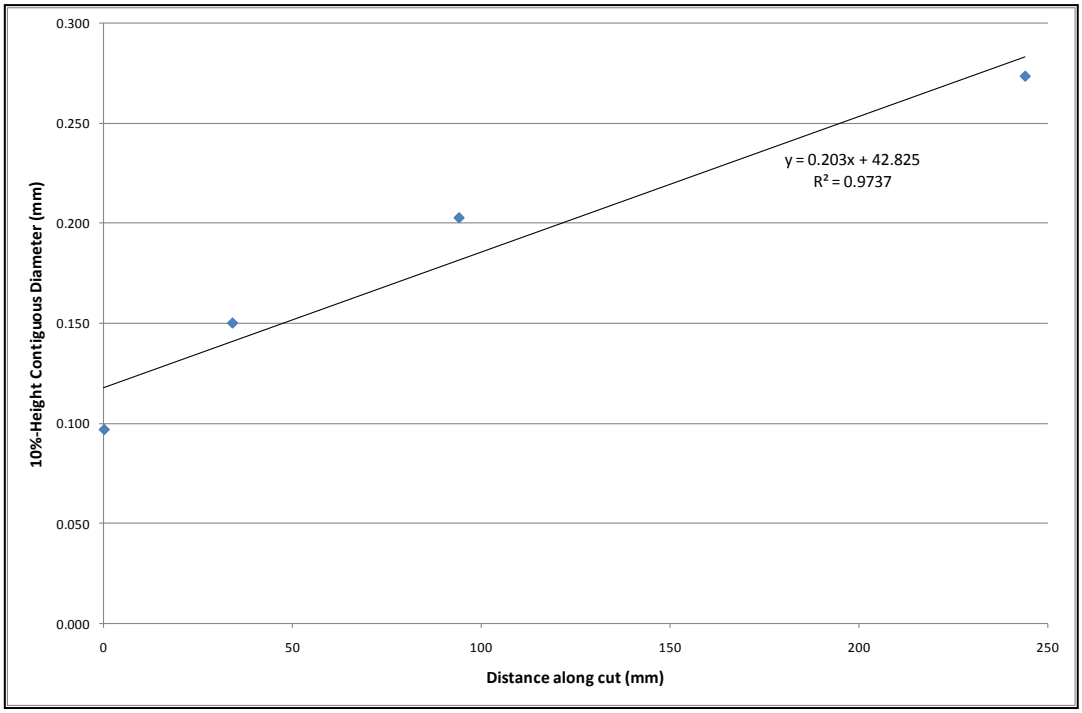

Figure 94: Variation of the 10%-Height Contiguous Diameter along a cut (5A, 0.0133ms^{-1}, Run #2)

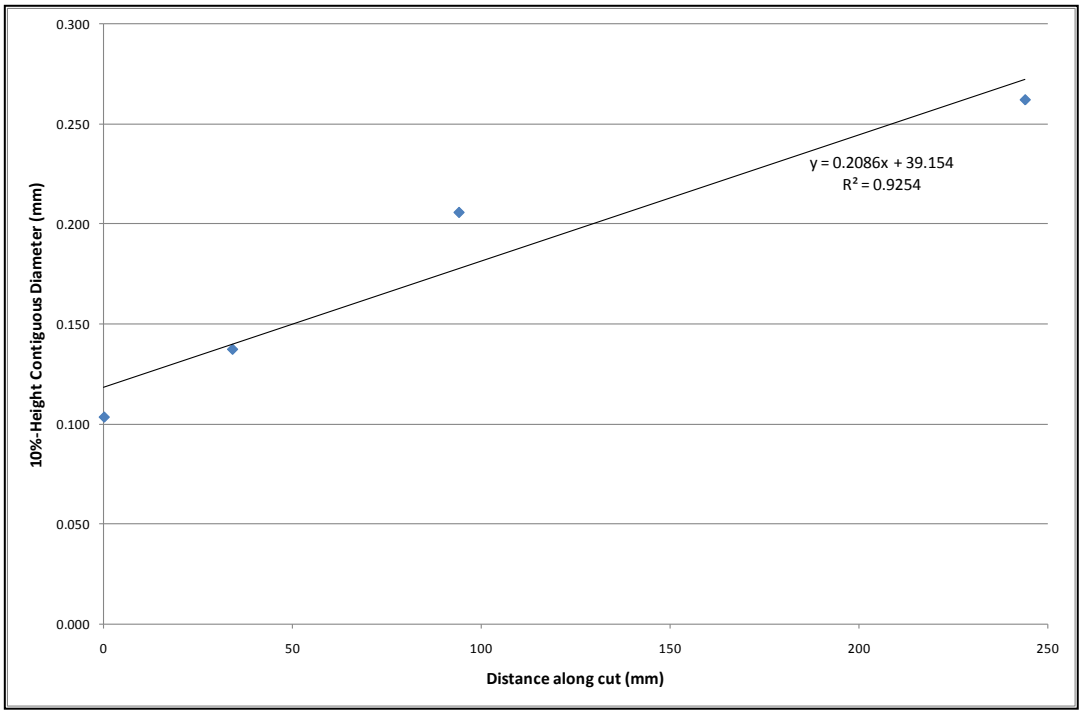

Figure 95: Variation of the 10%-Height Contiguous Diameter along a cut (5A, 0.0133ms^{-1}, Run #14)

Table 12: Values of ${}^{\emptyset}S_{10\%}$ along a cut with the same cutting conditions (5A, 0.0133ms^{-1}, hot-wire)

Run Number	${}^{\emptyset}S_{10\%}$ Values (mm)			
	0mm	**34mm**	**94mm**	**244mm**
#1	0.101	0.148	0.206	0.291
#2	0.097	0.150	0.203	0.274
#14	0.104	0.137	0.206	0.262
Range (Absolute)	0.007	0.013	0.003	0.029
Deviation (% of Run #1)	6.9	8.8	1.5	9.9

This work has established that the variation of ${}^{\emptyset}S_{10\%}$ can be modelled as a linear trend through the transition cutting stage with a high level of accuracy. However, this does not give the full picture of the variation of surface texture along the cut. As outlined in the experimental design section above, the last value of distance along the cut (244mm) was chosen because at this point in all the samples a steady-state surface appeared to have been achieved when the surfaces were assessed qualitatively. Therefore, it was expected that if measurements of ${}^{\emptyset}S_{10\%}$ were taken at larger further along the cut, these would have the same value at the 244mm data point. To test this and ensure that the 244mm data point was reflecting the steady-state surface texture value, samples at 344mm and 544mm were measured for two sets of cutting conditions (5A, 0.0133ms^{-1} and 7A, 0.0217ms^{-1}). The results for the 5A, 0.0133ms^{-1} case are shown in Figure 96. As can be seen, the measured texture at the 244mm data point accurately reflects the steady-state surface texture. In addition, the trend shown when more steady-state data is incorporated looks significantly more like what would be expected given the behaviour of the cutting force, tool centre temperature and thermomechanical balance along the cut. Although the linear trends plotted above show a good fit to the measured data, and can be used to model the variation of texture along the transition region of the cut, the trend through the transition region is better thought of as a curved trend closing in on the steady-state value.

A statistical analysis was undertaken on the steady-state surface texture values to determine which input parameters had a significant effect on the output surface texture, and to develop a model for the prediction of the surface texture based on input cutting conditions. Separate analyses were carried out for hot-wire and hot-blade tools, since although it was expected that the significant input parameters would be the same in both cases, it seemed likely from observation of the cutting processes with different tools that the exact nature of the relationships between the input parameters and the output texture would be different.

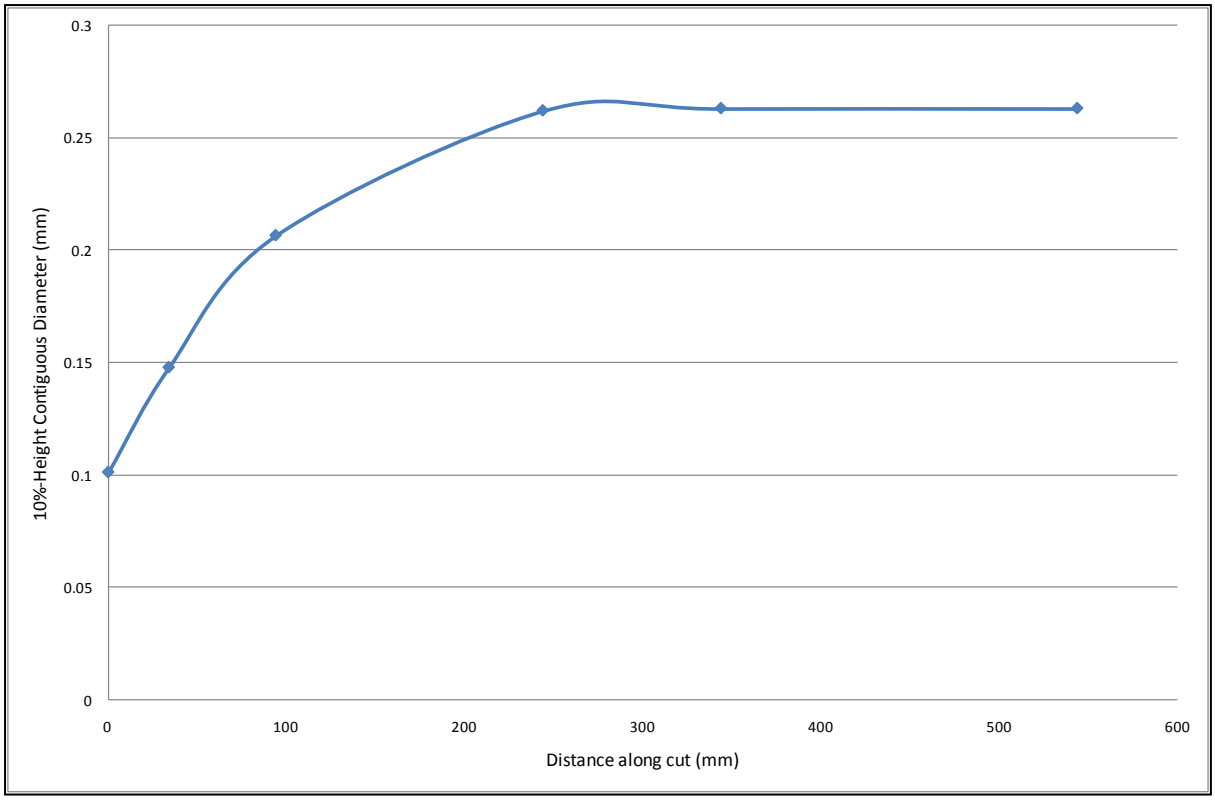

Figure 96: Variation of the 10%-Height Contiguous Diameter along a cut with 344mm and 544mm samples included (5A, 0.0133ms^{-1})

The analysis established that the only significant parameter influencing the steady-state surface texture, ${}^{ø}S_{10\%}$, was the effective heat input, Q_{eff}. It was found that the value of the 10%-Height Surface Texture was inversely proportional to the effective heat input. The statistical analysis produced models which allowed the prediction of the surface texture based on effective heat input to a high degree of accuracy. These models were:

$${}^{ø}S_{10\%,\,wire} = -(7\text{x}10^{-5})Q_{eff} + 0.3087 \quad (12)$$

$${}^{ø}S_{10\%,\,blade} = -(8\text{x}10^{-6})Q_{eff} + 0.3592 \quad (13)$$

Where the units of ${}^{ø}S_{10\%}$ are millimetres (mm) and the units of Q_{eff} are Joules per square meter (Jm^{-2}).

The model for the surface texture in hot-wire cutting had an R^2 value of 0.95, and the hot-blade cutting model had an R^2 of 0.98. These indicate that the models exhibit a very good conformance between the measured data and the predicted results. The trends of ${}^{ø}S_{10\%}$ with effective heat input for hot-wire and hot-blade cutting are shown in Figure 97 for hot-wire cutting and Figure 98 for hot-blade cutting.

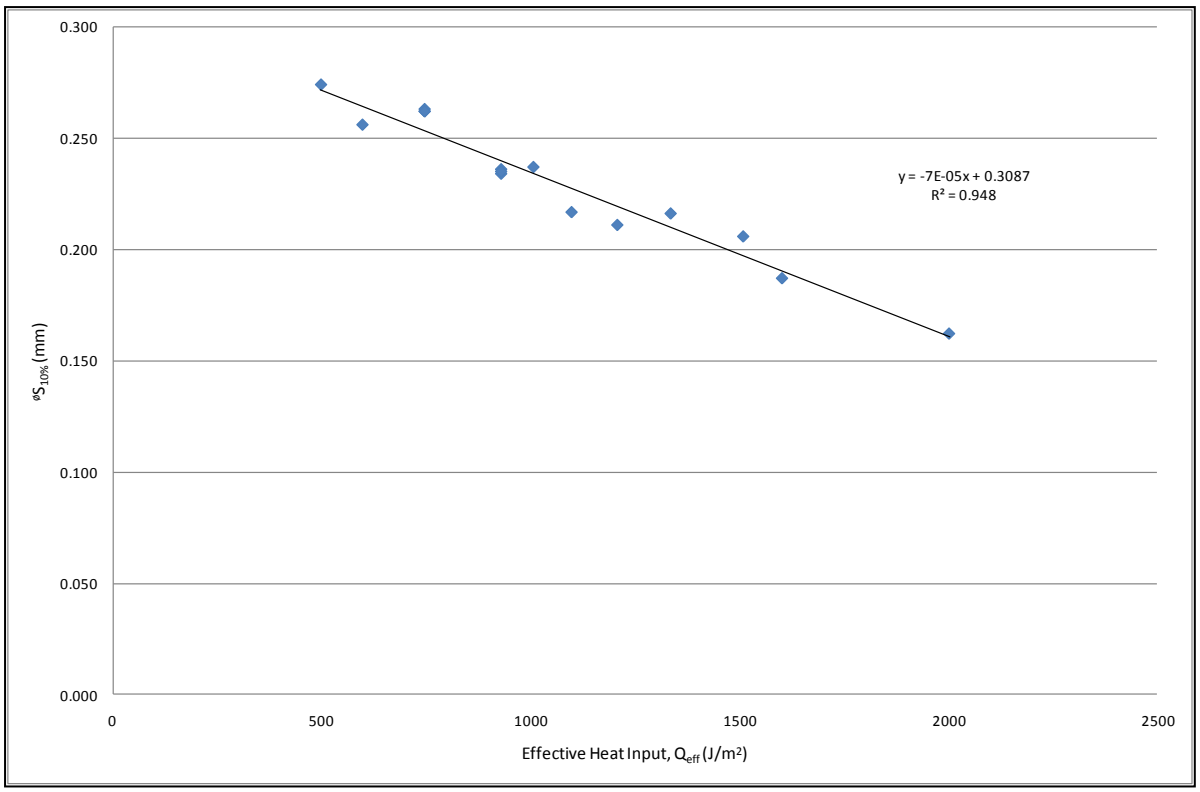

Figure 97: Trend of steady-state 10%-Height Contiguous Diameter with effective heat input, Q_{eff}, for hot-wire cutting

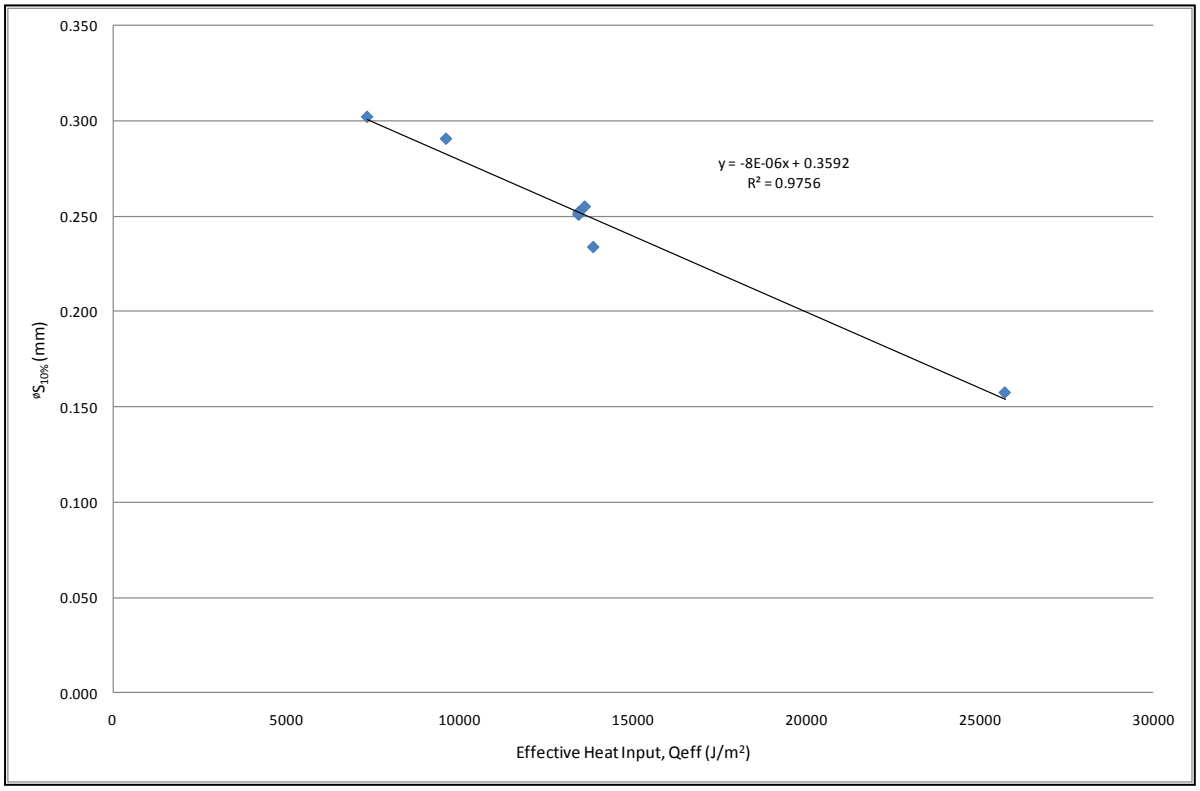

Figure 98: Trend of steady-state 10%-Height Contiguous Diameter with effective heat input, Q_{eff}, for hot-blade cutting

As is clear from these results, when using the 10%-Height Contiguous Diameter, $^{\varnothing}S_{10\%}$ it is possible to produce a good conformance between measured surface texture values and the observations of surface texture made during the qualitative assessments discussed earlier, and to generate models that allow accurate and reliable prediction of the surface texture parameter values based on the input cutting conditions. This is in contrast with the results achieved using height-based parameters, which did not show either repeatable measurements or any reliable conformance between the measured parameter values and the observed surface texture behaviour. The models produced using the 10%-Height Contiguous Diameter have R^2 values of very nearly 1, indicating an extremely good fit, which stands in stark contrast to the R^2 values of between about 0.15 and 0.55 for models generated using height-based parameters for either all the surfaces or only the surfaces produced using vapourised cutting.

The surface texture models produced above provide a very useful tool for predicting the texture based on the effective heat input, and therefore for developing a suitable cutting strategy to achieve a desired surface texture. To extract the maximum possible benefit from these models, it is necessary to relate the values of $^{\varnothing}S_{10\%}$ to the qualitative surface texture categories so that range of effective heat inputs that will lead to 'smooth' surfaces can be established.

The calculated values of $^{\varnothing}S_{10\%}$ can be sorted based on the qualitative surface type that each sample was categorised as. When this is done and the range of values in each category are compared, it becomes clear that, generally speaking, visually disturbed surfaces have higher values of $^{\varnothing}S_{10\%}$ than smooth surfaces, which in turn have greater values than vapourised surfaces. This is essentially what was expected from the increase of $^{\varnothing}S_{10\%}$ along the length of a cut. However, some overlap between the parameter values does occur at the boundary between each surface zone. The ranges of $^{\varnothing}S_{10\%}$ for each category are shown in Figure 99, where the overlap at each boundary can clearly be seen. The maximum and minimum values are also summarised for each surface category and for hot-wire and hot-blade cutting in Table 13.

This overlap between the different surface types was not entirely unexpected, given the subjectivity of the surface categorisation. Since it is very difficult to categorise surfaces with complete accuracy and repeatability, and since the different surface categories are really arbitrary segments of a surface texture continuum rather than discrete surface types, it is unsurprising that some surfaces should have been miscategorised, and it seems likely that such mis-categorisation is the cause of the overlap of $^{\varnothing}S_{10\%}$ values around the boundaries between the different surface categories.

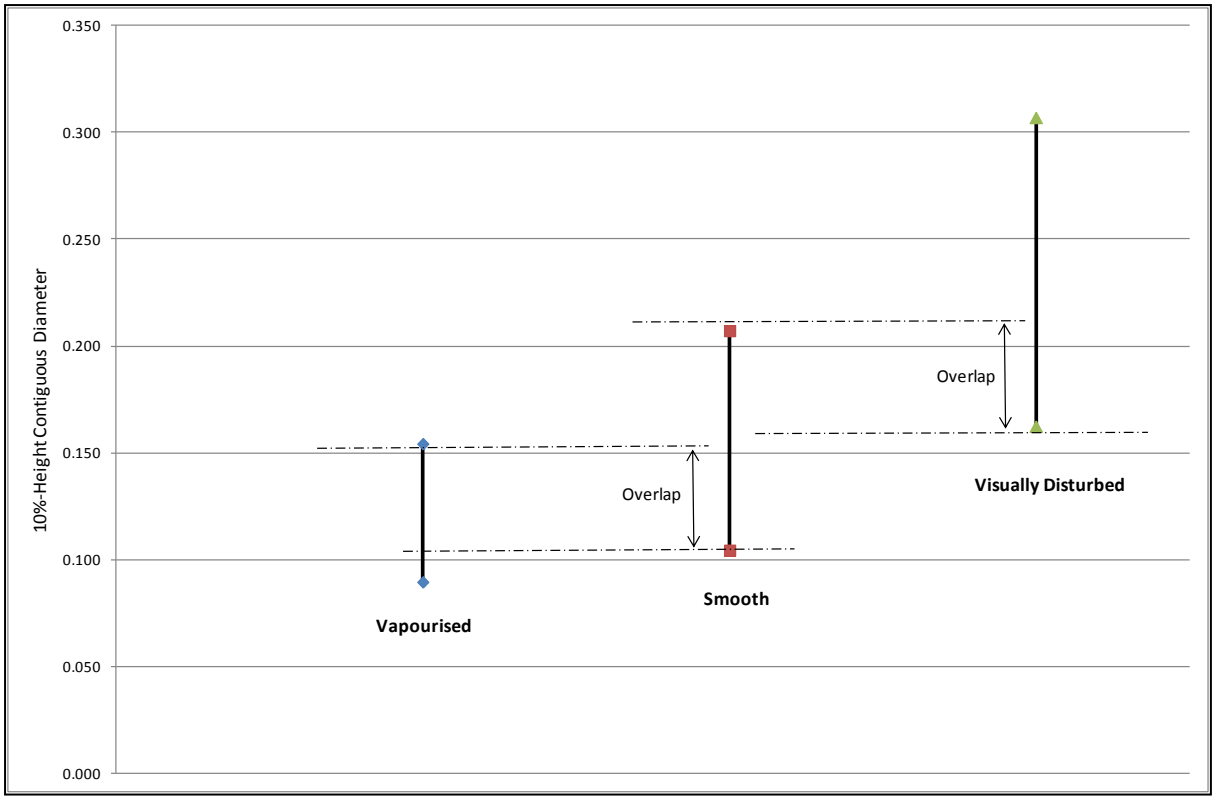

Figure 99: Ranges of ${}^{\emptyset}S_{10\%}$ values for each surface category for hot-wire cutting

Table 13: Minimum and maximum ${}^{\emptyset}S_{10\%}$ Values for each surface category

Surface Category	${}^{\emptyset}S_{10\%}$ Values (mm)			
	Wire Minimum	**Wire Maximum**	**Blade Minimum**	**Blade Maximum**
Vapourised	0.089	0.154	0.088	0.116
Smooth	0.104	0.207	0.098	0.0188
Visually Disturbed	0.162	0.307	0.165	0.315

The conclusion that the overlaps in ${}^{\emptyset}S_{10\%}$ values are the result of inaccurate surface categorisation is supported by comparison of the surface topography images for the 'vapourised' surface with the largest measured ${}^{\emptyset}S_{10\%}$ and the 'smooth' surface with the smallest measured ${}^{\emptyset}S_{10\%}$. These two cases are shown in Figure 100 and Figure 101, respectively. As can be seen, there is in fact very little substantive difference between these two topographies, despite the different surface categories into which they were placed. The arrangement of the particular surface features is somewhat different, but the size and type of those features is essentially the same. This indicates that the two surfaces were

actually both cut by approximately the same balance of thermal and mechanical cutting. The same observation was made when the topographies of the 'smooth' surface with the largest ${}^{\emptyset}S_{10\%}$ value and the 'visually disturbed' surface with the smallest ${}^{\emptyset}S_{10\%}$ value.

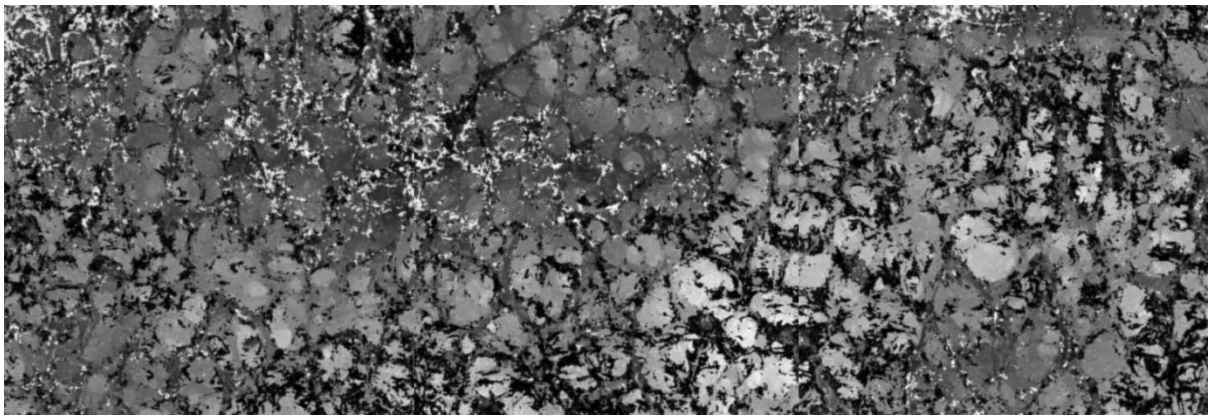

Figure 100: Surface topography for the vapourised surface with maximum measured ${}^{\emptyset}S_{10\%}$ (7A, 0.0217ms^{-1}, 34mm into cut, wire cutting)

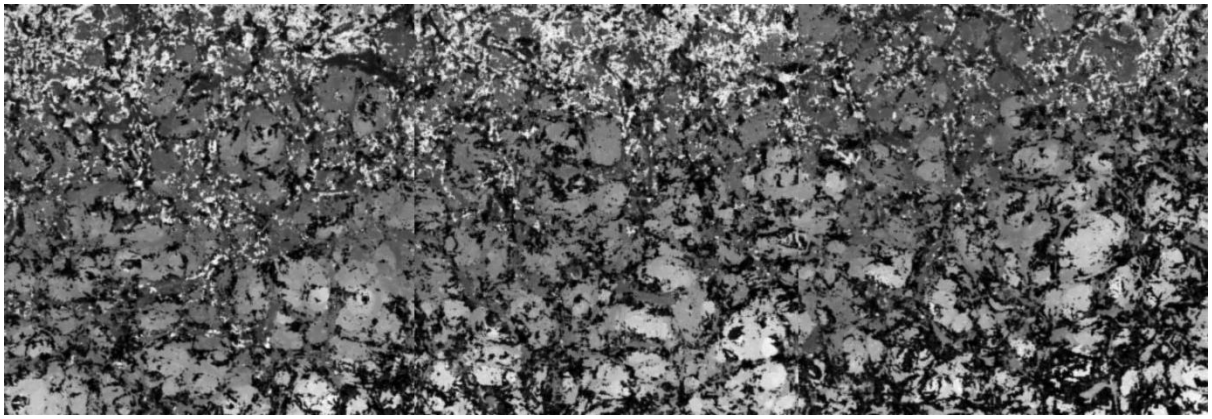

Figure 101: Surface topography for the smooth surface with minimum measured ${}^{\emptyset}S_{10\%}$ (8A, 0.0167ms^{-1}, 34mm into cut, wire cutting)

Based on the calculated values of ${}^{\emptyset}S_{10\%}$, it is possible to define threshold values for each surface category. Although the surface texture categories are essentially arbitrary, and not especially useful, they can still be used as an aid to define an 'optimum' range of ${}^{\emptyset}S_{10\%}$ values which correspond to smooth surfaces, and are therefore desirable. These threshold values were defined with reference to the range of surface texture values exhibited by the surfaces in each category, the overlap in measured texture at the boundaries, and the nature of the cutting process.

As was observed above, surfaces that were qualitatively categorised as 'smooth' were found to have ${}^{\emptyset}S_{10\%}$ values that overlapped with measured values for the 'vapourised' and 'visually disturbed' surfaces. However, these surfaces are still visually smooth and so the surfaces categorised as 'smooth' form the most appropriate reference point for defining a smooth-surface range for the 10%-Height Contiguous Diameter.

At the transition between smooth and visually disturbed surfaces, there is no fundamental change in cutting mechanics taking place, merely a transition along the continuum formed by the thermomechanical balance. As such, it is reasonable to expect that surfaces categorised as visually disturbed that had lower values of ${}^{ø}S_{10\%}$ than the maximum smooth value recorded could as easily be classified as smooth. When these surface samples were re-examined, this was found to be the case. Since the boundary between the two categories is essentially arbitrary, the most practical place to define this threshold is at the maximum recorded smooth-surface value, of 0.210mm. This will give the largest realistic range of effective heat input that can be expected to result in a smooth steady-state surface.

The transition between vapourised and smooth surfaces is somewhat more complicated, since at this boundary there is a change in cutting mode taking place, from purely-thermal to thermomechanical cutting. Without further investigation, it is difficult to define exactly the value of ${}^{ø}S_{10\%}$ at which the transition can be expected to take place, and as has been demonstrated above the surfaces in this transition region are not substantively different in any case. As such, the best definition of this threshold that can be achieved at this stage will inevitably be an approximation. To define a value for this approximation, the threshold was set at the mid-point of the overlap between the maximum vapourised value and the minimum smooth value. In the event, this midpoint value was found to be very similar for both the hot-wire and the hot-blade case, so the two values were averaged to define the threshold. This gave a boundary ${}^{ø}S_{10\%}$ value of 0.120mm

These thresholds are summarised in Table 14, and as can be seen ‘smooth’ surfaces are those with ${}^{ø}S_{10\%}$ values of between 0.120mm and 0.210mm. This provides a target range for the final finishes of surfaces cut by single-pass cutting, although as has already been noted in some cases vapourised or visually disturbed surfaces may be more desirable.

Table 14: ${}^{ø}S_{10\%}$ thresholds for each surface category

Category	**${}^{ø}S_{10\%}$ Values (mm)**
Vapourised	< 0.120
Smooth	0.120 – 0.210
Visually Disturbed	> 0.210

From these threshold values of ${}^{ø}S_{10\%}$ and the steady-state surface texture models developed above, it becomes possible to define a range of effective heat input Q_{eff} for each tool type that will produce a smooth surface. Any value of effective heat input within these ranges results in a smooth surface, while lower effective heat inputs result in visually disturbed surfaces and higher effective heat inputs result in vapourised surfaces.

The predictive models presented above for the steady-state surface texture based on effective heat input are useful in uncontrolled cutting, but are of most value in cuts where current control is applied. In controlled-current cuts qualitative assessment indicated that the surface texture was effectively constant along the cut length, with no vapourised region and no transition to steady-state cutting. As far as could be ascertained within the limit of qualitative surface assessment, current control made the texture constant along the cut length as well as the kerf. To verify this, a sample was produced using equivalent-kerf cutting conditions (see Section 5.5) with a steady-state effective heat input of 928.36 J/m^2 (i.e. 7A of applied current and a feedrate of 0.0217ms^{-1}). Surface texture measurements were taken at five points along the cut, and the results can be seen in Figure 102. As is clear, using current control results in a surface texture along the cut length that is essentially constant, subject to the inherent variability resulting from the use of a cellular material. This indicates that the use of the steady-state surface texture models developed above and controlled-current cutting results in constant, controllable and repeatable surface texture throughout the cut.

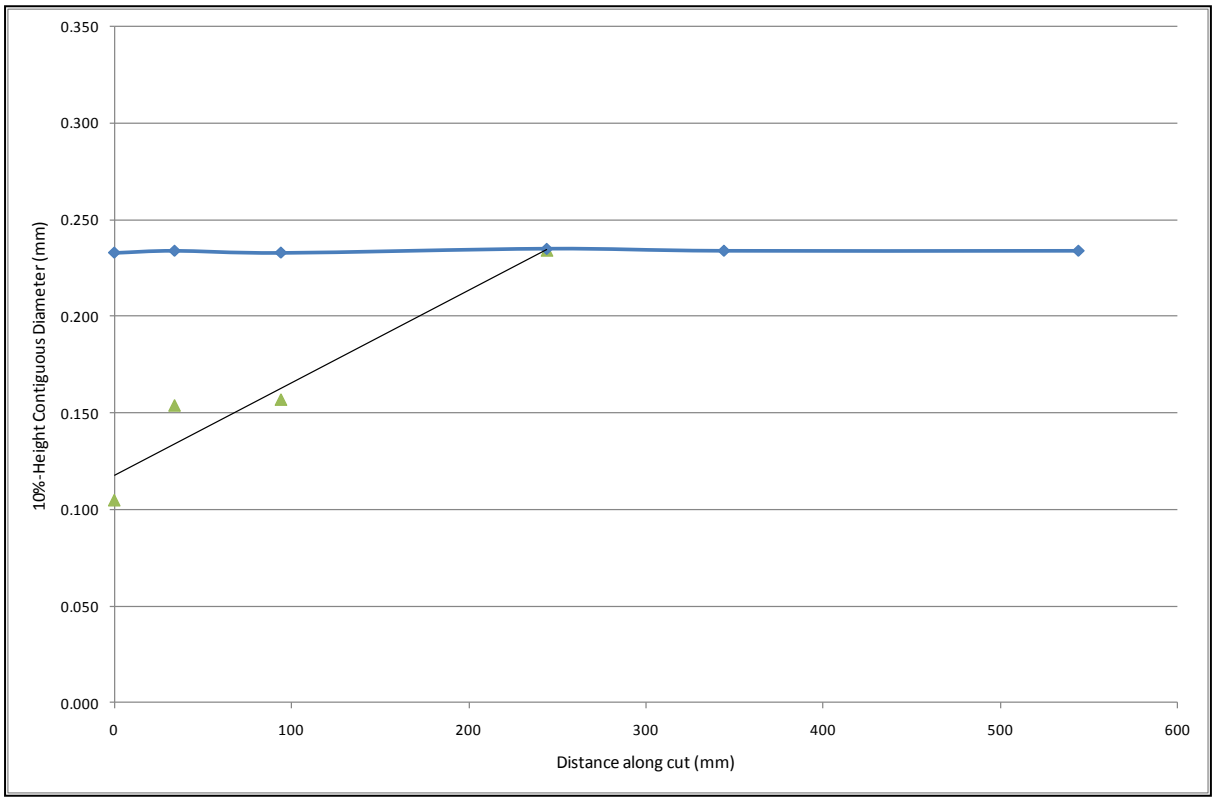

Figure 102: Trend of surface texture along a cut when current control is applied, showing the uncontrolled 7A, 0.0217ms^{-1} case and equivalent controlled-current case

Based on the work reported here, it is possible to develop a cause-and-effect diagram for the primary surface texture of polystyrene foam surfaces produced by hot-tool cutting. As has been shown, the texture is a function of a number of different parameters. The most significant is the effective heat input, Q_{eff}. This is in turn a function of the supplied current, the tool feedrate, the engaged tool length and the tool resistance. In addition, the distance along the cut is significant in cuts made without current control, since the surface texture varies between initial and steady-state values in the same

way as the tool temperature and cutting force. The tool type is also of significance, since although the nature of the behaviour of the surface texture is the same for hot-wire and hot-blade tools, the quantitative relationships between input cutting strategy parameters and output surface texture are different for each tool type. Finally, the material and the thermomechanical balance are also of significance (although the inclusion of material as an important factor here is based only on qualitative assessment, since materials other than XPS were excluded from the scope of this experimental work. The cause-and-effect diagram that summarises these conclusions is presented as Figure 103.

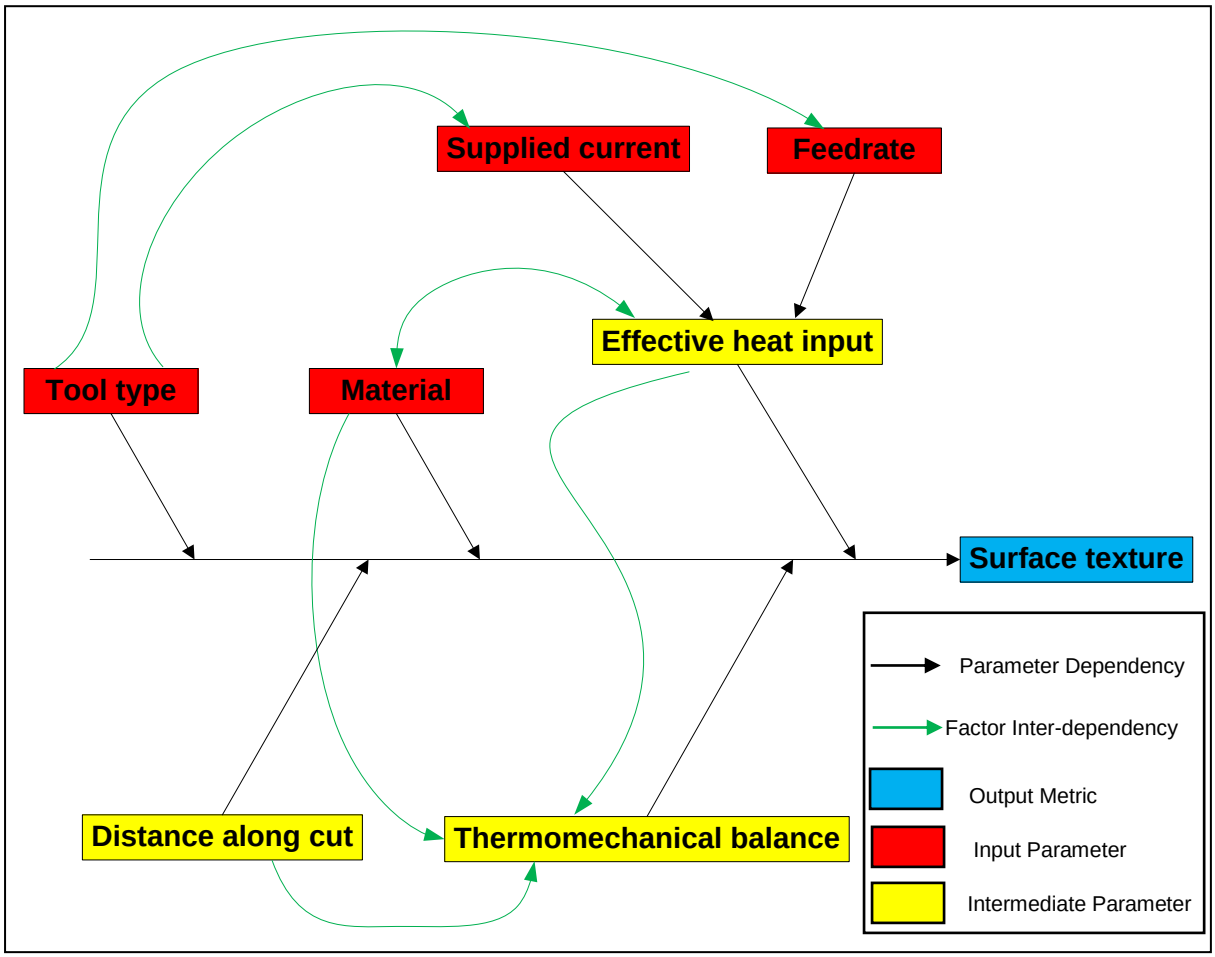

Figure 103: Cutting strategy factors and interactions that influence the surface texture

4.5 Limitations of the Surface Roughness Investigation

While useful, the surface texture investigation results summarised in this chapter do have several limitations. These are generally a function of the experimental designs used to gather the surface texture data, and in turn result from the nature of the confocal-microscope system used to measure the surface texture.

The first significant limitation is the relatively small number of surface texture samples measured. Sixty samples were measured for hot-wire cutting, and an additional 40 for hot-blade cutting: while these did cover the full range of cutting conditions within the operational space of the RFS system, the

models and understanding resulting from the investigation would have been more comprehensive, and therefore more accurate, if a larger number of samples could have been investigated practically. The small number of samples generated by the experiment design was a function of the process developed for measuring the surface texture: since measuring each sample by confocal microscopy was a very time-consuming (and therefore expensive) process, the available time and resources did not allow the measurement of more than the one hundred samples included in this investigation. With a measurement process that was less time-intensive and required less data processing, each sample could have been measured faster and therefore more samples could have been measured in the time available. Alternatively, if greater resources had been available to secure confocal microscope time, a larger sample size could have been investigated. In particular, more samples around the transition from vapourised to smooth surfaces would allow a much finer definition of the threshold values of ${}^{\emptyset}S_{10\%}$ between these two categories.

The second major limitation of the surface texture investigation is that it was limited to a single type of foam, XPS. As such, the experiment designs excluded expanded polystyrene foam (EPS), the other common material used by the RFS system. This was a result of the limited number of objective lenses available for the confocal microscope being used to gather surface topography data: in order to get large enough surface areas for the accurate evaluation of surface texture parameters, a low-magnification objective lens had to be used. The smallest magnification lens available had a 10x magnification, which gave square surface patches measuring 1.51mm on each side. Even at this low magnification, three or more adjacent surface topography patches had to be stitched together to give a large enough surface area to measure texture parameters. If EPS foam had been included in the investigation, then a much larger number of surface patches would have needed to be gathered to provide accurate topography data, as a result of the large beads in the cellular structure of EPS. Since more surface patches would have been needed for each sample, and since each set of cutting conditions used for XPS would have had to be completely replicated, the same resource constraints that limited the number of samples that could be measured also made it impractical to include EPS foam in the surface texture investigation.

4.6 Conclusions and Recommendations

This chapter has summarised the results of an investigation into the texture of surfaces produced using hot-tool cutting of extruded polystyrene foam. At the beginning of the work reported here, the assessment of surface texture was limited to some very basic qualitative categories that were not particularly reliable, were inherently subjective and were very difficult to communicate to interested parties outside the RFS project. There was very little understanding of the nature of foam surfaces after hot-tool cutting, no method of measuring them quantitatively, and no means of expressing the nature of the surfaces numerically. Most importantly, the factors that influenced the surface texture were only poorly understood.

The research reported here has made a significant contribution to the understanding of the surface texture of thermomechanically-cut foam surfaces. A robust, reliable and repeatable method of

measuring the texture of polystyrene foam using a confocal microscope was developed and validated, and this allowed detailed examination of the nature of foam surfaces at a small scale. It was further found that the fundamental differences between the different surface types that had already been identified was a function of the horizontal distribution of surface features rather than of the relative heights of those features, as is the case for most surfaces commonly of interest in engineering.

It was found that, because of the nature of the foam surfaces and the underlying foam material, common surface texture parameters like R_a, S_a and S_q were of no real use for distinguishing between or quantifying the surfaces of interest to RFS. It was found when values of these parameters were calculated that they were essentially randomly distributed, with a mean value equal to approximately half the cell size of the foam being used for the experiment. This strongly indicated that the cell size had as much, if not more, effect on the surface texture as the cutting strategy and cutting conditions. Height-based parameters were found to be of some limited applicability in vapourised cutting, but of no use when trying to measure surfaces that resulted from thermomechanical cutting. Even for surfaces that had been cut solely with vapourised cutting, the height-based parameters were only of limited use and it was not possible to develop robust predictive models for these parameters based on input cutting conditions.

In order to express the texture of foam surfaces numerically, a new parameter was developed, the 10%-Height Contiguous Diameter ($^{ø}S_{10\%}$). This parameter was proposed based on extensive qualitative inspection of surface topography data, and was a hybrid parameter that was based on both the heights of surface features and the horizontal distribution of those features, and was capable of distinguishing between the different surface categories found in thermomechanically-cut foam surfaces based on measurements of the relatively large flat areas on the surfaces that resulted from the smearing of the plastic by the mechanical action of the cutting tool.

Using the 10%-Height Contiguous Diameter, predictive models were developed for the steady-state surface texture of foam surfaces using statistical analysis of the surface data. This analysis found that the effective heat input, Q_{eff}, could be used to predict the steady-state texture with a high degree of reliability. Two models were produced, one for hot-wire cutting and one for hot-blade cutting. The models had R^2 values of 0.95 and 0.98, respectively, indicating a very good conformance between the values predicted by the models and the measured data. The models were:

$$^{ø}S_{10\%,\ wire} = -(7\text{x}10^{-5})Q_{eff} + 0.3087 \quad (12)$$

$$^{ø}S_{10\%,\ blade} = -(8\text{x}10^{-6})Q_{eff} + 0.3592 \quad (13)$$

Where the units of $^{ø}S_{10\%}$ are millimetres (mm) and the units of Q_{eff} are Joules per square meter (Jm^{-2}).

Based on the measurement results achieved using $^{ø}S_{10\%}$, a smooth surface range was defined. Surfaces that would previously have been assessed only qualitatively as being ‘smooth’ can now be quantitatively defined as surfaces with $^{ø}S_{10\%}$ values between 0.120mm and 0.210mm. Surface texture

values below 0.120mm are associated with vapourised surfaces, while surface texture values above 0.210 are associated with visually disturbed surfaces.

The steady-state models developed during this investigation are of use when cutting without current control, but really become powerful when used in conjunction with controlled current cutting and other cutting strategy knowledge that will be developed in subsequent chapters. Surfaces produced using controlled-current cutting were found to exhibit an effectively constant surface texture along the cut, so when the surface texture models developed here are combined with the steady-state and initial kerf models that will be developed in the following chapter it becomes possible to choose cutting conditions and implement controlled-current cutting in order to achieve a desired constant surface texture (this will be discussed further in section 5.5)

While the research reported here has significantly advanced the understanding of the surface texture produced by hot-tool cutting of polystyrene foam, there are a number of limitations to this research that should be rectified by further research to develop a complete understanding of foam surface texture. The most significant limitation is the fact that this investigation only used extruded polystyrene foam (XPS) without any consideration of the other major material used in the RFS system, expanded polystyrene foam (EPS). The investigation was restricted to XPS due to primarily to resource constraints, and it is very likely that the input cutting strategy parameters of significance for the texture of EPS foam will be the same as the parameters of significance for XPS foam, but in order to develop predictive models for the EPS surface texture another experimental investigation focused on this material will be necessary.

The second major limitation of this work was that only a relatively small number of samples were measured. This does not impair the results of the investigation, since an experimental design was used that gave a good overview of the behaviour of the surface texture across the operational space of the RFS system, but there are areas in which more measured samples would be desirable In particular, a more detailed investigation of the texture around the threshold that separates vapourised from smooth surfaces would be advisable, to define the threshold between these surface categories with greater accuracy.

It will be recalled that the desired outcomes from this investigation were:

- An accurate and quantitative method of gathering surface texture data for polystyrene foam surfaces.
- A better understanding of the features of surface texture that determine the visual nature of these surfaces.
- A useful quantitative measure of the surface texture of foam that was consistent, repeatable and communicable.
- Threshold values of this quantitative parameter for the different surface finish categories that have already been identified.

- A statistical model that could predict the expected surface texture of surfaces cut with hot-wires and hot-blades based on the values of input parameters, so that the texture could be considered along with other output metrics to optimise the cutting strategy used to sculpt a given part.

All of these desired outcomes were achieved, so the surface texture investigation has to be considered a success. The knowledge of foam surface texture within the RFS project has been advanced significantly by this work, and this new understanding can be used as part of the set of tools used to select a cutting strategy to sculpt a given part with the RFS system (see Chapter 8). In addition, measurement procedures are now established that can be used for further investigations of surface texture, to refine the conclusions of this investigation or to expand them to other types of foam.

5 Cutting Strategy for Single – Pass Cutting

While surface texture is an important parameter for assessing the quality of the surface, it is not the only significant aspect of surface quality, or even the largest. It is also necessary to consider the geometric form errors present in a surface due to the nature of the hot-tool cutting process. The geometric form errors present vary depending on whether single-pass or multi-pass cutting strategies are being used to produce a surface. This chapter will consider the cutting strategy in single-pass cutting, with particular emphasis on the geometric form errors present and the cutting force resulting from the cutting process. The form errors found in multi-pass cutting are considered in the next chapter.

5.1 Introduction

As discussed in the previous chapter, the surface texture is an important surface quality output metric, since the surface character of a foam surface has a significant influence on the aesthetic and interfacial quality of that surface. However, surface texture is by no means the most important surface quality output metric. Of more general importance is the geometric form of the cut surface.

Geometric form errors are the larger-scale deviations between the nominal and the actual surfaces, with magnitudes of the order of millimeters, rather than the micrometer-order errors of surface texture. The geometric form is important because these larger-scale surface deviations have a significant impact on the quality of the output part, since the relatively large form deviations control whether the sculpted part is within or outside the initial specification.

Despite the much larger scale of the form errors relative to surface texture errors, the underlying causes of these errors are the same. In single-pass cutting, the form errors are the result of thermomechanical factors and geometric factors like distance along the cut. As such, the geometric form errors for single-pass cutting are somewhat different from those for multi-pass cutting, since the nature of the cutting strategy is fundamentally different and no lay occurs in the surfaces. For this reason, the geometric form errors of single-pass and multi-pass cutting have been considered separately, despite the many similarities between them.

There are two basic geometric form errors that have been observed in surfaces produced by single-pass hot-tool cutting. These are the kerfwidth (denoted by λ) and the surface barrelling (denoted by ΔH). From qualitative observation of the cutting process, these errors were thought to be essentially the result of the effective heat input and the thermomechanical balance.

When a hot tool passes through a foam workpart, there is an initial zone during which the tool is surrounded by a thermal field sufficient to vapourise the foam without any physical contact between the tool and the foam. This field collapses as the cut progresses until steady-state thermomechanical cutting is reached, in which state the foam is being cut by both the heat of the tool and the mechanical slicing of the foam resulting from the physical contact between the tool and the foam. The nature of

this cutting mechanism results in the first significant single-pass geometric form error, the kerfwidth, which is a measure of the volume of foam lost as a result of the cutting process. This is essentially the same as the kerf experienced in sawing, where the width of the tool itself results in a dimensional error that has to be compensated for. If the central axis of the cutting tool is passing along the nominal surface that is being sculpted, then this kerfwidth will mean that the as-manufactured part will have surfaces that are offset from the nominal surfaces of the as-designed part. As such, there is a clear need to compensate for the kerf produced during cutting, and to do this it is necessary to develop a full understanding of the nature of the kerf and its variation along a cut. While some work in this area has been carried out by Brooks [1], and a basic current-control system developed to stabilise the kerfwidth along the cut, this work was based on a very limited number of cutting conditions and took no account of the exact nature of the kerfwidth variation along the cut, so a more thorough investigation is necessary to develop a full understanding of the behaviour of the kerf error.

The second significant surface form error in single-pass cutting is the surface barrelling, ΔH. This is an error in the shape of the surface that occurs in a direction normal to the direction of tool travel. It is thought that this error results is caused by the thermal profile along the tool, which is the result of the transfer of energy from the tool to the foam with which it is engaged. In the cut, once the vapourised stage is complete and thermomechanical cutting is taking place, the tool in the centre of the cut is significantly colder than the tool at its free-air temperature. At the centre of the engaged length, the tool is at its in-cut temperature, but the parts of the tool that are not engaged with the foam are still at the free-air temperature associated with the relevant level of power input. As a result, there is of necessity a thermal gradient along the tool from the centre of the engaged length to the unengaged length of the tool. This thermal gradient results in the geometric form error denoted by ΔH. It is important to note that, although ΔH is referred to as ‘surface barrelling’ because of the characteristic observed surface form in steady-state cutting, which showed a convex surface form error referred to as ‘barrelling’ within the RFS project, a surface can have ΔH values that are negative (indicating a concave surface) or near-zero (indicating an effectively flat surface). The nature of the observed ΔH configurations will be discussed in more detail in the next section.

This chapter begins with a discussion of the characteristic geometric form errors found in single-pass cutting, based on qualitative observations of the results of experimental work. Next is a discussion of the problem posed by the task of measuring the form error of foam surfaces, and the definition of an appropriate measurement process and suitable metrics for expressing the usual geometric form errors. An outline is then given of the design of a thorough experiment used to capture data to allow the characterisation of the form errors, followed by separate sections presenting detailed results for both the kerfwidth (λ) and surface barrelling (ΔH) errors. This is followed by a section discussing the cutting force measured in single-pass cutting, and presenting models that can be used to predict the expected cutting force based on the cutting conditions. The chapter concludes with a section discussing the results of the investigation and drawing conclusions.

5.2 Characteristic Geometric Form for Single-Pass Hot-Tool Cutting of Polystyrene Foam

As outlined above, the kerfwidth is the lost area resulting from the thermal field around the cutting tool and the physical size of the cutting tool. In a manner analogous to sawing, the tool has a finite thickness and so material equal to or greater than this thickness must be lost during the cutting process in order for the tool to be able to pass through the foam workpart. In the case of thermomechanical foam cutting, the tool 'thickness' is made up of both the physical size of the tool and the size of the thermal field around the tool. As a result, the kerfwidth along a cut exhibits characteristic behaviour that is related to the tool centre temperature and the feedrate, and therefore is a function of the thermomechanical balance.

At the beginning of a cut where no current control is implemented, the tool is initially at a free-air temperature that is a function of the power supplied to the tool. This temperature is significantly higher than the melting point of the foam, and so when the tool enters the foam the tool is surrounded by a thermal field that vapourises the foam around the tool without the tool coming into physical contact with the foam. As a result, the lost area (and therefore the kerf) is significantly larger than the physical size of the tool. The thermal field and the physical tool can be thought of as being summed together to make a 'virtual tool' which produces a relatively large kerfwidth.

As already noted, the size of the vapourising thermal field is not constant along a cut. As energy is transferred to the foam in order to melt the plastic, the tool cools down and the thermal field gets smaller (or, in other words, the kerf gets smaller). Eventually, under typical conditions, the thermal field is no longer large enough to vapourise the foam without physical contact between the tool and the foam, and so the tool begins to touch the foam and adds an element of mechanical slicing to the cutting process. Ultimately, steady-state conditions are reached at which the cutting force and tool centre temperature stabilise: at this point the kerfwidth also stabilises and remains essentially constant (subject to occasional random errors) for the remainder of the cut.

This trend of kerf along the cut is shown by Figure 104. During vapourised cutting the kerf is large as a result of the uncollapsed thermal field around the tool. During the transition region after thermomechanical cutting has begun, the kerf gets progressively smaller until steady-state conditions are reached, at which point the kerf has the lowest value it will exhibit for the set of conditions in use. There is a theoretical minimum kerf, i.e. the physical size of the tool, but in practice the steady-state kerf is usually slightly larger than this for the cutting conditions that define the operational space of the RFS system.

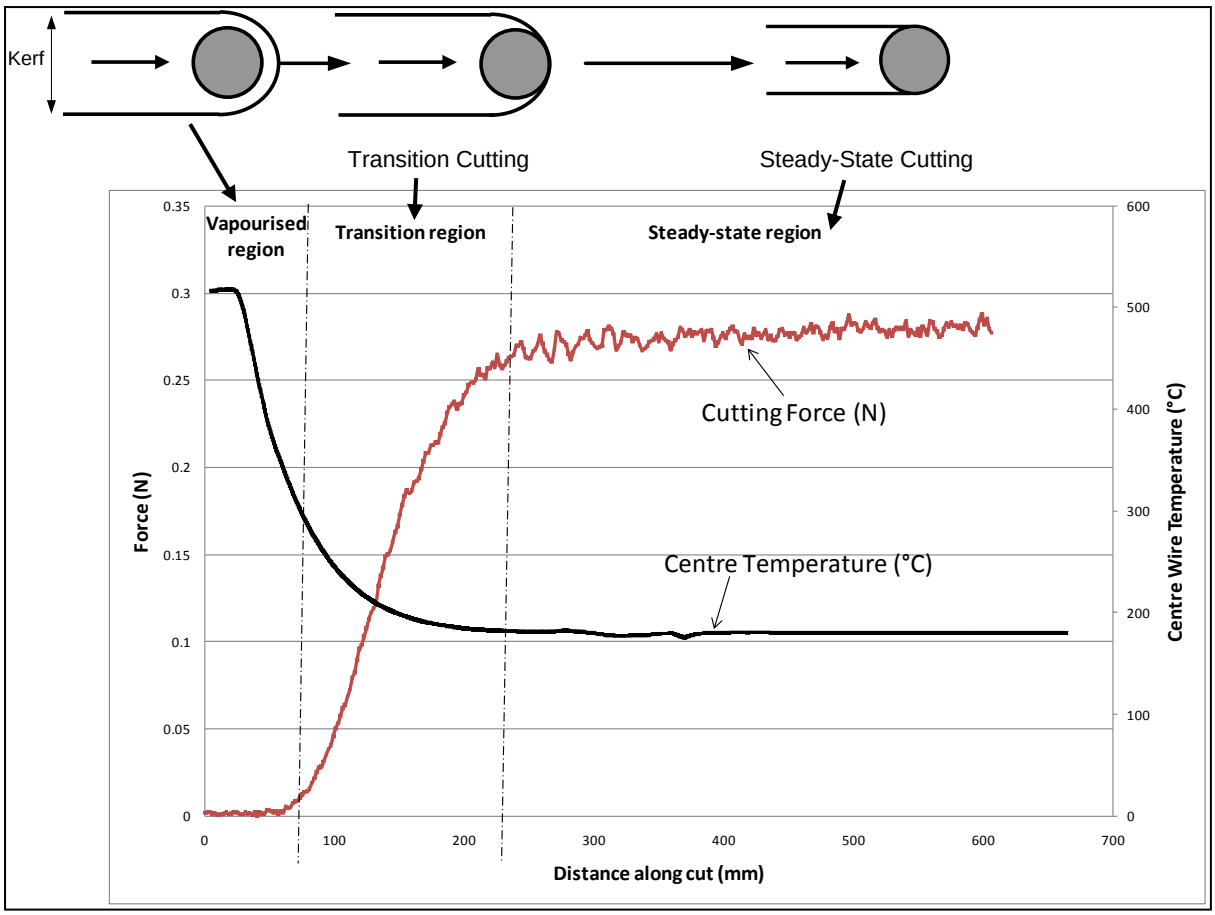

Figure 104: General trend of kerfwidth along a cut, as related to tool temperature, cutting force and cutting mode

The surface barrelling also exhibits a characteristic trend along a cut, which is also related to the thermomechanical balance. At the beginning of the cut, the tool is at its free-air temperature and there is no thermal gradient along the tool: all points on the cutting tool are at the same temperature. As such, when the cut begins the cutting mode is vapourisation, and the kerf is essentially constant for all points along the engaged length. This results in a transverse surface profile that is effectively flat, as shown on the left in Figure 105. As the cut progresses, energy is lost to the foam and the cutting tool cools down, but only along the engaged length. The length of the tool that is not engaged with the foam is still at the free-air temperature. As a result, there is a thermal gradient from the coldest point on the tool, at the centre of the engaged length, to the hottest points, which are outside the foam to either side. This thermal gradient occurs mostly in the few millimetres of tool length either side of the ends of the engaged length. As a result of the thermal gradient, the areas of foam at the ends of the engaged length are effectively being cut by vapourisation even when most of the engaged length is in steady-state thermomechanical cutting conditions. This means that the kerf at the ends of the engaged length is larger than the kerf in the centre of the cut, which manifests on the cut surface as a barrelled surface profile. The cross-sectional profile of a surface of this type is shown to the right of Figure 105.

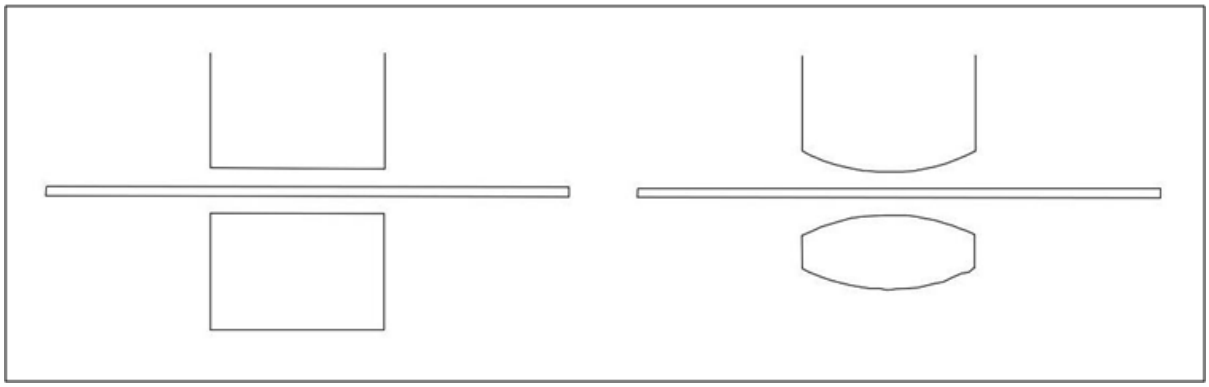

Figure 105: Characteristic transverse kerf profiles for single-pass cutting, showing the vapourised profile on the left and the thermomechanical profile on the right (tool feed direction is into the page)

In some circumstances it was observed that the transverse surface profile at the beginning of the cut is actually concave, as shown in Figure 106. This occurred frequently when producing sample surfaces for the detailed investigation of single-pass surface form, especially when cutting with relatively high effective heat input, and was thought to be a result of the cutting strategy used to produce samples. To make the production of workparts easier, the engaged length values used for these experiments were simply the thicknesses of available sheets of foam, so that the surfaces produced could be made by single cuts though as-manufactured sheets. However, as a result of the manufacturing process used, the sheets of foam have a higher-density 'skin' on the outer surfaces where the cellular structure of the bulk material is replaced by a layer of effectively solid polystyrene. It seemed likely that, during vapourised cutting, the higher-density skin at the edges of the foam (and therefore at the ends of the engaged length) required more energy to vapourise than the cellular bulk material, and so did not vapourise as far away from the wire as the bulk material at the centre of the engaged length, resulting in a concave surface profile.

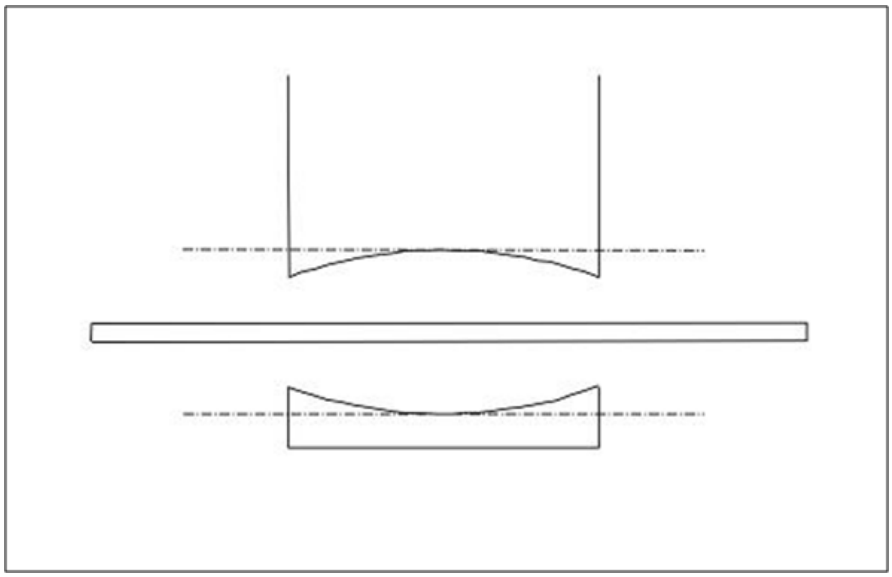

Figure 106: Transverse profile concavity for surfaces cut with high Q_{eff} and where the tool passes through the higher-density skin at the edges of as-manufactured foam sheets

When it occurred, this concavity was a function purely of the nature of the foam material (and of the cutting strategy used to produce the samples). In samples that were cut from workparts that had been prepared so as to ensure that the cut did not pass though the as-manufactured skin of the foam, concave surfaces were not produced. Based on this work, a correction was applied to the existing samples to compensate for the presence of the skin, as will be discussed in more detail later in this chapter.

The general trend of surface barrelling along a single-pass cut is shown in Figure 107, along with the characteristic cutting force and centre-cut temperature profiles. At the beginning of a cut the surface produced is either concave or flat, depending on whether the tool passes through the skin on the edges of sheets of foam. This remains the case until thermomechanical cutting begins, at which point convexity starts to develop in the surface. When steady-state cutting conditions are achieved, the surface barrelling appeared to reach its maximum value and remain there until the end of the cut.

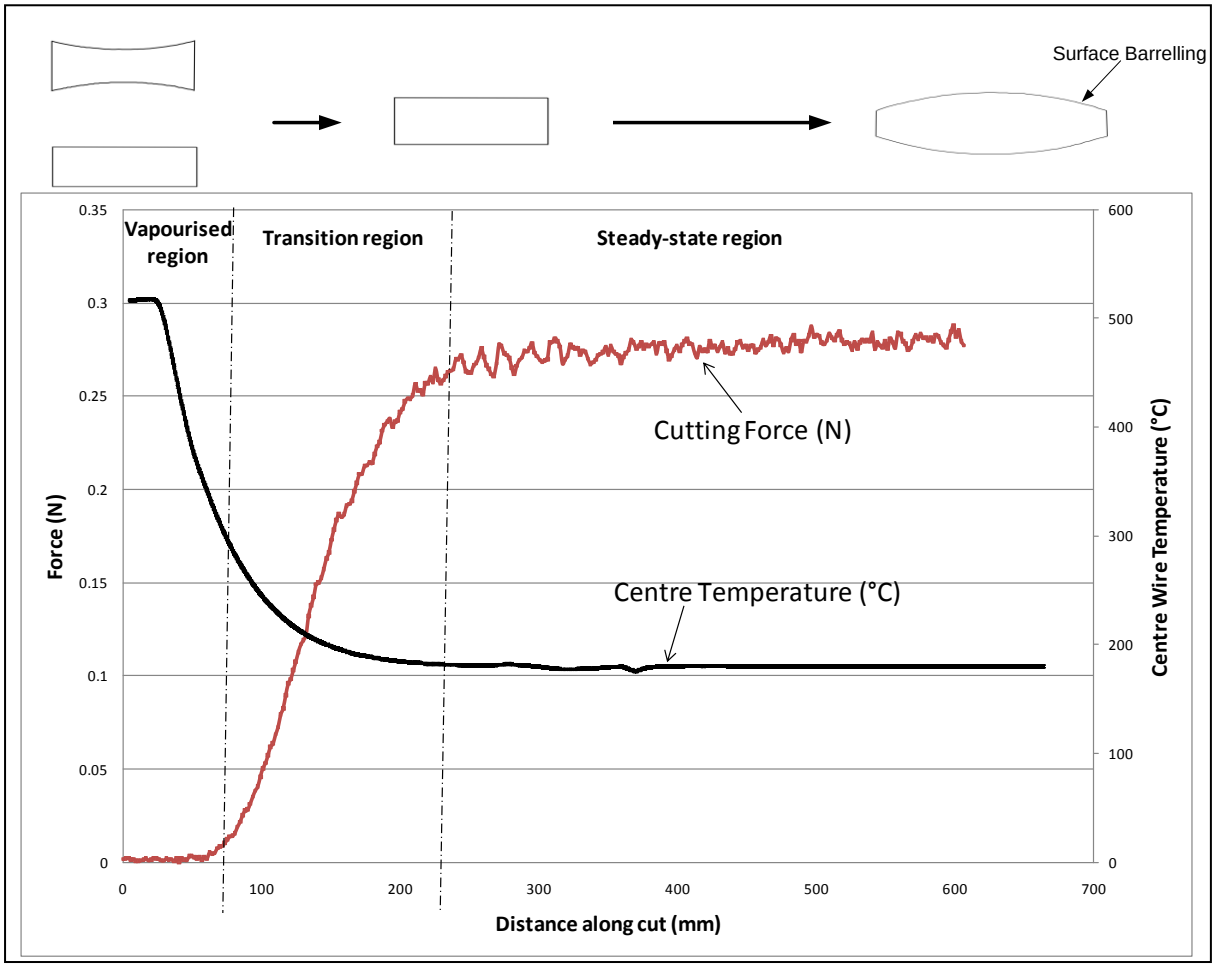

Figure 107: General trend of surface barrelling along a cut, as related to tool temperature, cutting force and cutting mode

Based on these qualitative observations, a number of hypotheses were developed for testing. These were:

1. That the kerfwidth and surface barrelling along a cut were functions of the tool temperature differential, ΔT, and were therefore in turn dependent on the cutting conditions (current and feedrate) and the distance along the cut.
2. That the kerfwidth and surface barrelling would both settle to steady values when steady-state conditions were achieved.
3. That the kerfwidth and surface barrelling along a cut would be repeatable and consistent for the same cutting parameters, and that the surface errors could be predicted based on the values of the input parameters.
4. That the steady-state cutting force would be a function of the effective heat input and the engaged tool length, and that a predictive model for the cutting force could be developed to allow tool durability predictions during the production planning stage.

In order to test these hypotheses, it was first necessary to determine a suitable and available method of measuring the geometric form of polystyrene foam. The measurement procedure developed is outlined in the following section.

5.3 Measurement Procedure and Metrics for Single-Pass Geometric Form

To develop a comprehensive quantitative understanding of the behaviour of the geometric form errors produced during single-pass cutting, it was necessary to be able to measure the surfaces produced so that the errors could be quantified for further analysis. This presented a number of unique challenges resulting from the nature of the material and the production and measuring equipment available. This section discusses the nature of the measurement problem, the measurement procedure developed to gather geometric form information, and the metrics developed to express this information.

The first consideration was the nature of the material. As with the measurement of surface texture discussed in the previous chapter, the soft cellular structure of polystyrene foam presented a measurement challenge. Since the material was soft, it was easily deformed by contact-based measurement systems. This was proven when an attempt was made to gather surface form data with a coordinate measuring machine (CMM): it was found that any tips with a diameter of less than 10mm left a visible dimple on the surface due to relatively high contact stress. Tips with a diameter greater than 10mm did not leave any surface deformation that was visible to the naked eye, but it was thought that they would be deforming the surface to some degree either elastically or plastically. In any case, using tips larger than 10mm would have made it almost impossible to discern fine detail in any of the surface data gathered, so a more suitable method was desirable.

The second consideration was the order of magnitude of the errors. Based on observation and crude measurement of a number of cut surfaces, an estimate of the general size of the kerf and barrelling errors was made. This estimate was that kerf errors had a maximum value of about 5mm, and that barrelling errors had a maximum value of about 0.5mm (these are maximum values: smaller error

values were also found, depending on the cutting conditions). As such, it was decided that a suitable measurement system needed to have a resolution of at least 0.1mm for measuring kerf and at least 0.01mm for measuring barrelling. It was felt that resolutions of this magnitude would provide a sufficient level of detail to discern surface features of interest.

The third consideration was the need for a suitable datum that could be used for as a reference for the measurements of geometric form. For example, if the surfaces were going to be measured on an instrument that used a table as a reference plane (like a CMM) then a suitable datum surface would need to exist. The exact nature of the datum that would be required would depend on the measurement instrument ultimately used.

Finally, it was not necessary to gather kerf and surface barrelling information at all points along a cut. If data about the entire surface was required this would have severely limited the range of possible measurement solutions, and would almost certainly have meant that an appropriate measurement tool would not be readily available at Canterbury University (resource constraints made it desirable to use an instrument that was available in-house). In any case, measuring the kerf and barrelling at all points along a cut would in all likelihood have produced an excess of information that would have made it harder to conduct analyses. It seemed logical that gathering kerf and barrelling information at a number of discrete points along a cut would be sufficient, as long as those discrete points were carefully chosen to provide a full picture of the variation in geometric form error along the cut.

Based on these considerations, a measurement procedure was developed that was able to capture surface profile data at discrete points along the length of a cut surface, using a 2D flatbed scanner as the data capture device. This procedure has four basic stages: sample generation, sample processing, data harvesting and data processing. Brief outlines of each stage follow.

The sample generation stage consisted of cutting samples for measurement. These cuts were carried out on the Kuka KR6 robot that forms the core of the RFS system. The procedure used to produce surfaces that could be easily measured was as follows:

1. Select the cutting conditions (feed and current) appropriate to the samples being generated, and make a cut with these cutting conditions. Discard the piece of foam cut from the workpart.
2. Move the sample vertically downwards a known distance and make a second cut, parallel to the first and in the same direction, with the same cutting conditions. This produced a sample strip which was measured.
3. Select the appropriate cutting conditions for the next sample and repeat 1 – 3 until all required sample strips have been produced.

This process generated a set of sample strips that had been cut with the same cutting conditions at top and bottom, and in the same direction. This meant that at any distance along the cut, the top and bottom surfaces should be the same, and therefore there existed a virtual datum plane through the centre of the foam strip. Since the distance between the two tool passes was known (for most of the

samples used in this investigation the distance used was 10mm), measurements of the thickness of the strip at the centre and the edges allowed the evaluation of parameters for both the kerfwidth and the surface barrelling. The process of generating the sample strips is shown in Figure 108.

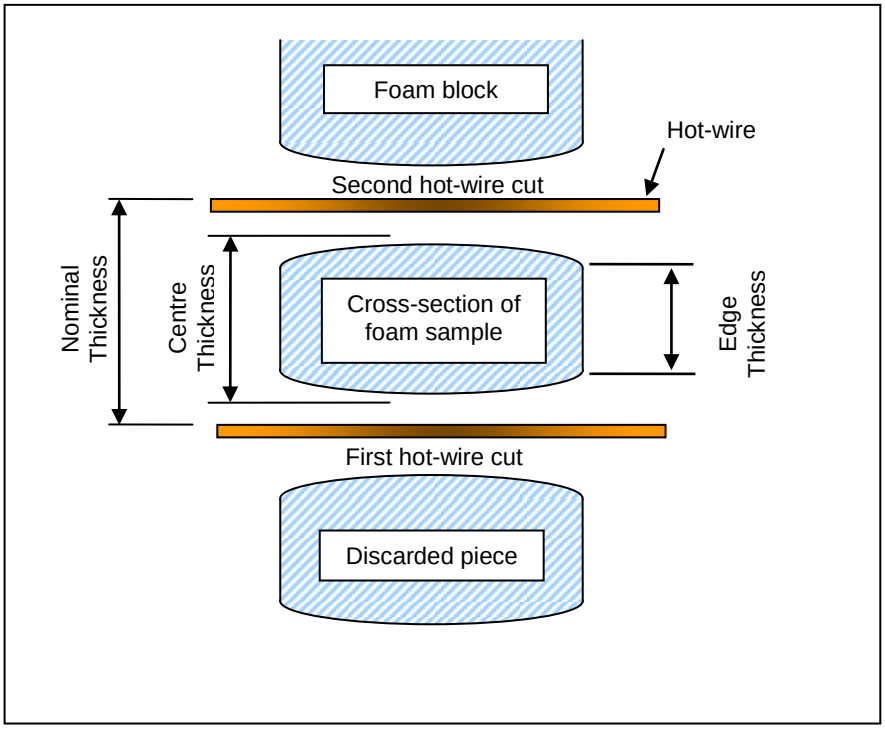

Figure 108: Sample generation and measurement strategy for surfaces produced by single-pass cuts

The next stage of the measurement procedure was sample processing. During this stage the sample strips generated in the previous stage were prepared for measurement on the flatbed scanner.

Since the only points of interest were at discrete distances along the cut, and since it was desirable to capture data from a cross-section of the sample strip for ease of data processing, the sample processing stage consisted of manually sectioning the samples in preparation for scanning. To do this, the points of interest along the sample strip were marked off (having been carefully measured using a steel rule) and the strip was then sectioned very carefully using a sharp razor blade and a square, to ensure that the cross-sections were normal to the longitudinal axis of the strip. Since the razor blade used to section the sample was very thin and very sharp (to avoid blunt razors each blade was used no more than five times before being replaced with a new one) it was possible to section the foam samples with a high degree of confidence that the sectioning process was not introducing any significant deformation to the surfaces of interest. A graphical representation of the manual sectioning process is shown in Figure 109.

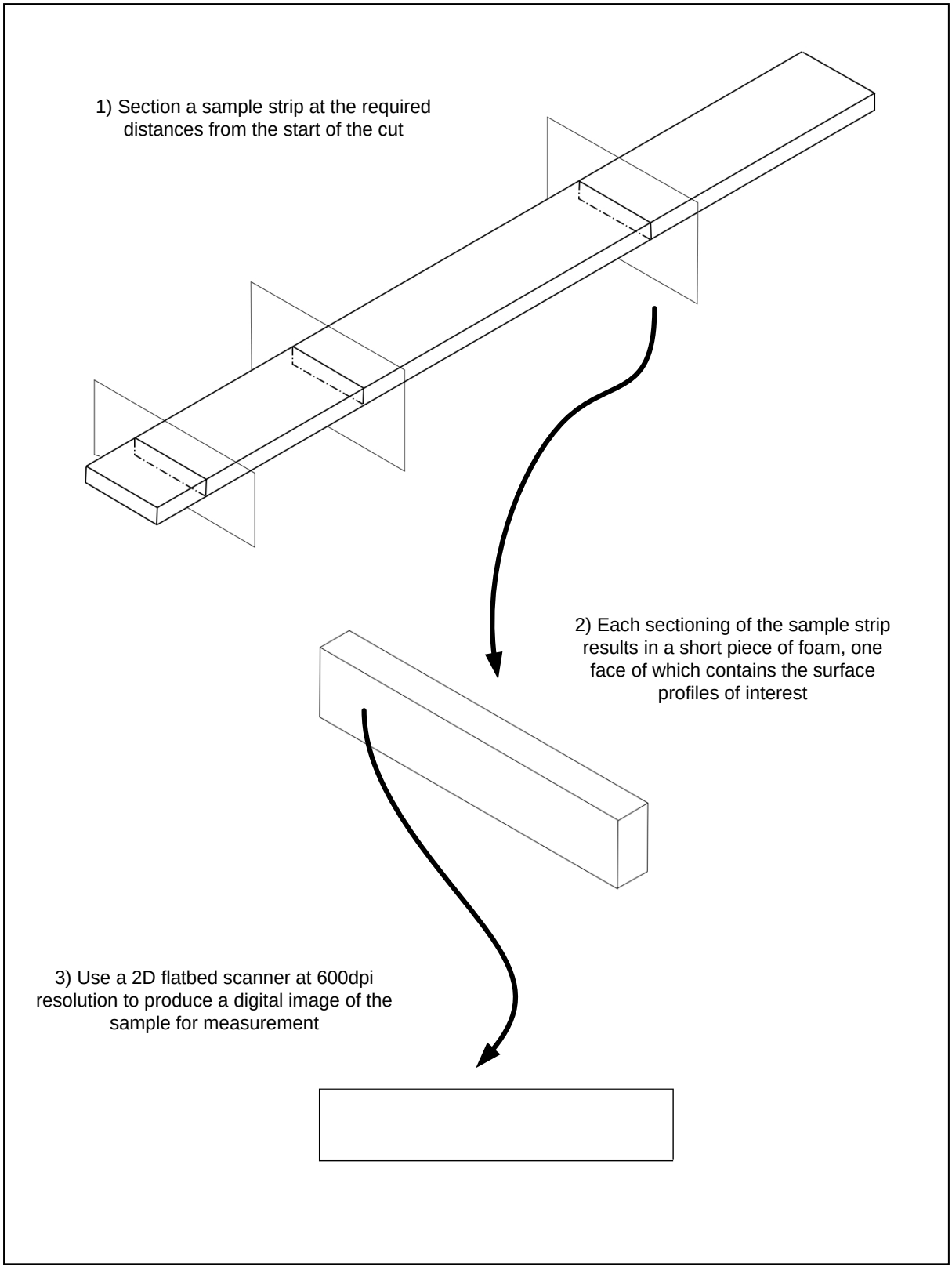

Figure 109: Surface profile sample preparation for measuring geometric form

In order to harvest surface profile data from these sample sections, they were mounted on a Perspex baseplate measuring 210mm x 200mm. This plate would fit into the scanning area of the scanner

used and allowed the scanning of a large number of samples at the same time. These plates with their attached samples were then scanned on a 2D flatbed document scanner, in colour, at a resolution of 600dpi. In effect, this produced a photograph at 600dpi of each sample section. The single images from each plate were then manually separated into digital photographs of each individual sectional sample.

Once each sample image was available, they were processed using Matlab to evaluate geometric form parameters. This was the data processing stage mentioned earlier. Each sample image was loaded in Matlab and the 'ginput' command was used to display the image and allow the selection of points of interest using the mouse (as shown in Figure 110). The mouse and cross-hairs were used to manually select points along the top and bottom surfaces of the sample, and the coordinates of these points were saved by Matlab. When all the desired points had been gathered, the Matlab script levelled the data, calculated the size of each pixel based on the image resolution, and calculated values for the geometric form metrics (the nature of these metrics will be outlined shortly). The resulting values were then saved and output as a data file. The data gathered from this procedure included values for the centre thickness and the edge thickness on each side of the sample (see Figure 108, above). These values, combined with the nominal thickness (the distance between the two adjacent tool passes used to produce the sample strip in the first instance) allowed the evaluation of both the kerfwidth and the surface barrelling.

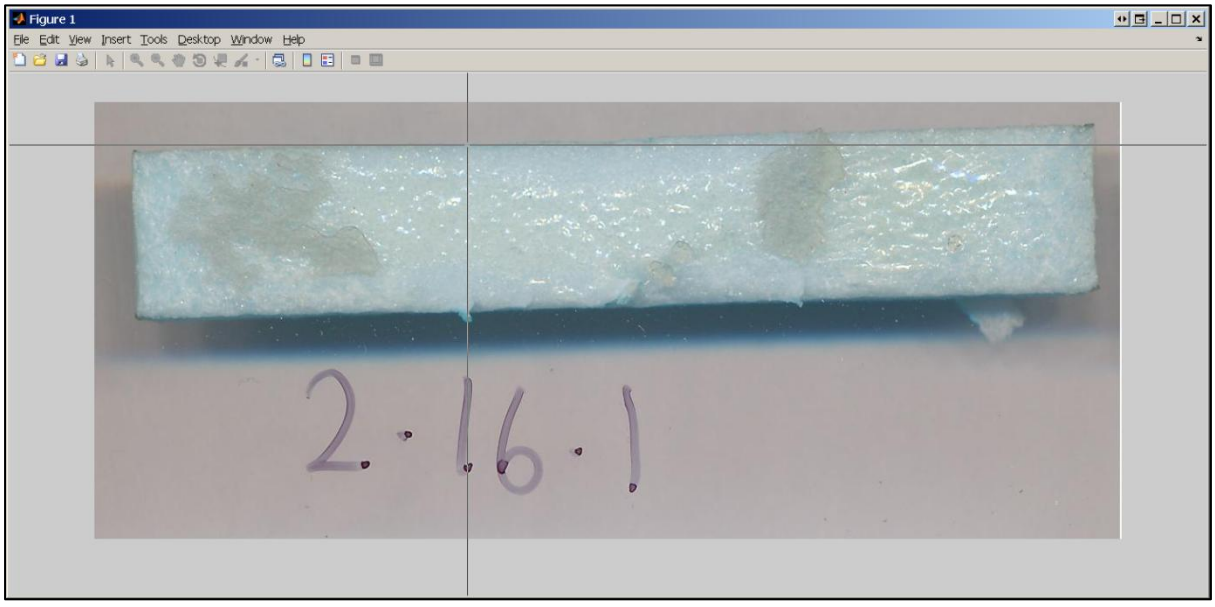

Figure 110: Screenshot of the manual surface profile capture process

The scanner resolution of 600dpi meant that the sample section images had a great deal of information contained within them, and could be displayed at a very large size during the selection of surface profile points, which made this stage more accurate than it would have been with smaller images. However, this step was still the most likely to introduce error into the measurements since the selection of points was a manual process. Other sources of potential error include the manual

sectioning process, which could have introduced parallax error into the data capture process. It is difficult to accurately quantify the magnitude of these potential errors, but an estimate of their effect on the uncertainty of the final outputs was made. It is expected that the final uncertainty of the geometric form metrics would be of the order of approximately ±0.05mm.

To facilitate comparison of the geometric form errors for different cutting conditions, numerical parameters were necessary. The parameters used were the kerfwidth (denoted by λ) and the surface height variation (denoted by *ΔH*). Both of these parameters had units of millimetres.

The kerfwidth was calculated as follows:

$$\lambda_{Centre} = Nominal\ Thickness - Centre\ Thickness \quad (14)$$

Attention must also be given to the local kerf at the ends of the engaged length of the tool, where vapourised cutting is always taking place. This is measured in the same way as the central kerfwidth:

$$\lambda_{Edge} = Nominal\ thickness - Edge\ Thickness \quad (15)$$

Since the samples being measured are vertically symmetric, the total kerfwidth being measured is spread evenly between the top and the bottom surfaces. Essentially half the kerf for each of the two cuts is being measured, but when added together this will be the same as measuring the entire kerf for a single cut. The samples were generated in this way because it was simpler to derive kerf and surface barrelling measurements like this than to implement a reliable external datum and measure the surfaces resulting from a single cut.

The surface height variation is the difference in thickness between the centre of the cut surface and the edge of the surface. This value will be referred to as the ‘Surface Height Variation’ or *ΔH*, and is measured as shown in Figure 111. The centre and edge thicknesses were measured, and the surface height variation was calculated using the following formula:

$$\Delta H = (Centre\ Thickness - Edge\ Thickness)/2 \quad (16)$$

In effect, the parameter *ΔH* is a profile-of-a-line geometric tolerance, defining the upper and lower bounds within which the actual surface is known to lie with the measurement procedure described. *ΔH* can be negative, zero or positive: negative values indicate concave surfaces and will only occur in cases where the tool passes through the skin at the surfaces of foams, zero values indicate that the surface is basically flat and are associated with purely-thermal cutting, and positive values indicate that surface barrelling is present and are associated with thermomechanical cutting.

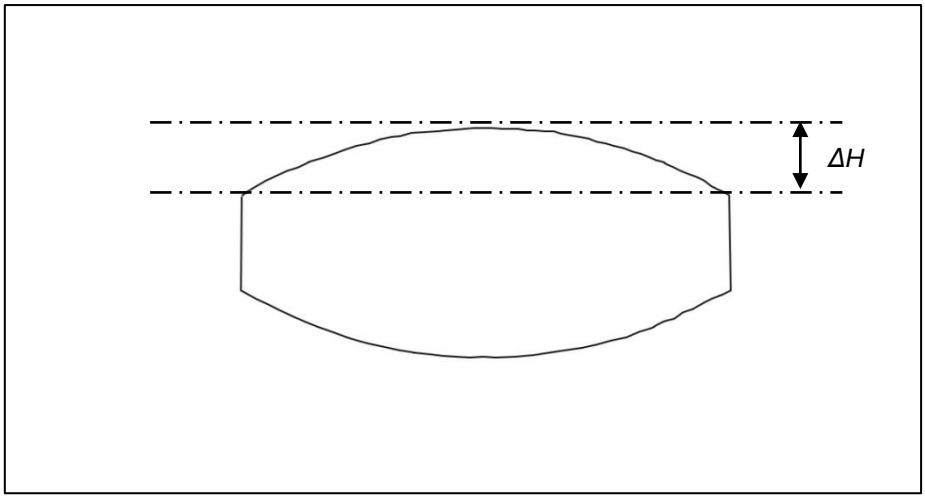

Figure 111: *ΔH* for single-pass cut surfaces

The fundamental difference between these two metrics (surface barrelling *ΔH* and kerfwidth *λ*) is that *ΔH* is measuring a surface profile, while *λ* is effectively measuring a 'lost area,' being the area of foam that is lost as a result of cutting. *ΔH* provides a simple measure of the magnitude of the surface deviation from a nominally flat surface, but provides no information about the actual shape of the surface profile. For the purposes of this work, it was deemed that the magnitude of the deviation was more important than the actual shape and so *ΔH* would be a suitable parameter for assessing the single-pass geometric form.

5.4 Experiment Design for Investigation of Single-Pass Geometric Form

In order to develop a comprehensive and quantitative understanding of the behaviour of kerf and surface barrelling along a cut, an experiment was designed to capture measured data for surfaces produced using both hot-wire and hot-blade tools. This experiment used values of current and feedrate across the full range of the operational space of the RFS system, and also investigated the effect of engaged length, foam type, and distance along the cut.

The cutting conditions used for the hot-wire cuts are shown in Table 15. The cutting conditions marked by '+' or 'x' were not used for the statistical analysis or the development of predictive models (described below) but were kept separate to be used for checking the results of the models against the measured values of samples produced using those cutting conditions. The cuts marked by '+' markers were used only for 50mm thick EPS, while the 'x' markers indicate cuts carried out with 50mm XPS foam. Where there are three '•,' three samples were produced and measured with that set of conditions, to provide an indication of the repeatability of the surface height variation.

Table 15: Cutting Conditions for Single Pass Taut Hot Wire Geometric Form Investigation

Feed (ms^{-1})	Current (A)			
	5	**6**	**7**	**8**
0.0133	●●●	X	●	●
0.0150	+		X	
0.0167	●	+	●	●
0.0183			●	
0.0200	●		●	●
0.0217			●●●	

The investigation of hot-wire cutting used two types of foam, EPS and XPS, and two values of engaged length (30mm and 50mm). Samples were measured at discrete distances along the cut, with more frequent measurements being taken near the start of the cut to capture transition data. These distances were selected based on visual inspection of a wide range of samples to determine levels that seemed likely to capture transition data adequately. The levels of distance used were 0mm, 9mm, 34mm, 64mm, 94mm, 144mm, 244mm, 344mm, 444mm, 544mm, and 644mm, and the total length of the cuts was 750mm. Only one type of wire was used, ø0.6mm Nikrothal N80 nichrome wire. Current control was not used for this work since it was desirable to capture the behaviour of uncontrolled cutting due to the limitations of the current control system, as discussed in the Background Material chapter. This experiment design gave a total of 420 samples for measurement and analysis.

The cutting conditions used for the hot-blade cuts are shown in Table 16 for the cuts carried out with expanded polystyrene foam (EPS) and Table 17 for the cuts carried out with extruded polystyrene foam (XPS). Different cutting conditions were used for the two foams because it was found that EPS could be cut at higher speeds than XPS for a given current without damaging the surface or causing tool failure. Based on qualitative assessment of the thermomechanical balance and the surfaces produced, the ranges of cutting conditions for the two foam types are broadly equivalent. In other words, the cut with the lowest values of feed and current for XPS are at essentially the same point in the operational space as the corresponding cut for EPS. Each set of cutting conditions used for producing a sample is marked by an ‘X’ in the two tables, with ‘XXXXX’ indicating that the cut was carried out five times to provide a repeatability measure. As for the hot-wire form investigation, these

cutting conditions were chosen to provide a snapshot of the form behaviour across the whole operational space of the RFS system.

Table 16: Cutting Conditions for Investigation of Single-pass Hot-blade cuts of Expanded Polystyrene Foam

Current (A)	**Feed (ms^{-1})**			
	0.038	0.050	0.062	0.086
16	X		X	
19	X	X	XXXXX	X
22	X		X	X

Table 17: Conditions for Investigation of Single-pass Hot-blade cuts of Extruded Polystyrene Foam

Current (A)	**Feed (ms^{-1})**				
	0.028	0.040	0.052	0.064	0.076
16	X		X		
19	X	X	XXXXX	X	X
22	X		X		X

The tool used for these hot-blade cuts consisted of a straight length of 1/8” by 0.018 inch nichrome ribbon, held under tension by a pneumatic cylinder in the same way as the hot-wire cutting tool. Two values of engaged length were used, 30mm and 50mm, and the values of distance along the cut used were 0, 20, 60, 100, 200, 300, 400, 500, and 600mm. This experimental design gave a total of 360 samples for measurement and analysis.

5.5 Characterisation of Kerfwidth in Single-Pass Cutting

As outlined above, the kerf along a hot-tool cut is important because it results in a discrepancy between the path followed by the tool and the final position of the cut surface. This must be well understood so that an offset can be applied between the desired surfaces and the toolpath, so that the as-cut surface matches the desired surface. Kerf has been examined to a limited extent by Brooks [1] but this investigation was somewhat limited. It was restricted almost entirely to steady-state kerf,

with no consideration of the change in kerf prior to the establishment of the steady-state cutting mode. The kerf along the cut was considered to a very limited extent when seeking to validate the force-feedback current control system, and this system was able to make the kerf effectively constant along the cut, but it was only implemented for a very small range of cutting conditions and had the significant drawback that it was based on a real-time measurement of the cutting force (see section 2.1.2). The investigation carried out by Brooks was also limited in that it did not consider a range of engaged lengths in any comprehensive manner.

As a result of the drawbacks in the kerf investigations carried out to date, there was a significant need for a much more comprehensive investigation that builds on the previous research and develops a full understanding of the behaviour of the kerf along the cut. This investigation is the subject of this section.

The first observation that can be made about the behaviour of the kerf along the cut is that there is a theoretical minimum value of kerf resulting from the physical size of the tool: in effect, the kerf cannot be smaller than the size of the cutting tool in the direction normal to the cutting direction. In hot-wire cutting, the theoretical minimum is the diameter of the wire, which is 0.6mm for the wire tools used in this investigation. For hot-blade cutting the theoretical minimum is the thickness of the blade, which is 0.018in (0.46mm) for the blades used in this research. While the size of the tool provides a minimum possible kerf value, this constraint was not reached in any of the cuts undertaken during this investigation. The reasons for this will be discussed below.

The next observation was that, at the start of the cut, the kerfwidth was a function solely of the supplied current. The feedrate (and therefore the effective heat input) had no effect. For two cuts made with the same current but different feedrates, the initial kerf was the same. This can be seen in the kerf profiles shown in Figure 112, where the kerf values at the start of the cut are the same (within the uncertainty of the measurements). This makes sense, because the kerf at the start of the cut is essentially a function of the free-air temperature of the tool, since at the start of the cut the thermal field around the tool is at its maximum extent and has not begun to decay as a result of the cutting process. It is possible to expand this observation to conclude that the kerf at the start of the cut is a function of the power input (where $P = i^2R$ and R is the resistance of the cutting tool material).

Observation of the kerf trends along a cut allowed another observation: that the steady-state and transition kerf were dependent on the effective heat input, Q_{eff}. Figure 112 shows the kerf along a cut for two cuts made with the same applied current, but different tool feedrates. As a result, these cuts had different values of effective heat input. Although both cuts produce the same kerfwidth initially, by the time the second data point has been reached (34mm into the cut) a clear difference has been established between the kerf resulting from the two cuts. This difference continues to develop until the steady-state cutting mode is established, at which point the difference between the two kerf measurements stabilises and remains effectively constant (to within measurement uncertainty) until the end of the cut. Generally speaking, cuts made with lower effective heat inputs have smaller kerfwidths than cuts made with higher effective heat inputs. It can also be observed that, before

steady-state cutting is achieved, the rate of change of the kerfwidth with distance varies depending on the effective heat input. For a given supplied current, a faster-moving tool will cool more quickly than a slower-moving tool. This variation in the rate of change is necessary to allow the establishment of the Q_{eff}-dependent steady-state kerf already observed.

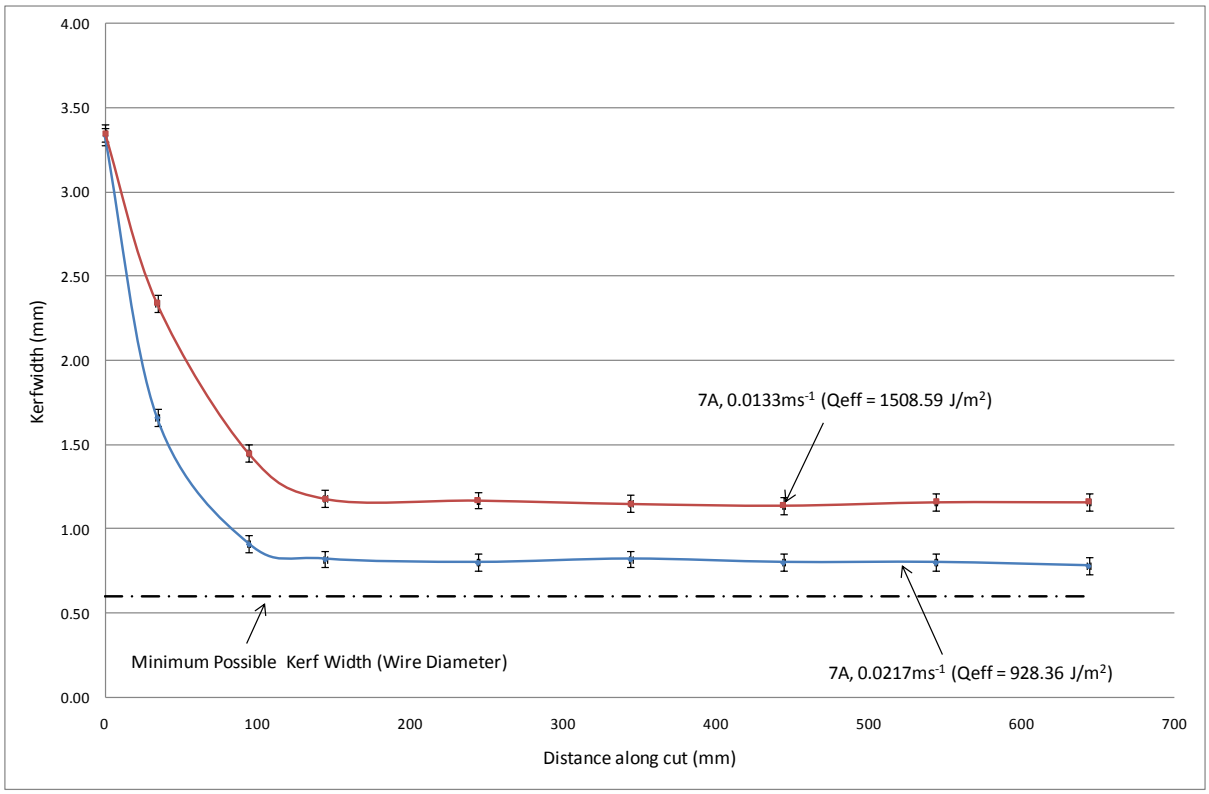

Figure 112: Trend of kerfwidth along a cut showing the variation resulting from changes in the level of effective heat input

Another observation that could be made from the trends of kerf against distance along the cut is that the trend follows a pattern broadly similar to the tool centre temperature, and broadly the inverse of the cutting force. This, added to observation of a wide range of cuts during the sample generation process, strongly suggests that the kerf is related to the thermomechanical balance along the cut.

While qualitative observation of the patterns exhibited by the kerf for different cutting conditions provides a valuable insight into the mechanics of kerf formation, there is a limit to the value of conclusions drawn by this method. In order to gain a more detailed quantitative understanding, the data sets produced by the experimental design outlined above were used as a basis for statistical analysis of the data, to fit predictive models and to develop a quantitative understanding of the significance of different input parameters for determining the kerf. The statistical analysis essentially took the form of linear regression, and was conducted using the software package R. Initially the analysis was restricted to the initial and steady-state kerf, taking no account of the transition, for two reasons. First, this approach allowed the significance of each input factor to be investigated without needing to go through the significantly more difficult process of fitting curves to the kerf

measurements along a cut, and secondly by taking this approach it was possible to build models for the initial and final kerf that could be used in conjunction with adaptive current control to control the kerf along the full length of the cut. The statistical investigation of initial and steady-state kerf builds on the work conducted by Brooks but uses a much larger data set that accounts for a wide range of potential input factors, and the use of statistical analysis allows a quantitative evaluation of the significance of each individual input factor.

When considering the initial kerf case, it was expected (as outlined above) that the effective heat input would have no significance and that the magnitude of the kerf would be proportional to the applied current (and therefore to the free-air tool temperature. It was also expected that the amount of vapourisation experienced by each foam type for a given tool temperature would be different due to the differences in cellular structure between the two foams, so they were analysed separately. The expectation of current-dependency was borne out by the statistical analysis of the initial kerf data for hot-wire cutting of XPS, which produced the following model in terms of supplied current, i and engaged length, l_e:

$$^{initial}\lambda_{xps,\ wire} = 0.484409i - 0.008267l_e + 0.077863 \quad (17)$$

This model had an R^2 value of 0.98. Recall that the closer the R^2 value is to 1, the more accurately the model is fitting the measured data. The R^2 value achieved here indicates that this model achieved a very accurate fit to the measured data, and therefore can comfortably be used to predict the kerf expected at the start of the cut for hot-wire cutting (it should be noted at this point that R produced R^2 values to four decimal places, and that these have been rounded to two decimal places for presentation in this thesis). During the development of this model, the statistical parameter $P_r(>|t|)$ was used to assess the significance of each of the input parameters (initially, all the possible input parameters were included in the regression analysis, and insignificant parameters were then filtered out based on the value of $P_r(>|t|)$. Recall that $P_r(>|t|)$ is the probability that a parameter is *not* significant in determining the value of the output metric (in this case kerfwidth). Therefore, the smaller the value of $P_r(>|t|)$ for a given parameter, the *more* likely it is to be significant. The $P_r(>|t|)$ values for the two parameters that were determined to be statistically significant were:

$P_r(>|t|)$: $i = <2\text{x}10^{-16}$

$l_e = 4.39\text{x}10^{-5}$

Since the $P_r(>|t|)$ value for current was so much smaller than that for engaged length, it can be said that the current is the most important determining factor for the steady-state kerf. However, the engaged length is still sufficiently significant to be included in the model: if it is removed and the model predicts $^{initial}\lambda_{xps}$ solely in terms of current i, the R^2 value of the model drops to 0.94. This is still a very good fit, but inclusion of the engaged length still results in a significant improvement to the fit between the model and the observed data. All the other possible input parameters that were included in the initial data set were determined to be statistically insignificant for determining the initial kerf.

This result matched the observations made above (Figure 112) that the initial kerf depended solely on the current supplied to the tool, and therefore was a function of the free-air temperature of the tool.

The significance of engaged length was not entirely expected, since it had previously been thought within the RFS research group that the engaged length of the tool had no effect on kerf. This will be discussed in more detail below.

The same analysis process was carried out for the initial kerf of cuts in EPS foam. This analysis produced equivalent results to those found for XPS. It was found that the only factors of statistical significance for the initial kerf in EPS were the supplied current, i, and the engaged length, l_e: this result is the same as the XPS conclusion. The model produced was:

$$^{initial}\lambda_{eps,\ wire} = 0.406749\text{i} - 0.008004 l_e + 0.043864 \quad (18)$$

The R^2 value for this model was 0.97, which again indicates a very good fit between the measured data and the predictive model. The fit is slightly less accurate than the fit for the XPS model, which was not unexpected given that it has been frequently observed during the RFS project that surfaces produced with XPS foam are more repeatable than those produced with EPS: this is thought to be a result of the different cellular structures of the two foams. When a regression model was produced for the EPS initial kerf solely in terms of supplied current, i, the R^2 value dropped to 0.93 (essentially the same size of drop that was found when excluding engaged length from the XPS model). This, in conjunction with the values of $P_r(>|t|)$ for the current and engaged length, indicated that both of these parameters had a statistically significant effect on the initial kerf. The $P_r(>|t|)$ values for these two parameters were:

Pr(>|t|): $i = <2\text{x}10^{-6}$

$l_e = 3.95\text{x}10^{-5}$

As for XPS, the current is the most statistically significant parameter for EPS, with l_e somewhat less significant but still important for an accurate model.

In order to validate the initial assumption that the different material structures would have an effect on the initial kerf, and that separate regression models were therefore necessary for each foam type, a single analysis was conducted that used all of the initial kerf data. When this was done, the regression model produced had an R^2 value of only 0.78 for the same general form and input parameters. This indicates that, when the two foam types are treated as identical, it is much harder to produce a model that fits the data well. Although R^2 values of 0.78 can be acceptable under certain circumstances, if a more accurate model can be achieved by simply separating the foam types then the gain in accuracy more than compensates for the minor inconvenience of needing to use multiple models. The loss of accuracy when the two foams are analysed together also acts to confirm the initial expectation that they would behave differently under vapourisation due to their different cellular structures.

A similar analysis was conducted using the measured steady-state kerf data and all of the available input parameters to determine which parameters were significant and to develop regression models that could be used to predict the kerf for a given set of cutting conditions. As for the initial kerf analysis, separate analyses were carried out for the two different types of foam.

For hot-wire cutting of XPS, the regression analysis produced the following model:

$$^{steady\text{-}state}\lambda_{xps,\ wire} = (5.905\text{x}10^{-4})Q_{eff} + (7.194\text{x}10^{-3})l_e + (6.748\text{x}10^{-2}) \quad (19)$$

This model had an R^2 value of 0.92, which indicated a very good fit between the model and the measured data. While this fit is not as good as the fit established for the initial kerf model, it is more than enough to make the model useful for predictive purposes. Only two input parameters were determined to have a statistically significant influence on the output kerf: these were the effective heat input, Q_{eff}, and the engaged length, l_e. The $P_r(>|t|)$ values for these two parameters were:

$P_r(>|t|)$: $Q_{eff} = 1.01\text{x}10^{-15}$

$l_e = 1.78\text{x}10^{-5}$

As is clear from these values, the effective heat input is by far the most significant parameter for determining the steady-state kerf. This was expected, and accords with the conclusions drawn by Brooks in his preliminary investigation of the influence of cutting conditions on kerf. As has been previously explained, the effective heat input is the energy input per unit area during the cutting process, and is calculated from the supplied current and the tool feedrate. Although the engaged length is much less significant that the effective heat input, the Pr(>|t|) value is still low enough to indicate that it is not negligible. When a regression model was developed for the steady-state kerf solely in terms of effective heat input, the R^2 value dropped to 0.84, which is an even larger loss of accuracy that was experienced when leaving engaged length out of the initial-kerf models. Based on this, it seems apparent that the engaged tool length is still of significant importance in determining what the output kerf of a given cut will be.

A similar analysis and model was developed for the steady-state kerf in hot-wire cutting of EPS. This produced the following model:

$$^{steady\text{-}state}\lambda_{eps,\ wire} = (1.488\text{x}10^{-3})Q_{eff} + (1.260\text{x}10^{-2})l_e - 0.905 \quad (20)$$

This model had an R^2 value of 0.92, the same as the steady-state model for XPS. Also as for XPS, effective heat input and engaged length were determined to be the statistically-significant input parameters with an influence on the steady-state kerf. The Pr(>|t|) values for each of these parameters were:

Pr(>|t|): $Q_{eff} = 6.59\text{x}10^{-15}$

$l_e = 0.000787$

Once again, the effective heat input was much more significant that the engaged length, but in the model developed solely in terms of effective heat input the R^2 value was only 0.88, indicating that a substantial improvement in the fit of the model could be achieved by including engaged length in the model. While engaged length in all of these cases was, based on Pr(>|t|) values, much less significant that the applied current or effective heat input, it was also in all cases much more significant than any of the other parameters tested.

As with the initial kerf investigation, it was found that the material had a significant influence on the steady-state kerf: if a single model was produced for the steady state kerf for both foam types, the R^2 value of this model was only 0.76, so treating the two foams separately resulted in a major improvement in the fit between the models and the measured data.

These models for initial and final kerf in hot-wire cutting have very high R^2 values, indicating that the models provide a very good fit to the measured data. As such, they are sufficiently accurate to be used for predictive purposes, as will be particularly relevant for selecting cutting conditions for controlled-current cutting.

It had been thought prior to this work that the engaged length of the tool had no effect on the kerfwidth, since the steady-state tool temperature for a given set of cutting conditions did not appear to make a difference to the kerfwidth when qualitative assessments were undertaken. However, as the values of Pr(>|t|) above have demonstrated, the engaged length l_e is a statistically significant parameter for determining the kerfwidth. While it is true that Q_{eff} is the predominant parameter for influencing the steady-state kerf (R^2 values of 0.84 and 0.88 for XPS and EPS respectively, when models using only Q_{eff} are generated), the engaged length is still significant and including it in the models leads to a substantial improvement in the fit between the models and the measured data.

An equivalent analysis was carried out for the initial and steady-state kerf resulting from hot-blade cutting of both EPS and XPS foam. This analysis had essentially the same results as the investigation of the initial and steady-state kerf for hot-wire cutting. Four models were developed for hot blade cutting, one steady-state and one initial model for each foam type.

The analysis of initial kerf for XPS produced the following model in terms of applied current and engaged length:

$$^{initial}\lambda_{xps,\,blade} = 0.135073i + 0.006857l_e - 0.886744 \qquad (21)$$

The R^2 of this model was 0.89. Although somewhat lower than the R^2 values achieved with the other equivalent models, this is still more than adequate for predictive purposes. The $P_r(>|t|)$ values for each statistically-significant parameter were:

$P_r(>|t|)$: $i = 4.82\text{x}10^{-11}$

$l_e = 0.004319$

As was the case for the hot-wire cutting models, this analysis revealed that the current was much more significant for determining the kerf than the engaged length. However, the engaged length was still necessary to achieve a good fit between the model and the measured data. When a regression model was developed for the kerf solely in terms of current, the R^2 value dropped to 0.83. This would still be an acceptable fit if the resulting model had to be used for predicting the kerf, but including the engaged length in the model results in a significantly better fit.

The model developed for the initial kerf of EPS was:

$$^{initial}\lambda_{eps,\ blade} = 0.094433i + 0.008436l_e - 0.359689 \quad (22)$$

This model had an R^2 value of 0.95, indicating a very good fit between the model and the measured data. The $P_r(>|t|)$ values for current and engaged length were:

$P_r(>|t|)$: $i = 1.67\text{x}10^{-13}$

$l_e = 6.95\text{x}10^{-8}$

When current is the only input variable used for the model, the R^2 value drops to 0.78, so as has been noted for the other cases the inclusion of engaged length results in a much better fit than using current alone.

The steady-state kerf investigation for hot-blade cutting achieved essentially the same results as the investigation of hot-wire cutting. The model for the steady-state kerf of XPS was:

$$^{steady\text{-}state}\lambda_{xps,\ blade} = (4.689\text{x}10^{-5})Q_{eff} - (7.452\text{x}10^{-3})l_e + 0.3909 \quad (23)$$

This model had an R^2 value of 0.99, indicating an extremely good fit between the measured data and the model. The $P_r(>|t|)$ values for each of the input parameters were:

$P_r(>|t|)$: $Q_{eff} = <2\text{x}10^{-16}$

$l_e = 4.08\text{x}10^{-10}$

If the engaged length was removed from the model, the R^2 drops to 0.90, so once again the inclusion of engaged length results in significantly better conformance between the model and the data.

Finally, the model for the steady-state kerf for EPS cut by hot-blades was:

$$^{steady\text{-}state}\lambda_{eps,\ blade} = (5.946\text{x}10^{-5})Q_{eff} - (1.652\text{x}10^{-2})l_e + 0.8480 \quad (24)$$

This model had an R^2 value of 0.86. This was somewhat lower than for most of the other models, but as has already been observed cuts in EPS foam tend to be less repeatable and more error-prone than cuts in XPS. The $P_r(>|t|)$ values for the input parameters in this model were:

$P_r(>|t|)$: $Q_{eff} = 8.42 \times 10^{-8}$

$I_e = 1.77 \times 10^{-7}$

The values of $P_r(>|t|)$ indicate, once again, that the effective heat input is the most significant input parameter. If the engaged length is removed from the model, the R^2 value drops to 0.45, so once again the incorporation of the engaged length results in a significant increase in the conformance of the model to the data.

As for the case of hot-wire cutting, in hot-blade cutting a much higher degree of accuracy was achieved by treating the two types of foam separately. When a single model was developed using both foam types, the R^2 was only 0.75 for the initial kerf model and 0.34 for the steady-state kerf model: clearly, treating the two foams separately is justified and desirable for the sake of accuracy.

These models for the initial and final kerf are able to reliably predict the extreme cases of kerf based on input cutting conditions, and as such have a number of uses. They can be used to select cutting conditions for controlled-current cutting, to evaluate the necessary offsets to apply to toolpaths in order to achieve high levels of dimensional accuracy, and to incorporate into models for multi-pass cutting to account for the influence of kerf on the thermomechanical errors in these cases, as will be discussed in the following chapter (see section 6.3.3.2). While these steady-state models are useful, they do not provide a full picture of the kerfwidth along a cut, since they ignore the details of the transition between the initial and final kerfs for constant-current cutting. As such, it is not possible to determine using these models exactly how far into the cut steady-state conditions become established, and therefore it is not possible to know with any degree of certainty when the steady-state kerf model can reliably be used. As a result of these drawbacks, an investigation of the nature of the transition between initial and steady-state kerf data is desirable.

As has already been established, the initial kerf is primarily a function of the applied current and the steady-state kerf is primarily a function of the effective heat input. The transition that occurs between these kerfs is also clearly a function of distance along the cut and Q_{eff}. This is obvious from Figure 112, which shows the kerf along a hot-wire cut in 30mm XPS for two different levels of effective heat input but the same applied current. Since the initial kerfs are the same, and since the steady-state kerf is smaller for lower effective heat inputs, the steepness of the transition must be larger for lower values of Q_{eff} (all other parameters being equal) since the magnitude of the change in kerf is larger.

It is clear from inspection of the general shape of the kerf transition that it should be possible to model this transition as a polynomial curve in terms of effective heat input, Q_{eff}, and distance along the cut, d, with d taking the form of both d and d^2 to provide a model based on a second-order polynomial. Based on the investigations of initial and steady-state kerf, it also seemed likely that engaged length l_e would be a relevant input parameter.

Models for the kerf through the transition cutting region were developed and the significance of different cutting strategy conditions was assessed. Although interesting, these models are not as accurate or as useful as the initial steady-state models, so while they will be presented here they will not be discussed in great detail.

$$^{Transition}\lambda_{wire,xps} = (1.129\text{x}10^{-3})Q_{eff} + (3.390\text{x}10^{-5})d^2 - (1.742\text{x}10^{-2})d + (2.119\text{x}10^{-2})l_e + 0.7415 \quad (25)$$

$R^2 = 0.80$

The $P_r(>|t|)$ values were all $<2\text{x}10^{-16}$ except for l_e, which was $3.46\text{x}10^{-6}$.

$$^{Transition}\lambda_{wire,eps} = (1.406\text{x}10^{-3})Q_{eff} + (1.374\text{x}10^{-5})d^2 - (8.671\text{x}10^{-3})d + (1.116\text{x}10^{-2})l_e + 0.4723 \quad (26)$$

$R^2 = 0.87$

The $P_r(>|t|)$ values for this model were all $<2\text{x}10^{-16}$, except l_e which was $1.78\text{x}10^{-5}$.

$$^{Transition}\lambda_{blade,xps} = (5.105\text{x}10^{-5})Q_{eff} + (1.518\text{x}10^{-5})d^2 - (8.252\text{x}10^{-3})d + (9.707\text{x}10^{-3})l_e + 0.9327 \quad (27)$$

$R^2 = 0.89$

$P_r(>|t|)$ values were all <2x10-16 for all except l_e, which was $3.80\text{x}10^{-8}$.

$$^{Transition}\lambda_{blade,eps} = (4.011\text{x}10^{-5})Q_{eff} + (1.208\text{x}10^{-5})d^2 - (6.631\text{x}10^{-3})d + (6.226\text{x}10^{-3})l_e + 1.116 \quad (28)$$

$R^2 = 0.80$

Without l_e, the R^2 drops to 0.70, so a small but valuable improvement in accuracy is achieved by incorporating engaged length into these models.

$P_r(>|t|)$: $Q_{eff} = 4.23\text{x}10^{-9}$

$d^2 = 1.49\text{x}10^{-11}$

$d = <2\text{x}10^{-16}$

$l_e = 0.00182$

Based on this work for steady-state, initial and transition kerfwidth, it is possible to construct a cause-and-effect diagram showing which user-controllable and intermediate parameters have an effect on the kerfwidth in single-pass cutting. This diagram is shown in Figure 113. As has been determined, the important user-controllable input parameters for determining the kerfwidth are the engaged length of the tool and either the supplied current or the effective heat input. In addition, as has been established by the statistical analyses undertaken, the exact quantitative relationships between these parameters and the kerf depend on the type of tool being used (wire or blade) and the type of foam

being cut (EPS or XPS). The thermomechanical balance and the distance along the cut are also important, since the nature of the trend of kerf along the cut is fairly obviously related to the behaviour of cutting force and tool centre temperature along the cut.

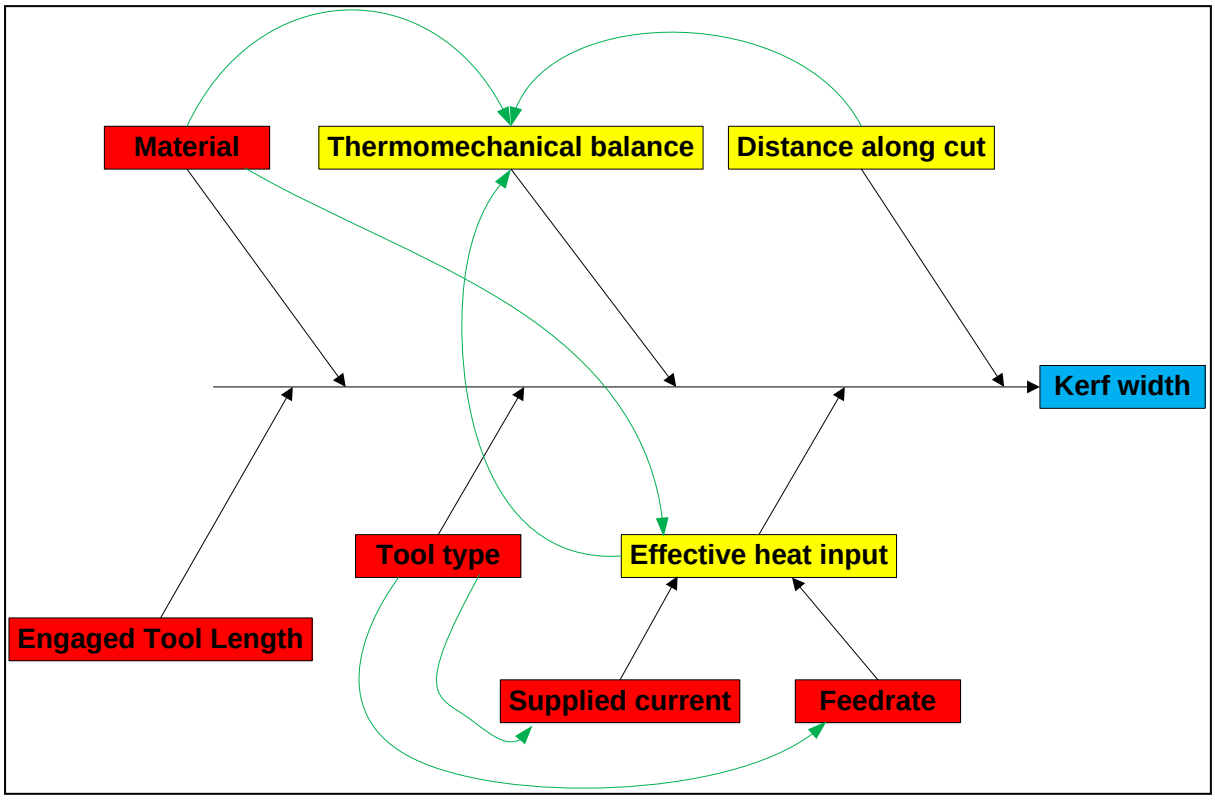

Figure 113: Factor interactions that contribute to the kerfwidth of single-pass cutting

The statistical models developed during this work provide very good conformance with the measured data, as shown by the summary of R^2 values presented in Table 18. These are all greater than 0.80, and for the initial and steady-state kerf models the minimum R^2 value is 0.86. This indicates that all of the models are sufficiently accurate to use for predictive purposes, but that the initial and steady-state models are the most accurate. As it happens, they are also the most useful, since they allow the calculation of equivalent-kerf cutting conditions for use in controlled-current cutting.

If a cut is to be made with a known effective heat input, or if the effective heat input can be determined from the required surface texture or some other functional requirement, the expected steady-state kerf can be calculated. This kerf value can then be substituted into the appropriate initial kerf model to determine cutting conditions that will give the same kerf during the vapourised cutting stage. Then, when a cutting force signal is detected, the force-feedback current control system can switch from the initial set of cutting conditions to the steady-state set of conditions, which will maintain a constant kerf along the full length of the cut.

Table 18: Summary of Coefficients of Determination (R^2) values for kerf models

Tool Type	Material	Initial Kerf	Transition Kerf	Steady-state kerf
Wire	XPS	0.98	0.80	0.92
	EPS	0.97	0.87	0.92
Blade	XPS	0.89	0.89	0.99
	EPS	0.95	0.80	0.86

5.6 Characterisation of Surface Barrelling in Single-Pass Cutting

In order to develop a full understanding of the geometric form errors present in a surface cut by single-pass cutting, it was also necessary to carry out a detailed analysis of the surface barrelling phenomenon that was observed in foam surfaces. This analysis was based on samples produced using the experimental design outlined above, and made use of the parameter Surface Height Variation, *ΔH*.

As was discussed earlier, the 'barrelling' of a surface can have one of three states: concave, flat or convex. The hypothesis at the outset of this investigation was that the primary cause of the surface barrelling was the temperature gradient that exists along the engaged length of the cutting tool during the cutting process. It was also hypothesised that concave surface barrelling was the result of the cutting strategy used to produce samples, in that when the tool was passing through the higher-density skin on the surfaces of as-manufactured foam sheets, this skin was melted less during vapourised cutting than the cellular bulk material, and so the centre of the cut had a wider kerf than the edges, leading to a concave surface barrelling profile. While this is an important aspect of cutting strategy, it does make it harder to determine which input parameters have an effect on the surface barrelling, since it confounds a material-property effect with the thermomechanical effects of the cutting process. As a result, it was desirable to either apply a correction to the concave *ΔH* results or to produce samples for which the cutting tool did not pass through the higher-density skin of the foam. In order to make the sample generation process significantly easier, it was most desirable to apply a correction to the surface height results.

Since concavity occurs only when vapourised cutting is taking place and since it is thought that the concavity is the result of the edges of the cut surface vapourising less than the centre, it seems logical that the surface would be essentially flat in the absence of the surface skin on the foam. If any mechanical cutting component was present this surmise would not be valid, but the tool in the centre of the cut is clearly hot enough that the thermal field has not yet collapse, so a nominally-flat surface

should be produced if the skin isn't present. This suggests that samples with negative *ΔH* values would have zero *ΔH* if the surface skin was not present.

To test this hypothesis, ten samples were produced using XPS foam that had been prepared in such a way that the tool did not pass through the surface skin. Five sets of cutting conditions were chosen to cover the RFS system operational space, and two levels of engaged length were used (30mm and 50mm). The cutting conditions used are shown in Table 19. These samples were prepared for hot-wire cutting only, and it was assumed that if the proposed *ΔH* correction was valid for hot-wire cutting then it would also be valid for hot-blade cutting, since the mechanism producing the surface concavity was the same.

Table 19: Cutting conditions used for skinless samples to correct negative *ΔH*

Current (A)	**Feed (ms^{-1})**
5	0.0133
5	0.0200
7	0.0217
8	0.0133
8	0.0200

Once the no-skin samples had been produced, the *ΔH* was measured at the same distances along the cut that produced negative *ΔH* in samples where a surface skin was present. It was found that the surfaces produced from workparts with no higher-density skin had zero surface barrelling in all cases where concave surface profiles had previously been produced.

This is demonstrated by Figure 114, which shows the variation in surface barrelling along a cut made with cutting conditions of 7A and $0.0217ms^{-1}$, and an engaged length of 30mm, for both the skin and no-skin cases. As is immediately clear, at most points along the cut there is no difference between the *ΔH* measurements for the two cases (within the uncertainty of the measurement process). However, for the sample at the start of the cut, where the *ΔH* value was negative when cutting through the skin it was zero when the tool did not pass through a surface skin.

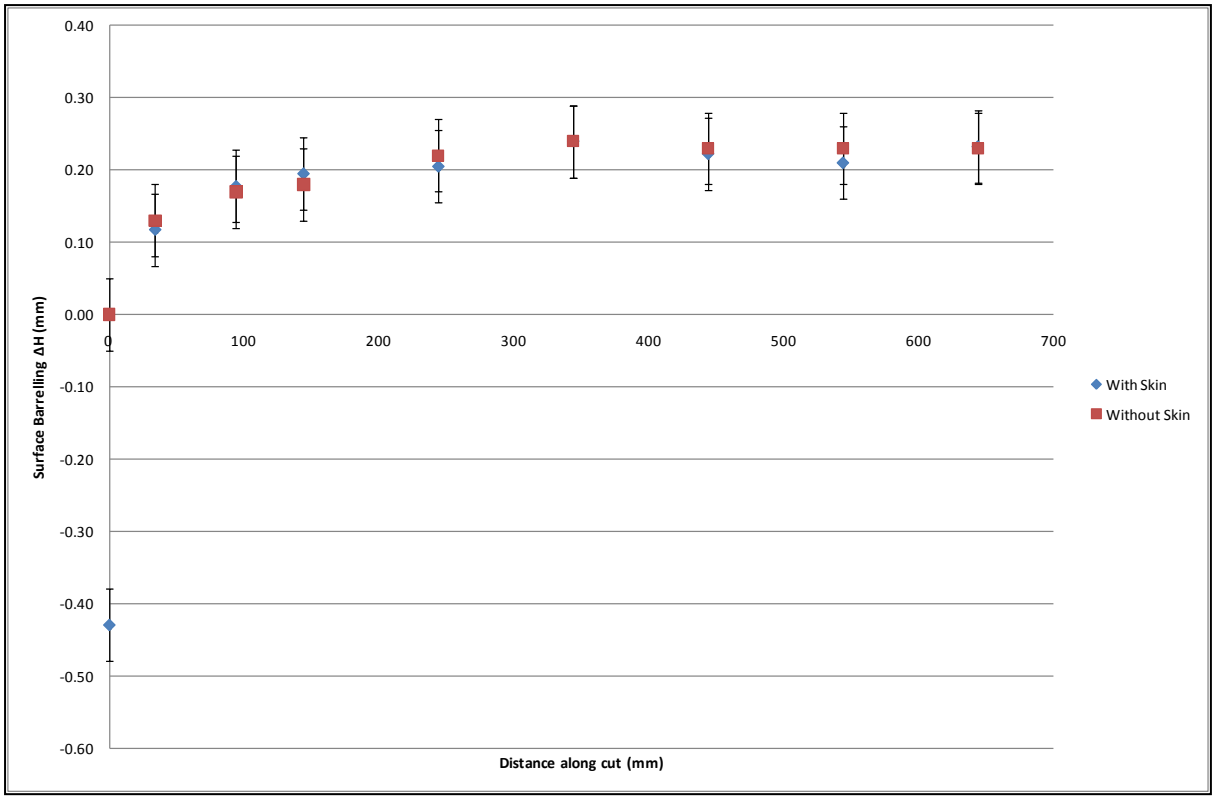

Figure 114: Surface barrelling for a single-pass cut, showing values for the through-skin and no-skin cases (XPS, l_e = 30mm, 7A, 0.0217ms^{-1})

Based on this work, it was concluded that the pre-existing surface barrelling samples could be used for further investigation if a correction was applied to compensate for the presence of the surface skin, and that an appropriate correction was to set all negative ΔH values to zero without making any changes to any other zero or positive ΔH values. Once this was established, the investigation of the parameters influencing the surface barrelling could proceed.

The first stage of the investigation of surface barrelling was to assess whether the barrelling was repeatable. It will be recalled that several sets of cutting conditions were used to make multiple samples, so that the measured values could be compared to see if the same cutting conditions resulted in the same values of ΔH at points along the cut. The outcome of one of these repeatability assessments is shown in Figure 115. As can be seen, within the accuracy limitations of the measuring system used the surface barrelling is definitely repeatable and produces very similar values at all points along the cut length.

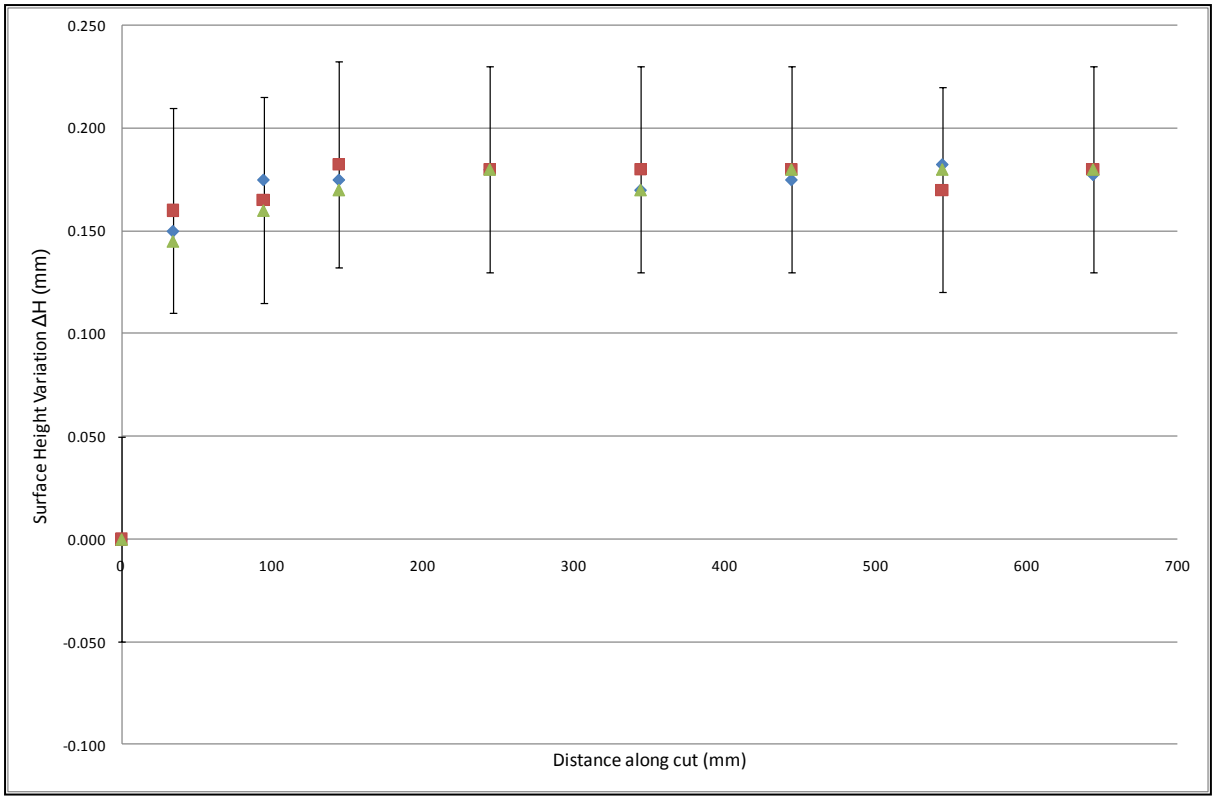

Figure 115: Repeatability of the surface height variation along the cut length (5A, 0.0133ms^{-1}, XPS, l_e = 30mm)

As has been stated earlier, it was thought initially that the surface barrelling was closely related to the tool temperature differential, ΔT. This was a surmise based on the apparently inverse profiles of ΔH and ΔT, with lower ΔT values (and hence locally hotter tools) resulting in higher local kerf widths and therefore contributing to the barrelling of the surface, and on observation of the cutting process. Before proceeding further, it was desirable to confirm this hypothesis. To do this, centre-cut temperature data was gathered for hot-wire cuts in 30mm XPS with the same cutting conditions used to produce the surface barrelling samples. Temperature data was gathered with a thermocouple attached to the cutting tool at the centre of the engaged length. The data provided a temperature profile along the full length of the cut, from which centre cut temperature data was harvested for the relevant levels of distance along the cut. The centre cut temperature was then subtracted from the known free-air temperature of the wire for the relevant level of current to give a value of ΔT. This data had to be gathered using equivalent cuts rather than during the cuts used to produce the samples because the thermocouple leaves a groove in the cut surfaces and so would have rendered these useless for surface barrelling measurement. This data was restricted to the case of 30mm cutting of XPS with a hot wire because the goal was to confirm the relationship between ΔT and ΔH, rather than to develop a complete model for ΔT in terms of ΔH: such a model would not actually be very useful for any kind of predictive purposes because it would not be based on user-controllable input parameters, and so would require another model for ΔT in terms of input parameters. For predictive purposes it

seemed simpler, more useful and more accurate to have a model for the surface barrelling solely in terms of variables that the production planner could directly control, if at all possible.

To determine the significance of the temperature differential for determining the surface barrelling, a data set that included corresponding values of ΔH and ΔT (amongst other parameters) was analysed statistically using the software package R. Based on this analysis, the following model for ΔH in terms of ΔT and distance along the cut was produced, with an R^2 value of 0.81:

$$^{Wire}\Delta H = (4.391x10^{-4})\Delta T + (3.252x10^{-2})\sqrt{d} - (9.313x10^{-4})d - 0.2288 \quad (29)$$

Although the R^2 value might be taken to indicate that this model provides a good predictive tool for the surface barrelling in terms of the temperature differential and the distance along the cut, it must be remembered that this is only for hot-wire cutting, for a single foam type and for one value of engaged length, and that it has a parabolic shape that results in poor conformance with the measured data at high levels of distance. In any case, the important outcome of this analysis was not the model itself but the $P_r(>|t|)$ values for each input parameter. These were as follows:

$P_r(>|t|)$: $\Delta T = 2.33x10^{-5}$

$d = 2.04x10^{-7}$

$\sqrt{d} = 3.61x10^{-8}$

The $P_r(>|t|)$ value for the tool temperature differential, ΔT, is very small. Although the values for distance are smaller, indicating that distance is statistically more significant for the surface barrelling outcome for this data set, the very small value of ΔT indicates that it still has a statistically significant effect on the measured ΔH value. Therefore, the hypothesis that the surface barrelling is a function of the thermal gradient along the length of the tool within the engaged length appears to be confirmed. There are two problems with this result. The first is that the ability to predict ΔH in terms of ΔT is not particularly useful, since ΔT is not an input cutting strategy condition. The second problem is that the dependence of ΔH on ΔT is not quite as clear cut as this model would seem to indicate.

Figure 116 shows a scatter plot of the ΔT and ΔH values for cuts made in 30mm XPS (the same data which the regression model above was based on), with a linear line of best fit. As can be seen, the R^2 value of this linear fit is only 0.4892, which indicates that the fit is not very good at all. There are also clearly data points on this scatter plot for which higher values of ΔT result in lower values of ΔH, rather than the reverse. It seems apparent that the causes of the surface barrelling are somewhat more complex than had first been thought.

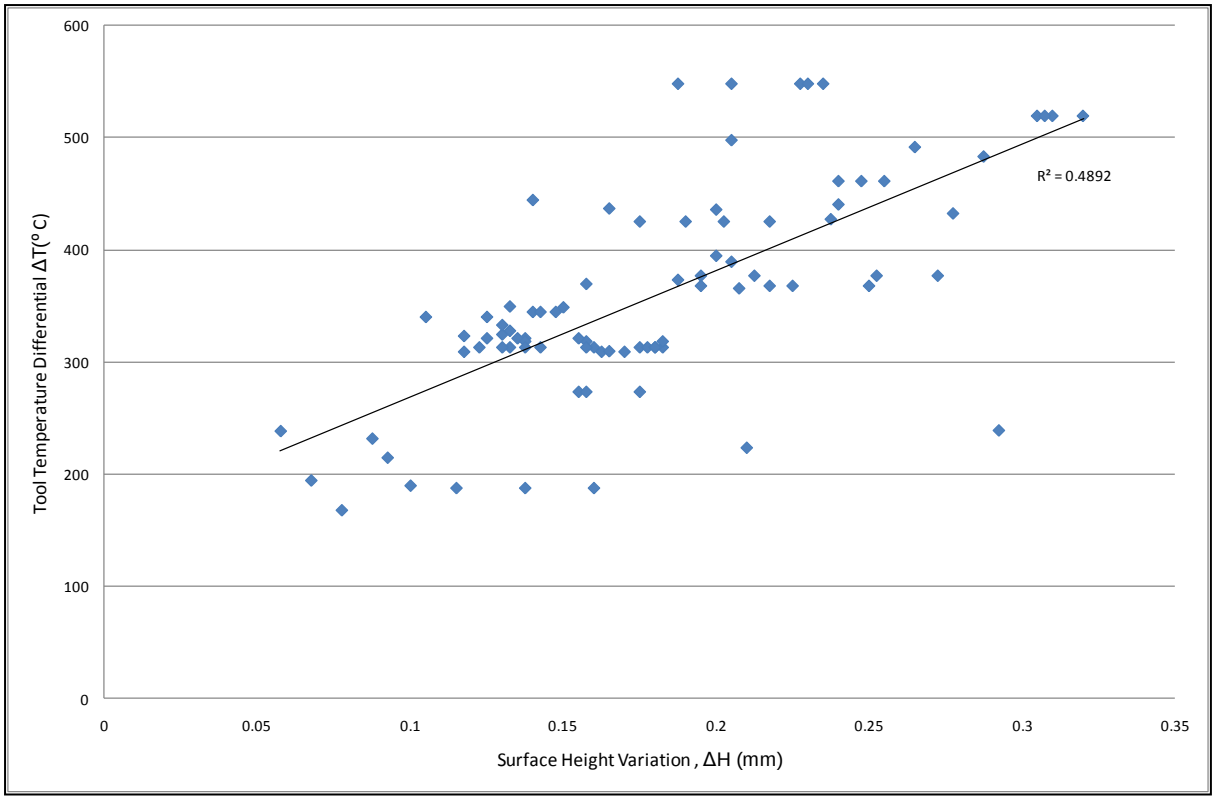

Figure 116: Relationship between Tool Temperature Differential ΔT and Surface Height Variation ΔH

If the surface barrelling ΔH were a simple function of tool temperature differential ΔT, it would also be expected that, for a given supplied current, higher effective heat input values would result in a smaller ΔH. This is because, as was found in the kerf investigation above, the effective heat input plays a strong role in determining the centre-cut temperature of the tool, and higher values of Q_{eff} result in hotter tools (and hence wider kerf). Since the supplied current determines the free-air temperature, and since the difference between the free-air temperature and the centre-cut temperature defines the tool temperature differential ΔT, a higher Q_{eff} results in a hotter centre-cut temperature, and therefore the difference between this temperature and the free-air temperature would be smaller, resulting in a smaller ΔH. The relationship between higher effective heat input and smaller ΔT was not expected to be simple and linear, since the value of ΔT depends on both the centre cut temperature and the free-air temperature of the tool during the cut. Effective heat input influences the centre-cut temperature, but the free-air temperature for a given tool is most strongly influenced by the supplied current. Since the effective heat input is determined by both the current and the tool feedrate, it is possible for cuts made with the same effective heat input to have different supplied currents, simply by varying the feedrate. This is illustrated by Figure 118, which shows a contour plot of the effective heat input for cuts made with an engaged length l_e of 30mm. As can be clearly seen, there exist "iso-Q_{eff}" contours, demonstrating that supplied current can vary while still achieving the same effective heat input Q_{eff}. This means that the tool temperature differential, ΔT, must be a function of both the effective heat input and the supplied current, even though the effective heat input is also a function of the supplied current.

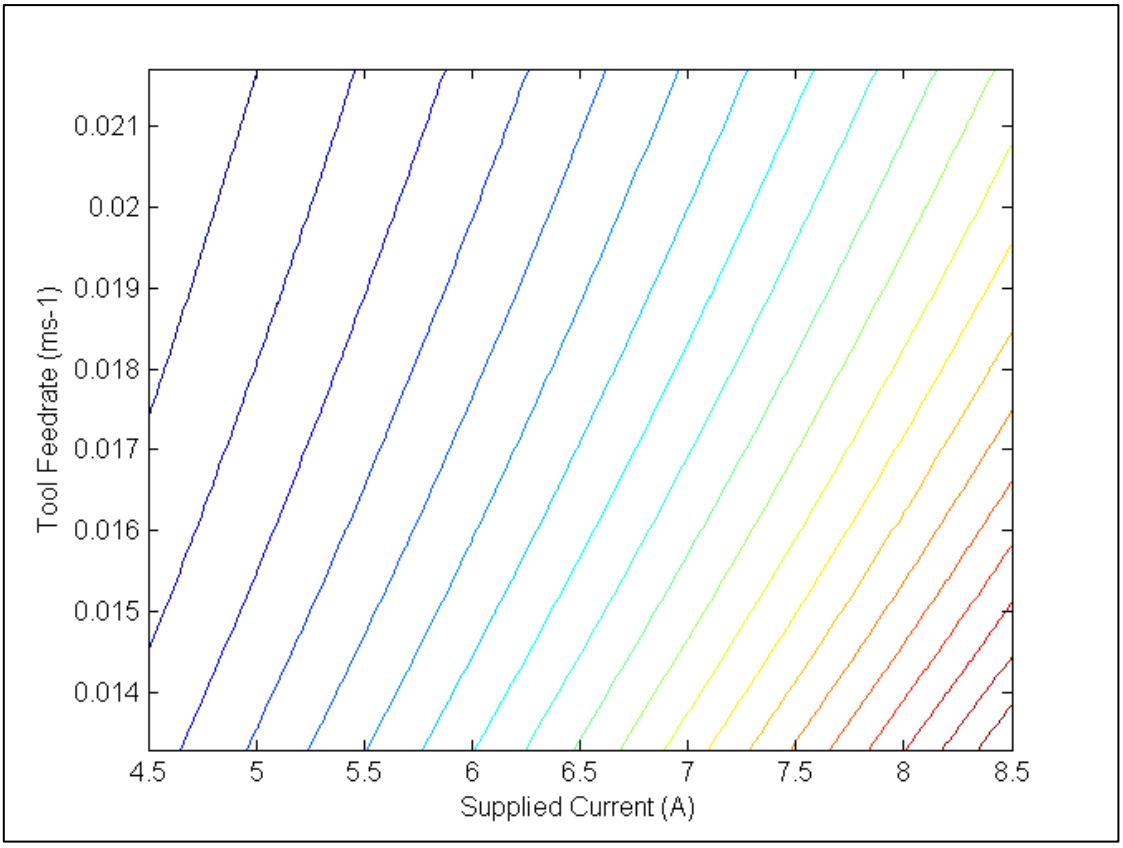

Figure 117: Contour Plot of the Distribution of Effective Heat Input Q_{eff} with changes in Feedrate and Supplied Current (for l_e = 30mm)

The expectation that higher effective heat input would result in smaller surface barrelling for a given supplied current was not supported by the data gathered for this investigation. Figure 118 shows the surface height variation data plotted against effective heat input, broken down by applied current. As immediately becomes obvious, this graph is showing that higher effective heat inputs result in larger surface height variation for a given supplied current, which is in direct contradiction to the theoretical implications of a relationship between the tool temperature differential and the surface height variation.

To explore this apparent contradiction in the data set more fully, a statistical analysis was undertaken on the whole data set to identify input cutting strategy parameters that had a significant effect on the value of surface height variation, and to see if a model could be developed to predict ΔH. This analysis was also inconclusive and contradictory. The best R^2 value that could be achieved was 0.385 for XPS, and the best achievable models for EPS were even worse. None of the input parameters tested showed any particular statistical significance for determining the value of ΔH.

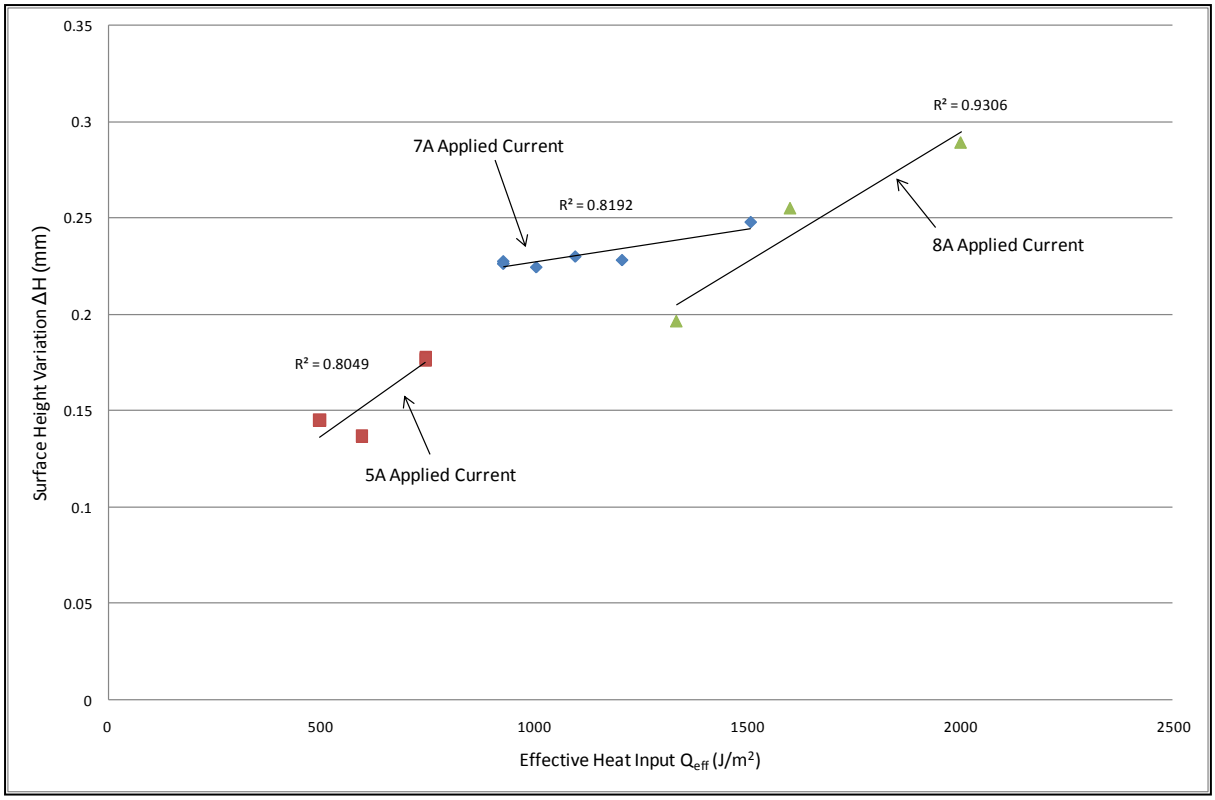

Figure 118: Variation of Steady-State Surface Height Variation ΔH with Effective Heat Input Q_{eff}, broken down by Applied Current

The discrepancy between the expected and measured surface barrelling trends with increasing effective heat input indicate that the factor interactions that result in surface barrelling are more complex than was first thought. While it seems clear from the initial statistical analysis and from observation of the cutting process that the surface barrelling is a direct function of the tool temperature differential, ΔT, there is reason to think that the relationship between input cutting conditions, cutting mode and tool temperature differential is more complex than expected.

As outlined above, the working assumption at the beginning of the surface barrelling investigation was that the temperature of the tool in the centre of the cut was proportional to the effective heat input, with higher Q_{eff} values leading to higher centre-cut temperatures, and therefore lower values of ΔT. However, further investigation of the tool temperature data indicates that this trend is not as clear-cut as it at first seemed.

Figure 119 shows the measured values for the centre-cut temperature of a wire cutting tool during steady-state cutting, plotted against effective heat input. These values are for the cutting of XPS with an engaged length of 30mm. The data is shown as a set of independent points with no attempt at fitting a trendline, since the limited number of data points does not really provide sufficient information for the development of a quantified trend. However, some general observations can be made from this graph.

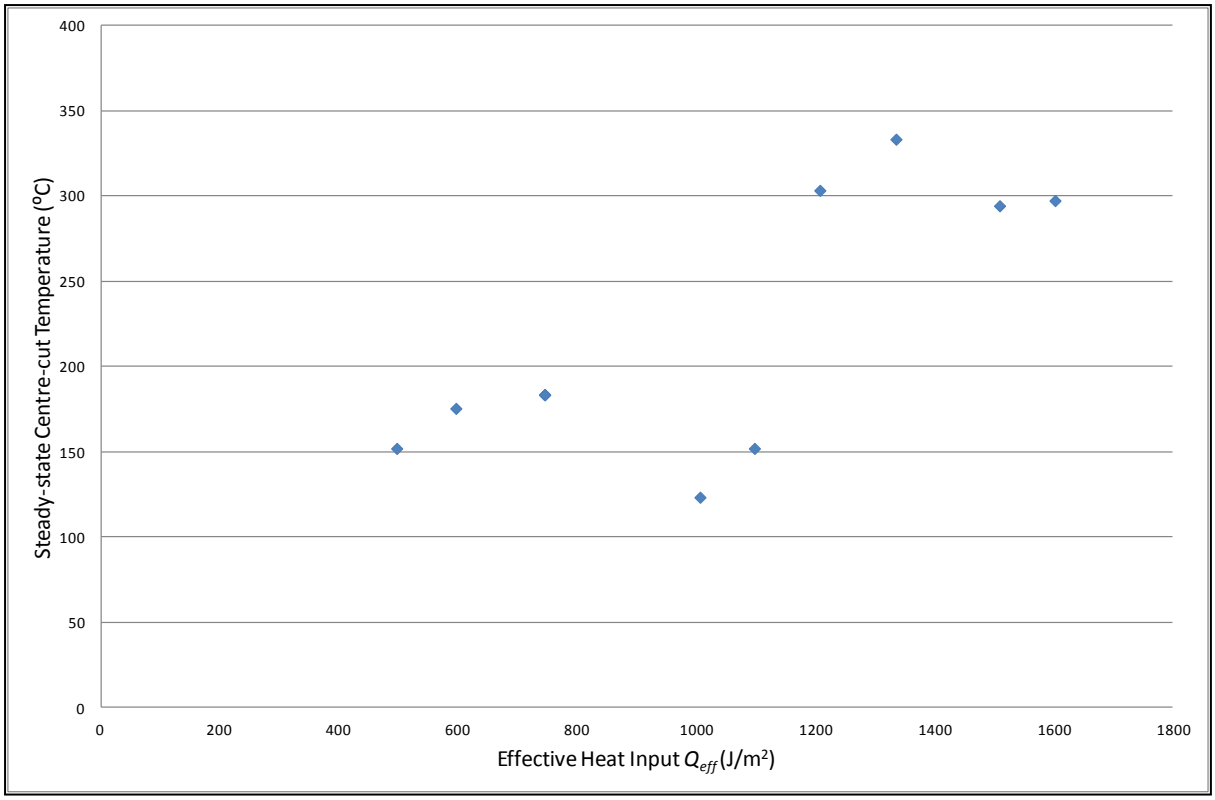

Figure 119: Variation of Steady-state Centre-cut Temperature with Effective Heat Input Q_{eff} (XPS, l_e = 30mm)

It will be recalled that the initial expectation for the behaviour of centre-cut temperature was that higher effective heat inputs would result in higher centre-cut temperatures, and therefore lower ΔT values for a given current. Broadly speaking, this expectation is valid, with a proportional relationship being observable between centre-cut temperature and effective heat input. However, this relationship is not linear. As can be seen, at Q_{eff} values between 800 J/m^2 and 1200 J/m^2, the centre cut temperature is actually lower than it was at lower values of Q_{eff}. It seems likely that this unexpected behaviour is due to a change in the steady-state cutting mechanics within this energy input range, so that the predominant mode of cutting at higher effective heat inputs is different from that at lower effective heat inputs.

As was outlined in section 2.1.1, previous research on the cutting mechanics of hot-tool cutting of polystyrene foam identified a series of different cutting modes, any or all of which could occur in sequence along a cut depending on the exact cutting conditions being used. It seems likely that, at some value of effective heat input between 800 J/m^2 and 1200 J/m^2 for an engaged length of 30mm, a transition between two of these cutting modes takes place. At values of effective heat input below this transition threshold, one cutting mode predominates in steady-state cutting, while another mode predominates at values of effective heat input above the threshold. At values of effective heat input below the cutting mode transition threshold (i.e. using tool temperatures at the colder end of the operational range and tool feedrates at the higher end) the cutting mode is more likely to be ‘solid

contact' cutting, whereas at higher values of effective heat input (hotter and slower cutting conditions) the cutting mode is more likely to be 'line contact' or 'stick and slip' cutting.

The change in cutting mode at varying levels of effective heat input would have a direct influence on the steady-state temperature of the tool due to the different mechanisms of heat transfer predominating in each cutting mode. The rate at which energy is transferred from the cutting tool to the cutting zone or the foam will naturally differ depending on the physical nature of the cut around the foam: physical parameters that are likely to be of significance include the amount of molten polystyrene surrounding the cutting tool, the degree of physical contact between the tool and the foam, and the rate of heat transfer to the air and vapourisation products occupying the kerf behind the cutting tool.

While it can be said with confidence that the surface barrelling exhibited by hot-tool single-pass cutting is a result of the thermal gradient present along the engaged length of the tool, the exact links between the input cutting conditions and the output surface barrelling are much more complex than was first thought. In order to fully understand the relationships between input conditions and output surface height variation, a thorough and comprehensive understanding of the cutting mechanics will be necessary. Developing this understanding would be a significant body of work in its own right, and was beyond the scope of this research (since this work was undertaken with the intention of treating the detail of the cutting mechanics largely as a black box), so further research into the nature of surface barrelling is recommended but has not been undertaken. It seems likely that such research could benefit from the development of a multi-physics FEA model of the hot-tool cutting process, and that such a model once developed could also be used to further the understanding of the hot-tool cutting process and its effect on surface quality in a range of other areas. As such, further investigation and modelling work on the cutting mechanics of hot-tool cutting of polystyrene foam is recommended for future work.

Despite the inconclusive outcomes of this research, some progress has still been made in characterising the surface height variation ΔH. Based on the current understanding of the nature of this surface error, a cause and effect diagram has been constructed to show the relationships between input strategy parameters and the surface barrelling, and to show the interactions and dependencies between these input parameters. This diagram is presented as Figure 120. This diagram is almost certainly not the last word in mapping the factors that affect the surface barrelling, and there are no quantitative predictive models associated with it to determine which parameters are the most significant, but it reflects the best current understanding of the nature of surface barrelling and should serve as a useful starting point for a further investigation of this surface error.

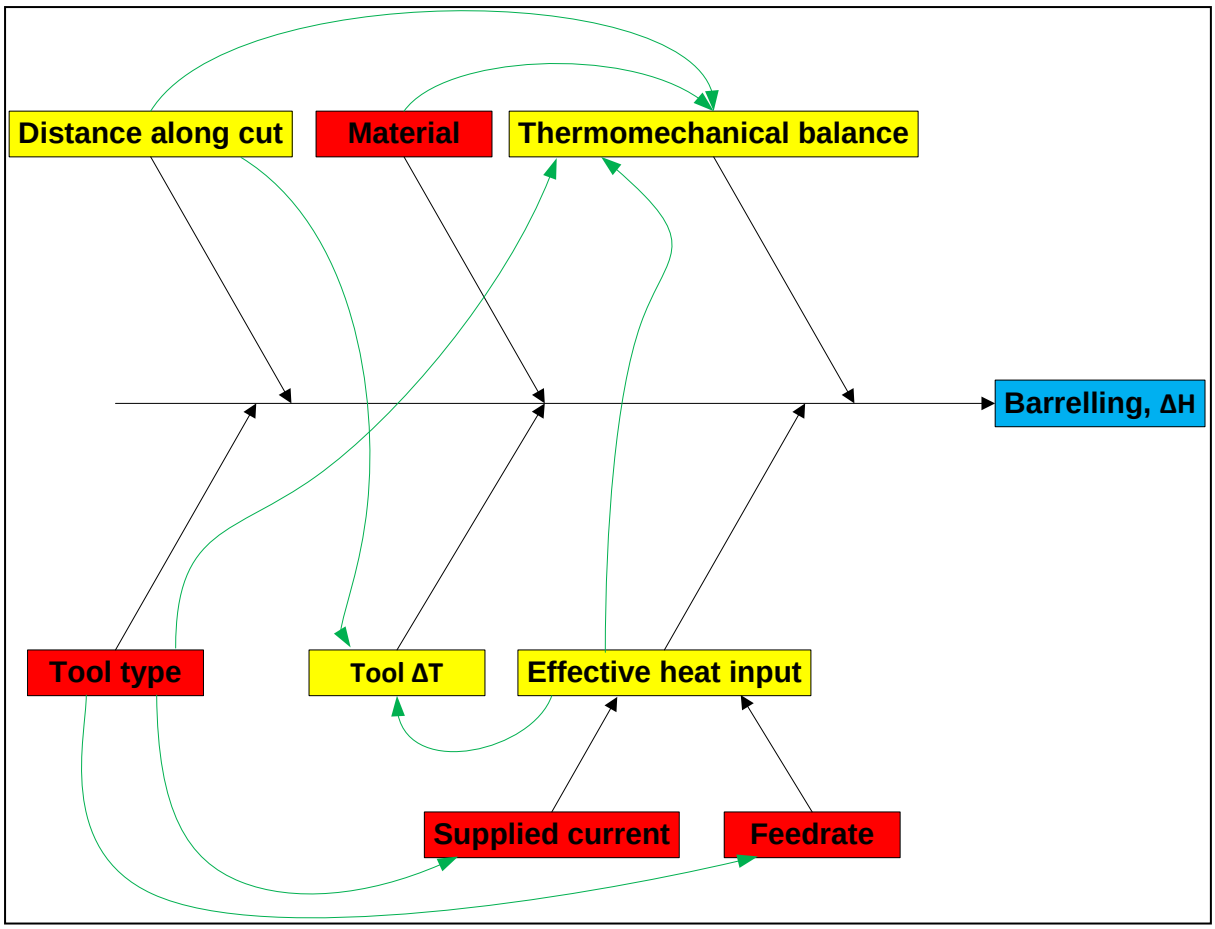

Figure 120: Factor interactions that contribute to the surface barrelling in single-pass cutting

As the final point in this section, it is necessary to consider the effect of force-feedback current control on the surface barrelling along a single-pass cut. To do this, a small number of the cutting conditions used for the constant-current samples above were repeated using the equivalent controlled-current cutting conditions. Given the 'conclusions' drawn about the cause and nature of the surface barrelling above, it seemed likely that the initial surface barrelling would still be zero, since the initial tool temperature is still constant along the cutting tool prior to engagement with the foam, with no thermal gradient between the free-air temperature and the centre-cut temperature. It also seemed likely that the steady-state surface barrelling would be unchanged by the use of controlled-current cutting, since the steady-state cutting conditions are unchanged by the current-control system. It was hypothesised that the only effect of current control on the surface barrelling would be to make steady-state barrelling conditions occur earlier in the cut than they otherwise would.

Figure 121 shows the surface height variation (ΔH) along a cut made with constant-current cutting conditions of 7A and 0.0183ms^{-1} in XPS with an engaged length of 30mm, and the trend of ΔH in the equivalent controlled-current case. As can be clearly seen, the surface barrelling at the start of the cut and in steady-state cutting are the same, but the steady-state value of ΔH is achieved much sooner in controlled-current cutting. This confirms the hypothesis above.

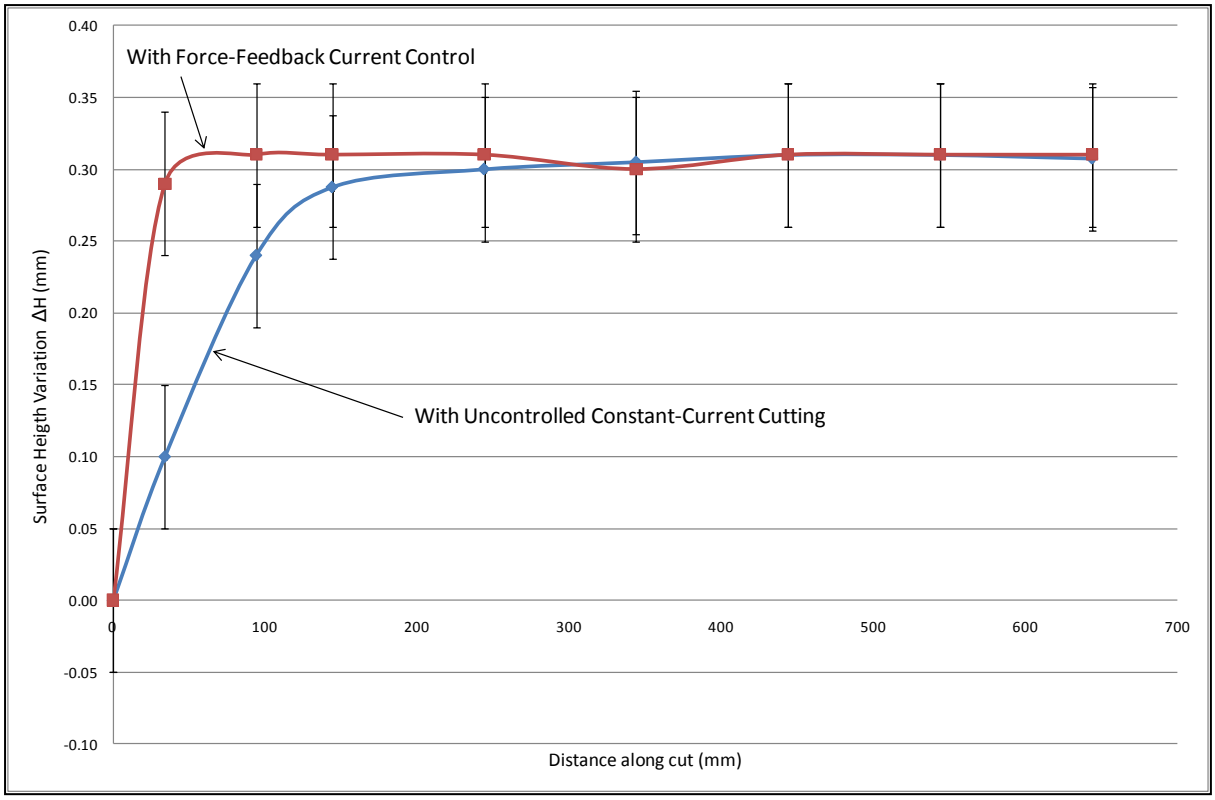

Figure 121: Comparison between the surface height variation *ΔH* with and without force-feedback current control (XPS, l_e = 30mm, 7A, 0.0183ms^{-1})

There is a significant implication of this result, which is that it is not really possible or practical to control the cutting process to eliminate the surface barrelling. Cuts with zero values of *ΔH* can be produced using purely-vapourised cutting, but this results in poor surface finishes and relatively slow cutting, and requires relatively high energy input. In addition, the high temperatures at which cutting tools must operate in purely-vapourised cutting have a detrimental effect on the tool life and durability. It is possible to force the cutting process directly into steady-state thermomechanical cutting with current-control, and as a result the steady-state kerf can be achieved directly from the start of the cut, but this does not force the surface barrelling into steady-state conditions immediately. Since the barrelling is the result of a thermal gradient along the engaged length of the tool, and since no thermal gradient exists in the tool prior to engagement with the foam, a transition from zero barrelling to the steady-state barrelling value is inevitable in all cuts.

While it is not yet possible to predict the magnitude of the surface barrelling based on input cutting strategy conditions, or to control the cutting process to eliminate surface barrelling, this is actually not a very serious problem from a practical point of view. This is because the typical magnitudes of the surface barrelling are really quite low, and it is likely that for most of the large-size parts being sculpted with the RFS system the dimensional tolerances are such that the barrelling can simply be left uncontrolled. In addition, the magnitudes of typical errors in multi-pass cutting are so much larger than the surface barrelling that, frankly, there are bigger problems to solve before investing significant time and effort trying to develop more conclusive results regarding the surface barrelling.

5.7 Cutting Force in Single-Pass Cutting

The cutting force in thermomechanical cutting of foam is important because it has a significant effect on the durability and life of the cutting tools, and on the surface finish produced by the cut. For a given design of cutting tool (hot-wire or hot-blade tools designed for multi-pass or single-pass cutting), there will be a critical cutting force that it can withstand before failing. The exact value of this critical cutting force varies depending on the cutting conditions, the tool temperature, the tool design and the cutting strategy. Cutting force has been briefly examined by Brooks [1] but only for a limited range of cutting conditions and without giving due consideration to the effect of engaged length, and with no attempt to develop a tool to allow the prediction of the cutting force based on input cutting conditions. As such, it is necessary to conduct a much more thorough investigation of the cutting force to determine exactly which input parameters are significant and quantitative relationships between these parameters and the final cutting force.

As has been noted above, the cutting force in hot-tool cutting of foam is initially zero due to the thermal field around the cutting tool, and remains so as long as the vapourised cutting mode lasts. When the thermal field collapses and physical contact starts to occur between the tool and the foam, the cutting force begins to increase until steady-state conditions are reached, at which point the cutting force plateaus and remains effectively constant until the end of the cut. From a practical point of view, only the steady-state cutting force is important for tool durability assessment, since this is the worst-case cutting force that will be experienced for a given set of cutting conditions. As such, only the steady-state kerf will be considered in this section.

Preliminary qualitative observations of the patterns of cutting force resulted in a number of tentative conclusions being drawn. These were:

1. That a cut made in EPS foam would have a lower steady-state cutting force than a cut made in XPS foam with the same cutting conditions, engaged length and tool type.
2. That for a given set of cutting conditions and the same type of foam, a cut made with a longer engaged length would have a higher steady-state cutting force than a cut made with a shorter engaged length.
3. That higher values of effective heat input Q_{eff} (i.e. greater energy input per unit area of cut surface) would result in a lower steady-state cutting force than a cut made with a lower effective heat input, all other parameters being equal.

Trends of steady-state cutting force with effective heat input for cutting of XPS foam with hot-wire tools are shown in Figure 122 (other tool types and foams result in cutting force trends that are qualitatively the same but have different specific values, so for conciseness only one curve has been reproduced here). As can be seen, the cutting force approaches zero as the effective heat input increases: this is a result of high effective heat inputs leading to steady-state conditions that stay in the vapourised cutting mode. Since no physical contact between the wire and the foam occurs in these instances, the cutting force is zero. Below the critical point of Q_{eff} at which the force reaches

zero, higher effective heat inputs also lead to smaller cutting forces due to the greater energy input to the foam.

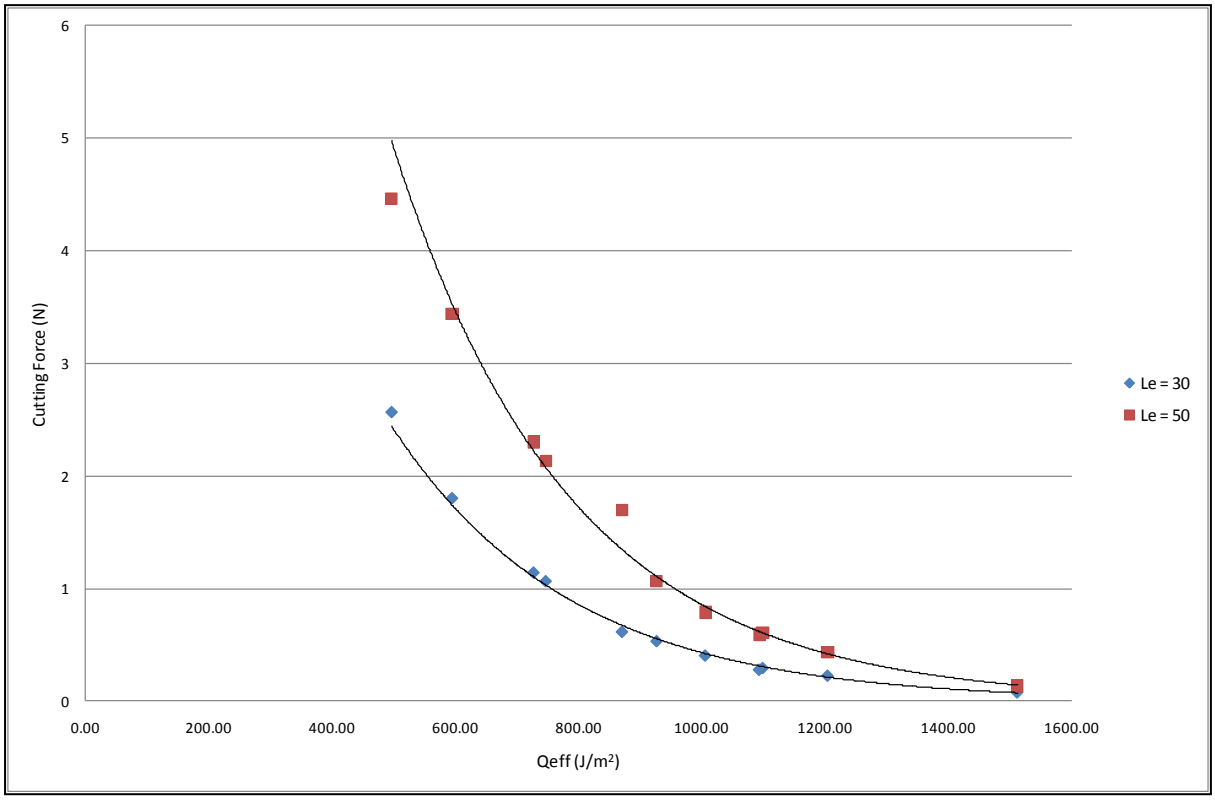

Figure 122: Trend of steady-state cutting force with Q_{eff} for hot-wire cutting of XPS with different engaged tool lengths, showing the exponential decay of cutting force with increasing Q_{eff}

It can also be seen that, at levels of Q_{eff} below the critical point where the cutting force trends to zero, the engaged length has a significant effect on the steady-state cutting force. For a given value of effective heat input, a cut made with a longer engaged length will experience a higher cutting force than a cut made with smaller engaged length.

Based on these cutting force curves, it is clear that the initial qualitative observations made above are valid, but this is of only limited practical use. In order to use this understanding of how the cutting force behaves with variations in engaged length, effective heat input, workpart material and tool type, it is necessary to develop quantitative models that will allow the prediction of the cutting force based on cutting conditions, so that these models can be added to the cutting strategy toolbox being developed progressively throughout this thesis.

It is fairly clear from Figure 122 that the trend of cutting force with effective heat input can be modelled as an exponential decay with an “asymptotic” approach to 0N at high values of Q_{eff} (the word asymptotic is used loosely here, since clearly the cutting force does reach zero in practice for purely vapourised cutting even though in an exponential fitted model it will not). The high level of correspondence between the measured cutting force data and an exponential decay is shown by the

trendlines in Figure 122: these are exponential trendlines for the l_e = 30mm and l_e = 50mm cases, and clearly fit the data very well. This correspondence between the data and an exponential trend is also observed for the other tool types and materials, although the exact shape of the curve differs. It is also reasonably clear from the observed trends that the engaged length acts as a multiplier for the cutting force, and so an appropriate exponential model can reasonably be expected to have to form:

$$F = \mathbf{A} l_e e^{(-\mathbf{B} Q_{eff})} + \mathbf{C} \quad (30)$$

Where **A**, **B** and **C** are coefficients that must be evaluated to develop an accurate model. Model fitting was carried out using the R software in a manner similar to the development of the models for the 10%-Height Contiguous Diameter ${}^{\emptyset}S_{10\%}$ and the kerfwidth λ, although this fitting process was complicated somewhat by the exponential nature of the model. The exact details of the curve fitting process are not particularly pertinent to the results, and so will not be discussed here in detail. It must be noted that the data set used to fit this curve to measured cutting force data was not limited to the data set produced by the single-pass kerf and barrelling experimental work outlined earlier. For cutting force analysis, a wide range of data was available that has been built up by the RFS project over several years, covering a very broad range of cutting conditions. As long as valid comparisons could be made, all of this data was used for developing cutting force models, in order to improve the accuracy of the models.

Separate models were developed for each relevant combination of tool type and foam material, resulting in a total of four cutting force models (since there are two types of single pass tool and two types of foam that are relevant). These models are presented in Table 20. For these models to function accurately engaged length l_e must have units of millimetres and effective heat input Q_{eff} must have units of J/m^2.

Table 20: Predictive Cutting Force Models for different tools and foams in terms of engaged length and effective heat input

Cutting Force Model		**R^2**
$F_{xps,\ wire} = 0.415156 l_e e^{(-0.003 Qeff)} - 0.159992$	(31)	0.99
$F_{eps,\ wire} = 1.0998 l_e e^{(-0.005 Qeff)} + 0.4162$	(32)	0.91
$F_{xps,\ blade} = 0.48525 l_e e^{(-0.0003 Qeff)} + 0.02874$	(33)	0.98
$F_{eps,\ blade} = 0.58121 l_e e^{(-0.0003 Qeff)} + 0.42289$	(34)	0.95

As can be seen from the R^2 values of these models, the equations in Table 20 provide a very good conformance to the measured steady-state cutting force. Cutting force has been shown to be primarily dependent on the effective heat input, the engaged length, the type of tool being used and the foam

being sculpted. When these four variables are included as the input parameters, very accurate models can be generated for cutting force.

Although these models were developed from the measurement of cutting force in single-pass cutting, it is highly relevant to multi-pass cutting. Cutting force in the multi-pass cutting case generally has shorter engaged tool lengths than in single-pass cutting, but the same fundamental mechanisms are operating as for single-pass cutting, so the models above can be used to predict the cutting force in multi-pass cutting using the appropriate values of the input parameters. The relevance of this to tool life, tool durability and tool failure modes will be discussed in the next chapter.

Based on this work, it is possible to develop a cause and effect diagram for the cutting force in terms of user-controllable and intermediate cutting strategy parameters, to aid in the control of the RFS system. This diagram is shown in Figure 123.

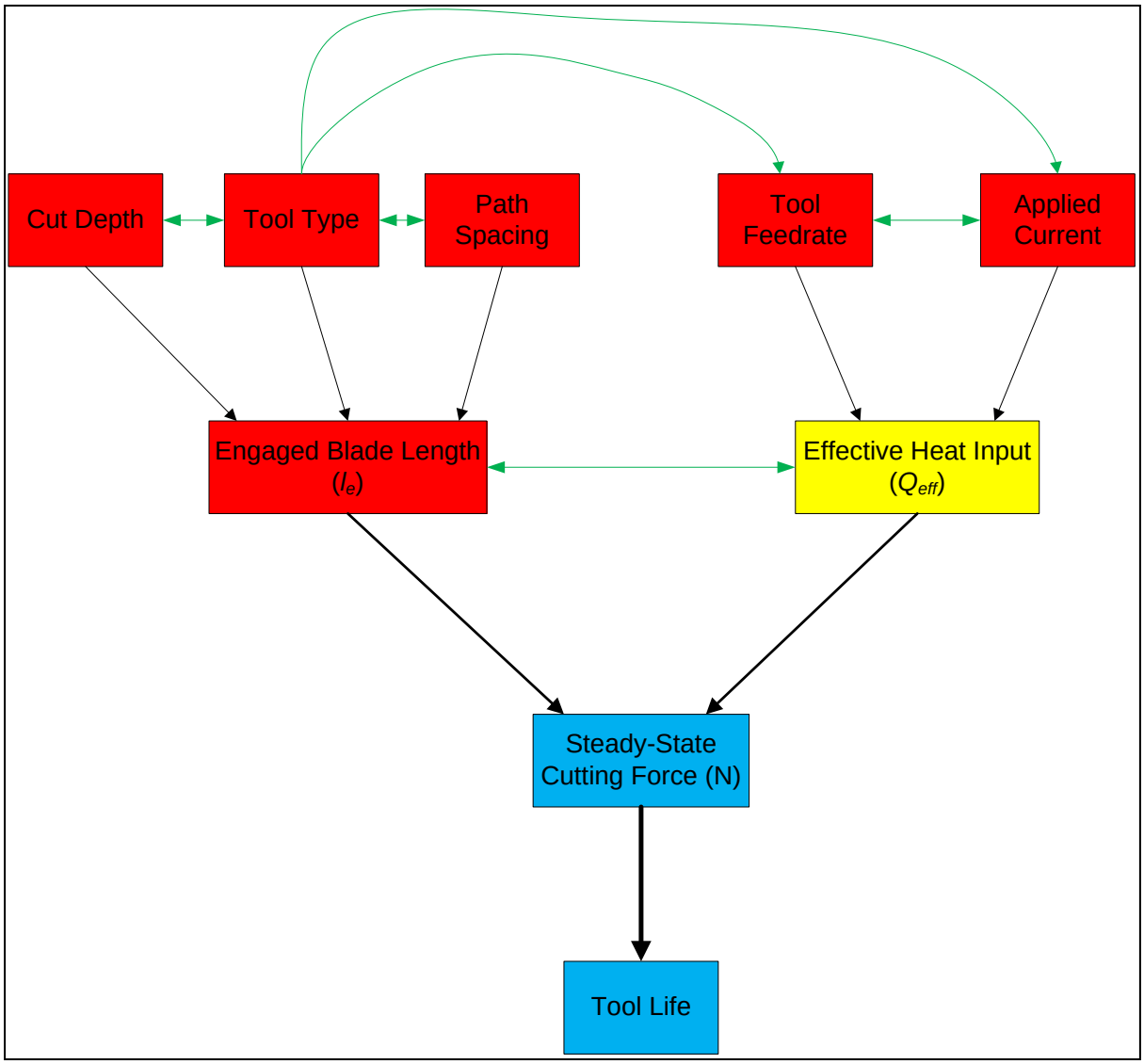

Figure 123: Factors and interactions that determine the cutting force

5.8 Conclusions and Limitations

As a result of the investigation into single-pass cutting strategy presented here, a number of conclusions can be drawn about the nature of the geometric form errors found in single-pass cutting. It is also possible to identify some limitations of this investigation that result in suggested areas for further research. These conclusions and limitations are the subject of this section.

5.8.1 Limitations of this Research

The investigation reported here has contributed significantly to the understanding of cutting strategy for single-pass hot-tool cutting of foam, but there are still some significant limitations to this work that must be kept in mind when applying the conclusions drawn here.

The kerf and barrelling investigations only considered two values of engaged length, and the supposition is that models developed using these engaged length values can be extrapolated to engaged lengths both larger and smaller than the range investigated. This supposition may not be accurate, so in future it may be desirable to conduct a similar investigation with a wider range of engaged lengths incorporated into the experimental design

The models developed above for the initial kerf are based on the supplied current, which is essentially a power input. As a result of the use of current as a key input parameter, these models are only really relevant to tools identical to those used for the experiment (i.e. with the same resistance). These models would be more generally useful if the initial kerf model was based on power, so that the models could be considered to be independent of the tool.

Finally, and most significantly, the results of the investigation of surface barrelling ΔH were highly inconclusive. There are indications that the value of ΔH is a function of the tool temperature differential ΔH, but there are also indications that the full picture of the causes of surface barrelling is not yet available. This is an area where a significant amount of future research is recommended.

5.8.2 Conclusions

This investigation has made a significant contribution to the body of knowledge concerning the cutting strategy for single-pass cutting, and has made a major contribution to the capability of the RFS system by defining models for the initial and final kerf that can be used to define equivalent-kerf cutting conditions for use in controlled-current cutting. Key results of this study were:

- Both kerf and surface height variation were found to be repeatable errors of the cutting process and will (within experimental error) be the same for a given set of cutting conditions every time those conditions are used.
- Statistical predictive models for the initial and steady-state kerf have been developed that can be used to establish equivalent-kerf cutting conditions that dramatically increase the range of currents, feeds and effective heat inputs for which force-feedback current control can be used.

- The parameters that have a significant effect on the kerf have been identified and the relationships between them have been mapped, so now the key parameters are known with a high degree of confidence. It was also concluded that, contrary to previous theories held within the RFS project team, the tool engaged length does have a significant effect on the kerf in single-pass cutting.
- The key factors influencing cutting force in single-pass cutting were identified as being the effective heat input Q_{eff} and the engaged tool length l_e. Statistical models were developed for the cutting force for different tool types and foams based on these input parameters, and these models allow the prediction of the expected maximum steady-state cutting force for a given set of cutting conditions with a high degree of accuracy.

6 Cutting Strategy for Multi – Pass Cutting

Since the RFS system uses a combination of single-pass and multi-pass cutting strategies to produce 3D sculpted objects, it is necessary to consider the cutting strategy and geometric form errors found in multi-pass cutting as well as those found in single-pass cutting. The investigation of the effect of multi-pass cutting strategy on surface quality is the subject of this chapter. There are two main types of geometric form errors in multi-pass cutting, which are superimposed upon each other to produce a net surface error. These are geometric errors and thermomechanical errors. Each of these will be dealt with separately. In addition, the cutting force in multi-pass cutting will be considered.

6.1 Introduction

Single-pass cutting using straight hot-wire and hot-blade tools is a useful element of cutting strategy in foam sculpting, but this type of cutting is only really of use for sculpting planar prismatic surfaces or in some cases for roughing a workpart close to the final desired shape. The primary limitation of single-pass cutting is a combination of tool shape and tool access: it is simply not possible to sculpt freeform curved surfaces using single-pass cutting tools.

In order to sculpt such 3D surfaces, the RFS system uses a multi-pass cutting strategy. The only viable alternative would be to combine single-pass cutting with the layered manufacturing approach used by the FF-TLOM and VLM systems discussed in the literature review, but this would have increased the complexity of the system in that an additional system would have been necessary to assemble the layers.

Surfaces produced by multi-pass cutting are characterised by relatively large-scale lay ridges resulting from the tool passes (visible in Figure 124) with areas between the ridges that possess primary texture, of the type considered in Chapter 3. These lay features are technically a surface texture feature, but have been treated as a geometric form feature due to the fact that they are much larger than lay in other machining processes.

There are two significant sources of error in multi-pass cutting operations. These are the geometric and the thermomechanical surface errors. The additional sources of error make the optimisation and prediction of errors in multi-pass cutting somewhat more complex than was the case in single-pass cutting.

Geometric errors are a function of the multi-pass cutting paradigm itself: the RFS system produces freeform surfaces by approximating each element of the surface with a cut. For example, when using a square-end tool, a curved surface is produced by approximating the curve with a large number of nominally straight surfaces of varying orientation. This approach allows the production of curved surfaces but produces an inevitable error that is largely a function of the path spacing, tool shape, and tool size. Analysis and prediction of the geometric errors is relatively simple, and will be discussed in more detail in section 6.2.

Thermomechanical errors are a function of the cutting process itself, and are actually very similar to the thermomechanical errors in single-pass cutting, which result in kerf and surface barrelling. These errors depend on such things as the cutting conditions, the effective heat input, and the engaged length. As such, the analysis and prediction of the thermomechanical errors is more complex than that for the geometric errors. Thermomechanical errors are considered in section 6.3.

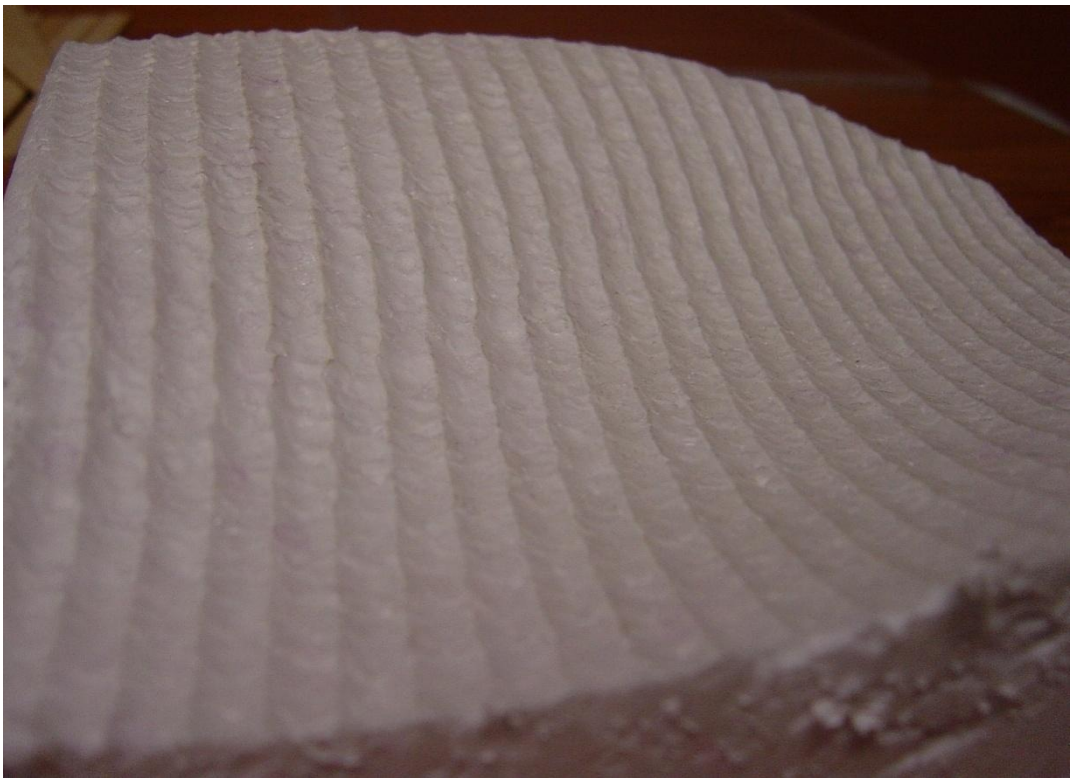

Figure 124: An arbitrary freeform surface sculpted in EPS with a round-nose tool

As with surfaces produced by single-pass cuts, surface flaws are often found on surfaces if the buildup of molten plastic on the blade or wire is not controlled. These flaws take the form of melted pockets in the surface with size of the same order as the lay features. Flaws can be avoided by simply allowing the cutting tool to rest in free-space for a few seconds between cutting passes, so that molten plastic on the tool is burned off. In practice this is achieved using a unidirectional cutting strategy, so that plastic can burn off when the tool is traversing in open air between cutting passes.

During the research conducted by Posthuma [7], a number of rules of thumb for multi-pass cutting were postulated. These were qualitative guidelines to achieving good surface quality with multi-pass cutting, and were based on the assessment of a range of different surfaces produced with different combinations of cutting conditions, tool size, and path spacing. The only drawback of this work from the point of view of this thesis was that no surfaces were produced with round-nose tools during Posthuma's research. Nevertheless, the rules of thumb provide the starting point for this investigation, and they are documented here for this reason. These provide some basic groundwork on which to base the detailed quantitative assessment of geometric form error for multi-pass cutting. The

assessment of these surfaces was extremely qualitative, and essentially consisted of ranking the surfaces produced from ‘best’ to ‘worst’ based on how they appeared to the naked eye. As such, the assessment of surface quality undertaken for this work was heavily predicated on those parameters that were most apparent to the eye, such as surface flaws, regularity of the lay and the surface texture. The dimensional accuracy of the surfaces was not considered.

Multi-Pass Cutting Rules of Thumb

- A certain amount of overlap between cutter passes was necessary to avoid major surface inaccuracy, but this overlap was also a significant factor influencing the number of surface defects. A trade-off between these conflicting effects must be made to achieve the desired and/or optimum surface geometry.
- Unidirectional cutting (where each tool pass is in the same direction) results in fewer surface defects (i.e. melted pockets) than bidirectional cutting, since the blade has more time in free air between cuts for residual liquid plastic on the blade to vapourise.
- When sculpting concave surfaces with square-ended tools, it was necessary for the tool width to be low with respect to the local surface curvature, otherwise gouging occurs due to the corners of the blade being too far from the tool centre point.
- Concave surfaces resulted in a greater frequency of surface flaws than convex surfaces. The reason for this is not clear.
- The ‘best’ surface finish was achieved with the smallest tools and the smallest step over, as assessed qualitatively.
- The cut depth should be kept to less than 20mm, since deeper cuts tend to result in higher cutting forces and this leads to more frequent bending of the blades. This is undesirable as it necessitated replacement of the blade. For this reason, roughing and finishing passes are often necessary.
- EPS requires less thermal input to cut than XPS, so the cutting forces and blade temperature variations are smaller. This seems to result in smaller lay heights (R_{max}, see below).

The surface gouging that occurred when sculpting concave surfaces with square-nose tools that were too large relative to the surface curvature inspired the development of round-nose tools, since these would not cause gouging when sculpting concave surfaces. These tools were first developed during the research that forms the basis for this thesis, and the surface errors resulting from these tools have been considered in this chapter along with those resulting from square-nose tools.

6.2 Geometric Surface Errors in Multi-Pass Cutting

When a curved surface is sculpted with multi-pass cutting, the curvature of the surface is approximated by a number of facets, each produced by a single tool pass. Together these facets produce a final surface that is close to the nominal surface shape. However, producing a surface in this way will inevitably lead to deviation between the actual approximated surface and the nominal surface. These deviations are referred to as geometric errors throughout this thesis.

Geometric errors are a function of geometric factors like the tool shape, tool size, path spacing and surface curvature. In order to determine exactly which geometric factors were important, mathematical models were developed for the idealised geometric error that would result from a given cutting strategy. These models produced formulae that could be used to determine the expected geometric error in the hypothetical case where there were no thermomechanical errors, which meant they could be used to provide a baseline surface error for given samples. This baseline error could then be compared to the as-measured error to provide a quantitative measure of the net thermomechanical component of the surface error.

Due to the different tool shapes used for square-nose and round-nose multi-pass cutting, the two tool shapes have been treated separately. Section 6.2.1 presents the geometric models for square-nose cutting, while section 6.2.2 presents the geometric models for round-nose cutting.

6.2.1 Geometric Surface Errors for Square-Nose Multi-Pass Cutting

When calculating the geometric error of surfaces sculpted by square-nose multi-pass cutting, there are two cases of interest. These are (from the point of view of the tool) surfaces that are concave and surfaces that are convex. If multi-pass cutting is used to sculpt nominally flat surfaces, then there is theoretically no geometric error that needs to be considered.

This section presents the development of geometric models for the error resulting from the approximation of a curved surface with multiple passes of a square-nose tool. Convex surfaces will be considered first, followed by concave surfaces. The development of these models is actually reasonably straightforward: comments throughout the mathematical derivations explain what is happening at each step.

6.2.1.1 Geometric Error of a Convex Surface cut with a square-nose tool

The first geometric error case that must be considered is that resulting from the approximation of a convex surface with multiple passes of a square-nosed tool. The geometry of this case is shown in Figure 125, and the development of a mathematical model for this error in terms of the geometric conditions is presented below.

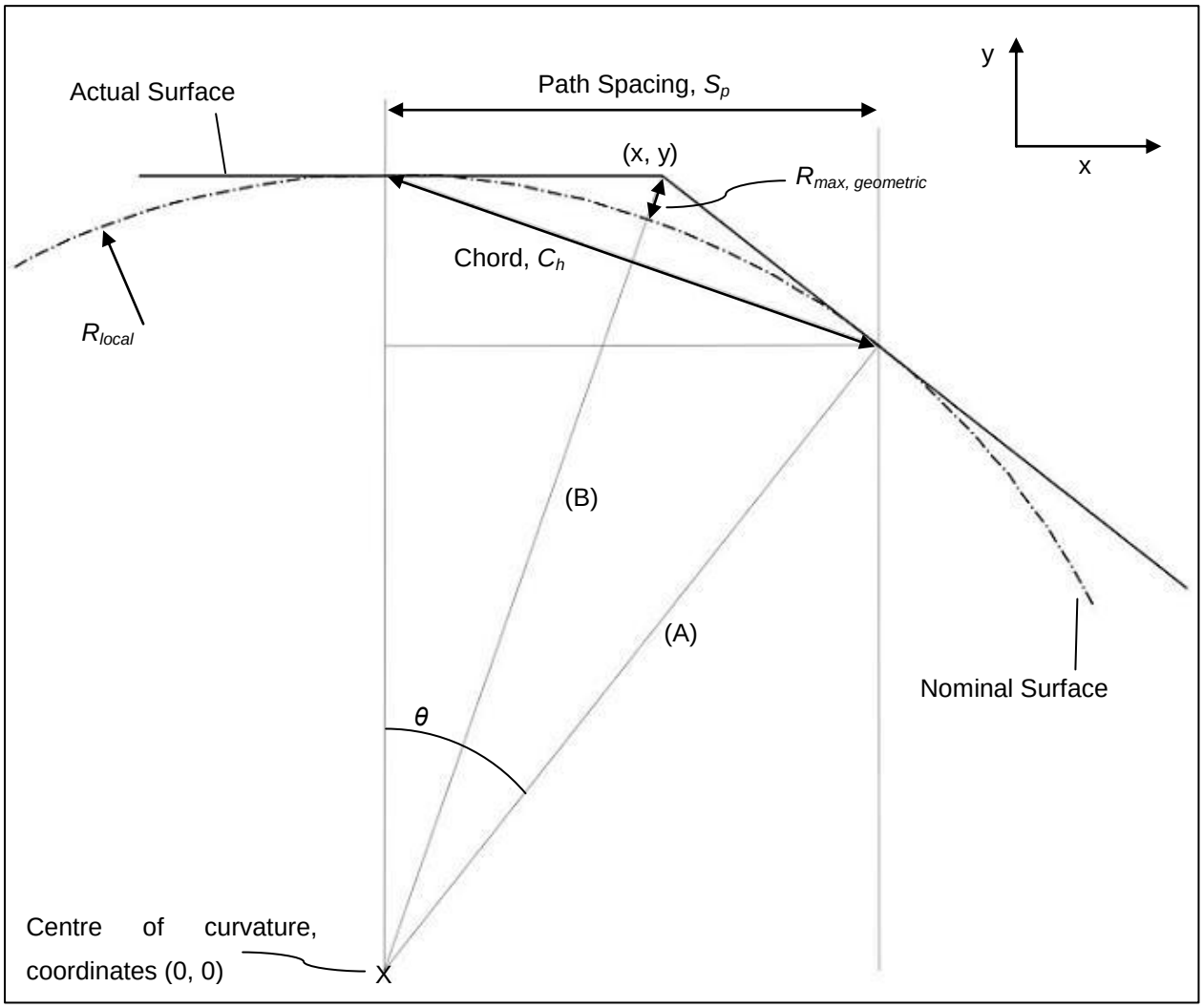

Figure 125: Cross-sectional geometry of a convex surface cut with a square-nose tool

First, we find θ:

$$\theta = \sin^{-1}\left(\frac{S_p}{R_{local}}\right) \tag{35}$$

Then determine the chord length C_h:

$$C_h = 2R_{local}\sin\left(\frac{\theta}{2}\right) \tag{36}$$

$$C_h = 2R_{local} \sin\left(\frac{\sin^{-1}\left(\frac{S_p}{R_{l.ocal}} \right)}{2} \right) \tag{37}$$

From Pythagoras, we know that:

$$S_p{}^2 = l^2 = C_h{}^2 \tag{38}$$

$$\therefore l = \sqrt{C_h{}^2 - S_p{}^2} \tag{39}$$

In this model there are two linear components of the actual surface which are tangential to the local curvature. One is horizontal, and (relative to the origin of the coordinate system at the centre of the radius of curvature) has the equation:

$$y = R_{local} \tag{40}$$

The other is angled and passes through the point defined by $(S_p, R_{local} - \sqrt{(C_h{}^2 - S_p{}^2)})$. An equation for this line is needed in order to determine the intercept between the two actual-surface components.

The slope of the radial line (A) is defined by:

$$\frac{rise}{run} = \frac{R_{local} - \sqrt{C_h{}^2 - S_p{}^2}}{S_p} \tag{41}$$

The surface component for which we need an equation is tangential to this line, so the slope of the surface component will be:

$$Slope = -\frac{S_p}{R_{local} - \sqrt{C_h{}^2 - S_p{}^2}} \tag{42}$$

Now, using the form y = mx + c for the equation of a straight line, we can generate the equation for the line segment of interest, using the known x an y coordinates, and find an equation for the coefficient c using known terms only:

$$\left(R_{local} - \sqrt{C_h{}^2 - S_p{}^2} \right) = -\left(\frac{S_p}{R_{local} - \sqrt{C_h{}^2 - S_p{}^2}} \right) S_p + c \tag{43}$$

$$\therefore c = \left(R_{local} - \sqrt{C_h{}^2 - S_p{}^2} \right) + \left(\frac{S_p}{R_{local} - \sqrt{C_h{}^2 - S_p{}^2}} \right) S_p \tag{44}$$

Based on this, the equation of the angled line segment, in the form y = mx + c, is:

$$y = -\left(\frac{S_p}{R_{local} - \sqrt{C_h{}^2 - S_p{}^2}} \right) x + \left(R_{local} - \sqrt{C_h{}^2 - S_p{}^2} + \frac{S_p{}^2}{R_{local} - \sqrt{C_h{}^2 - S_p{}^2}} \right) \tag{45}$$

This equation could be simplified, but for computational purposes this isn't really necessary. In addition, leaving these equations in the unsimplified form makes it easier to understand the process followed to derive them.

There are now two equations, 40 and 45, with two unknowns, x and y. These unknowns are the coordinates of the intercept between the two line segments that make up the as-cut surface in this geometric model, so it is necessary to find the values of x and y in order to calculate the geometric R_{max}. To do this, we solve the two equations simultaneously.

Substitute equation (40) into equation (45) and solve for x:

$$R_{local} = -\left(\frac{S_p}{R_{local} - \sqrt{C_h{}^2 - S_p{}^2}} \right) x + \left(R_{local} - \sqrt{C_h{}^2 - S_p{}^2} + \frac{S_p{}^2}{R_{local} - \sqrt{C_h{}^2 - S_p{}^2}} \right) \tag{46}$$

$$-R_{local} + \left(R_{local} - \sqrt{C_h{}^2 - S_p{}^2} + \frac{S_p{}^2}{R_{local} - \sqrt{C_h{}^2 - S_p{}^2}} \right) = \left(\frac{S_p}{R_{local} - \sqrt{C_h{}^2 - S_p{}^2}} \right) x \tag{47}$$

Rearranging for x:

$$\therefore x = \frac{R_{local} - \left(R_{local} - \sqrt{C_h{}^2 - S_p{}^2} + \frac{S_p{}^2}{R_{local} - \sqrt{C_h{}^2 - S_p{}^2}} \right)}{\left(\frac{S_p}{R_{local} - \sqrt{C_h{}^2 - S_p{}^2}} \right)} \tag{48}$$

Once this value of x is evaluated, substitute x into equation (45) and solve for y. A full equation for this will not be presented here as it is the value of x that is most useful for determining the value of $R_{max,\ geometric}$.

This now gives the x, y coordinates of the intercept between the two line segments that make up the surface approximation.

From the geometry of the model (shown in the diagrams above and below) we know that line (B) is equal to the sum of R_{local} and $R_{max,\ geometric}$. Therefore, from Pythagoras:

$$B = \sqrt{R_{local}{}^2 + x^2} \tag{49}$$

In this case x is evaluated using equation (48), above. Finally, this gives:

$$R_{\max,geometric} = \left(\sqrt{R_{local}{}^2 + x^2} - R_{local} \right) \tag{50}$$

6.2.1.2 Geometric Error of a Concave Surface cut with a Square-nose Tool

There are two basic types of cutting strategy that can be used in this case: under-cutting and over-cutting. Under-cutting is the most appropriate in almost all cases, since if desired post-processing can be used to improve the surface accuracy by removing excess material. This is not the case in when the surface has been approximated by over-cutting, since in this case the dimensions of the sculpted part will be smaller than the ideal dimensions and there is no excess material to remove. The geometry of these two cases is shown in Figure 126, and the geometric model is derived below.

When cutting a concave surface, the path spacing is not of direct importance for the geometric R_{max}. The blade width W_b is of more importance, although the path spacing will be restricted to less than the blade width. Since path spacing is of less importance, the development of a geometric model for R_{max} is much simpler for concave surfaces than was the case for convex surfaces.

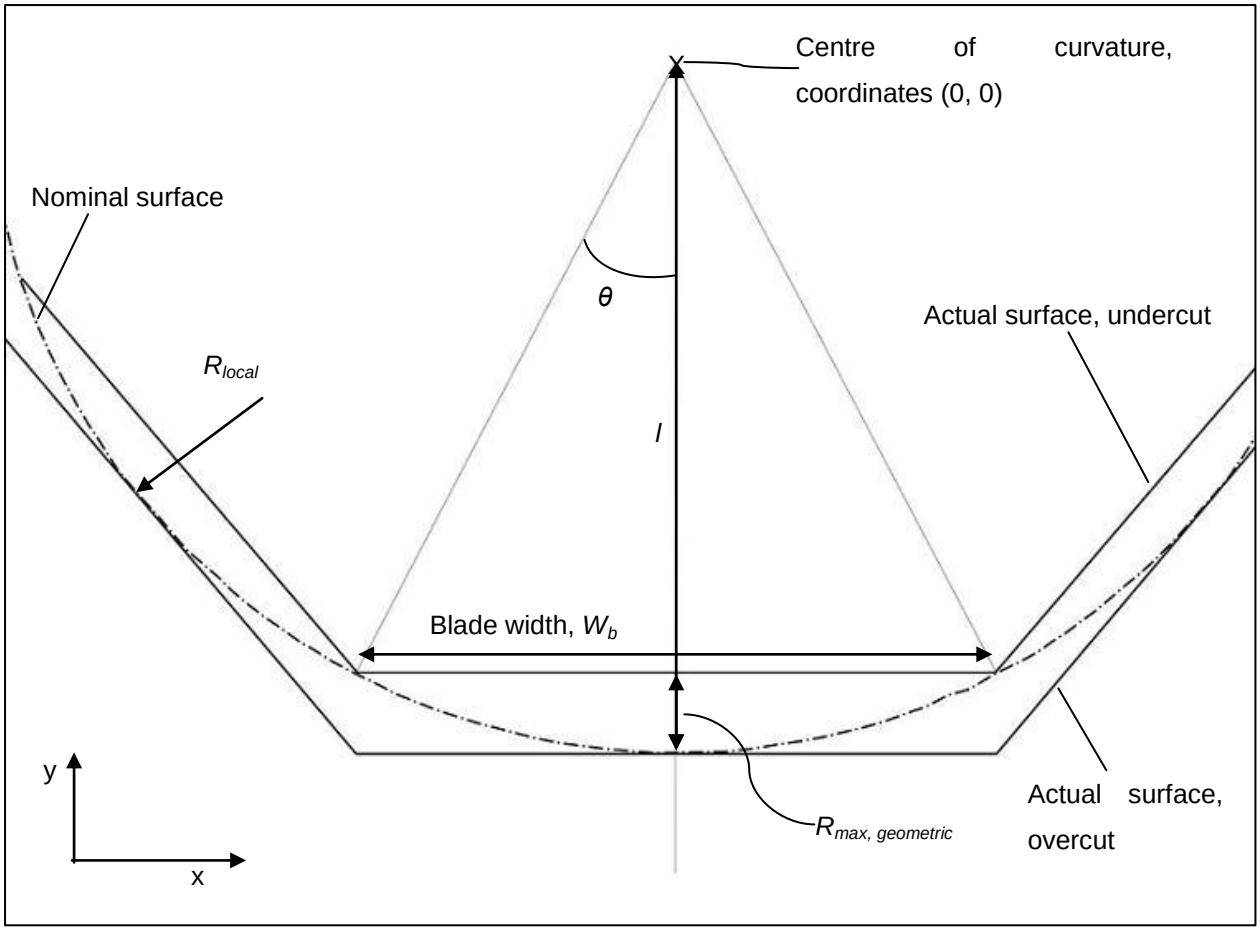

Figure 126: Cross-sectional geometry of a concave surface cut with a square-nose tool

First, determine the length *l*:

$$\left(\frac{W_b}{2}\right)^2 + l^2 = {R_{local}}^2 \tag{51}$$

$$\therefore l^2 = {R_{local}}^2 - \left(\frac{W_b}{2}\right)^2 \tag{52}$$

$$l = \sqrt{{R_{local}}^2 - \left(\frac{W_b}{2}\right)^2} \tag{53}$$

From the geometry of the model above, we know that:

$$R_{\max,geometric} = R_{local} - l \tag{54}$$

$$\therefore R_{\max,geometric} = R_{local} - \sqrt{R_{local}{}^2 - \left(\frac{W_b}{2}\right)^2} \tag{55}$$

6.2.2 Geometric Surface Errors for Round-Nose Multi-Pass Cutting

When sculpting surfaces with multi-pass cutting and round-nose tools, there are three cases that must be considered: concave, convex and flat surfaces. As a result of the shape of the tool, there is a geometric error even when sculpting flat surfaces. This geometric error due to the tool shape increases as path spacing increases, but cannot be larger than the tool radius.

In this section, all three of these cases will be considered and geometric error models will be developed. Flat surfaces will be considered first, followed by convex surfaces and finally concave surfaces.

6.2.2.1 Geometric Error of a Flat Surface cut with a Round-nose Tool

When sculpting flat surfaces with round-nose tools, the most significant input parameters determining the geometric error are the path spacing and the tool radius. The geometry of this case is shown in Figure 127, with the derivation of the geometric model presented subsequently.

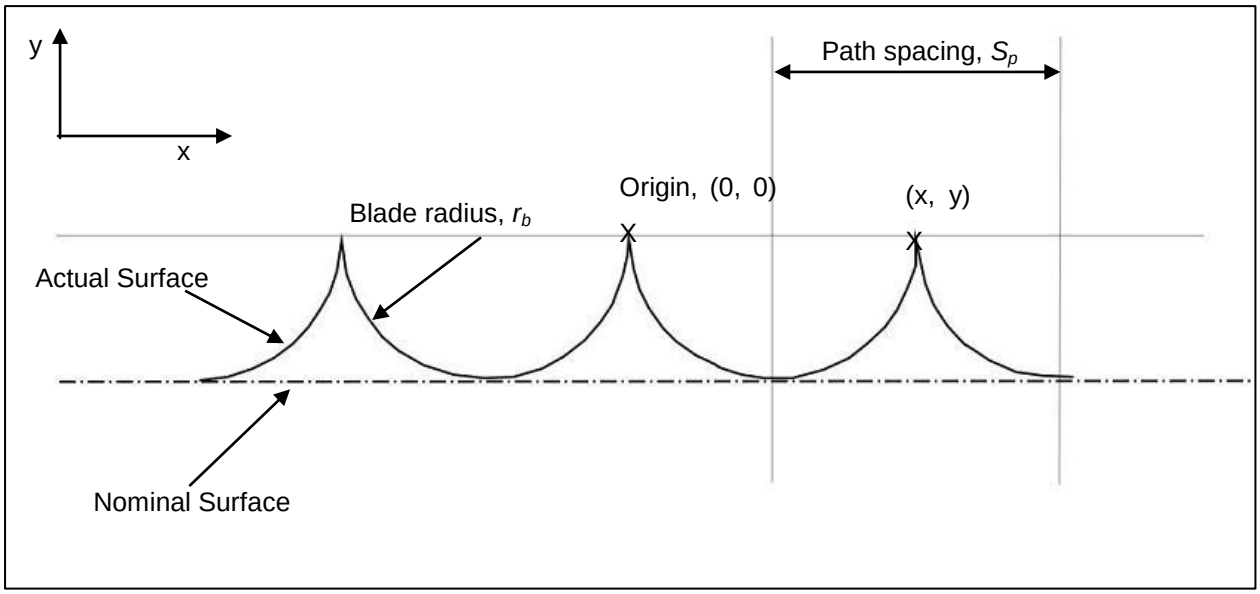

Figure 127: Cross-sectional geometry of a flat surface cut with a round-nose tool

For this model, we want to determine the height of the intercept between adjacent surface segments above the nominal surface. To do this, we need to find the value of y in the coordinates x, y, in terms of blade radius and path spacing.

Each surface segment is an arc that can be modelled relative to the origin defined above as:

$$x^2 + y^2 = r_b{}^2 \tag{56}$$

In the case above, it is clear from the geometry that:

$$x = \frac{S_p}{2} \tag{57}$$

It is also clear that this is true for all cases of blade radius and path spacing. Substituting equation (57) into equation (56) gives:

$$\left(\frac{S_p}{2}\right)^2 + y^2 = {r_b}^2 \tag{58}$$

Rearranging gives:

$$y = \sqrt{{r_b}^2 - \left(\frac{S_p}{2}\right)^2} \tag{59}$$

And, finally:

$$R_{\max,geometric} = r_b - \sqrt{{r_b}^2 - \left(\frac{S_p}{2}\right)^2} \tag{60}$$

6.2.2.2 Geometric Error of a Convex Surface cut with a Round-nose Tool

The geometric error resulting when sculpting a convex surface with a round-nose tool is significantly more complex than the case of sculpting a flat surface, because the curvature of the nominal surface must also be considered. The geometry of this case is shown in Figure 128, with the model derivation presented below.

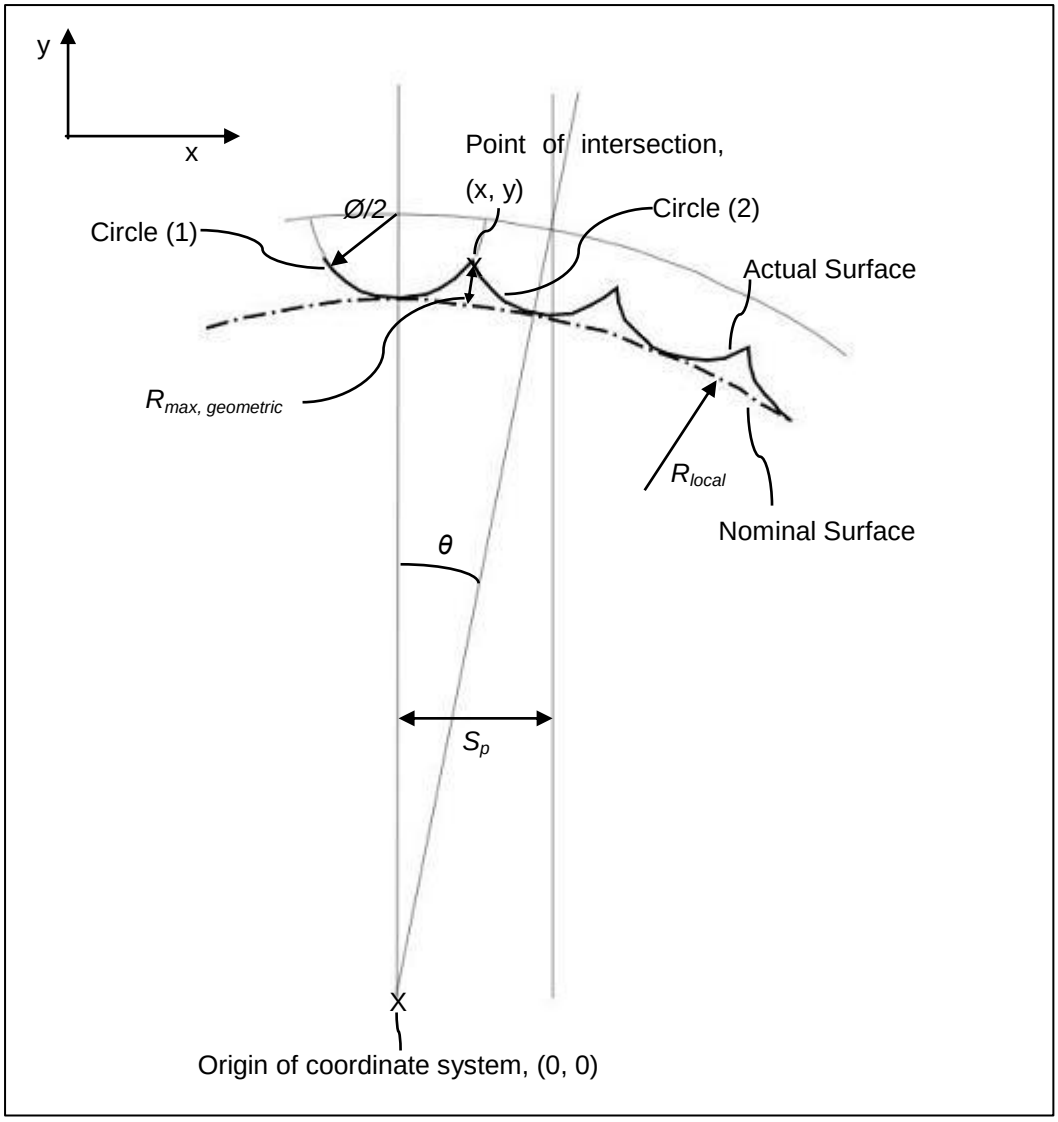

Figure 128: Cross-sectional geometry of a convex surface cut with a round-nose tool

First find an equation for circle (1):

$$x^2 + \left(y - \left(R_{local} + \frac{\phi}{2} \right) \right)^2 = r^2 \tag{61}$$

$$x^2 + \left(y - R_{local} - \frac{\phi}{2} \right)^2 = \left(\frac{\phi}{2} \right)^2 \tag{62}$$

Now find an equation for circle (2). The first problem is to find the x, y coordinates of the centre of this circle.

$$x = \sin\theta \left(R_{local} + \frac{\phi}{2} \right) \tag{63}$$

$$y = \cos\theta\left(R_{local} + \frac{\phi}{2}\right) \tag{64}$$

Therefore the equation for circle (2) is:

$$\left(x - \sin\theta\left(R_{local} + \frac{\phi}{2}\right)\right)^2 + \left(y - \cos\theta\left(R_{local} + \frac{\phi}{2}\right)\right)^2 = \left(\frac{\phi}{2}\right)^2 \tag{65}$$

This gives two equations and two unknowns, so they can be solved simultaneously to determine the coordinates (x, y) of the intercept between two adjacent surface segments.

Equation (62) can be rearranged to:

$$x = \sqrt{\left(\frac{\phi}{2}\right)^2 - \left(y - R_{local} - \frac{\phi}{2}\right)^2} \tag{66}$$

Substitute this into equation (65) to give:

$$\left(\sqrt{\left(\frac{\phi}{2}\right)^2 - \left(y - R_{local} - \frac{\phi}{2}\right)^2} - \sin\theta\left(R_{local} + \frac{\phi}{2}\right)\right)^2 + \left(y - \cos\theta\left(R_{local} + \frac{\phi}{2}\right)\right)^2 = \left(\frac{\phi}{2}\right)^2 \tag{67}$$

This can be rearranged to give:

$$y = \sqrt{\left(\frac{\phi}{2}\right)^2 - \left(\sqrt{\left(\frac{\phi}{2}\right)^2 - \left(y - R_{local} - \frac{\phi}{2}\right)^2} - \sin\theta\left(R_{local} + \frac{\phi}{2}\right)\right)^2} + \cos\theta\left(R_{local} + \frac{\phi}{2}\right) \tag{68}$$

This equation gives y in terms of the local radius of curvature, R_{local}, and the blade diameter ø. Clearly y exists on both sides of this equation. While it is possible to simplify this equation to put y on only one side, there is little point since the equation can more easily be evaluated iteratively by a computer.

Substituting equation (68) into equation (62) gives equation (69)

$$x = \sqrt{\left(\frac{\phi}{2}\right)^2 - \left(\left(\sqrt{\left(\frac{\phi}{2}\right)^2 - \left(\sqrt{\left(\frac{\phi}{2}\right)^2 - \left(y - R_{local} - \frac{\phi}{2}\right)^2} - \sin\theta\left(R_{local} + \frac{\phi}{2}\right)\right)^2} + \cos\theta\left(R_{local} + \frac{\phi}{2}\right)\right) - R_{local} - \frac{\phi}{2}\right)^2}$$

The x, y coordinates of the intercept between two adjacent surface segments can be evaluated iteratively from equations (68) and (69).

Now, with the known x and y values of the intercept, it is possible to calculate the value of $R_{max,\ geometric}$:

$$\left(R_{local} + R_{\max,geometric}\right)^2 = x^2 + y^2 \tag{70}$$

$$R_{\max,geometric} = \sqrt{x^2 + y^2} - R_{local} \tag{71}$$

6.2.2.3 Geometric Error of a Concave Surface cut with a Round-nose Tool

The derivation of a geometric model for this case is very similar to the derivation of the model for the geometric error of a convex surface cut with a round-nose tool, with different signs in the equations. Figure 129 shows the geometry used for this model, and the derivation of the model is presented below.

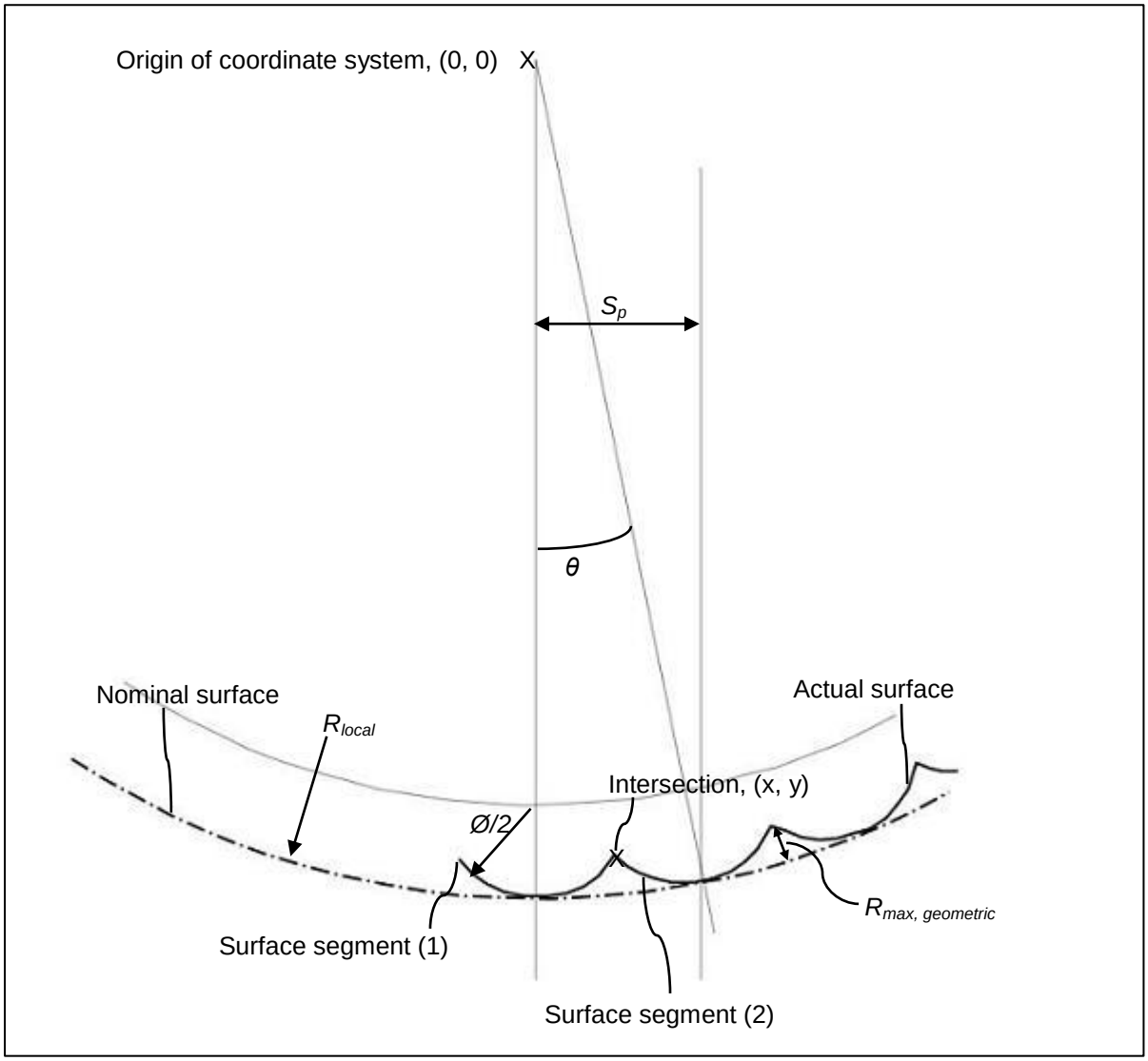

Figure 129: Cross-sectional geometry of a concave surface cut with a round-nose tool

First we find the equation for surface segment (1):

$$x^2 + \left(y - \left(R_{local} - \frac{\phi}{2} \right) \right)^2 = \left(\frac{\phi}{2} \right)^2 \tag{72}$$

Now find the equation for line segment (2):

$$\left(x - \sin\theta \left(R_{local} - \frac{\phi}{2} \right) \right)^2 + \left(y + \cos\theta \left(R_{local} - \frac{\phi}{2} \right) \right)^2 = \left(\frac{\phi}{2} \right)^2 \tag{73}$$

Rearranging (72) to give an equation for x, substituting into equation (73) and rearranging gives:

$$y = \sqrt{\left(\frac{\phi}{2} \right)^2 - \left(\sqrt{\left(\frac{\phi}{2} \right)^2 - \left(y - R_{local} - \frac{\phi}{2} \right)^2} - \sin\theta \left(R_{local} - \frac{\phi}{2} \right) \right)^2} - \cos\theta \left(R_{local} - \frac{\phi}{2} \right) \tag{74}$$

This can be substituted back into equation (72) and rearranged to give equation (75):

$$x = \sqrt{\left(\frac{\phi}{2} \right)^2 - \left(\left(\sqrt{\left(\frac{\phi}{2} \right)^2 - \left(\sqrt{\left(\frac{\phi}{2} \right)^2 - \left(y - R_{local} - \frac{\phi}{2} \right)^2} - \sin\theta \left(R_{local} - \frac{\phi}{2} \right) \right)^2} - \cos\theta \left(R_{local} - \frac{\phi}{2} \right) \right) - R_{local} - \frac{\phi}{2} \right)^2}$$

From these equations and the geometry of the model, we can define the value of $R_{max,\ geometric}$ as:

$$R_{\max,geometric} = -\sqrt{x^2 + y^2} + R_{local} \tag{76}$$

6.2.3 Discussion and Conclusions

These models for the geometric error resulting from the approximation of curved surfaces with multiple tool passes allowed the mapping of the significant input parameters that determine the geometric surface errors. The important input parameters for each combination of surface curvature and tool shape are summarised in Table 21.

.

Table 21: Summary of input parameters affecting the geometric surface errors in multi-pass cutting

Tool Shape	**Surface Curvature**	**Input Parameters**
Square	Convex	Surface Curvature R_{local}, Path Spacing S_p
	Concave	Surface Curvature R_{local}, Blade Width W_b
Round	Flat	Blade Diameter ø, Path Spacing S_p
	Convex	Surface Curvature R_{local}, Blade Diameter ø, Path Spacing S_p
	Concave	Surface Curvature R_{local}, Blade Diameter ø, Path Spacing S_p

From the models, a cause and effect diagram for the geometric surface error was developed. This diagram is shown in Figure 130. It was also possible, from the multi-pass cutting rules of thumb and from existing understanding of the nature of multi-pass cutting strategy, to map the interactions between the input parameters. The geometric R_{max} is directly influenced by the surface curvature, the tool size, the tool shape, and the path spacing. These input parameters also affect each other. For example, the tool shape, tool size and path spacing must be selected based on the curvature of the surface being sculpted, and the value of path spacing used must be appropriate for the tool size and the tool shape being used. As has been explained, red parameters in these diagrams indicate cutting strategy parameters that are directly controllable by the production planner, and the hatching on the surface curvature parameter indicates that this parameter is controllable only within the limits of functional requirements. In other words, to ensure that a part can be easily and accurately sculpted it is necessary to consider the cutting strategy at the part design stage.

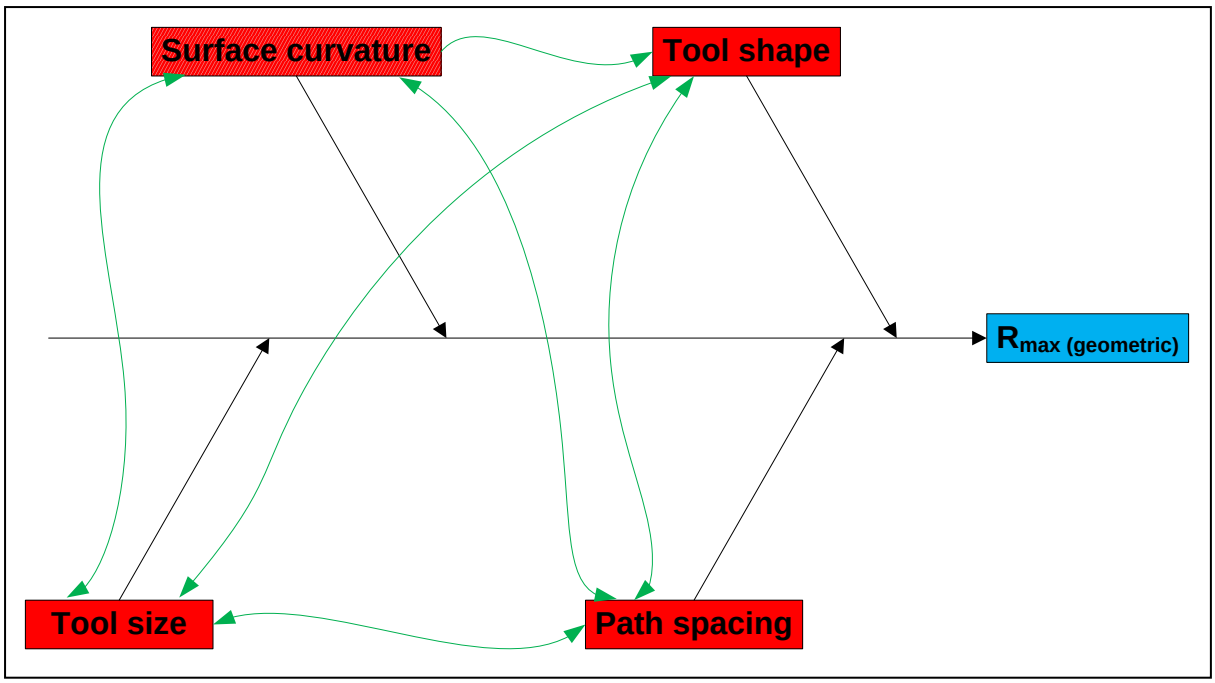

Figure 130: Factor interactions influencing the value of $R_{max\ (geometric)}$ in multi-pass cutting

The other significant surface error in multi-pass cutting is the peak spacing. Geometric models for this did not need to be developed in order to map the parameters that influenced the process. Instead, by inspection of a range of multi-pass sample surfaces and by consideration of the geometric cases outlined above, it was clear that the peak spacing would be controlled by the same input parameters as the geometric R_{max}, and that the interactions between these input parameters would also be the same. The cause and effect diagram for multi-pass peak spacing is shown in Figure 131.

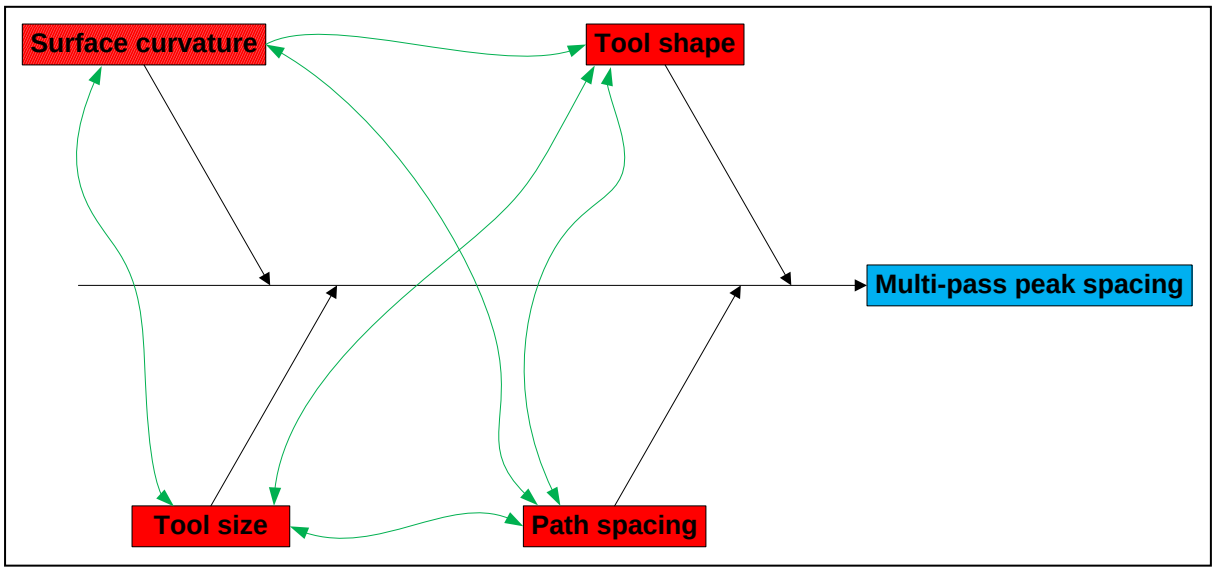

Figure 131: Factor interactions influencing the value of peak spacing in multi-pass cutting

These models allow the prediction of the geometric component of surface errors in multi-pass cutting, and as such provide a useful starting point for the assessment and prediction of multi-pass surface accuracy, but the geometric error does not provide a complete picture of the sources of error. Since the geometric models were based on an assumption that there were no thermomechanical effects like kerf or surface barrelling, the thermomechanical errors have not yet been considered. It is necessary to consider the effects of thermomechanical error in order to develop a full understanding of the surface error in multi-pass cutting. When an understanding of thermomechanical errors is available, this can be combined with the geometric error models presented here to help choose input cutting parameters to achieve a required surface accuracy, and therefore to optimise the cutting strategy for sculpting a given part. The investigation of the thermomechanical errors in multi-pass cutting is the subject of the next section.

6.3 Thermomechanical Surface Errors in Multi-Pass Cutting

The previous section demonstrated how geometric surface errors are introduced by the shapes of the cutting tools used, the curvature of the surfaces being sculpted, and the toolpath used to sculpt the surface. These surface errors are denoted by $R_{max,\ geometric}$, and are demonstrated for the case of a flat surface sculpted by a round-nose tool in Figure 132. Mathematical models for the calculation of this error based on relevant input conditions have already been presented.

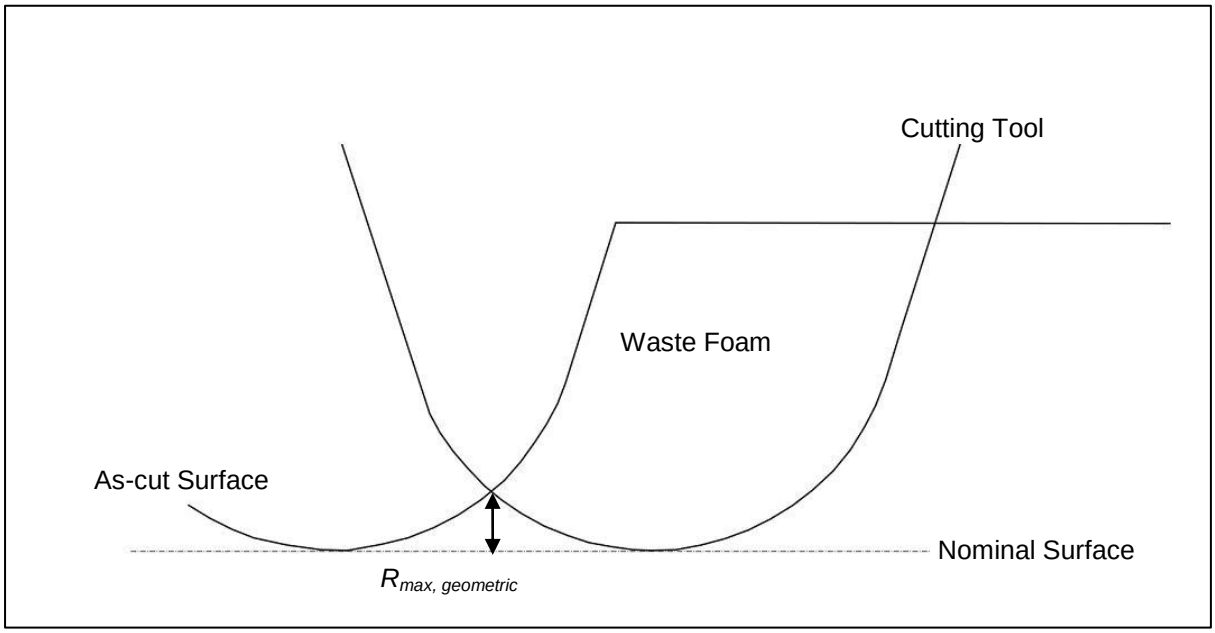

Figure 132: Ideal $R_{max,\ geometric}$ in the case where a flat surface is sculpted with a round-nose tool

Although the geometric surface errors are important, and in many cases will be the most significant source of the total error in a sculpted surface, the full picture of the sources of error is somewhat more complex and several other factors must be considered to allow a more complete understanding of the sources of error, and to facilitate the more accurate prediction of the error that can be expected from a given cutting strategy.

The multi-pass cutting process is, in principle, the same as the process of making a cut with a single-pass of a straight hot blade. The ribbon used to make the loop in the tool is the same; it is simply shaped instead of being straight. The range of cutting conditions used (i.e. the operational space) is the same, and therefore the nature of the thermomechanical cutting process will also be the same. The only real difference is that, in most multi-pass cutting, the engaged length of the tool is significantly smaller than is usually the case in single-pass cutting, as a result of relatively low values for path spacing and cut depth. This difference does not negate the fundamental similarity between the two cases of hot-blade cutting of foam, since the magnitude of the thermomechanical errors in single-pass cutting was partially dependent on the value of engaged length in any case.

As a result of this similarity, it is reasonable to expect that thermomechanical errors will be present in multi-pass cutting as they were in single-pass cutting, and that these thermomechanical errors will be superimposed on the geometric surface errors. It will be recalled that the two significant thermomechanical errors in single-pass cutting were the kerf (λ) and the surface barrelling (ΔH), and before going on to a detailed quantitative analysis of the nature of these errors it is worth spending some time to outline what effect the kerf and surface barrelling can be expected to have on the surface errors in a multi-pass cut.

Consider a cut with a round-nose tool (like that shown in Figure 132) where kerf is superimposed on the geometric error resulting from the shape of the tool. This kerf results from the thermal field around the tool, and in effect increases the radius of the cutting tool, as shown in Figure 133 (this assumes for the moment that the kerf is constant along the engaged length, with no barrelling present). From examination of the geometry in this case, it is clear that the effect of kerf should be to increase the effective tool radius and therefore to cause an actual surface error that is *smaller* than the ideal geometric surface error.

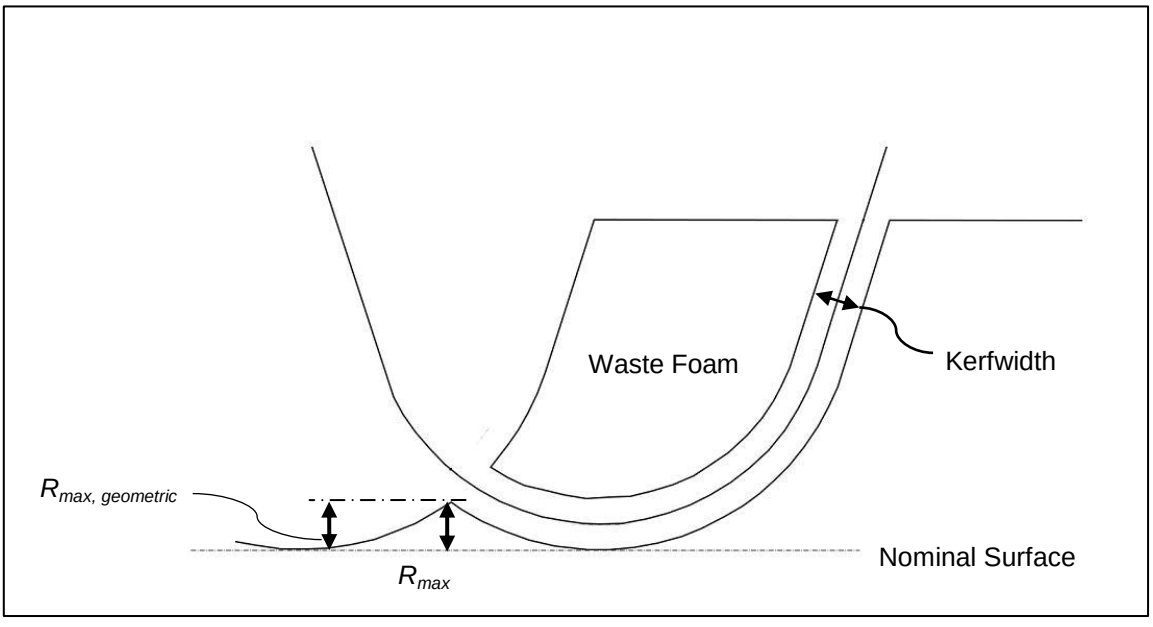

Figure 133: Effect of the kerf on the surface error when sculpting a flat surface with a round-nose tool

The ‘surface barrelling’ can now be superimposed on the kerf and geometry of this case, as shown in Figure 134. The term surface barrelling is used here loosely because this is the term that has been used previously for the error resulting from the thermal gradient along the engaged length of the tool, even though in the multi-pass case the resulting surface error isn’t really a barrelling like that exhibited in single-pass cutting. In multi-pass cutting the thermal gradient results in a wider kerfwidth at the ends of the engaged length than in the centre, and therefore adds another increase to the effective radius of the tool in addition to that resulting from the basic kerf. As a result, the surface barrelling should make the actual surface error somewhat smaller again than the error to be expected from the superposition of geometric error and kerf.

It should be noted at this point that, as with single-pass cutting, the error resulting from the thermal gradient along the tool is concentrated at the ends of the engaged length. As a result, only the surface barrelling at one end of the engaged length (denoted by ‘A’ in Figure 134) is relevant to the final surface error in multi-pass cutting, since the barrelling at the other end of the engaged length is affecting a piece of foam that will be cut off by the next tool pass in any case.

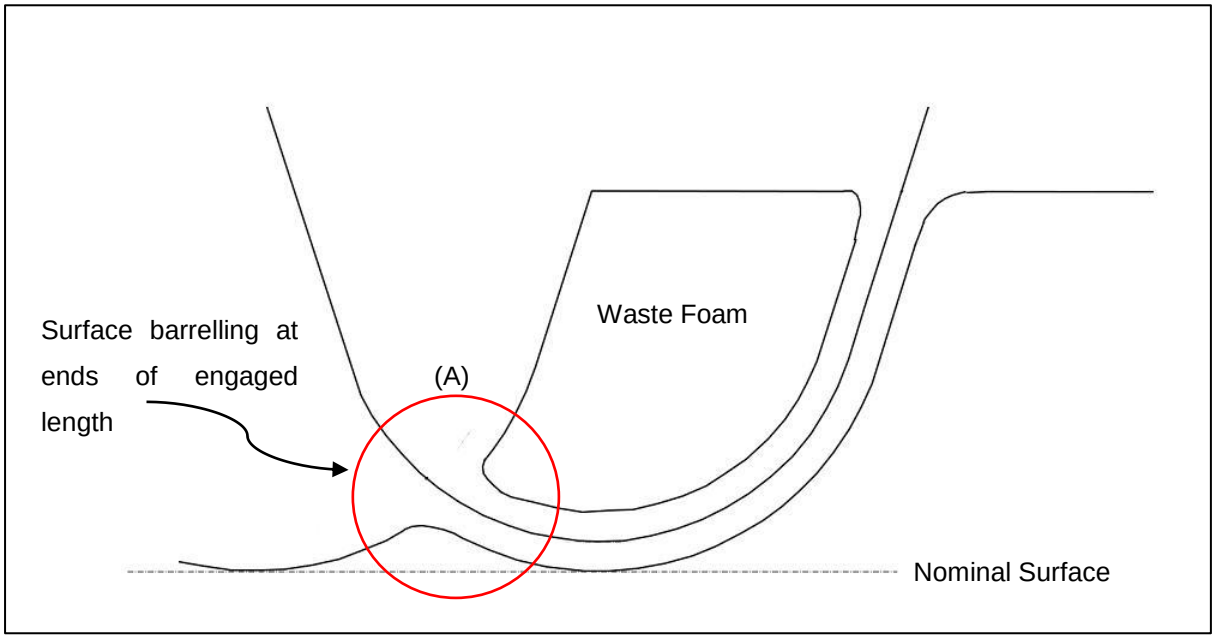

Figure 134: Effect of the ‘surface barrelling’ on the surface error when sculpting a flat surface with a round-nose tool

From this consideration of surface error superposition, it is possible to conclude that, unless there are other, unconsidered, factors at work, the actual errors (or, in other words, the net surface error) in surfaces cut with round-nose tools should be smaller than the geometric errors predicted by the models developed in the previous section. As such, these models provide a means of calculating, in advance, the worst-case error to be expected for a given combination of tool radius, surface curvature and path spacing.

The case of multi-pass cutting with square-nose tools is somewhat different from the round-nose case. When sculpting with square-nose tools, the effect of kerf in producing thermomechanical surface error is much less significant. Consider the sculpting of a nominally-flat surface with multiple passes of square-nose tools: the geometric surface error in this case should be zero. If the same cutting conditions are used the kerf for each pass will be the same, and (as long as a suitable offset has been applied to ensure dimensional accuracy) will not have any actual effect on the surface error if the kerf is considered to be constant along the engaged length of the tool. So, considering only the geometric error and the error resulting from kerf, this surface should be flat. However, this is not the case, as shown in Figure 135. This figure shows a cross-section of a foam sample, the top edge of which was sculpted with multiple passes of a square-nose tool. Clearly, there is an error in this surface, which has been previously referred to within the RFS project as the 'weatherboard' effect. This error is significant and readily apparent when visually inspecting the sculpted surface, and so must be explained in order to determine a method of minimising the achieved error.

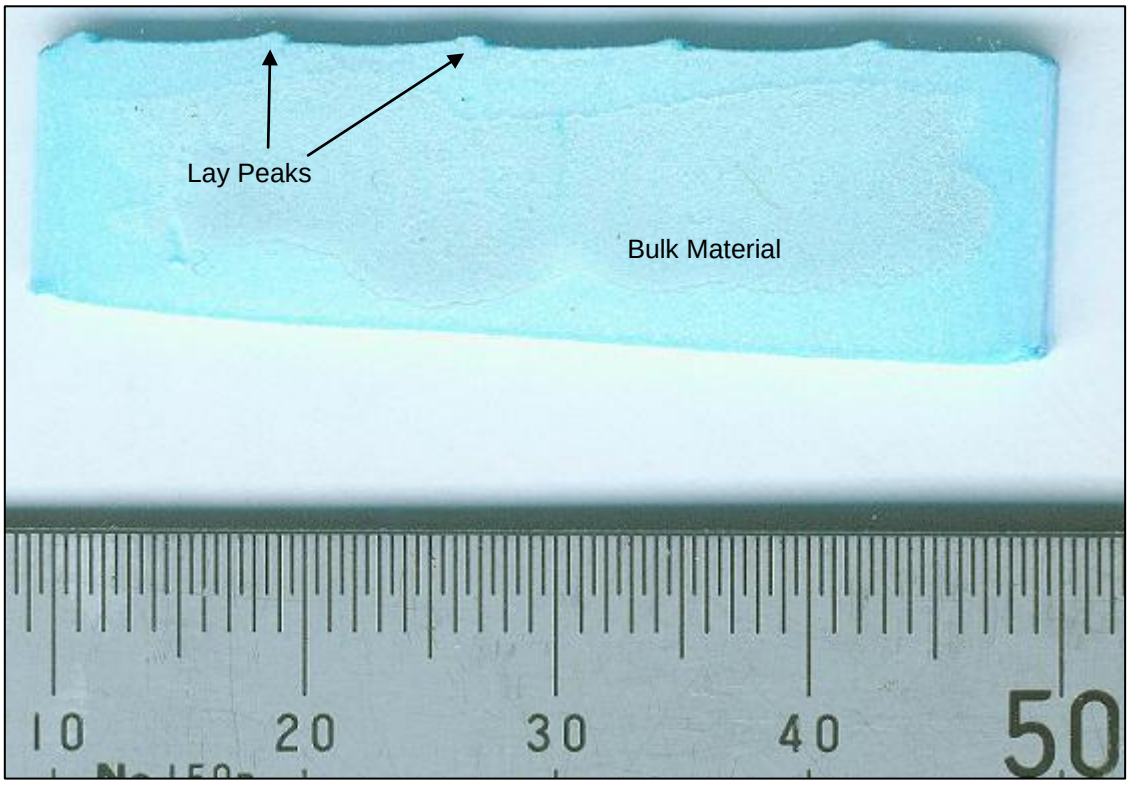

Figure 135: Sectioned view showing lay resulting from multi-pass cutting of a flat surface (8mm square-nose tool, 8mm path spacing)

Since the weatherboard effect was clearly not due to geometric error or kerf, it was deduced that the error was caused by the thermal gradient along the engaged length of the cutting tool, and was therefore analogous to surface barrelling in the single-pass cutting case. In order to test this, a brief experiment was carried out. Five cuts were carried out in EPS using an 8mm square-nose tool with a path spacing of 8mm and cutting conditions of 16A and $0.050ms^{-1}$, and the temperature of the tool was recorded using a thermocouple (reference to paper for method) along the length of the cut.

Temperature data was gathered at five different points on the tool, as marked in Figure 136. The temperature profiles along the cut length recorded at these points on the tool are shown in Figure 137.

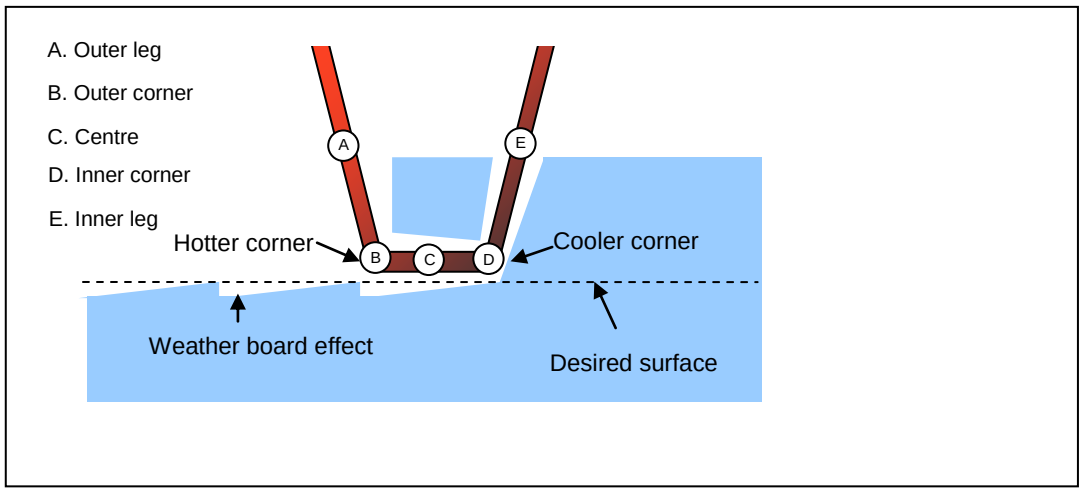

Figure 136: Points of interest for measuring longitudinal tool temperature profiles in multi-pass cutting

Based on the observed relationships between tool position and as-cut surface position it was expected that the most significant points on the tool would be the outer corner (B) and the inner corner (D). It was expected that the outer corner would be consistently hotter than the inner corner, since the inner corner is further into the engaged length, and that the temperature profile at the tool centre (C) would be somewhere between the temperatures at the two corners. It was also expected that the temperature difference between these points would be negligible at the start of the cut, and would then develop to a steady-state temperature difference analogous to ΔT in single-pass cutting.

These expectations were borne out by the measured temperature data. At the beginning of the cut the temperature difference between the two tool corners was negligible, but a difference developed very quickly and increased to approximately 300ºC after 4s, before eventually stabilising at approximately 200ºC. This was expected from visual inspection of multi-pass cut surfaces, where the weatherboard effect seemed to be largest near the start of the cut and smaller once steady-state conditions were established. That said, even when cutting with steady-state conditions that weatherboard effect was still quite pronounced.

The temperature of the tool centre (C) was between the temperatures of the two corners at all points along the cut, and was closer to the temperature of the inner corner than that of the outer. This is what would have been expected if measurements were made of analogous points in single-pass cutting, since the thermal gradient between free-air and centre-cut temperatures is most pronounced at the ends of the engaged length.

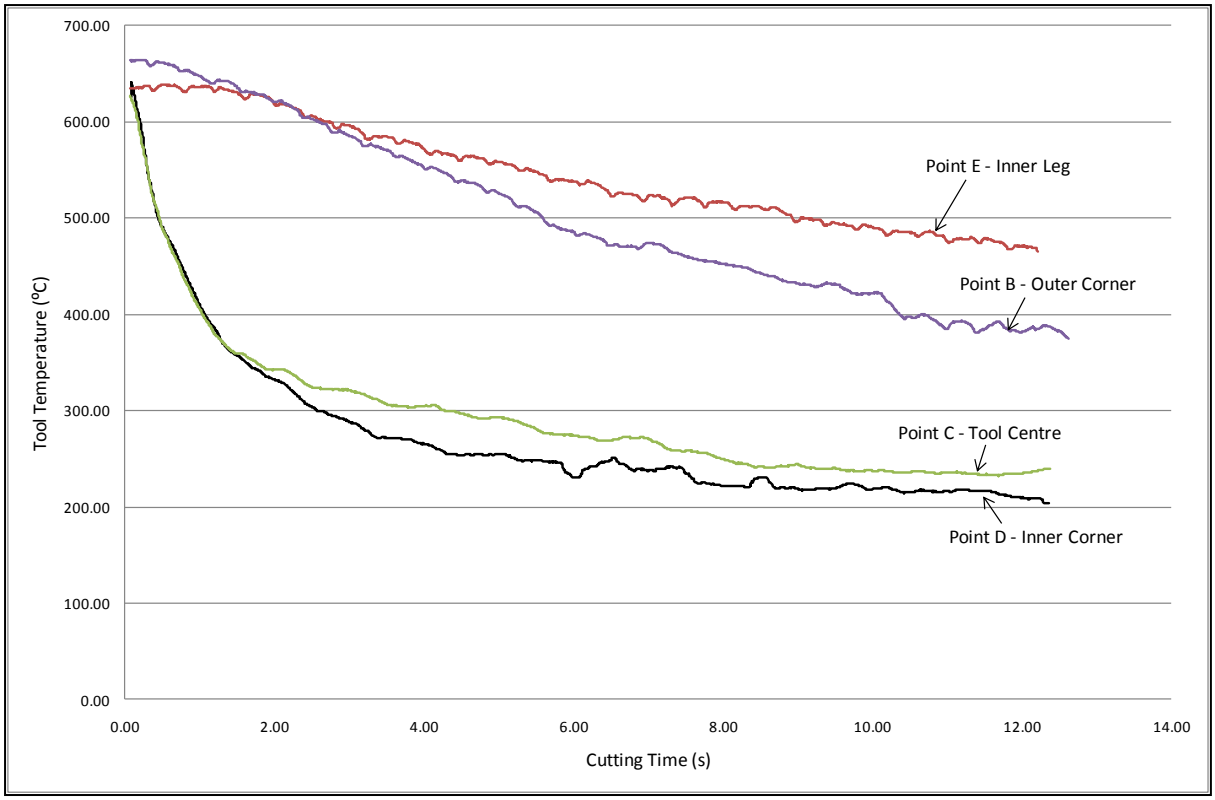

Figure 137: Longitudinal tool temperature profiles for multi-pass cutting of a flat surface (0.050ms^{-1}, 16A, EPS, Square 8mm tool, 8mm path spacing)

This work seemed to support the initial supposition, based on qualitative observation of the multi-pass cutting process, that the surface error in square-nose multi-pass cutting was strongly related to the thermal gradient along the engaged length of the tool. Since it was thought that the kerf would have no effect on the lay in square-nose cutting (while still affecting the dimensional accuracy), this seemed to indicate that the R_{max} in multi-pass surfaces cut by square-nose tools was essentially the multi-pass equivalent of ΔH in single-pass cutting. However, as will be seen, the causes of the weatherboard surface error are somewhat more complicated.

6.3.1 Measurement of Multi-Pass Thermomechanical Errors

In order for the conceptual model of the thermomechanical error in multi-pass cutting outlined above to be useful, it was necessary to relate the magnitude of the net surface error to the cutting strategy. To achieve this, it was first necessary to quantify the errors, and so a procedure for the measurement of multi-pass surface error was necessary.

For the purposes of the investigation carried out here (with the experimental design described in the next section) the net surface error in multi-pass cutting was measured using a similar procedure to that used for the measurement of surface error in single-pass cutting. Foam surface samples were produced, and then manually sectioned at specified values of distance along the cut: these cross-sectional samples were then scanned with a 2D flatbed scanner at a resolution of 600dpi to produce full-colour images of the sample sections. Since the multi-pass surface data was gathered using the

same data acquisition process as for the single-pass data, the measurement uncertainty is the same: that is, linear measurements have an uncertainty of approximately ±0.05mm.

Up to this point the procedure for measuring multi-pass surface error was the same as that used for single-pass surface error. However, once the sample section data had been captured the two procedures diverged. For the analysis of multi-pass surface error, a different set of measurement parameters was necessary, so a different Matlab script was used. This script can be found in Appendix B. Using this script, points on the surface of interest were harvested manually, and then the data set resulting from this was processed to evaluate the two measurement parameters used.

The two measurement parameters were chosen to express the information that defines the net surface error. These were the R_{max} and the peak spacing. Both of these are parameters originally developed to measure surface texture, and are relevant here because (as was outlined earlier) the thermomechanical component of surface error in multi-pass cutting is lay, which is technically a type of surface texture error that has been treated as a geometric form error in the RFS system because it has a very large magnitude relative to the primary surface texture.

R_{max} is the maximum distance between a peak and a valley in a surface sample, and therefore measures the absolute magnitude of the surface deviation normal to the nominal surface. Essentially this parameter measures the height of the ridges that are readily apparent on multi-pass surfaces when they are visually inspected.

Peak spacing is the distance (parallel to the nominal surface) between a lay peak and its neighbour. It is expected that this will be largely a function of the path spacing used for the surface in question.

Both of these metrics are shown qualitatively in Figure 138, for flat surfaces cut with a round-nose blade. The relative magnitude of the surface errors has been exaggerated for clarity. Surfaces cut with square-nose blades exhibit errors of the same basic type.

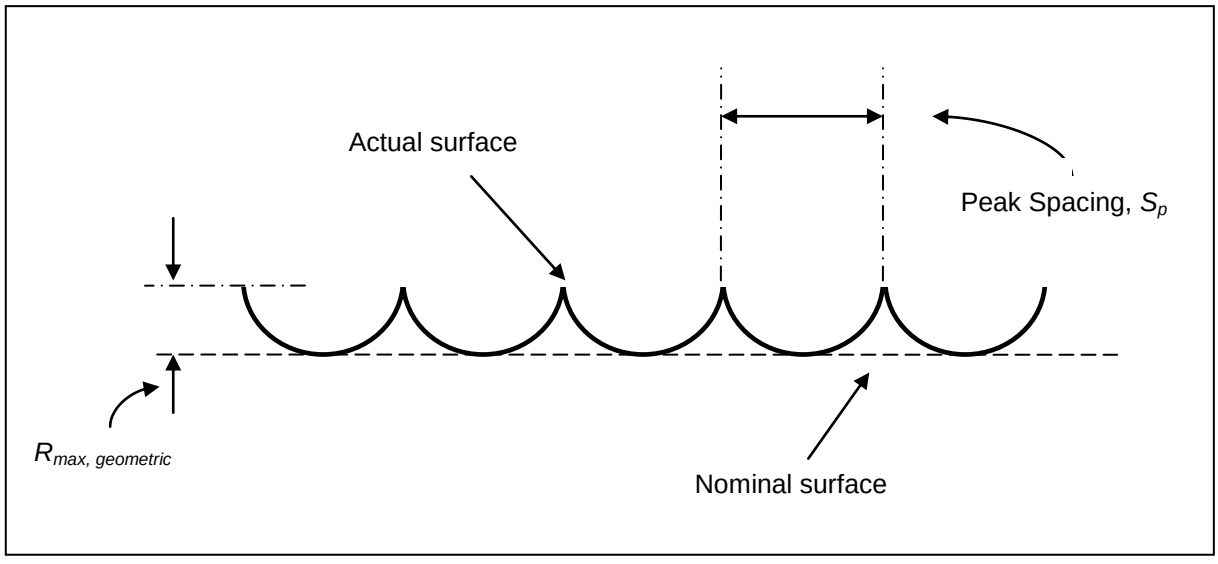

Figure 138: Geometric Form Measurement Parameters for Multi-Pass Cutting

Using these two metrics in concert, it is possible to quantitatively express both the magnitude and the distribution of the net surface errors, and this makes it possible to compare the errors for surfaces cut with different cutting strategies. It must be stressed that these metrics will measure the net surface error, not just the thermomechanical component of the error. For example, a flat surface cut with a round-nose tool will have a given R_{max}, which will be made up of three constituent components: the $R_{max,\ geometric}$ resulting from the tool shape and path spacing, the $R_{max,\ thermomechanical}$ resulting from the kerf, and the $R_{max,\ thermomechanical}$ resulting from the thermal gradient along the engaged length. In order to isolate the magnitudes of these different components, the absolute R_{max} values must be considered in conjunction with the geometric R_{max} values determined by the models in the previous section and in conjunction with the kerf and barrelling analysis carried out in the previous chapter. This will be discussed in detail below.

6.3.2 Experimental Investigation of Multi-Pass Thermomechanical Errors

Since the net error of a surface produced by multi-pass cutting is made up of superimposed geometric and thermomechanical components, it is necessary to have a thorough understanding of how these errors vary with changes in cutting strategy. While the theoretical geometric error can be evaluated using the geometric models developed earlier, it is still necessary to develop an understanding of the behaviour of the thermomechanical errors in order to gain a full understanding of the causes of net surface error. The development of this understanding from an experimental investigation is the subject of this chapter.

As outlined earlier, the total thermomechanical error when cutting with a round-nose tool is a function of the thermal field around the cutting tool (the kerf) and the thermal gradient along the engaged length of the tool (or ‘surface barrelling’). This contrasts with the total thermomechanical error when cutting with a square-nose tool, which is a function solely of the thermal gradient along the tool. This different is important, especially for the analysis of experimental data, since it means that the total thermomechanical error in square-nose cutting is the result of a single property of the cutting process and so can be analysed relatively simply, while the total thermomechanical error in round-nose cutting has confounded causes which need to be teased apart in order to quantify the effects of each source of error.

To investigate the thermomechanical error, an experiment was designed that incorporated a wide range of input factors that were thought to be of relevance, with levels selected to cover the operational space of the RFS system in multi-pass cutting without resulting in an unwieldy number of samples requiring measurement. As a result, measurements of the surface error were taken at discrete points throughout the operational space, rather than continuously across the whole operational space.

The most important factors chosen for inclusion in this investigation were the cutting conditions (tool feed and supplied current, which in turn determine the effective heat input, Q_{eff}), the distance along the cut, the tool shape, the tool size, the path spacing and the type of foam. These factors were identified as being important based on qualitative observation of a wide range of cuts, a brainstormed

list of potentially-significant factors, and the results of the surface texture and single-pass surface form investigations discussed in previous chapters.

As for the single-pass surface form experimental investigation, two types of foam were used: XPS and EPS. These are, as has previously been observed, the two primary materials used for sculpting objects with the RFS system, and so both need to be considered to develop a full model of the cutting strategy for optimisation. The cutting conditions used for XPS are shown in Table 22, and the cutting conditions used for EPS are shown in Table 23. These cover the same range of cutting conditions as were used for the single-pass surface form investigation. Combinations of cutting conditions marked with a '+' in these tables were used in this investigation. Six combinations of cutting conditions were defined for each foam type.

Table 22: XPS Cutting Conditions for Multi-Pass Geometric Form Investigation

Current (A)	Feed (ms^{-1})			
	0.040	0.052	0.064	0.076
16	+	+		
18			+	
20		+		
22	+			+

Table 23: EPS Cutting Conditions for Multi-Pass Geometric Form Investigation

Current (A)	Feed (ms^{-1})		
	0.052	0.074	0.098
16	+	+	
18		+	
22	+	+	+

Five levels of distance along the cut were selected. These were 0mm, 100mm, 250mm, 400mm and 600mm. The total cut length for each cut was 700mm. These values were chosen based on observation of a wide range of surfaces previously produced using multi-pass cutting, and were

selected because they seemed likely to provide a full picture of the behaviour of the surface error along the cut without making the experiment too large to conduct efficiently.

The experimental investigation incorporated both square-nose and round-nose tools, with two sizes of each tool shape selected. Square-nose blades with widths of 8mm and 22mm, and round-nose blades with diameters of 15mm and 25mm were chosen. These sizes were selected because they represent the respectively the smallest and largest sizes of each tool type that are commonly used in the RFS system, and experience of sculpting freeform surfaces with these tools has established that these sizes are the most useful, especially for finishing cuts. Since we are concerned here with defining a cutting strategy to optimise the surface quality of a particular part, it makes sense to focus on the tools most commonly used for finishing cuts, since the surface quality resulting from roughing cuts is irrelevant to the surface quality of the final sculpted item.

Based on these tool sizes, values of path spacing were selected. These were chosen based on the rule of thumb (specified above) that the path spacing should be less than the tool width or diameter to achieve good surfaces. The values of path spacing used for each tool type and size are summarised in Table 24. With the exception of the 8mm square tool, three levels of path spacing were defined for each tool: a value that was small relative to the tool size, a value that was moderate relative to the tool size, and a value that was high relative to the tool size. In the case of the 8mm square tool, only two levels were chosen because the small size of the tool made any more levels unnecessary.

Table 24: Tool Sizes and Path Spacing Values for Investigation of Multi-Pass Surface Form Errors

Blade Shape	Blade Size (mm)	Path Spacing Levels (mm)		
Square-nose	8	4	8	---------
Square-nose	22	10	15	20
Round-nose	15	5	10	15
Round-nose	25	5	15	25

To make it easier to isolate thermomechanical surface errors from geometric surface errors, the samples produced were restricted to nominally flat surfaces. Since the nominal surfaces had no curvature, the geometric error when cutting with square-nose tools was zero and the geometric error when cutting with round-nose tools was easy to calculate, and could therefore be readily subtracted from the measured total surface error. It seemed likely that an understanding of the thermomechanical errors based on sculpting nominally flat surfaces could be easily transferred to the sculpting of curved surfaces simply by adding expected thermomechanical error to the expected geometric error calculated using the geometric error models, since these components of error are superimposed on each other in practice.

This experiment design resulted in a total of 660 samples being produced for measurement, spread across the entire multi-pass operational space of the RFS system. The large size of this data set allowed a thorough analysis of the relationships between the thermomechanical surface error and the cutting strategy, and the development of models to predict the expected thermomechanical error for a given strategy.

6.3.3 Investigation Results

The experiment plan outlined above produced 660 sample surfaces, from which R_{max} and peak spacing measurements were taken. These measurements were analysed in conjunction with visual inspection of the surfaces and the surface sections to develop a thorough understanding of the nature of the cutting process that produces the surfaces, and to quantify the surface errors to be expected from a given set of cutting conditions.

The R_{max} measurement results for square-nose and round-nose tools were considered separately, since the different geometric conditions in these two types of cutting fundamentally changed the nature of the cutting factor interactions that influenced the surfaces. The peak spacing results are dealt with together since for this surface error the conclusions drawn held for both tool types.

The characteristic nature of the surfaces produced by both square-nose and round-nose tools will be discussed here, with some examples of the behaviour of surface error along a cut presented. The examples presented are representative of the results found, and the conclusions drawn hold true for all of the measured data.

6.3.3.1 Square-Nose Tool Multi-Pass Surface Error

Figure 139 and Figure 140 show the values of R_{max} along the length of a surface sculpted with an 8mm square nose tool with the same cutting conditions with path spacing values of 4mm and 8mm respectively. As can be seen, the trend of R_{max} along the cut exhibits a characteristic trend where the total surface error is quite large at the beginning of the cut and gets smaller through a transition region until stead-state conditions are achieved, at which point the surface error becomes constant for the remainder of the cut length. This characteristic pattern is exhibited by all the surfaces produced using square-nose cutting for this research.

In the case of square-nose cutting of flat surfaces, the as-measured total surface error is made up entirely of thermomechanical error, since the geometric error in these cases is zero. When round-nose tools are considered in the next question, an effort must be made to distinguish the geometric error from the thermomechanical error, but for the square-nose case this is unnecessary.

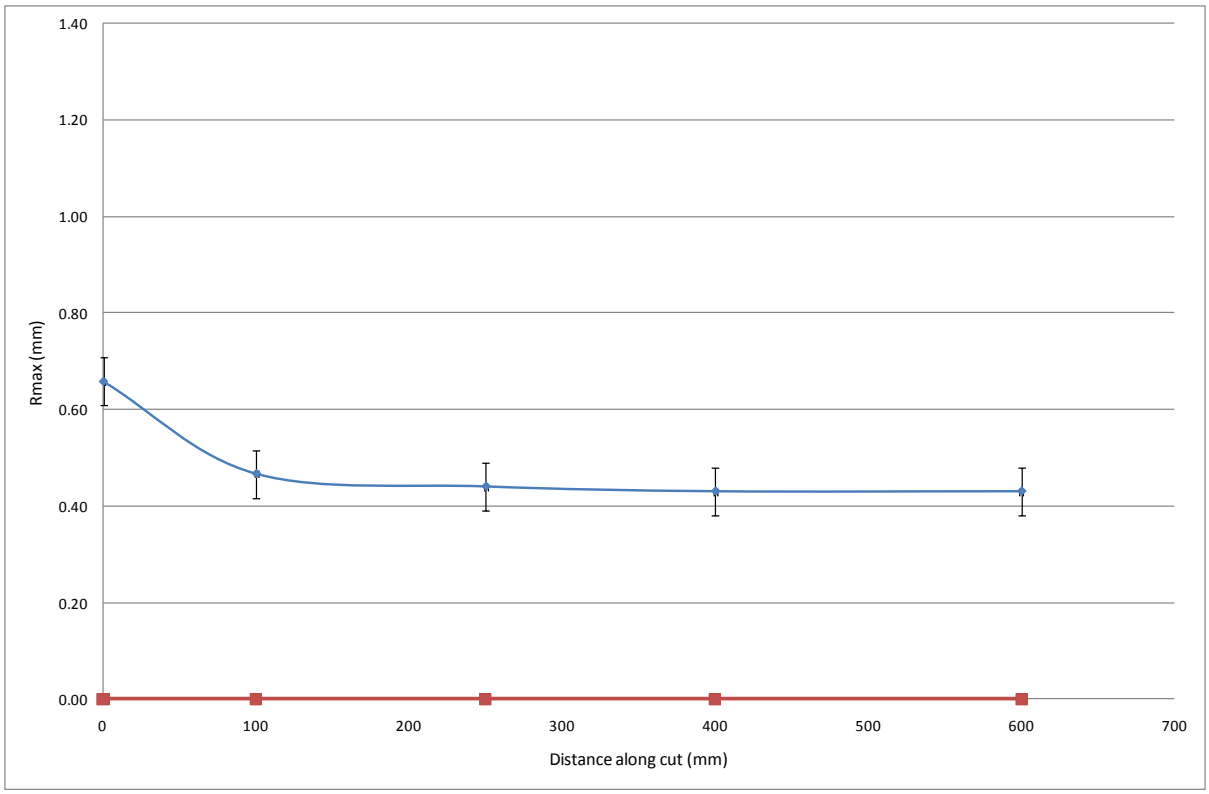

Figure 139: General trend of R_{max} along a surface produced using multi-pass cutting with a square-nose tool (0.040ms^{-1}, 19A, 8mm square-nose tool, S_p = 4mm)

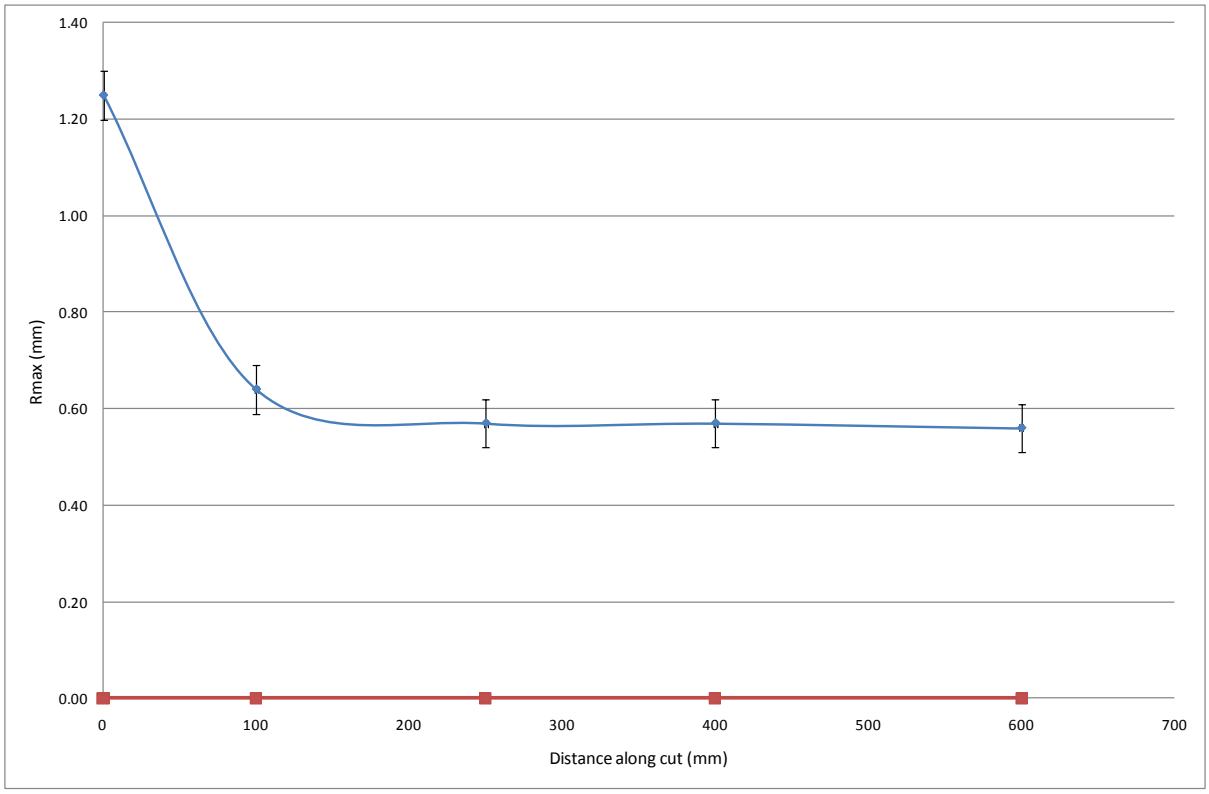

Figure 140: General trend of R_{max} along a surface produced using multi-pass cutting with a square-nose tool (0.040ms^{-1}, 19A, 8mm square-nose tool, S_p = 8mm)

Comparing the surface error for these two cases it becomes clear that, for the same tool size and cutting conditions, surfaces produced with smaller path spacing have smaller total surface errors. This is shown most clearly by Figure 141, which shows the surface errors for the two cases presented above on the same graph. The reasons for this result will be discussed below.

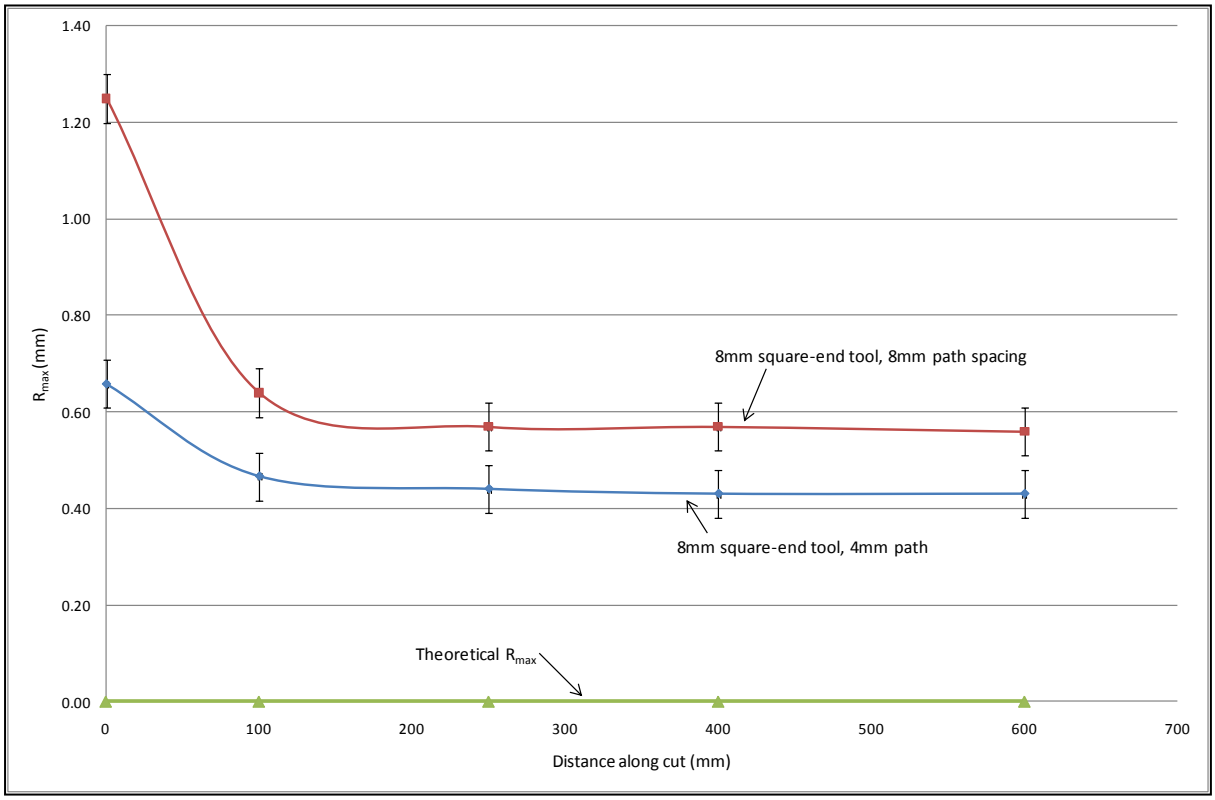

Figure 141: Effect of increasing path spacing on R_{max} of surfaces cut by multi-pass cutting (XPS, 0.040ms^{-1}, 19A, 8mm square-nose tool)

These results did not initially appear to make much sense. The initial supposition was that the weatherboard effect in square-nose cutting was solely the result of the thermal gradient along the engaged length of the tool, and was the multi-pass equivalent of surface barrelling in single-pass cutting. If this was the case, it would be expected that the surface error would be small or zero at the start of the cut where the tool temperature differential ΔT was zero, and that the error would increase until steady-state conditions were reached, at which both R_{max} and ΔT would be at their maximum. Clearly, this is not the case, which indicates that the surface error in square-nose multi-pass cutting is either the result of some other property of the cutting process, or that another factor causes a component of thermomechanical surface error which is confounded with the effects of the thermal gradient. In fact, given the magnitude of the change between the initial and steady-state R_{max} values, there is strong reason to suspect that if there is another effect compounded with the thermal gradient, it actually has a more significant influence on the final error than the thermal gradient does.

When the longitudinal thermal profiles presented in Figure 137 were considered in slightly more detail, it became even more apparent that the thermal gradient was not responsible for the entirety of the

surface error. Figure 142 shows the difference between the temperatures measured at points B and D (Figure 136) along the cut and the measured R_{max} for the corresponding set of cutting conditions. As immediately becomes clear from inspection of this graph, there is no clear correlation between the thermal gradient and the surface error. Clearly, the surface error in square-nose cutting is more complicated than was previously thought.

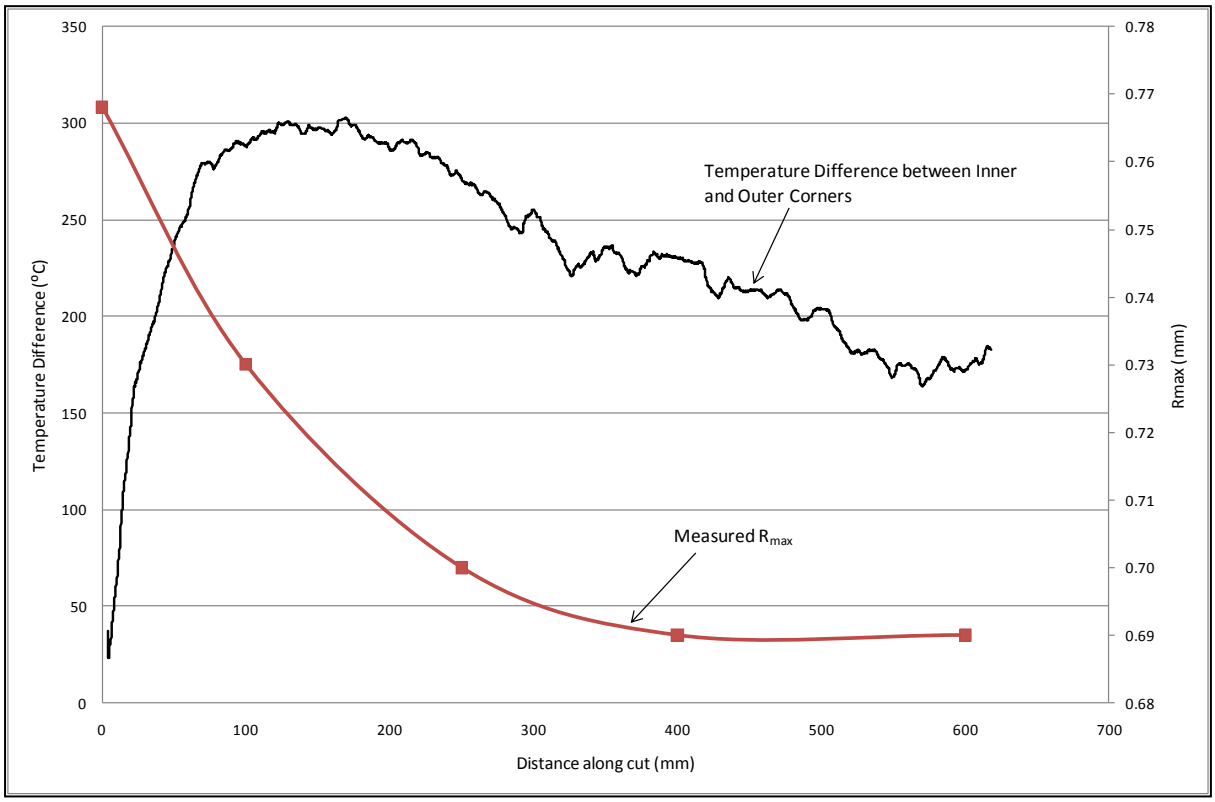

Figure 142: Comparison of the thermal gradient along the engaged length of the tool with the corresponding R_{max} along a cut (EPS, 16A, 0.050ms^{-1}, 8mm Square-nosed tool, 8mm Path Spacing)

The characteristic trend of R_{max} along the length of multi-pass square-nose cuts resembled the trend of kerfwidth along a single-pass cut more closely than it did the trend of surface barrelling, in that it starts out at a high initial value and decays to a lower but non-zero steady-state value. This suggested that the kerf might actually be having an effect on the surface error even for square-nose cutting.

An examination of the cross-section sample images from which the R_{max} measurements were taken cast further light on the unexpected surface error. The first three cross-sections of a cut in XPS with cutting conditions of 0.052ms^{-1} and 20A with a 22mm square-nose tool and a path spacing of 15mm are shown in Figure 143. The fourth and fifth samples for this surface were omitted since they are essentially the same as the third sample, as they all reflect steady-state cutting conditions.

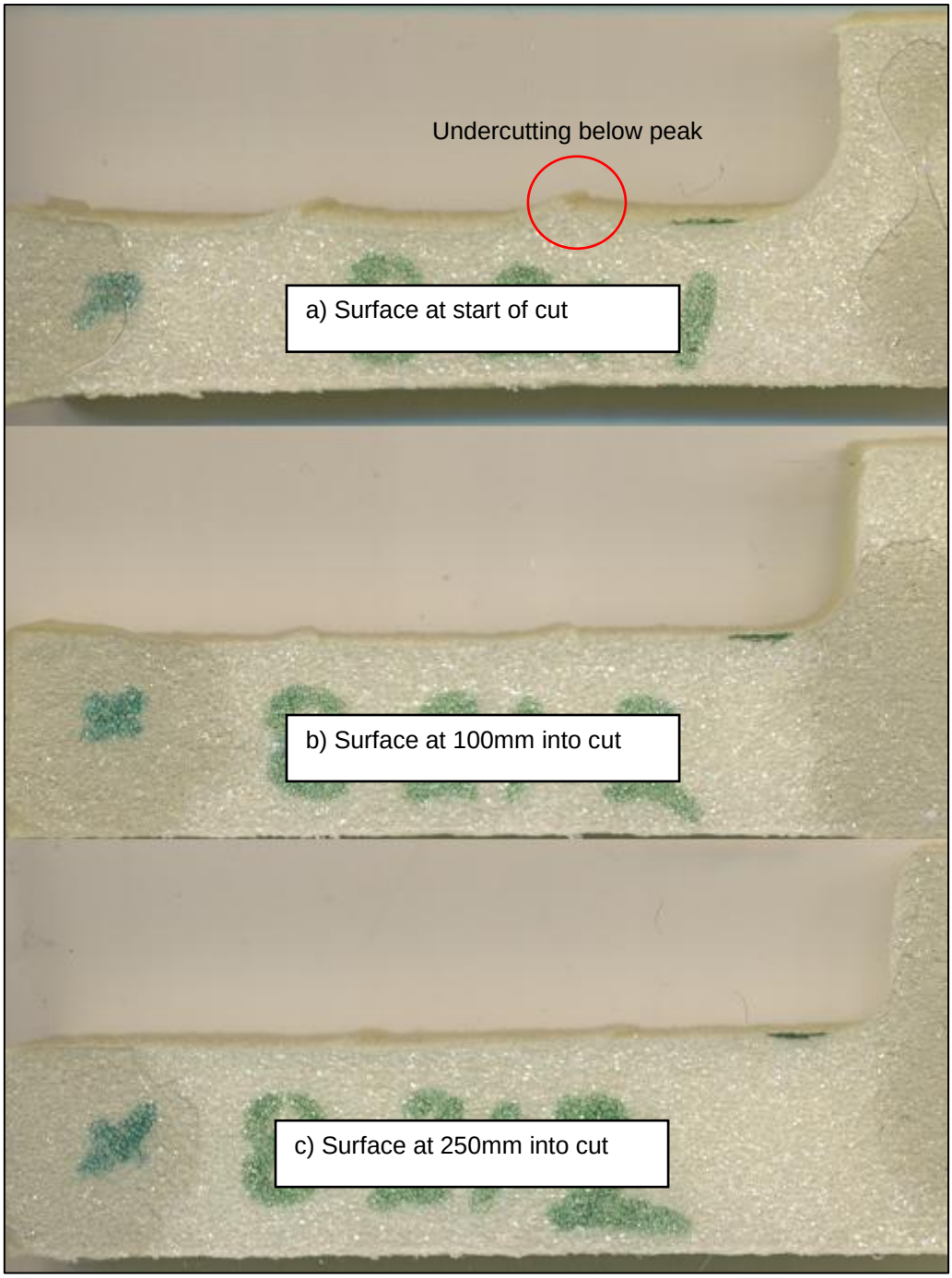

Figure 143: Cross-sections of surfaces at the start of a cut (top), 100mm into the cut (middle), and 250mm into the cut (bottom) (0.052ms^{-1}, 20A, XPS, 22mm square-nosed tool, 15mm path spacing)

It is immediately clear from examination of these samples that the initial surface error is very different from the steady-state surface error. The steady-state error resembles the theoretical weatherboard effect that has already been discussed, with relatively straight segments of actual surface between the lay peaks. This steady-state error does seem likely to be a function of the thermal gradient along the engaged length of the tool, as was expected.

However, the nature of the surface at the beginning of the cut is very different indeed. This surface has a scalloped cross-section that resembles surfaces sculpted with round-nose tools, even though a square-nose tool was used. The peaks of the cross-section of the initial surface are at the same points across the surface as in the steady-state surfaces, with the spacing of these peaks determined by the path spacing. These peaks are also at approximately the same height as the peaks in the steady-state samples.

The key difference between the initial and steady-state surfaces (and the difference in R_{max} between them) lies between the peaks, where the surface has been vapourised away significantly more than on the steady-state surface. These vapourisations during the tool pass results from the modification of the structure of the foam material by the previous tool path, and from the thermal field around the cutting tool.

When a hot tool cuts polystyrene foam, it changes the cellular structure of the foam adjacent to the cut surface, producing a heat affected zone (HAZ) as shown in Figure 144. This heat affected zone is characterised by collapsed cells and semi-melted plastic. This heat affected zone has significantly higher density than the unaffected bulk material.

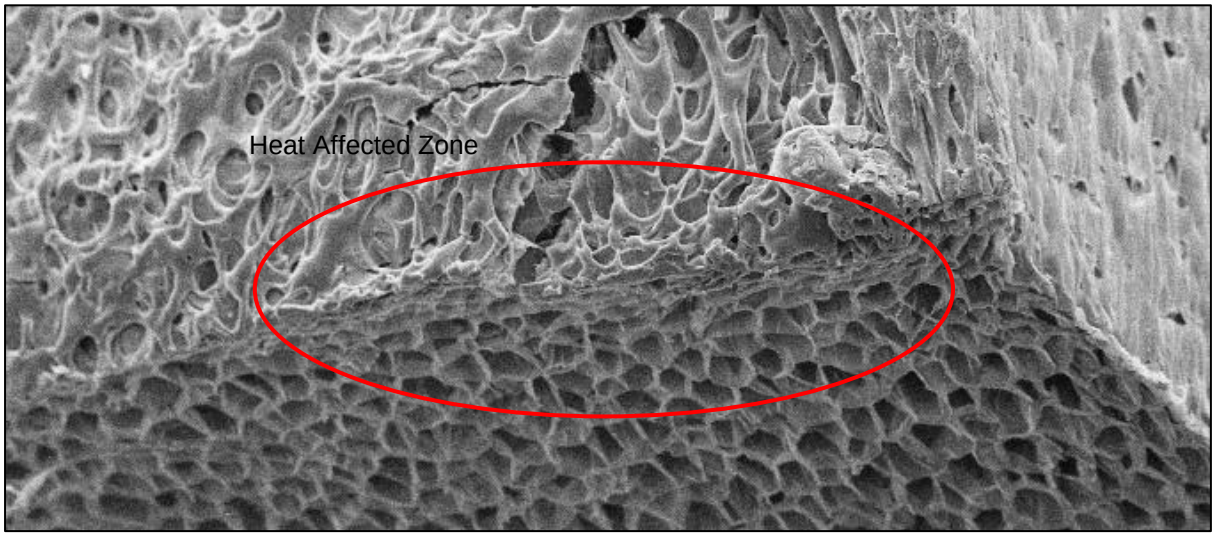

Figure 144: Cellular structure of XPS foam showing the heat affected zone resulting from thermomechanical foam cutting

Since this skin has a higher density, it vapourises less than the bulk material when being cut by a hot tool. In other words, for a given state of the thermal field around the tool, an already-cut surface will be less susceptible to melting that unaltered bulk material. When multi-pass cutting is taking place, the engaged length of the tool is cutting unaltered bulk material, while heated parts of the tool are passing over already-cut surface.

As the tool passes through the foam, it is surrounded by a thermal field in the same way as when straight hot tools are being used for single-pass cutting. This thermal field has the effect of creating a

kerfwidth around the tool. However, unlike the single-pass cutting case, the effect of this thermal field is asymmetric because of the heat affected zone on the already-cut surface. When the thermal field around the tool is large and the primary cutting mode is vapourisation, the heat radiated from the blade vapourises the unmodified bulk material more than the higher-density skin caused by the HAZ. As a result, the valleys in the surface profile are deeper than they would be if the kerf was having no significant effect, and (in some cases) the peaks formed by the previous tool pass display undercutting. This suggests that the magnitude of the surface error R_{max} is more a function of the depth of the valleys on the surface than of the height of the peaks, since the valleys are cut from unmodified bulk material whereas the peaks are established in an existing HAZ. The effect of kerf and the HAZ skin are shown in Figure 145, for the case where the path spacing is equal to the tool width. Note that in this case and in Figure 146 the offcut piece of waste foam has been omitted for clarity.

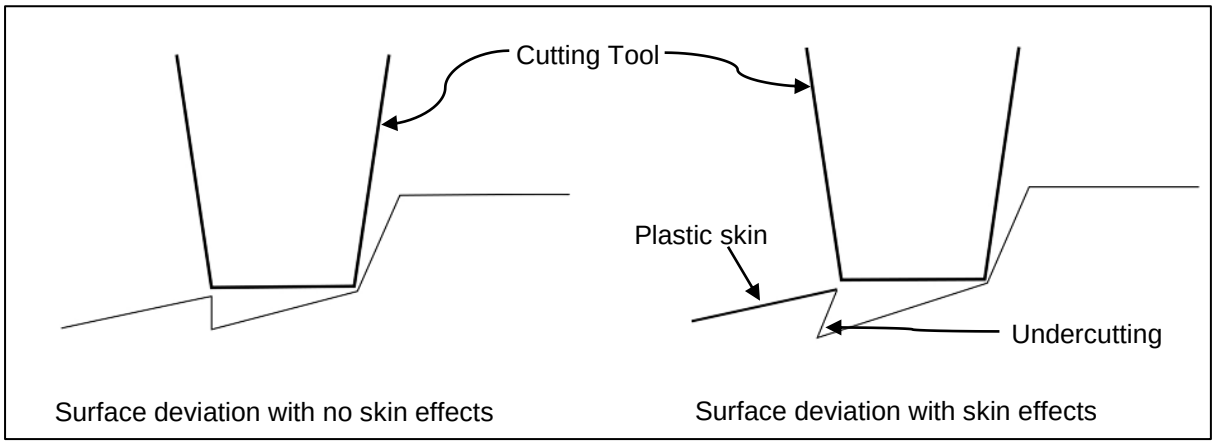

Figure 145: Effects of collapsed plastic skin on surface deviation of a surface cut with a square-nose tool

If the path spacing is significantly less than the tool width (i.e. less than half the width), the nature of the surface error is more complex. The same basic cutting process is operating, and the effect of the skin causes by the HAZ is still present, but in addition each surface peak is re-ablated by the tool during the subsequent tool pass. This ablation is the result of the hot, unengaged length of the tool passing over the established peak: the thermal field around the tool re-melts the plastic that forms the peak, reducing its height. The effect of kerf on unmodified bulk material is approximately the same as for the case where the path spacing is a large proportion of the blade width, so the lowest points of the surface profile are at approximately the same height relative to the toolpath, but the peaks of the surface are lower due to the re-ablation process. As a result, the absolute magnitude of the vertical deviation between these two reference points (the R_{max}) is smaller for cases where path spacing is low relative to the toolpath. This net effect of the peak re-ablation and the HAZ skin is shown by Figure 146. Since the peaks in this case, with low relative path spacing, are established in material that has a heat affected zone, the material here is still more resistant to melting than the bulk material, but some re-melting does still take place. The effect of this peak re-melting will be less pronounced in surfaces with convex curvature, since the unengaged length of the tool will be further from the peak and so the temperature of the thermal field at the peak will be lower.

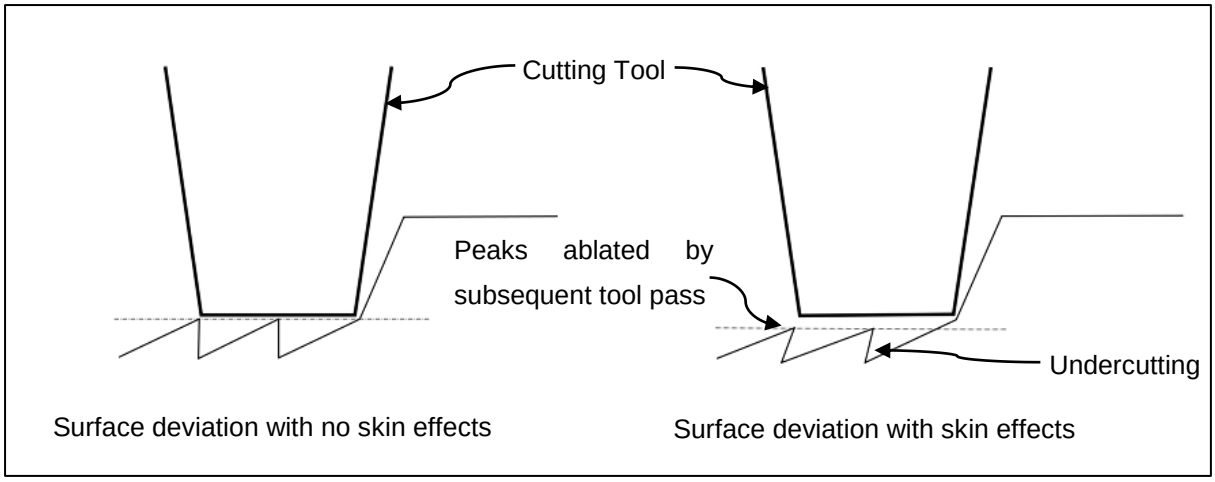

Figure 146: Effects of collapsed plastic skin and peak ablation on surface deviation of surfaces cut with a square-nose tool when the path spacing is less than the tool width

Based on the measurements of surface error, observations of the cutting process and the reasoning above, it seems fairly obvious that the multi-pass surface error when using square-nose tools is not solely a result of the thermal gradient along the tool, as had been previously thought. In fact, there is a component of the error that is essentially dependent on kerfwidth.

It had been thought that, since the kerf would be the same at any point long the cut for each tool pass, the effect of kerf on surface error when using square-nose tools would be negligible. However, when the effect of a higher-density skin on the already-cut surface is considered, the causes of the net surface error become clearer. As a result of the higher-density skin, the thermal field around the tool causes an uneven distribution of the final surface (the scalloped surface effect shown in Figure 143 (a)): this is broadly speaking the same mechanism that results in negative surface barrelling results in some cases of single-pass cutting, but due to the nature of the multi-pass cutting process it cannot be avoided completely by careful selection of cutting strategy.

Therefore, it was concluded that kerfwidth had an effect on the surface error in multi-pass cutting with square-nose tools, which leads to a promising conclusion. As has previously been noted, the surface error was qualitatively observed to start out relatively large before settling to a lower steady-state value, and this was thought to be the result of the thermal gradient along the engaged length of the tool. As such, since this thermal gradient is not controllable (in the same way that the surface barrelling in single-pass cutting was not controllable), it was thought that the surface error in multi-pass cutting would not be amenable to minimisation by control of the cutting conditions. However, once it was known that the kerf has an effect on surface error, and since it seems that the kerf has a significant effect on the transient surface error between initial and steady-state R_{max}, this raised the possibility that, if the kerf was controlled using force-feedback current control, the effect of kerf on R_{max} would be stabilised and, as a result, the value of R_{max} would be much closer to constant along the cut length.

To test this, a multi-pass sample was produced using cutting conditions that resulted in a kerf equivalent to that resulting from conditions of 22A and 0.076ms^{-1}, with an 8mm square-nose tool and 4mm path spacing, using XPS as the material. The values of R_{max} were measured along the cut at the same levels of distance used for the constant-current samples, and these results were compared with the equivalent constant-current data. The expectation was that if controlling the kerf eliminated the transient kerf error, the error with current control would be solely the result of the thermal gradient along the tool. As such, it was expected that the surface error would initially be very small due to the low tool temperature differential ΔT, and would increase to a steady-state value approximately the same as the steady-state value in the constant current case. The results of this test are shown in Figure 147, and as can be seen the use of current control has resulted in a dramatic improvement in the consistency of the surface deviation R_{max} along the length of the cut.

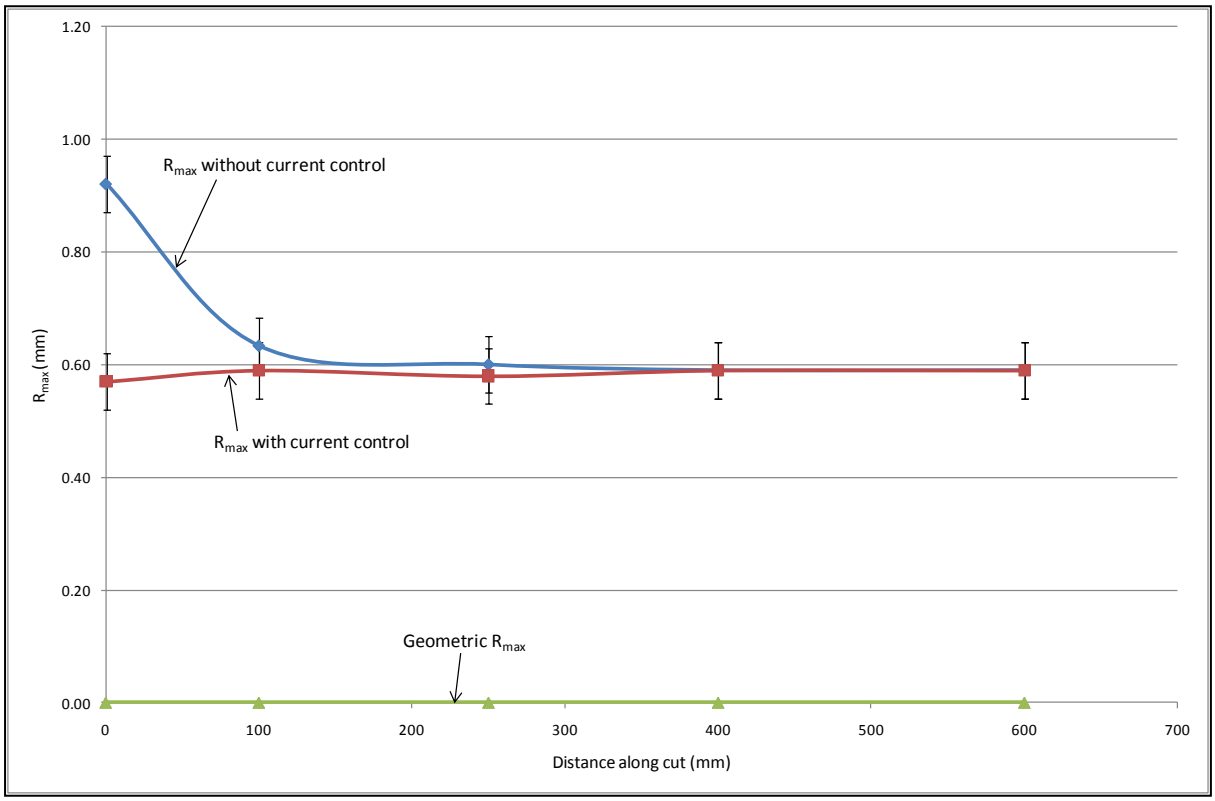

Figure 147: Variation of R_{max} along a cut with and without force-feedback current control (0.076ms^{-1}, 22A, 8mm square-nose tool, 4mm path spacing, XPS)

This test broadly confirmed the hypothesis that a significant amount of the multi-pass surface error could be eliminated using controlled-current cutting, but the behaviour of the controlled-current surface error is not exactly what would be expected if the remaining error is solely the result of the thermal gradient along the tool. Since the thermal gradient at the beginning of the cut is zero, it would make more sense of the surface error at the start of the cut was also zero. This phenomenon remains unexplained, since the time available did not allow a fuller investigation of the surface error behaviour in controlled-current cutting: study of this behaviour is one of the recommended areas for further research resulting from this thesis.

When controlled-current cutting is used, the value of R_{max} is effectively constant along the cut length. There is some variation as the thermal gradient along the tool establishes, but the surface error is still constant within the limits of experimental uncertainty. To assess the significance of each input parameter and to develop predictive models for the R_{max} that could be used to develop an optimised cutting strategy, a statistical analysis of the data for the steady-state surface error was undertaken. This analysis was restricted to steady-state cutting because it was fairly clear that the magnitude of the error resulting from constant-current cutting meant that controlled-current cutting was going to be the most useful cutting paradigm in almost all cases.

For steady-state cutting, statistical analysis produces the following models:

$$^{Steady\text{-}state}R_{max,\ xps} = 0.0272541i - 4.2964059f + 0.0024307\,^{Rel}S_p + 0.0013234l_e + 0.1842151 \quad (77)$$

Where i is the supplied current, f is tool feedrate, l_e is the engaged tool length and $^{Rel}S_p$ is the relative path spacing (path spacing as a percentage of blade size). These were the only four parameters determined to be of statistical significance, based on assessment of the $P_r(>|t|)$ values. This model had an R^2 value of 0.85, and the $P_r(>|t|)$ values for each input parameter were:

$i = 3.73\text{x}10^{-7}$

$f = 7.60\text{x}10^{-6}$

$^{Rel}S_p = 7.97\text{x}10^{-6}$

$l_e = 0.4563$

The corresponding model for EPS foam was found to be:

$$^{Steady\text{-}state}R_{max,\ eps} = 0.0264009i - 3.8627453f + 0.0017336\,^{Rel}S_p + 0.0004843l_e + 0.2309475 \quad (78)$$

This model had an R^2 value of 0.82, and $P_r(>|t|)$ values of:

$i = 2.25\text{x}10^{-7}$

$f = 5.89\text{x}10^{-6}$

$^{Rel}S_p = 6.63\text{x}10^{-4}$

$l_e = 0.6696$

As is clear from the $P_r(>|t|)$ values for these models, l_e is the least statistically-significant of the input parameters, and based solely on the statistical analysis there was no reason to use it as an input parameter for these models. However, based on observation of the cutting process it was strongly believed that the engaged length was actually significant, but that it wasn't appearing to be statistically significant because the experimental design resulted in only a limited range of engaged lengths

actually being considered. Since the cut depth was essentially the same for almost all the samples, the engaged length was dependent solely on the path spacing, so only limited range of actual engaged length values was considered. A further investigation of this, using a wider range of values for cut depth and path spacing, is one of the recommended areas for further research.

These models allow a reasonably accurate prediction of the magnitude of R_{max} when steady-state cutting conditions have been achieved, in terms of the current, feed, relative path spacing and engaged tool length. With these models in hand, and using controlled-current cutting to compensate for the effect of kerf outlined above, it is possible to devise strategies for minimising the remaining thermomechanical R_{max} along a cut.

The remaining R_{max} once the effect of kerf has been eliminated can only be due to the thermal gradient along the engaged length of the tool, and is effectively the same type of surface error as the surface barrelling encountered when making single-pass cuts with wires and blades (see Chapter 5). It will be recalled that the surface barrelling was an inevitable consequence of straight-tool cutting, and that nothing could be done to control, minimise or eliminate the surface barrelling resulting from a cut made with given cutting conditions, since the thermal gradient between the free-air temperature and the in-cut temperature of the tool was a fundamental feature of the cutting process itself. This remains true of the thermal gradient along the engaged length in multi-pass cutting, but because of the different cutting paradigm operating in multi-pass cutting it is possible to take steps to compensate for the effects of the thermal gradient and therefore to directly influence the surface error R_{max}.

The R_{max} error due to thermal gradient along the engaged length is effectively an asymmetric kerf, and can be compensated for in the same way as regular kerf with an offset. This offset will need to be larger at the hotter end of the engaged length than at the cooler end. In effect, an angular offset can be applied by rotating the tool as shown in Figure 148, so that the hotter corner of the tool is further away from the surface by a value equal to the expected Rmax, should significantly reduce or possibly eliminate the R_{max} error resulting from square-nose multi-pass cutting.

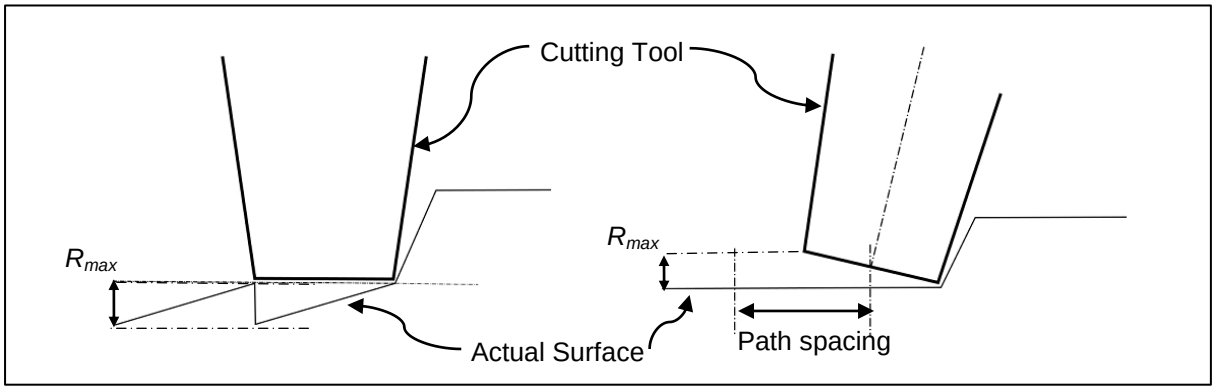

Figure 148: Minimisation of R_{max} in square-nose multi-pass cutting by applying angular offset to the tool

This strategy for reducing the multi-pass surface error for square-nose cutting has significant potential, and there are no obvious obstacles to its implementation, but insufficient time was available to trial the strategy during this research project. As such, further testing and refinement of this idea is proposed as an area for future research.

6.3.3.2 Round-Nose Tool Multi-Pass Surface Error

When sculpting a surface using multiple passes of a round-nose tool, the thermomechanical component of the surface error (resulting from the kerf and the thermal gradient along the engaged length of the tool) does not exist in isolation. Unlike the case of square-nose tools cutting nominally-flat surfaces, there is a considerable geometric component to the surface error resulting from the shape of the cutting tool and the path spacing. This geometric component is small when the path spacing is small relative to the blade diameter, but at values of path spacing close to or equal to the blade diameter the geometric component of the surface error trends towards a value that is half of the blade diameter. Clearly, this makes high values of path spacing undesirable from the outset, since they introduce significant additional error into the surface being sculpted. Round-nose tools are of most use when sculpting concave 3D surfaces, since they have no corners which can result in gouging at the edges of the tool pass, and there is little point using a specific tool shape to increase the surface accuracy if the tool is going to be used in such a way that the surface accuracy is impaired.

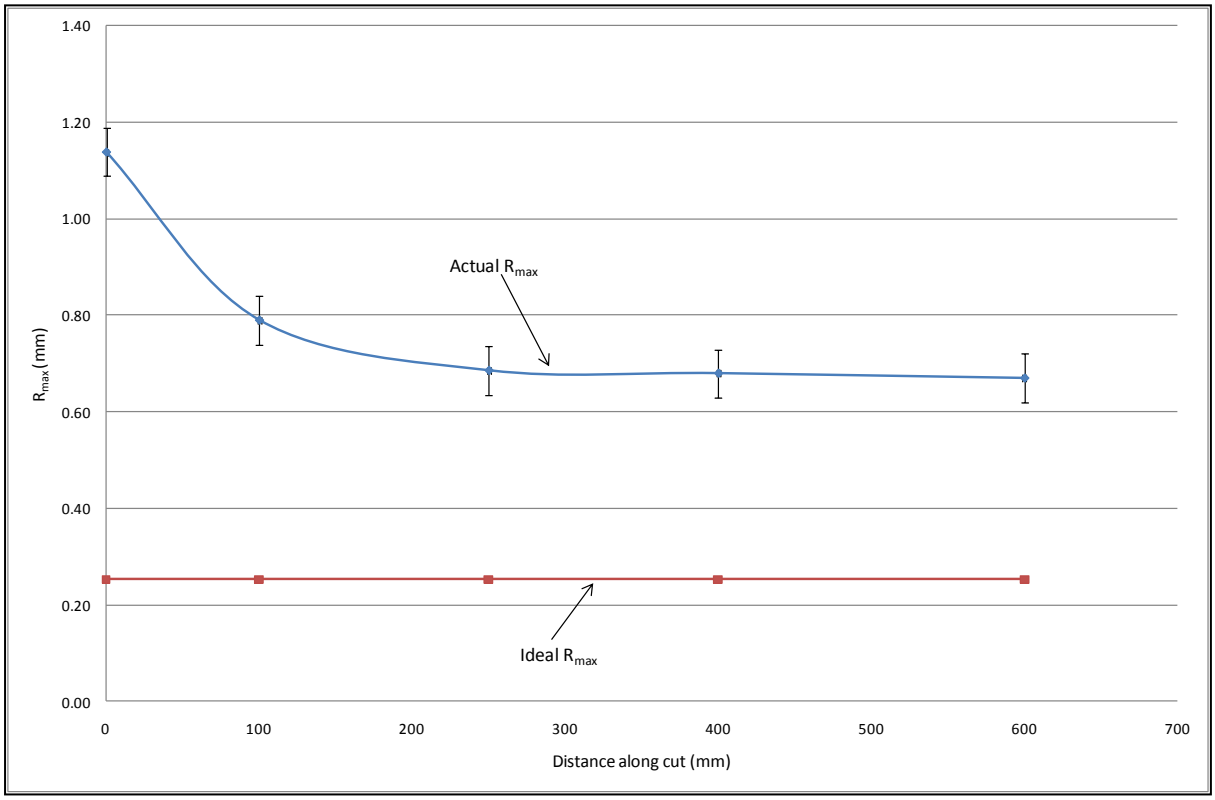

Figure 149: R_{max} variation along a cut with a round-nose tool and low path spacing (0.052ms^{-1}, 16A, ø25mm tool, 5mm path spacing)

Surfaces cut with round-nose tools exhibit the same basic trend of R_{max} along the cut as was found for square-nose tools, with the R_{max} value starting relatively high at the beginning of the cut and then trending down until it stabilises when steady-state cutting is achieved. This basic trend is shown in Figure 149.

In the case of round-nose cutting it makes sense for the development of the thermal gradient to result in a decrease in R_{max} from the initial value to the steady-state value, since at the beginning of the cut where the thermal gradient is zero the reduction in R_{max} from 'barrelling' is not present, while later in the cut the reduction does occur resulting in a smaller actual measurement. This will be confounded with the effect of kerfwidth, where the kerf at the beginning of the cut is wide and therefore results in a relatively large reduction in as-measured R_{max}, and then reduces to the steady-state kerf value with a corresponding increase in the component of as-measured R_{max} resulting from the kerf.

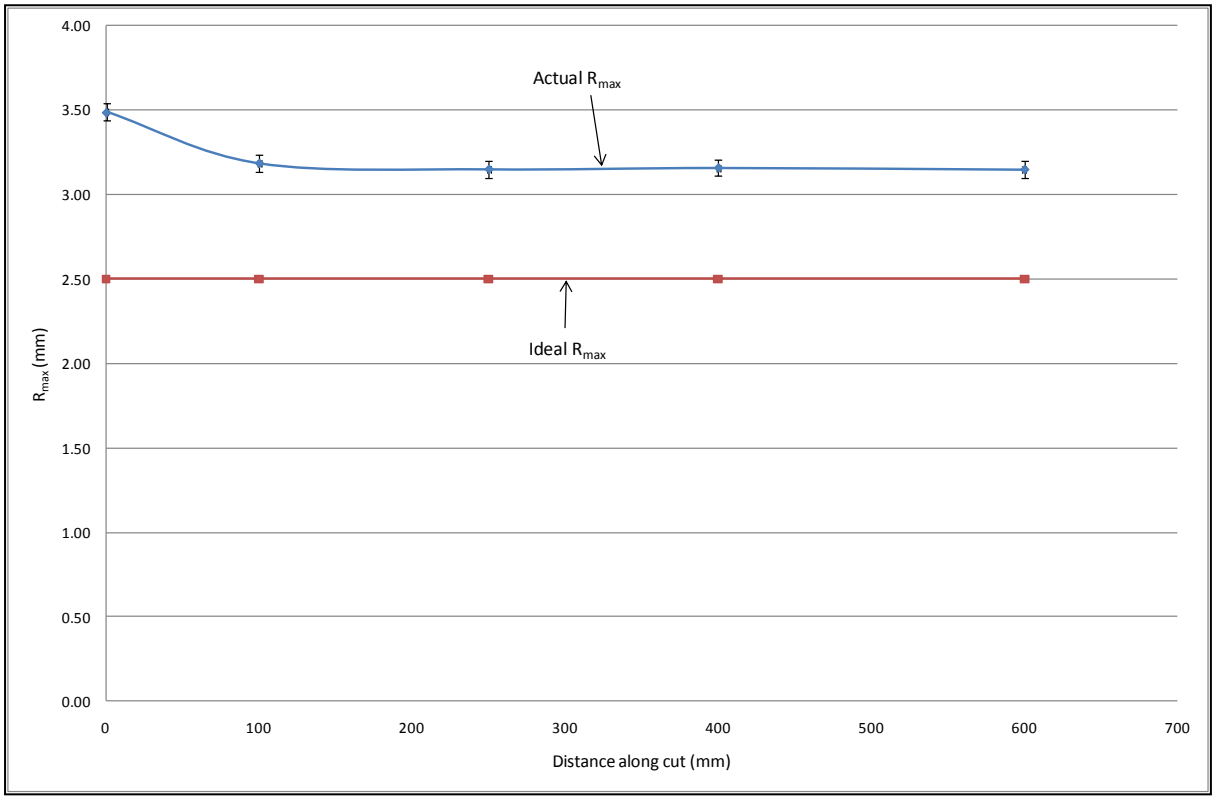

Figure 150: R_{max} variation along a cut with a round-nose tool and moderate path spacing (0.052ms^{-1}, 16A, ø25mm tool, 15mm path spacing)

When cutting with round-nose tools, the magnitude of the path spacing relative to the tool diameter turns out to have an effect on the nature of the as-measured R_{max}. At low values of path spacing, the actual R_{max} is larger than the R_{max} predicted by the geometric models at all points along the cut (Figure 149). At moderate values of path spacing, the actual R_{max} is still larger than the predicted geometric R_{max}, but the steady-state as-measured R_{max} is closer to the geometric R_{max} than at low values of path spacing (Figure 150). At high values of path spacing (i.e. path spacing values close to the blade diameter) the actual R_{max} is less than the predicted geometric R_{max}. The same characteristic

decay trend of R_{max} along the cut is exhibited, with approximately the same magnitude of change between initial and steady-state R_{max}, but this change is much less significant in these cases relative to the significantly greater steady-state R_{max} and the predicted geometric R_{max} (Figure 151).

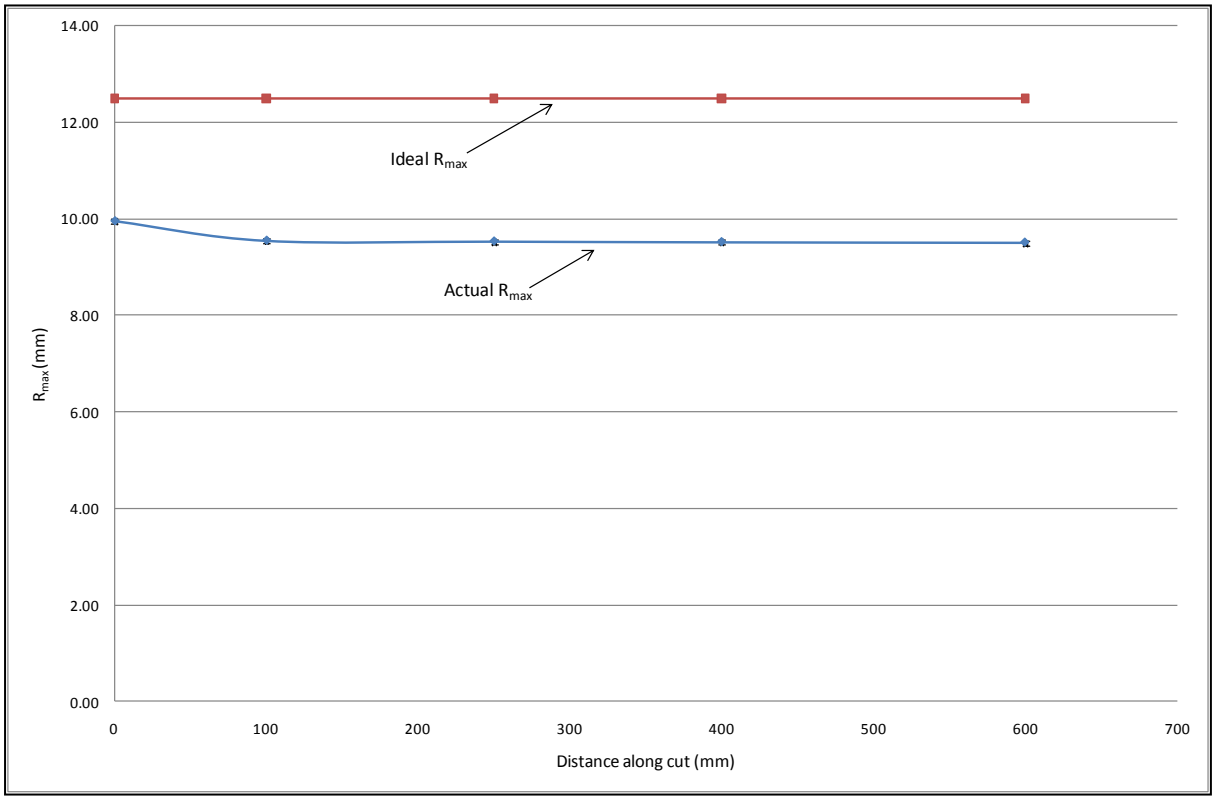

Figure 151: R_{max} variation along a cut with a round-nose tool and high path spacing (0.052ms^{-1}, 16A, ø25mm tool, 25mm path spacing)

These observed behaviours of R_{max} along the cut with changes in path spacing are useful, but not entirely unexpected. What is really of interest in this research is the differences between the predicted geometric R_{max} and the as-measured R_{max}, since these differences are the total thermomechanical error.

Figure 152 shows the deviation between the predicted $R_{max,\ geometric}$ value and the as-measured R_{max} value (which includes both geometric and thermomechanical components) for nominally-flat surfaces cut with round nose tools, plotted against the path spacing expressed as a percentage of the blade diameter. This difference between the geometric R_{max} and the as-measured R_{max} is due to the thermomechanical component of surface error. It is the superimposed sum of the surface deviations resulting from the errors due to the kerfwidth and the errors due to the thermal gradient along the engaged length of the tool.

As can be observed from Figure 152, when the path spacing is small relative to the blade diameter (below about 65%), the deviation is negative, but when the path spacing is large relative to the path spacing the deviation is positive. Since the deviation is the result of subtracting the as-measured R_{max}

from the predicted R_{max} derived from the geometric models, this means that when the path spacing is small relative to the blade diameter, the actual R_{max} is larger than would be expected from the geometric models and the hypothetical thermomechanical effects outlined earlier (see section 6.3), and if the path spacing is large relative to the blade diameter the actual R_{max} is smaller than would be expected from the geometric models, which is what was expected from the consideration of thermomechanical effects above. This observation accords with the results for individual cuts described above. This result seems somewhat counter-intuitive, given the theoretical behaviour of the error in a surface cut with round-nose tools.

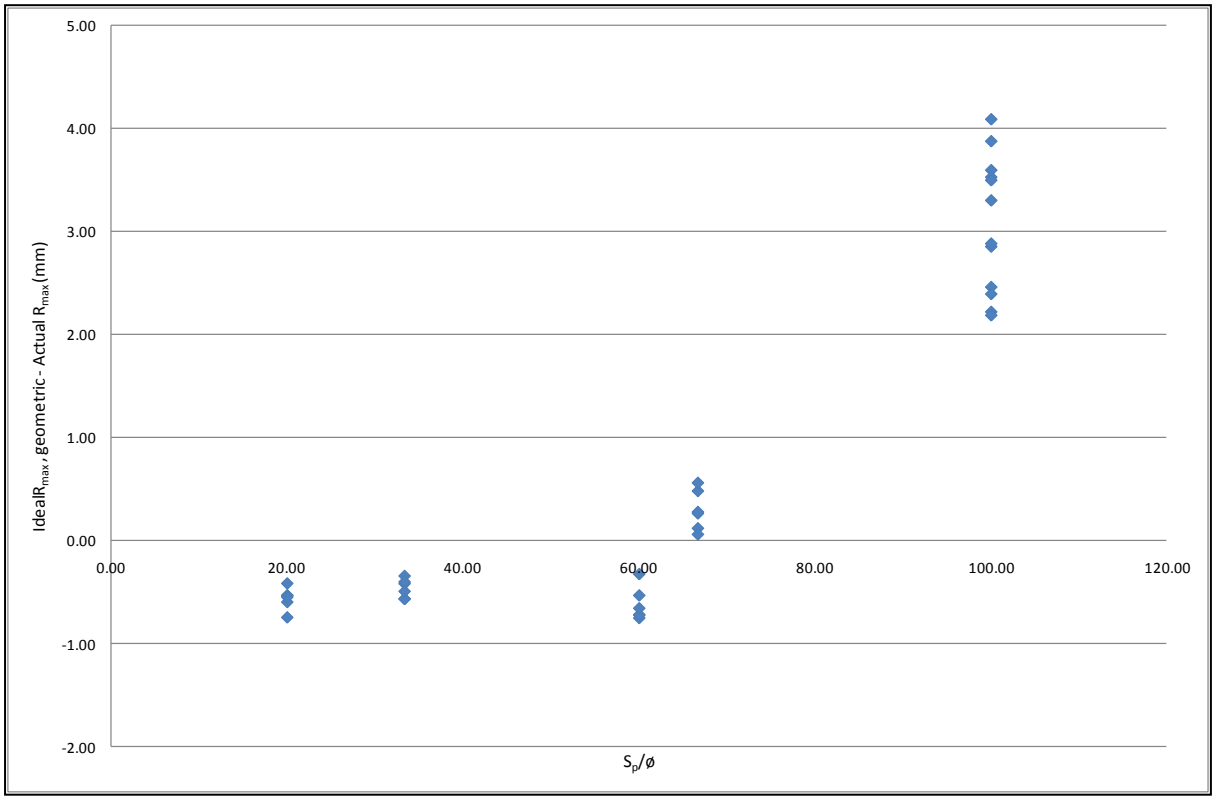

Figure 152: Difference between $R_{max,\ geometric}$ and as-measured R_{max} plotted against Path Spacing as a percentage of Blade Diameter for Round-nose tools cutting XPS foam

As discussed above, when cutting with round-nose tools the presence of a kerf should, in theory, act to increase the effective diameter of the tool, thus resulting in as-measured errors that are smaller than the predicted errors. From this observation, and using the models for steady-state kerf developed for single-pass cutting, it is possible to calculate a 'virtual tool diameter' that takes into account both the diameter of the tool and the size of the thermal field around the tool when steady-state cutting conditions have been achieved. This virtual tool diameter can then be used in place of the actual tool diameter in the geometric models of the surface error in multi-pass cutting, which in theory should result in more accurate predictions of the as-measured R_{max}.

As shown in the figures below, the effectiveness of this technique depends on the relative magnitude of the path spacing. When the path spacing is large relative to the blade diameter (Figure 153) the

R_{max} predicted using the virtual tool approach is significantly closer to the as-measured R_{max} than the R_{max} predicted based solely on the physical tool diameter, as would be expected. The remaining discrepancy was not unexpected, since this will be the result of the surface deviation due to the thermal gradient along the tool (i.e. the surface barrelling) as well as any random error resulting from factors like blade oscillation.

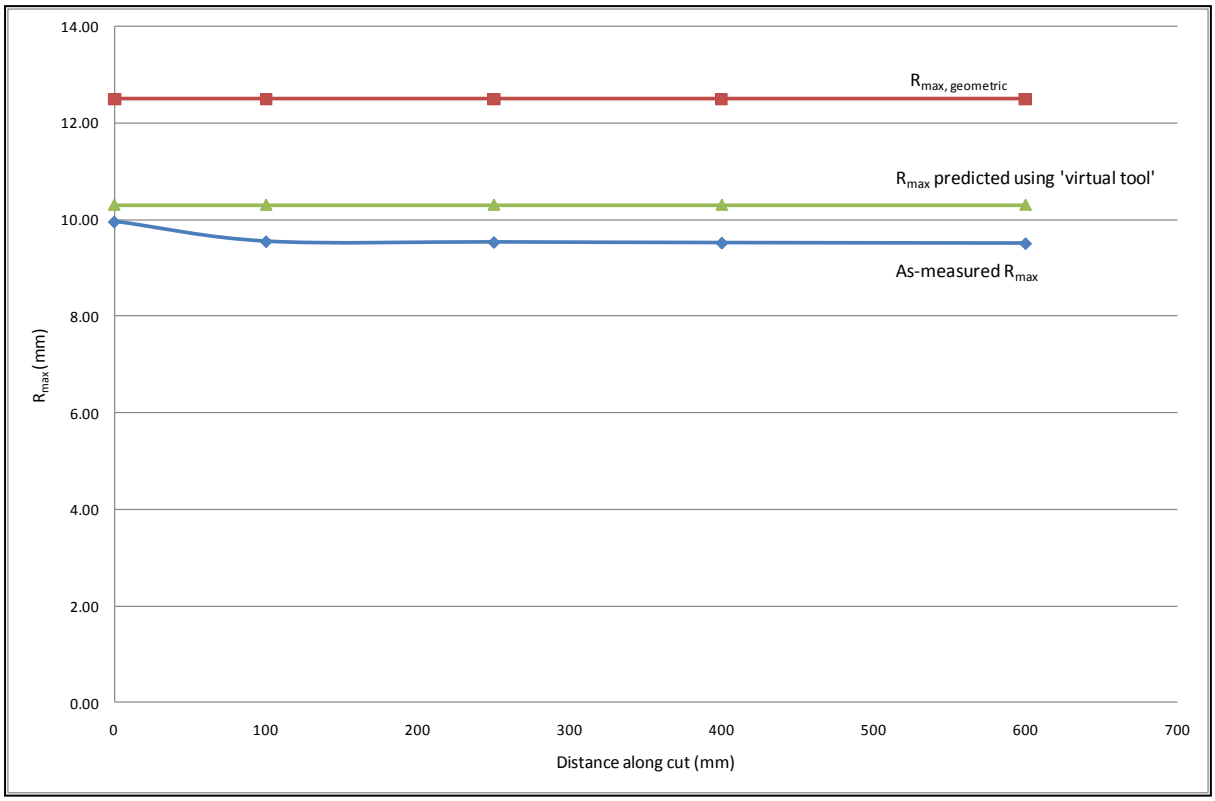

Figure 153: R_{max} variation along a cut with a round-nose tool and high path spacing, showing the R_{max} predicted using the virtual tool diameter in the geometric model outlined earlier ($0.052ms^{-1}$, 16A, ø25mm tool, 25mm path spacing)

However, for cases where the path spacing is small or moderate relative to the tool diameter, the virtual tool approach is significantly less successful, with the difference resulting from incorporating the kerf into these models explaining none of the discrepancy between the as-measured and the predicted R_{max} values along the cut length. This is shown in the Figure 154 for the case with 15mm path spacing and a 25mm tool diameter. As can be seen in this case, incorporating the kerf into the expected-R_{max} model actually makes the discrepancy between the expected and as-measured surface error larger.

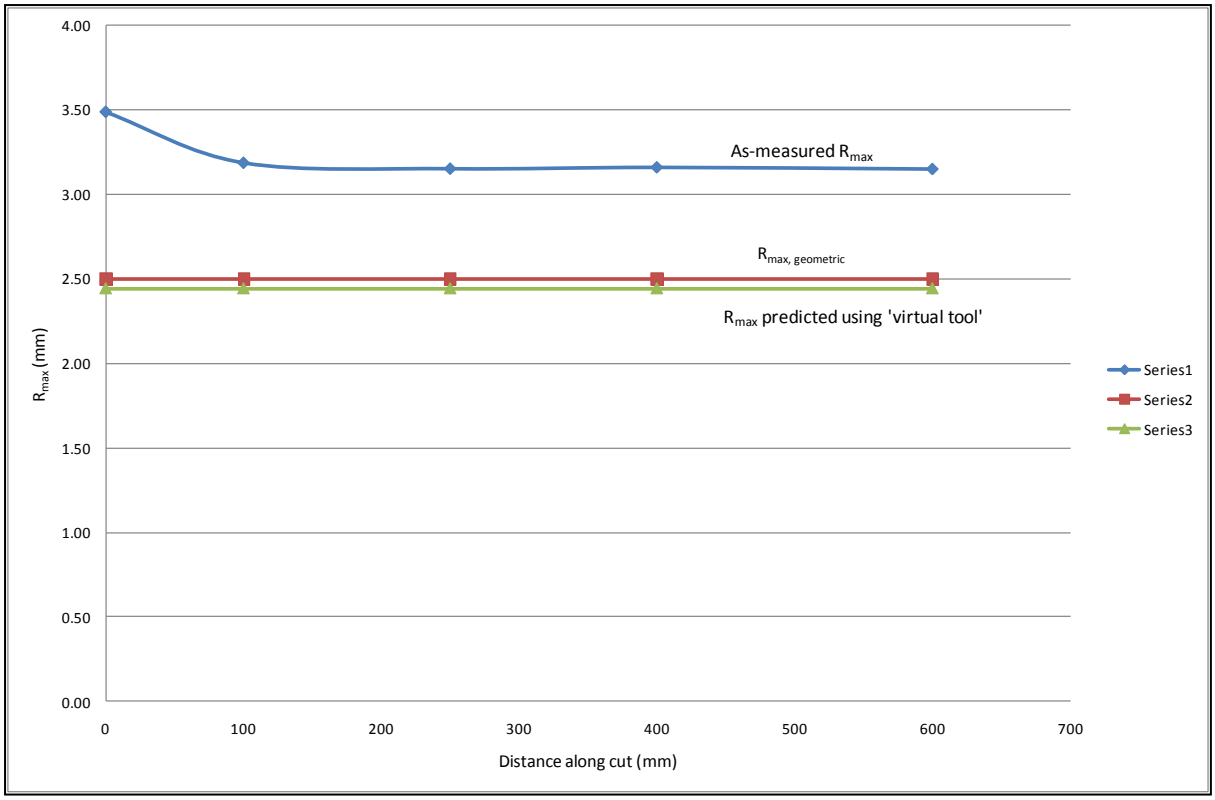

Figure 154: R_{max} variation along a cut with a round-nose tool and moderate path spacing, showing the R_{max} predicted using the virtual tool diameter in the geometric model outlined earlier ($0.052ms^{-1}$, 16A, ø25mm tool, 15mm path spacing)

Clearly, when path spacing is low relative to the blade diameter, something unexpected is going on in the cutting process that affects the magnitude of the surface error. The causes of this characteristic pattern of R_{max} variation with changes in the relative path spacing lie in the same basic process that caused the R_{max} in square-nose cutting to vary along the length of the cut when the applied current was not controlled.

When the path spacing is low relative to the blade diameter, the engaged length of the tool is quite short and the section of the tool that actually has a significant effect on the final surface is that part of the tool close to the central axis either side of the tool centre point (TCP). This section of the tool has relatively little curvature relative to the surface being cut, so from the point of view of the cutting process it more closely resembles a square-nose tool than a theoretical round-nose tool. As a result, the theoretical superposition of thermomechanical and geometric errors postulated earlier breaks down at low values of relative path spacing, and the effects of the kerf and HAZ become more important. At low path spacing values, the kerf and the HAZ cause asymmetric surface melting analogous to that found in square-nose cutting: since unmodified bulk material melts more than already-cut adjacent surfaces that have a heat affected zone, the depth of the surface valleys relative to the height of the surface peaks is larger than it would be in the absence of the heat affected zone, so the measured values of R_{max} are larger than the predicted errors resulting from the geometric models. The characteristic trend of R_{max} along the cut, starting at a high value and decaying to a

steady-state value, strongly suggests that kerf is the strongest influence on the R_{max} variation in multi-pass cutting, which also suggests that the use of controlled-current cutting will be able to stabilise the R_{max} along the cut length. This would be a useful result in itself, but would not really allow the minimisation of the surface error in the same way as it did for the square-nose cutting case, since applying an angular offset to a round-nose tool would make no real difference to the tool shape engaged in the cut.

A statistical analysis of the data set for round-nose R_{max} was undertaken for both initial and steady-state conditions, to determine which input parameters had the most significance for the final surface error value and to develop models that could be used to predict the expected error for a given cutting strategy. Since the geometric error is a fundamental property of the round-nose cutting process, and since there is no apparent way of eliminating the geometric error for these tool types, the net surface error was considered to be the most appropriate output parameter for these models, and no effort was made to predict the thermomechanical component of error separately.

The statistical analysis found that the geometric parameters of tool diameter ($ø$) and path spacing (S_p) were the most significant inputs, and that thermomechanical effects were of very little significance compared to the geometric effects. As such, there was no statistical merit in developing separate models for XPS and EPS foam, since the models and accuracies achieved were the same for both foams treated separately as for both foams treated together. The round-nose multi-pass cutting case is the only one in this thesis where the nature of the material has no statistically significant effect on the values of the surface quality output metric.

The analysis also found that the best conformance between the predictive models and the measured data was achieved when the samples made with a path spacing less than the blade diameter were treated separately from the samples made with path spacing equal to the blade diameter. The models developed are presented below.

For path spacing < blade ø:

$$^{initial}R_{max} = 0.02063ø + 0.22447S_p + 4.74550f - 0.01874i - 0.40731 \quad (79)$$

The R^2 value for this model was 0.9534, indicating a very good conformance between the predicted and measured data. The values of $P_r(>|t|)$ for each parameter were:

$ø$ = 0.0597

S_p = 2.10×10^{-13}

f = 0.2541

i = 0.3728

It is clear from these that the geometric conditions are by far the most important, and that path spacing is the single most important parameter influencing the total surface error. This makes sense, and accords well with the results of the geometric model for the round-nose cutting of a flat surface. Feed and current are the least significant input parameters: if these are removed from the model so that a model based solely on geometric conditions is used, the R^2 value drops to 0.9462, which is very nearly the same as that for the primary model above.

The same basic comments can be made about the steady-state Rmax model:

$$^{Steady}R_{max} = 0.016017ø + 0.211600S_p + 5.540956f - 0.018288i - 0.583983 \quad (80)$$

The R^2 for this model is 0.9658, indicating a very good fit, and this drops to 0.9598 if feed and current are removed to leave a model based solely on geometric conditions. The Pr(>|t|) values for each parameter are:

ø = 0.0661

S_p = 9.6x10-15

f = 0.1012

i = 0.2778

For path spacing = blade *ø*:

The models produced for the case where path spacing was equal to the blade diameter, the geometric conditions were even more predominant. The initial R_{max} model developed was:

$$^{Initial}R_{max} = 0.2185ø + 0.4318S_p + 5.045f - 0.00007102i - 6.216 \quad (81)$$

This model had an R^2 value of 0.9953, which dropped to 0.995 if feed and current were dropped from the model, indicating that the thermomechanical parameters have a negligible effect on the surface error at large values of relative path spacing. The $P_r(>|t|)$ values for each parameter supporting this, with those for feed and current being much, much larger than those for blade diameter and path spacing.

ø = 0.024806

S_p = 0.000366

f = 0.499881

i = 0.998488

The results for the steady-state R_{max} case were basically the same as for the initial R_{max} case. The final model was:

$$^{steady}R_{max} = 0.10807ø + 0.49327S_p + 10.24266f + 0.01435i - 5.98916 \quad (82)$$

This had an R^2 value of 0.9952, which drops to 0.9953 if feed and current are removed. This (and the $P_r(>|t|)$ values below) indicates that the thermomechanical component of the surface error is actually more significant in steady-state cutting than in vapourised cutting. The $P_r(>|t|)$ values for the parameters in this model were:

$ø$ = 0.193476

S_p = 0.000112

f = 0.173576

i = 0.691593

Based on the examination of square-nose and round-nose multi-pass cutting surface errors carried out here, it is possible to develop a cause and effect diagram detailing the parameters that have a significant effect on the thermomechanical surface errors in multi-pass cutting and the relationships between them. This diagram is shown in Figure 155. This is a general diagram for multi-pass cutting, and as such there are input parameters documented in it that may not actually be relevant to the specific case being considered. For example, the material is important for square-nose multi-pass cutting but of no significance when predicting the error to be expected in round-nose multi-pass cutting.

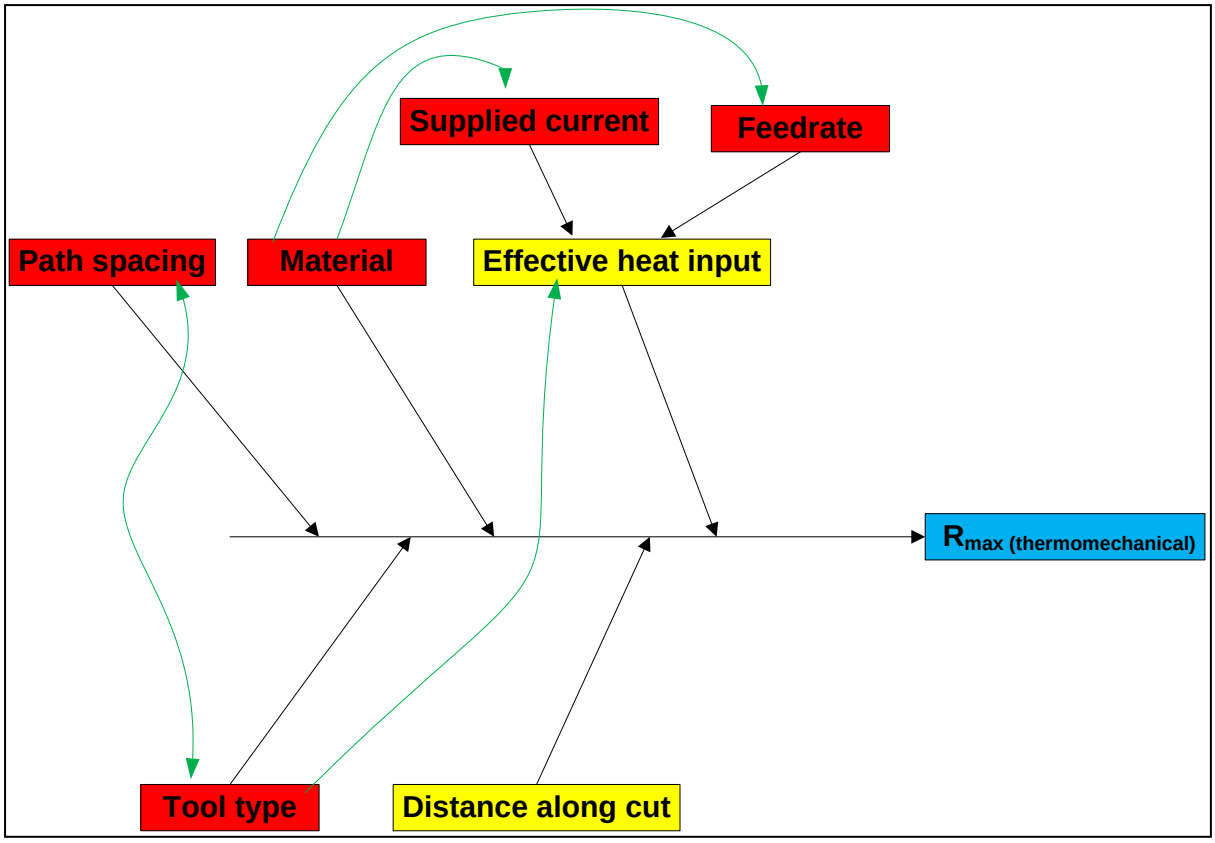

Figure 155: Factor interactions that influence the thermomechanical R_{max} in surfaces cut with multi-pass cutting

6.3.3.3 Multi-Pass Peak Spacing

Peak spacing has already been discussed from a geometric point of view, and it has been found that the ideal peak spacing is a function of the path spacing used to sculpt the surface in question. It is now necessary to consider any thermomechanical effects on the peak spacing, so that these can be superimposed on the geometric peak spacing to allow accurate predictions of the value of this error for a given cutting strategy.

Figure 156 shows the as-measured peak spacing values for the surface samples generated by the experiment outlined above, plotted against the path spacing used to produce each sample. As can be seen from the linear trend, there exists a strong correlation between the as-measured peak spacing and the path spacing. The gradient of the best-fit line is 0.9744, which is very close to the value of 1 that would indicate that peak spacing is equal to path spacing. The linear best-fit line has an R^2 value of 0.9942, indicating an extremely good fit to the measured data.

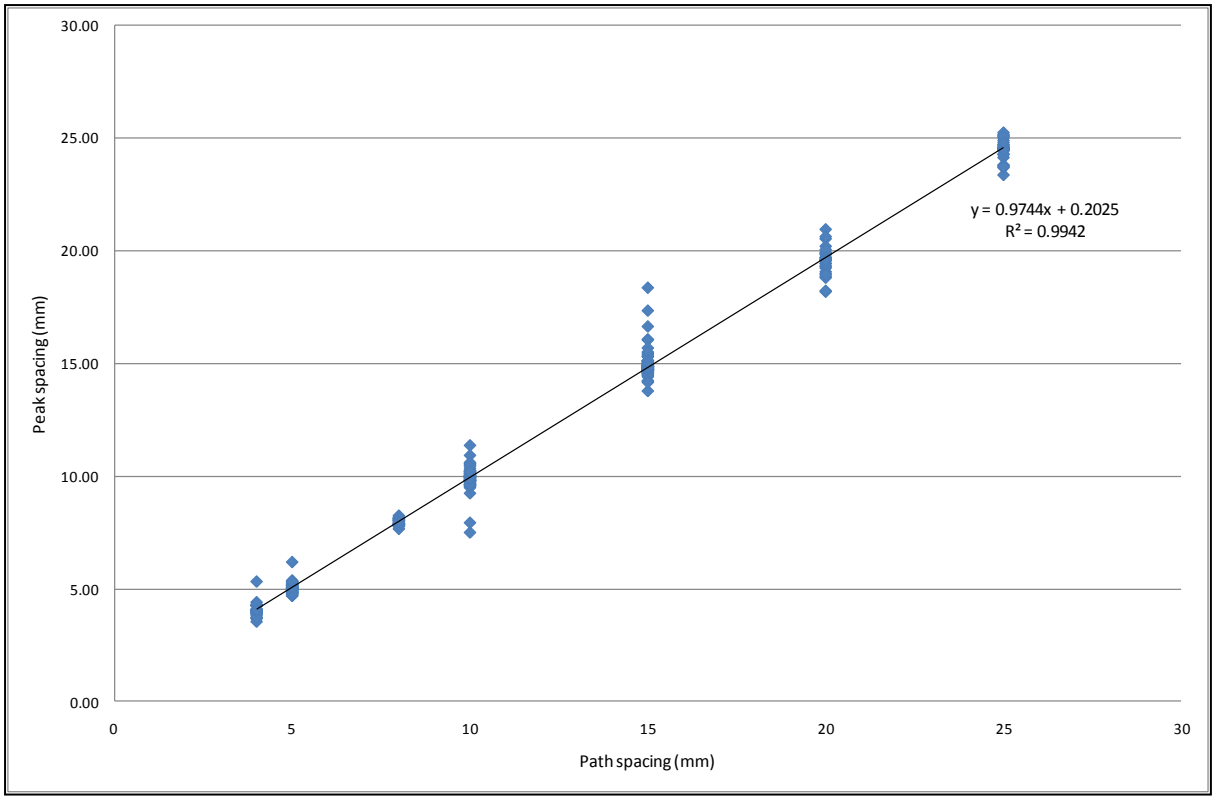

Figure 156: Relationship between peak spacing and path spacing for all multi-pass surface samples

This indicates that, broadly speaking, the final as-measured peak spacing of a surface is almost entirely dependent on the path spacing used to sculpt that surface. There may be an element of thermomechanical component to this error, but it is not of any real significance. As such, the geometric understanding of the causes of peak spacing developed earlier can stand on its own, without needing to be supplemented with a thermomechanical understanding of peak spacing.

6.4 Cutting Force and Tool Failure in Multi-Pass Cutting

In multi-pass cutting, there are two basic tool failure models, which are generally referred to as bending failure and torsion failure. Bending failure occurs when the cutting force is too high and the engaged length is symmetric around the tool centre point, while torsion failure occurs when the cutting force is too high and the engaged length is offset to one side of the tool centre point. Examples of these two basic types of failure are shown in Figure 157. Torsion failure generally results from cases where the path spacing is low.

Although these two failure modes manifest in different ways, the mechanism that causes tool failure is the same in both cases. The only difference between them is the geometric conditions of the toolpath, and therefore the point of action of the cutting force (since although the cutting force is technically a distributed load along the engaged length it can be modelled as a point load acting at the centre of the engaged length. For a given tool length and tool free-air temperature there will exist a critical cutting force above which the blade is not capable of resisting the cutting force to maintain its shape. The tool

temperature is important here because the yield stress of nichrome materials varies depending on the temperature of the sample, with higher temperatures leading to lower yield stresses. The free-air temperature is the relevant tool temperature because tools never fail in the engaged length: the hottest parts of the tools, and therefore the points that have the lowest yield stress, are the sections that are not transferring energy to the foam.

Figure 157: Failure modes of multi-pass cutting tools (Bending Failure on the left, Torsion Failure on the right)

Tool failures during cutting are obviously undesirable, and can be avoided by ensuring that the cutting force expected during a cut is lower than the critical cutting force for the tool temperature being used. In order to be able to assess the likelihood of tool failure without cutting, it is necessary to know the temperature-dependent yield stress of the specific nichrome material used for the tool, and to be able to predict the cutting force that can be expected for a given cutting strategy.

Data concerning the temperature dependent yield stress of the nichrome tools used in the RFS system was not available, and time constraints did not permit experiments to be carried out to determine the relationship between temperature and yield stress, so this part of the puzzle is still missing. As such, one recommended area for future research is to determine the relationship between temperature and yield stress for the tool materials used in RFS. However, it was possible to predict the cutting force based on input cutting strategy using models developed from statistical analysis.

It seemed reasonable to expect that the cutting force models generated during the single-pass cutting strategy investigation would produce accurate predictions for the cutting force in multi-pass cutting if appropriate values of effective heat input Q_{eff} and engaged tool length l_e were used in the models.

This expectation was based on the understanding that the cutting processes for single-pass cutting with straight blades and for multi-pass cutting with looped blades were basically the same. As far as the interaction between the blade and the foam was concerned, it seemed likely that the bent-ribbon blades used for multi-pass cutting would behave in fundamentally the same way as straight-blade tools.

To test this surmise, measured cutting force data gathered during experiment used above to generate multi-pass surface samples for measurement was compared with the cutting force predicted by the single-pass hot-blade models developed in Chapter 5. Due to time constraints, this was not done for every combination of multi-pass cutting conditions for which information was available: three XPS and three EPS cases chosen at random and compared. This was considered acceptable since it would quickly become apparent if the predicted data did not conform to the measured data, and if this did prove to be the case then a more comprehensive investigation could be carried out. In the event that the cases considered did show good conformance between the predicted and measured cutting force data, it was thought that six cases would provide a sufficiently large sample that conformance could reasonably be expected for all other cases.

Figure 158 shows the steady-state cutting force as a function of effective heat input for multi-pass cutting of XPS with a ø15mm round-nose tool using a path spacing of 15mm (giving an engaged length of 11.61mm). The values predicted by the single-pass model and the as-measured values are both shown.

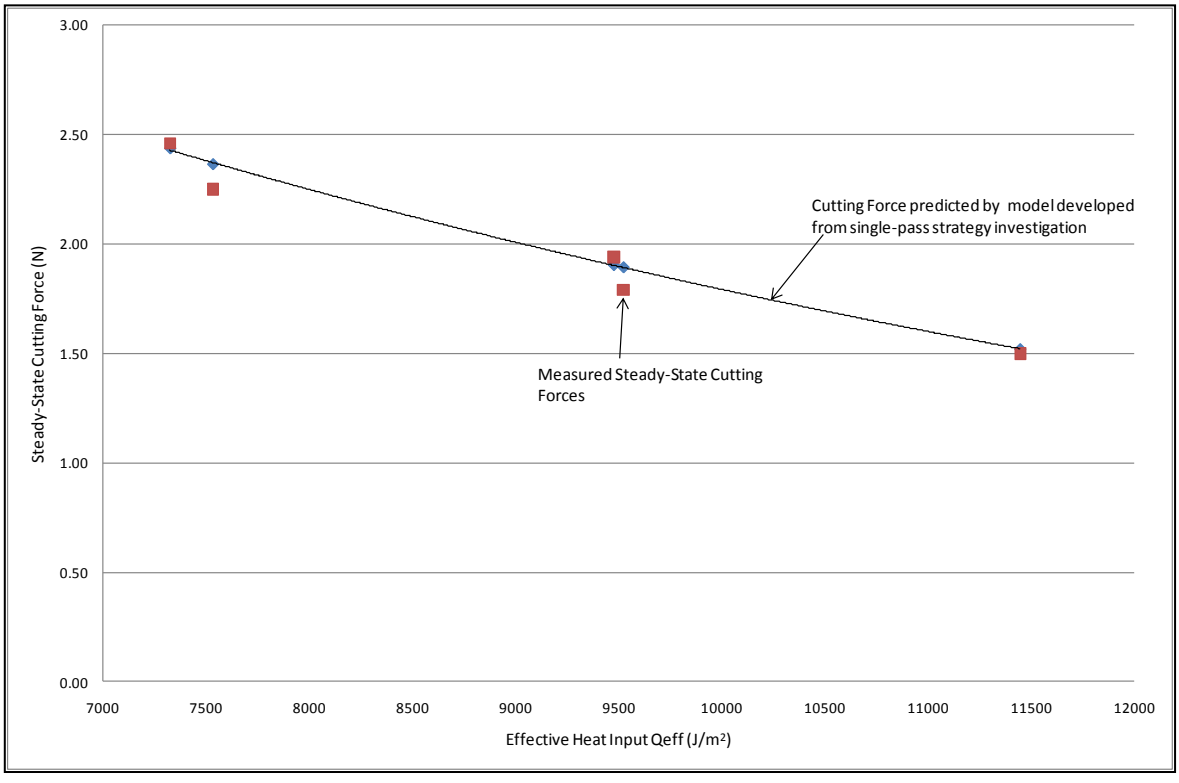

Figure 158: Comparison of Predicted and Measured Steady-State Cutting Forces for Multi-Pass Cutting of XPS (ø15mm tool, S_p = 15mm)

As is clear from this plot, the measured maximum values of steady-state cutting force in multi-pass cutting of XPS conform very closely to the cutting force values predicted by the single-pass cutting force models when appropriate values of input cutting conditions (Effective heat input Q_{eff} and engaged tool length l_e) are used. In this instance, when the as-measured force values are plotted directly against the predicted force values for the relevant level of effective heat input, a linear best-fit line fitted to this data has an R^2 value of 0.97, indicating an extremely good fit between the measured and predicted force data. The case shown here is for a round-nose tool with a diameter of 15mm and a path spacing of 15mm, but the same very close conformance was seen for all the cutting force examples that were tested.

Figure 159 shows an example of the cutting forces when cutting EPS foam, in this case for a ø25mm tool with a path spacing of 15mm. As is clear, the conformance between the measured and predicted cutting force values is also quite good, although slightly less so than was found for XPS, with particularly noticeable deviations at high and low values of effective heat input. It seems likely that this is a result of the different cellular structure of EPS foam, where localised regions of higher or lower foam density can result in extraneous cutting forces. In this case a linear fit between the as-measured and predicted force has an R^2 of 0.98, which is more than adequate to validate the use of the single-pass cutting force model for predicted the cutting force in multi-pass cutting with EPS foam.

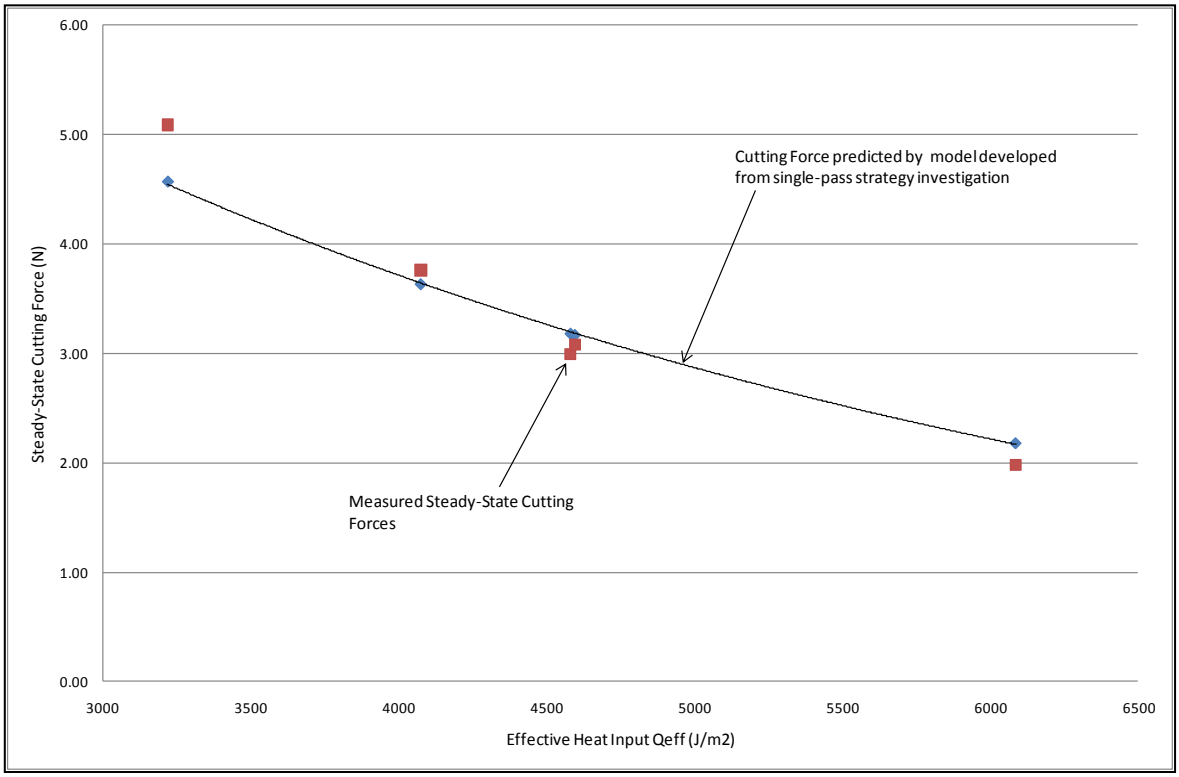

Figure 159: Comparison of Predicted and Measured Steady-State Cutting Forces for Multi-Pass Cutting of EPS (ø25mm tool, S_p = 15mm)

It was found that the cutting-force predictive models developed for single-pass hot-blade cutting were applicable to the multi-pass cutting case and that if the appropriate values of effective heat input and

engaged length were substituted into the models the predicted force values had very good conformance with the measured multi-pass steady-state cutting force values. Once further research has been carried out to determine the relationship between the temperature and the yield stress of the nichrome material, it will be possible to assess whether a given cutting strategy is likely to result in tool failure, and therefore to choose a cutting strategy that will not result in tool failure.

6.5 Conclusions and Limitations

Based on the research reported in this chapter, it is possible to draw a number of useful conclusions that can be applied to the problem of optimising the cutting strategy for robotic foam sculpting. It is also possible to identify a number of limitations of this research that should form the basis for future work. This section presents both the conclusions and limitations of the multi-pass cutting strategy investigation.

6.5.1 Limitations of this Research

This study has a number of limitations that could benefit from future research. The most important of these are summarised here.

- The postulated method of reducing or eliminating the surface deviation in square-nose multi-pass cutting has not yet been implemented. There are no obvious obstacles preventing this technique from working, but it has yet to be practically validated.
- The experimental investigation of the thermomechanical error in multi-pass cutting was restricted to the sculpting of nominally-flat surfaces. This means that the exact nature of the confounding between geometric and thermomechanical errors, especially on concave and convex surfaces, has not yet been fully characterised. This will form a promising area for future research.
- In order to avoid tool failure based on cutting force predicted from the statistical models and calculations of the critical cutting force for a given tool and temperature, information on the temperature-dependent yield stress of nichrome materials is required. During this research project this information could not be found, so to make the cutting force models really useful this data should either be sourced or developed form experimental work.

6.5.2 Conclusions

This investigation has explored the nature of multi-pass cutting and the causes of the characteristic surface errors of this cutting paradigm in a considerable level of detail. A number of important conclusions have been drawn, the most significant of which are summarised below:

- It was determined that the surface deviation R_{max} found in surfaces produced with multi-pass cutting were the result of the superposition of geometric and thermomechanical errors. Geometric errors are the result of the approximation of curved surfaces with multiple surface facets, while thermomechanical errors are the result of the hot-tool cutting process.

- The factors that influence the geometric surface deviation, the thermomechanical surface deviation and the peak spacing were defined and the relationships between them identified. Quantitative statistical models were also developed that allow the prediction of key output metrics based on input cutting strategy conditions.
- Contrary to initial expectations, it was found that the kerf around the tool was one of the most significant sources of thermomechanical error, and was certainly responsible for the largest transient surface errors prior to the establishment of steady-state cutting.
- The higher-density heat affected zone resulting from the hot-tool cutting of foam was found to have an effect on the surface deviation, since the HAZ from each tool pass resulted in the establishment of peaks (sometimes undercut) by the subsequent tool pass. This was primarily of importance when vapourisation was the cutting mode.
- The effect of kerf on the surface deviation could be stabilised by using force-feedback current control. It was also possible to predict the magnitude of steady-state error with a satisfactory degree of accuracy using statistical models. This presented the possibility of being able to compensate for the surface height deviation in square-nose cutting by applying an angular offset to the tool, although tool geometry means that this option is not available for controlling the surface errors in round-nose cutting.
- The most significant input parameters for determining the surface deviation of round-nose cutting were found to be the geometric conditions of tool diameter and path spacing. Relative to the effects of these parameters, thermomechanical errors were insignificant. Since only geometric conditions were really relevant, it was also found that a single model could be used for both XPS and EPS foam.
- The peak spacing in multi-pass cut surfaces was found to be almost exclusively a function of geometric conditions, with no significant or repeatable thermomechanical effects.
- The cutting force experienced by the tool in multi-pass cutting was found to conform to the predictions made with the single-pass hot-blade cutting force models when appropriate values of engaged length and effective heat input were used to predict output values. This confirmed that these models were appropriate tools for the prediction of cutting force.

7 Acoustic Output Characterisation for Current Control

One key problem with the robotic foam sculpting system is presented by the need to control the current throughout the length of a cut so as to stabilise the kerf and cutting force and allow more accurate prediction of the surface errors from the start of the cut to the end. At present, such current control depends on the use of a real-time measure of the cutting force using a loadcell, which has a number of drawbacks that have already been summarised (section 2.1.2). In an attempt to circumvent these drawbacks, it was postulated that the acoustic output of the cutting process could serve as a substitute for the cutting force as a trigger signal for active current control. This chapter summarises the results of an investigation into the acoustic output of the hot-tool cutting process and identifies an acoustic signal that should provide a method of identifying the beginning of thermomechanical cutting without the need for a loadcell to measure the cutting force.

7.1 Introduction

For some time, a major focus of the research into the RFS system has been the development of a method of controlling the tool temperature to ensure that the cutting mode is constant throughout the length of the cut. This has gone through several iterations, starting with work based on hot-wire anemometry and the resistivity of the cutting tool [17] and developing into a system that applies a step change to the applied current when the cutting force indicates that thermomechanical cutting is taking place, based on a real-time measure of the cutting force using a loadcell [1, 19]. There has also been some limited published work on the control issues associated with hot-wire cutting for EPS foam, which was only partially applicable to the RFS system [68-70].

The current control system implemented at present uses a loadcell on the hot-wire or hot-blade cutting tool to measure the cutting force, and when the cutting force indicates that cutting is taking place the current supplied to the tool is increased. This results in a higher wire or blade temperature, which compensates for the cooling that naturally takes place during cutting to maintain the tool temperature at about the same level as its free-air temperature. This system has been implemented and surfaces produced with it were assessed: it was found that the result was a kerf width that was much more stable along the cut, without the lead-in transient kerf width that was characteristic of cuts made with constant current. Cuts made using force-feedback current control had a kerf that varied by about 0.1mm along the cut instead of the approximately 1.5mm variation found in constant-current cutting. The constant nature of surface quality in controlled-current cutting has also been demonstrated (earlier in this thesis) for the surface texture and the multi-pas R_{max}, and the usefulness of the system has been improved by the development of the initial and steady-state kerf models developed in the single-pass cutting strategy investigation.

This system does have one very serious remaining drawback: since the cutting force has to be measured, a loadcell is needed on the cutting tool. Within the context of Robotic Foam Sculpting, this

has meant that the tool has had to be mounted on a fixed support and the robot used to move the foam workpiece, since if the tool and loadcell are on the robot the accelerations resulting from movement of the robot results in extraneous readings from the loadcell. This is not the optimum arrangement of tool and workpiece: it is easier to program the robot and to achieve surface details on a sculpted part if the robot is moving the tool and the workpiece is mostly fixed in place, as well as being easier to move a small tool in space without collisions than it is to move a large block of polystyrene foam.

During the cutting investigations carried out for other purposes (reported above) it was noticed that the cutting process produced a distinct sound, and that this sound output varied during the cut in a way that seemed, to the human ear, to be predictable, repeatable and to follow a pattern similar to that routinely displayed by the cutting force during a cut. As a result of this insight, it was surmised that it might be possible to implement an acoustic-feedback current control system in place of the force-feedback system already in place. A system like this would allow current control to be used even if the robot was moving the tool, but first a more thorough understanding of the nature of the acoustic output of polystyrene foam cutting was necessary. The investigation carried out to develop this understanding is the focus of this chapter.

7.2 Acoustic Output Scoping Investigation

In order to develop an acoustic-feedback current control system, it first had to be established that the acoustic output could be used to identify when cutting was taking place. In order to establish this, a scoping experiment was carried out. For a number of sets of cutting conditions, acoustic data was gathered (using a Bruel and Kjaer Type 2250 acoustic data analyser, see Appendix C) for two different states: cutting and not-cutting. In each of these, the robot was moved along exactly the same path: the only difference was that in one case a heated wire was passed through the foam to conduct a cut, and in the other no cutting took place. As a result, any differences between captured acoustic data for the two states could be attributed solely to the thermomechanical cutting process with a high degree of confidence.

The acoustic output for one of these sets of cutting conditions (7A, 0.0217ms^{-1}) is shown in Figure 160 and Figure 161, below. Figure 160 shows the output when no cutting is taking place, while Figure 161 shows the output when cutting is present. These plots are of the octave-band centre frequencies aggregated along the entire cut, and are not broken down by distance along the cut. When no cutting occurs, the acoustic output was made up of robot noise, background noise and other extraneous data. When cutting occurs, the background noise was much the same but the acoustic output caused by cutting was also present. The vertical amplitude of the bars has units of dB.

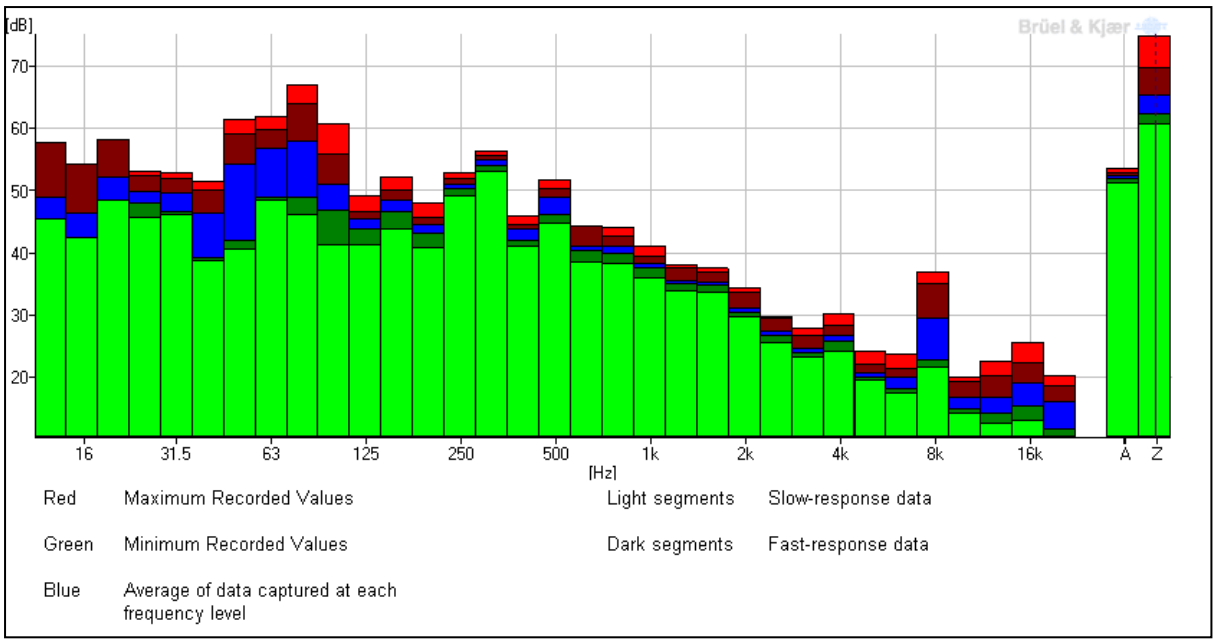

Figure 160: Acoustic Background without Foam Cutting (1300mm/min robot feedrate)

The coloured bars in these graphs contain a significant amount of information. The vertical bar on the right, labelled ‘Z’ is the total output across the entire frequency range, while the bar beside it labelled ‘A’ is the total output weighted to approximate what the human ear would hear listening to the same data. The red bar segments are the maximum values recorded, the green bars are the minimum values, and the blue bar segments represent the average of the data captured at each frequency level. Light-coloured segments indicate slow-response data, gathered at a sampling rate of one sample every second, while the darker segments indicate fast-response data collected at a sampling rate of one sample every 0.125 seconds. In practice, the details of these graphs were not especially important for the purposes of this scoping investigation: of more interest were the differences between the two graphs.

Comparing these output plots, it is possible to see at a glance that there is a clear difference between the acoustic output when no cutting takes place and when cutting does take place: this difference is the acoustic output of the cutting process itself. This makes it clear that the acoustic output of cutting is both present and measureable, so at the least it will be possible to tell the difference between the cutting and not-cutting states: this is the basic requirement for an acoustic-feedback current control system, so these results validated the basic concept behind this study. It was also possible to use this data to define the scope of a more detailed acoustic-output investigation.

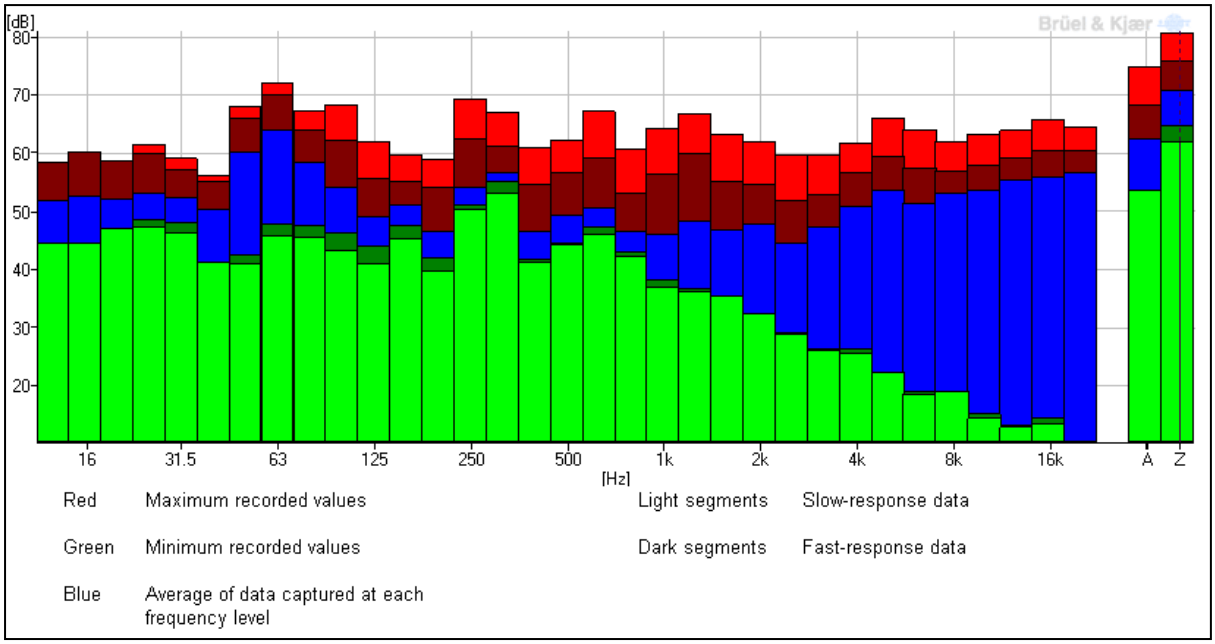

Figure 161: Acoustic Data Logged During Foam Cutting (7A, 1300mm/min)

It is clear that the acoustic output at frequencies below 1 kHz is essentially the same in both cases, but that there are large (and therefore more easily measured) acoustic outputs related to the cutting process at frequencies between 1 kHz and 16 kHz. For this reason, the more detailed characterisation of the acoustic output can be restricted to frequencies above 1 kHz, since this is clearly going to be the frequency range that will provide the most useful measurement metric for a current control system. It is also clear that the cutting-related acoustic output is more significant at frequencies closer to 16 kHz than at frequencies closer to 1 kHz.

7.3 Detailed Investigation of Acoustic Output for Thermal Plastic Foam Cutting

Since the initial scoping investigation seemed to indicate that there was a clear and measureable acoustic output resulting from the hot-tool cutting process, it was necessary to conduct a thorough investigation of the acoustic output with respect to input cutting conditions and cutting force. The goal of this investigation was to determine if there was a repeatable and identifiable relationship between the acoustic output and the cutting force, so that the acoustic signal could be substituted for the force signal currently used to control the current supplied to the tool. The details of this investigation are presented in this section.

7.3.1 Experimental Apparatus and Method

In order to use the acoustic output of the thermomechanical cutting process as a trigger metric for the current-control system, it is necessary to have a full understanding of the behaviour of the acoustic output along the length of the cut with different cutting conditions, tool types and materials. To develop this understanding, a detailed investigation of the acoustic output was undertaken. A large

number of cuts were made using the Kuka robot, hot-wire and hot-blade tools, and recordings of the acoustic output and cutting force were taken for each cut. The cutting force measurement were taken with the same loadcell-based experimental setup used in [1]: this system will not be summarised here.

The acoustic data for this investigation was gathered using the same Bruel and Kjaer Type 2250 acoustic data analyser as was used for the scoping investigation, with a microphone positioned adjacent to the tool so as to be close to the cut, as shown in Figure 162. As usual for the investigations carried out for this thesis, both EPS and XPS foam were considered, and two foam thicknesses were used, 30mm and 50mm. This investigation only considered single-pass cutting using wires and blades, so the foam thicknesses used were also the engaged tool lengths.

The acoustic output of multi-pass cuts was not included in this investigation. The reason for this was that, if the hypothesis that acoustic output was related to cutting force proved correct, then conclusions drawn for single-pass cutting would be equally valid for multi-pass cutting, since the cutting forces for single and multi-pass cutting exhibit basically the same behaviour for given values of effective heat input and engaged length.

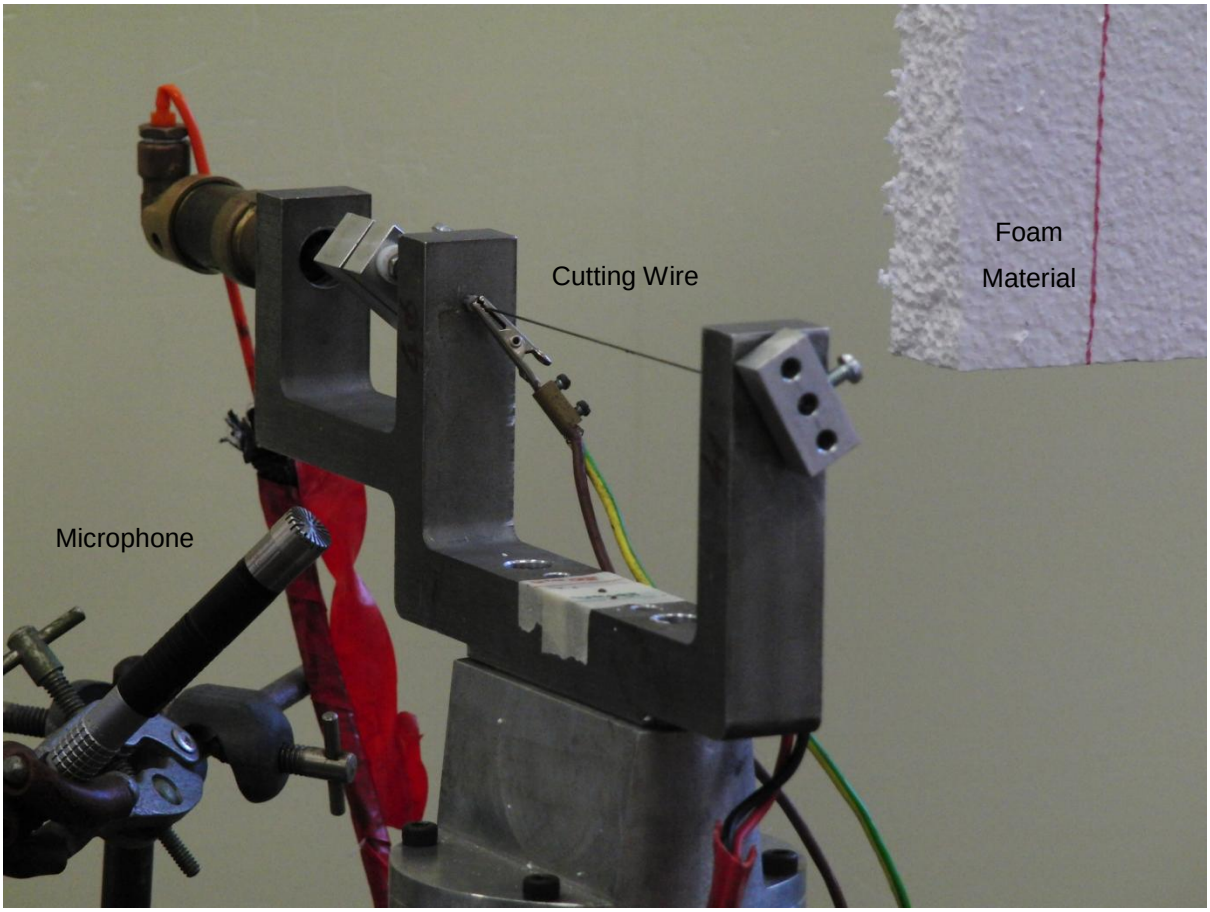

Figure 162: Experimental Setup for gathering Acoustic Output Data (in this case for 30mm EPS)

Based on the scoping exercise outlined above, acoustic data was gathered for frequencies between 1 kHz and 16 kHz. This was done in four bands, as follows:

- 1 – 4 kHz
- 4 – 8 kHz
- 8 – 12 kHz
- 12 – 16 kHz

These frequency bands were chosen to cover the full range of frequencies of interest identified by the scoping exercise, from 1 kHz to 16 kHz. This range was divided into four bands of 4 kHz each in order to investigate the characteristics of the output in each band separately from the others. The selection of four 4 kHz bands was somewhat arbitrary, the intention being to conduct a first-pass characterisation of the behaviour of different bands and then refine the experiment design further for a second-pass investigation. As it transpired, the 4 kHz bands initially chosen provided a sufficiently detailed understanding of the acoustic output of the foam cutting process that a trigger signal for current control could be identified without any need for investigation of different frequency bands.

The cutting conditions used for this investigation are shown by Table 25 to Table 27. Table 25 shows the cutting conditions used for hot-wire cutting with both EPS and XPS foam, Table 26 shows the conditions used for hot-blade cutting of EPS, and Table 27 shows the conditions used for hot-blade cutting of XPS. Cutting conditions denoted by '+' were carried out once and the acoustic output recorded, while for the cutting conditions denoted by 'X' the cut was repeated six times for 30mm foam so that the repeatability and consistency of the output could be verified. This repeatability investigation was necessary since the acoustic output would be of no use as a trigger for current control unless the output for a given set of cutting conditions could be expected to be highly similar in all circumstances.

Table 25: Cutting conditions for investigation of acoustic output for hot-wire cutting of EPS and XPS

Current (A)	**Tool Feedrate (ms^{-1})**					
	0.0133	**0.0167**	**0.0183**	**0.0187**	**0.0200**	**0.0217**
5	+	+			+	
6	+	+			+	
7	+	+	X	+	+	+

Table 26: Cutting conditions for investigation of acoustic output for hot-blade cutting of EPS

Current (A)	Tool Feedrate (ms^{-1})				
	0.038	**0.050**	**0.062**	**0.074**	**0.086**
16	+		+		
19	+	+	X	+	+
22	+		+		+

Table 27: Cutting conditions for investigation of acoustic output for hot-blade cutting of XPS

Current (A)	Tool Feedrate (ms^{-1})				
	0.028	**0.040**	**0.052**	**0.064**	**0.076**
16	+		+		
19	+	+	X	+	+
22	+		+		+

This experimental design resulted in a total of 142 cuts being made, with readings of the acoustic output at intervals of 0.1s for the entire length of the cut. The cut length was at least 650mm in all cases, so this resulted in a very large amount of acoustic data that could be used to characterise the cutting process. The order in which the cuts were made was randomised to minimise the effect of any errors that built up over time.

The cutting force data and the acoustic output data were gathered using two separate systems, which meant that the data did not have a common time stamp. In order to associate a given time on the cutting force time series with the same point on the acoustic output time series, registration of the data was necessary. To do this, the end of the cut was identified in both time series. This point is characterised by a rapid fall-off in the cutting force and by a spike in the acoustic output as the offcut piece of foam falls onto the base of the cutting tool, as illustrated by Figure 163. These points in the two time-series plots were therefore aligned with each other to give a single time-series data set. There is some potential for error in this method, since the fall-off in cutting force and the spike in acoustic output occurred over several data points and some user interpretation was required to determine the two relevant points on each data series. However, that potential for error was not considered to be significant since it was relatively clear how the acoustic output varied for different cutting modes, and even allowing for some small misalignment associated features of the cutting force and acoustic output plots could be clearly identified.

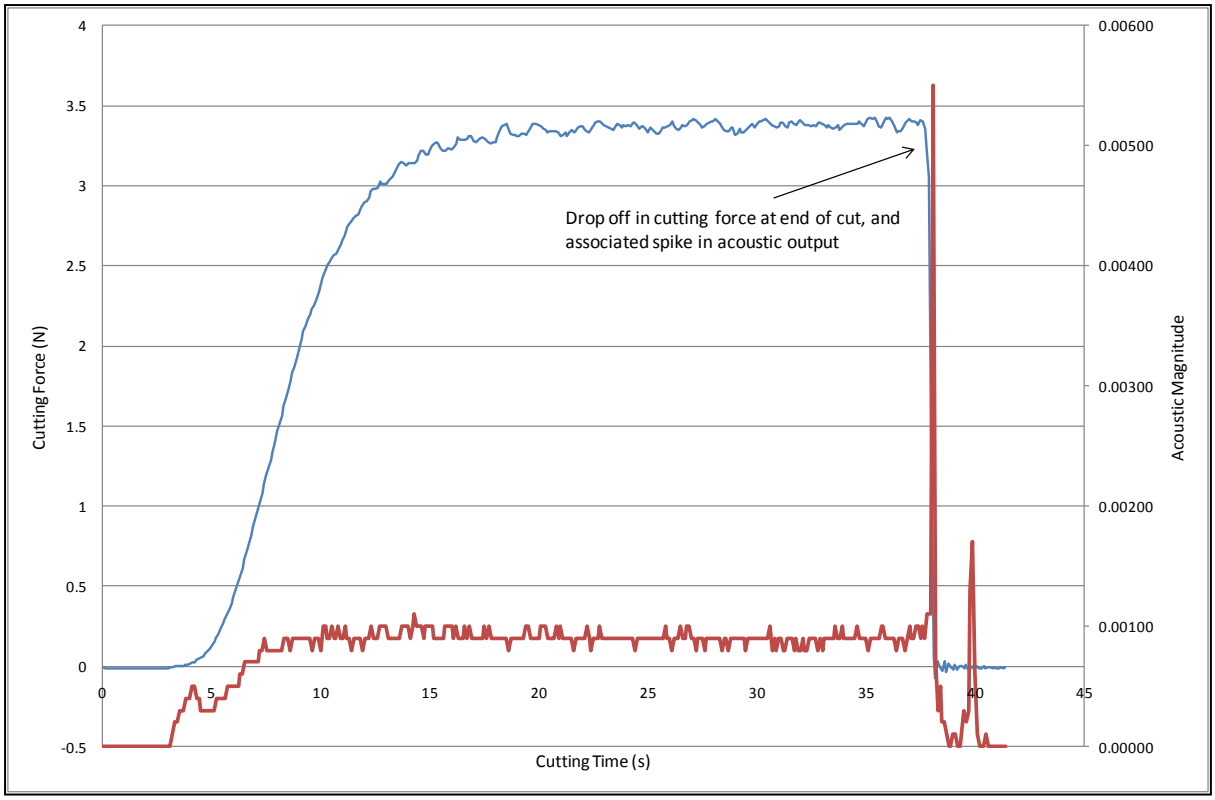

Figure 163: Drop in cutting force and associated spike in acoustic output at the end of a cut (5A, 0.0167ms^{-1}, 4 - 8 kHz)

7.3.2 Results

The captured acoustic data was compared to the cutting force and the cutting mode (vapourised or thermomechanical) along the length of the cut, since a relationship between the acoustic data and the cutting force is desirable so that acoustic output can replace cutting force as a trigger for current control. In order for the acoustic output to be useful as a current-control trigger metric, it must be consistent, repeatable, predictable and related to the cutting force.

The units used for the acoustic magnitude in this work are a proprietary dimensionless unit built into the analysis software provided with the acoustic data analyser, and are analogous to dB. This was not considered to be a problem since the main focus of this work only required an understanding of the relative magnitudes of the acoustic outputs, not absolute values. As it turned out, the most reliable potential trigger signal went from having no value in vapourised-only cutting to having a value in thermomechanical cutting, so the actual magnitude of the units used to measure the acoustic output were essentially irrelevant.

All of the results presented below are for the acoustic output of the cutting process itself: recordings were also taken of the background noise for each set of cutting conditions and the background acoustic data was subtracted from the data gathered during cutting, to leave only the acoustic readings that are a direct result of the thermomechanical cutting process.

Based on qualitative observation of the acoustic output during cutting trials, three basic hypotheses were developed for testing by this investigation. These were:

1. That the acoustic output was proportional to the cutting force and the cutting mode during the cutting process and higher cutting forces would result in larger acoustic outputs.
2. That the acoustic output would have a greater magnitude for cutting of XPS foam than EPS foam, since the cutting forces when cutting XPS are higher, which is believed to be due to the more regular cellular structure of the foam.
3. That the acoustic output would have a greater magnitude for larger values of l_e, the engaged tool length, since the cutting force is proportional to the engaged length.

For all tool types and foams, comparison of the acoustic outputs for different cutting conditions showed that there was definite proportionality between the acoustic output and the cutting force for all of the frequency bands investigated. For cuts where the steady-state cutting force was relatively high due to relatively low effective heat input, the magnitudes of the acoustic outputs were also higher than for cuts made with relatively high effective heat input and relatively low cutting forces. The link between cutting force and acoustic output is best illustrated by Figure 164, which shows the cutting force and 4 – 8 kHz acoustic output for a hot-blade cut of EPS with a current of 19A and a feedrate of $0.064 ms^{-1}$. In this case, there was an extraneous spike in the cutting force data during the thermomechanical cutting stage (just under 12s from the start of the cut), before steady-state cutting had been achieved: these spikes occur occasionally, particularly when cutting EPS foam, which is thought to result from the cutting tool passing through areas of locally higher foam density. Normally such spikes are ignored since they occur essentially randomly and are not a consistent or important feature of the thermomechanical cutting process. However, in this case the spike in cutting force serves a useful purpose because there is also an associated spike in the acoustic output, which demonstrates clearly the link between acoustic output and the cutting force. It should be noted that for all the plots of acoustic magnitude and cutting force against time in this chapter, the point 0s on the time axis corresponds to the point at which the cutting tool first ‘engages’ with the foam (i.e. where cutting begins).

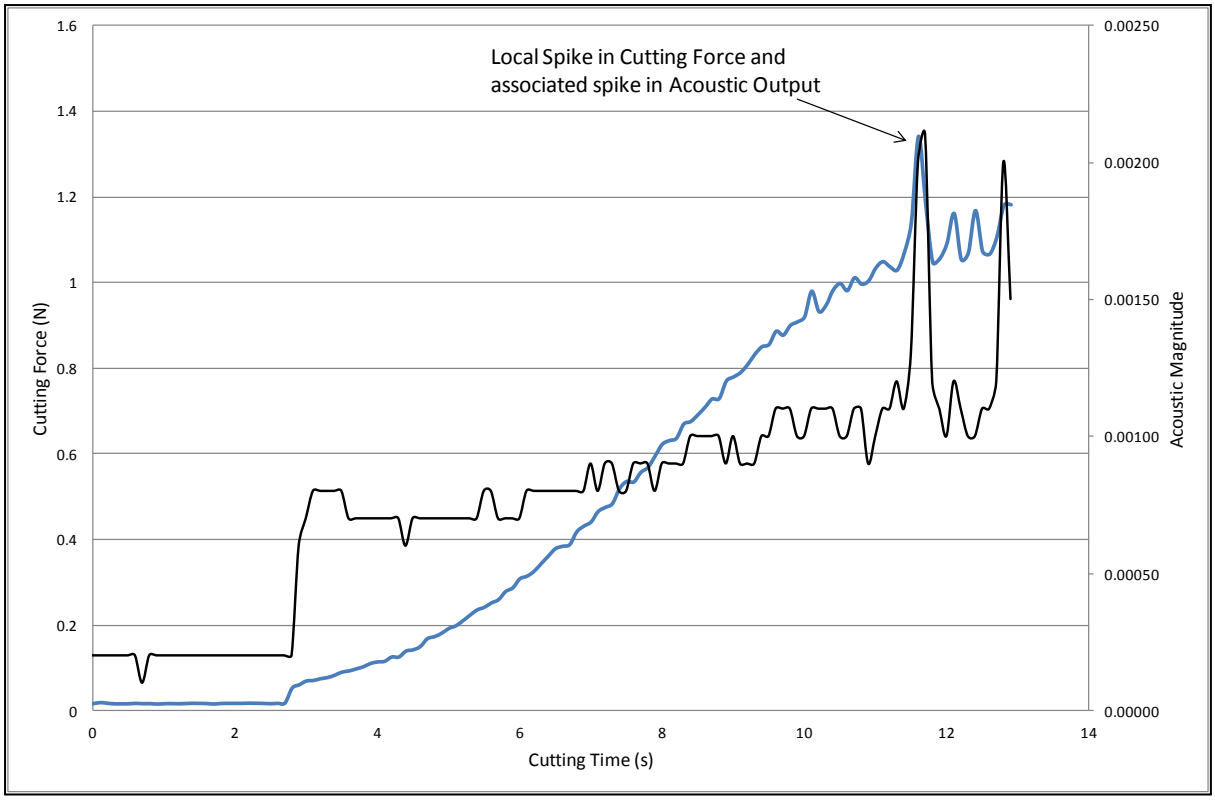

Figure 164: Cutting Force and Acoustic Output showing an extraneous spike in Cutting Force and the associated spike in Acoustic Output (XPS, blade cutting, 19A, 0.064ms^{-1}, 1 - 4 kHz)

It was also found that, for the same effective heat input, the magnitude of the acoustic output for XPS was greater than that for EPS. This was expected, since during cutting the sound made while cutting XPS is noticeably louder than the sound made while cutting EPS. This phenomenon is demonstrated by Figure 165, which shows the 1 – 4 kHz acoustic signal generated by cutting 30mm XPS with a hot-wire tool at a current of 5A and a feed of 0.0200ms^{-1}, and Figure 166, which shows the acoustic output produced when cutting EPS at the same cutting conditions. In the case of XPS, the magnitude of the acoustic signal settles to a mean value of 0.00090 (allowing for the noise of the signal) in the steady-state cutting region, while the acoustic magnitude for EPS in the steady-state cutting region settles at a mean value of only 0.00030. The greater magnitude of the acoustic output for cutting of XPS was found in all cases where direct comparisons could be made, and is thought to be a result of the regular cellular structure of XPS, which results in significantly higher and more regular cutting force readings when cutting XPS than when cutting EPS.

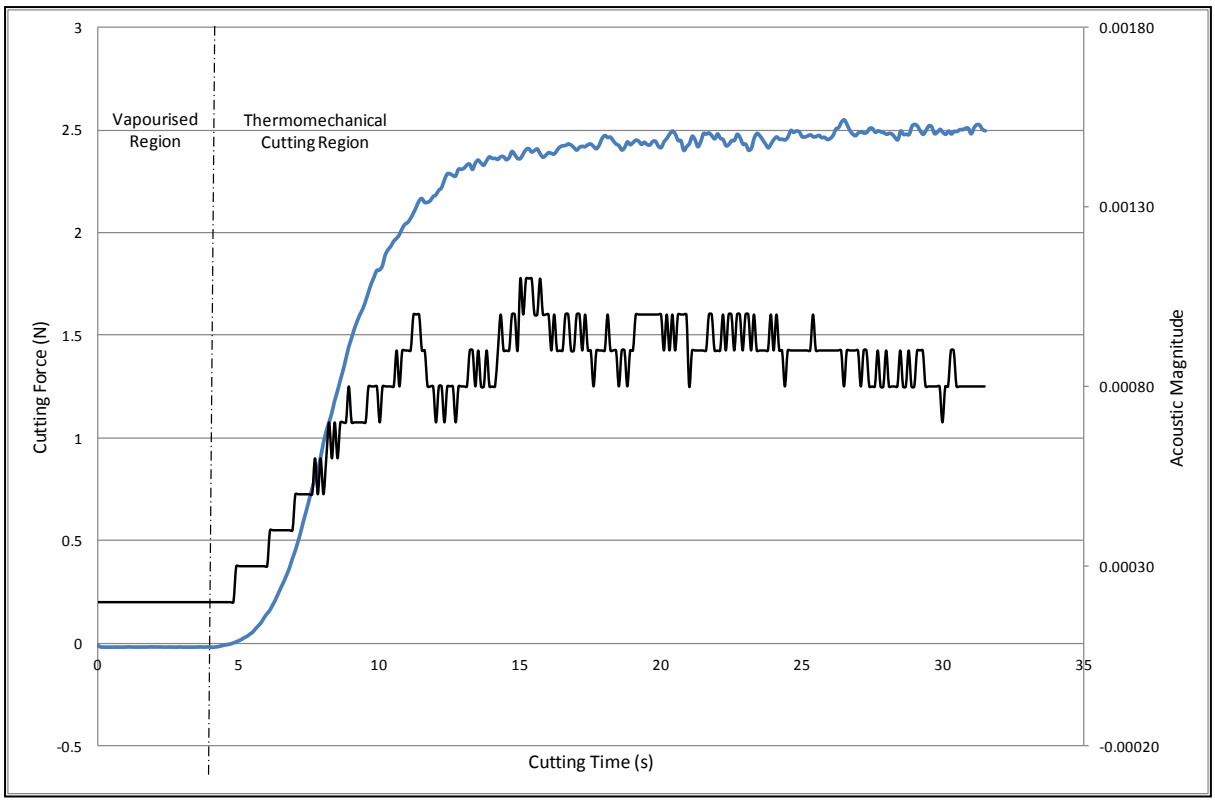

Figure 165: Cutting Force and Acoustic Output for 30mm XPS (5A, 0.0200ms^{-1}, 1 - 4 kHz)

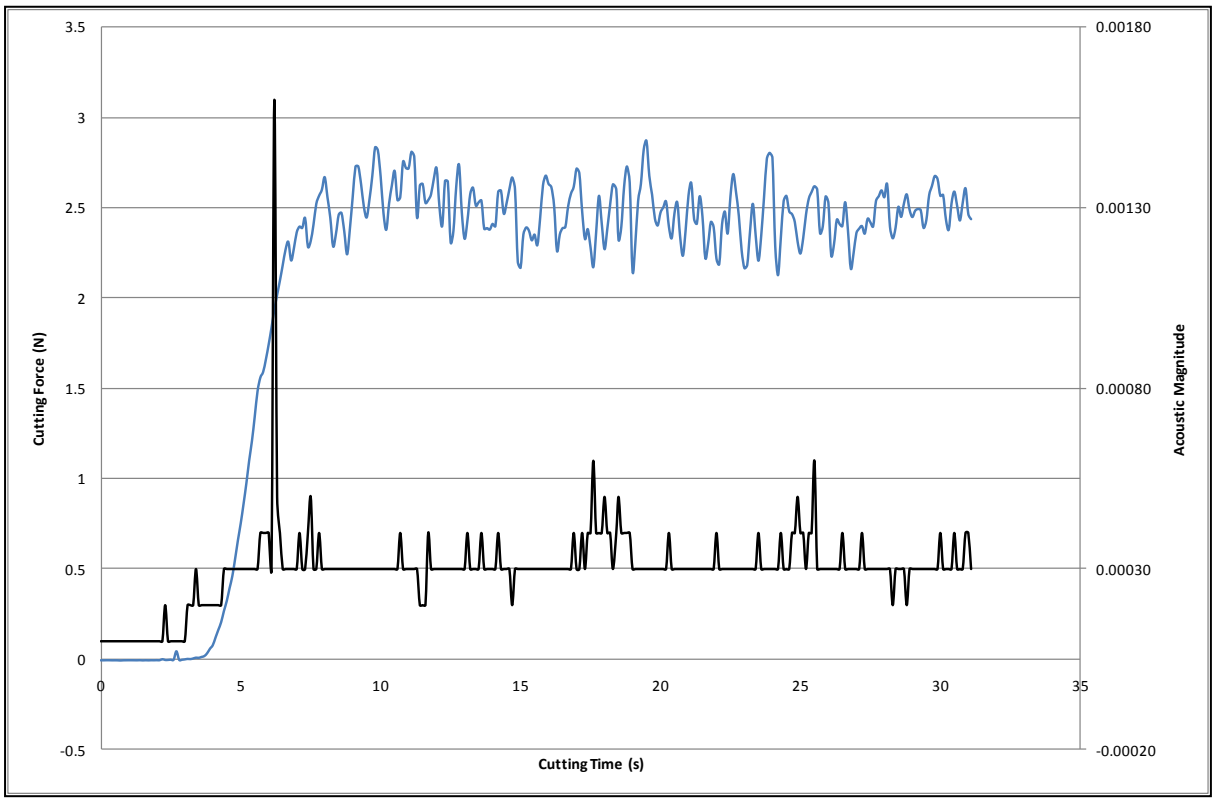

Figure 166: Cutting Force and Acoustic Output for 30mm EPS (5A, 0.0200ms^{-1}, 1 - 4 kHz)

It was also found that the magnitude of the acoustic output, like the cutting force, was consistently proportional to the engaged tool length, l_e. This is demonstrated by Figure 167, which shows the 4 – 8 kHz output for an XPS cut with an engaged length of 30mm with cutting conditions of 7A and 0.0217ms^{-1}, and Figure 168, which shows the output for a cut with the same cutting conditions but a 50mm engaged length. In the case where l_e = 30mm, the acoustic output settles to a mean steady-state value of 0.00050, while in the l_e = 50mm case the mean steady-state value is 0.00070.

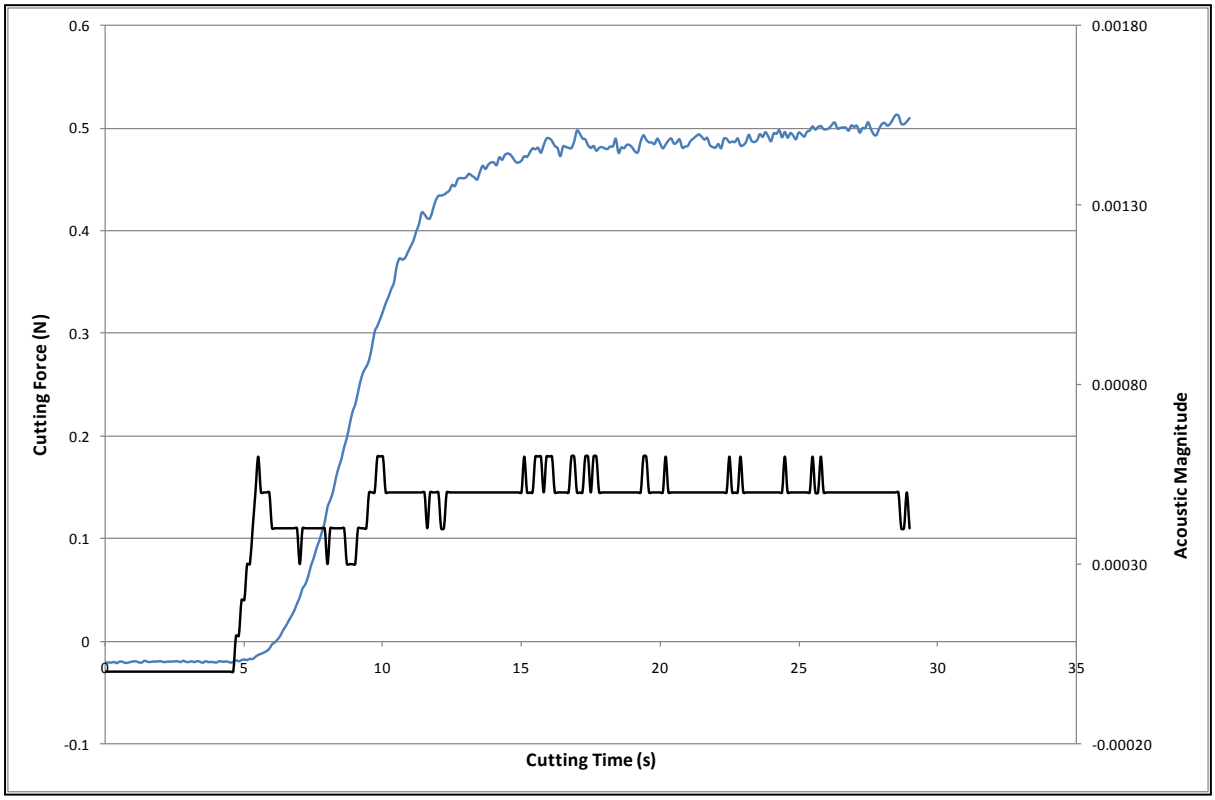

Figure 167: Acoustic Output and Cutting Force for an engaged length of 30mm (XPS, wire tool, 7A, 0.0217ms^{-1}, 4 - 8 kHz)

The proportionality of the acoustic output to the engaged length is an important result, with particular relevance to multi-pass cutting. An acoustic-feedback current control system will only really be useful as part of the RFS system if it can be used to control the applied current for all tool types and cutting strategies, so it must be capable of working in the multi-pass cutting case. Due to the nature of multi-pass cutting, the tool engaged length is a function of the exact tool shape and size, and the path spacing, and is generally much shorter than the engaged length in the single-pass cutting cases, so the magnitude of the acoustic output would be smaller.

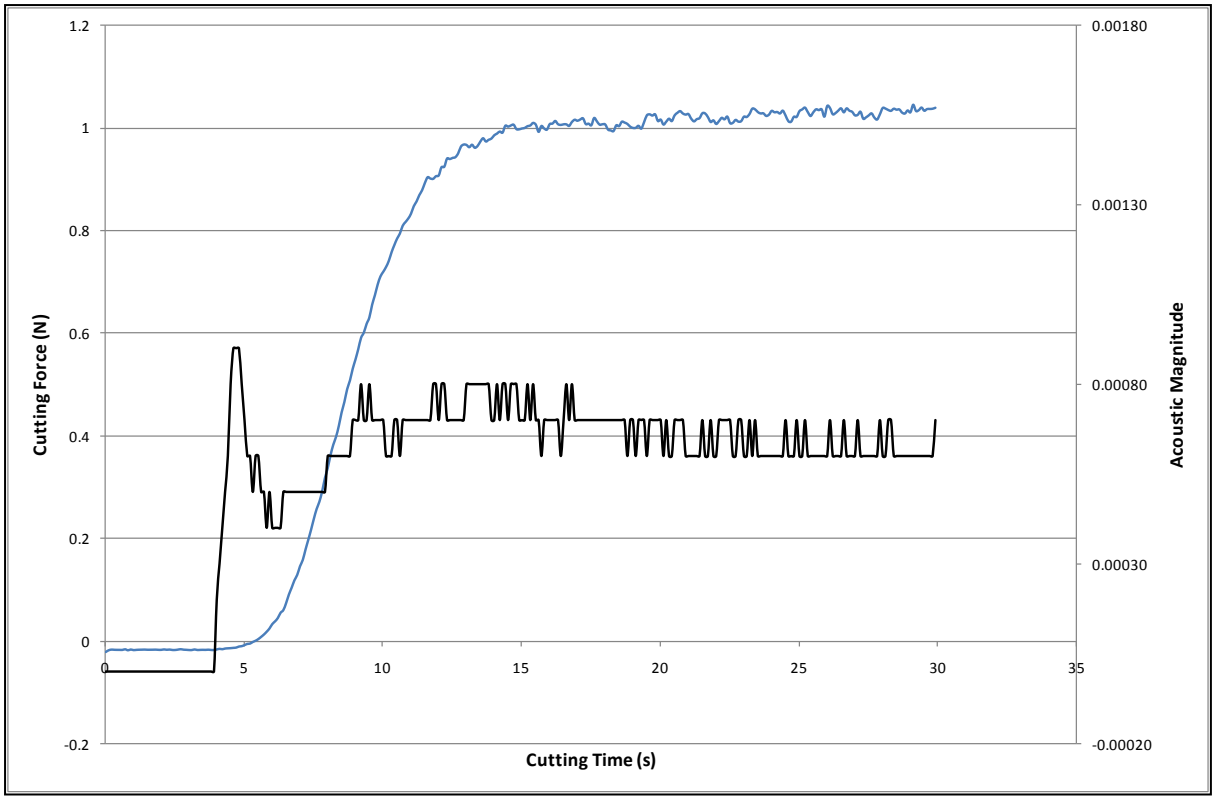

Figure 168: Acoustic Output and Cutting Force for an engaged length of 50mm (XPS, wire tool, 7A, 0.0217ms^{-1}, 4 - 8 kHz)

It can also be observed from these graphs that the nature of the potential acoustic-output trigger signal is very different from the nature of the cutting force trigger signal at the transition from vapourised to thermomechanical cutting. Whereas the cutting force initially increases very slowly from zero, with a low rate of change, before starting to increase faster through the transition-cutting region, the acoustic output undergoes what is essentially a step change. The sampling rate for this experiment was one sample every 0.1s, and in all cases the change from the acoustic output in vapourised cutting to the acoustic output in thermomechanical cutting takes place between one data point and the next. As such, the change in acoustic output is very close to instantaneous. The much faster response to changes in the cutting mode of the acoustic output means that the acoustic signal should be a much better trigger signal for a control system, since changes can be discerned easily, rather than having to apply a force threshold value above which thermomechanical cutting can be expected to be taking place.

It has been established that the magnitude of the acoustic output is proportional to the foam type being cut, the type of tool, the engaged length and the cutting conditions. From the point of view of developing an acoustic-feedback current control system, this presents a problem, since the magnitude of the acoustic output will be different for each combination of the above variables and therefore there will need to be different trigger levels of the acoustic output for each combination. In other words, for a cut made with high current, low feed, EPS foam and a hot-wire tool and a second cut made with low current, high feed, XPS and a hot-blade, the magnitude of acoustic output

corresponding to the appropriate trigger-point for the current step would be different. As such, it would be highly desirable to find some aspect of the acoustic output of cutting that was independent of the engaged length, cutting conditions and foam type to use as the trigger for the current step This would be simpler than having a control system that used different values of the trigger signal for different circumstances, since only a single rule would have to be implemented. In order to see of such a characteristic acoustic signal, it is necessary to examine the characteristic outputs in each frequency band.

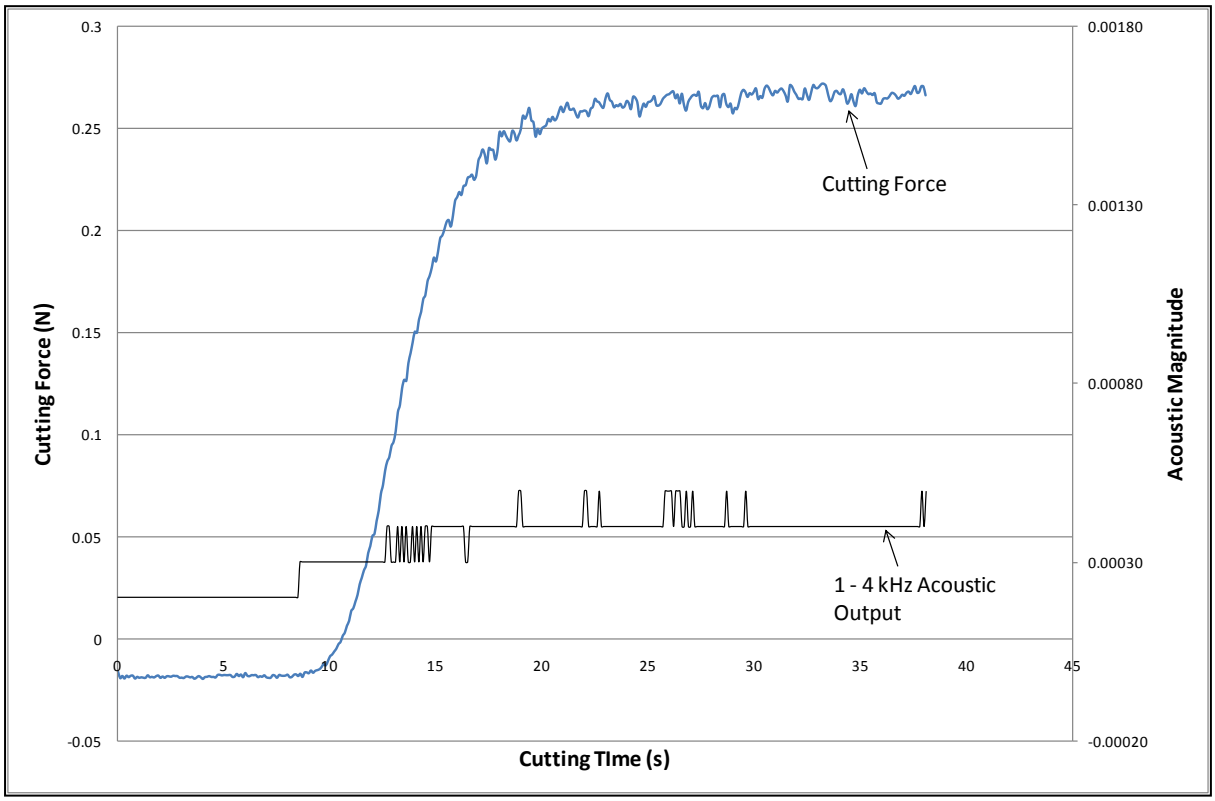

Figure 169: Acoustic Output and Cutting Force for 1 - 4 kHz band (XPS, wire cutting, 30mm, 7A, and 0.0183ms^{-1})

The 1 – 4 kHz band for all cuts is very similar in trend to that shown in Figure 169, for 30mm XPS cut by a hot-wire at a current of 7A and a feed of 0.0183ms^{-1}. During the vapourised cutting region, the acoustic output has constant magnitude, and this increases at the beginning of the thermomechanical cutting region. The overall increase from the vapourised cutting region to the thermomechanical cutting region is generally not that large. In the case of XPS, the value of the acoustic magnitude in the vapourised region is always 0.00020, regardless of the cutting conditions, engaged length or tool type. Hot, fast hot-wire cuts with short engaged lengths have the same output magnitude as cold, slow, blade cuts with long engaged lengths. When cutting EPS, the same steady behaviour is exhibited in the vapourised region but not all cutting conditions produced vapourised-region outputs of the same magnitude. In EPS cutting, the vapourised region magnitude is either 0.00010 or 0.00020, and there appears to be no predictable relationship between the cutting conditions, tool type and engaged length and the magnitude of the vapourised region acoustic output.

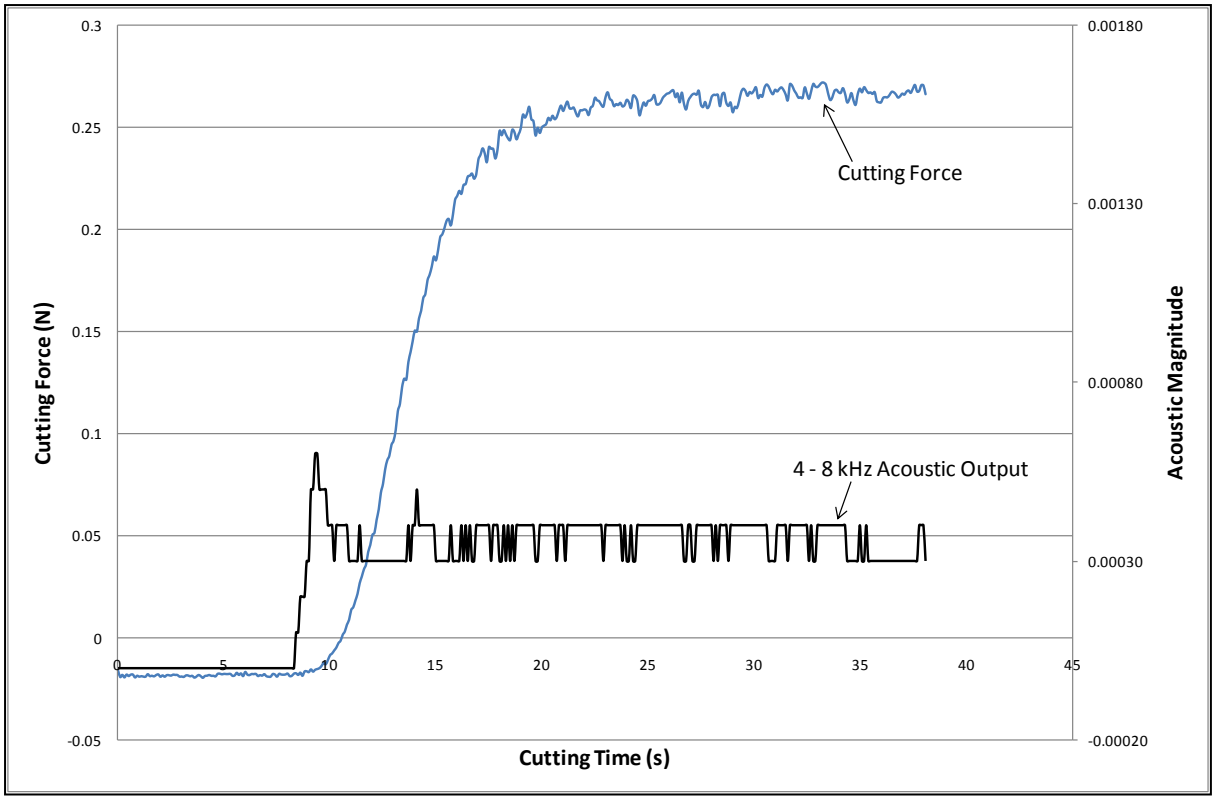

Figure 170: Acoustic Output and Cutting Force for 4 - 8 kHz band (XPS, wire cutting, 30mm, 7A, and 0.0183ms^{-1})

The acoustic output for the 4 – 8 kHz and 8 – 12 kHz bands shows a similar pattern, with a constant value in the vapourised cutting region and an increase in the acoustic magnitude once thermo-mechanical cutting is taking place. Generally the change in magnitude from the vapourised region to the steady-state region is larger than for the 1 – 4 kHz band, and the steady-state signal exhibits somewhat more variability.

It is also clear that the acoustic output for the 4 – 8 kHz band and the 8 – 12 kHz band are the same. In the case presented here in Figure 170 and Figure 171 the acoustic output is exactly the same, and this is true for all of the cuts carried out in this investigation. Some small discrepancies were observed between the acoustic outputs for these two frequency bands, but these discrepancies are limited to the occasional data point which can be regarded as random error. The largest number of differing data points found was 3 in a 35s cut, or 3 data points out of 350, and less than 5% of the samples cut exhibited any discrepancy. This result means that an acoustic-feedback current control system could be implemented based on the 8 kHz-wide band from 4 – 12 kHz: since this band is wider than the 4 kHz bands investigated in this study, it would be easier to measure and such a current control system would be somewhat more robust

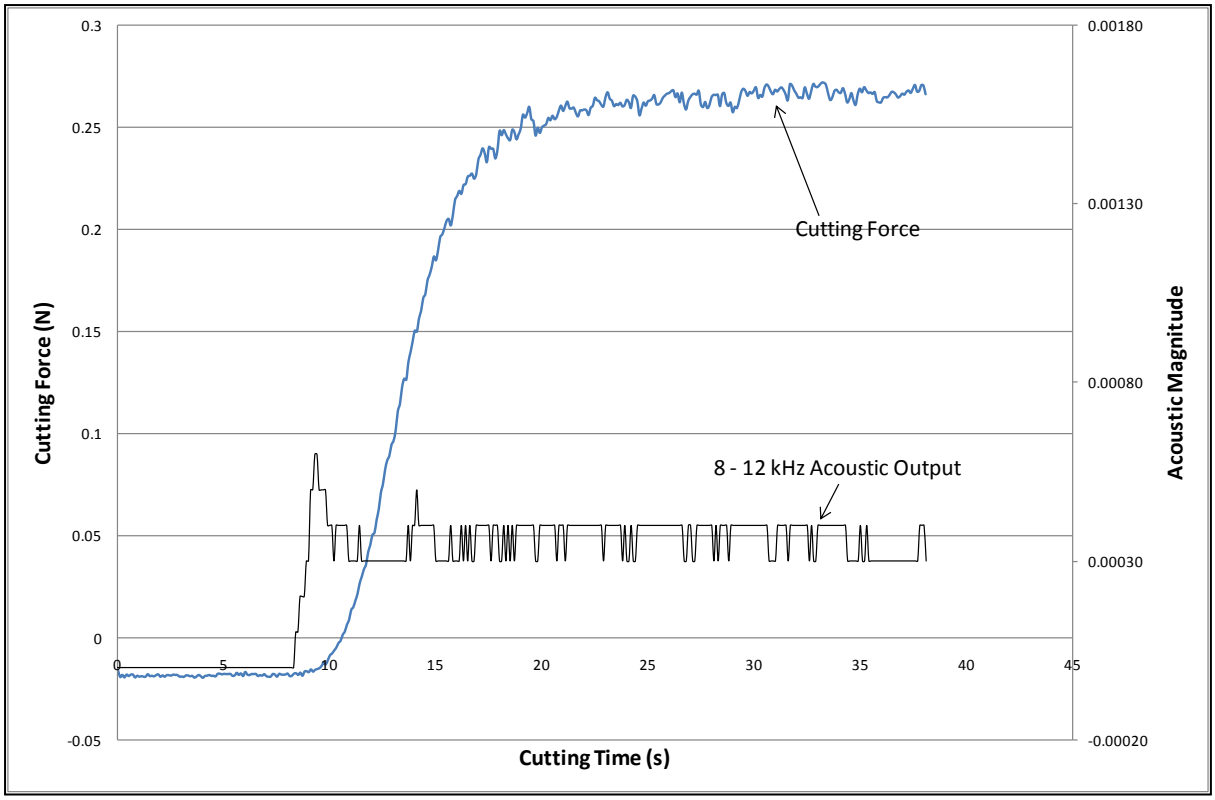

Figure 171: Acoustic Output and Cutting Force for 8 – 12 kHz band (XPS, wire cutting, 30mm, 7A, and 0.0183ms^{-1})

As for the 1 – 4 kHz band, the value of the acoustic output in the vapourised region in the 4 – 12 kHz band was constant, and increased markedly when thermomechanical cutting began to take place. In this frequency band, the acoustic recording had zero magnitude in the vapourised region. Unlike the 1 – 4 kHz band, in the 4 – 12 kHz band the output in the vapourised region was consistent for all possible combinations of tool type, engaged length, cutting conditions and foam type. Regardless of the exact values of the input parameters, the vapourised cutting region always exhibited no acoustic output above background noise, with a substantial and discernable increase in output at the beginning of the thermomechanical cutting region. This is a very useful result, because an adaptive-current control system essentially only needs to be able to identify the point at which thermomechanical cutting starts. It is this point that the loadcell in the current force-feedback control system is used to identify. In the 4 – 12 kHz acoustic output band, any acoustic output measured above the background noise indicates that thermomechanical cutting is taking place, so the current step could be applied as soon as such an output is detected. Since the characteristic output in the vapourised region is independent of the parameters of the cut, a single current-control rule can be applied to all cutting strategies, which greatly simplifies the requirements of the control system.

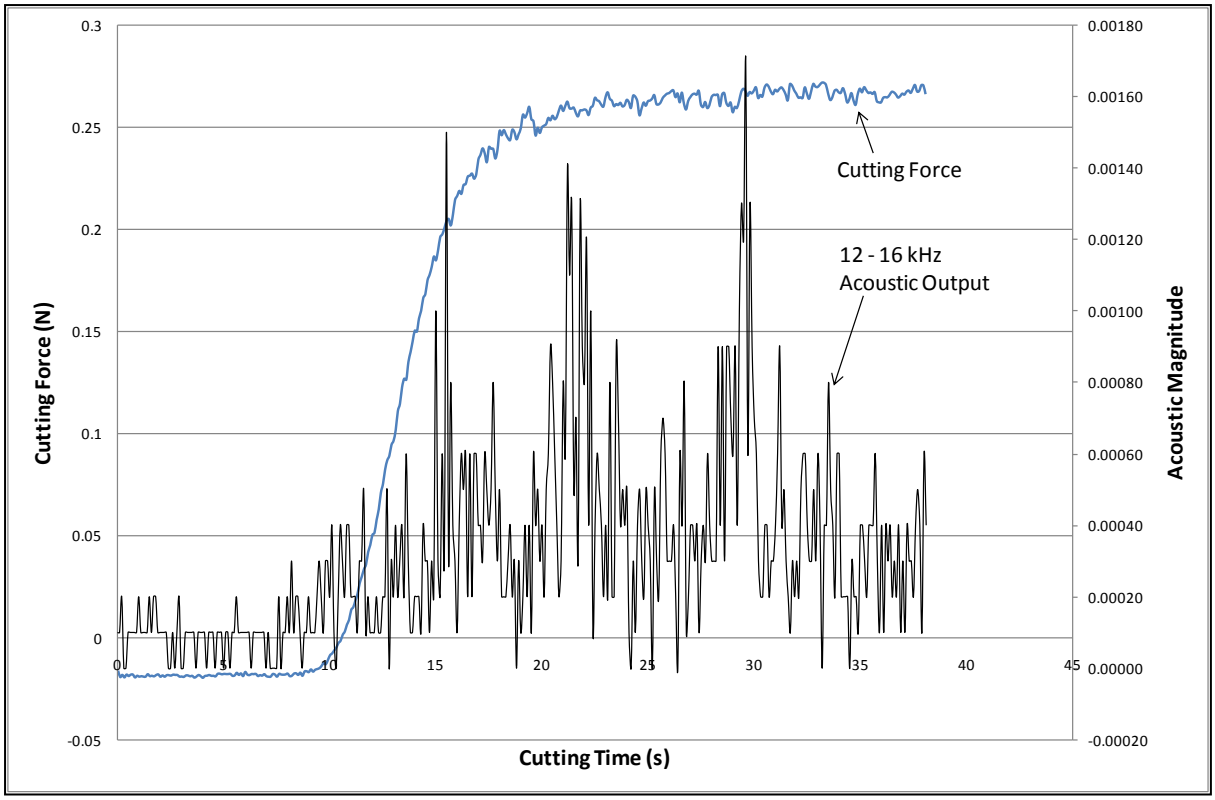

Figure 172: Acoustic Output and Cutting Force for 12 - 16 kHz band (XPS, wire cutting, 30mm, 7A, and 0.0183ms^{-1})

The behaviour of the acoustic signal in the 12 – 16 kHz band was much less consistent than behaviour in the lower frequency bands, as shown in Figure 172. For all cutting stages, the signal was very variable, and especially so in the thermomechanical cutting region. The magnitude of the acoustic output in this frequency band in thermomechanical cutting can vary from more than 0.00175 to zero within the space of three data points, or 0.3s. In the vapourised-cutting region the variation is smaller, lying between zero and 0.00020, but the data is still unpredictable. As such, it seems likely that the 12 – 16 kHz band can be ruled out as a potentially useful acoustic trigger signal, since there is no consistency, repeatability or predictability in the results.

As noted above, the magnitude of the acoustic output was proportional to the cutting force. It is also true that, for a given cut, the mean and peak acoustic magnitudes were larger for higher frequency bands. This suggests that the acoustic output measured in the higher frequency bands is mostly a result of the mechanical component of thermomechanical cutting, while the acoustic output resulting from the thermal component is mostly (but not entirely) present in the lower frequency bands examined. This can be confirmed by comparing Figure 169 with Figure 172. These are both charts of the same cut, but show different frequency bands. The change in the 1 – 4 kHz band as the cutting force increases is a relatively small 0.00040, while the 12 – 16 kHz band has a maximum change of 0.00170.

The behaviour exhibited by the acoustic output with increasing effective heat input Q_{eff} is shown by Figure 173 to Figure 175, which show the acoustic output in the 4 – 8 kHz band for three cuts made with a feedrate of 0.0167ms^{-1} in 30mm XPS with increasing supplied current, and therefore increasing Q_{eff}. As can clearly be seen, at relatively low effective heat input (Figure 173), the acoustic output in steady-state conditions settles at an average value of about 0.00090, while at relatively high effective heat input (Figure 175) the acoustic output settles at an average value of 0.00030. The acoustic output for an intermediate value of effective heat input has a steady-state value between these two extreme cases. It can also be observed that the steady-state acoustic output exhibits significantly more variability and noise at low values of Q_{eff} than it does at high effective heat input.

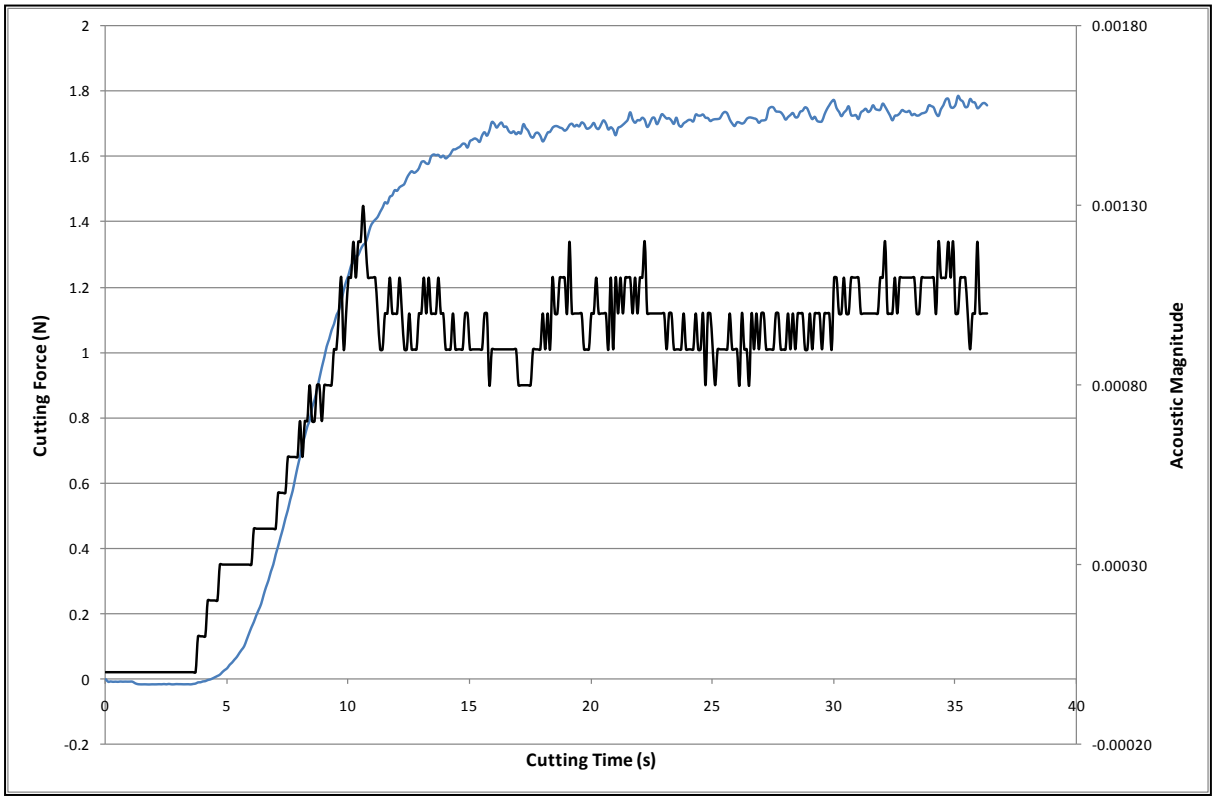

Figure 173: Acoustic output and cutting force for 5A, 0.0167ms^{-1}, 30mm XPS, 4 - 8 kHz band

Since these graphs are all of the 4 – 8 kHz band, they confirm the observation made above that the acoustic output above background in this band and the 8 – 12 kHz band is zero-valued during vapourised cutting, has a positive non-zero value when thermomechanical cutting is taking place, and that the step change in the acoustic output reliably occurs at the transition from vapourised to thermomechanical cutting.

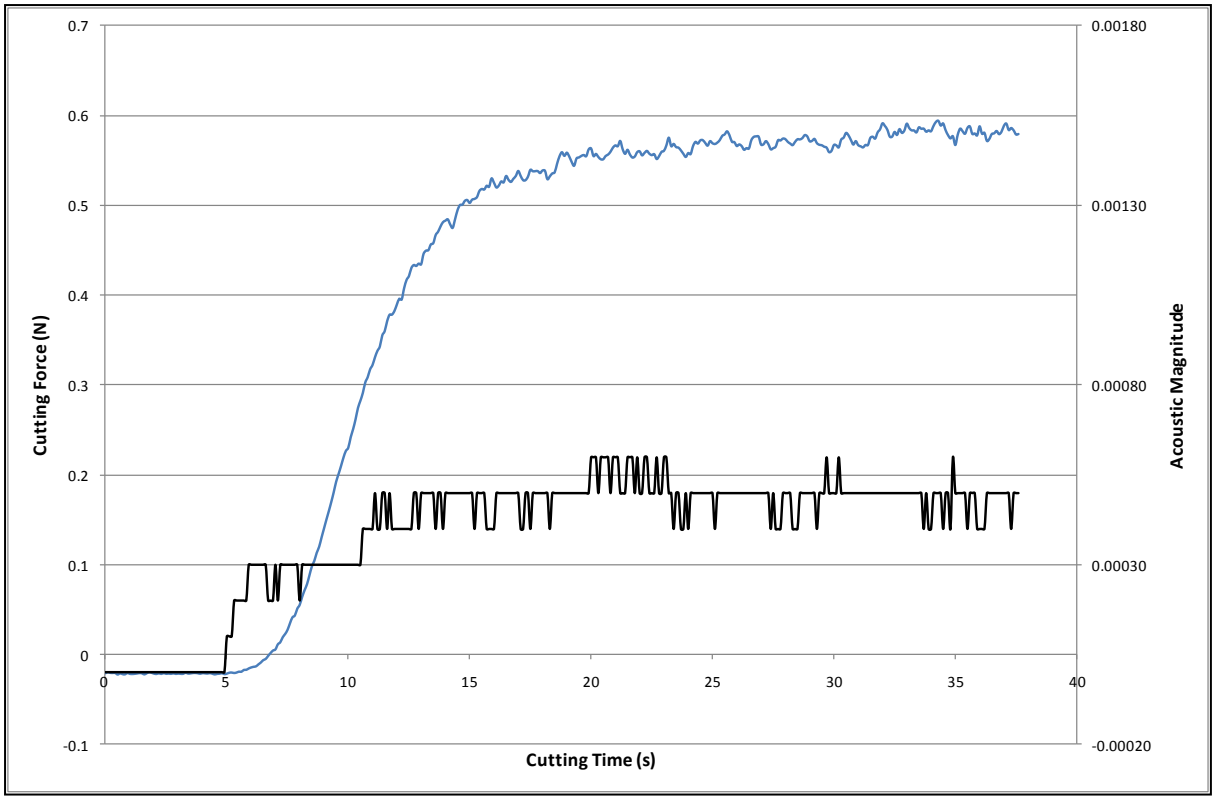

Figure 174: Acoustic output and cutting force for 6A, 0.0167ms^{-1}, 30mm XPS, 4 - 8 kHz band

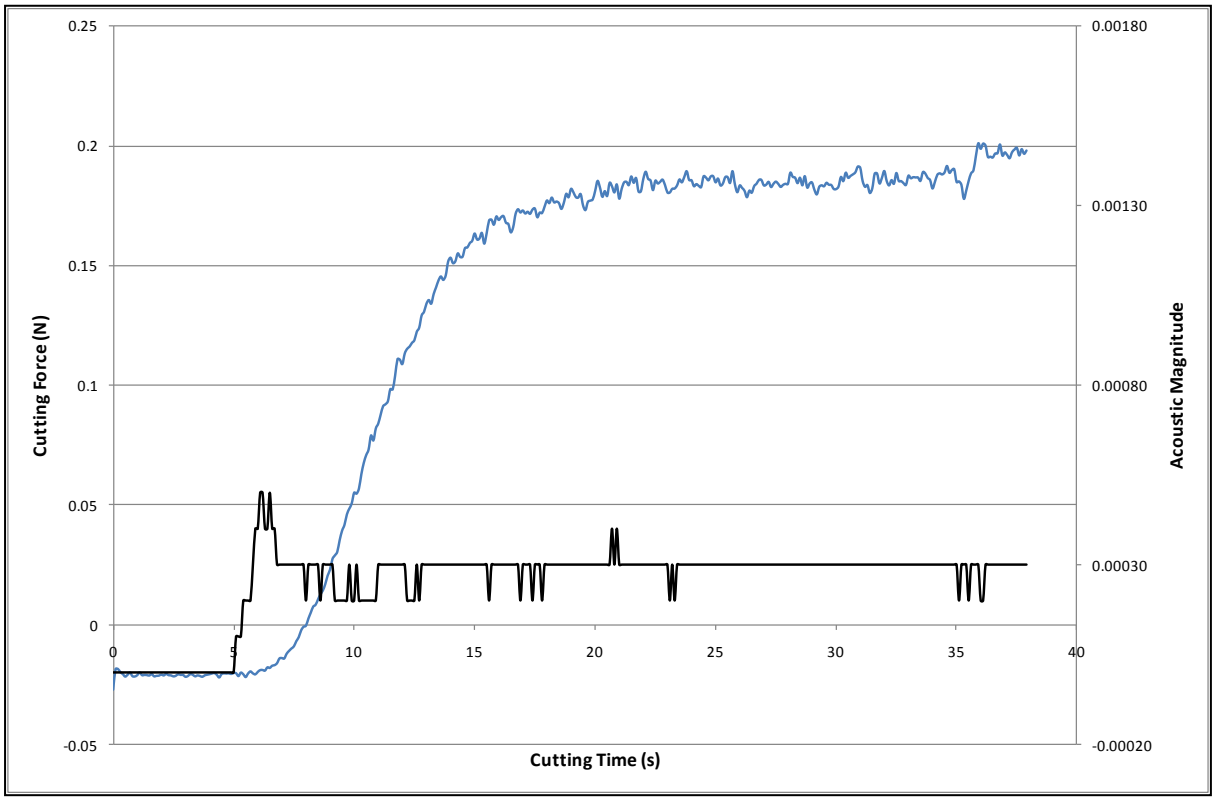

Figure 175: Acoustic output and cutting force for 7A, 0.0167ms^{-1}, 30mm XPS, 4 - 8 kHz band

7.4 Discussion and Conclusions

From a practical point of view, to implement an acoustic-feedback current control system for RFS it is only necessary to be able to identify when thermomechanical cutting is taking place from the acoustic output, or in other words to identify the point at which the cutting force begins to increase at the end of the vapourised region. This work has established that the acoustic output is definitely correlated to the cutting force, and there are a number of ways in which an acoustic-feedback control system could be implemented. Any or all of the frequency bands examined here could serve as a trigger signal for adaptive current control, but some are more suitable than others and the exact trigger signal used in practice will depend on the nature of the control system and sensors available. The 12 – 16 kHz band has the greatest magnitude of acoustic output, and therefore may be the easiest frequency band to measure. However, the very variable nature of the acoustic signal in this band at all stages of cutting will probably substantially increase the complexity of the control rule required to differentiate the separate cutting stages, because there are no clear and stable acoustic signals associated with the vapourised and thermomechanical cutting stages across all cutting conditions and tool types.

In the lower frequency bands, there are stable and reliable acoustic characteristics of this type. As noted above, the 1 – 4 kHz band has a value of 0.00020 when in the vapourised cutting zone, for all sets of cutting conditions, all engaged lengths, and all tool types. I should be noted that despite the large number of decimal places used for these acoustic magnitude readings, the sounds they are referring to are easily discernable by both the human ear and the acoustic data analyser. The 4 – 8 kHz and 8 – 12 kHz bands also have a stable level during vapourised cutting regardless of conditions, engaged length and tool type: there is no acoustic output in these frequency bands during vapourised cutting. These three frequency bands also exhibit substantially lower levels of variability during thermomechanical cutting than the 12 – 16 kHz band. The acoustic output magnitudes for vapourised cutting are summarised in Table 28.

Table 28: Summary of Vapourised-Cutting Acoustic Outputs for different Frequency Bands, Tools and Materials

Frequency Band (kHz)	**Material and Tool Type**			
	XPS, Wire	**XPS, Blade**	**EPS, Wire**	**EPS, Blade**
1 – 4	0.00020	0.00020	0.00010 / 0.00020	0.00010 / 0.00020
4 – 8	Zero	Zero	Zero	Zero
8 – 12	Zero	Zero	Zero	Zero
12 – 16	Inconsistent	Inconsistent	Inconsistent	Inconsistent

Based on the characteristic patterns of acoustic output that have been observed, it seems likely that the best trigger signal for acoustic-feedback current control will be the acoustic output in the 4 – 12 kHz band. The 1 – 4 kHz band would be suitable, with the current step being triggered whenever the acoustic reading is greater than 0.00020. However, in this band the relative size of the increase in acoustic output is relatively small in this frequency band, and the vapourised-cutting value of acoustic output is not consistent for both types of foam. In the 4 – 12 kHz band (made up of the examined 4 – 8 kHz and 8 – 12 kHz bands, which exhibited the same behaviour), the higher current level would be triggered whenever the acoustic output magnitude in this frequency band was greater than zero. Additionally, using the 4 – 12 kHz frequency band as the trigger signal means that a wider input range can be used which should also simplify the acoustic-feedback current control system.

At the beginning of this investigation three hypotheses were developed. These were based on qualitative observation of the acoustic output during hot-tool cutting of polystyrene, and on the results of the preliminary scoping investigation, and in order for the acoustic output to be a useful control signal for controlled-current cutting all three of these hypotheses had to be verified. The hypotheses were:

1. That the acoustic output was proportional to the cutting force and the cutting mode during the cutting process and higher cutting forces would result in larger acoustic outputs.
2. That the acoustic output would have a greater magnitude for cutting of XPS foam than EPS foam, since the cutting forces when cutting XPS are higher, which is believed to be due to the more regular cellular structure of the foam.
3. That the acoustic output would have a greater magnitude for larger values of l_e, the engaged tool length, since the cutting force is proportional to the engaged length.

From the investigation discussed above, it was concluded that all three of these hypotheses were correct and had been verified. The acoustic output during hot-tool cutting exhibited clear proportionality to the cutting force and to the cutting mode, and higher acoustic outputs were associated with higher cutting forces. Cutting of XPS foam did produce higher average acoustic outputs than cutting of EPS, and longer engaged lengths (which are associated with higher cutting forces) did result in larger acoustic magnitude than shorter engaged lengths.

Based on this work, it was possible to conclude that the acoustic output of hot-tool cutting was a potentially useful trigger signal for a feedback current control system. The acoustic output is clearly related to the cutting force and cutting mode, is consistent, is repeatable, and is predictable for certain frequency bands. The most useful of the potential trigger signals considered is likely to be the acoustic output between 4 and 12 kHz. In this frequency range, there is no acoustic output above background during vapourised cutting, but as soon as there is a mechanical component to the cutting process the acoustic output increases to a positive, non-zero value within 0.1s. This means that a current control system could be implemented to apply the required step change in current as soon as an acoustic output in this frequency band is detected.

A current control system using a real time acoustic output measurement as the control signal (in place of a cutting force reading) can now be developed based on this research. Such a system would not suffer from the system configuration issues inherent in the force-feedback control system currently in place on the RFS system. Since the only sensor required will be a microphone, this can easily be mounted on the robot along with the cutting tool, so with such a system the robot would be able to move the tool rather than the workpart without impairing the function of the current control system.

While an acoustic-feedback current control system has not at this stage been implemented, a few general comments can be made regarding the nature and configuration of such a system. In principle it would be similar to the force-feedback current control system already implemented, with the only difference being the in the nature of the triggering input. The key feature of an acoustic-feedback control system would be the input device, a microphone, which would ideally be positioned as close as possible to the cut itself. As such, it would most likely be mounted directly onto the tool, a sufficient distance from the cutting element that it would not interfere with the cut itself. In addition, another microphone would be positioned in the workcell some distance from the robot itself, to gather background noise data. The outputs from these two microphones would be fed into a computer which could subtract one from the other to give a net reading of the acoustic output resulting solely from the cutting process. It is possible that a filtering process would need to be applied to this data to remove occasional extraneous background noise spikes that could cause confusion for the control system.

Once this reading of the acoustic data resulting from the thermomechanical cutting process has been produced (and the reading should be generated in as close to real-time as possible) then the output in the 4 – 12 kHz band can be monitored by software. When an acoustic output in this frequency band is detected, a signal would be sent to the power supply used to supply current to the tool, and the appropriate current step would be applied. When acoustic output in the 4 – 12 kHz band ceased (indicating the end of thermomechanical cutting, which would in practice correlate with the end of all cutting) another signal could be sent to the power supply instructing it to step the current back down to the starting value in preparation for the next cut.

The exact nature of the physical equipment necessary to implement an acoustic-feedback control system will vary depending on the power supply used and the exact electrical properties of the cutting tool elements. In addition, the type of microphones and the nature of filtering systems required will depend on the environment in which the RFS system is being operated at the time of implementation. For example, if the robot is operating in a workcell that can be acoustically insulated, then there will be less need to filter out extraneous external noise than if there is no acoustic insulation surrounding the workcell. Such detailed questions can be considered when a detailed design of an acoustic-output control system is being undertaken, and this work can proceed now that the usefulness of the acoustic output as a control signal has been validated.

The research reported in this chapter has been published as [71]. A copy of this paper can be found in Appendix C.

7.5 Limitations and Future Work

Although this work on the acoustic output of hot-tool cutting of polystyrene foam produced very good results and shows great promise as a trigger signal for an acoustic-feedback current control system, there are some limitations to the research and valuable work remains to be carried out in the future.

The most significant limitation is that, although the acoustic output has been shown to be a valid trigger signal for current control, this has not been validated by implementation. Time constraints prevented the construction of an acoustic-feedback current control system based on the outcomes of this research, so it is not possible to present cutting trial results demonstrating that an acoustic-output current control system works. That said, the underlying research required to identify an appropriate trigger signal has been undertaken and there is no apparent reason why an acoustic-feedback control system would not work as well as the force-feedback control system.

8 Discussions and Conclusions

This thesis has presented the results of a thorough investigation undertaken into the cutting strategy of robotic foam sculpting, with particular emphasis being focused on the relationships between controllable cutting strategy parameters and the quality of the sculpted surfaces produced. The findings of this research are generally applicable to hot-tool cutting of polystyrene foam, but are of particular relevance to the RFS system being developed at the University of Canterbury.

The investigation covered the following specific topics:

- The assessment of existing foam-based rapid prototyping systems and the associated understanding of surface texture found in the published literature.
- Identification of the parameters that influence the quality of surfaces produced by hot-tool cutting and mapping of the relationships and interactions between these parameters.
- Development of a suitable method for measuring the primary surface texture of polystyrene foam surfaces, characterisation of those surfaces based on the cutting mode, development of a suitable parameter for expressing the surface texture of foam, and the development of a mathematical model capable of predicting the surface texture based on input cutting conditions.
- Investigation of the parameters affecting the surface quality and geometric form in single-pass hot-tool cutting, especially with respect to kerfwidth and surface barrelling, and the development of mathematical models to predict values of these parameters based on input cutting conditions.
- Investigation of the parameters affecting the surface quality and geometric form in multi-pass hot-tool cutting using both square-nose and round-nose tools, and the development of mathematical models to predict values of the appropriate surface quality parameters based on input cutting conditions.
- The development of models for the cutting force in hot-tool cutting, to enable the force to be predicted for a given cutting strategy to achieve optimum tool life.
- Empirical investigation of the acoustic output of hot-tool cutting of polystyrene foam to assess the suitability of the acoustic output as a trigger signal for controlled-current cutting.

This research has made a significant contribution to the understanding of Robotic Foam Sculpting cutting strategy and more generally of hot-tool cutting of polystyrene foam. It has also systematically explored the effects of the cutting strategy on the output surface quality. In this chapter, the outcomes of the research are summarised and assessed against the research objectives outlined in the introduction. In addition, the limitations of the research undertaken are discussed and some recommendations for future work are presented. Finally, the novel intellectual contributions of this research are outlined.

8.1 Summary of Results

This research into the cutting strategy and surface quality of robotic foam sculpting achieved a wide range of results that have significantly advanced the understanding of how the hot-tool cutting process works and how the achieved surface quality is determined. The scope of the research work has ranged widely, from mapping the interactions between input and output cutting strategy parameters through to the development of new measurement systems and metrics for assessing the quality of foam surfaces.

In this section, the most significant results of the research are summarised and briefly discussed. For clarity, these summaries are broken down into separate subsections for each key research area.

8.1.1 Cutting Strategy Factor Interactions and Dependencies

One major outcome of this research is that the key parameters that were relevant to the cutting strategy were identified, and the relationships between these parameters defined and mapped. The relevant parameters fell into one of three categories: the user-controllable input parameters, the output parameters used to measure the surface quality, and the intermediate parameters that influenced the value of dependent outputs but could not be directly controlled by the process planner in the same way that the input parameters could be.

The relationships between all of these parameters were mapped and have been presented earlier as cause-and-effect diagrams. The mapping of these relationships was based on statistical analysis of the data sets produced by the experiments used to investigate each specific surface quality output and on observation and qualitative assessment of the cuts and the cut surfaces produced during these experiments. This resulted in the relationship maps mentioned above, and in most cases on statistical models that provide a mathematical expression of the relationship between input parameters and output metrics. These models allow the prediction of the expected value of a given surface quality metric based on the cutting strategy used, or the selection of a cutting strategy to achieve a desired surface quality. As such, they are very powerful tools that can help to achieve an optimised cutting strategy for sculpting a given part with the RFS system. However, this does not mean that the cutting strategy is easy to optimise, since the surface quality output metrics are not independent of each other.

One of the key results of the relationship mapping research was the finding that in many cases the same input and intermediate cutting strategy parameters keep recurring as significant parameters influencing multiple dependent output metrics. In other words, any one of these recurring parameters influences several surface aspects of surface quality. As a result, if one of these recurring parameters is adjusted to achieve a desired value of a specific output metric, then this will in turn change the value of any other parameter that is dependent on the input parameter being changed.

This result is summarised in Table 29. This table presents the same data that is contained in the cause-and-effect diagrams for each surface quality metric, but reverses the emphasis. Instead of

presenting the relevant input parameters for each separate output metric, the table lists the controllable input parameters and the intermediate parameters, and then lists all the surface quality outputs that are in some way dependent on those input and intermediate parameters.

Table 29: Summary of the Output Cutting Strategy Metrics dependent on Controllable and Intermediate Strategy Parameters

Controllable Parameter	**Intermediate Parameter**	**Dependent Outputs**
Tool Type		Surface Texture, Kerfwidth, Surface Barrelling ΔH, $R_{max,\ thermomechanical}$, $R_{max,\ geometric}$, Cutting Force
Material		Surface Texture, Kerfwidth, Surface Barrelling ΔH, $R_{max,\ thermomechanical}$, $R_{max,\ geometric}$, Cutting Force
Supplied Current	Effective Heat Input, Q_{eff}	Surface Texture, Kerfwidth, Surface Barrelling ΔH, $R_{max,\ thermomechanical}$, Cutting Force
Tool Feedrate		
	Distance along cut	Surface Texture, Kerfwidth, Surface Barrelling ΔH, $R_{max,\ thermomechanical}$
Path Spacing		$R_{max,\ geometric}$, Peak Spacing, $R_{max,\ thermomechanical}$, Cutting Force
	Engaged Tool Length	Kerfwidth, Surface Barrelling ΔH, $R_{max,\ thermomechanical}$, Cutting Force

As becomes clear from examination of this table, changes to an input parameter to fine-tune a given output parameter cannot be made in isolation. It is also necessary to consider the effect that these changes have on other surface output metrics, and to assess whether those effects are significant. The key conclusion that can be drawn from this is that the selection of the most appropriate cutting strategy for sculpting a given part is not a trivial problem, and requires an optimisation process. The process maps and statistical models developed during this research provide a very useful and reliable body of underlying knowledge that this optimisation work can be based on.

8.1.2 Surface Texture of Polystyrene Foam

The detailed investigation of the surface texture of foam surfaces produced by hot-tool cutting has contributed significantly to the understanding of the nature of these surfaces and the most suitable method of measuring and defining them. The first significant problem that had to be resolved to conduct this investigation was the identification of an appropriate and available instrument for the measurement of surface texture. After consideration of a range of instruments it was concluded that a suitable system had to use non-contact data capture to avoid damaging the surface being measured, and eventually a process was developed that used a confocal microscope to capture data about the relative heights and distribution of surface features. A Matlab script was developed to process this data into numerical surface texture parameters. The parameters used to evaluate the surface texture initially were all standard texture parameters like R_a and S_a.

Experimental investigation of the factors of significance for the surface texture concluded that standard parameters based solely on the relative heights of surface features were of limited use for assessing foam surface texture. Parameters of this type were of some use for assessing surfaces that had been produced using vapourised cutting, but even in this limited case it was not possible to develop an accurate statistical model of the surface textures based on input cutting strategy conditions. Height-based texture parameters were of no use whatsoever for surfaces that had been produced by thermomechanical cutting, since these surfaces are produced in part by smearing of molten foam along the surface by the cutting tool. From these results, it was concluded that the height of surface features on foam surfaces was strongly correlated with the size of the cells in the foam, and that height-based texture parameters were not suitable metrics for the texture of foam surfaces.

Despite this, it was still desirable to have a numerical parameter for expressing the surface texture and for statistical analysis, so a new parameter was developed. This parameter was called the 10%-Height Contiguous Diameter (denoted by ${}^{\varnothing}S_{10\%}$) and was based on both the vertical and horizontal distributions of the surface features. ${}^{\varnothing}S_{10\%}$ proved to be a very useful parameter for communicating the nature of foam surfaces, and was capable of discriminating between thermally-cut and thermomechanically-cut surfaces. Most importantly, ${}^{\varnothing}S_{10\%}$ could be used for all surfaces, regardless of the cutting mode used to produce them.

Using the 10%-Height Contiguous Diameter, it was possible to produce statistical regression models that allowed the prediction of stead-state ${}^{\varnothing}S_{10\%}$ based on the effective heat input Q_{eff}. These models had very good conformance between predicted and measured data, with R^2 values of 0.95 and 0.98 for hot-wire cutting and hot-blade cutting, respectively. These models are presented in Table 30. The units of ${}^{\varnothing}S_{10\%}$ are millimetres and the units of Q_{eff} are Joules per square meter. With these models, it is possible to predict the surface texture to be expected from a given effective heat input, or to choose an effective heat input that can be expected to achieve a desired surface texture. If force-feedback current control was used during cutting, then the steady-state surface texture was maintained along the entire length of the cut.

Table 30: Statistical models for predicting the steady-state surface texture based on effective heat input

Property	Model		R^2
Texture, ${}^{ø}S_{10\%}$ (mm)	${}^{ø}S_{10\%,\ wire} = -(7x10^{-5})Q_{eff} + 0.3087$	(12)	0.95
	${}^{ø}S_{10\%,\ blade} = -(8x10^{-6})Q_{eff} + 0.3592$	(13)	0.98

To relate the measured values of the 10%-Height Contiguous Diameter to the qualitative surface texture categories previously used for assessing foam surface texture, threshold values of ${}^{ø}S_{10\%}$ were defined that marked the (fairly arbitrary) boundaries between the vapourised and smooth surface categories, and between the smooth and visually disturbed surface categories. These thresholds are shown in Table 31.

Table 31: ${}^{ø}S_{10\%}$ thresholds for each surface category

Category	${}^{ø}S_{10\%}$ Values (mm)
Vapourised	< 0.120
Smooth	0.120 – 0.210
Visually Disturbed	> 0.210

The investigation into the foam surface texture made a significant contribution to the existing body of knowledge on the nature of cutting strategy for hot-tool foam cutting. It must be noted that this work is not in any way restricted to the RFS system, but can be applied in any case where polystyrene foam is being cut by hot tools. The key conclusions of this research were:

- That the surface texture of foam cut by hot-tools is a function of the effective heat input, material, thermomechanical balance and distance along the cut.
- That surface texture parameters based solely on the relative heights of surface features were not suitable for the measurement of foam surfaces.
- That the new parameter 10%-Height Contiguous Diameter allowed accurate, repeatable and useful measurements of foam surface texture.

8.1.3 Cutting Strategy for Single-Pass Cutting

The cutting strategy and its influence on the output surface quality in single-pass cutting were thoroughly investigated. This investigation built upon the results of earlier kerf research but was much

more comprehensive, covering more foam types, a wider range of cutting conditions and considering the engaged tool length. The two key surface errors in single-pass cutting were identified as the kerfwidth, λ, and the surface barrelling, ΔH, both of which had units of mm. This investigation also determined that the input parameters that affected these two surface outputs were the effective heat input, the engaged tool length, the distance along the cut, the material, the thermomechanical balance and the tool type.

In order to develop a quantitative understanding of the cutting strategy in single-pass cutting, a measurement procedure had to be developed to facilitate the measurement of the surface errors. The procedure used was based on producing foam samples using a double-cut cutting strategy to provide symmetric samples with a virtual datum through the centre, and then manually sectioning these samples and scanning the sections with a flatbed scanner to produce high-resolution colour images of the samples cross-sections. These images were then processed with Matlab to evaluate the kerfwidth and surface barrelling for each sample.

Using the data sets produced by the experiment, statistical analyses of both the kerfwidth and the barrelling were carried out. The kerfwidth analysis established statistical models for the initial kerf, the steady-state kerf and the transition kerf that had high R^2 values indicating a good conformance between the models and the measured data. The least accurate models were the models for the transition kerf.

Of these kerfwidth models, the most useful were the initial kerf and steady-state kerf models, since these can be used to greatly increase the capability of the existing force-feedback current control system implemented on the RFS system. One of the major drawbacks of this control system was that it could only be implemented for a small number of cutting conditions, where it was known that the kerf for the initial cutting conditions would be the same as the kerf for the final cutting conditions. The initial and steady-state kerf models developed during this investigation allow much more fine-tuned selection of cutting conditions. For a given steady-state effective heat input and engaged length, the expected kerf can be calculated. This expected kerf and the known engaged length can then be used in the appropriate initial-kerf model to determine what initial power input (i.e. current) is needed to achieve an initial kerf equal to the expected steady-state kerf. The equivalent-kerf cutting conditions determined in this way can then be programmed in to the force-feedback current control system. As a result of this work, feedback current control is no longer limited to use with a few discrete sets of cutting conditions, but can be applied to any cutting conditions within the operational space of the RFS system. The statistical models for the kerfwidth are summarised in Table 32.

Table 32: Summary of statistical models developed for the kerfwidth in single-pass cutting

Property	Model		R^2
Kerf, λ (mm)	$^{initial}\lambda_{xps,\ wire} = 0.484409i - 0.008267l_e + 0.077863$	(17)	0.98
	$^{initial}\lambda_{eps,\ wire} = 0.406749i - 0.008004l_e + 0.043864$	(18)	0.97
	$^{steady\text{-}state}\lambda_{xps,\ wire} = (5.905\text{x}10^{-4})Q_{eff} + (7.194\text{x}10^{-3})l_e + 0.0675$	(19)	0.92
	$^{steady\text{-}state}\lambda_{eps,\ wire} = (1.488\text{x}10^{-3})Q_{eff} + (1.260\text{x}10^{-2})l_e - 0.9050$	(20)	0.92
	$^{initial}\lambda_{xps,\ blade} = 0.135073i + 0.006857l_e - 0.886744$	(21)	0.89
	$^{initial}\lambda_{eps,\ blade} = 0.094433i + 0.008436l_e - 0.359689$	(22)	0.95
	$^{steady\text{-}state}\lambda_{xps,\ blade} = (4.689\text{x}10^{-5})Q_{eff} - (7.452\text{x}10^{-3})l_e + 0.3909$	(23)	0.99
	$^{steady\text{-}state}\lambda_{eps,\ blade} = (5.946\text{x}10^{-5})Q_{eff} - (1.652\text{x}10^{-2})l_e + 0.8480$	(24)	0.86

The nature of the surface barrelling in single-pass cutting was also within the scope of this investigation, but the results of this part of the study were much less conclusive. There were indications that the surface barrelling was proportional to the tool temperature differential ΔH, but there were also strong indications that the barrelling at least to some extent inversely proportional to the temperature differential. No solid conclusions could be drawn regarding the nature and causes of this surface quality output metric, and further investigation in this area would be appropriate. At present a tentative map of the dependencies between strategy conditions that influence the barrelling has been established, but this will in all likelihood have to be revised when further research in this area is undertaken.

The steady-state cutting force was also investigated during the single-pass cutting strategy investigation. It was found that the maximum measured cutting force for a given cut was a function of the effective heat input Q_{eff} and the engaged tool length, l_e. Further, it was found that the cutting force could be accurately modelled as an exponential function of effective heat input, and that models of this form had very high R^2 values. The models produced for hot-wire and hot-blade cutting of XPS and EPS foams are summarised in Table 33.

Table 33: Summary of cutting force models developed for single-pass cutting

Property	Model		R^2
Cutting Force, F (N)	$F_{xps,\ wire} = 0.415156 l_e e^{(-0.003Qeff)} - 0.159992$	(31)	0.99
	$F_{eps,\ wire} = 1.0998 l_e e^{(-0.005Qeff)} + 0.4162$	(32)	0.91
	$F_{xps,\ blade} = 0.48525 l_e e^{(-0.0003Qeff)} + 0.02874$	(33)	0.98
	$F_{eps,\ blade} = 0.58121 l_e e^{(-0.0003Qeff)} + 0.42289$	(34)	0.95

These models allowed the prediction of the cutting force that can be expected for a given single-pass cutting strategy (and it was found in the multi-pass investigation that the cutting force models developed for single-pass cutting remained valid when used for multi-pass cutting). Predictions of the cutting force are useful for developing a cutting strategy because the cutting force has a significant influence on the tool life and the likelihood of tool failure, since tool durability is determined by the cutting strategy.

8.1.4 Cutting Strategy for Multi-Pass Cutting

An investigation into the cutting strategy for multi-pass cutting with RFS was also undertaken, to characterise and quantify the surface errors resulting from different cutting strategies. This investigation identified the two most significant errors in multi-pass cutting, explored the cutting mechanics that cause those surface errors and developed models that allowed the errors to be predicted based on input cutting conditions. Two tool types were used for the investigation, square-nose and round-nose. The selection of an appropriate tool depends on the type of surface being sculpted, but generally speaking round-nose tools are of most use for sculpting surfaces with significant concave curvature.

The two significant surface quality metrics in multi-pass cutting were found to be the maximum vertical deviation between the highest and lowest points on a surface, R_{max}, and the peak spacing. R_{max} was essentially a result of lay, and so was technically a surface texture error, but due to the size of the features relative to the primary surface texture it was treated separately as a geometric error. Peak spacing was essentially a function of the path spacing (S_p) used to sculpt the surface.

These multi-pass surface errors were found to be caused by several different sources of error that confounded each other and resulted in distinct components of error that were superimposed to make the total surface error. The following sources of error were found to be relevant:

- Geometric error resulting from the tool shape, tool size, nominal surface curvature and path spacing.

- Thermomechanical error resulting from the thermomechanical cutting process. This can be further subdivided into:
    - Thermomechanical error resulting from the kerf around the tool
    - Thermomechanical error resulting from the thermal gradient along the engaged length
- There was also potential for robot positional or orientation error to be introduced into the surfaces being sculpted, but for this thesis experimental designs and surface quality metrics were chosen to minimise the effects of any such errors.

This study concluded that, while it was a relatively simple matter to separate the geometric and thermomechanical components of the surface error, it was much more difficult to separate the confounded effects of kerf and thermal gradient. It was also found that the significance of the kerf and thermal gradient, and the relationship between these sources of error and the net surface error, were influenced by the path spacing and tool size being used, and by the behaviour of the foam when cut by hot-tools. Path spacing and tool size were found to be significant because, if the path spacing was significantly less than the tool size, and therefore if some of the unengaged length of the tool was passing over already-established surface peaks, these peaks were ablated and resulted in a smaller total surface error than if the peaks were not re-ablated by subsequent tool passes. The behaviour of the foam was significant because the structure of the material is altered by hot-tool cutting. When a heated tool passes through foam, the surface produced has a heat affected zone of higher-density unfoamed polystyrene adjacent to the surface, which is more resistant to melting than unmodified bulk material. This HAZ can result in larger R_{max} deviations and in undercutting under the surface peaks.

Table 34: Statistical models for the steady-state R_{max} surface error with square-nose tools

Model	R^2
$^{Steady\text{-}state}R_{max,xps} = 0.0272541i - 4.2964059f + 0.0024307^{Rel}S_p + 0.0013234l_e + 0.184215$ (77)	0.85
$^{Steady\text{-}state}R_{max,eps} = 0.0264009i - 3.8627453f + 0.0017336^{Rel}S_p + 0.0004843l_e + 0.2309475$ (78)	0.82

The investigation of the surface error resulting from round-nose multi-pass cutting found that the geometric component of these errors was generally far more significant than the thermomechanical component, and that at values of path spacing that were low relative to the tool diameter a round-nose tool behaved in a fashion similar to a square-nose tool, with the magnitude of the surface error being exacerbated by the heat affected zone.

Predictive models for the surface error in round-nose multi-pass cutting were developed, for the cases where path spacing was less than the blade diameter and where path spacing was equal to the blade diameter. These models are presented in Table 35 and Table 36.

Table 35: Statistical models for the surface error in round-nose multi-pass cutting when path spacing is less than blade diameter

Model (for path spacing < blade ø)		R^2
$^{initial}R_{max} = 0.02063ø + 0.22447S_p + 4.74550f - 0.01874i - 0.40731$	(79)	0.9534
$^{Steady}R_{max} = 0.016017ø + 0.211600S_p + 5.540956f - 0.018288i - 0.583983$	(80)	0.9658

Table 36: Statistical models for the surface error in round-nose multi-pass cutting when path spacing is equal to blade diameter

Model (for path spacing = blade ø)		R^2
$^{Initial}R_{max} = 0.2185ø + 0.4318S_p + 5.045f - 0.00007102i - 6.216$	(81)	0.9953
$^{Steady}R_{max} = 0.10807ø + 0.49327S_p + 10.24266f + 0.01435i - 5.98916$	(82)	0.9952

This study also concluded that the peak spacing of the final sculpted surface was almost entirely a function of geometric factors. Thermomechanical factors did result in some deviation between the peak spacing predicted from geometric factors, but the degree of this deviation was negligible compared to the expected geometric peak spacing. As such, it was decided that the thermomechanical effect on peak spacing could be ignored and that the as-cut peak spacing could be predicted based solely on geometric factors. In many cases, this simply meant that the peak spacing was equal to the path spacing used to sculpt the surface.

The cutting force in multi-pass cutting was also considered by this investigation. The measured steady-state cutting forces being compared to the values predicted by the single-pass cutting force models with appropriate values of effective heat input and engaged length. It was expected that the models would provide accurate predictions of the multi-pass cutting force, since the basic nature of the cutting process is the same, even though multi-pass tools are shaped rather than straight blades. This was found to be the case, with the correlation between the measured and predicted cutting forces being 0.97 for cuts made in XPS foam and 0.98 for cuts made in EPS foam. This means that the cutting force models developed for single-pass cutting can be reliably used to predict the cutting force in multi-pass cutting, and therefore to design a cutting strategy that will not result in tool failure, although some further work is required before this capability is achieved.

8.1.5 Acoustic Output Characterisation

The most significant remaining drawback of the force-feedback current control system (after the development of predictive models for kerf in the single-pass strategy investigation) was the need for a

loadcell to provide measurements of cutting force to use as a trigger signal for the current step applied at the end of the vapourised cutting region. During cutting trials it was noticed that the sound made by the cutting process varied along the cut and sounded like it might be related to the cutting force, so an investigation into the acoustic output of hot-tool cutting was carried out to determine whether the sound of cutting could be used as a trigger signal for current control. A literature survey carried out on this subject indicated that there was no published work on the acoustic behaviour of hot-tool cutting.

This investigation found that the acoustic output was very strongly correlated with the cutting force and the engaged length, and that the acoustic output was more measurable for XPS foam than it was for EPS. It was also found that, by and large, the acoustic output signal was quite noisy: it was surmised that this was the result of local variations in the cutting process due to the cellular nature of the foam. Further, it was found that the acoustic output was consistent and repeatable, so as long as sound could be used to identify the transition from vapourised cutting to thermomechanical cutting the acoustic output would be a very useful potential trigger signal.

The most significant conclusion of this research was that, in the frequency band from 4 – 12 kHz, there was no acoustic output above background noise when vapourisation was the cutting mode, but that as soon as there was a mechanical component to the cutting the acoustic output in this frequency band became positive and non-zero. The exact magnitude of the acoustic output for this frequency band varied depending on the cutting force, but without exception the output was positive and non-zero. This finding was true for all the combinations of cutting conditions, tool types and foams used in the investigation.

This result provided a very useful and very simple potential trigger signal for an acoustic-feedback current control system (although such a system has yet to be implemented, see section 8.4). During a controlled-current cut, the current step can be applied as soon as any positive non-zero reading above background was recorded in the 4 – 12 kHz frequency band, since this acoustic signal was reliably associated with the transition from vapourised to thermomechanical cutting. This was determined to be a better trigger signal than the cutting force, since it could be reliably measured while the tool was mounted on the robot and since the acoustic signal underwent a step change at the vapourised-thermomechanical transition, unlike the cutting force which initially had a very small rate of change at the beginning of mechanical cutting. As a result, the acoustic output was able to reliably identify the transition point more easily than the cutting force.

8.2 Conclusions

At the start of the research that forms the basis for this thesis, the cutting strategy of Robotic Foam Sculpting was only very poorly understood. This resulted in significant limitations to the capability of the RFS system. The fundamental limitations included:

- The lack of any quantitative understanding of the surface texture being produced by thermal plastic foam cutting, the lack of a suitable means of measuring the foam texture, and the lack of detailed understanding of the factors that affected the surface texture.
- The lack of a quantitative understanding of the macroscopic surface form errors present in surfaces that were cut using single-pass and multi-pass tools, and the lack of detailed understanding of the factors that influence these errors of form.
- The lack of a comprehensive model of the inter-relationships between input cutting conditions and the output surface quality (surface texture and errors of form) of the cut surface.

These limitations meant that anyone planning to use RFS to sculpt a given part, or designing a part that will be sculpted, had no knowledge to guide them in the selection of tool feedrate, applied current, tool types, tool sizes, material, path spacing and path orientation. Production planners and design engineers had no idea how to design parts in such a way that they can be easily made with RFS, for example by avoiding surface curvatures that cannot be accurately sculpted. Finally, for a given set of cutting conditions the production planner has no idea what sort of surface quality (surface texture and surface accuracy) could be expected, and no mechanism to select cutting conditions based on desired surface quality. The purpose of this research was to develop an understanding of the cutting strategy and its effect on surface quality that could be used to select an appropriate cutting strategy to achieve a desired surface quality, or to predict the expected surface quality based on the cutting strategy. The fundamental goal was to develop a set of quantitative, evidence-based tools that could be used to develop an optimised cutting strategy for sculpting a given part with the RFS system. The goals of this research were embodied in a set of fundamental questions for which answers were required (section 1.2). These questions were:

1. What elements of cutting strategy have an effect on the surface quality of parts produced from polystyrene foam using hot tools?
2. What are the most significant surface errors that must be considered when choosing a cutting strategy for a given part?
3. How can the surface errors be measured accurately?
4. Is it possible to develop models that allow the prediction of the value of a given type of surface error based on input cutting strategy conditions?
5. Is there an alternative output metric that can be used as a trigger signal for controlled-current cutting, in place of the cutting force used at present?

The vision for this research was that it would produce a set of tools that could be used to configure the cutting strategy to achieve a desired level of surface quality, and to optimise the cutting strategy to achieve the best possible surface quality in the minimum possible time, while considering other factors such as tool life.

To a very significant degree, these research objectives have been met, and answers have been determined for all of the fundamental research questions. The research reported in this thesis has achieved the following outcomes.

- The key parameters that constitute the cutting strategy and the surface quality have been identified, and the relationships and interactions between these parameters have been mapped.
- A detailed investigation has been carried out into the nature of the surface texture and the most appropriate methods of measuring and expressing it. This investigation resulted in the development of a new surface texture parameter that reliably and consistently expresses the nature of the surface texture, and allows the selection of cutting conditions to achieve a desired texture on the sculpted surface.
- A detailed investigation of the cutting strategy in single-pass cutting as been carried out. This resulted in the identification of the most significant errors on surfaces cut with single-pass cutting, the development of mathematical models that allowed the reliable prediction of the steady-state and initial kerf based on cutting strategy conditions, and a fuller understanding of the nature of the surface barrelling error (although more work in this area is necessary to allow the reliable prediction of surface barrelling). Models were also developed for the steady-state cutting force in single-pass cutting with different tools and foams.
- A detailed investigation of the cutting strategy in multi-pass cutting, which identified the nature of the significant surface errors and developed a detailed understanding of the processes within the cut that cause these errors. This investigation also resulted in statistical models that allow the prediction of the steady-state errors based on the cutting strategy, and postulated a technique that could allow the elimination of multi-pass surface error (at least in square-nose cutting). It was also confirmed that the cutting force models developed for single-pass cutting could be used to accurately predict the cutting force in multi-pass cutting.
- The acoustic output of hot-tool cutting of polystyrene foam has been identified as a new and potentially valuable trigger signal for a current control system, and the acoustic output for different cutting strategies and cutting modes has been characterised.

Viewed as a whole, the research underlying this thesis can be considered a success. A detailed and quantitative understanding of the effects of cutting strategy on surface quality is now available for the use of anyone who wants to sculpt a part with Robotic Foam Sculpting. There is now a quantitative understanding of the relationships between all the cutting strategy parameters and the output surface quality metrics, the causes of each of the significant surface errors have been identified, and mathematical models are available that can predict the expected magnitude of different surface errors based on the cutting strategy conditions.

However, this research does still have significant limitations that need to be resolved before the understanding of cutting strategy can be said to be complete. These limitations, and recommendations for future work, can be found in section 8.4, below.

8.3 Novel Contributions of This Research

The research reported in this thesis has covered a significant range of different aspects of the cutting strategy and output surface quality of hot-tool cutting of polystyrene foam, and has significantly advanced the understanding of the cutting process within the Robotic Foam Sculpting research group. The key novel contributions of this research include:

- Mapping of the factor interactions and dependencies that as a whole constitute the cutting strategy. This has involved identifying the relationships between a wide range of input factors and the output surface quality metrics, as well as identifying the significant surface errors. As a result of this research, a thorough understanding of the causes of the total surface error on a given sculpted part is available for the first time. Previous research has been limited to only some of the surface errors present, to only steady-state errors, or to errors that could only be assessed qualitatively.
- Development of a technique for the measurement of polystyrene foam surface texture using confocal microscopy.
- Development of a new surface texture parameter (the 10%-Height Contiguous Diameter, ${}^{ø}S_{10\%}$, which is capable of distinguishing between the different types of primary surfaces produced by hot-tool cutting of foam and identifying the varying degrees of mechanical cutting action along the length of the cut.
- A thorough investigation of the relationships between the cutting strategy and the kerfwidth in single-pass cutting, and the development of models to allow the prediction of steady-state and initial kerf based on cutting strategy conditions.
- An investigation of the relationships between the cutting strategy and the surface errors in multi-pass cutting, which achieved a detailed understanding of the causes of the surface errors and developed statistical models capable of predicting the surface errors from the cutting strategy conditions.
- The development of a quantitative understanding of the surface errors and the relationships between these errors and the input cutting strategy parameters, and the development from this of a set of tools that can be used to determine the optimum cutting strategy for sculpting a given part using the RFS system.
- A new and novel method of controlling the cutting conditions based on a real-time reading of the acoustic output of the cutting process has been postulated, and research has been undertaken to determine aspects of the acoustic output that can be used as a trigger signal. It was found that any acoustic output in the 4 – 12 kHz band indicated the presence of thermomechanical cutting, and so the presence of acoustic readings in this band can be used to trigger the current step associated with feedback current control.

8.4 Limitations and Future Research

Although the research presented in this thesis has made a significant contribution to the understanding of cutting strategy for robotic foam sculpting, and provides a very valuable set of tools

for the selection of an appropriate cutting strategy for sculpting a given part, there are still a number of limitations to this research that should be addressed in future research work. These limitations and recommendations for future research are summarised in this section.

8.4.1 Limitations of This Research

The research reported in this thesis has significantly advanced the understanding of cutting strategy for hot-tool cutting and its effect on the quality of the surfaces produced. However, there are significant limitations to the research that need to be rectified to obtain a complete understanding of the cutting strategy and surface quality. The most significant of these limitations are outlined below:

- The surface texture investigation was restricted to only a single type of foam (XPS) and a relatively small number of samples. A further investigation should be carried out into the surface texture of EPS foam, and more samples should be measured around the transition from vapourised to smooth surfaces to refine the threshold value defined earlier.
- The investigation of surface barrelling in single-pass cutting was inconclusive and incomplete. More work should be undertaken to develop a model that can predict the surface barrelling based on cutting strategy.
- The postulated method of reducing or eliminating the lay in square-nose multi-pass cutting by applying an angular offset to the tool has not actually been tested. There do not appear to be any obstacles to the success of this technique, but it does need to be practically validated.
- A real-time feedback current control system based on the acoustic output of the cut has not yet been implemented.

8.4.2 Recommendations for Future Research

The RFS system is far from being a commercially practical system, and a significant amount of further research is required before it can be commercialised. This section contains recommendations for future research and development. Some of these recommendations are intended to correct limitations of this research and complete the understanding of cutting strategy developed here, while others are more general recommendations based on an assessment of the limitations of the RFS system.

The key areas items of beneficial further research are as follows:

- Gather information on the behaviour of the yield stress of the nichrome tool material at different temperatures, so that the critical cutting force for different cutting strategies can be calculated and compared to the predicted cutting force, to aid in avoiding strategies that will result in tool failure.
- Conduct a wider surface texture investigation including EPS foam and with more samples around the vapourised to smooth transition.
- Test and validate the angular-offset method of reducing the lay in square-nose multi-pass cutting.
- Implement an acoustic-feedback current control system.

- Conduct a more comprehensive investigation of the nature of surface barrelling in single-pass cutting, with more data gathered, to develop a model for the prediction of this surface error.
- Develop an expert system or CAM package that uses the understanding of cutting strategy developed here, and the future research outlined above, to semi-automate the selection of an appropriate cutting strategy for RFS, and calculates things like the sculpting time.
- Conduct research to identify a wider range of foam materials that would be suitable for use in the RFS system.
- Expand the range of tools available for use in the RFS system. In particular, tools capable of drilling and plunge cutting operations, and capable of cutting pockets and undercuts, would be very useful. Tools using ultrasonic excitation could also be developed to achieve good surface finishes with lower energy input.
- Further research into workholding. For example, if the workpart could be spun during sculpting then operations analogous to turning could be used to shape desired parts. This would also require research into aspects of work holding like sculpting orientation optimisation.
- Some research should be carried out into the ecological implications of using polystyrene foam as a prototyping and manufacturing material. Polystyrene foam is a non-biodegradable material, and waste material spends years taking up space in landfills, so it would be desirable to have alternative, more ecologically-friendly materials. It is possible that a bio-foam could be developed for use in RFS, and research should be carried out in this area to develop a list of characteristics that would be desirable in such a foam.

References

1. Brooks, H., *Plastic Foam Cutting Mechanics for Rapid Prototyping and Manufacturing Purposes*, in *Department of Mechanical Engineering*. 2009, University of Canterbury: Christchurch. p. 165.
2. Lawrence, L.L., *Expanded Polystyrene Craft*. 1974: Sir Isaac Pitman and Sons Ltd.
3. Products, D. *Hobby and Craft*. 2011 [cited 2011 March 2011]; Available from: http://www.demandproducts.com/Hobby-and-Craft-items/.
4. Products, D. *Jobcut 4 ft Hot Wire Foam Cutter*. 2011 [cited 2011 February 2011]; Available from: http://www.demandproducts.com/Themeing-and-3D-Props-items/item.php?l2=4,16,33&sku=GROUPJOBCUT.
5. Products, D. *Themeing and 3D Props*. 2011 [cited 2011 February 2011]; Available from: http://www.demandproducts.com/Themeing-and-3D-Props-items/search.php?l1=4,16.
6. Megaplot. *Foam Cutters*. 2011 [cited 2011 March 2011]; Available from: http://www.foamcutter.pl/index.php?s=fcutt.
7. Posthuma, A., *Development of a Novel Robotically Effected Plastic Foam Sculpting System for Rapid Prototyping and Manufacturing*, in *Department of Mechanical Engineering*. 2007, University of Canterbury: Christchurch. p. 120.
8. Groover, M.P., *Automation, Production Systems and Computer-Aided Manufacturing*. 2001: Prentice-Hall, Inc. 856.
9. Kandula, R., *Implementation of a Multiple Axis Robot as an Autonomous Rapid Prototyping Facility*, in *Mechanical Engineering Department*. 2006, University of Canterbury.
10. Aitchison, D.R., T.S. Germann, and M. Taylor. *Sculpting of Expanded Foam Plastics for Rapid Prototyping Applications*. in *Virtual Modelling and Rapid Manufacturing*. 2005. Leiria, Portugal.
11. Aitchison, D., et al., *Feed-rate, temperature and feed-force relationships for foam plastics cut by a taut hot-wire*, in *ICOMAST2006: International Conference on Manufacturing Science and Technology*. 2006: Melaka, Malaysia.
12. Aitchison, D. and R. Sulaiman, *Determining the surface form of polystyrene through the coordinate measurement machine.* Proceedings of the Institution of Mechanical Engineers, Part C: Journal of Mechanical Engineering Science, 2003. **217**(7): p. 839-844.
13. Aitchison, D. and R. Sulaiman. *Cutting expanded polystyrene: Feed-rate and temperature effects on surface roughness*. in *IASTED International Conference Modelling, Simulation and Optimisation*. 2003. Banff, Alta., Canada: Int. Assoc. of Science and Technology for Development.
14. Aitchison, D. and R. Sulaiman, *A new adaptable rapid prototyping & manufacturing approach for producing a variety of foam-based product solutions*, in *NordDesign 2004 - Product Design in Changing Environment*. 2004: Tampere, Finland.
15. Aitchison, D., et al., *An investigation into the prediction of optimal machining conditions for polystyrene foam cut with a taut hot-wire*, in *International Conference New Technologies in Manufacturing*. 2009: Galati, Romania.
16. Ahn, D.G., S.H. Lee, and D.Y. Yang, *A study on the influence of the sloped cutting angle on kerfwidth and part quality in the hotwire cutting of EPS foam for the VLM-s rapid prototyping process.* International Journal of Machine Tools & Manufacture, 2003. **43**(14): p. 1447-64.
17. Bain, J., et al., *Robotic Foam Sculpting: Final Year Project Report*. 2006, University of Canterbury. p. 48.
18. Taylor, M.G., D.R. Aitchison, and A.J. Posthuma, *Semi-automated Robotic Sculpting of Freeform Surfaces for Direct Digital Manufacture*, in *International Conference on Mechanical and Manufacturing Engineering (ICME2008)*. 2008: Malaysia.
19. Brooks, H.L. and D.R. Aitchison, *Force feedback temperature control for hot-tool plastic foam cutting.* Proceedings of the Institution of Mechanical Engineers, Part B: Journal of Engineering Manufacture. **224**(5): p. 709-719.
20. Hope, R.L., P.A. Jacobs, and R.N. Roth, *Rapid Prototyping with sloping surfaces.* Rapid Prototyping Journal, 1997. **3**: p. 12 - 19.
21. Hope, R.L., A.T. Riek, and R.N. Roth. *Layer building with sloping edges for rapid prototyping of large objects*. 1996. Nottingham, UK: Univ. Nottingham.

22. Ahn, D.G., et al., *Development and Design of variable lamination manufacturing (VLM) process by using expandable polystyrene foam.* Proceedings of the Korean Society of Precision Engineering, 2000: p. 719 - 762.
23. Ahn, D.G., H.S. Lee, and D.Y. Yang, *Investigation into development of progressive-type variable lamination manfacturing using expandable polystyrene foam and its apparatus.* Proceedings of the I MECH E Part B Journal of Engineering Manufacture, 2002. **216**: p. 1239 - 1252.
24. Ahn, D.G., H.S. Lee, and D.Y. Yang, *Development of transfer-type variable lamination manufacturing (VLM-) process.* International Journal of Machine Tools and Manufacture, 2003. **43**: p. 1447 - 1464.
25. Ahn, D.G., S.H. Lee, and D.Y. Yang, *Investigation into thermal characteristics of linear hotwire cutting system for variable lamination manufacturing (VLM) process by using expandable polystyrene foam.* International Journal of Machine Tools and Manufacture, 2002. **42**(4): p. 427-439.
26. Ahn, D.-G., S.H. Lee, and D.-Y. Yang, *Mechanical properties and anisotropy of expanded polystyrene foam sheet for the VLM-S rapid prototyping process.* Journal of Materials Science Letters, 2002. **21**(9): p. 747-749.
27. Lee, S.H., D.G. Ahn, and D.Y. Yang. *Surface reconstruction for mid-slice generation on variable lamination manufacturing*. 2002. Switzerland: Elsevier.
28. Menix Engineering Co, L., *Rapid Shaper http:/www.rapidshaper.com*. 2008.
29. Ahn, D.G., S.H. Lee, and D.Y. Yang, *Influence of process parameters on the surface roughness in hotwire cutting of EPS foam sheet for VLM-S rapid prototyping process.* Journal of Materials Science, 2005. **40**: p. 5699 - 5702.
30. Broek, J., J. , et al., *Survey of the State of Art in Thick Layered Manufacturing of Large Objects and the Presentation of a Newly Developed System*. 1998.
31. De Smit, B., et al., *Experimental results on the application of FF-TLOM technology for the creation of a large freeform shape*, in *Proceedings of the 2nd Annual Conference with International Participation on Rapid Technologies*. 2001. p. 93 - 101.
32. Lennings, A.F., et al., *Prototyping large-sized objects using freeform thick layers of plastic foam*, in *Proceedings of the Solid Free Fabrication Symposium*. 1998. p. 97 - 104.
33. Broek, J.J., A. Kooijman, and H. Rademacher, *Exploration of flexible blade curvature for free form thick layered object manufacturing*, in *Proceedings of the TMCE 2004*. 2004: Lausanne, Switzerland. p. 707 - 718.
34. Kooijman, A. and J.J. Broek. *Improving minimum strain energy curve calculations for flexible blade cutting*. 2006. Piscataway, NJ, USA: IEEE.
35. Horvath, I., et al., *Tool profile and tool path calculation for free-form thick layered fabrication.* Computer Aided Design, 1998. **30**(14): p. 1097-110.
36. De Smit, B., et al. *Developing a Tool for the Direct Cutting of Freeform Surfaces out of Extruded Polystyrene Foam*. in *Euro-u Rapid 2002 Conference*. 2002.
37. Broek, J.J., et al., *Free-form thick layer object manufacturing technology for large-sized physical models.* Automation in Construction, 2002. **11**(3): p. 335-47.
38. De Smit, B., et al., *Implementation of the freeform thick layered object manufacturing technology (FF-TLOM), a status review*, in *Proceedings of the Ninth European Conference on Rapid prototyping and manufacturing*. 2000. p. 311 – 321.
39. De Smit, B., J. Broek, and I. Horvath. *Experimental Investigation Of Factors Influential For The Flexible Blade Based Prototyping Process*. in *The 1999 ASME Design Engineering Technical Conference*. 1999. Las Vegas, Nevada, USA: ASME.
40. De Smit, B., et al., *Tool- and Process Control Issues relating to the use of a Flexible Cutting Tool*, in *CIRP International Design Seminar*, H. Kals and F. van Houten, Editors. 1999, Kluwer Academic Publishers: University of Twente, The Netherlands. p. 405 - 414.
41. Kim, H.C., S.H. Lee, and D.Y. Yang, *Toolpath planning algorithm for the ablation process using energy sources.* CAD Computer Aided Design, 2009. **41**(1): p. 59-64.
42. Kim, H.C., S.H. Lee, and D.Y. Yang, *A study of tool design for minimization of heat-affected zone in rapid heat ablation process.* Journal of Materials Processing Technology, 2007. **187-188**: p. 51-55.
43. Kim, H.C., et al., *A study on thermal characteristics of non-contact hot-tool for rapid feature detailing (RFD) process.* International Journal of Machine Tools and Manufacture, 2005. **45**(3): p. 345-353.

44. Kim, H.C., S.H. Lee, and D.Y. Yang, *Development of a rapid heat ablation (RHA) process using a hot tool.* International Journal of Machine Tools and Manufacture, 2007. **47**(1): p. 124-132.
45. Zhu, J., et al. *An 8-axis robot based rough cutting system for surface sculpturing*. in *11th International Conference on Precision Engineering (11th ICPE)*. 2006. Tokyo, Japan: .
46. Tanaka, T. and Y. Saito, *On the mechanism of the hot wire cutting of polystyrene foam (cutting characteristics of the dwelling wire).* Nihon Kikai Gakkai Ronbunshu, C Hen/Transactions of the Japan Society of Mechanical Engineers, Part C, 2006. **72**(10): p. 3383-3389.
47. Jouaneh, M., A. Hammad, and P. Datseris, *Flexible automated foam cutting system.* International Journal of Machine Tools and Manufacture, 1997. **37**(4): p. 437-449.
48. Hamade, R.F., et al., *Modelangelo: a subtractive 5-axis robotic arm for rapid prototyping.* Robotics and Computer-Integrated Manufacturing, 2005. **21**(2): p. 133-44.
49. Croma, *"Foam Processing Technologies"* http://www.croma-foamcutter.com/default.aspx. 18/10/2010.
50. Sun, K., et al., *Influence of process parameters on surface roughness in rapid manufacturing for expandable polystyrene pattern.* Journal of Xi'an Jiaotong University, 2007. **41**(3): p. 344-7.
51. British Standards Institution, *Manual of British Standards in Engineering Metrology*. 1984, London: Hutchinson Publishing Group. 235.
52. British Standards Institution, *Centre-Line Average Method for the Assessment of Surface Texture (B.S.1134:1961)*. 1961: British Standards Institution.
53. Zygo. *MetroPro Surface Texture Parameters*. 2010 [cited 2010 8 October 2010]; Available from: http://www.zygo.com/library/papers/SurfText.pdf.
54. Veeco. *Surface Measurement Parameters for Wyko Optical Profilers*. 2010 [cited 2010 8 October 2010]; Available from: http://www.veeco.com/pdfs/appnotes/AN505-Surface_05083_63.pdf.
55. Whitehouse, D., *Surfaces and their Measurement*. 1 ed. Vol. 1. 2002, London: Kogan Page Science. 371.
56. Griffiths, B., *Manufacturing Surface Technology: Surface Integrity and Functional Performance*. 2001: Penton Press. 237.
57. Blateyron, F., *A Revolution in 3-D Surface Metrology.* Quality, 2007. **46**(10): p. B8.
58. Lange, D.A., H.M. Jennings, and S.P. Shah, *Analysis of surface roughness using confocal microscopy.* Journal of Materials Science, 1993. **28**(14): p. 3879-84.
59. Al-Shammery, H.A.O., et al., *The use of confocal microscopy to assess surface roughness of two milled CAD-CAM ceramics following two polishing techniques.* Dental Materials, 2007. **23**(6): p. 736-741.
60. Brigitte Forster, D.V.D.V., Jesse Berent, Daniel Sage, Michael Unser, *Complex wavelets for extended depth-of-field: A new method for the fusion of multichannel microscopy images.* Microscopy Research and Technique, 2004. **65**(1-2): p. 33-42.
61. Montgomery, D.C., *Design and analysis of experiments*. 5th ed. 2001, New York: John Wiley. xii, 684 p.
62. Mendenhall, W., *Introduction to Probability and Statistics*. 1983: PWS Publishers.
63. McClave, J.T., F.H. Dietrich, and T. Sincich, *Statistics*. 1997.
64. Christensen, R., *Analysis of Variance, Design and Regression*. 1996: Chapman and Hall.
65. Lou, M., J. Chen, and C. Li, *Surface Roughness Prediction Technique for CNC End-Milling.* Journal of Industrial Technology, 1998. **15**(1).
66. Thomas, T.R., *Rough Surfaces*. 2 ed. 1999: Imperial College Press. 278.
67. Institution, B.S., *Geometrical product specifications (GPS) - Surface Texture: Areal*, in *Classification of methods for measuring surface texture (ISO 25178)*. 2010.
68. Gallina, P., *Delayed Reference Control for Hotwire Cutting of Expandable Polystyrene Foam.* Journal of Manufacturing Science and Engineering, 2006.
69. Pascutto, P. and P. Gallina, *Improvement of a delayed velocity reference control (DVRC) for machining operations.* International Journal of Machine Tools & Manufacture, 2007. **47**(3-4): p. 496-508.
70. Gallina, P., N. Scuor, and G. Mosetti, *Delayed-reference control (DRC) applied to machining operations.* International Journal of Machine Tools & Manufacture, 2005. **45**(12-13): p. 1386-92.

71. Bain, J., et al., *Acoustic-Feedback Current Control for Thermomechanical Cutting of Polystyrene Foam*, in *NZ Rapid Product Development Conference 2011*. 2011: Auckland, New Zealand.

Appendix A: Surface Texture Assessment Material

Appendix A1: Surface Texture Assessment Parameter Results

Table 1: 10%-Height Contiguous Diameters for Hot-Wire Cutting

Sample #	Feed (ms^{-1})	Current (A)	Distance (mm)	Qeff (J/m^2)	${}^{ø}S_{10\%}$ (mm)
1.1.1	0.0133	5	0	744.94	0.101
1.1.2	0.0133	5	34	744.94	0.148
1.1.3	0.0133	5	94	744.94	0.206
1.1.4	0.0133	5	244	744.94	0.262
1.2.1	0.0133	5	0	744.94	0.097
1.2.2	0.0133	5	34	744.94	0.150
1.2.3	0.0133	5	94	744.94	0.203
1.2.4	0.0133	5	244	744.94	0.263
1.3.1	0.0183	7	0	1097.15	0.091
1.3.2	0.0183	7	34	1097.15	0.124
1.3.3	0.0183	7	94	1097.15	0.162

1.3.4	0.0183	7	244	1097.15	0.217
1.4.1	0.0217	7	0	928.36	0.105
1.4.2	0.0217	7	34	928.36	0.154
1.4.3	0.0217	7	94	928.36	0.174
1.4.4	0.0217	7	244	928.36	0.234
1.5.1	Damaged Sample – no data				
1.5.2	0.0217	7	34	928.36	0.153
1.5.3	0.0217	7	94	928.36	0.167
1.5.4	0.0217	7	244	928.36	0.236
1.6.1	0.0167	5	0	595.95	0.111
1.6.2	0.0167	5	34	595.95	0.148
1.6.3	0.0167	5	94	595.95	0.202
1.6.4	0.0167	5	244	595.95	0.256

1.7.1	0.0200	5	0	496.63	0.107
1.7.2	0.0200	5	34	496.63	0.199
1.7.3	0.0200	5	94	496.63	0.254
1.7.4	0.0200	5	244	496.63	0.274
1.8.1	0.0200	7	0	1005.73	0.114
1.8.2	0.0200	7	34	1005.73	0.137
1.8.3	0.0200	7	94	1005.73	0.185
1.8.4	0.0200	7	244	1005.73	0.237
1.9.1	0.0167	7	0	1206.87	0.110
1.9.2	0.0167	7	34	1206.87	0.124
1.9.3	0.0167	7	94	1206.87	0.162
1.9.4	0.0167	7	244	1206.87	0.211
1.10.1	0.0133	7	0	1508.59	0.131

1.10.2	0.0133	7	34	1508.59	0.151
1.10.3	0.0133	7	94	1508.59	0.189
1.10.4	0.0133	7	244	1508.59	0.206
1.11.1	0.0217	7	0	928.36	0.114
1.11.2	0.0217	7	34	928.36	0.154
1.11.3	0.0217	7	94	928.36	0.204
1.11.4	0.0217	7	244	928.36	0.235
1.12.1	0.0133	8	0	2002.08	0.116
1.12.2	0.0133	8	34	2002.08	0.125
1.12.3	0.0133	8	94	2002.08	0.150
1.12.4	0.0133	8	244	2002.08	0.162
1.13.1	0.0167	8	0	1601.66	0.089
1.13.2	0.0167	8	34	1601.66	0.104

1.13.3	0.0167	8	94	1601.66	0.164
1.13.4	0.0167	8	244	1601.66	0.187
1.14.1	0.0133	5	0	744.94	0.104
1.14.2	0.0133	5	34	744.94	0.137
1.14.3	0.0133	5	94	744.94	0.206
1.14.4	0.0133	5	244	744.94	0.262
1.15.1	0.0200	8	0	1334.72	0.117
1.15.2	0.0200	8	34	1334.72	0.124
1.15.3	0.0200	8	94	1334.72	0.152
1.15.4	0.0200	8	244	1334.72	0.216

Table 2: 10%-Height Contiguous Diameter Values for Hot-Blade Cutting

Sample #	Feed (ms^{-1})	Current (A)	Distance (mm)	Qeff (J/m^2)	${}^{ø}S_{10\%}$ (mm)
5.1.1	0.028	16	0	13604.57	0.088
5.1.2	0.028	16	50	13604.57	0.098
5.1.3	0.028	16	250	13604.57	0.165
5.1.4	0.028	16	400	13604.57	0.201
5.1.5	0.028	16	550	13604.57	0.255
5.2.1	0.028	22	0	25721.14	0.098
5.2.2	0.028	22	50	25721.14	0.135
5.2.3	0.028	22	250	25721.14	0.152
5.2.4	0.028	22	400	25721.14	0.111
5.2.5	0.028	22	550	25721.14	0.157
5.3.1	0.052	16	0	7325.54	0.111
5.3.2	0.052	16	50	7325.54	0.130

5.3.3	0.052	16	250	7325.54	0.213
5.3.4	0.052	16	400	7325.54	0.249
5.3.5	0.052	16	550	7325.54	0.302
5.4.1	0.052	22	0	13849.85	0.094
5.4.2	0.052	22	50	13849.85	0.128
5.4.3	0.052	22	250	13849.85	0.163
5.4.4	0.052	22	400	13849.85	0.194
5.4.5	0.052	22	550	13849.85	0.234
5.5.1	0.04	19	0	13429.20	0.116
5.5.2	0.04	19	50	13429.20	0.143
5.5.3	0.04	19	250	13429.20	0.188
5.5.4	0.04	19	400	13429.20	0.231
5.5.5	0.04	19	550	13429.20	0.252

5.6.1	0.04	19	0	13429.20	0.105
5.6.2	0.04	19	50	13429.20	0.116
5.6.3	0.04	19	250	13429.20	0.170
5.6.4	0.04	19	400	13429.20	0.192
5.6.5	0.04	19	550	13429.20	0.251
5.7.1	0.04	19	0	13429.20	0.104
5.7.2	0.04	19	50	13429.20	0.125
5.7.3	0.04	19	250	13429.20	0.206
5.7.4	0.04	19	400	13429.20	0.247
5.7.5	0.04	19	550	13429.20	0.251
5.8.1	0.075	22	0	9602.56	0.095
5.8.2	0.075	22	50	9602.56	0.124
5.8.3	0.075	22	250	9602.56	0.233

5.8.4	0.075	22	400	9602.56	0.270
5.8.5	0.075	22	550	9602.56	0.291

Appendix A2: Surface Topology Images

Surface Topology Images for Hot-Wire Samples

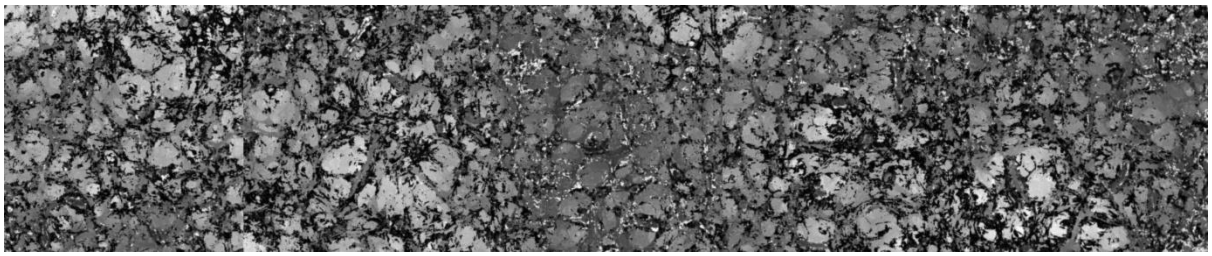

Figure 1: Sample 1.1.1 Surface Topology (5A, 0.0133ms^{-1}, 0mm from start of cut)

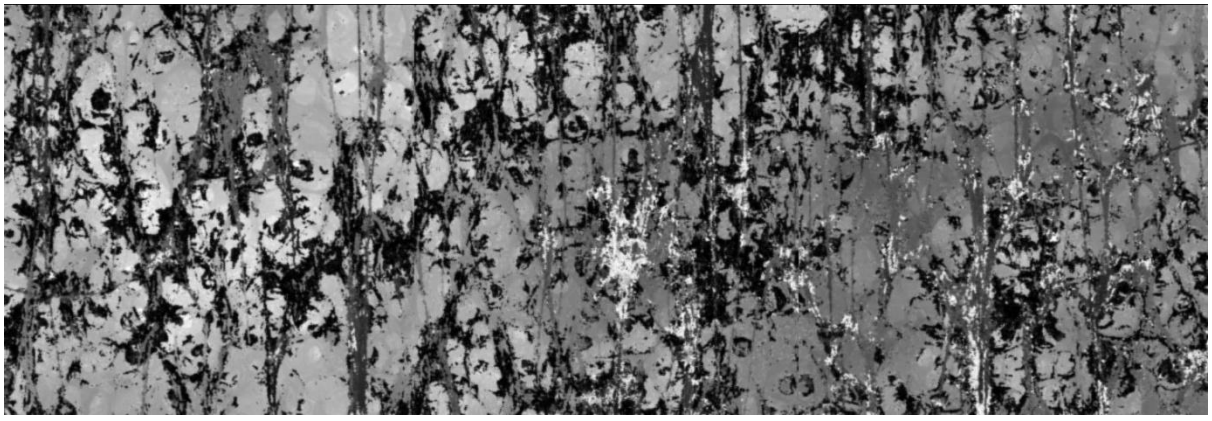

Figure 2: Sample 1.1.2 Surface Topology (5A, 0.0133ms^{-1}, 34mm from start of cut)

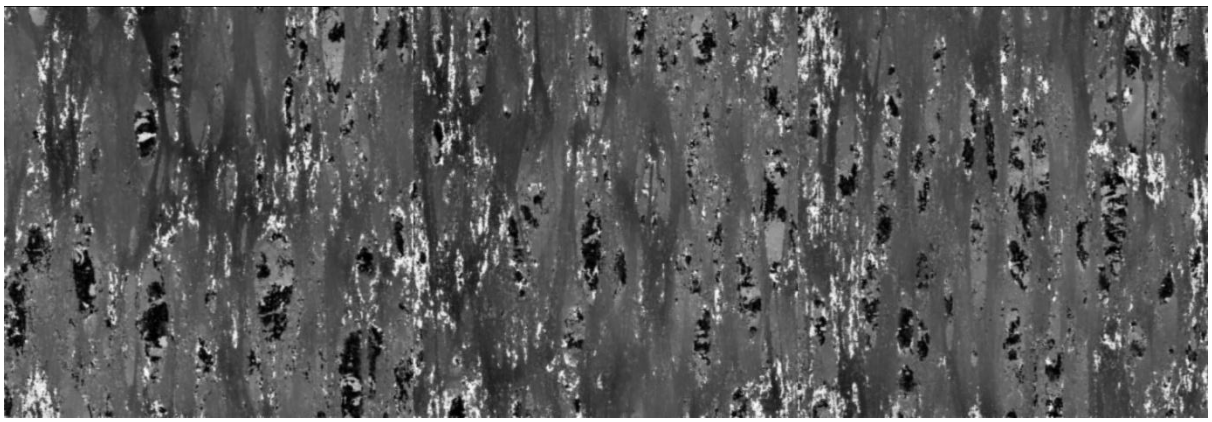

Figure 3: Sample 1.1.3 Surface Topology (5A, 0.0133ms^{-1}, 94mm from start of cut)

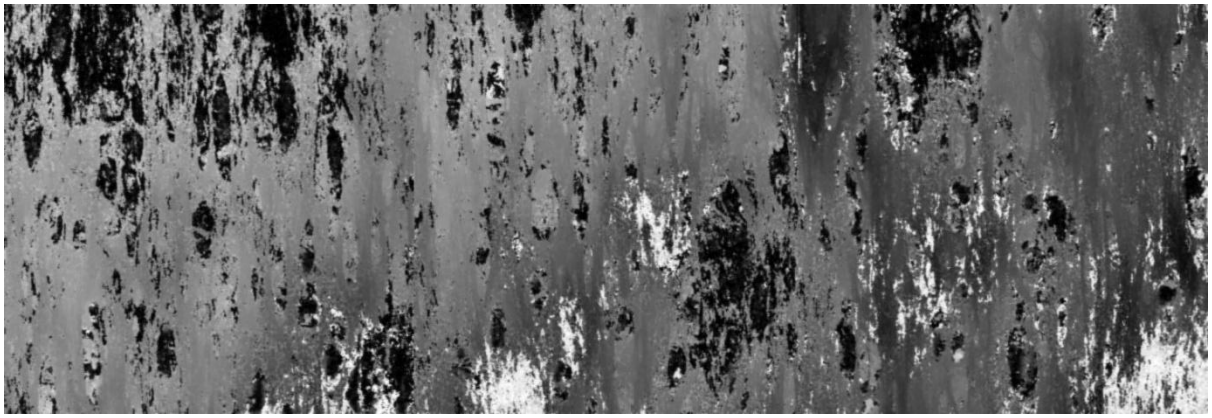

Figure 4: Sample 1.1.4 Surface Topology (5A, 0.0133ms^{-1}, 244mm from start of cut)

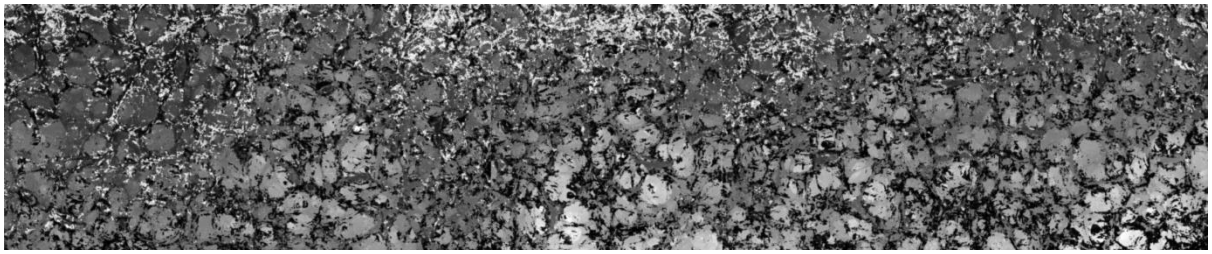

Figure 5: Sample 1.2.1 Surface Topology (5A, 0.0133ms^{-1}, 0mm from start of cut)

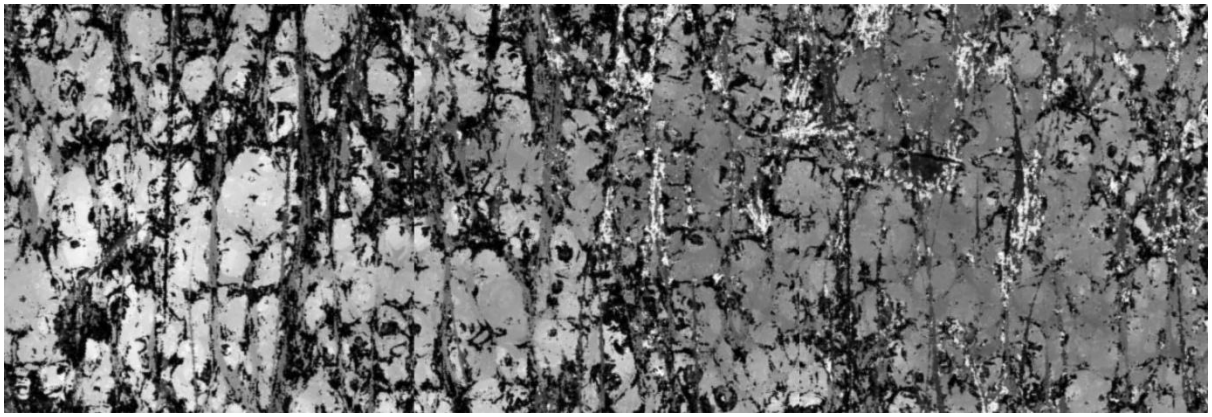

Figure 6: Sample 1.2.2 Surface Topology (5A, 0.0133ms^{-1}, 34mm from start of cut)

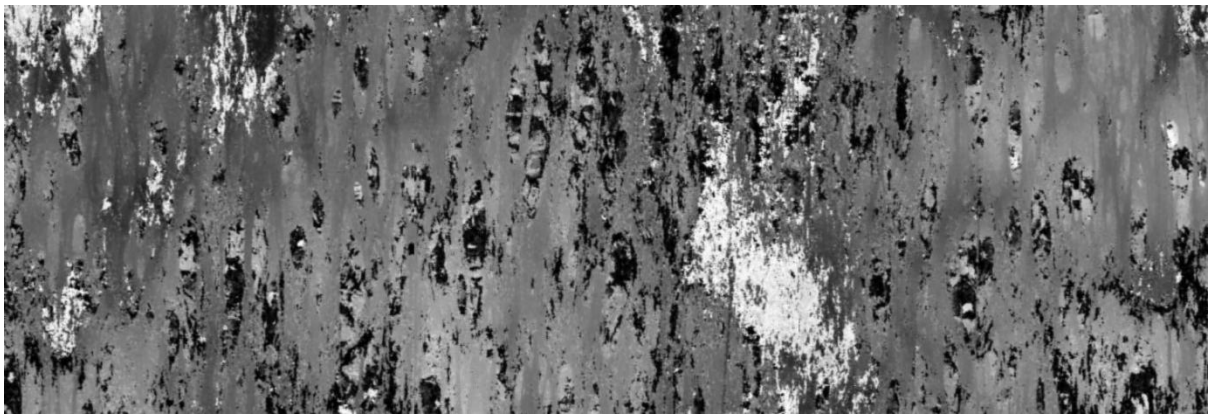

Figure 7: Sample 1.2.3 Surface Topology (5A, 0.0133ms^{-1}, 94mm from start of cut)

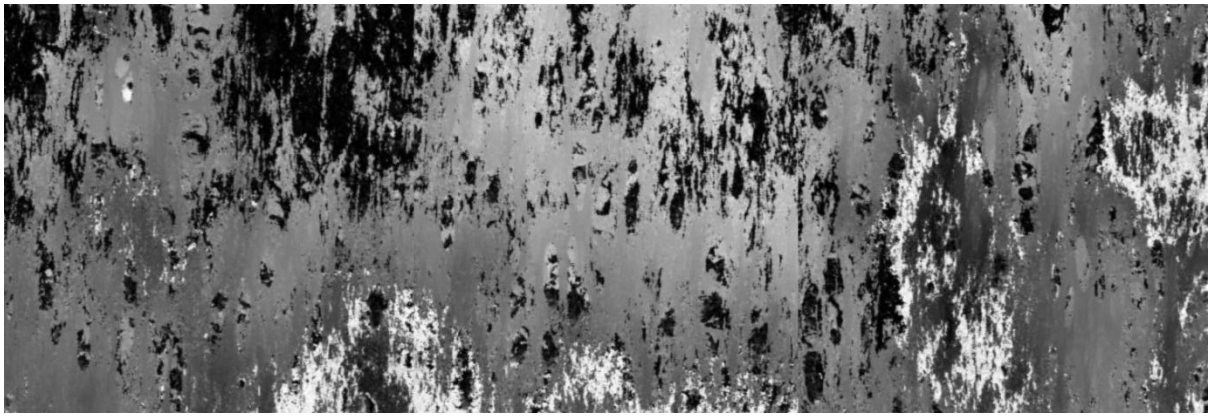

Figure 8: Sample 1.2.4 Surface Topology (5A, 0.0133ms^{-1}, 244mm from start of cut)

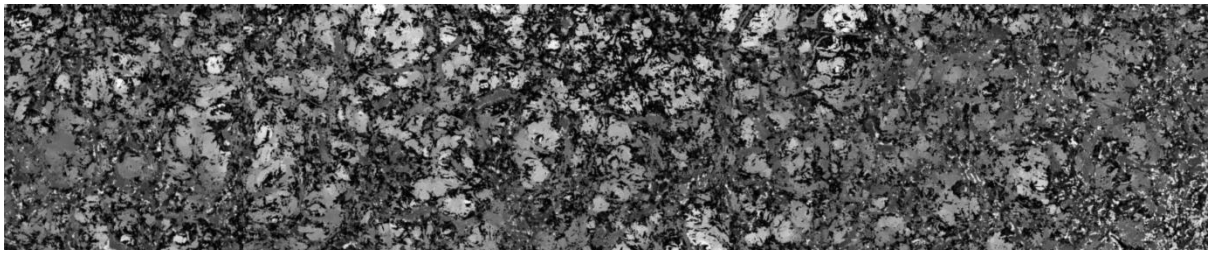

Figure 9: Sample 1.3.1 Surface Topology (7A, 0.0133ms^{-1}, 0mm from start of cut)

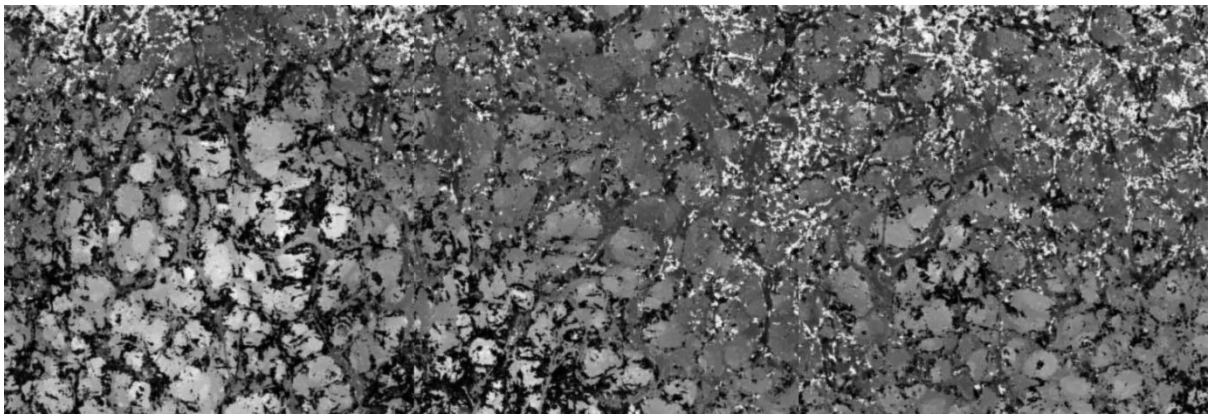

Figure 10: Sample 1.3.2 Surface Topology (7A, 0.0133ms^{-1}, 34mm from start of cut)

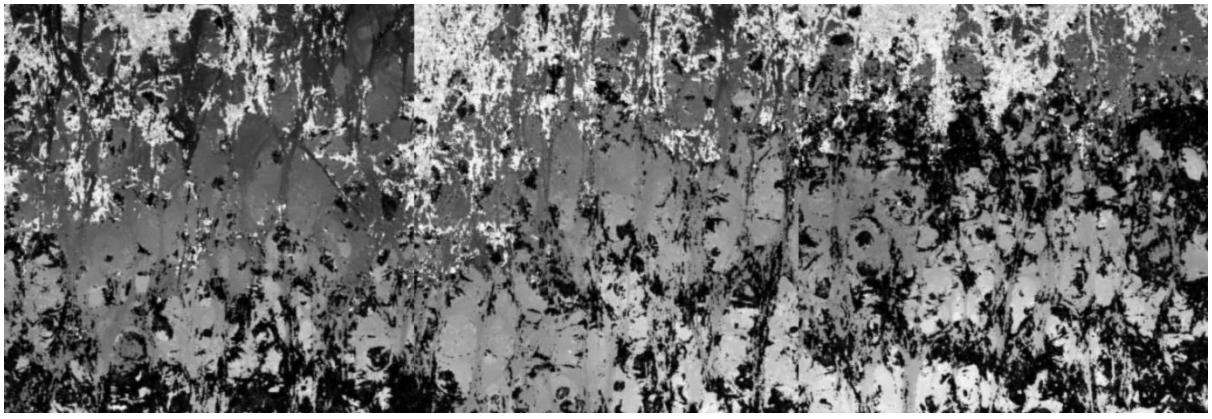

Figure 11: Sample 1.3.3 Surface Topology (7A, 0.0133ms^{-1}, 94mm from start of cut)

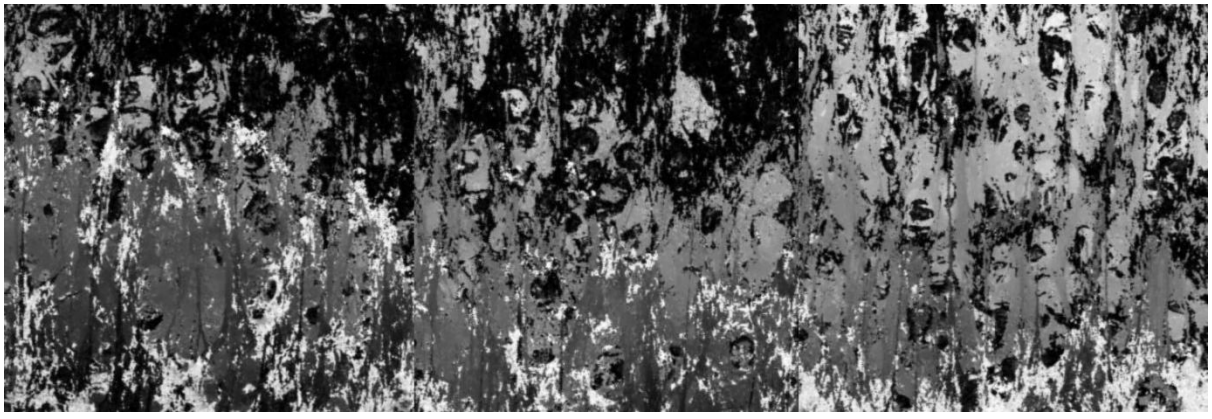

Figure 12: Sample 1.3.4 Surface Topology (7A, 0.0133ms^{-1}, 244mm from start of cut)

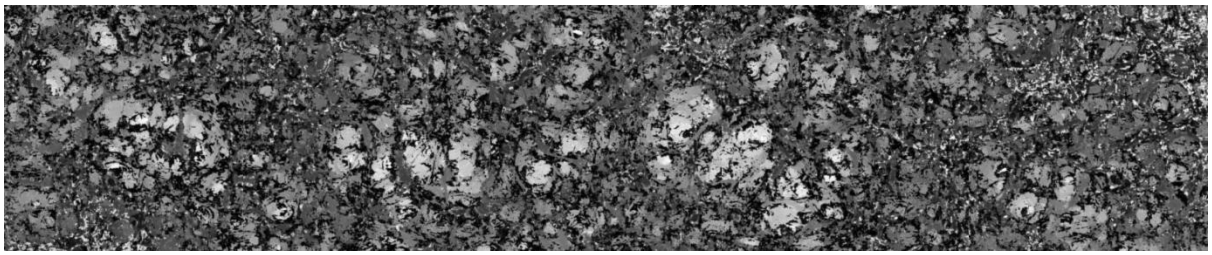

Figure 13: Sample 1.4.1 Surface Topology (7A, 0.0217ms^{-1}, 0mm from start of cut)

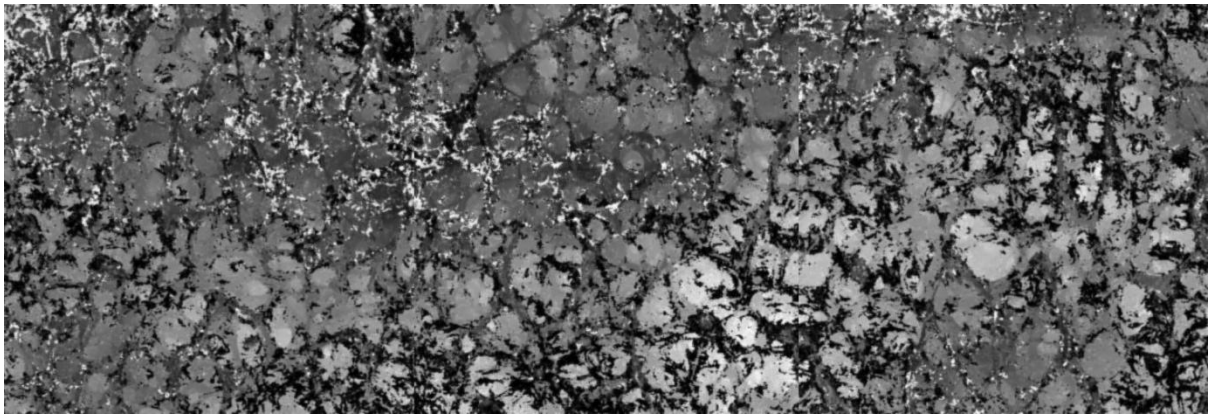

Figure 14: Sample 1.4.2 Surface Topology (7A, 0.0217ms^{-1}, 34mm from start of cut)

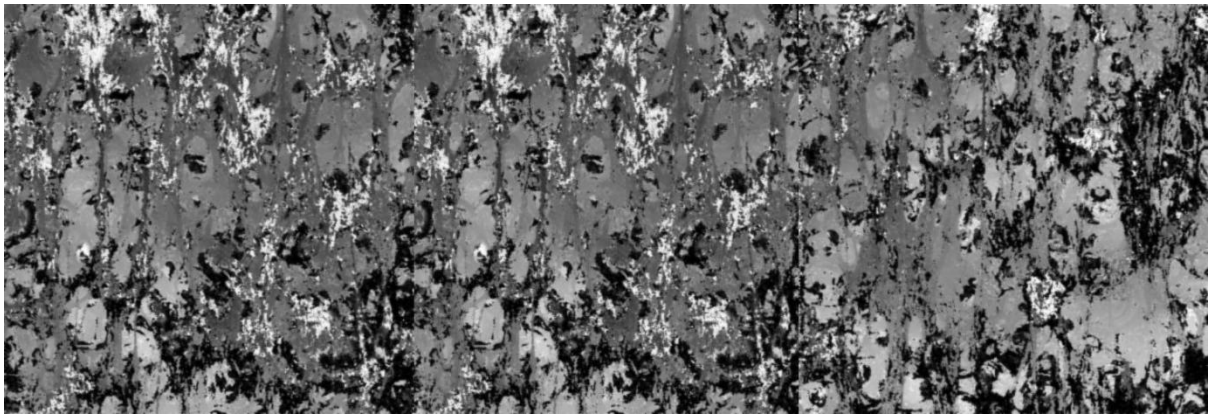

Figure 15: Sample 1.4.3 Surface Topology (7A, 0.0217ms^{-1}, 94mm from start of cut)

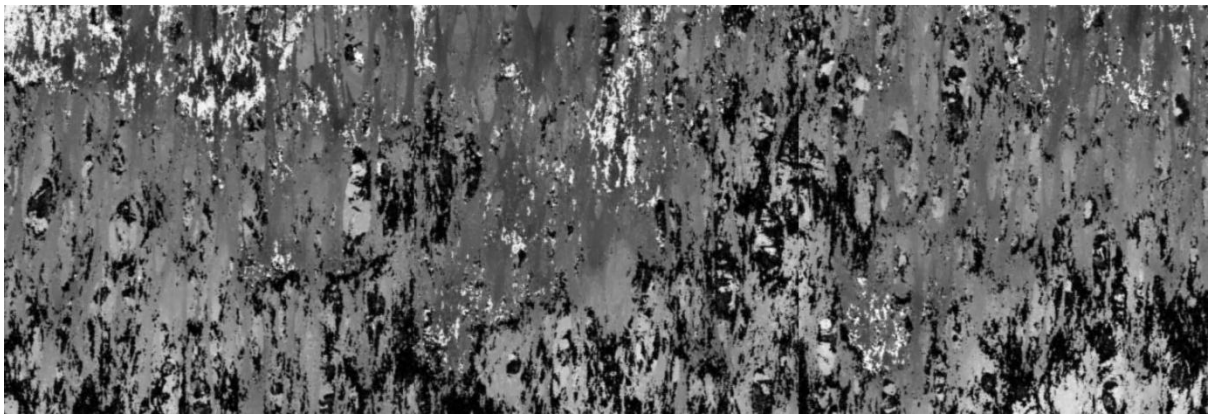

Figure 16: Sample 1.4.4 Surface Topology (7A, 0.0217ms^{-1}, 244mm from start of cut)

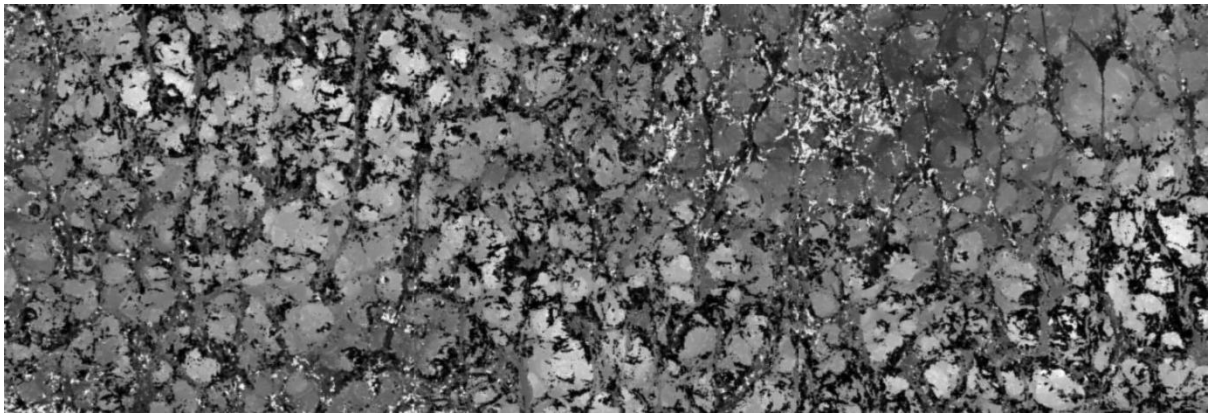

Figure 17: Sample 1.5.2 Surface Topology (7A, 0.0217ms^{-1}, 34mm from start of cut)

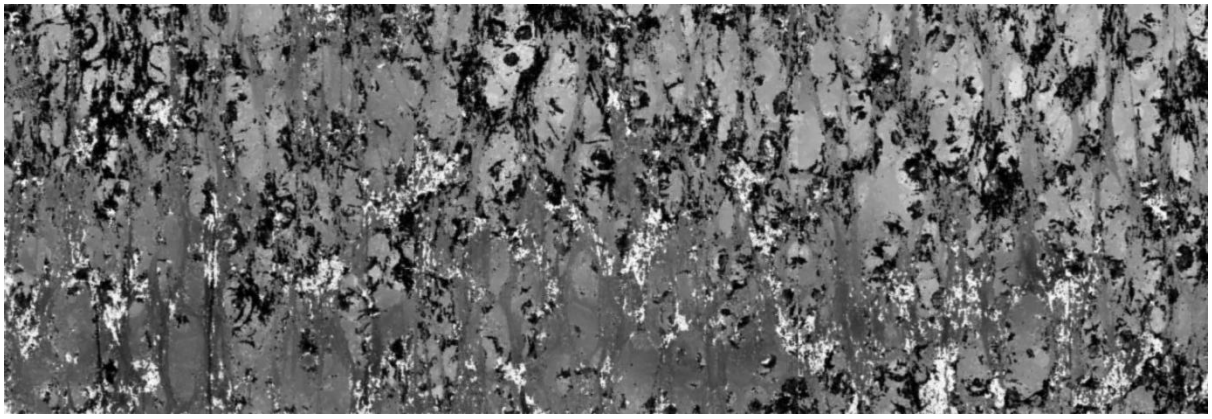

Figure 18: Sample 1.5.3 Surface Topology (7A, 0.0217ms^{-1}, 94mm from start of cut)

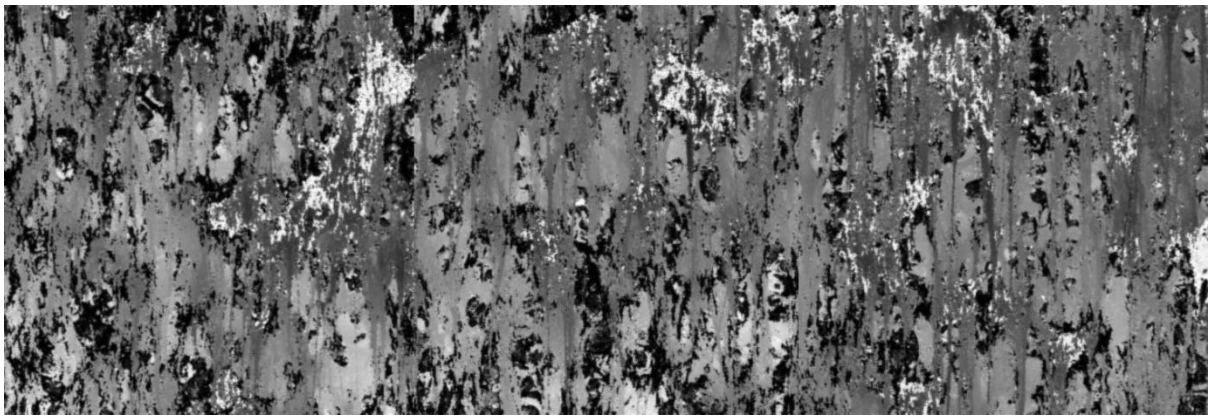

Figure 19: Sample 1.5.4 Surface Topology (7A, 0.0217ms^{-1}, 244mm from start of cut)

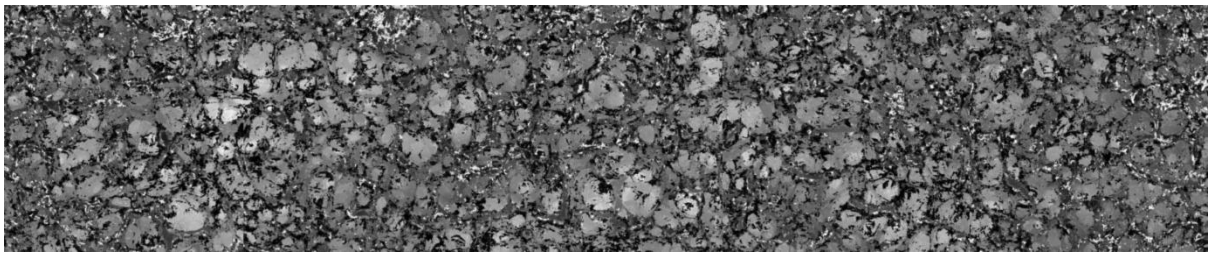

Figure 20: Sample 1.6.1 Surface Topology (5A, 0.0167ms^{-1}, 0mm from start of cut)

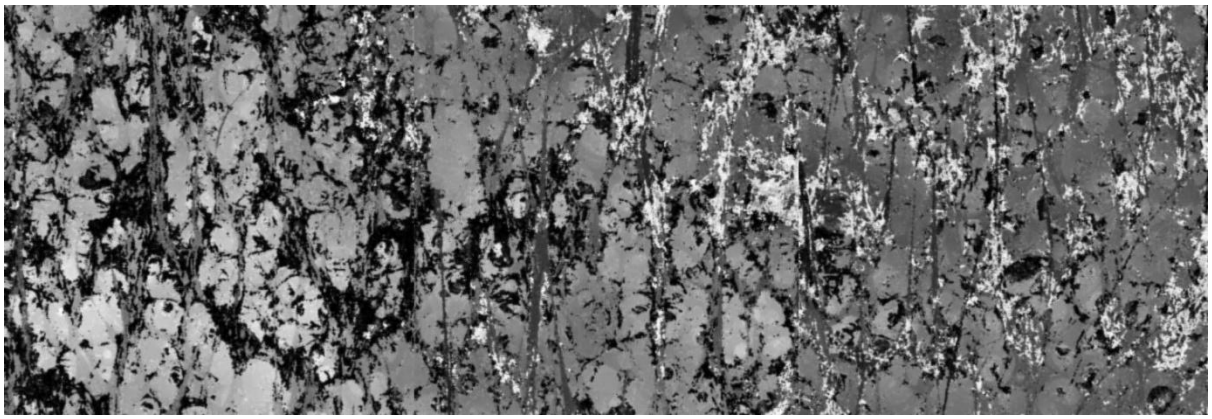

Figure 21: Sample 1.6.2 Surface Topology (5A, 0.0167ms^{-1}, 34mm from start of cut)

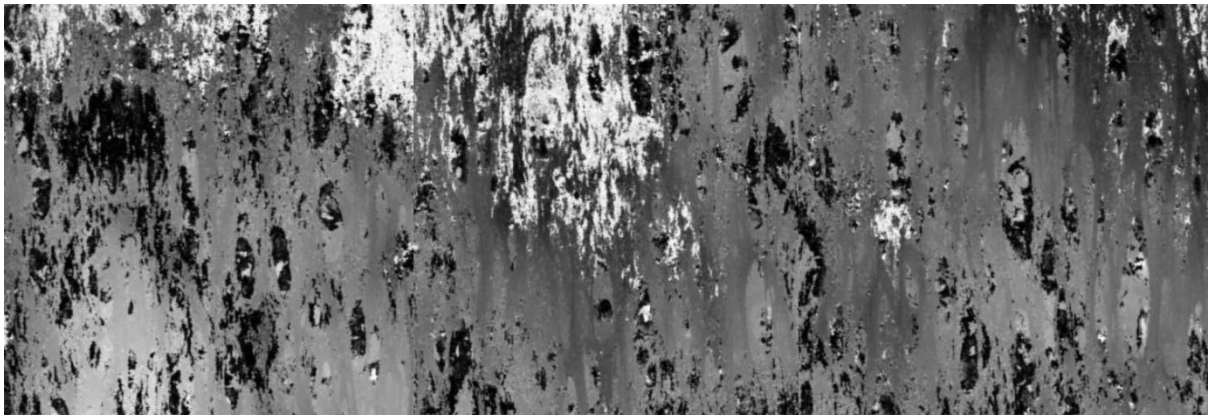

Figure 22: Sample 1.6.3 Surface Topology (5A, 0.0167ms^{-1}, 94mm from start of cut)

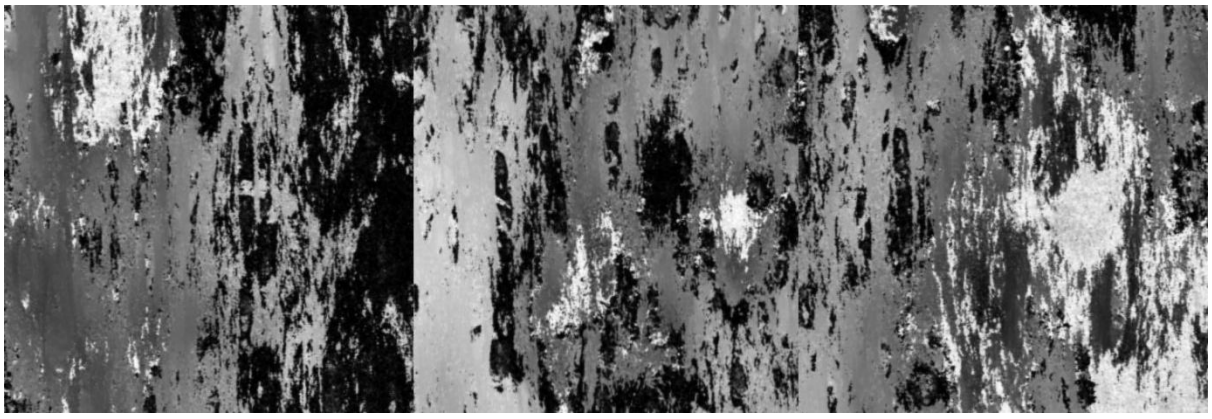

Figure 23: Sample 1.6.4 Surface Topology (5A, 0.0167ms^{-1}, 244mm from start of cut)

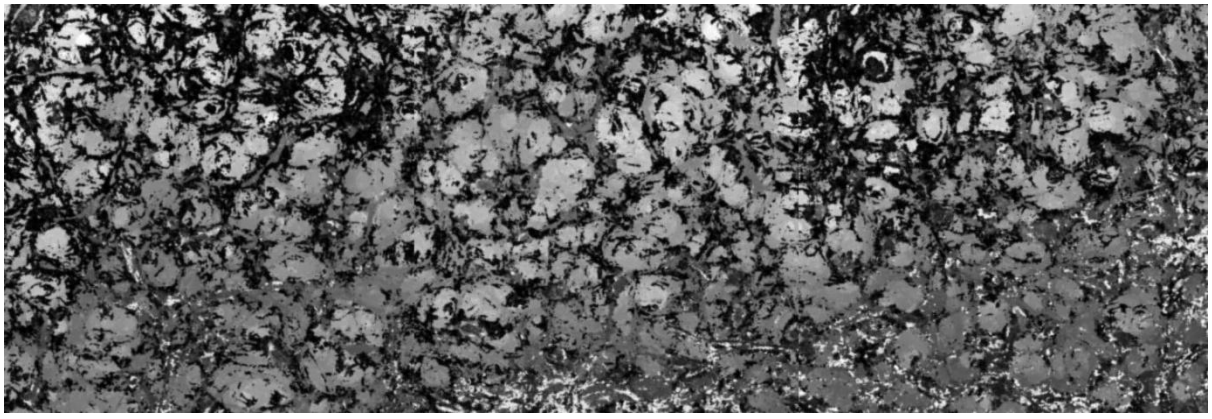

Figure 24: Sample 1.7.1 Surface Topology (5A, 0.0200ms^{-1}, 0mm from start of cut)

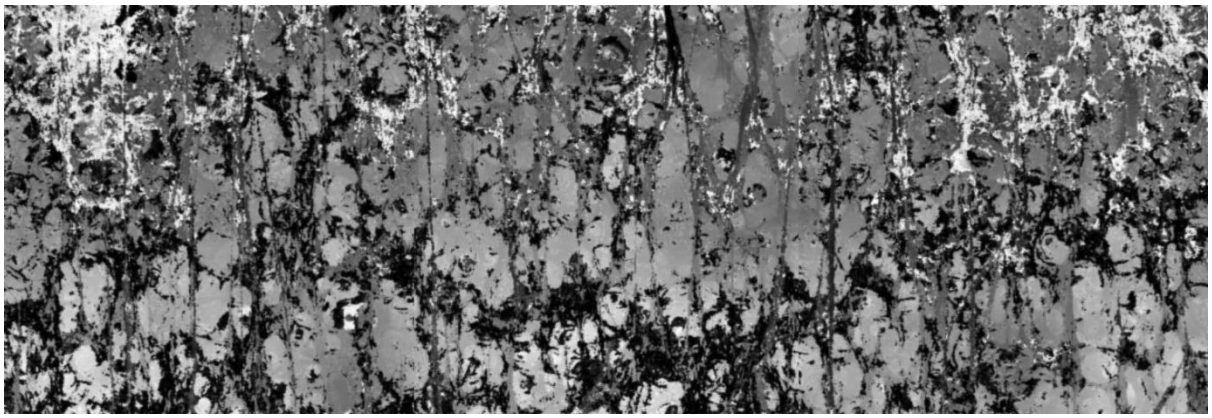

Figure 25: Sample 1.7.2 Surface Topology (5A, 0.0200ms^{-1}, 34mm from start of cut)

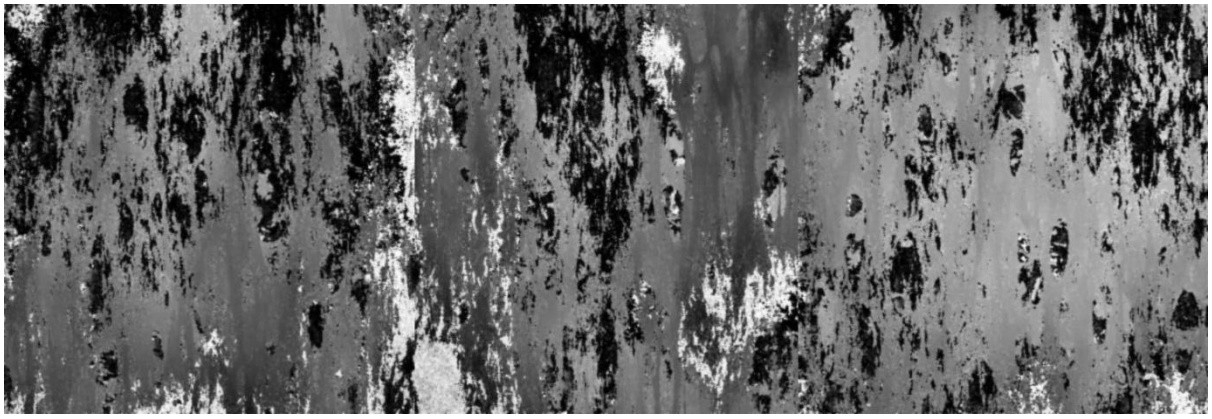

Figure 26: Sample 1.7.3 Surface Topology (5A, 0.0200ms^{-1}, 94mm from start of cut)

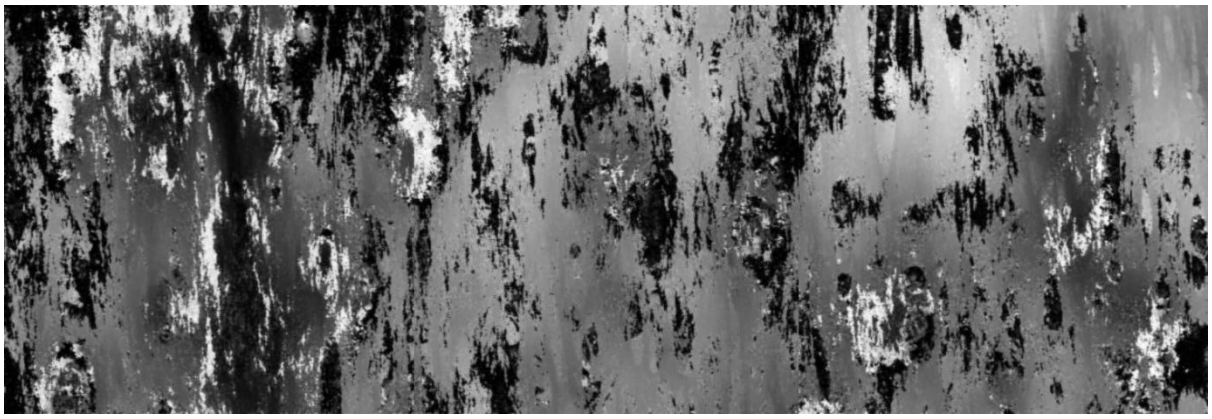

Figure 27: Sample 1.7.4 Surface Topology (5A, 0.0200ms^{-1}, 244mm from start of cut)

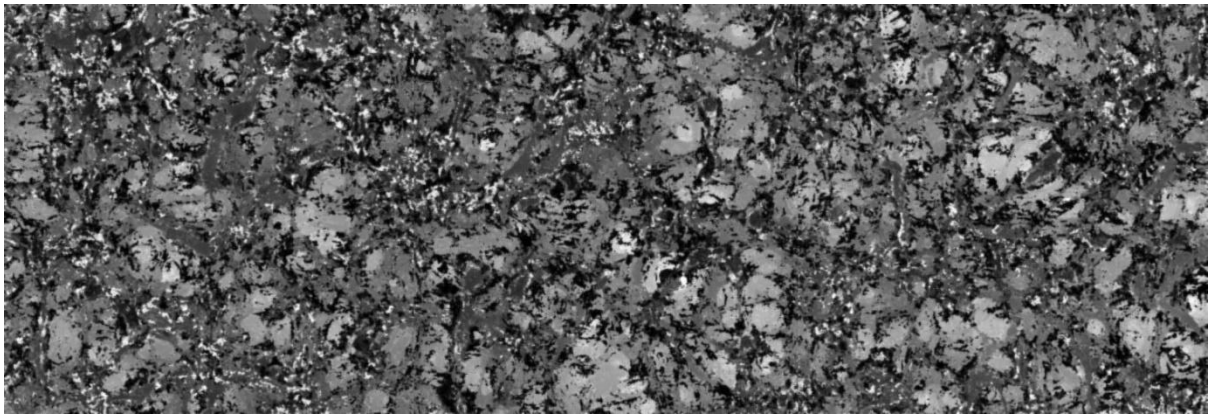

Figure 28: Sample 1.8.1 Surface Topology (7A, 0.0200ms^{-1}, 0mm from start of cut)

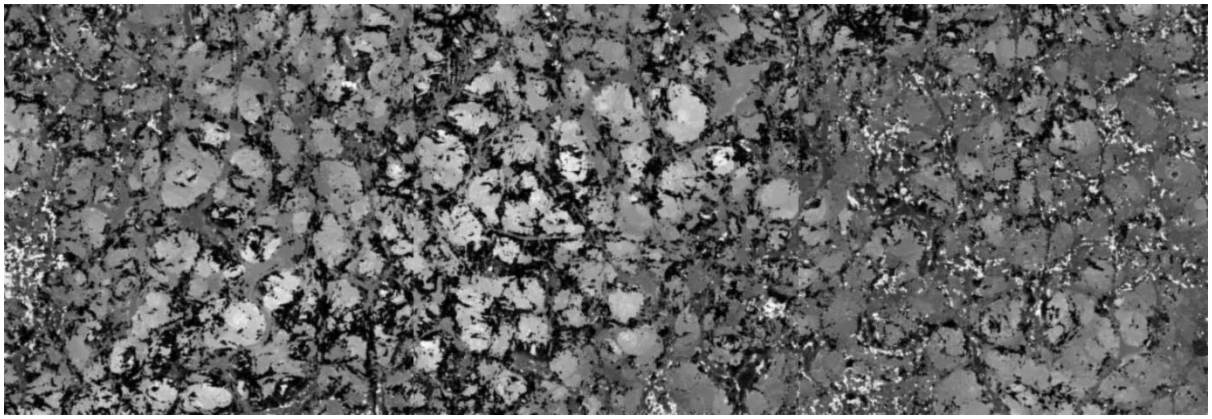

Figure 29: Sample 1.8.2 Surface Topology (7A, 0.0200ms^{-1}, 34mm from start of cut)

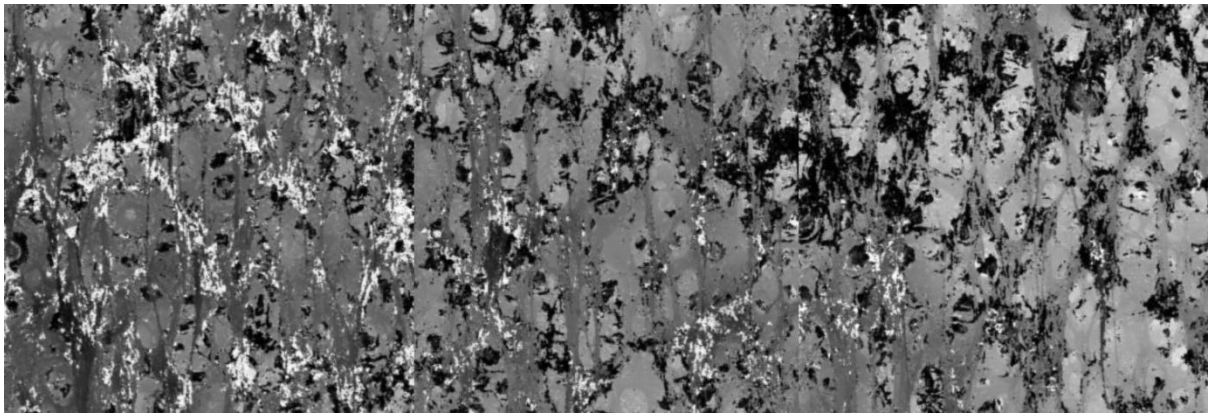

Figure 30: Sample 1.8.3 Surface Topology (7A, 0.0200ms^{-1}, 94mm from start of cut)

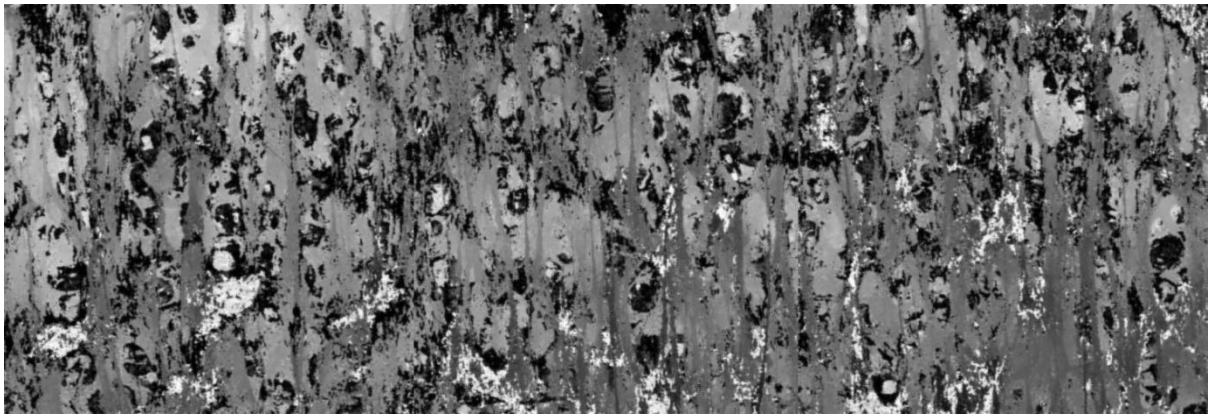

Figure 31: Sample 1.8.4 Surface Topology (7A, 0.0200ms^{-1}, 244mm from start of cut)

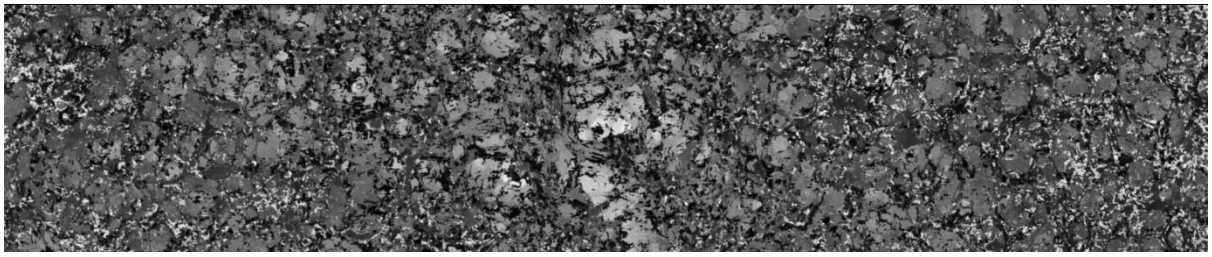

Figure 32: Sample 1.9.1 Surface Topology (7A, 0.0167ms^{-1}, 0mm from start of cut)

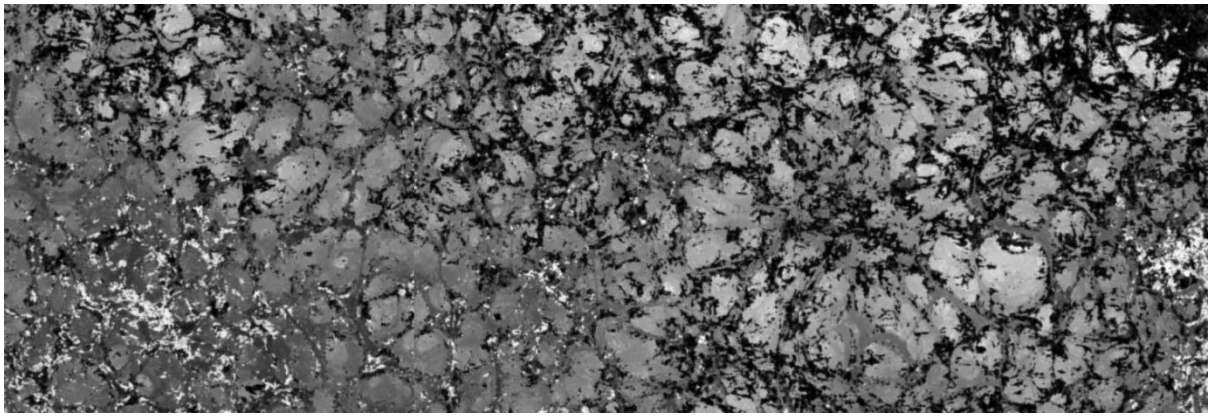

Figure 33: Sample 1.9.2 Surface Topology (7A, 0.0167ms^{-1}, 34mm from start of cut)

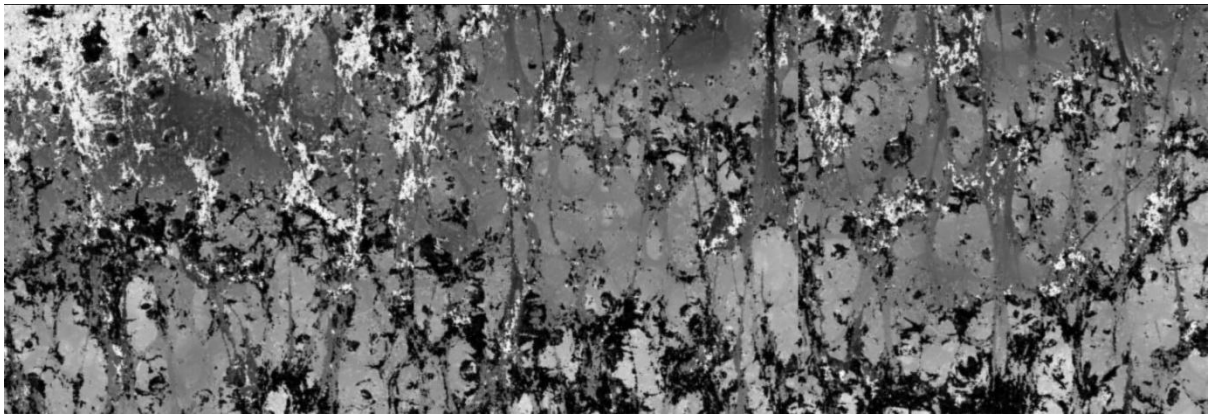

Figure 34: Sample 1.9.3 Surface Topology (7A, 0.0167ms^{-1}, 94mm from start of cut)

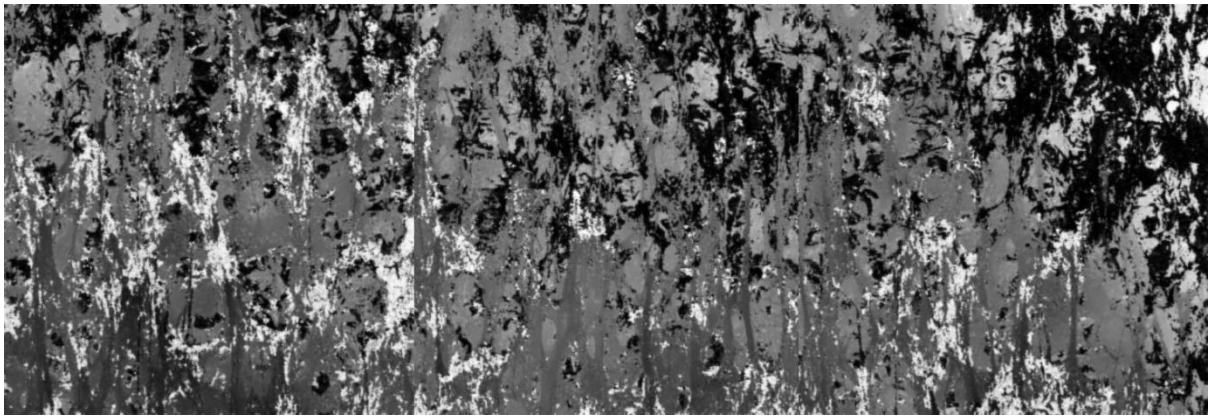

Figure 35: Sample 1.9.4 Surface Topology (7A, 0.0167ms^{-1}, 244mm from start of cut)

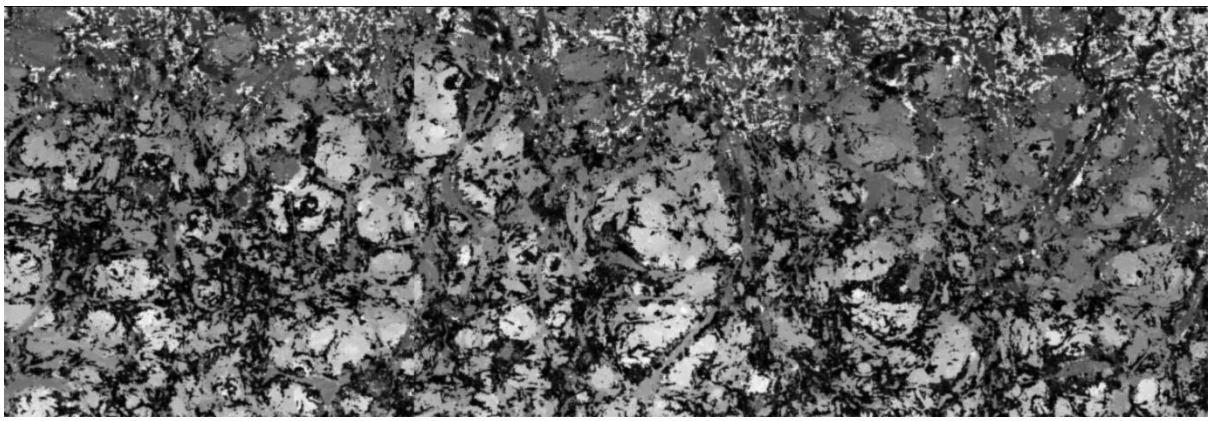

Figure 36: Sample 1.10.1 Surface Topology (7A, 0.0133ms^{-1}, 0mm from start of cut)

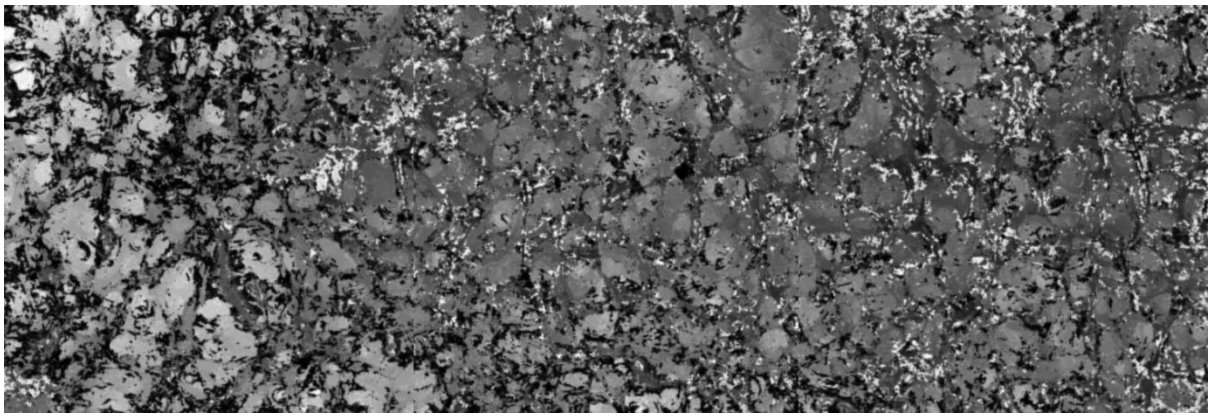

Figure 37: Sample 1.10.2 Surface Topology (7A, 0.0133ms^{-1}, 34mm from start of cut)

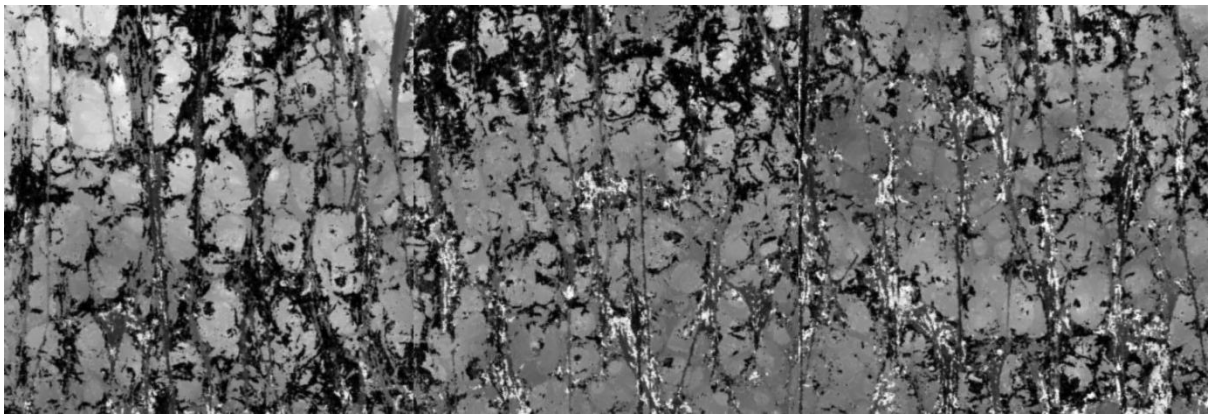

Figure 38: Sample 1.10.3 Surface Topology (7A, 0.0133ms^{-1}, 94mm from start of cut)

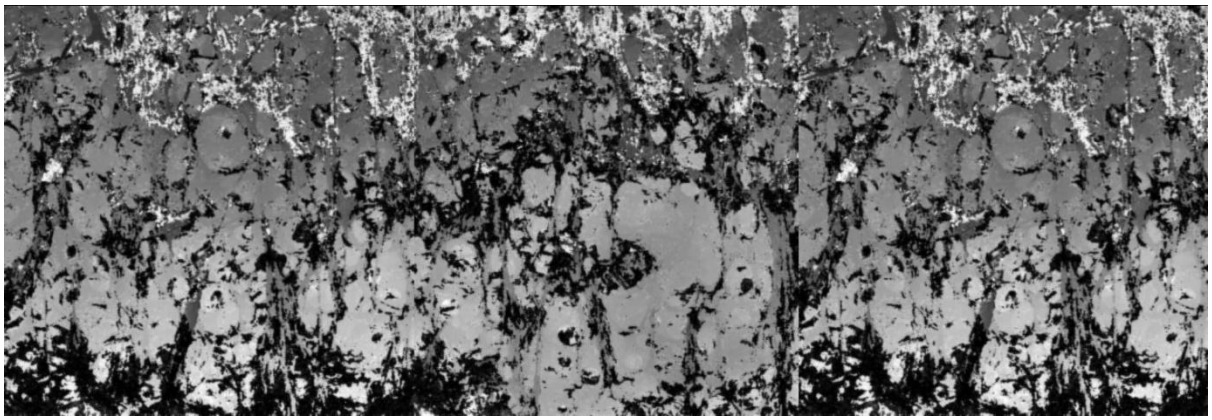

Figure 39: Sample 1.10.4 Surface Topology (7A, 0.0133ms^{-1}, 244mm from start of cut)

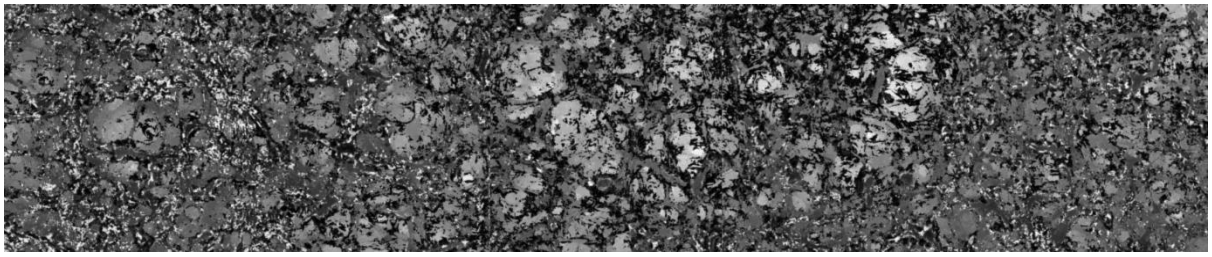

Figure 40: Sample 1.11.1 Surface Topology (7A, 0.0217ms^{-1}, 0mm from start of cut)

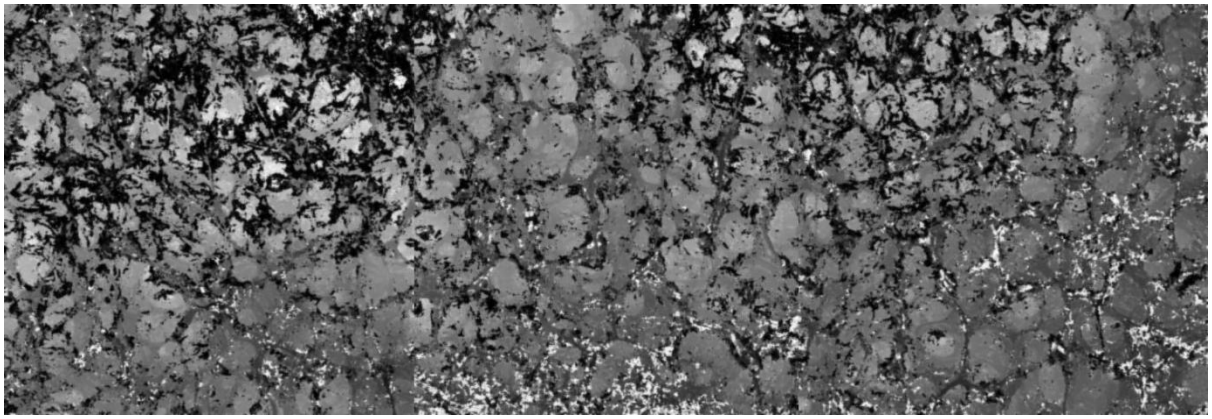

Figure 41: Sample 1.11.2 Surface Topology (7A, 0.0217ms^{-1}, 34mm from start of cut)

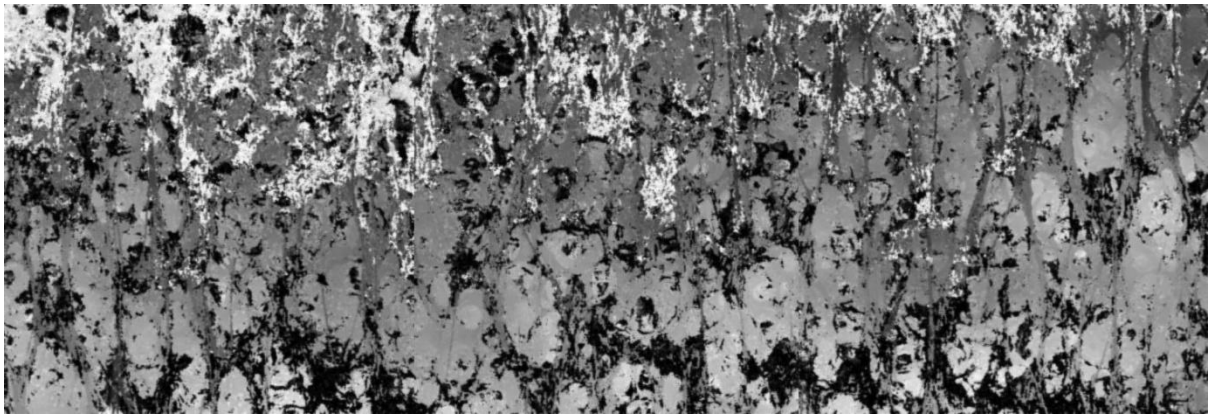

Figure 42: Sample 1.11.3 Surface Topology (7A, 0.0217ms^{-1}, 94mm from start of cut)

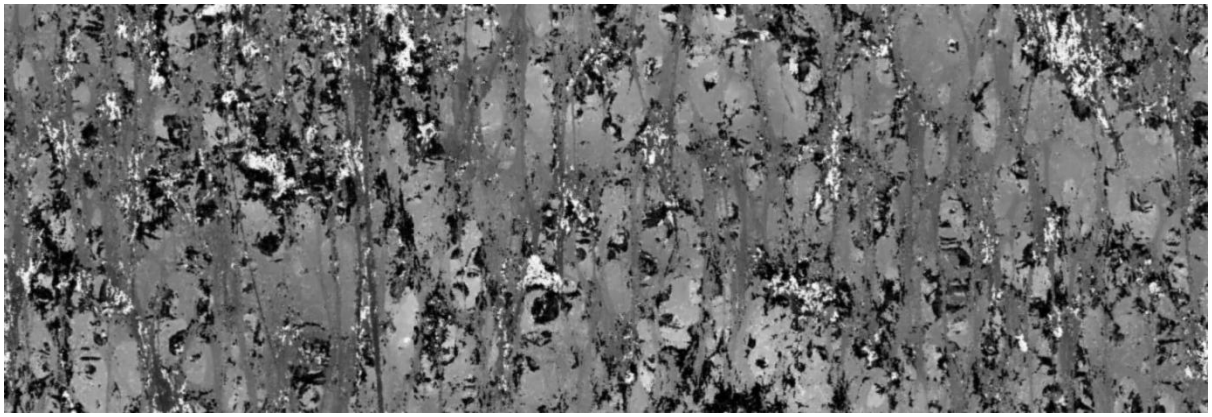

Figure 43: Sample 1.11.4 Surface Topology (7A, 0.0217ms^{-1}, 244mm from start of cut)

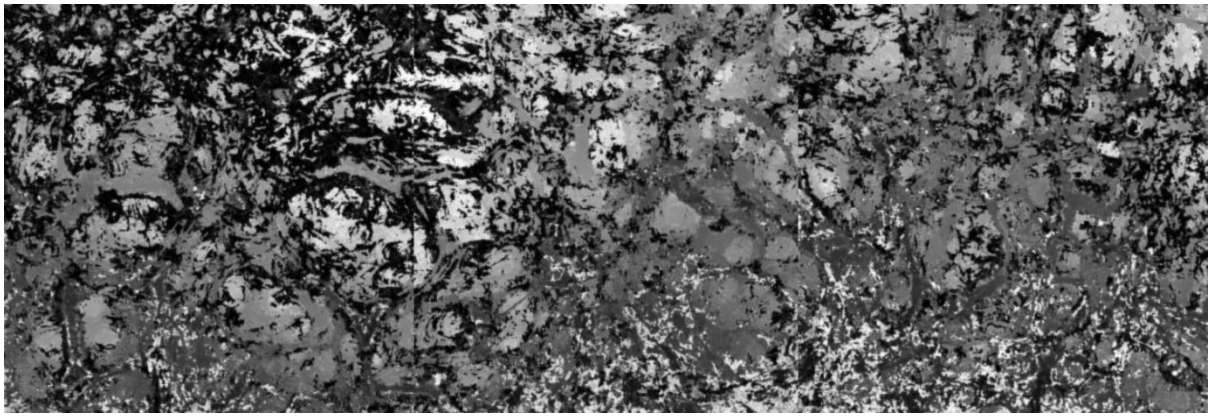

Figure 44: Sample 1.12.1 Surface Topology (8A, 0.0133ms^{-1}, 0mm from start of cut)

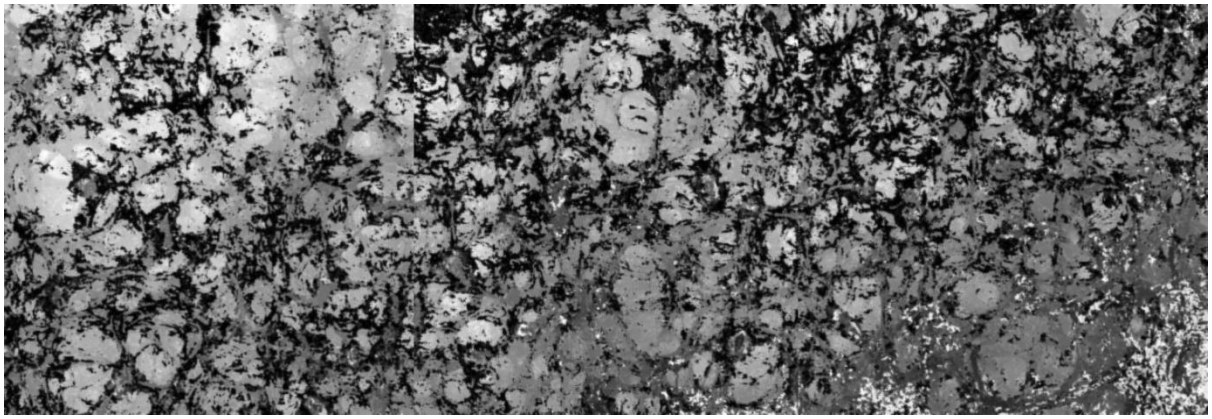

Figure 45: Sample 1.12.2 Surface Topology (8A, 0.0133ms^{-1}, 34mm from start of cut)

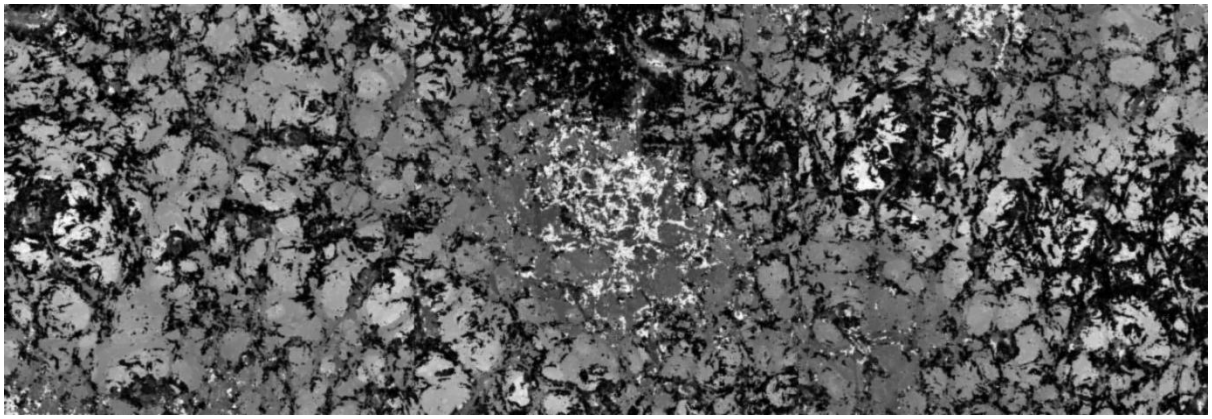

Figure 46: Sample 1.12.3 Surface Topology (8A, 0.0133ms^{-1}, 94mm from start of cut)

Figure 47: Sample 1.12.4 Surface Topology (8A, 0.0133ms^{-1}, 244mm from start of cut)

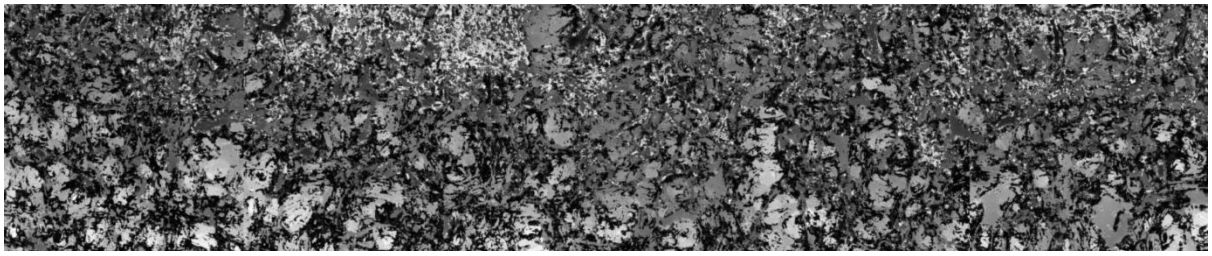

Figure 48: Sample 1.13.1 Surface Topology (8A, 0.0167ms^{-1}, 0mm from start of cut)

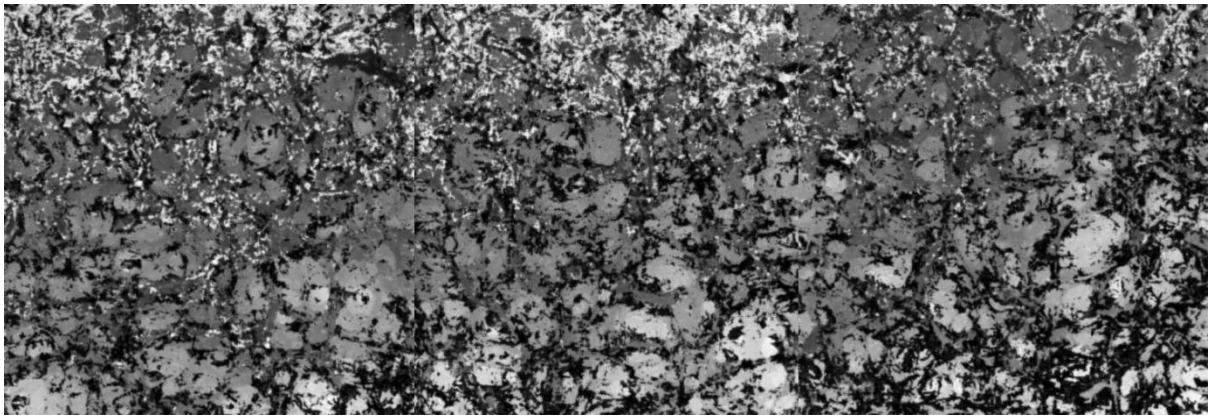

Figure 49: Sample 1.13.2 Surface Topology (8A, 0.0167ms^{-1}, 34mm from start of cut)

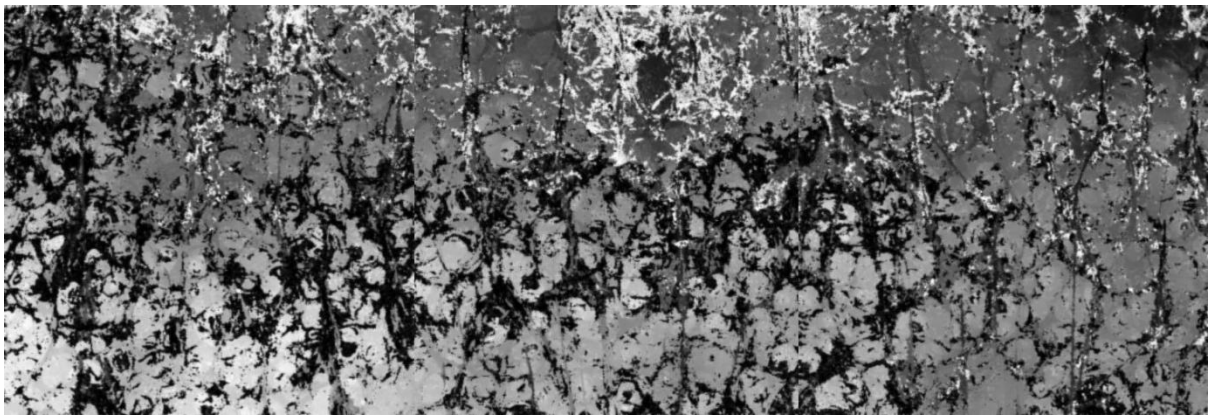

Figure 50: Sample 1.13.3 Surface Topology (8A, 0.0167ms^{-1}, 94mm from start of cut)

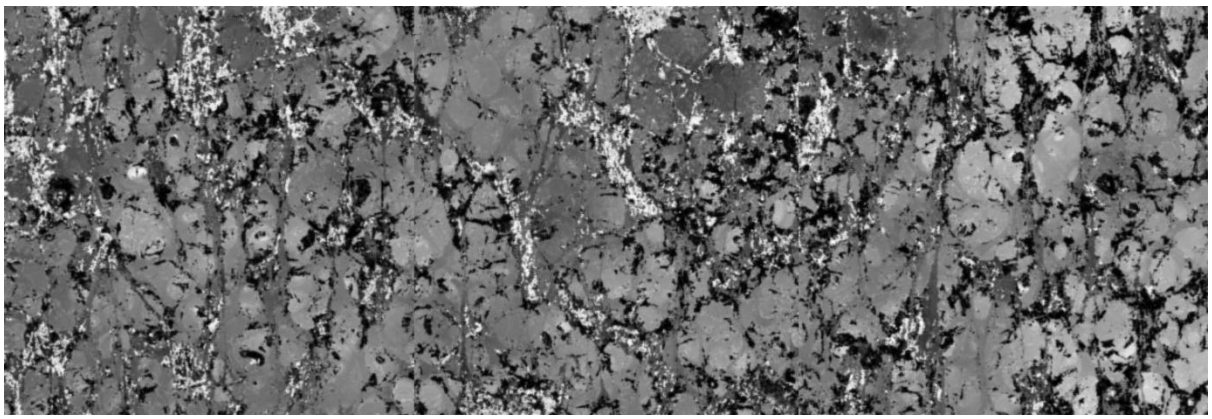

Figure 51: Sample 1.13.4 Surface Topology (8A, 0.0167ms^{-1}, 244mm from start of cut)

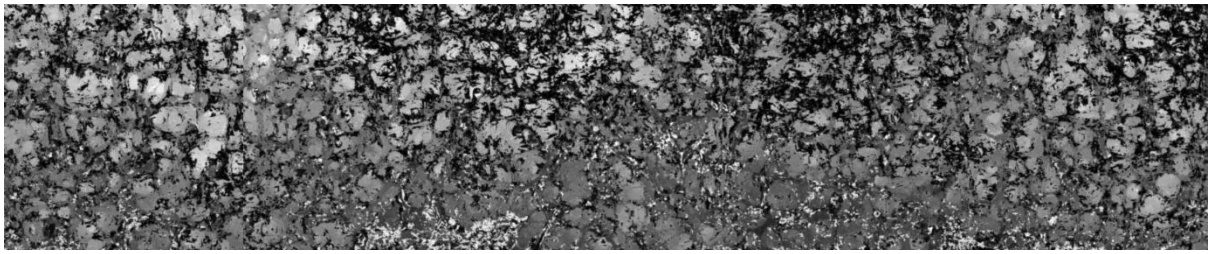

Figure 52: Sample 1.14.1 Surface Topology (5A, 0.0133ms^{-1}, 0mm from start of cut)

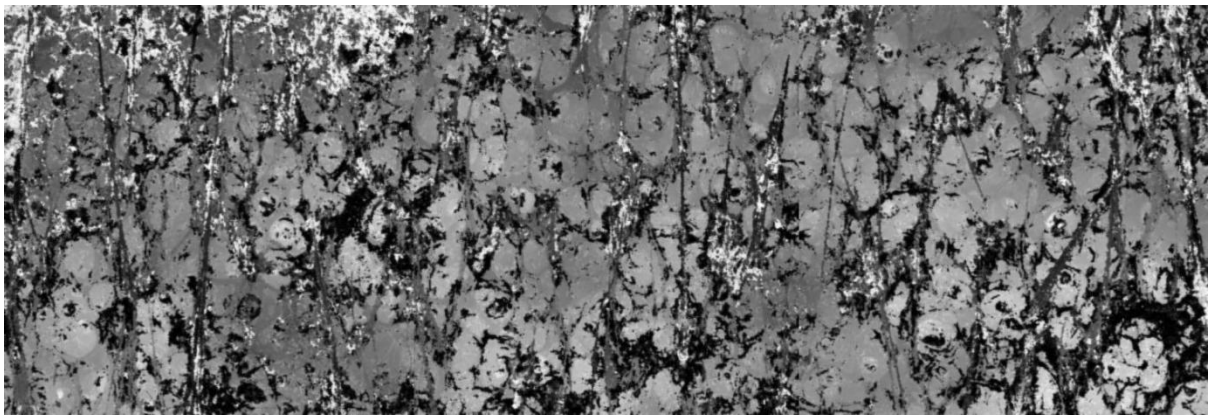

Figure 53: Sample 1.14.2 Surface Topology (5A, 0.0133ms^{-1}, 34mm from start of cut)

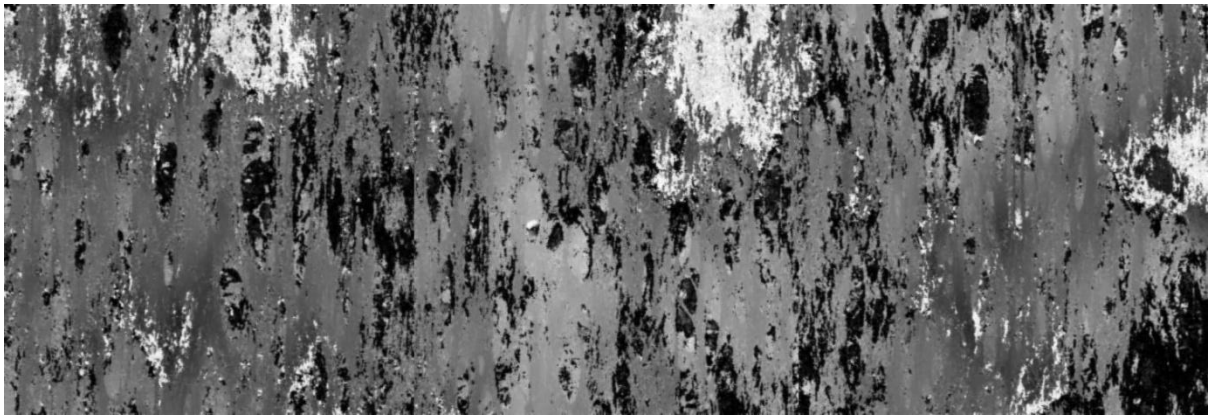

Figure 54: Sample 1.14.3 Surface Topology (5A, 0.0133ms^{-1}, 94mm from start of cut)

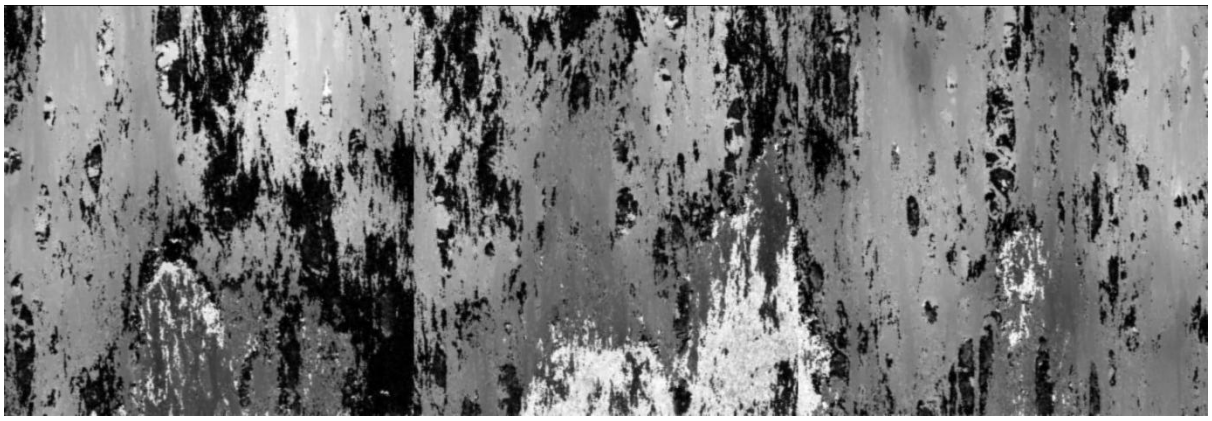

Figure 55: Sample 1.14.4 Surface Topology (5A, 0.0133ms^{-1}, 244mm from start of cut)

Figure 56: Sample 1.15.1 Surface Topology (8A, 0.0200ms^{-1}, 0mm from start of cut)

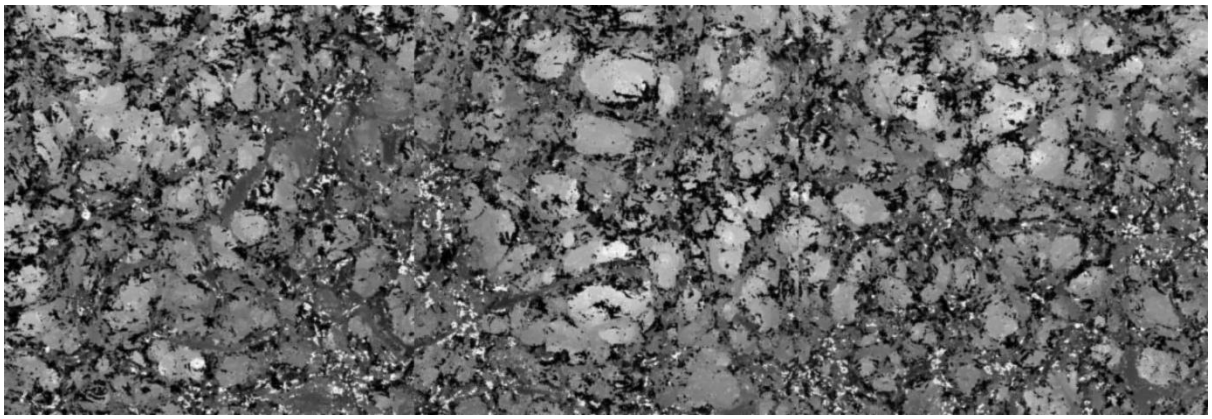

Figure 57: Sample 1.15.2 Surface Topology (8A, 0.0200ms^{-1}, 34mm from start of cut)

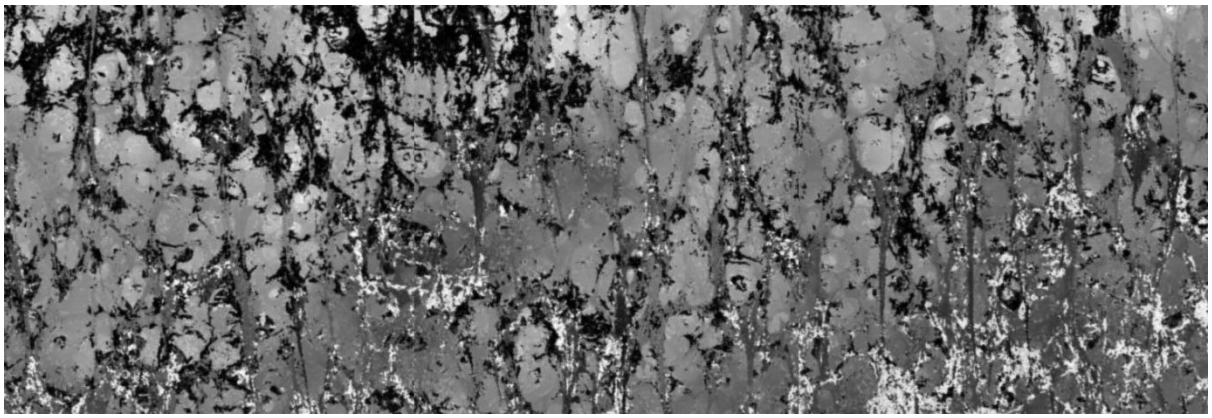

Figure 58: Sample 1.15.3 Surface Topology (8A, 0.0200ms^{-1}, 94mm from start of cut)

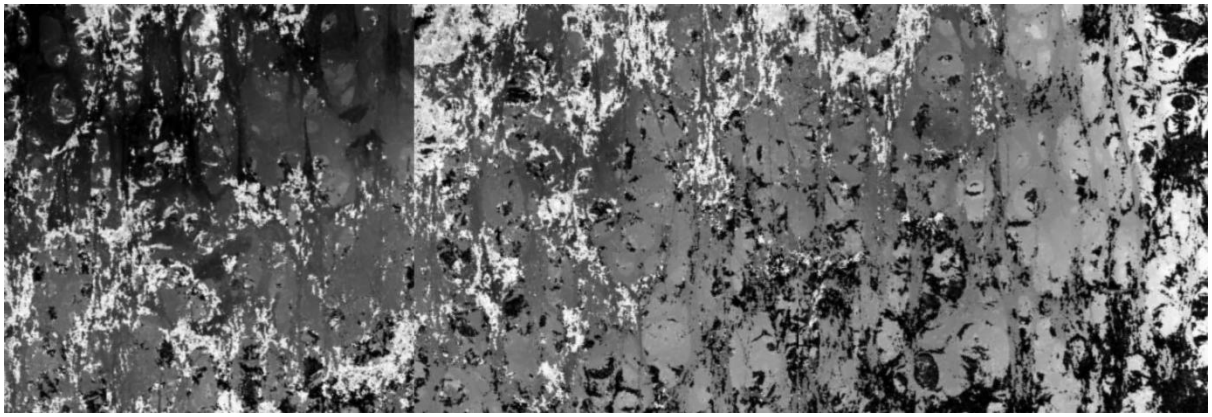

Figure 59: Sample 1.15.4 Surface Topology (8A, 0.0200ms^{-1}, 244mm from start of cut)

Surface Topology Images for Hot-Blade Samples

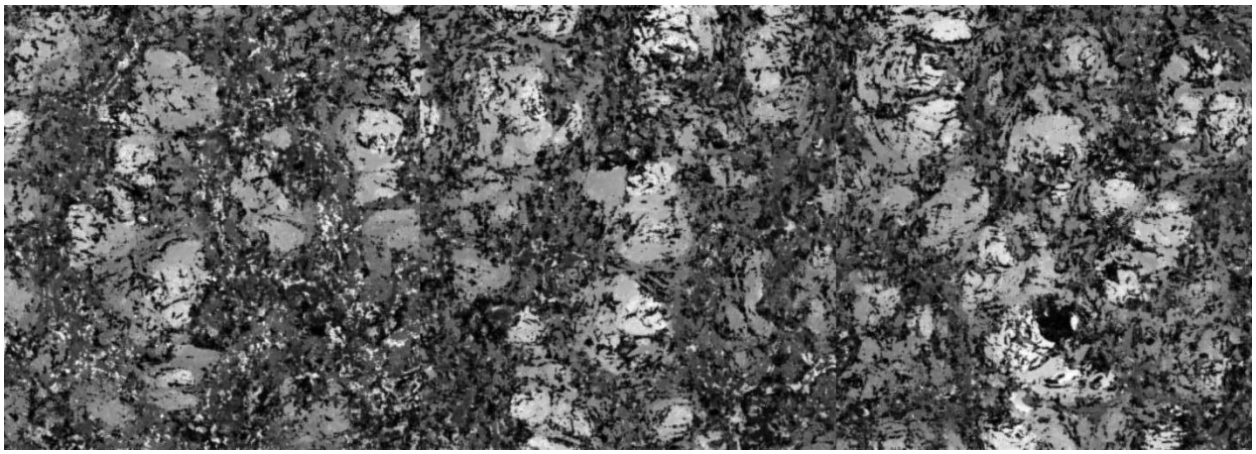

Figure 60: Sample 5.1.1 Surface Topology (16A, 0.028ms^{-1}, 0mm from start of cut)

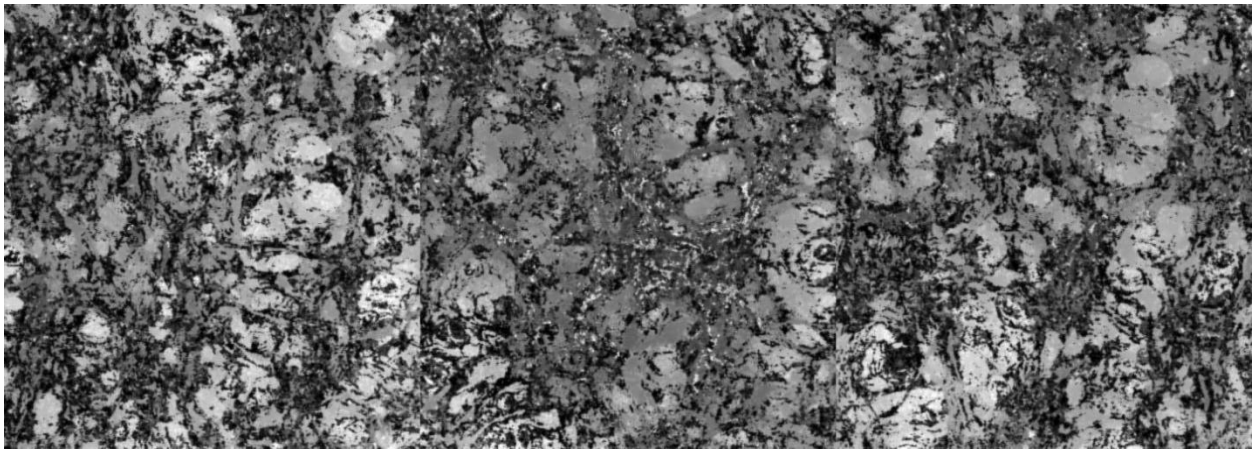

Figure 61: Sample 5.1.2 Surface Topology (16A, 0.028ms^{-1}, 50mm from start of cut)

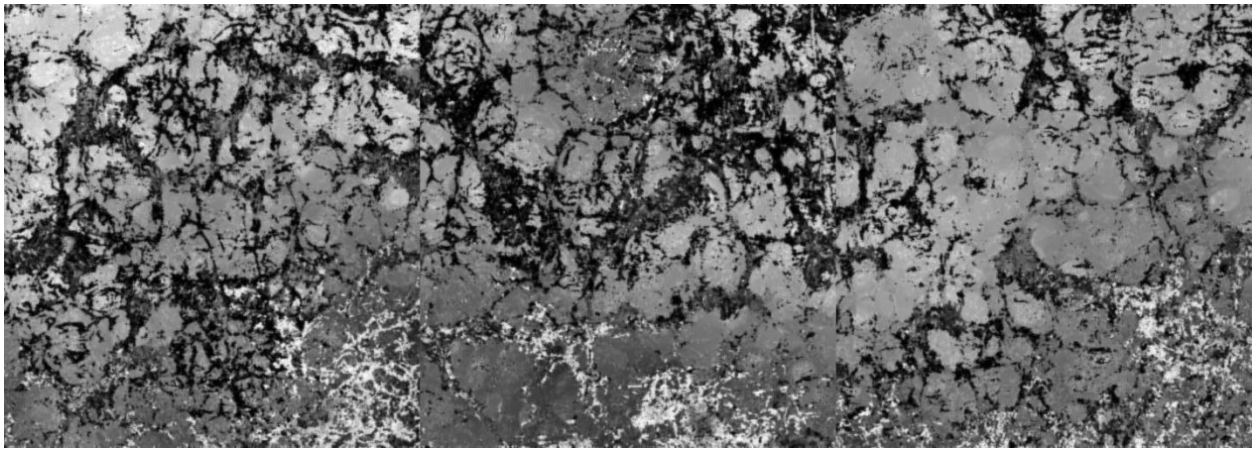

Figure 62: Sample 5.1.3 Surface Topology (16A, 0.028ms^{-1}, 250mm from start of cut)

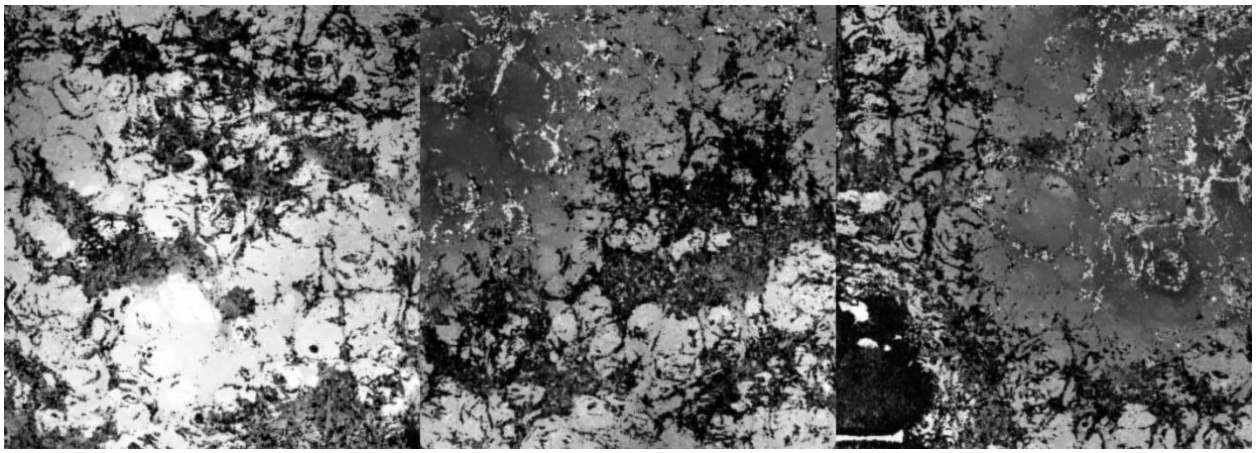

Figure 63: Sample 5.1.4 Surface Topology (16A, 0.028ms^{-1}, 400mm from start of cut)

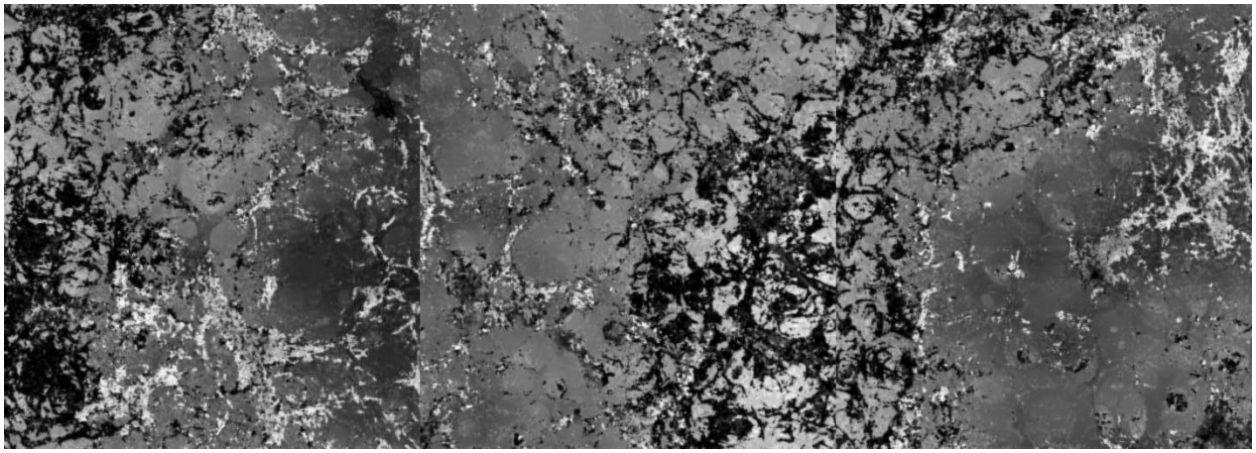

Figure 64: Sample 5.1.5 Surface Topology (16A, 0.028ms^{-1}, 550mm from start of cut)

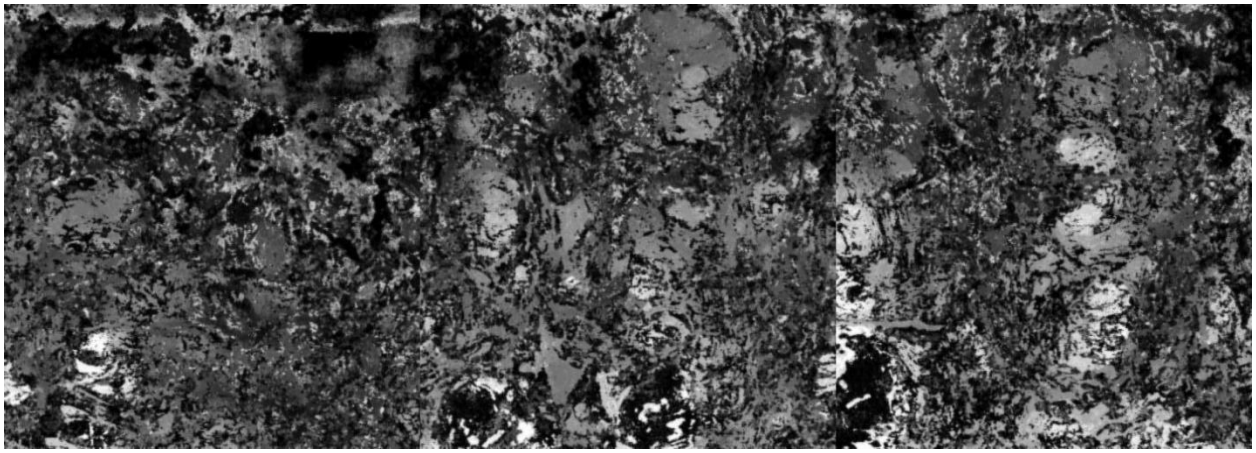

Figure 65: Sample 5.2.1 Surface Topology (22A, 0.028ms^{-1}, 0mm from start of cut)

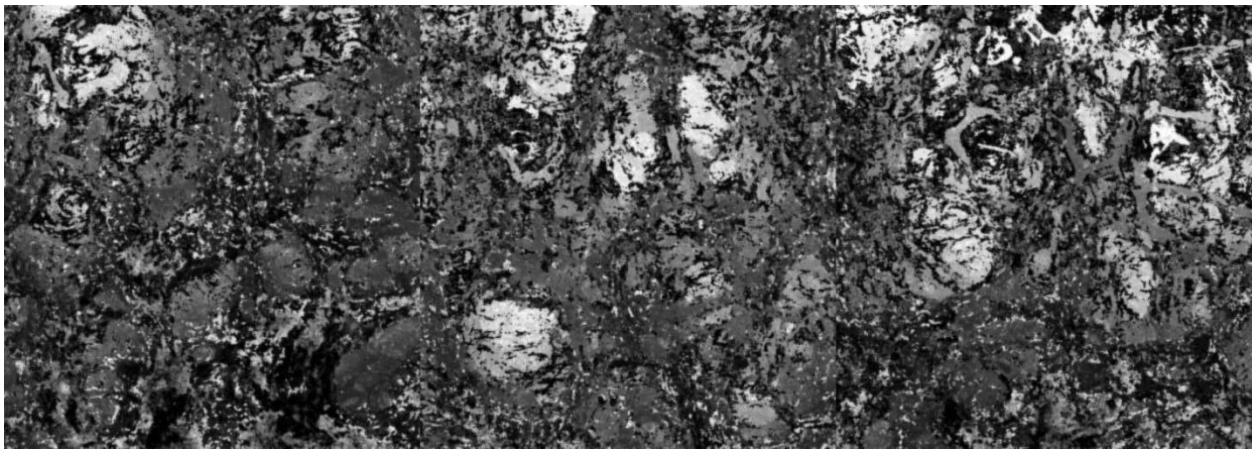

Figure 66: Sample 5.2.2 Surface Topology (22A, 0.028ms^{-1}, 50mm from start of cut)

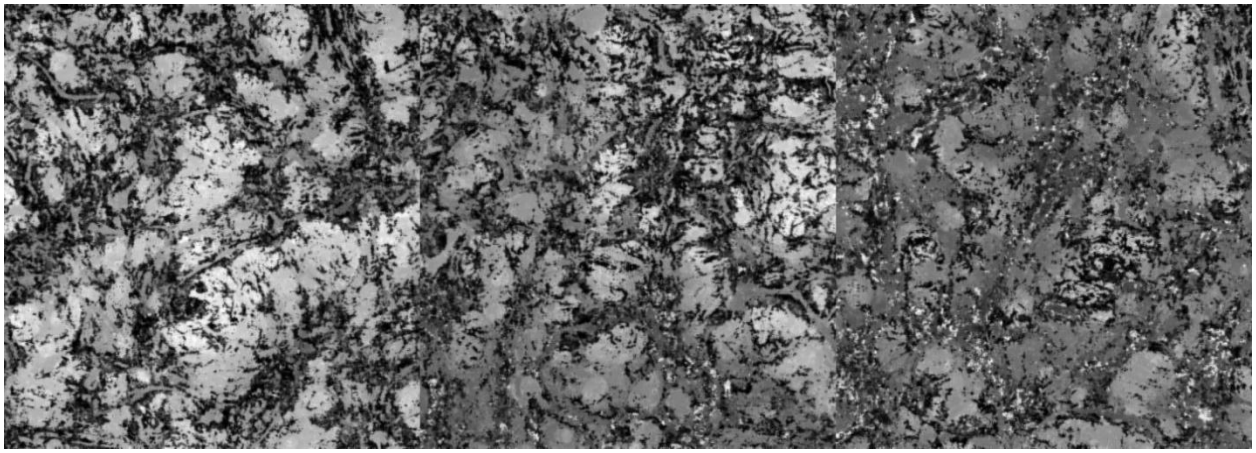

Figure 67: Sample 5.2.3 Surface Topology (22A, 0.028ms^{-1}, 250mm from start of cut)

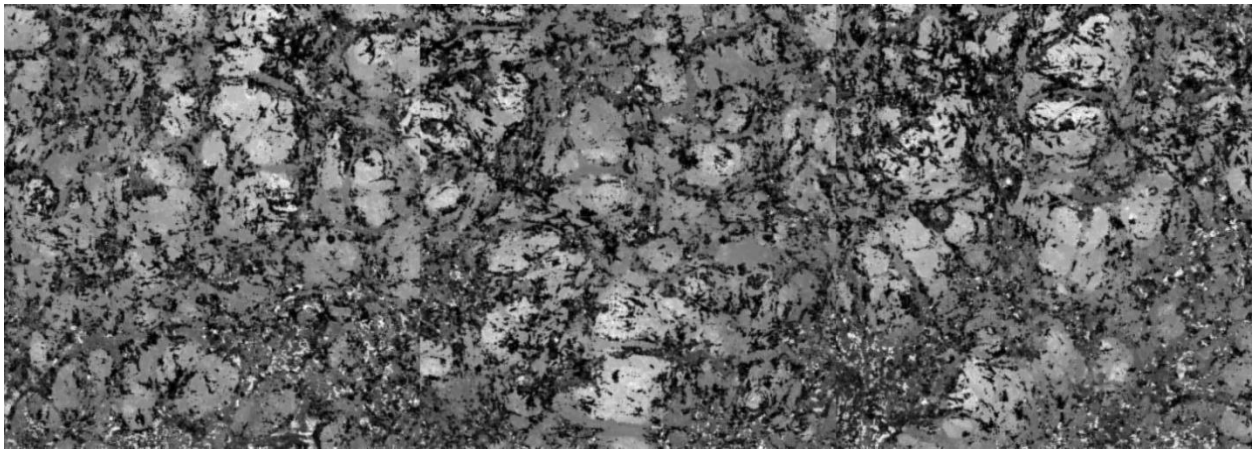

Figure 68: Sample 5.2.4 Surface Topology (22A, 0.028ms^{-1}, 400mm from start of cut)

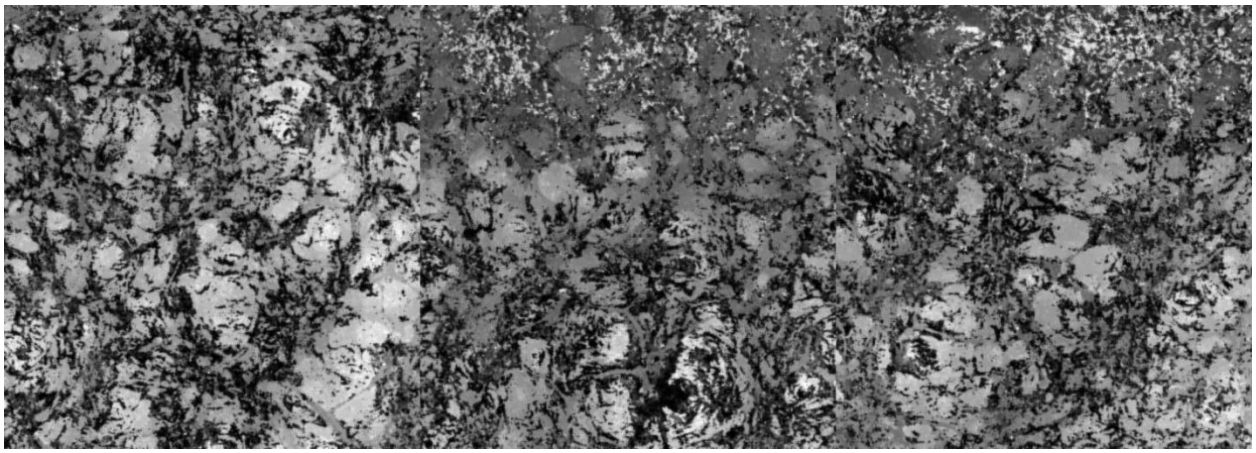

Figure 69: Sample 5.2.5 Surface Topology (22A, 0.028ms^{-1}, 550mm from start of cut)

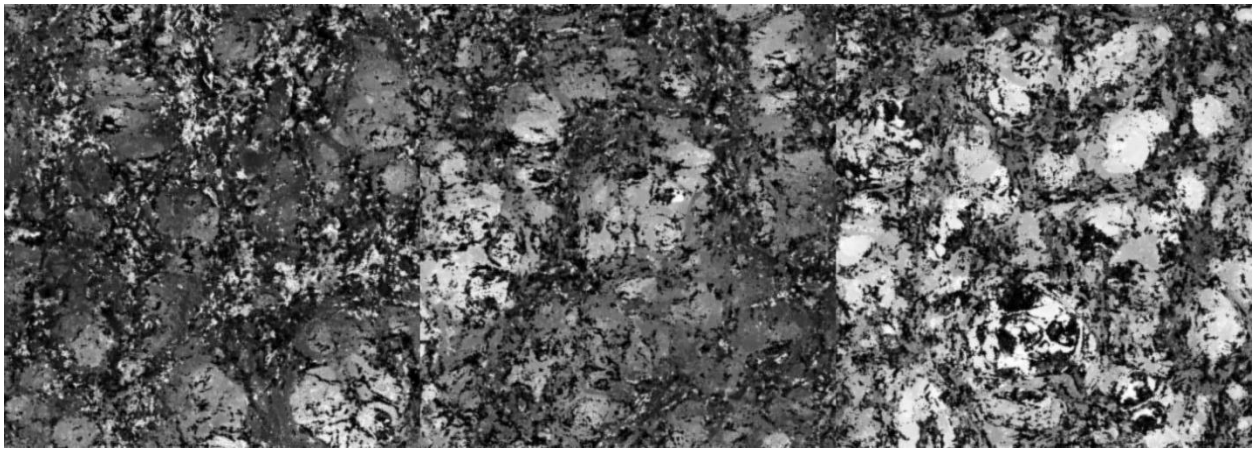

Figure 70: Sample 5.3.1 Surface Topology (16A, 0.052ms^{-1}, 0mm from start of cut)

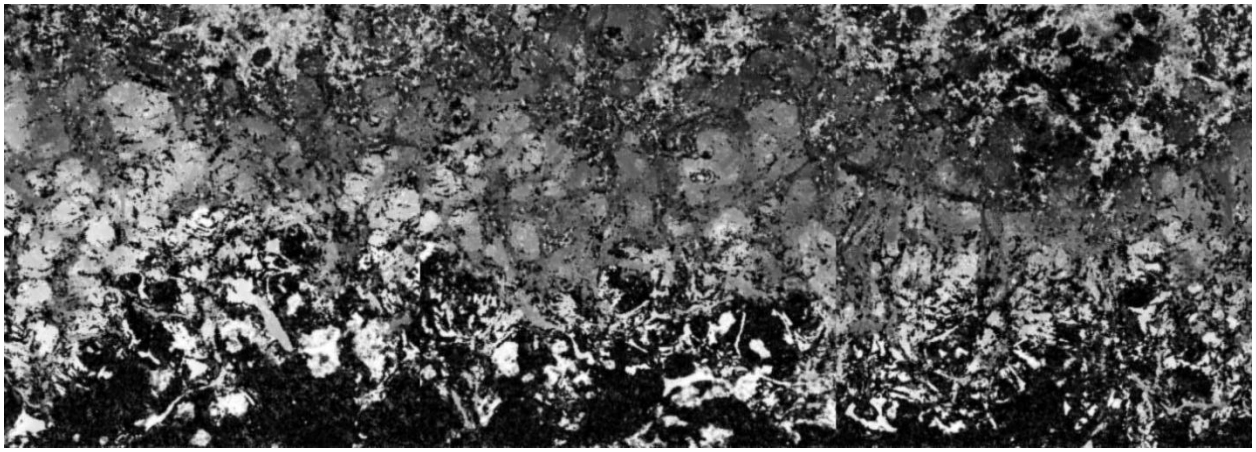

Figure 71: Sample 5.3.2 Surface Topology (16A, 0.052ms^{-1}, 50mm from start of cut)

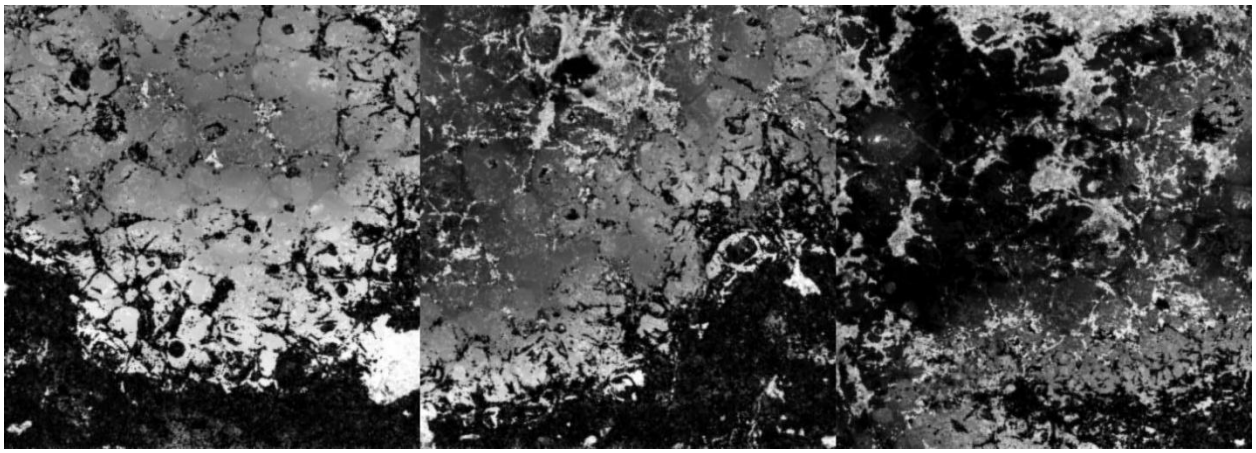

Figure 72: Sample 5.3.3 Surface Topology (16A, 0.052ms^{-1}, 250mm from start of cut)

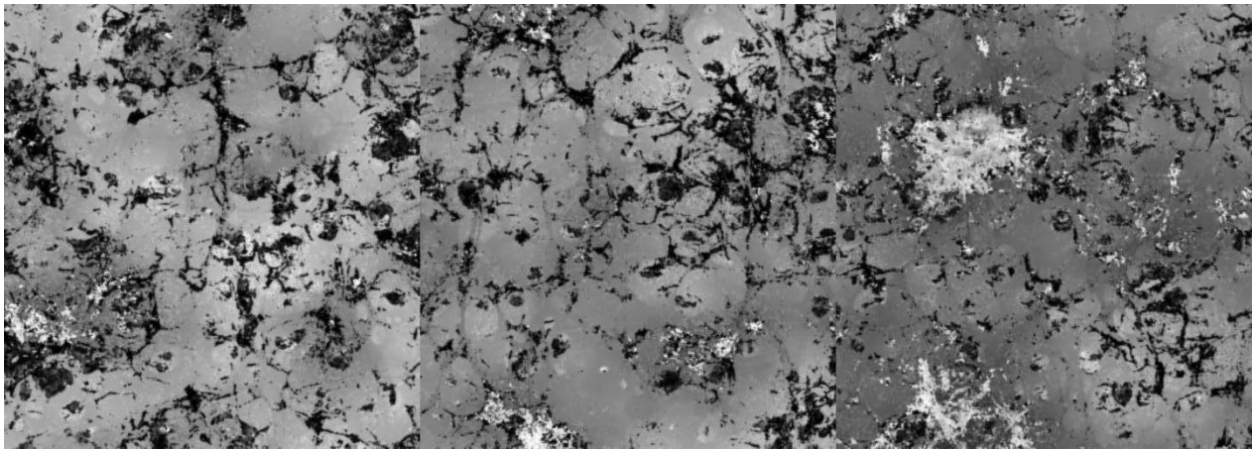

Figure 73: Sample 5.3.4 Surface Topology (16A, 0.052ms^{-1}, 400mm from start of cut)

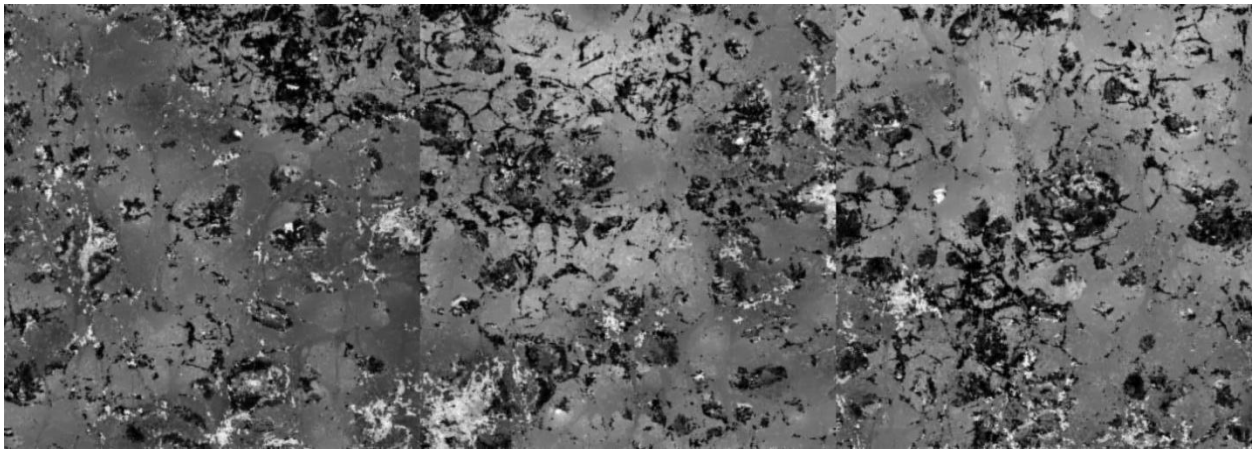

Figure 74: Sample 5.3.5 Surface Topology (16A, 0.052ms^{-1}, 550mm from start of cut)

Figure 75: Sample 5.4.1 Surface Topology (22A, 0.052ms^{-1}, 0mm from start of cut)

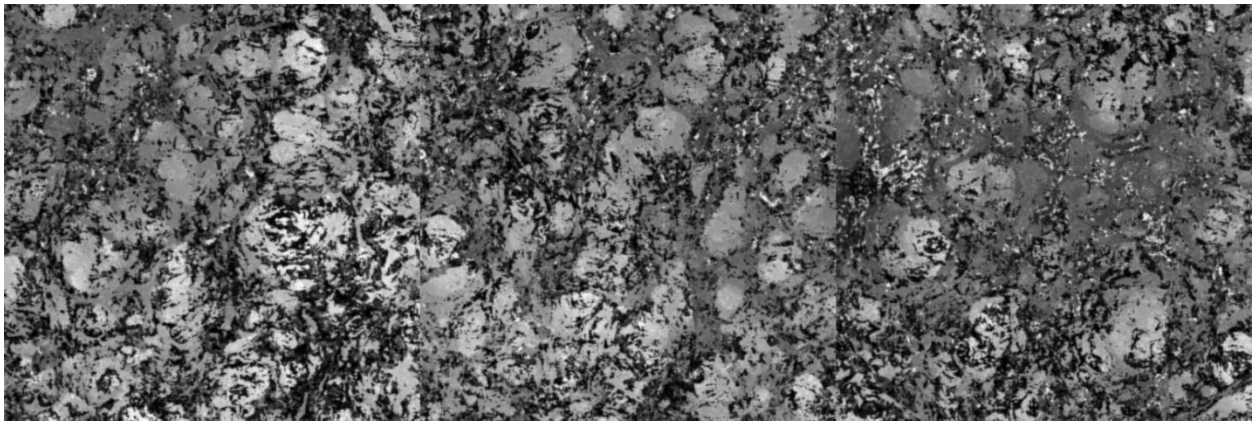

Figure 76: Sample 5.4.2 Surface Topology (22A, 0.052ms^{-1}, 50mm from start of cut)

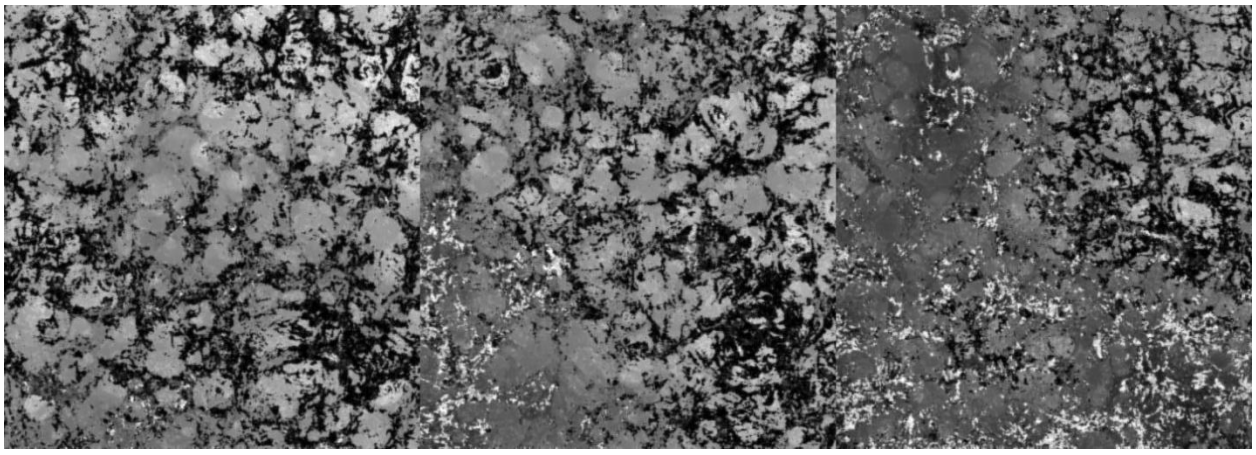

Figure 77: Sample 5.4.3 Surface Topology (22A, 0.052ms^{-1}, 250mm from start of cut)

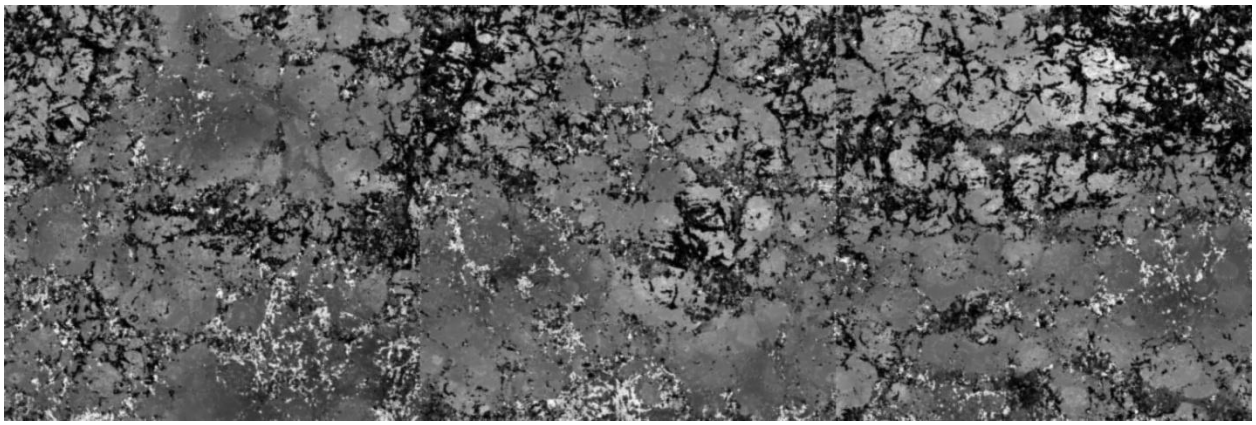

Figure 78: Sample 5.4.4 Surface Topology (22A, 0.052ms^{-1}, 400mm from start of cut)

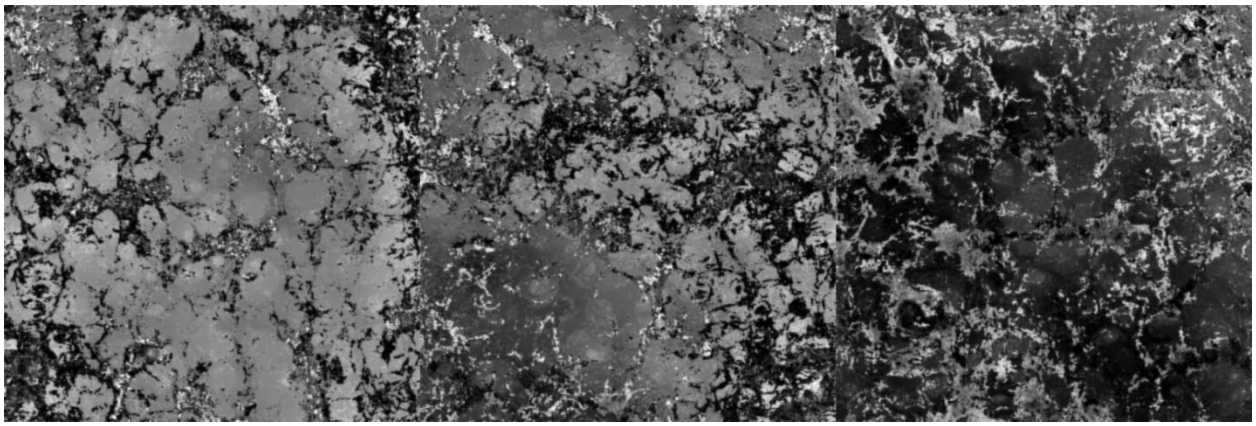

Figure 79: Sample 5.4.5 Surface Topology (22A, 0.052ms^{-1}, 550mm from start of cut)

Figure 80: Sample 5.5.1 Surface Topology (19A, 0.040ms^{-1}, 0mm from start of cut)

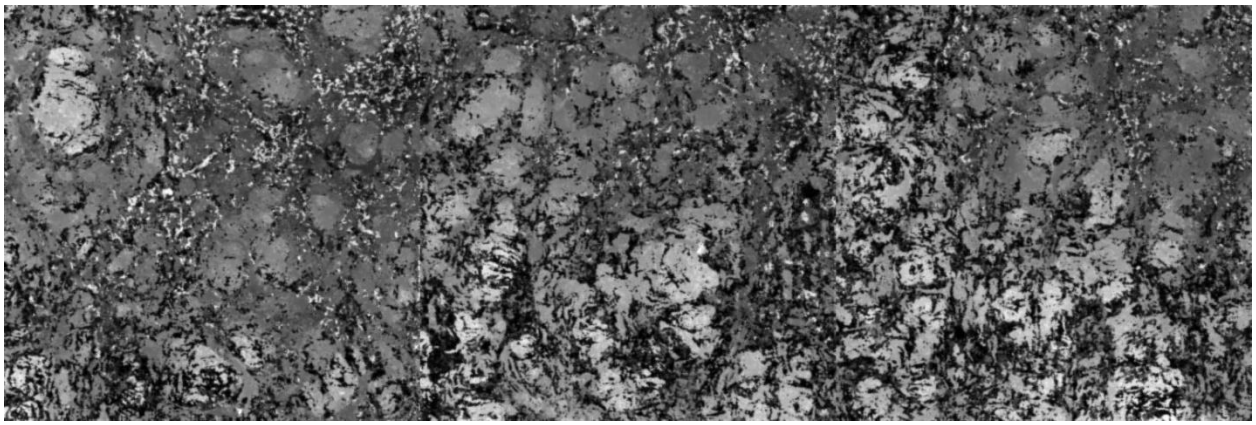

Figure 81: Sample 5.5.2 Surface Topology (19A, 0.040ms^{-1}, 50mm from start of cut)

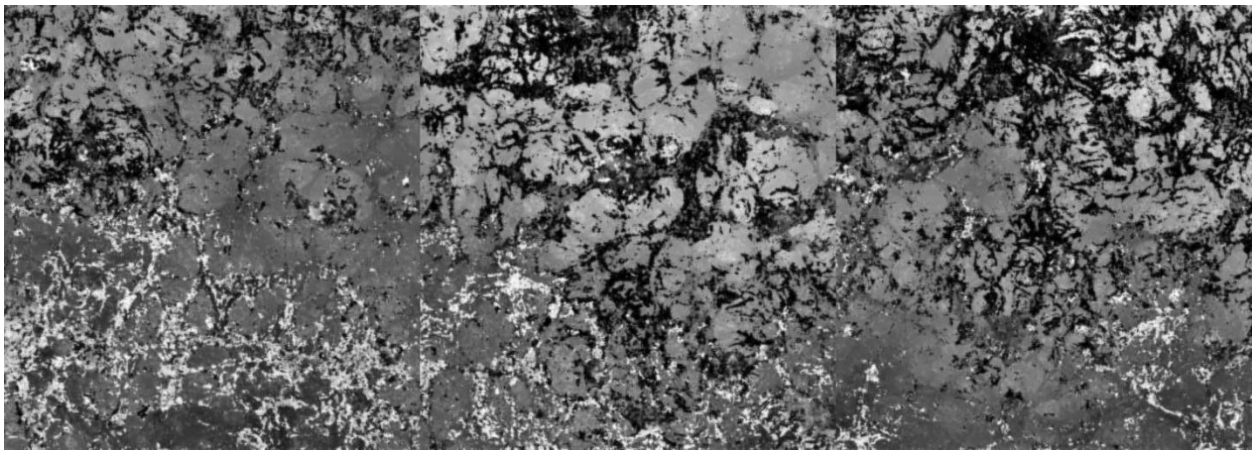

Figure 82: Sample 5.5.3 Surface Topology (19A, 0.040ms^{-1}, 250mm from start of cut)

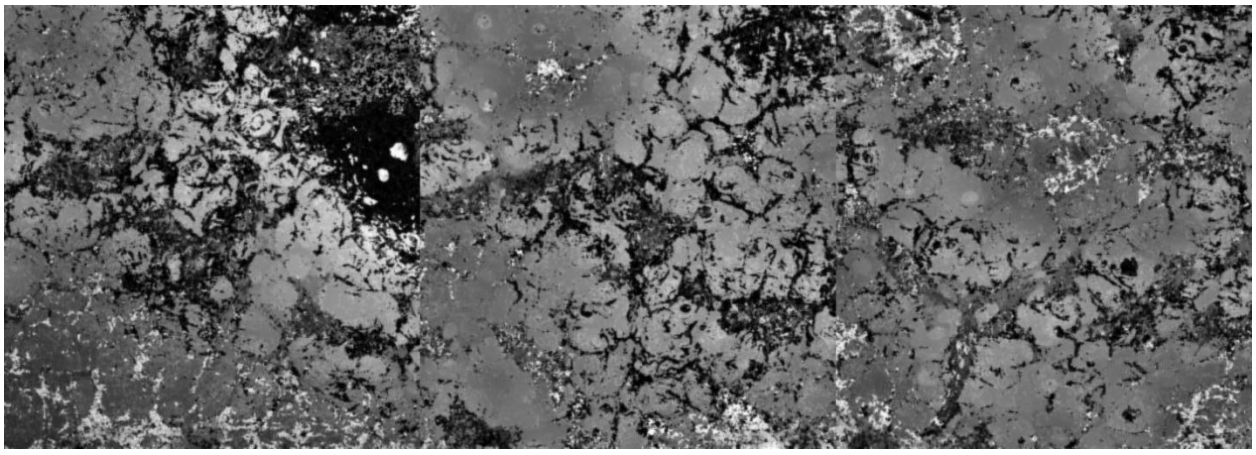

Figure 83: Sample 5.5.4 Surface Topology (19A, 0.040ms^{-1}, 400mm from start of cut)

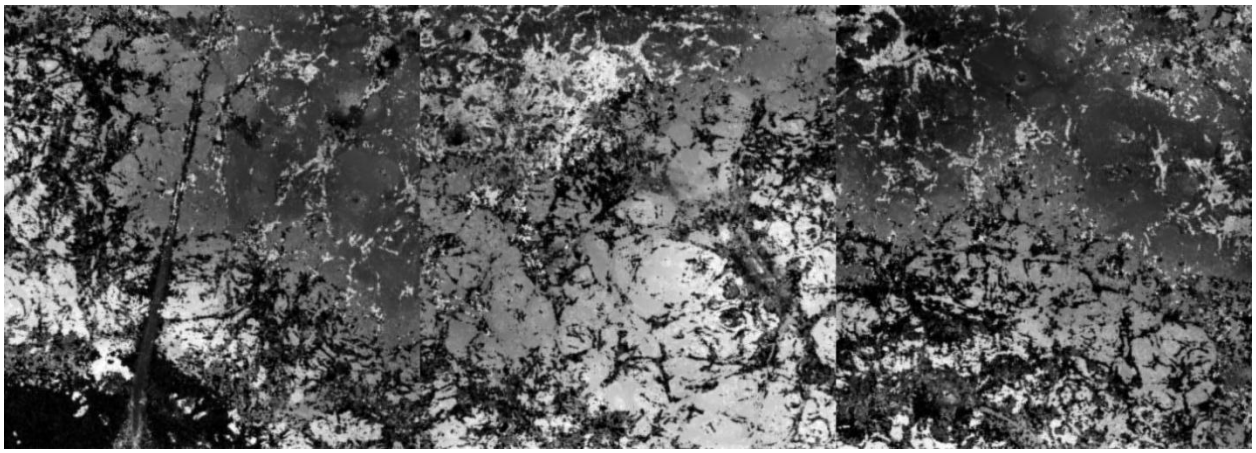

Figure 84: Sample 5.5.5 Surface Topology (19A, 0.040ms^{-1}, 550mm from start of cut)

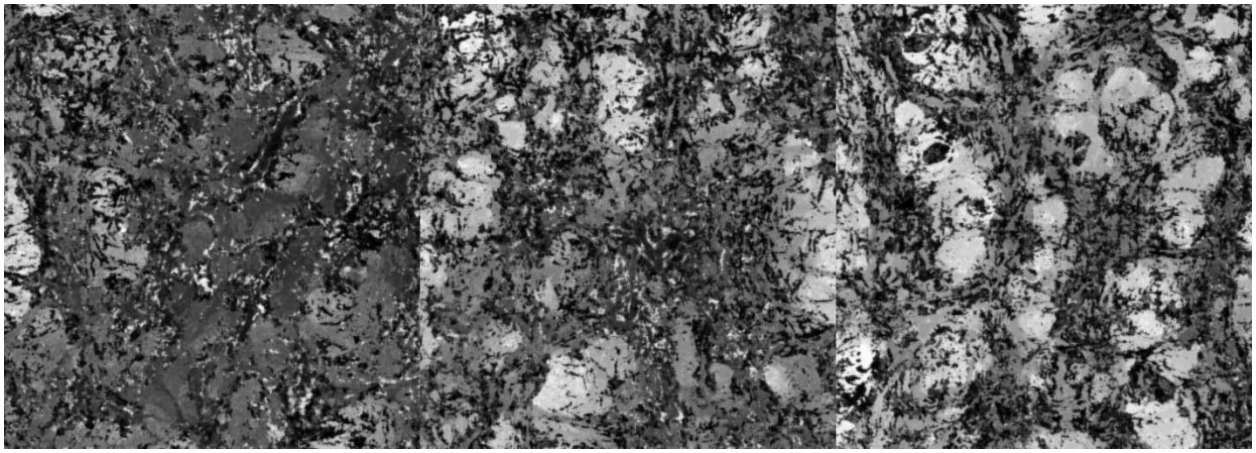

Figure 85: Sample 5.6.1 Surface Topology (19A, 0.040ms^{-1}, 0mm from start of cut)

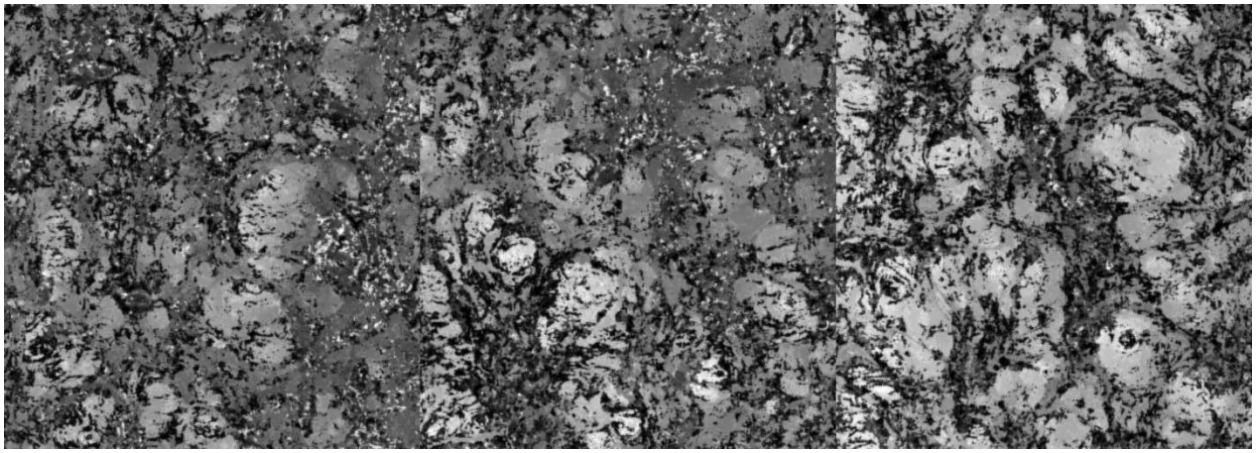

Figure 86: Sample 5.6.2 Surface Topology (19A, 0.040ms^{-1}, 50mm from start of cut)

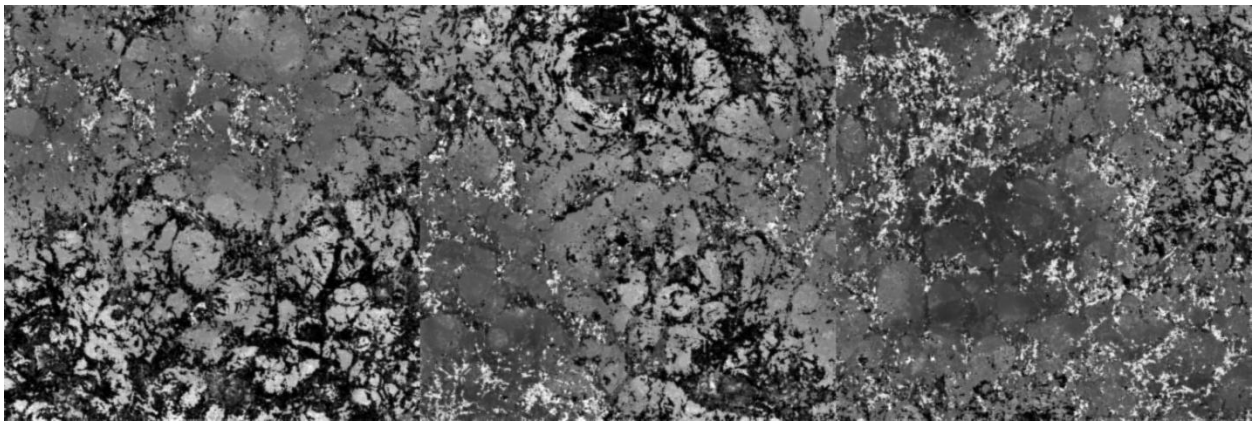

Figure 87: Sample 5.6.3 Surface Topology (19A, 0.040ms^{-1}, 250mm from start of cut)

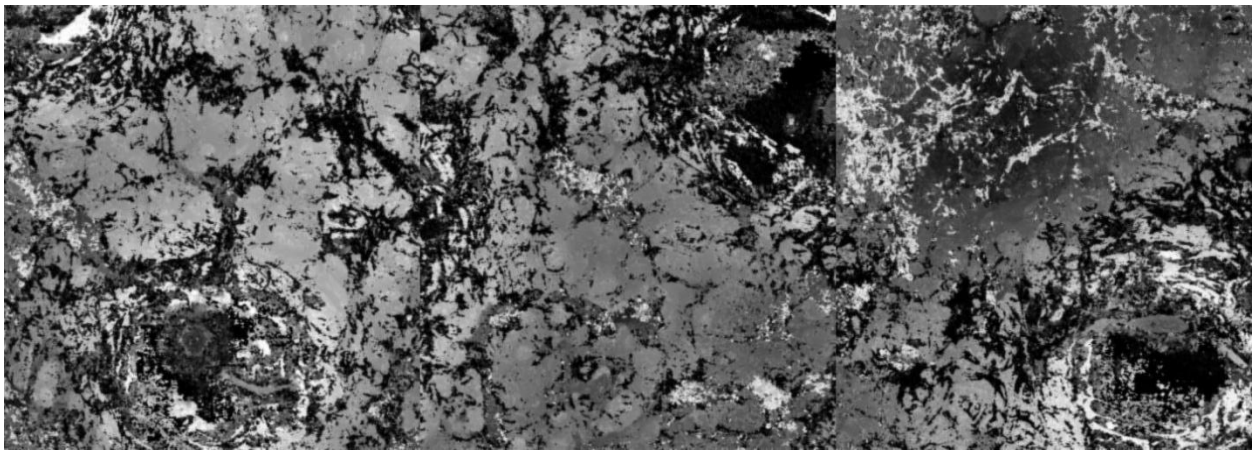

Figure 88: Sample 5.6.4 Surface Topology (19A, 0.040ms^{-1}, 400mm from start of cut)

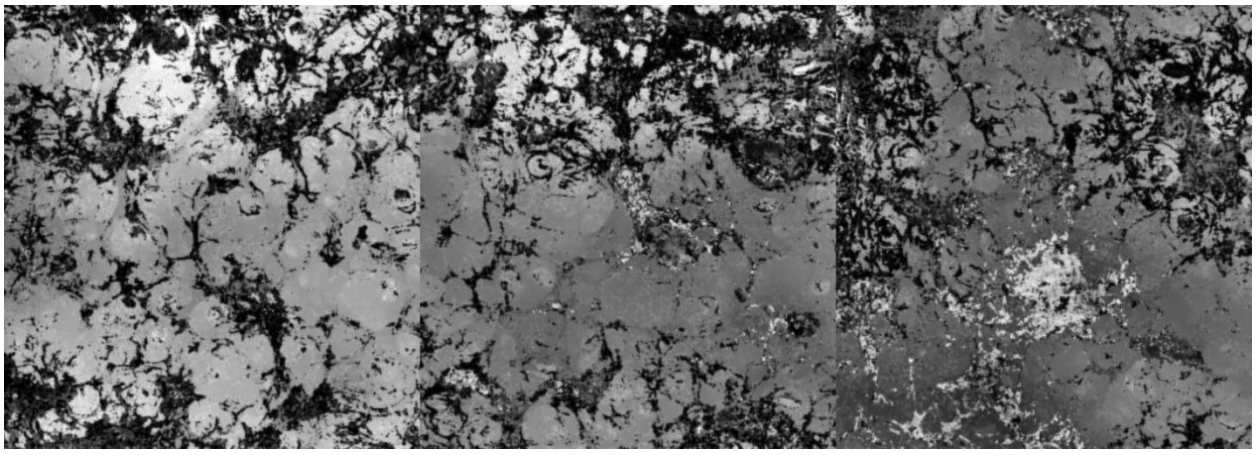

Figure 89: Sample 5.6.5 Surface Topology (19A, 0.040ms^{-1}, 550mm from start of cut)

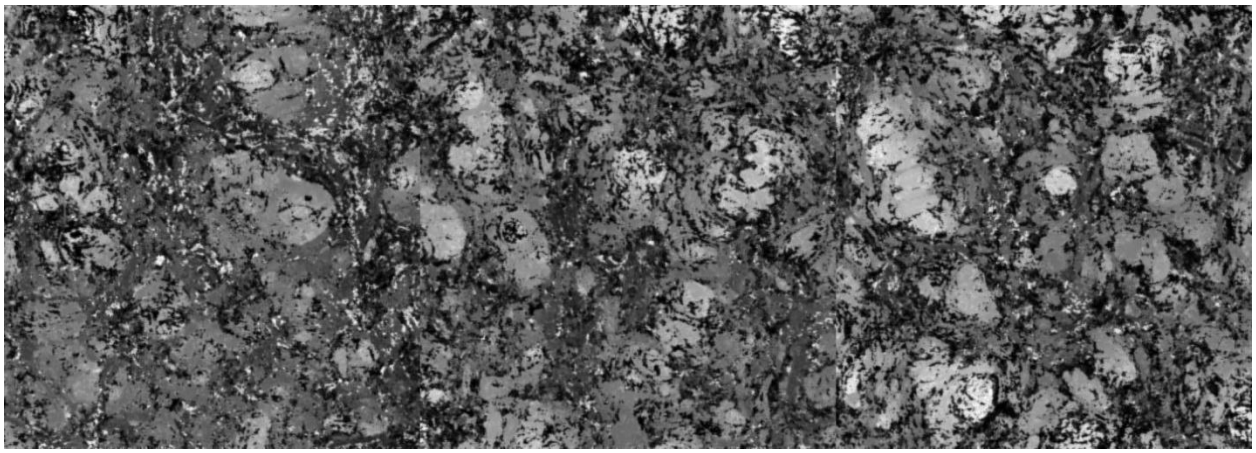

Figure 90: Sample 5.7.1 Surface Topology (19A, 0.040ms^{-1}, 0mm from start of cut)

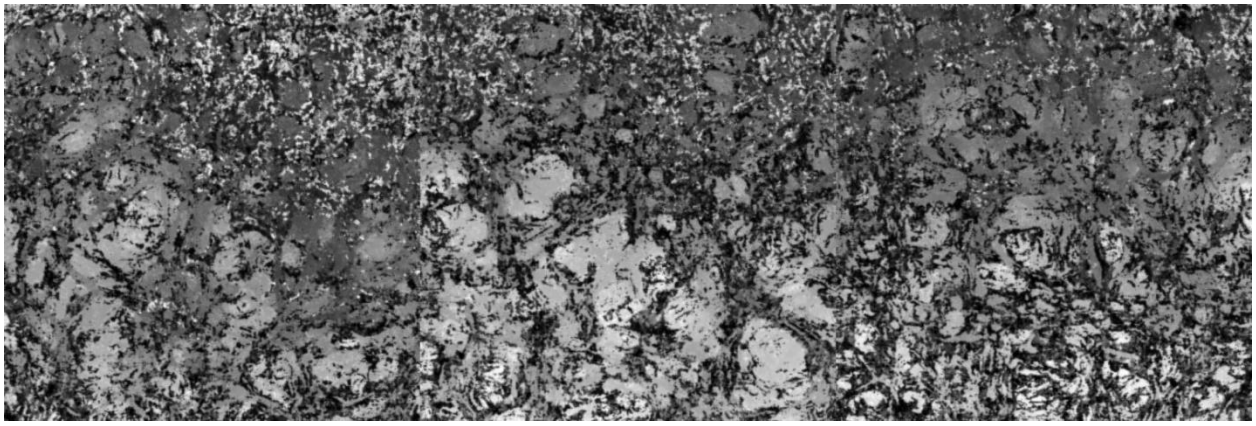

Figure 91: Sample 5.7.2 Surface Topology (19A, 0.040ms^{-1}, 50mm from start of cut)

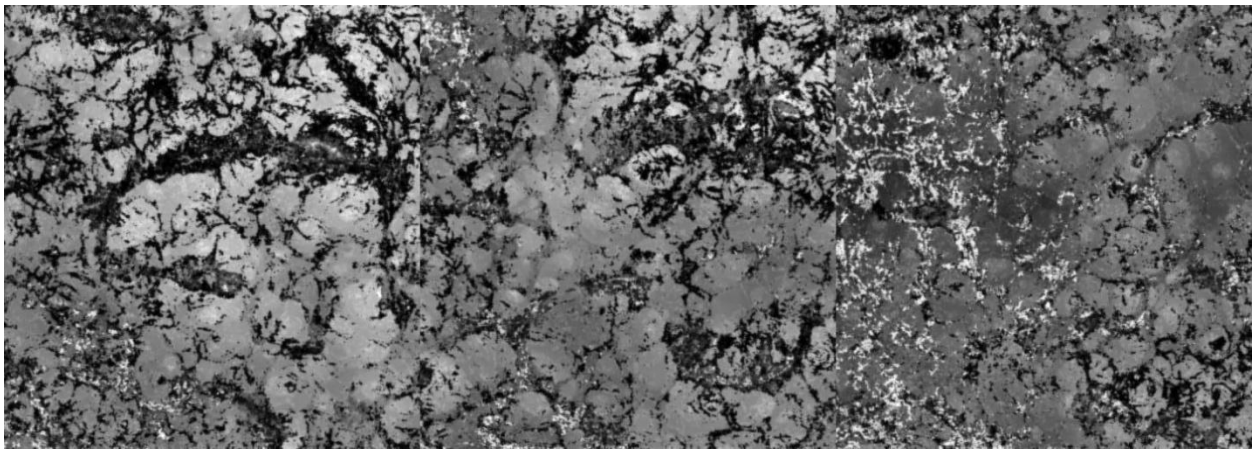

Figure 92: Sample 5.7.3 Surface Topology (19A, 0.040ms^{-1}, 250mm from start of cut)

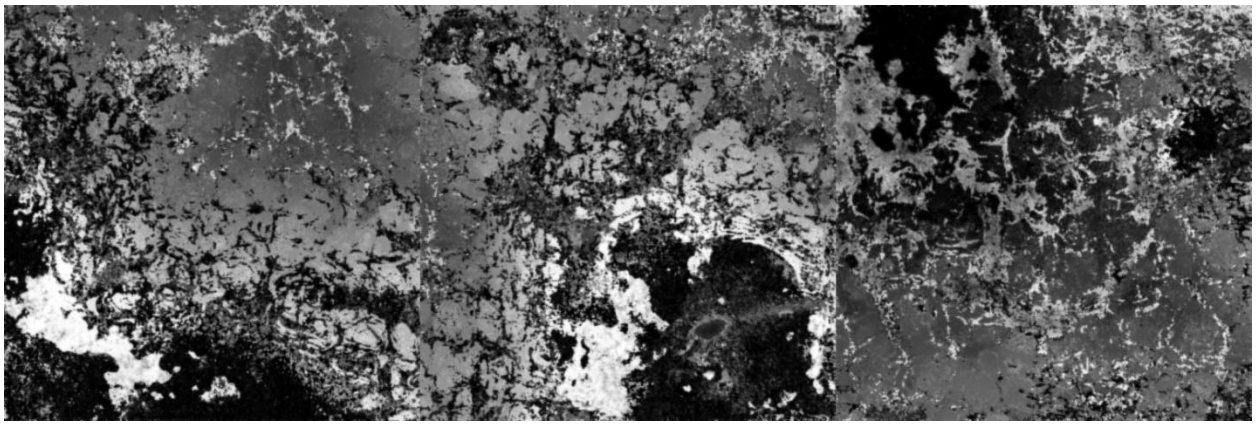

Figure 93: Sample 5.7.4 Surface Topology (19A, 0.040ms^{-1}, 400mm from start of cut)

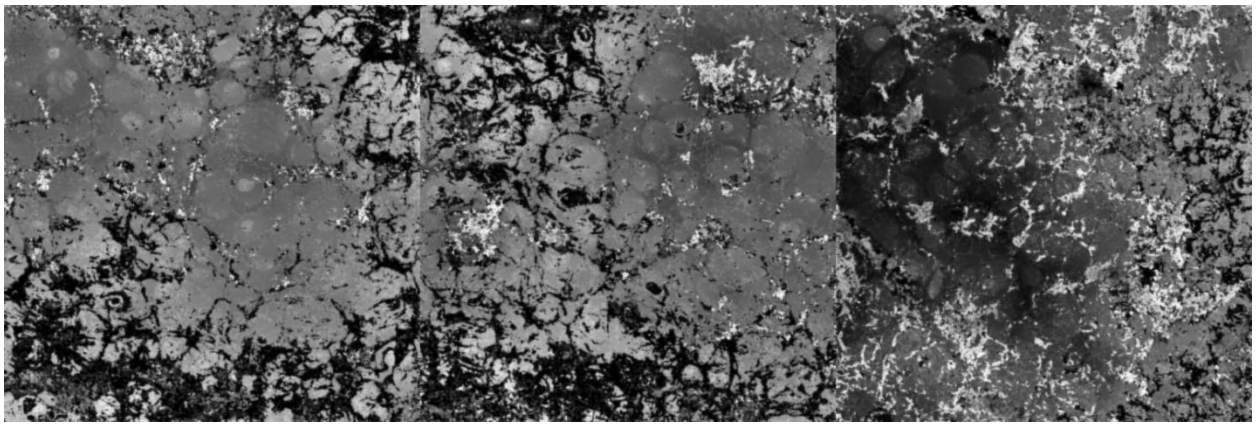

Figure 94: Sample 5.7.5 Surface Topology (19A, 0.040ms^{-1}, 550mm from start of cut)

Figure 95: Sample 5.8.1 Surface Topology (22A, 0.075ms^{-1}, 0mm from start of cut)

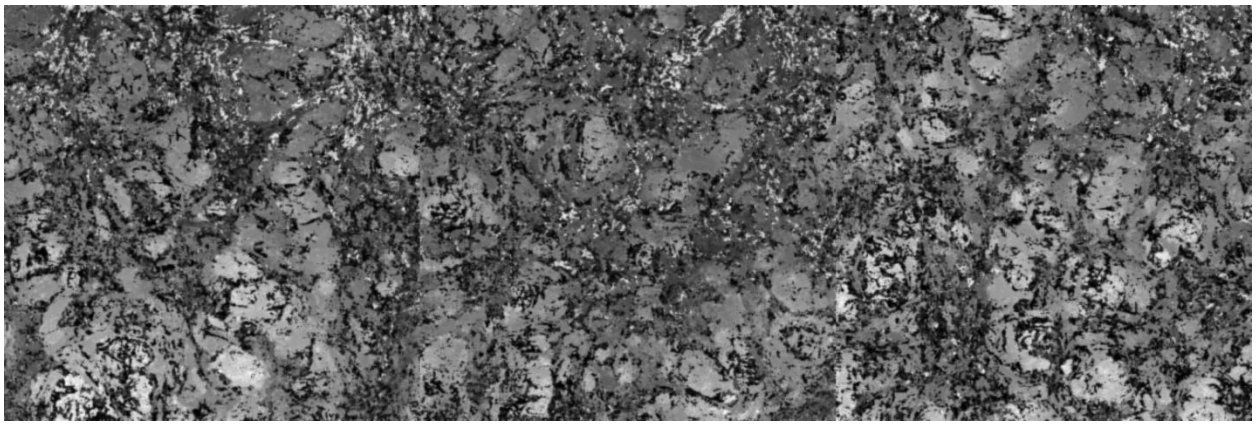

Figure 96: Sample 5.8.2 Surface Topology (22A, 0.075ms^{-1}, 50mm from start of cut)

Figure 97: Sample 5.8.3 Surface Topology (22A, 0.075ms^{-1}, 250mm from start of cut)

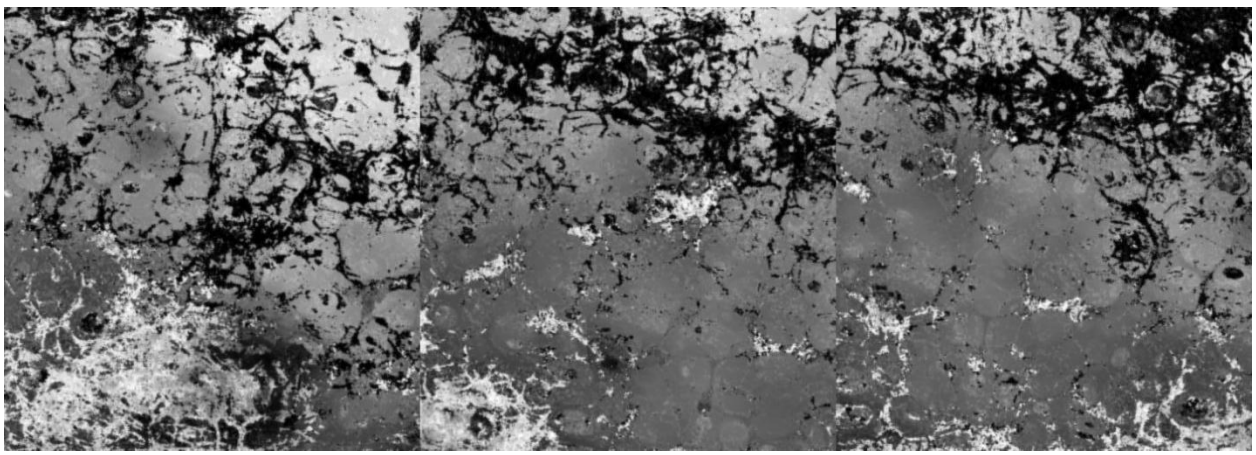

Figure 98: Sample 5.8.4 Surface Topology (22A, 0.075ms^{-1}, 400mm from start of cut)

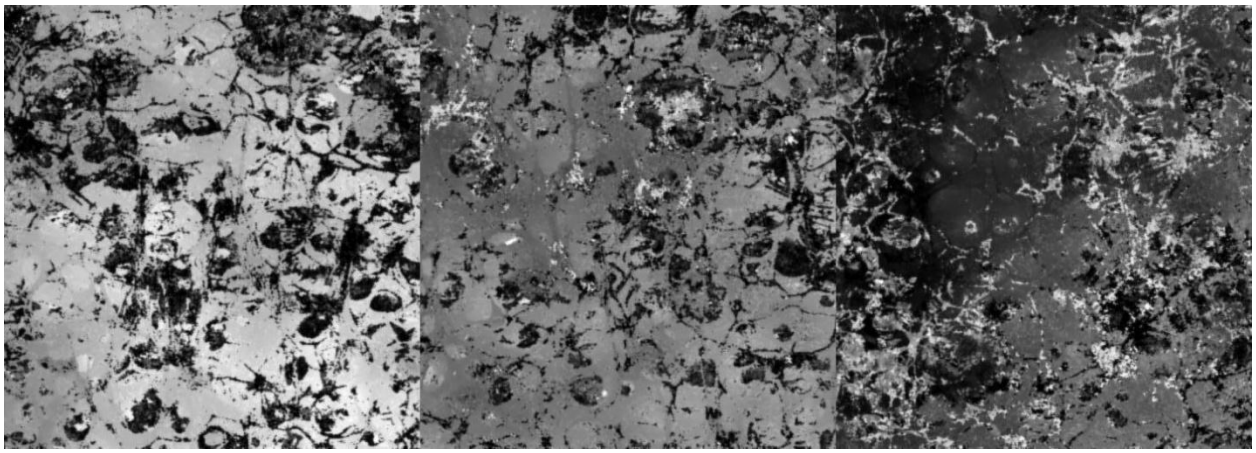

Figure 99: Sample 5.8.5 Surface Topology (22A, 0.075ms^{-1}, 550mm from start of cut)

Appendix A3: Matlab Scripts for Calculating Surface Texture Parameters

Profile-Based Parameter Calculation Script (Ra, Rz, Rmax, etc)

```
% Roughness Parameter Calculator

% Script file to calculate the values of roughness parameters for surface
% profile data harvested using the Biological Sciences Confocal Microscope.

% Written by Joe Bain, Ph.D Candidate, February 2008.

% First, process Confocal Microscope image stacks in accordance with the
%  procedures outlined in the document 'Surface Roughness Measurement
Procedure'

% Note the need to remove the X and Y column headers from the text file
% before importing into Matlab.

% Now load the resulting text file of surface profile coordinates into
% Matlab. Copy the text file into the Matlab workspace and change the
% filename below to match the file to be processed.

clc
clear all
A = load ('Plot Values.txt');

% Now enter the physical parameters which the script will need to calculate
% roughness parameters:

maxheight = -110; %input('Enter the maximum height of the image stack in
microns')
minheight = 112; %input('Enter the minimum height of the image stack in
microns')
    % These determine the physical sie of the image stack, against which
    % greyscale values must be calibrated.

    % Then convert to mm of height:
maxheight = maxheight/1000;
minheight = minheight/1000;

maxgrey = 255; %input('Enter the maximum grey value of the composite image')
mingrey = 0; %input('Enter the minimum grey value of the composite image')
    % These determine the extreme grey values to calibrate with the extreme
    % physical size.

pixelsize = 1.55/1024;    % Determines the pixel size in mm for a 10x dry
confocal objective.
loopsize = size(A,1);
```

```
% Now calibrate the pixel number and greyscale values to create an array
% where each entry reflects the physical size of the surface profile.
    % Calibrate pixel numbers fist:
    for i = 1:loopsize
        A(i,1) = A(i,1)*pixelsize;
    end
    % Now calibrate grey values to height
    for i = 1:loopsize
        A(i,2) = (((A(i,2) - mingrey)/(maxgrey - mingrey)) * (maxheight -
minheight)) + minheight;
    end

% The next phase is to level the surface data to minimise the inaccuracies
% resulting from a sloped sample. To do this, a first-order linear
% trendline for the data is developed, and the raw data is rotated until
% the trendline is horizontal.

% Plot the linear trend line using the subroutine createfigure.m. This
% subroutine was automatically generated by Matlab to repeat curve fitting
% carried out using the GUI, with additions to return the gradient and y
% intercept of the linear trend as useful variables.

[trend] = createfigure((A(:,1)),(A(:,2)));
gradient = trend(1);
yintercept = trend(2);

% Now calculate the angle theta through which the surface data must be
rotated so
% that the linear trendline is horizontal. For this we will use a default
% dx of 1mm.

dx = 1;
dy = dx * gradient;
theta = atand(dy/dx); % To give the necessary angle of rotation in degrees
thetar = theta *((2*pi)/360); % To convert theta into radians

% Then enter the appropriate command to rotate the graphics object by theta
% degrees
% Determine object label for the raw data line on the graph
 h1 = findobj(gca,'type','line','color','b');
 h2 = findobj(gca,'type','line','color','r');
 rotate(h1,[0 0 1],-theta) % To rotate object h around the Z axis by theta
degrees
 rotate(h2,[0 0 1],-theta) % To perform the same rotation on the trendline
for verification purposes

% Establish rotation matrix Ar:

Ar = [cos(thetar) sin(thetar); -sin(thetar) cos(thetar)];

for i=1:loopsize
    X = A(i,:);
        Xt = X';  % This transposes each row of A into a column vector Xt
        Xbart = Ar * Xt;
```

```
        Xbar = Xbart';
        A(i,:) = Xbar;   % Writes the new row vector of coordinates into each
Row of A.
end

plot(A(:,1),A(:,2),'k')

% Note that I still need to make the sign of the rotation less dependent on
% operator input

% Next apply smoothing to the profile line to compensate for the greater
% resolution of an optical measurement system (calibration, effectively).

aa=smooth(A(:,2),11, 'moving'); % Applies a moving average to the data prior
to calculation of roughness parameters.
BBB = [A(:,1) aa];
hold on
plot(BBB(:,1),BBB(:,2),'r')
plot(BBB(:,1),BBB(:,2),'m')

%Now we can begin the calculation of Ra.
% Initially need to find the lowest point of the surface, surface height
% coordinates are in the second column of the array BBB.

minint = min(BBB); % Defines an intermediate row vector with the minimum
elements of each column of A.
maxint = max(BBB);
lowpoint = minint(2);    % The second element of minint, the lowest surface
height recorded.

% Next step is to determine the area enclosed by the surface and the
% horizontal line through the lowest point. This will be done by
% approximating each surface data point as a vertical rectangle and summing
% together the area of these rectangles for a total area.

areaP = 0;
for i = 1:loopsize
    areaP = areaP + (abs((BBB(i,2))-lowpoint) * pixelsize);    % This gives
the total area enclosed in square mm.
end

% Now determine the sampling length L, the difference between the minimum
% and maximum horizontal coordinates (1st column of A).

horimin = minint(1);
horimax = maxint(1);
L = (horimax - horimin);  % This gives the horizontal range in mm.

% Now determine reference line height Hm:

Hm = areaP/L + lowpoint;   % Which gives the absolute height of the surface
centre line.

% Next find the areas R and S, those enclosed by the surface above and
```

```
% below the centreline respectively.

areaR = 0;
areaS = 0;
for i = 1:loopsize
    if BBB(i,2) > Hm;
        areaR = areaR + (abs(BBB(i,2) - Hm) * pixelsize);
    else
        areaS = areaS + (abs(BBB(i,2) - Hm) * pixelsize);
    end
end

% Finally, it is possible to determine the parameter value Ra.

Ra = (areaR + areaS)/L * 1000   % Determines the value of Ra in microns.

% Calculate Rmax, the Maximum peak to valley height:

Rmax = (maxint(2) - minint(2)) * 1000 % To determine Rmax in microns.

% Calculate Rz, the Ten-Point Height:
    % First sort array A so elements are in ascending order
B = sort(BBB);
        % Now extract the five highest values:
    Bsize = size(B);
    Bmax = Bsize(1);
    ref = lowpoint - 5;
    r1 = abs(B(Bmax,2) - ref);
    r3 = abs(B(Bmax - 1,2) - ref);
    r5 = abs(B(Bmax - 2,2) - ref);
    r7 = abs(B(Bmax - 3,2) - ref);
    r9 = abs(B(Bmax - 4,2) - ref);

    % And the five lowest values
    r2 = abs(B(1,2) - ref);
    r4 = abs(B(2,2) - ref);
    r6 = abs(B(3,2) - ref);
    r8 = abs(B(4,2) - ref);
    r10 = abs(B(5,2) - ref);

    % Now Rz can be calculated and returned to the user:
    Rz = (((r1 + r3 + r5 + r7 + r9) - (r2 + r4 + r6 + r8 + r10))/5) * 1000

% Return sampling length L:

L
```

Areal Parameter Calculation Script (Sa, Sq, Ssk, etc)

```
% Roughness Parameter Calculator for Areal data

% Script file to calculate the values of roughness parameters for surface
% profile data harvested using the Biological Sciences Confocal Microscope.
```

```
% Written by Joe Bain, Ph.D Candidate, April 2010.

% First, process Confocal Microscope image stacks in accordance with the
% procedures outlined in the document 'Surface Roughness Measurement
% Procedure' and produce greyscale composite images of the surface
% topology. Name these according to the sample naming convention, i.e.
% 'Xnum.Runnum.Samplenum Composite.jpg'

% Copy these images into the matlab workspace, then run this script.

clc
clear all

%==========================================================================

% Define parameters needed for the data processing in this space:

Xnum = 5;    %Defines the experiment number for the current data set
Runnum = 8;     %Defines the number of runs (i.e sets of cutting conditions)
in the experiment
Samplenum = 5;  %Defines the number of samples made from each set of cutting
conditions
pixelsize = 1.55/512;     % Determines the pixel size in mm for a 10x dry
confocal objective.

%==========================================================================

% Load in the height data for the images. These data points are found in
% the text files with name format 'X(Xnum) Height Data'

Xnumstr1 = num2str(Xnum);
heightname = strcat('X',Xnumstr1,' Height Data.txt');
heightdata = load(heightname);

normalsarraysize = Runnum * Samplenum;
normalsarray = zeros(3,normalsarraysize);

% Define a zeros array for output data to be stored in, and enter titles in
% the top row of this array.
outputrows = (Runnum*Samplenum);
outputarray = zeros(outputrows,7);

rowcount = 0;

for mainloop = 1:Runnum
    for j = 1: Samplenum
    %mainloop = 1;   % For a single run-through of 1.1.1 Composite.
    %j = 1;
    %======================================================================
    % Clear out all variables from previous loops:
    clear Xnumstr Runnumstr Samplenumstr picname I heightrank maxheight
minheight imagerows imagecols A maxint minint maxgrey mingrey gradient
yintercept dx dy theta thetar outputfilename X Xt Xbart Xbar aa BBB lowpoint
```

```
areaP horimin horimax L Hm areaR areaS Ra Rmax B Bsize Bmax ref r1 r2 r3 r4
r5 r6 r7 r8 r9 r10 Rz
    %=========================================================================
        rowcount = rowcount + 1;

        Xnumstr = num2str(Xnum);
        Runnumstr = num2str(mainloop);
        Samplenumstr = num2str(j);
        picname       =       strcat(Xnumstr,'.',Runnumstr,'.',Samplenumstr,'
Composite.jpg');

       I = imread (picname);    % Loads the relevant image into the matlab
workspace 'I = imread (picname);'
        % ensure image is in greyscale:
       I = rgb2gray(I);

        % Now determine relevant height data from the heightdata text file:

        heightrank = ((mainloop-1)*4)+j;
        maxheight = heightdata(heightrank,1);
        minheight = heightdata(heightrank,2);

        %Convert height values to mm measurements:
        maxheight = maxheight/1000;
        minheight = minheight/1000;

        % Determine the number of rows and columns of pixels in the image:
        imagerows = size(I,1);
        imagecols = size(I,2);
        imagewidth = imagerows*pixelsize;
        imagelength = imagecols*pixelsize;

        arraysize = size(I,1) * size(I,2);
        A = zeros(arraysize,3);

        % Now write values from Image array I to an xyz point cloud
        % three-column array, A:

            for y = 1:imagerows
                for x = 1:imagecols
                    A((x+(imagecols*(y-1))),1) = x*pixelsize;
                    A((x+(imagecols*(y-1))),2) = y*pixelsize;
                    A((x+(imagecols*(y-1))),3) = I(y,x);
                end
            end

            for p = 1:arraysize
                A(p,3)            =            ((A(p,3)-0)/(255-0)*(maxheight-
minheight))+minheight;
            end

            % Fit a plane to the xyz data in matrix A:

            [coeff,score,roots] = princomp(A);
```

```
 Qmat = coeff(:,1);
 Pmat = coeff(:,2);
 normal = coeff(:,3);

% Establish target vector for the rotation:

z = [0 0 1];

% Determine rotation angle and direction:

rotterms = vrrotvec(normal,z);

% Determine rotation matrix:

Rotmat = vrrotvec2mat(rotterms);

% Now apply rotation:
loopsize = size(A,1);
 for s = 1:loopsize
     Vtemp = A(s,:);
     Vtemp = Vtemp';

     Vnew = Rotmat*Vtemp;
     Vnew = Vnew';

     A(s,:) = Vnew;
 end
% Re-fit plane to rotated data to check results:
 [coeff,score,roots] = princomp(A);
 normal = coeff(:,3);

 % Now proceed with evaluating surface roughness parameters:

 % First determine the height of the reference plane above the
 % minimum point on the surface. This height is denoted as
 % hrefplane

 minsurf = min(A(:,3));
 volint = 0;
 for i =1:loopsize
     volint = volint + (pixelsize^2)* (A(i,3) - minsurf);
 end
 hrefplane  =  volint/(imagelength*imagewidth);       %To  give  the
height of the reference plane above the lowest point of the surface, in mm

 % Now proceed to the calculation of amplitude-based parameters:

 % Calculate Sa:
 saint = 0;
 for i = 1:loopsize
     saint = saint + abs(A(i,3) - hrefplane);
 end
 Sa = (1/(imagerows*imagecols))*saint;
```

```
            % Calculate RMS roughness Sq:
            sqint = 0;
            for i = 1:loopsize
                sqint = sqint + ((A(i,3) - hrefplane)^2);
            end
            Sq = sqrt((1/(imagerows*imagecols)) * sqint);

            % Calculate skew Ssk:
            sskint = 0;
            for i = 1:loopsize
                sskint = sskint + ((A(i,3) - hrefplane)^3);
            end
            Ssk = (1/(imagerows * imagecols * Sq^3)) * sskint;

            % Calculate kurtosis Sku:
            skuint = 0;
            for i = 1:loopsize
                skuint = skuint + ((A(i,3) - hrefplane)^4);
            end
            Sku = (1/(imagerows*imagecols*Sq^4)) * skuint;

            % Calculate the peak-to-valley height (Sz, St, Sy - all the
            % same thing):

            maxpix = max(A(:,3));
            minpix = min(A(:,3));
            Sz = maxpix - minpix;

        % Now need to generate some surface parameters that are not based on
        % the amplitude of the surface data

        % First write rotated data from matrix A back into a new image
        % matrix I2. This involves a slight approximation since some data
        % points do not maintain regular coordinates, but given the high
        % resolution and the large amount of data available this is deemed
        % acceptable.

        I2 = zeros(imagerows,imagecols);
        for p = 1:imagerows
            for c = 1:imagecols
                I2(p,c) = A(((p-1)*imagecols) + c, 3);
            end
        end

        % Now find the number of local maxima and minima, defined as a pixel
which is
        % higher than all eight surrounding pixels. This variable is called
        % 'peakcount'
        summitcount = 0;
        for p = 2:(imagerows-1)
            for c = 2:(imagecols-1)
                if I2(p,c) > I2(p-1,c-1) && I2(p,c) > I2(p,c-1) && I2(p,c) >
I2(p+1,c+1) && I2(p,c) > I2(p+1,c) && I2(p,c) > I2(p-1,c) && I2(p,c) > I2(p-
1,c+1) && I2(p,c) > I2(p,c+1) && I2(p,c) > I2(p+1,c+1)
                    summitcount = summitcount + 1;
```

```
                end
            end
        end

        % Now determine Sds, the summit density (e.g the number of peaks,
        % peakcount, divided by the area of the image.

        imagearea = (imagecols * pixelsize) * (imagerows * pixelsize);    %To
give area in mm^2

        Sds = summitcount/imagearea;     %To give peak density in peaks per
square mm

        % Repeat this process to determine the density of local minima in
        % the image:

        valleycount = 0;
        for p = 2:(imagerows-1)
            for c = 2:(imagecols-1)
                if I2(p,c) < I2(p-1,c-1) && I2(p,c) < I2(p,c-1) && I2(p,c) <
I2(p+1,c+1) && I2(p,c) < I2(p+1,c) && I2(p,c) < I2(p-1,c) && I2(p,c) < I2(p-
1,c+1) && I2(p,c) < I2(p,c+1) && I2(p,c) < I2(p+1,c+1)
                 valleycount = valleycount + 1;
                end
            end
        end

        Vds = valleycount/imagearea;      %To give the density of local minima
in minima per square mm

        outputarray(rowcount,1) = Sa;
        outputarray(rowcount,2) = Sq;
        outputarray(rowcount,3) = Ssk;
        outputarray(rowcount,4) = Sku;
        outputarray(rowcount,5) = Sz;
        outputarray(rowcount,6) = Sds;
        outputarray(rowcount,7) = Vds;

    end
end

save X5arealdata outputarray -ascii -tabs;
```

Calculation Script for Autocorrelation-Based Parameters (Str, etc)

```
clc
clear all

% Enter number of image files to be processed (these will be sequentially
numbered):
filecount = 316;
```

```
% Initialise output array of zeros:
outputarray = zeros(filecount,4);

for mainloop = 1:filecount
    filecountstr = num2str(mainloop);
    picname = strcat(filecountstr,'.',jpg.jpg');

% Clear out variables from previous loops
%=========================================================================
clear I IAACF maxint maxvalue Inormaacf aacffilename plotname rowpeak colpeak
arrayrows  arraycols  binaryarray  counter0  counter1  counter2  counter3
belowarray abovearray Rmaxint Rmax Rminint Rmin Str Sal
%=========================================================================


%Read in relevant surface topology image
I = imread(picname);
%Convert image to greyscale
I = rgb2gray(I);
% Now convert to double precision elements
I = double(I);

% Determine physical size of each pixel:
pixelsize = 1.55/512;

%Calculate autocorrelation function:
IAACF = xcorr2(I);

% Determine maximum value of raw autocorrelation function (2-step process):
maxint = max(IAACF);
maxvalue = max(maxint);

% Normalise autocorrelation function by dividing by the maximum value. This
% gives the central spike an amplitude of 1.
Inormaacf = IAACF/maxvalue;
% Save the basic normalised AACF array for possible later use to generate
% plots
aacffilename = strcat(filecountstr,' AACF array');
save aacffilename Inormaacf -ascii -tabs;

% Now generate and save a 2D contour plot of the autocorrelation function
% surface:

contour(Inormaacf,'DisplayName','Inormaacf');figure(gcf);
plotname = strcat(filecountstr,' contour plot');
saveas(gcf,plotname,'jpg');
close all

% Determine indices of maximum value of this array (and hence of the central
peak):
[rowpeak,colpeak] = find(Inormaacf==max(Inormaacf(:)));

% Determine size of the normaacf array:
arrayrows = size(Inormaacf,1);
```

```
arraycols = size(Inormaacf,2);

% Initialise variables:
binaryarray = zeros(arrayrows,arraycols);
counter0 = 0;
counter1 = 0;

% Now go through the AACF array and apply thresholding at 0.2. Set cell
% values less than 0.2 to 0, and values above 0.2 to 1. Also count the
% number of data points that fall into each category.
for i = 1:arrayrows;
    for j = 1:arraycols;
        if Inormaacf(i,j) < 0.2;
            binaryarray(i,j) = 0;
            counter0 = counter0 + 1;
        elseif Inormaacf(i,j) >=0.2;
            binaryarray(i,j) = 1;
            counter1 = counter1 + 1;
        end
    end
end

belowarray = zeros(counter0,3);
abovearray = zeros(counter1,3);

counter2 = 0;
counter3 = 0;

for i = 1:arrayrows;
    for j =1:arraycols;
        if binaryarray(i,j) == 0;
            counter2 = counter2 + 1;
            belowarray(counter2,1) = i;
            belowarray(counter2,2) = j;
            belowarray(counter2,3) = sqrt(((abs(i - rowpeak))^2) + ((abs(j -
colpeak))^2));
        elseif binaryarray(i,j) ==1;
            counter3 = counter3 + 1;
            abovearray(counter3,1) = i;
            abovearray(counter3,2) = j;
            abovearray(counter3,3) = sqrt(((abs(i - rowpeak))^2) + ((abs(j -
colpeak))^2));
        end
    end
end

% Now we have two arrays, belowarray and above array, with the coordinates
% and the horizontal distance from the peak for every pixel both above and
% below the 0.2 threshold.

% The maximum distance from the centre point to the threshold (Rmax) in pixel
lengths will be the
% largest value of the third column of abovearray. Then convert to mm.

Rmaxint = max(abovearray);
```

```
Rmax = Rmaxint(3);
Rmax = Rmax * pixelsize;

%The minimum distance from the centre to the threshold (Rmin) in pixel
%lengths will be the smallest value of the third column of belowarray. Then
%convert to mm.

Rminint = min(belowarray);
Rmin = Rminint(3);
Rmin = Rmin * pixelsize;

% The texture aspect ratio Str is the ratio nof Rmin to Rmax:

Str = Rmin/Rmax;

% The fastest decay autocorrelation length Sal is the same as Rmin:

Sal = Rmin;

% Save Str, Sal data to an array in order to save it later:

outputarray(mainloop,1) = Rmin;
outputarray(mainloop,2) = Rmax;
outputarray(mainloop,3) = Str;
outputarray(mainloop,4) = Sal;

end

save AACFparameters outputarray -ascii -tabs;
```

10%-Height Band Processing Script

```
clc
clear all

%========================================================================

% Define parameters needed for the data processing in this space:

Xnum = 5;    %Defines the experiment number for the current data set
Runnum = 8;     %Defines the number of runs (i.e sets of cutting conditions)
in the experiment
Samplenum = 5;  %Defines the number of samples made from each set of cutting
conditions
pixelsize = 1.55/512;    % Determines the pixel size in mm for a 10x dry
confocal objective.

%========================================================================

% Load in the height data for the images. These data points are found in
% the text files with name format 'X(Xnum) Height Data'
```

```
Xnumstr1 = num2str(Xnum);
heightname = strcat('X',Xnumstr1,' Height Data.txt');
heightdata = load(heightname);

normalsarraysize = Runnum * Samplenum;
normalsarray = zeros(3,normalsarraysize);

% Define a zeros array for output data to be stored in, and enter titles in
% the top row of this array.
outputrows = (Runnum*Samplenum);
outputarray = zeros(outputrows,7);

rowcount = 0;

for mainloop = 1:Runnum
    for j = 1: Samplenum

    %=========================================================================
    % Clear out all variables from previous loops:
    clear Xnumstr Runnumstr Samplenumstr picname I heightrank maxheight
minheight imagerows imagecols imagewidth imagelength arraysize A rotterms
rotmat I2 I1avg10 I2avg10
    %=========================================================================
        rowcount = rowcount + 1;

        Xnumstr = num2str(Xnum);
        Runnumstr = num2str(mainloop);
        Samplenumstr = num2str(j);
        picname       =       strcat(Xnumstr,'.',Runnumstr,'.',Samplenumstr,'
Composite.jpg');

       I = imread (picname);    % Loads the relevant image into the matlab
workspace 'I = imread (picname);'
        % ensure image is in greyscale:
       I = rgb2gray(I);

        % Now determine relevant height data from the heightdata text file:

        heightrank = ((mainloop-1)*4)+j;
        maxheight = heightdata(heightrank,1);
        minheight = heightdata(heightrank,2);

        %Convert height values to mm measurements:
        maxheight = maxheight/1000;
        minheight = minheight/1000;

        % Determine the number of rows and columns of pixels in the image:
        imagerows = size(I,1);
        imagecols = size(I,2);
        imagewidth = imagerows*pixelsize;
        imagelength = imagecols*pixelsize;

        arraysize = size(I,1) * size(I,2);
        A = zeros(arraysize,3);
```

```
        % Now write values from Image array I to an xyz point cloud
        % three-column array, A:

            for y = 1:imagerows
                for x = 1:imagecols
                    A((x+(imagecols*(y-1))),1) = x*pixelsize;
                    A((x+(imagecols*(y-1))),2) = y*pixelsize;
                    A((x+(imagecols*(y-1))),3) = I(y,x);
                end
            end
            % Now calibrate grey pixel values to physical height information:
            for p = 1:arraysize
                A(p,3)            =            ((A(p,3)-0)/(255-0)*(maxheight-
minheight))+minheight;
            end

            % Fit a plane to the xyz data in matrix A:

            [coeff,score,roots] = princomp(A);
            Qmat = coeff(:,1);
            Pmat = coeff(:,2);
            normal = coeff(:,3);

           % Establish target vector for the rotation:

           z = [0 0 1];

           % Determine rotation angle and direction:

           rotterms = vrrotvec(normal,z);

           % Determine rotation matrix:

           Rotmat = vrrotvec2mat(rotterms);

           % Now apply rotation:
           loopsize = size(A,1);
            for s = 1:loopsize
                Vtemp = A(s,:);
                Vtemp = Vtemp';

                Vnew = Rotmat*Vtemp;
                Vnew = Vnew';

                A(s,:) = Vnew;
            end
            % Now write rotated pixel height data back into a M x N image
            % matrix I2.
           I2 = zeros(imagerows,imagecols);
           for p = 1:imagerows
            for c = 1:imagecols
                I2(p,c) = A(((p-1)*imagecols) + c, 3);
            end
```

```
            end
            % Now we have M x N array I2 which represents the entire surface
            % texture sample as generated by the confocal microscope.

            % Next step is to take this data and process it into the 10% and
            % 20% bands, setting pixels within that height band to black (grey
value = 0) and
            % pixels outside that band to white (grey value = 255).

            % I is the non-levelled surface texture data. Process this one
            % first:
            Imeanheight = mean2(I);
            maxint = max(I);
            Imax = max(maxint);
            minint = min(I);
            Imin = min(minint);
            Irange = Imax - Imin;
            I1tenpc = 0.1*Irange;
            I1upper10 = Imeanheight + I1tenpc;
            I1lower10 = Imeanheight - I1tenpc;

            I1avg10 = zeros(imagerows, imagecols);
            % Set values of I1 within 10% of the mean to 0, others to 255;
            for i = 1:imagerows;
                for j =1:imagecols;
                    if I(i,j) <= I1upper10 && I(i,j) >= I1lower10
                        I1avg10(i,j) = 0;
                    else I1avg10(i,j) = 255;
                    end
                end
            end

            % I2 is the levelled and re-written surface texture data
            I2meanheight = mean2(I2);
            maxint = max(I2);
            I2max = max(maxint);
            minint = min(I2);
            I2min = min(minint);
            I2range = I2max - I2min;
            I2tenpc = 0.1*I2range;
            %I2upper10 = I2meanheight + I2tenpc;
            %I2lower10 = I2meanheight - I2tenpc;
            I2upper10 = I2meanheight + halfstdev;
            I2lower10 = I2meanheight - halfstdev;

            I2avg10 = zeros(imagerows, imagecols);
            % Set values of I2 within 10% of the mean to 0, others to 255;
            for i = 1:imagerows;
                for j =1:imagecols;
                    if I2(i,j) <= I2upper10 && I2(i,j) >= I2lower10
                        I2avg10(i,j) = 0;
                    else I2avg10(i,j) = 255;
                    end
                end
            end
```

```
            % Now export the two binary surface topography images I1avg10
            % and I2avg10 as TIFF files.

            filename2 = strcat(Xnumstr,'.',Runnumstr,'.',Samplenumstr,' 10%','
levelled.tif');
            imwrite(I2avg10, filename2, 'tiff')

    end
end
```

Appendix B: Geometric Form Assessment Material

Appendix B1: Single-Pass Form Results

This section presents the measured surface form results, along with values for the input parameters deemed to be of importance for determining the surface form results. The data is presented in the following tables.

Table 1: Geometric Form Data for Single-Pass Cutting with a Hot-Wire Tool

Sample #	Feed (ms-1)	Current (A)	Distance (mm)	Material	Engaged Length (mm)	Qeff	Kerfwidth	Edge Kerf	ΔH (mm)
2.1.1	0.0133	5	0	XPS	30	744.94	2.23	2.05	-0.09
2.1.2	0.0133	5	34	XPS	30	744.94	1.10	1.38	0.14
2.1.3	0.0133	5	94	XPS	30	744.94	0.71	1.06	0.17
2.1.4	0.0133	5	144	XPS	30	744.94	0.65	0.97	0.16
2.1.5	0.0133	5	244	XPS	30	744.94	0.69	1.03	0.17
2.1.6	0.0133	5	344	XPS	30	744.94	0.65	0.91	0.13
2.1.7	0.0133	5	444	XPS	30	744.94	0.64	0.99	0.18
2.1.8	0.0133	5	544	XPS	30	744.94	0.64	1.01	0.18
2.1.9	0.0133	5	644	XPS	30	744.94	0.64	1.00	0.18
2.2.1	0.0133	5	0	XPS	30	744.94	2.04	1.92	-0.06
2.2.2	0.0133	5	34	XPS	30	744.94	0.96	1.28	0.16
2.2.3	0.0133	5	94	XPS	30	744.94	0.74	1.05	0.16
2.2.4	0.0133	5	144	XPS	30	744.94	0.66	1.03	0.18
2.2.5	0.0133	5	244	XPS	30	744.94	0.73	1.06	0.16
2.2.6	0.0133	5	344	XPS	30	744.94	0.66	1.02	0.18
2.2.7	0.0133	5	444	XPS	30	744.94	0.67	0.99	0.16

2.2.8	0.0133	5	544	XPS	30	744.94	0.65	0.97	0.16
2.2.9	0.0133	5	644	XPS	30	744.94	0.63	0.99	0.18
2.3.1	0.0183	7	0	XPS	30	1097.15	3.37	2.69	-0.34
2.3.2	0.0183	7	34	XPS	30	1097.15	1.74	1.94	0.10
2.3.3	0.0183	7	94	XPS	30	1097.15	0.97	1.45	0.24
2.3.4	0.0183	7	144	XPS	30	1097.15	0.87	1.45	0.29
2.3.5	0.0183	7	244	XPS	30	1097.15	0.79	1.32	0.30
2.3.6	0.0183	7	344	XPS	30	1097.15	0.81	1.42	0.31
2.3.7	0.0183	7	444	XPS	30	1097.15	0.78	1.42	0.32
2.3.8	0.0183	7	544	XPS	30	1097.15	0.78	1.40	0.31
2.3.9	0.0183	7	644	XPS	30	1097.15	0.78	1.40	0.31
2.4.1	0.0217	7	0	XPS	30	928.36	3.22	2.36	-0.43
2.4.2	0.0217	7	34	XPS	30	928.36	1.53	1.77	0.12
2.4.3	0.0217	7	94	XPS	30	928.36	0.90	1.26	0.18
2.4.4	0.0217	7	144	XPS	30	928.36	0.89	1.28	0.19
2.4.5	0.0217	7	244	XPS	30	928.36	0.83	1.24	0.21
2.4.6	0.0217	7	344	XPS	30	928.36	0.81	1.29	0.24
2.4.7	0.0217	7	444	XPS	30	928.36	0.81	1.26	0.22

2.4.8	0.0217	7	544	XPS	30	928.36	0.81	1.23	0.21
2.4.9	0.0217	7	644	XPS	30	928.36	0.78	1.25	0.23
2.5.1	0.0217	7	0	XPS	30	928.36	3.18	2.48	-0.35
2.5.2	0.0217	7	34	XPS	30	928.36	1.66	1.76	0.05
2.5.3	0.0217	7	94	XPS	30	928.36	0.91	1.34	0.21
2.5.4	0.0217	7	144	XPS	30	928.36	0.87	1.23	0.18
2.5.5	0.0217	7	244	XPS	30	928.36	0.80	1.24	0.22
2.5.6	0.0217	7	344	XPS	30	928.36	0.82	1.30	0.24
2.5.7	0.0217	7	444	XPS	30	928.36	0.80	1.27	0.23
2.5.8	0.0217	7	544	XPS	30	928.36	0.80	1.26	0.23
2.5.9	0.0217	7	644	XPS	30	928.36	0.78	1.24	0.23
2.6.1	0.0167	5	0	XPS	30	595.95	2.30	1.73	-0.29
2.6.2	0.0167	5	34	XPS	30	595.95	0.97	1.15	0.09
2.6.3	0.0167	5	94	XPS	30	595.95	0.81	1.14	0.17
2.6.4	0.0167	5	144	XPS	30	595.95	0.77	1.03	0.13
2.6.5	0.0167	5	244	XPS	30	595.95	0.69	0.93	0.12
2.6.6	0.0167	5	344	XPS	30	595.95	0.66	0.91	0.13
2.6.7	0.0167	5	444	XPS	30	595.95	0.64	0.91	0.14

2.6.8	0.0167	5	544	XPS	30	595.95	0.61	0.92	0.16
2.6.9	0.0167	5	644	XPS	30	595.95	0.62	0.89	0.14
2.7.1	0.0200	5	0	XPS	30	496.63	1.96	1.71	-0.13
2.7.2	0.0200	5	34	XPS	30	496.63	0.95	1.07	0.06
2.7.3	0.0200	5	94	XPS	30	496.63	0.66	0.92	0.13
2.7.4	0.0200	5	144	XPS	30	496.63	0.66	0.93	0.13
2.7.5	0.0200	5	244	XPS	30	496.63	0.64	0.89	0.13
2.7.6	0.0200	5	344	XPS	30	496.63	0.64	0.94	0.15
2.7.7	0.0200	5	444	XPS	30	496.63	0.64	0.93	0.15
2.7.8	0.0200	5	544	XPS	30	496.63	0.62	0.90	0.14
2.7.9	0.0200	5	644	XPS	30	496.63	0.60	0.89	0.14
2.8.1	0.0200	7	0	XPS	30	1005.73	3.18	2.31	-0.44
2.8.2	0.0200	7	34	XPS	30	1005.73	1.52	1.66	0.07
2.8.3	0.0200	7	94	XPS	30	1005.73	0.86	1.14	0.14
2.8.4	0.0200	7	144	XPS	30	1005.73	0.80	1.21	0.21
2.8.5	0.0200	7	244	XPS	30	1005.73	0.91	1.29	0.19
2.8.6	0.0200	7	344	XPS	30	1005.73	0.83	1.29	0.23
2.8.7	0.0200	7	444	XPS	30	1005.73	0.97	1.38	0.20

2.8.8	0.0200	7	544	XPS	30	1005.73	0.93	1.40	0.24
2.8.9	0.0200	7	644	XPS	30	1005.73	0.88	1.34	0.23
2.9.1	0.0167	7	0	XPS	30	1206.87	3.72	2.76	-0.48
2.9.2	0.0167	7	34	XPS	30	1206.87	1.61	1.88	0.13
2.9.3	0.0167	7	94	XPS	30	1206.87	1.06	1.39	0.17
2.9.4	0.0167	7	144	XPS	30	1206.87	1.02	1.44	0.21
2.9.5	0.0167	7	244	XPS	30	1206.87	0.97	1.29	0.16
2.9.6	0.0167	7	344	XPS	30	1206.87	0.99	1.38	0.19
2.9.7	0.0167	7	444	XPS	30	1206.87	0.94	1.39	0.23
2.9.8	0.0167	7	544	XPS	30	1206.87	0.97	1.41	0.22
2.9.9	0.0167	7	644	XPS	30	1206.87	0.95	1.45	0.25
2.10.1	0.0133	7	0	XPS	30	1508.59	3.50	3.11	-0.20
2.10.2	0.0133	7	34	XPS	30	1508.59	2.34	2.17	-0.09
2.10.3	0.0133	7	94	XPS	30	1508.59	1.45	1.87	0.21
2.10.4	0.0133	7	144	XPS	30	1508.59	1.18	1.77	0.29
2.10.5	0.0133	7	244	XPS	30	1508.59	1.17	1.65	0.24
2.10.6	0.0133	7	344	XPS	30	1508.59	1.15	1.70	0.27
2.10.7	0.0133	7	444	XPS	30	1508.59	1.26	1.65	0.20

2.10.8	0.0133	7	544	XPS	30	1508.59	1.26	1.69	0.21
2.10.9	0.0133	7	644	XPS	30	1508.59	1.16	1.67	0.25
2.11.1	0.0217	7	0	XPS	30	928.36	3.05	2.39	-0.33
2.11.2	0.0217	7	34	XPS	30	928.36	1.47	1.56	0.04
2.11.3	0.0217	7	94	XPS	30	928.36	0.98	1.32	0.17
2.11.4	0.0217	7	144	XPS	30	928.36	0.97	1.35	0.19
2.11.5	0.0217	7	244	XPS	30	928.36	0.97	1.38	0.20
2.11.6	0.0217	7	344	XPS	30	928.36	0.91	1.32	0.21
2.11.7	0.0217	7	444	XPS	30	928.36	0.91	1.27	0.18
2.11.8	0.0217	7	544	XPS	30	928.36	0.90	1.28	0.19
2.11.9	0.0217	7	644	XPS	30	928.36	0.89	1.28	0.19
2.12.1	0.0133	8	0	XPS	30	2002.08	3.79	3.49	-0.15
2.12.2	0.0133	8	34	XPS	30	2002.08	2.45	2.63	0.09
2.12.3	0.0133	8	94	XPS	30	2002.08	1.97	2.44	0.23
2.12.4	0.0133	8	144	XPS	30	2002.08	1.88	2.44	0.28
2.12.5	0.0133	8	244	XPS	30	2002.08	1.84	2.42	0.29
2.12.6	0.0133	8	344	XPS	30	2002.08	1.82	2.37	0.28
2.12.7	0.0133	8	444	XPS	30	2002.08	1.84	2.45	0.31

2.12.8	0.0133	8	544	XPS	30	2002.08	Damaged	Damaged	Damaged
2.12.9	0.0133	8	644	XPS	30	2002.08	Damaged	Damaged	Damaged
2.13.1	0.0167	8	0	XPS	30	1601.66	3.47	2.72	-0.38
2.13.2	0.0167	8	34	XPS	30	1601.66	1.94	2.13	0.09
2.13.3	0.0167	8	94	XPS	30	1601.66	1.43	1.64	0.11
2.13.4	0.0167	8	144	XPS	30	1601.66	1.29	1.70	0.21
2.13.5	0.0167	8	244	XPS	30	1601.66	1.22	1.78	0.28
2.13.6	0.0167	8	344	XPS	30	1601.66	1.22	1.73	0.26
2.13.7	0.0167	8	444	XPS	30	1601.66	1.24	1.72	0.24
2.13.8	0.0167	8	544	XPS	30	1601.66	1.22	1.72	0.25
2.13.9	0.0167	8	644	XPS	30	1601.66	Damaged	Damaged	Damaged
2.14.1	0.0133	5	0	XPS	30	744.94	2.34	1.85	-0.25
2.14.2	0.0133	5	34	XPS	30	744.94	1.22	1.45	0.11
2.14.3	0.0133	5	94	XPS	30	744.94	0.86	1.18	0.16
2.14.4	0.0133	5	144	XPS	30	744.94	0.81	1.09	0.14
2.14.5	0.0133	5	244	XPS	30	744.94	0.78	1.02	0.12
2.14.6	0.0133	5	344	XPS	30	744.94	0.79	1.04	0.12
2.14.7	0.0133	5	444	XPS	30	744.94	0.79	1.07	0.14
2.14.8	0.0133	5	544	XPS	30	744.94	0.74	1.03	0.14

2.14.9	0.0133	5	644	XPS	30	744.94	0.80	1.06	0.13
2.15.1	0.0200	8	0	XPS	30	1334.72	3.43	2.73	-0.35
2.15.2	0.0200	8	34	XPS	30	1334.72	2.01	2.17	0.08
2.15.3	0.0200	8	94	XPS	30	1334.72	1.37	1.75	0.19
2.15.4	0.0200	8	144	XPS	30	1334.72	1.36	1.76	0.20
2.15.5	0.0200	8	244	XPS	30	1334.72	1.33	1.73	0.20
2.15.6	0.0200	8	344	XPS	30	1334.72	1.37	1.72	0.18
2.15.7	0.0200	8	444	XPS	30	1334.72	1.35	1.73	0.19
2.15.8	0.0200	8	544	XPS	30	1334.72	1.37	1.78	0.20
2.15.9	0.0200	8	644	XPS	30	1334.72	1.35	1.79	0.22
2.16.1	0.0133	5	0	XPS	50	744.94	2.02	1.83	-0.10
2.16.2	0.0133	5	34	XPS	50	744.94	0.97	1.30	0.16
2.16.3	0.0133	5	94	XPS	50	744.94	0.73	1.04	0.15
2.16.4	0.0133	5	144	XPS	50	744.94	0.67	0.93	0.13
2.16.5	0.0133	5	244	XPS	50	744.94	0.67	0.94	0.14
2.16.6	0.0133	5	344	XPS	50	744.94	0.69	0.95	0.13
2.16.7	0.0133	5	444	XPS	50	744.94	0.66	0.90	0.12
2.16.8	0.0133	5	544	XPS	50	744.94	0.68	0.95	0.13

2.16.9	0.0133	5	644	XPS	50	744.94	0.62	0.77	0.08
2.17.1	0.0133	5	0	XPS	50	744.94	2.10	1.89	-0.11
2.17.2	0.0133	5	34	XPS	50	744.94	1.11	1.48	0.19
2.17.3	0.0133	5	94	XPS	50	744.94	0.76	1.03	0.14
2.17.4	0.0133	5	144	XPS	50	744.94	0.77	1.03	0.13
2.17.5	0.0133	5	244	XPS	50	744.94	0.75	1.03	0.14
2.17.6	0.0133	5	344	XPS	50	744.94	0.74	1.01	0.14
2.17.7	0.0133	5	444	XPS	50	744.94	0.75	1.00	0.12
2.17.8	0.0133	5	544	XPS	50	744.94	0.72	0.94	0.11
2.17.9	0.0133	5	644	XPS	50	744.94	0.72	0.91	0.09
2.18.1	0.0183	7	0	XPS	50	1097.15	3.30	2.41	-0.45
2.18.2	0.0183	7	34	XPS	50	1097.15	1.67	1.79	0.06
2.18.3	0.0183	7	94	XPS	50	1097.15	0.83	1.45	0.31
2.18.4	0.0183	7	144	XPS	50	1097.15	0.89	1.36	0.23
2.18.5	0.0183	7	244	XPS	50	1097.15	0.79	1.38	0.29
2.18.6	0.0183	7	344	XPS	50	1097.15	0.75	1.28	0.26
2.18.7	0.0183	7	444	XPS	50	1097.15	0.73	1.26	0.27
2.18.8	0.0183	7	544	XPS	50	1097.15	0.72	1.19	0.23

2.18.9	0.0183	7	644	XPS	50	1097.15	0.71	1.19	0.24
2.19.1	0.0217	7	0	XPS	50	928.36	3.06	2.65	-0.21
2.19.2	0.0217	7	34	XPS	50	928.36	1.36	1.39	0.02
2.19.3	0.0217	7	94	XPS	50	928.36	0.81	1.18	0.18
2.19.4	0.0217	7	144	XPS	50	928.36	0.85	1.21	0.18
2.19.5	0.0217	7	244	XPS	50	928.36	0.81	1.13	0.16
2.19.6	0.0217	7	344	XPS	50	928.36	0.81	1.14	0.17
2.19.7	0.0217	7	444	XPS	50	928.36	0.80	1.14	0.17
2.19.8	0.0217	7	544	XPS	50	928.36	1.01	1.44	0.22
2.19.9	0.0217	7	644	XPS	50	928.36	1.60	1.98	0.19
2.20.1	0.0217	7	0	XPS	50	928.36	3.28	2.45	-0.42
2.10.2	0.0217	7	34	XPS	50	928.36	1.61	1.64	0.01
2.20.3	0.0217	7	94	XPS	50	928.36	0.90	1.27	0.19
2.20.4	0.0217	7	144	XPS	50	928.36	0.81	1.13	0.16
2.20.5	0.0217	7	244	XPS	50	928.36	0.83	1.14	0.16
2.20.6	0.0217	7	344	XPS	50	928.36	0.79	1.16	0.18
2.20.7	0.0217	7	444	XPS	50	928.36	0.79	1.15	0.18
2.20.8	0.0217	7	544	XPS	50	928.36	0.84	1.17	0.17

2.20.9	0.0217	7	644	XPS	50	928.36	1.15	1.69	0.27
2.21.1	0.0167	5	0	XPS	50	595.95	2.05	1.64	-0.21
2.21.2	0.0167	5	34	XPS	50	595.95	0.99	1.14	0.08
2.21.3	0.0167	5	94	XPS	50	595.95	0.71	1.01	0.15
2.21.4	0.0167	5	144	XPS	50	595.95	0.62	0.92	0.15
2.21.5	0.0167	5	244	XPS	50	595.95	0.65	0.91	0.13
2.21.6	0.0167	5	344	XPS	50	595.95	0.63	0.87	0.12
2.21.7	0.0167	5	444	XPS	50	595.95	0.65	0.90	0.13
2.21.8	0.0167	5	544	XPS	50	595.95	0.67	0.90	0.12
2.21.9	0.0167	5	644	XPS	50	595.95	0.72	1.03	0.15
2.22.1	0.0200	5	0	XPS	50	496.63	2.04	1.59	-0.23
2.22.2	0.0200	5	34	XPS	50	496.63	0.97	1.09	0.06
2.22.3	0.0200	5	94	XPS	50	496.63	0.71	0.93	0.11
2.22.4	0.0200	5	144	XPS	50	496.63	0.75	1.04	0.15
2.22.5	0.0200	5	244	XPS	50	496.63	0.72	0.91	0.10
2.22.6	0.0200	5	344	XPS	50	496.63	0.69	0.93	0.12
2.22.7	0.0200	5	444	XPS	50	496.63	0.67	0.95	0.14
2.22.8	0.0200	5	544	XPS	50	496.63	0.64	0.94	0.15

2.22.9	0.0200	5	644	XPS	50	496.63	0.65	0.98	0.16
2.23.1	0.0200	7	0	XPS	50	1005.73	3.35	2.64	-0.36
2.23.2	0.0200	7	34	XPS	50	1005.73	1.93	1.95	0.01
2.23.3	0.0200	7	94	XPS	50	1005.73	0.98	1.54	0.28
2.23.4	0.0200	7	144	XPS	50	1005.73	0.93	1.43	0.25
2.23.5	0.0200	7	244	XPS	50	1005.73	0.91	1.47	0.28
2.23.6	0.0200	7	344	XPS	50	1005.73	0.92	1.45	0.26
2.23.7	0.0200	7	444	XPS	50	1005.73	0.92	1.45	0.27
2.23.8	0.0200	7	544	XPS	50	1005.73	0.90	1.43	0.26
2.23.9	0.0200	7	644	XPS	50	1005.73	0.88	1.45	0.28
2.24.1	0.0167	7	0	XPS	50	1206.87	3.37	2.41	-0.48
2.24.2	0.0167	7	34	XPS	50	1206.87	1.64	1.97	0.17
2.24.3	0.0167	7	94	XPS	50	1206.87	1.00	1.53	0.26
2.24.4	0.0167	7	144	XPS	50	1206.87	1.01	1.53	0.26
2.24.5	0.0167	7	244	XPS	50	1206.87	0.99	1.45	0.23
2.24.6	0.0167	7	344	XPS	50	1206.87	0.95	1.42	0.24
2.24.7	0.0167	7	444	XPS	50	1206.87	0.97	1.43	0.23
2.24.8	0.0167	7	544	XPS	50	1206.87	0.96	1.43	0.23

2.24.9	0.0167	7	644	XPS	50	1206.87	0.93	1.47	0.27
2.25.1	0.0133	7	0	XPS	50	1508.59	3.38	2.63	-0.38
2.25.2	0.0133	7	34	XPS	50	1508.59	1.95	2.04	0.04
2.25.3	0.0133	7	94	XPS	50	1508.59	1.30	1.86	0.28
2.25.4	0.0133	7	144	XPS	50	1508.59	1.18	1.64	0.23
2.25.5	0.0133	7	244	XPS	50	1508.59	1.13	1.65	0.26
2.25.6	0.0133	7	344	XPS	50	1508.59	1.12	1.65	0.27
2.25.7	0.0133	7	444	XPS	50	1508.59	1.11	1.67	0.28
2.25.8	0.0133	7	544	XPS	50	1508.59	1.06	1.67	0.30
2.25.9	0.0133	7	644	XPS	50	1508.59	1.05	1.66	0.30
2.26.1	0.0217	7	0	XPS	50	928.36	3.12	2.19	-0.47
2.26.2	0.0217	7	34	XPS	50	928.36	1.56	1.76	0.10
2.26.3	0.0217	7	94	XPS	50	928.36	0.89	1.37	0.24
2.26.4	0.0217	7	144	XPS	50	928.36	0.79	1.26	0.24
2.26.5	0.0217	7	244	XPS	50	928.36	0.74	1.28	0.27
2.26.6	0.0217	7	344	XPS	50	928.36	0.73	1.25	0.26
2.26.7	0.0217	7	444	XPS	50	928.36	0.74	1.25	0.25
2.26.8	0.0217	7	544	XPS	50	928.36	0.73	1.25	0.26

2.26.9	0.0217	7	644	XPS	50	928.36	0.73	1.26	0.27
2.27.1	0.0133	8	0	XPS	50	2002.08	3.46	3.26	-0.10
2.27.2	0.0133	8	34	XPS	50	2002.08	2.55	2.82	0.13
2.27.3	0.0133	8	94	XPS	50	2002.08	1.90	2.44	0.27
2.27.4	0.0133	8	144	XPS	50	2002.08	1.71	2.36	0.32
2.27.5	0.0133	8	244	XPS	50	2002.08	1.56	2.15	0.30
2.27.6	0.0133	8	344	XPS	50	2002.08	1.44	2.03	0.29
2.27.7	0.0133	8	444	XPS	50	2002.08	1.29	1.84	0.28
2.27.8	0.0133	8	544	XPS	50	2002.08	1.12	1.77	0.33
2.27.9	0.0133	8	644	XPS	50	2002.08	Damaged	Damaged	Damaged
2.28.1	0.0167	8	0	XPS	50	1601.66	3.30	2.64	-0.33
2.28.2	0.0167	8	34	XPS	50	1601.66	1.97	2.12	0.07
2.28.3	0.0167	8	94	XPS	50	1601.66	1.25	1.67	0.21
2.28.4	0.0167	8	144	XPS	50	1601.66	1.18	1.67	0.25
2.28.5	0.0167	8	244	XPS	50	1601.66	1.01	1.58	0.29
2.28.6	0.0167	8	344	XPS	50	1601.66	0.89	1.58	0.34
2.28.7	0.0167	8	444	XPS	50	1601.66	0.98	1.35	0.18
2.28.8	0.0167	8	544	XPS	50	1601.66	1.00	1.81	0.40

2.28.9	0.0167	8	644	XPS	50	1601.66	0.97	1.78	0.41
2.29.1	0.0133	5	0	XPS	50	744.94	2.38	2.06	-0.16
2.29.2	0.0133	5	34	XPS	50	744.94	1.15	1.41	0.13
2.29.3	0.0133	5	94	XPS	50	744.94	0.69	1.06	0.18
2.29.4	0.0133	5	144	XPS	50	744.94	0.69	1.06	0.18
2.29.5	0.0133	5	244	XPS	50	744.94	0.66	1.04	0.19
2.29.6	0.0133	5	344	XPS	50	744.94	0.67	1.05	0.19
2.29.7	0.0133	5	444	XPS	50	744.94	0.65	1.06	0.21
2.29.8	0.0133	5	544	XPS	50	744.94	0.64	1.03	0.19
2.29.9	0.0133	5	644	XPS	50	744.94	0.55	0.80	0.12
2.30.1	0.0200	8	0	XPS	50	1334.72	3.52	2.62	-0.45
2.30.2	0.0200	8	34	XPS	50	1334.72	2.08	2.19	0.05
2.30.3	0.0200	8	94	XPS	50	1334.72	1.18	1.77	0.29
2.30.4	0.0200	8	144	XPS	50	1334.72	0.95	1.53	0.29
2.30.5	0.0200	8	244	XPS	50	1334.72	0.86	1.62	0.38
2.30.6	0.0200	8	344	XPS	50	1334.72	0.89	1.63	0.37
2.30.7	0.0200	8	444	XPS	50	1334.72	0.83	1.56	0.36
2.30.8	0.0200	8	544	XPS	50	1334.72	0.81	1.62	0.41

2.30.9	0.0200	8	644	XPS	50	1334.72	0.79	1.52	0.37
2.31.1	0.0133	5	0	EPS	30	744.94	1.98	2.03	0.02
2.31.2	0.0133	5	34	EPS	30	744.94	1.23	1.63	0.20
2.31.3	0.0133	5	94	EPS	30	744.94	0.94	1.41	0.24
2.31.4	0.0133	5	144	EPS	30	744.94	0.72	0.86	0.07
2.31.5	0.0133	5	244	EPS	30	744.94	0.67	1.05	0.19
2.31.6	0.0133	5	344	EPS	30	744.94	0.70	1.16	0.23
2.31.7	0.0133	5	444	EPS	30	744.94	0.75	1.25	0.25
2.31.8	0.0133	5	544	EPS	30	744.94	0.79	1.23	0.22
2.31.9	0.0133	5	644	EPS	30	744.94	0.40	1.08	0.34
2.32.1	0.0133	5	0	EPS	30	744.94	1.98	1.88	-0.05
2.32.2	0.0133	5	34	EPS	30	744.94	1.28	1.69	0.21
2.32.3	0.0133	5	94	EPS	30	744.94	0.91	1.26	0.17
2.32.4	0.0133	5	144	EPS	30	744.94	0.79	1.40	0.31
2.32.5	0.0133	5	244	EPS	30	744.94	0.45	0.98	0.27
2.32.6	0.0133	5	344	EPS	30	744.94	0.31	0.81	0.25
2.32.7	0.0133	5	444	EPS	30	744.94	-0.12	0.45	0.28
2.32.8	0.0133	5	544	EPS	30	744.94	0.01	0.67	0.33

2.32.9	0.0133	5	644	EPS	30	744.94	-0.22	0.43	0.33
2.33.1	0.0183	7	0	EPS	30	1097.15	2.93	2.38	-0.28
2.33.2	0.0183	7	34	EPS	30	1097.15	1.93	2.23	0.15
2.33.3	0.0183	7	94	EPS	30	1097.15	1.50	1.95	0.23
2.33.4	0.0183	7	144	EPS	30	1097.15	1.24	1.83	0.29
2.33.5	0.0183	7	244	EPS	30	1097.15	1.21	1.57	0.18
2.33.6	0.0183	7	344	EPS	30	1097.15	1.02	1.52	0.25
2.33.7	0.0183	7	444	EPS	30	1097.15	1.09	1.74	0.33
2.33.8	0.0183	7	544	EPS	30	1097.15	0.93	1.54	0.31
2.33.9	0.0183	7	644	EPS	30	1097.15	0.80	1.56	0.38
2.34.1	0.0217	7	0	EPS	30	928.36	2.29	2.05	-0.12
2.34.2	0.0217	7	34	EPS	30	928.36	1.79	2.03	0.12
2.34.3	0.0217	7	94	EPS	30	928.36	1.30	1.65	0.17
2.34.4	0.0217	7	144	EPS	30	928.36	1.11	1.52	0.21
2.34.5	0.0217	7	244	EPS	30	928.36	1.01	1.63	0.31
2.34.6	0.0217	7	344	EPS	30	928.36	1.00	1.68	0.34
2.34.7	0.0217	7	444	EPS	30	928.36	0.49	1.16	0.33
2.34.8	0.0217	7	544	EPS	30	928.36	1.20	1.68	0.24

2.34.9	0.0217	7	644	EPS	30	928.36	0.62	1.17	0.28
2.35.1	0.0217	7	0	EPS	30	928.36	2.49	2.52	0.01
2.35.2	0.0217	7	34	EPS	30	928.36	1.79	2.23	0.22
2.35.3	0.0217	7	94	EPS	30	928.36	1.30	1.73	0.22
2.35.4	0.0217	7	144	EPS	30	928.36	1.14	1.59	0.22
2.35.5	0.0217	7	244	EPS	30	928.36	0.92	1.40	0.24
2.35.6	0.0217	7	344	EPS	30	928.36	0.80	1.39	0.30
2.35.7	0.0217	7	444	EPS	30	928.36	1.06	1.38	0.16
2.35.8	0.0217	7	544	EPS	30	928.36	0.94	1.45	0.25
2.35.9	0.0217	7	644	EPS	30	928.36	0.77	1.22	0.22
2.36.1	0.0167	5	0	EPS	30	595.95	1.77	1.73	-0.02
2.36.2	0.0167	5	34	EPS	30	595.95	1.18	1.47	0.14
2.36.3	0.0167	5	94	EPS	30	595.95	0.85	1.15	0.15
2.36.4	0.0167	5	144	EPS	30	595.95	0.44	1.09	0.32
2.36.5	0.0167	5	244	EPS	30	595.95	0.60	1.13	0.26
2.36.6	0.0167	5	344	EPS	30	595.95	0.50	0.98	0.24
2.36.7	0.0167	5	444	EPS	30	595.95	0.46	0.95	0.24
2.36.8	0.0167	5	544	EPS	30	595.95	0.42	0.95	0.27

2.36.9	0.0167	5	644	EPS	30	595.95	0.50	0.94	0.22
2.37.1	0.0200	5	0	EPS	30	496.63	1.82	1.68	-0.07
2.37.2	0.0200	5	34	EPS	30	496.63	1.07	1.48	0.21
2.37.3	0.0200	5	94	EPS	30	496.63	0.97	1.37	0.20
2.37.4	0.0200	5	144	EPS	30	496.63	0.67	1.26	0.30
2.37.5	0.0200	5	244	EPS	30	496.63	0.25	0.52	0.13
2.37.6	0.0200	5	344	EPS	30	496.63	0.41	0.97	0.28
2.37.7	0.0200	5	444	EPS	30	496.63	0.30	0.60	0.15
2.37.8	0.0200	5	544	EPS	30	496.63	-0.47	0.21	0.34
2.37.9	0.0200	5	644	EPS	30	496.63	1.05	1.72	0.33
2.38.1	0.0200	7	0	EPS	30	1005.73	2.40	2.39	0.00
2.38.2	0.0200	7	34	EPS	30	1005.73	1.85	2.06	0.11
2.38.3	0.0200	7	94	EPS	30	1005.73	1.42	1.75	0.16
2.38.4	0.0200	7	144	EPS	30	1005.73	1.36	1.76	0.20
2.38.5	0.0200	7	244	EPS	30	1005.73	1.32	1.83	0.25
2.38.6	0.0200	7	344	EPS	30	1005.73	1.06	1.75	0.34
2.38.7	0.0200	7	444	EPS	30	1005.73	1.07	1.73	0.33
2.38.8	0.0200	7	544	EPS	30	1005.73	1.07	1.71	0.32

2.38.9	0.0200	7	644	EPS	30	1005.73	1.03	1.73	0.35
2.39.1	0.0167	7	0	EPS	30	1206.87	2.86	2.67	-0.10
2.39.2	0.0167	7	34	EPS	30	1206.87	2.03	2.39	0.18
2.39.3	0.0167	7	94	EPS	30	1206.87	1.69	2.07	0.19
2.39.4	0.0167	7	144	EPS	30	1206.87	1.53	1.94	0.20
2.39.5	0.0167	7	244	EPS	30	1206.87	1.46	1.85	0.19
2.39.6	0.0167	7	344	EPS	30	1206.87	1.34	1.86	0.26
2.39.7	0.0167	7	444	EPS	30	1206.87	1.37	1.80	0.21
2.39.8	0.0167	7	544	EPS	30	1206.87	1.31	1.87	0.28
2.39.9	0.0167	7	644	EPS	30	1206.87	1.32	1.81	0.24
2.40.1	0.0133	7	0	EPS	30	1508.59	3.03	3.00	-0.02
2.40.2	0.0133	7	34	EPS	30	1508.59	2.24	2.58	0.17
2.40.3	0.0133	7	94	EPS	30	1508.59	1.96	2.33	0.19
2.40.4	0.0133	7	144	EPS	30	1508.59	1.99	2.26	0.14
2.40.5	0.0133	7	244	EPS	30	1508.59	1.94	2.20	0.13
2.40.6	0.0133	7	344	EPS	30	1508.59	1.81	2.27	0.23
2.40.7	0.0133	7	444	EPS	30	1508.59	1.73	2.18	0.23
2.40.8	0.0133	7	544	EPS	30	1508.59	1.62	2.19	0.28

2.40.9	0.0133	7	644	EPS	30	1508.59	1.61	2.06	0.23
2.41.1	0.0217	7	0	EPS	30	928.36	2.50	2.34	-0.08
2.41.2	0.0217	7	34	EPS	30	928.36	1.85	2.14	0.14
2.41.3	0.0217	7	94	EPS	30	928.36	1.43	1.95	0.26
2.41.4	0.0217	7	144	EPS	30	928.36	1.36	1.76	0.20
2.41.5	0.0217	7	244	EPS	30	928.36	1.10	1.92	0.41
2.41.6	0.0217	7	344	EPS	30	928.36	1.04	1.72	0.34
2.41.7	0.0217	7	444	EPS	30	928.36	0.84	1.58	0.37
2.41.8	0.0217	7	544	EPS	30	928.36	1.02	1.62	0.30
2.41.9	0.0217	7	644	EPS	30	928.36	0.86	1.53	0.34
2.42.1	0.0133	8	0	EPS	30	2002.08	3.11	3.16	0.02
2.42.2	0.0133	8	34	EPS	30	2002.08	2.92	3.27	0.17
2.42.3	0.0133	8	94	EPS	30	2002.08	2.68	3.24	0.28
2.42.4	0.0133	8	144	EPS	30	2002.08	2.65	2.86	0.10
2.42.5	0.0133	8	244	EPS	30	2002.08	2.48	2.94	0.23
2.42.6	0.0133	8	344	EPS	30	2002.08	2.42	2.78	0.18
2.42.7	0.0133	8	444	EPS	30	2002.08	2.34	2.69	0.17
2.42.8	0.0133	8	544	EPS	30	2002.08	2.30	2.82	0.26

2.42.9	0.0133	8	644	EPS	30	2002.08	2.25	2.73	0.24
2.43.1	0.0167	8	0	EPS	30	1601.66	Damaged	Damaged	Damaged
2.43.2	0.0167	8	34	EPS	30	1601.66	Damaged	Damaged	Damaged
2.43.3	0.0167	8	94	EPS	30	1601.66	Damaged	Damaged	Damaged
2.43.4	0.0167	8	144	EPS	30	1601.66	Damaged	Damaged	Damaged
2.43.5	0.0167	8	244	EPS	30	1601.66	Damaged	Damaged	Damaged
2.43.6	0.0167	8	344	EPS	30	1601.66	Damaged	Damaged	Damaged
2.43.7	0.0167	8	444	EPS	30	1601.66	Damaged	Damaged	Damaged
2.43.8	0.0167	8	544	EPS	30	1601.66	Damaged	Damaged	Damaged
2.43.9	0.0167	8	644	EPS	30	1601.66	Damaged	Damaged	Damaged
2.44.1	0.0133	5	0	EPS	30	744.94	1.91	2.11	0.10
2.44.2	0.0133	5	34	EPS	30	744.94	1.32	1.69	0.19
2.44.3	0.0133	5	94	EPS	30	744.94	0.99	1.34	0.18
2.44.4	0.0133	5	144	EPS	30	744.94	0.79	1.30	0.25
2.44.5	0.0133	5	244	EPS	30	744.94	0.98	1.32	0.17
2.44.6	0.0133	5	344	EPS	30	744.94	0.90	1.35	0.22
2.44.7	0.0133	5	444	EPS	30	744.94	0.79	1.19	0.20
2.44.8	0.0133	5	544	EPS	30	744.94	0.72	1.25	0.27

2.44.9	0.0133	5	644	EPS	30	744.94	0.69	1.06	0.19
2.45.1	0.0200	8	0	EPS	30	1334.72	Damaged	Damaged	Damaged
2.45.2	0.0200	8	34	EPS	30	1334.72	Damaged	Damaged	Damaged
2.45.3	0.0200	8	94	EPS	30	1334.72	Damaged	Damaged	Damaged
2.45.4	0.0200	8	144	EPS	30	1334.72	Damaged	Damaged	Damaged
2.45.5	0.0200	8	244	EPS	30	1334.72	Damaged	Damaged	Damaged
2.45.6	0.0200	8	344	EPS	30	1334.72	Damaged	Damaged	Damaged
2.45.7	0.0200	8	444	EPS	30	1334.72	Damaged	Damaged	Damaged
2.45.8	0.0200	8	544	EPS	30	1334.72	Damaged	Damaged	Damaged
2.45.9	0.0200	8	644	EPS	30	1334.72	Damaged	Damaged	Damaged
2.46.1	0.0133	5	0	EPS	50	744.94	1.05	1.19	0.07
2.46.2	0.0133	5	34	EPS	50	744.94	0.50	0.89	0.20
2.46.3	0.0133	5	94	EPS	50	744.94	0.58	1.10	0.26
2.46.4	0.0133	5	144	EPS	50	744.94	0.47	1.36	0.44
2.46.5	0.0133	5	244	EPS	50	744.94	0.35	1.04	0.34
2.46.6	0.0133	5	344	EPS	50	744.94	0.26	0.79	0.26
2.46.7	0.0133	5	444	EPS	50	744.94	0.20	0.73	0.26
2.46.8	0.0133	5	544	EPS	50	744.94	0.24	0.98	0.37

2.46.9	0.0133	5	644	EPS	50	744.94	Damaged	Damaged	Damaged
2.47.1	0.0133	5	0	EPS	50	744.94	1.89	1.84	-0.03
2.47.2	0.0133	5	34	EPS	50	744.94	1.08	1.49	0.20
2.47.3	0.0133	5	94	EPS	50	744.94	0.64	1.10	0.23
2.47.4	0.0133	5	144	EPS	50	744.94	0.28	1.05	0.39
2.47.5	0.0133	5	244	EPS	50	744.94	0.36	0.96	0.30
2.47.6	0.0133	5	344	EPS	50	744.94	0.26	0.95	0.34
2.47.7	0.0133	5	444	EPS	50	744.94	0.22	0.88	0.33
2.47.8	0.0133	5	544	EPS	50	744.94	0.14	0.85	0.36
2.47.9	0.0133	5	644	EPS	50	744.94	0.12	0.92	0.40
2.48.1	0.0183	7	0	EPS	50	1097.15	2.37	2.35	-0.01
2.48.2	0.0183	7	34	EPS	50	1097.15	1.38	1.86	0.24
2.48.3	0.0183	7	94	EPS	50	1097.15	0.90	1.51	0.30
2.48.4	0.0183	7	144	EPS	50	1097.15	0.83	1.42	0.30
2.48.5	0.0183	7	244	EPS	50	1097.15	0.76	1.40	0.32
2.48.6	0.0183	7	344	EPS	50	1097.15	0.78	1.24	0.23
2.48.7	0.0183	7	444	EPS	50	1097.15	0.69	1.35	0.33
2.48.8	0.0183	7	544	EPS	50	1097.15	0.54	1.34	0.40

2.48.9	0.0183	7	644	EPS	50	1097.15	0.54	1.37	0.42
2.49.1	0.0217	7	0	EPS	50	928.36	2.17	2.17	0.00
2.59.2	0.0217	7	34	EPS	50	928.36	1.42	1.91	0.25
2.49.3	0.0217	7	94	EPS	50	928.36	0.94	1.54	0.30
2.49.4	0.0217	7	144	EPS	50	928.36	0.90	1.45	0.27
2.49.5	0.0217	7	244	EPS	50	928.36	0.58	1.24	0.33
2.49.6	0.0217	7	344	EPS	50	928.36	0.83	1.55	0.36
2.49.7	0.0217	7	444	EPS	50	928.36	0.47	1.23	0.38
2.49.8	0.0217	7	544	EPS	50	928.36	0.50	1.18	0.34
2.49.9	0.0217	7	644	EPS	50	928.36	0.38	1.24	0.43
2.50.1	0.0217	7	0	EPS	50	928.36	2.45	2.52	0.03
2.50.2	0.0217	7	34	EPS	50	928.36	1.43	1.78	0.17
2.50.3	0.0217	7	94	EPS	50	928.36	0.95	1.47	0.26
2.50.4	0.0217	7	144	EPS	50	928.36	0.75	1.53	0.39
2.50.5	0.0217	7	244	EPS	50	928.36	0.77	1.64	0.43
2.50.6	0.0217	7	344	EPS	50	928.36	0.35	1.08	0.36
2.50.7	0.0217	7	444	EPS	50	928.36	0.60	1.33	0.37
2.50.8	0.0217	7	544	EPS	50	928.36	0.51	1.27	0.38

2.50.9	0.0217	7	644	EPS	50	928.36	0.45	1.36	0.46
2.51.1	0.0167	5	0	EPS	50	595.95	1.46	1.44	-0.01
2.51.2	0.0167	5	34	EPS	50	595.95	0.69	1.38	0.35
2.51.3	0.0167	5	94	EPS	50	595.95	0.42	1.27	0.43
2.51.4	0.0167	5	144	EPS	50	595.95	0.27	0.99	0.36
2.51.5	0.0167	5	244	EPS	50	595.95	0.01	0.89	0.44
2.51.6	0.0167	5	344	EPS	50	595.95	0.07	1.09	0.51
2.51.7	0.0167	5	444	EPS	50	595.95	0.29	0.87	0.29
2.51.8	0.0167	5	544	EPS	50	595.95	0.02	0.82	0.40
2.51.9	0.0167	5	644	EPS	50	595.95	0.05	0.80	0.37
2.52.1	0.0200	5	0	EPS	50	496.63	1.95	1.92	-0.02
2.52.2	0.0200	5	34	EPS	50	496.63	1.17	1.73	0.28
2.52.3	0.0200	5	94	EPS	50	496.63	0.52	1.19	0.33
2.52.4	0.0200	5	144	EPS	50	496.63	0.20	0.88	0.34
2.52.5	0.0200	5	244	EPS	50	496.63	0.17	0.91	0.37
2.52.6	0.0200	5	344	EPS	50	496.63	0.34	1.17	0.42
2.52.7	0.0200	5	444	EPS	50	496.63	0.31	1.11	0.40
2.52.8	0.0200	5	544	EPS	50	496.63	0.10	0.84	0.37

2.52.9	0.0200	5	644	EPS	50	496.63	0.25	0.91	0.33
2.53.1	0.0200	7	0	EPS	50	1005.73	2.40	2.53	0.06
2.53.2	0.0200	7	34	EPS	50	1005.73	1.52	2.11	0.30
2.53.3	0.0200	7	94	EPS	50	1005.73	1.01	1.73	0.36
2.53.4	0.0200	7	144	EPS	50	1005.73	0.86	1.66	0.40
2.53.5	0.0200	7	244	EPS	50	1005.73	0.81	1.47	0.33
2.53.6	0.0200	7	344	EPS	50	1005.73	0.74	1.56	0.41
2.53.7	0.0200	7	444	EPS	50	1005.73	0.71	1.37	0.33
2.53.8	0.0200	7	544	EPS	50	1005.73	0.63	1.44	0.40
2.53.9	0.0200	7	644	EPS	50	1005.73	0.73	1.45	0.36
2.54.1	0.0167	7	0	EPS	50	1206.87	2.74	2.55	-0.10
2.54.2	0.0167	7	34	EPS	50	1206.87	1.44	2.14	0.35
2.54.3	0.0167	7	94	EPS	50	1206.87	1.14	1.69	0.28
2.54.4	0.0167	7	144	EPS	50	1206.87	1.00	1.73	0.37
2.54.5	0.0167	7	244	EPS	50	1206.87	1.05	1.84	0.39
2.54.6	0.0167	7	344	EPS	50	1206.87	0.84	1.54	0.35
2.54.7	0.0167	7	444	EPS	50	1206.87	0.84	1.62	0.39
2.54.8	0.0167	7	544	EPS	50	1206.87	0.95	1.56	0.31

2.54.9	0.0167	7	644	EPS	50	1206.87	0.77	1.67	0.45
2.55.1	0.0133	7	0	EPS	50	1508.59	2.90	2.72	-0.09
2.55.2	0.0133	7	34	EPS	50	1508.59	1.76	2.26	0.25
2.55.3	0.0133	7	94	EPS	50	1508.59	1.36	1.99	0.31
2.55.4	0.0133	7	144	EPS	50	1508.59	1.24	1.90	0.33
2.55.5	0.0133	7	244	EPS	50	1508.59	1.19	1.78	0.30
2.55.6	0.0133	7	344	EPS	50	1508.59	1.20	1.69	0.24
2.55.7	0.0133	7	444	EPS	50	1508.59	1.21	1.74	0.26
2.55.8	0.0133	7	544	EPS	50	1508.59	1.20	1.88	0.34
2.55.9	0.0133	7	644	EPS	50	1508.59	1.15	1.90	0.38
2.56.1	0.0217	7	0	EPS	50	928.36	2.52	2.47	-0.03
2.56.2	0.0217	7	34	EPS	50	928.36	1.60	2.01	0.21
2.56.3	0.0217	7	94	EPS	50	928.36	0.96	1.65	0.34
2.56.4	0.0217	7	144	EPS	50	928.36	0.90	1.52	0.31
2.56.5	0.0217	7	244	EPS	50	928.36	0.84	1.43	0.29
2.56.6	0.0217	7	344	EPS	50	928.36	0.79	1.33	0.27
2.56.7	0.0217	7	444	EPS	50	928.36	0.63	1.14	0.25
2.56.8	0.0217	7	544	EPS	50	928.36	0.86	1.45	0.30

2.56.9	0.0217	7	644	EPS	50	928.36	0.69	1.45	0.38
2.57.1	0.0133	8	0	EPS	50	2002.08	2.98	2.95	-0.02
2.57.2	0.0133	8	34	EPS	50	2002.08	2.45	2.86	0.21
2.57.3	0.0133	8	94	EPS	50	2002.08	1.83	2.46	0.31
2.57.4	0.0133	8	144	EPS	50	2002.08	1.88	2.68	0.40
2.57.5	0.0133	8	244	EPS	50	2002.08	1.81	2.26	0.23
2.57.6	0.0133	8	344	EPS	50	2002.08	1.64	2.24	0.30
2.57.7	0.0133	8	444	EPS	50	2002.08	1.60	2.25	0.32
2.57.8	0.0133	8	544	EPS	50	2002.08	1.69	2.48	0.40
2.57.9	0.0133	8	644	EPS	50	2002.08	Damaged	Damaged	Damaged
2.58.1	0.0167	8	0	EPS	50	1601.66	2.89	2.66	-0.12
2.58.2	0.0167	8	34	EPS	50	1601.66	2.06	2.35	0.14
2.58.3	0.0167	8	94	EPS	50	1601.66	1.50	2.18	0.34
2.58.4	0.0167	8	144	EPS	50	1601.66	1.42	1.93	0.26
2.58.5	0.0167	8	244	EPS	50	1601.66	1.35	1.91	0.28
2.58.6	0.0167	8	344	EPS	50	1601.66	1.23	1.86	0.32
2.58.7	0.0167	8	444	EPS	50	1601.66	1.31	1.77	0.23
2.58.8	0.0167	8	544	EPS	50	1601.66	1.21	1.95	0.37

2.58.9	0.0167	8	644	EPS	50	1601.66	1.20	1.90	0.35
2.59.1	0.0133	5	0	EPS	50	744.94	1.72	1.87	0.07
2.59.2	0.0133	5	34	EPS	50	744.94	1.17	1.43	0.13
2.59.3	0.0133	5	94	EPS	50	744.94	0.87	1.36	0.25
2.59.4	0.0133	5	144	EPS	50	744.94	0.50	1.02	0.26
2.59.5	0.0133	5	244	EPS	50	744.94	0.44	1.16	0.36
2.59.6	0.0133	5	344	EPS	50	744.94	0.39	0.98	0.30
2.59.7	0.0133	5	444	EPS	50	744.94	0.40	0.96	0.28
2.59.8	0.0133	5	544	EPS	50	744.94	0.60	1.07	0.24
2.59.9	0.0133	5	644	EPS	50	744.94	0.53	0.93	0.20
2.60.1	0.0200	8	0	EPS	50	1334.72	2.98	2.99	0.00
2.60.2	0.0200	8	34	EPS	50	1334.72	1.95	2.29	0.17
2.60.3	0.0200	8	94	EPS	50	1334.72	1.46	1.93	0.23
2.60.4	0.0200	8	144	EPS	50	1334.72	1.47	1.97	0.25
2.60.5	0.0200	8	244	EPS	50	1334.72	1.32	1.80	0.24
2.60.6	0.0200	8	344	EPS	50	1334.72	1.17	1.82	0.32
2.60.7	0.0200	8	444	EPS	50	1334.72	1.20	1.65	0.22
2.60.8	0.0200	8	544	EPS	50	1334.72	1.19	1.77	0.29

2.60.9	0.0200	8	644	EPS	50	1334.72	1.14	1.67	0.27

Table 2: Geometric Form Data for Single-Pass Cutting with a Hot-Blade Tool

Sample #	Feed (ms-1)	Current (A)	Distance (mm)	Material	Engaged Length (mm)	Qeff (J/m2)	Kerfwidth (mm)	Edge Kerf (mm)	ΔH (mm)
4.1.1	0.0380	22	0	EPS	30	18952.42	1.94	1.80	-0.14
4.1.2	0.0380	22	20	EPS	30	18952.42	1.58	2.00	0.43
4.1.3	0.0380	22	60	EPS	30	18952.42	1.67	1.88	0.21
4.1.4	0.0380	22	100	EPS	30	18952.42	1.55	1.82	0.27
4.1.5	0.0380	22	200	EPS	30	18952.42	1.59	1.84	0.25
4.1.6	0.0380	22	300	EPS	30	18952.42	1.54	1.78	0.25
4.1.7	0.0380	22	400	EPS	30	18952.42	1.50	1.79	0.29
4.1.8	0.0380	22	500	EPS	30	18952.42	1.36	1.52	0.16
4.1.9	0.0380	22	600	EPS	30	18952.42	1.39	1.56	0.17
4.2.1	0.0860	22	0	EPS	30	8374.33	1.40	1.31	-0.09
4.2.2	0.0860	22	20	EPS	30	8374.33	1.16	1.19	0.04
4.2.3	0.0860	22	60	EPS	30	8374.33	1.19	1.33	0.14
4.2.4	0.0860	22	100	EPS	30	8374.33	1.11	1.13	0.02
4.2.5	0.0860	22	200	EPS	30	8374.33	1.04	1.10	0.06

4.2.6	0.0860	22	300	EPS	30	8374.33	0.98	1.21	0.23
4.2.7	0.0860	22	400	EPS	30	8374.33	0.89	1.16	0.27
4.2.8	0.0860	22	500	EPS	30	8374.33	0.80	1.19	0.39
4.2.9	0.0860	22	600	EPS	30	8374.33	0.82	1.24	0.42
4.3.1	0.0380	16	0	EPS	30	10024.42	1.48	1.29	-0.18
4.3.2	0.0380	16	20	EPS	30	10024.42	1.36	1.42	0.06
4.3.3	0.0380	16	60	EPS	30	10024.42	1.17	1.33	0.16
4.3.4	0.0380	16	100	EPS	30	10024.42	1.13	1.23	0.10
4.3.5	0.0380	16	200	EPS	30	10024.42	1.03	1.17	0.15
4.3.6	0.0380	16	300	EPS	30	10024.42	0.91	1.16	0.26
4.3.7	0.0380	16	400	EPS	30	10024.42	0.84	1.10	0.26
4.3.8	0.0380	16	500	EPS	30	10024.42	0.81	1.16	0.35
4.3.9	0.0380	16	600	EPS	30	10024.42	0.82	1.15	0.32
4.4.1	0.0860	19	0	EPS	30	6246.14	1.28	1.32	0.04
4.4.2	0.0860	19	20	EPS	30	6246.14	1.15	1.13	-0.02
4.4.3	0.0860	19	60	EPS	30	6246.14	1.02	1.23	0.21
4.4.4	0.0860	19	100	EPS	30	6246.14	1.09	1.13	0.04
4.4.5	0.0860	19	200	EPS	30	6246.14	0.90	1.04	0.14

4.4.6	0.0860	19	300	EPS	30	6246.14	0.84	0.98	0.14
4.4.7	0.0860	19	400	EPS	30	6246.14	0.78	1.00	0.22
4.4.8	0.0860	19	500	EPS	30	6246.14	0.64	1.12	0.48
4.4.9	0.0860	19	600	EPS	30	6246.14	0.97	1.30	0.33
4.5.1	0.0380	19	0	EPS	30	14136.00	1.89	1.64	-0.25
4.5.2	0.0380	19	20	EPS	30	14136.00	1.53	1.56	0.03
4.5.3	0.0380	19	60	EPS	30	14136.00	1.52	1.56	0.04
4.5.4	0.0380	19	100	EPS	30	14136.00	1.36	1.56	0.21
4.5.5	0.0380	19	200	EPS	30	14136.00	1.36	1.47	0.11
4.5.6	0.0380	19	300	EPS	30	14136.00	1.26	1.42	0.17
4.5.7	0.0380	19	400	EPS	30	14136.00	1.24	1.39	0.15
4.5.8	0.0380	19	500	EPS	30	14136.00	1.18	1.34	0.16
4.5.9	0.0380	19	600	EPS	30	14136.00	1.17	1.35	0.19
4.6.1	0.0500	19	0	EPS	30	10743.36	1.59	1.38	-0.20
4.6.2	0.0500	19	20	EPS	30	10743.36	1.43	1.31	-0.12
4.6.3	0.0500	19	60	EPS	30	10743.36	1.29	1.47	0.19
4.6.4	0.0500	19	100	EPS	30	10743.36	1.22	1.35	0.13
4.6.5	0.0500	19	200	EPS	30	10743.36	1.13	1.29	0.16

4.6.6	0.0500	19	300	EPS	30	10743.36	1.06	1.21	0.15
4.6.7	0.0500	19	400	EPS	30	10743.36	0.98	1.14	0.16
4.6.8	0.0500	19	500	EPS	30	10743.36	1.00	1.22	0.22
4.6.9	0.0500	19	600	EPS	30	10743.36	0.97	1.15	0.19
4.7.1	0.0740	19	0	EPS	30	7259.03	1.57	1.36	-0.21
4.7.2	0.0740	19	20	EPS	30	7259.03	1.30	1.31	0.01
4.7.3	0.0740	19	60	EPS	30	7259.03	1.10	1.26	0.16
4.7.4	0.0740	19	100	EPS	30	7259.03	1.14	1.08	-0.06
4.7.5	0.0740	19	200	EPS	30	7259.03	0.92	1.10	0.18
4.7.6	0.0740	19	300	EPS	30	7259.03	0.89	1.09	0.20
4.7.7	0.0740	19	400	EPS	30	7259.03	0.88	1.08	0.20
4.7.8	0.0740	19	500	EPS	30	7259.03	0.82	1.08	0.27
4.7.9	0.0740	19	600	EPS	30	7259.03	0.73	1.11	0.38
4.8.1	0.0620	19	0	EPS	30	8664.00	1.47	1.44	-0.02
4.8.2	0.0620	19	20	EPS	30	8664.00	1.27	1.40	0.13
4.8.3	0.0620	19	60	EPS	30	8664.00	1.14	1.40	0.26
4.8.4	0.0620	19	100	EPS	30	8664.00	1.18	1.14	-0.04
4.8.5	0.0620	19	200	EPS	30	8664.00	1.02	1.22	0.20

4.8.6	0.0620	19	300	EPS	30	8664.00	0.95	1.16	0.21
4.8.7	0.0620	19	400	EPS	30	8664.00	0.88	1.00	0.12
4.8.8	0.0620	19	500	EPS	30	8664.00	0.91	1.14	0.23
4.8.9	0.0620	19	600	EPS	30	8664.00	0.79	0.99	0.20
4.9.1	0.0620	16	0	EPS	30	6144.00	1.39	1.24	-0.15
4.9.2	0.0620	16	20	EPS	30	6144.00	1.24	1.32	0.09
4.9.3	0.0620	16	60	EPS	30	6144.00	1.18	1.33	0.16
4.9.4	0.0620	16	100	EPS	30	6144.00	1.04	1.17	0.14
4.9.5	0.0620	16	200	EPS	30	6144.00	0.94	1.04	0.10
4.9.6	0.0620	16	300	EPS	30	6144.00	0.76	1.01	0.26
4.9.7	0.0620	16	400	EPS	30	6144.00	0.83	1.05	0.22
4.9.8	0.0620	16	500	EPS	30	6144.00	0.65	1.05	0.40
4.9.9	0.0620	16	600	EPS	30	6144.00	1.19	1.34	0.16
4.10.1	0.0620	22	0	EPS	30	11616.00	1.67	1.68	0.02
4.10.2	0.0620	22	20	EPS	30	11616.00	1.43	1.42	-0.01
4.10.3	0.0620	22	60	EPS	30	11616.00	1.28	1.44	0.16
4.10.4	0.0620	22	100	EPS	30	11616.00	1.24	1.38	0.14
4.10.5	0.0620	22	200	EPS	30	11616.00	1.22	1.27	0.05

4.10.6	0.0620	22	300	EPS	30	11616.00	1.11	1.32	0.21
4.10.7	0.0620	22	400	EPS	30	11616.00	1.13	1.35	0.22
4.10.8	0.0620	22	500	EPS	30	11616.00	1.11	1.39	0.28
4.10.9	0.0620	22	600	EPS	30	11616.00	1.12	1.34	0.22
4.11.1	0.0620	19	0	EPS	30	8664.00	1.67	1.30	-0.37
4.11.2	0.0620	19	20	EPS	30	8664.00	1.37	1.56	0.19
4.11.3	0.0620	19	60	EPS	30	8664.00	1.26	1.33	0.07
4.11.4	0.0620	19	100	EPS	30	8664.00	1.26	1.28	0.02
4.11.5	0.0620	19	200	EPS	30	8664.00	1.14	1.16	0.03
4.11.6	0.0620	19	300	EPS	30	8664.00	1.02	1.16	0.14
4.11.7	0.0620	19	400	EPS	30	8664.00	0.93	1.03	0.10
4.11.8	0.0620	19	500	EPS	30	8664.00	0.89	1.12	0.23
4.11.9	0.0620	19	600	EPS	30	8664.00	0.95	1.11	0.17
4.12.1	0.0620	19	0	EPS	30	8664.00	1.70	1.44	-0.26
4.12.2	0.0620	19	20	EPS	30	8664.00	1.32	1.45	0.14
4.12.3	0.0620	19	60	EPS	30	8664.00	1.34	1.41	0.07
4.12.4	0.0620	19	100	EPS	30	8664.00	1.22	1.41	0.19
4.12.5	0.0620	19	200	EPS	30	8664.00	1.15	1.32	0.17

4.12.6	0.0620	19	300	EPS	30	8664.00	1.08	1.26	0.18
4.12.7	0.0620	19	400	EPS	30	8664.00	0.97	1.18	0.22
4.12.8	0.0620	19	500	EPS	30	8664.00	0.91	1.21	0.30
4.12.9	0.0620	19	600	EPS	30	8664.00	0.90	1.15	0.25
4.13.1	0.0620	19	0	EPS	30	8664.00	1.66	1.46	-0.19
4.13.2	0.0620	19	20	EPS	30	8664.00	1.32	1.28	-0.04
4.13.3	0.0620	19	60	EPS	30	8664.00	1.28	1.35	0.07
4.13.4	0.0620	19	100	EPS	30	8664.00	1.16	1.33	0.17
4.13.5	0.0620	19	200	EPS	30	8664.00	1.07	1.17	0.10
4.13.6	0.0620	19	300	EPS	30	8664.00	0.97	1.06	0.09
4.13.7	0.0620	19	400	EPS	30	8664.00	0.90	1.14	0.24
4.13.8	0.0620	19	500	EPS	30	8664.00	0.85	1.10	0.25
4.13.9	0.0620	19	600	EPS	30	8664.00	0.84	1.10	0.26
4.14.1	0.0620	19	0	EPS	30	8664.00	1.43	1.44	0.01
4.14.2	0.0620	19	20	EPS	30	8664.00	1.29	1.39	0.10
4.14.3	0.0620	19	60	EPS	30	8664.00	1.22	1.37	0.15
4.14.4	0.0620	19	100	EPS	30	8664.00	1.17	1.36	0.20
4.14.5	0.0620	19	200	EPS	30	8664.00	1.07	1.29	0.22

4.14.6	0.0620	19	300	EPS	30	8664.00	1.06	1.22	0.17
4.14.7	0.0620	19	400	EPS	30	8664.00	0.89	1.12	0.23
4.14.8	0.0620	19	500	EPS	30	8664.00	0.90	1.14	0.25
4.14.9	0.0620	19	600	EPS	30	8664.00	0.86	1.13	0.27
4.15.1	0.0620	22	0	EPS	50	11616.00	2.15	1.83	-0.32
4.15.2	0.0620	22	20	EPS	50	11616.00	2.04	1.97	-0.07
4.15.3	0.0620	22	60	EPS	50	11616.00	1.58	1.70	0.13
4.15.4	0.0620	22	100	EPS	50	11616.00	1.49	1.71	0.22
4.15.5	0.0620	22	200	EPS	50	11616.00	1.28	1.63	0.35
4.15.6	0.0620	22	300	EPS	50	11616.00	1.15	1.39	0.24
4.15.7	0.0620	22	400	EPS	50	11616.00	1.11	1.44	0.33
4.15.8	0.0620	22	500	EPS	50	11616.00	0.99	1.33	0.34
4.15.9	0.0620	22	600	EPS	50	11616.00	0.98	1.32	0.34
4.16.1	0.0860	22	0	EPS	50	8374.33	0.77	0.77	0.00
4.16.2	0.0860	22	20	EPS	50	8374.33	0.73	0.78	0.04
4.16.3	0.0860	22	60	EPS	50	8374.33	0.64	0.73	0.09
4.16.4	0.0860	22	100	EPS	50	8374.33	0.61	0.73	0.13
4.16.5	0.0860	22	200	EPS	50	8374.33	0.57	0.74	0.17

4.16.6	0.0860	22	300	EPS	50	8374.33	0.58	0.73	0.15
4.16.7	0.0860	22	400	EPS	50	8374.33	0.60	0.76	0.16
4.16.8	0.0860	22	500	EPS	50	8374.33	0.60	1.01	0.41
4.16.9	0.0860	22	600	EPS	50	8374.33	0.64	1.11	0.48
4.17.1	0.0380	16	0	EPS	50	10024.42	1.51	1.64	0.14
4.17.2	0.0380	16	20	EPS	50	10024.42	1.38	1.40	0.02
4.17.3	0.0380	16	60	EPS	50	10024.42	1.10	1.17	0.07
4.17.4	0.0380	16	100	EPS	50	10024.42	1.02	1.18	0.16
4.17.5	0.0380	16	200	EPS	50	10024.42	0.79	0.97	0.18
4.17.6	0.0380	16	300	EPS	50	10024.42	0.65	0.88	0.23
4.17.7	0.0380	16	400	EPS	50	10024.42	0.54	0.84	0.30
4.17.8	0.0380	16	500	EPS	50	10024.42	0.65	0.97	0.32
4.17.9	0.0380	16	600	EPS	50	10024.42	0.43	0.75	0.32
4.18.1	0.0860	19	0	EPS	50	6246.14	0.80	0.63	-0.17
4.18.2	0.0860	19	20	EPS	50	6246.14	0.43	0.51	0.08
4.18.3	0.0860	19	60	EPS	50	6246.14	0.34	0.51	0.17
4.18.4	0.0860	19	100	EPS	50	6246.14	0.33	0.49	0.16
4.18.5	0.0860	19	200	EPS	50	6246.14	0.32	0.49	0.18

4.18.6	0.0860	19	300	EPS	50	6246.14	0.40	0.54	0.14
4.18.7	0.0860	19	400	EPS	50	6246.14	0.53	0.98	0.45
4.18.8	0.0860	19	500	EPS	50	6246.14	0.64	0.92	0.28
4.18.9	0.0860	19	600	EPS	50	6246.14	0.90	1.36	0.47
4.19.1	0.0830	19	0	EPS	50	14136.00	1.94	1.79	-0.15
4.19.2	0.0830	19	20	EPS	50	14136.00	1.79	1.42	-0.36
4.19.3	0.0830	19	60	EPS	50	14136.00	1.31	1.63	0.33
4.19.4	0.0830	19	100	EPS	50	14136.00	1.16	1.28	0.12
4.19.5	0.0830	19	200	EPS	50	14136.00	1.09	1.29	0.20
4.19.6	0.0830	19	300	EPS	50	14136.00	0.88	1.11	0.23
4.19.7	0.0830	19	400	EPS	50	14136.00	0.87	1.09	0.22
4.19.8	0.0830	19	500	EPS	50	14136.00	0.79	1.05	0.26
4.19.9	0.0830	19	600	EPS	50	14136.00	0.71	1.10	0.39
4.20.1	0.0500	19	0	EPS	50	10743.36	1.87	1.65	-0.22
4.20.2	0.0500	19	20	EPS	50	10743.36	1.47	1.65	0.18
4.20.3	0.0500	19	60	EPS	50	10743.36	1.27	1.41	0.15
4.20.4	0.0500	19	100	EPS	50	10743.36	0.97	1.25	0.28
4.20.5	0.0500	19	200	EPS	50	10743.36	0.89	1.07	0.18

4.20.6	0.0500	19	300	EPS	50	10743.36	0.72	1.06	0.34
4.20.7	0.0500	19	400	EPS	50	10743.36	0.62	0.93	0.31
4.20.8	0.0500	19	500	EPS	50	10743.36	0.60	0.88	0.28
4.20.9	0.0500	19	600	EPS	50	10743.36	0.53	1.03	0.50
4.21.1	0.0740	19	0	EPS	50	7259.03	1.83	1.70	-0.13
4.21.2	0.0740	19	20	EPS	50	7259.03	1.42	1.53	0.12
4.21.3	0.0740	19	60	EPS	50	7259.03	1.22	1.32	0.10
4.21.4	0.0740	19	100	EPS	50	7259.03	1.03	1.12	0.09
4.21.5	0.0740	19	200	EPS	50	7259.03	0.76	0.94	0.18
4.21.6	0.0740	19	300	EPS	50	7259.03	0.66	0.91	0.25
4.21.7	0.0740	19	400	EPS	50	7259.03	0.25	0.82	0.57
4.21.8	0.0740	19	500	EPS	50	7259.03	0.25	0.82	0.58
4.21.9	0.0740	19	600	EPS	50	7259.03	-0.27	0.35	0.61
4.22.1	0.0620	19	0	EPS	50	8664.00	1.76	1.58	-0.19
4.22.2	0.0620	19	20	EPS	50	8664.00	1.43	1.57	0.14
4.22.3	0.0620	19	60	EPS	50	8664.00	1.22	1.32	0.10
4.22.4	0.0620	19	100	EPS	50	8664.00	0.98	1.13	0.15
4.22.5	0.0620	19	200	EPS	50	8664.00	0.78	1.03	0.25

4.22.6	0.0620	19	300	EPS	50	8664.00	0.67	1.03	0.36
4.22.7	0.0620	19	400	EPS	50	8664.00	0.63	1.02	0.39
4.22.8	0.0620	19	500	EPS	50	8664.00	0.62	1.02	0.40
4.22.9	0.0620	19	600	EPS	50	8664.00	0.50	0.87	0.37
4.23.1	0.0620	19	0	EPS	50	8664.00	1.38	1.34	-0.03
4.23.2	0.0620	19	20	EPS	50	8664.00	1.19	1.37	0.19
4.23.3	0.0620	19	60	EPS	50	8664.00	1.03	1.15	0.12
4.23.4	0.0620	19	100	EPS	50	8664.00	0.83	0.90	0.07
4.23.5	0.0620	19	200	EPS	50	8664.00	0.63	0.77	0.14
4.23.6	0.0620	19	300	EPS	50	8664.00	0.49	0.76	0.27
4.23.7	0.0620	19	400	EPS	50	8664.00	0.50	0.73	0.23
4.23.8	0.0620	19	500	EPS	50	8664.00	0.38	0.73	0.36
4.23.9	0.0620	19	600	EPS	50	8664.00	0.17	0.67	0.51
4.24.1	0.0620	22	0	EPS	50	11616.00	1.73	1.73	0.00
4.24.2	0.0620	22	20	EPS	50	11616.00	1.42	1.52	0.10
4.24.3	0.0620	22	60	EPS	50	11616.00	1.23	1.55	0.32
4.24.4	0.0620	22	100	EPS	50	11616.00	1.23	1.34	0.11
4.24.5	0.0620	22	200	EPS	50	11616.00	1.03	1.14	0.11

4.24.6	0.0620	22	300	EPS	50	11616.00	0.87	1.03	0.16
4.24.7	0.0620	22	400	EPS	50	11616.00	0.80	1.02	0.22
4.24.8	0.0620	22	500	EPS	50	11616.00	0.76	1.02	0.26
4.24.9	0.0620	22	600	EPS	50	11616.00	0.65	1.02	0.37
4.25.1	0.0520	16	0	XPS	30	7325.54	1.50	0.96	-0.54
4.25.2	0.0520	16	20	XPS	30	7325.54	1.20	1.24	0.04
4.25.3	0.0520	16	60	XPS	30	7325.54	0.95	1.05	0.10
4.25.4	0.0520	16	100	XPS	30	7325.54	0.87	0.96	0.09
4.25.5	0.0520	16	200	XPS	30	7325.54	0.60	0.87	0.27
4.25.6	0.0520	16	300	XPS	30	7325.54	0.51	0.83	0.32
4.25.7	0.0520	16	400	XPS	30	7325.54	0.52	0.86	0.35
4.25.8	0.0520	16	500	XPS	30	7325.54	0.51	0.86	0.35
4.25.9	0.0520	16	600	XPS	30	7325.54	0.50	0.82	0.32
4.26.1	0.0520	22	0	XPS	30	13849.85	2.06	1.37	-0.69
4.26.2	0.0520	22	20	XPS	30	13849.85	1.72	1.59	-0.13
4.26.3	0.0520	22	60	XPS	30	13849.85	1.42	1.57	0.15
4.26.4	0.0520	22	100	XPS	30	13849.85	1.26	1.34	0.09
4.26.5	0.0520	22	200	XPS	30	13849.85	1.02	1.21	0.19

4.26.6	0.0520	22	300	XPS	30	13849.85	0.97	1.10	0.13
4.26.7	0.0520	22	400	XPS	30	13849.85	0.88	0.98	0.10
4.26.8	0.0520	22	500	XPS	30	13849.85	0.84	0.95	0.12
4.26.9	0.0520	22	600	XPS	30	13849.85	0.75	0.96	0.21
4.27.1	0.0280	16	0	XPS	30	13604.57	1.90	1.40	-0.51
4.27.2	0.0280	16	20	XPS	30	13604.57	1.59	1.68	0.09
4.27.3	0.0280	16	60	XPS	30	13604.57	1.29	1.48	0.19
4.27.4	0.0280	16	100	XPS	30	13604.57	1.05	1.21	0.16
4.27.5	0.0280	16	200	XPS	30	13604.57	0.90	1.11	0.21
4.27.6	0.0280	16	300	XPS	30	13604.57	0.82	1.11	0.29
4.27.7	0.0280	16	400	XPS	30	13604.57	0.72	1.01	0.29
4.27.8	0.0280	16	500	XPS	30	13604.57	0.72	1.13	0.42
4.27.9	0.0280	16	600	XPS	30	13604.57	0.71	1.08	0.37
4.28.1	0.0400	19	0	XPS	30	13429.20	2.13	1.34	-0.79
4.28.2	0.0400	19	20	XPS	30	13429.20	1.82	1.62	-0.20
4.28.3	0.0400	19	60	XPS	30	13429.20	1.43	1.46	0.03
4.28.4	0.0400	19	100	XPS	30	13429.20	1.22	1.33	0.11
4.28.5	0.0400	19	200	XPS	30	13429.20	1.00	1.11	0.12

4.28.6	0.0400	19	300	XPS	30	13429.20	0.79	0.96	0.17
4.28.7	0.0400	19	400	XPS	30	13429.20	0.82	0.93	0.11
4.28.8	0.0400	19	500	XPS	30	13429.20	0.74	1.02	0.27
4.28.9	0.0400	19	600	XPS	30	13429.20	0.72	1.00	0.28
4.29.1	0.0520	19	0	XPS	30	10330.15	1.77	1.22	-0.56
4.29.2	0.0520	19	20	XPS	30	10330.15	1.52	1.30	-0.21
4.29.3	0.0520	19	60	XPS	30	10330.15	1.33	1.13	-0.20
4.29.4	0.0520	19	100	XPS	30	10330.15	1.18	1.01	-0.17
4.29.5	0.0520	19	200	XPS	30	10330.15	0.85	0.96	0.12
4.29.6	0.0520	19	300	XPS	30	10330.15	0.69	0.91	0.23
4.29.7	0.0520	19	400	XPS	30	10330.15	0.63	0.90	0.27
4.29.8	0.0520	19	500	XPS	30	10330.15	0.60	0.87	0.28
4.29.9	0.0520	19	600	XPS	30	10330.15	0.64	0.89	0.25
4.30.1	0.0760	22	0	XPS	30	9476.21	1.68	1.17	-0.51
4.30.2	0.0760	22	20	XPS	30	9476.21	1.40	1.44	0.04
4.30.3	0.0760	22	60	XPS	30	9476.21	1.21	1.26	0.06
4.30.4	0.0760	22	100	XPS	30	9476.21	1.10	1.19	0.09
4.30.5	0.0760	22	200	XPS	30	9476.21	0.82	1.14	0.32

4.30.6	0.0760	22	300	XPS	30	9476.21	0.74	1.06	0.33
4.30.7	0.0760	22	400	XPS	30	9476.21	0.64	0.88	0.24
4.30.8	0.0760	22	500	XPS	30	9476.21	0.62	0.91	0.29
4.30.9	0.0760	22	600	XPS	30	9476.21	0.57	0.98	0.41
4.31.1	0.0280	19	0	XPS	30	19184.57	2.39	1.60	-0.79
4.31.2	0.0280	19	20	XPS	30	19184.57	2.08	1.69	-0.39
4.31.3	0.0280	19	60	XPS	30	19184.57	1.76	1.73	-0.03
4.31.4	0.0280	19	100	XPS	30	19184.57	1.29	1.57	0.28
4.31.5	0.0280	19	200	XPS	30	19184.57	1.17	1.38	0.21
4.31.6	0.0280	19	300	XPS	30	19184.57	1.15	1.32	0.17
4.31.7	0.0280	19	400	XPS	30	19184.57	1.05	1.20	0.15
4.31.8	0.0280	19	500	XPS	30	19184.57	1.13	1.21	0.09
4.31.9	0.0280	19	600	XPS	30	19184.57	1.07	1.30	0.24
4.32.1	0.0280	22	0	XPS	30	25721.14	2.65	1.92	-0.72
4.32.2	0.0280	22	20	XPS	30		2.56	2.18	-0.38
4.32.3	0.0280	22	60	XPS	30	25721.14	2.07	2.08	0.01
4.32.4	0.0280	22	100	XPS	30	25721.14	1.85	1.95	0.11
4.32.5	0.0280	22	200	XPS	30	25721.14	1.55	1.64	0.09

4.32.6	0.0280	22	300	XPS	30	25721.14	1.39	1.50	0.11
4.32.7	0.0280	22	400	XPS	30	25721.14	1.36	1.49	0.13
4.32.8	0.0280	22	500	XPS	30	25721.14	1.46	1.64	0.19
4.32.9	0.0280	22	600	XPS	30	25721.14	1.39	1.46	0.07
4.33.1	0.0640	19	0	XPS	30	8393.25	1.73	1.17	-0.56
4.33.2	0.0640	19	20	XPS	30	8393.25	1.14	1.37	0.23
4.33.3	0.0640	19	60	XPS	30	8393.25	1.15	1.16	0.01
4.33.4	0.0640	19	100	XPS	30	8393.25	0.97	1.14	0.17
4.33.5	0.0640	19	200	XPS	30	8393.25	0.77	0.89	0.13
4.33.6	0.0640	19	300	XPS	30	8393.25	0.56	0.84	0.28
4.33.7	0.0640	19	400	XPS	30	8393.25	0.56	0.90	0.34
4.33.8	0.0640	19	500	XPS	30	8393.25	0.52	0.88	0.36
4.33.9	0.0640	19	600	XPS	30	8393.25	0.50	0.89	0.39
4.34.1	0.0760	19	0	XPS	30	7068.00	1.58	1.11	-0.46
4.34.2	0.0760	19	20	XPS	30	7068.00	1.31	1.32	0.01
4.34.3	0.0760	19	60	XPS	30	7068.00	1.07	1.14	0.08
4.34.4	0.0760	19	100	XPS	30	7068.00	0.92	1.04	0.13
4.34.5	0.0760	19	200	XPS	30	7068.00	0.75	0.90	0.15

4.34.6	0.0760	19	300	XPS	30	7068.00	0.55	0.77	0.22
4.34.7	0.0760	19	400	XPS	30	7068.00	0.49	0.83	0.34
4.34.8	0.0760	19	500	XPS	30	7068.00	0.48	0.81	0.34
4.34.9	0.0760	19	600	XPS	30	7068.00	0.47	0.73	0.27
4.35.1	0.0520	19	0	XPS	30	10330.15	1.88	1.21	-0.67
4.35.2	0.0520	19	20	XPS	30	10330.15	1.56	1.57	0.01
4.35.3	0.0520	19	60	XPS	30	10330.15	1.30	1.33	0.04
4.35.4	0.0520	19	100	XPS	30	10330.15	1.10	1.18	0.08
4.35.5	0.0520	19	200	XPS	30	10330.15	0.80	0.97	0.17
4.35.6	0.0520	19	300	XPS	30	10330.15	0.76	0.96	0.21
4.35.7	0.0520	19	400	XPS	30	10330.15	0.65	0.88	0.24
4.35.8	0.0520	19	500	XPS	30	10330.15	0.65	0.86	0.22
4.35.9	0.0520	19	600	XPS	30	10330.15	0.64	0.87	0.24
4.36.1	0.0520	19	0	XPS	30	10330.15	1.93	1.17	-0.77
4.36.2	0.0520	19	20	XPS	30	10330.15	1.68	1.45	-0.23
4.36.3	0.0520	19	60	XPS	30	10330.15	1.41	1.29	-0.13
4.36.4	0.0520	19	100	XPS	30	10330.15	1.17	1.08	-0.09
4.36.5	0.0520	19	200	XPS	30	10330.15	0.82	1.04	0.22

4.36.6	0.0520	19	300	XPS	30	10330.15	0.75	1.06	0.31
4.36.7	0.0520	19	400	XPS	30	10330.15	0.66	0.85	0.19
4.36.8	0.0520	19	500	XPS	30	10330.15	0.66	0.88	0.22
4.36.9	0.0520	19	600	XPS	30	10330.15	0.58	0.82	0.24
4.37.1	0.0520	19	0	XPS	30	10330.15	1.90	1.10	-0.81
4.37.2	0.0520	19	20	XPS	30	10330.15	1.56	1.17	-0.39
4.37.3	0.0520	19	60	XPS	30	10330.15	1.29	1.15	-0.15
4.37.4	0.0520	19	100	XPS	30	10330.15	0.95	1.18	0.23
4.37.5	0.0520	19	200	XPS	30	10330.15	0.88	0.87	-0.01
4.37.6	0.0520	19	300	XPS	30	10330.15	0.88	0.74	-0.14
4.37.7	0.0520	19	400	XPS	30	10330.15	0.64	0.84	0.20
4.37.8	0.0520	19	500	XPS	30	10330.15	0.66	0.91	0.25
4.37.9	0.0520	19	600	XPS	30	10330.15	0.55	0.91	0.36
4.38.1	0.0520	19	0	XPS	30	10330.15	1.88	1.19	-0.69
4.38.2	0.0520	19	20	XPS	30	10330.15	1.52	1.55	0.02
4.38.3	0.0520	19	60	XPS	30	10330.15	1.23	1.34	0.11
4.38.4	0.0520	19	100	XPS	30	10330.15	1.11	1.22	0.11
4.38.5	0.0520	19	200	XPS	30	10330.15	0.86	1.11	0.26

4.38.6	0.0520	19	300	XPS	30	10330.15	0.75	1.02	0.28
4.38.7	0.0520	19	400	XPS	30	10330.15	0.69	0.92	0.23
4.38.8	0.0520	19	500	XPS	30	10330.15	0.68	0.94	0.27
4.38.9	0.0520	19	600	XPS	30	10330.15	0.67	0.92	0.25
4.39.1	0.0520	16	0	XPS	50	7325.54	1.39	0.84	-0.56
4.29.2	0.0520	16	20	XPS	50	7325.54	1.09	0.80	-0.29
4.29.3	0.0520	16	60	XPS	50	7325.54	0.95	0.77	-0.18
4.39.4	0.0520	16	100	XPS	50	7325.54	0.77	0.73	-0.03
4.39.5	0.0520	16	200	XPS	50	7325.54	0.54	0.67	0.14
4.39.6	0.0520	16	300	XPS	50	7325.54	0.43	0.58	0.15
4.39.7	0.0520	16	400	XPS	50	7325.54	0.35	0.55	0.20
4.39.8	0.0520	16	500	XPS	50	7325.54	0.51	0.67	0.17
4.39.9	0.0520	16	600	XPS	50	7325.54	0.52	0.34	-0.18
4.40.1	0.0520	22	0	XPS	50	13849.85	1.96	1.12	-0.83
4.40.2	0.0520	22	20	XPS	50	13849.85	1.65	1.20	-0.44
4.40.3	0.0520	22	60	XPS	50	13849.85	1.39	1.14	-0.25
4.40.4	0.0520	22	100	XPS	50	13849.85	1.20	1.09	-0.11
4.40.5	0.0520	22	200	XPS	50	13849.85	0.91	0.95	0.04

4.40.6	0.0520	22	300	XPS	50	13849.85	0.71	0.97	0.26
4.40.7	0.0520	22	400	XPS	50	13849.85	0.61	0.91	0.30
4.40.8	0.0520	22	500	XPS	50	13849.85	0.59	0.90	0.31
4.40.9	0.0520	22	600	XPS	50	13849.85	0.58	0.87	0.29
4.41.1	0.0280	16	0	XPS	50	13604.57	1.67	1.10	-0.57
4.41.2	0.0280	16	20	XPS	50	13604.57	1.47	1.09	-0.38
4.41.3	0.0280	16	60	XPS	50	13604.57	1.15	1.02	-0.13
4.41.4	0.0280	16	100	XPS	50	13604.57	1.01	0.99	-0.02
4.41.5	0.0280	16	200	XPS	50	13604.57	0.72	0.89	0.17
4.41.6	0.0280	16	300	XPS	50	13604.57	0.68	0.87	0.19
4.41.7	0.0280	16	400	XPS	50	13604.57	0.63	0.82	0.19
4.41.8	0.0280	16	500	XPS	50	13604.57	0.60	0.81	0.21
4.41.9	0.0280	16	600	XPS	50	13604.57	0.55	0.73	0.18
4.42.1	0.0400	19	0	XPS	50	13429.20	1.91	1.08	-0.83
4.42.2	0.0400	19	20	XPS	50	13429.20	1.56	1.16	-0.40
4.42.3	0.0400	19	60	XPS	50	13429.20	1.35	1.12	-0.23
4.42.4	0.0400	19	100	XPS	50	13429.20	1.16	1.10	-0.07
4.42.5	0.0400	19	200	XPS	50	13429.20	0.82	0.91	0.09

4.42.6	0.0400	19	300	XPS	50	13429.20	0.67	0.92	0.25
4.42.7	0.0400	19	400	XPS	50	13429.20	0.64	0.86	0.22
4.42.8	0.0400	19	500	XPS	50	13429.20	0.61	0.85	0.24
4.42.9	0.0400	19	600	XPS	50	13429.20	0.56	0.78	0.22
4.43.1	0.0520	19	0	XPS	50	10330.15	1.74	1.04	-0.70
4.43.2	0.0520	19	20	XPS	50	10330.15	1.58	1.03	-0.55
4.43.3	0.0520	19	60	XPS	50	10330.15	1.09	0.95	-0.14
4.43.4	0.0520	19	100	XPS	50	10330.15	0.98	0.92	-0.06
4.43.5	0.0520	19	200	XPS	50	10330.15	0.75	0.85	0.10
4.43.6	0.0520	19	300	XPS	50	10330.15	0.67	0.80	0.14
4.43.7	0.0520	19	400	XPS	50	10330.15	0.61	0.81	0.20
4.43.8	0.0520	19	500	XPS	50	10330.15	0.54	0.78	0.24
4.43.9	0.0520	19	600	XPS	50	10330.15	0.43	0.73	0.30
4.44.1	0.0760	22	0	XPS	50	9476.21	1.64	1.09	-0.55
4.44.2	0.0760	22	20	XPS	50	9476.21	1.53	1.02	-0.51
4.44.3	0.0760	22	60	XPS	50	9476.21	1.18	1.00	-0.18
4.44.4	0.0760	22	100	XPS	50	9476.21	1.01	0.93	-0.07
4.44.5	0.0760	22	200	XPS	50	9476.21	0.81	0.87	0.06

4.44.6	0.0760	22	300	XPS	50	9476.21	0.62	0.88	0.27
4.44.7	0.0760	22	400	XPS	50	9476.21	0.52	0.86	0.34
4.44.8	0.0760	22	500	XPS	50	9476.21	0.49	0.81	0.32
4.44.9	0.0760	22	600	XPS	50	9476.21	0.48	0.86	0.38
4.45.1	0.0280	19	0	XPS	50	19184.57	2.30	1.51	-0.79
4.45.2	0.0280	19	20	XPS	50	19184.57	2.01	1.40	-0.60
4.45.3	0.0280	19	60	XPS	50	19184.57	1.50	1.32	-0.18
4.45.4	0.0280	19	100	XPS	50	19184.57	1.36	1.25	-0.10
4.45.5	0.0280	19	200	XPS	50	19184.57	1.04	1.12	0.08
4.45.6	0.0280	19	300	XPS	50	19184.57	0.96	1.10	0.14
4.45.7	0.0280	19	400	XPS	50	19184.57	0.89	1.10	0.21
4.45.8	0.0280	19	500	XPS	50	19184.57	0.91	1.09	0.18
4.45.9	0.0280	19	600	XPS	50	19184.57	0.91	1.06	0.15
4.46.1	0.0280	22	0	XPS	50	25721.14	2.64	1.47	-1.17
4.46.2	0.0280	22	20	XPS	50	25721.14	2.30	1.55	-0.75
4.46.3	0.0280	22	60	XPS	50	25721.14	1.96	1.55	-0.41
4.46.4	0.0280	22	100	XPS	50	25721.14	1.67	1.56	-0.11
4.46.5	0.0280	22	200	XPS	50	25721.14	1.36	1.43	0.07

4.46.6	0.0280	22	300	XPS	50	25721.14	1.31	1.43	0.12
4.46.7	0.0280	22	400	XPS	50	25721.14	1.28	1.37	0.09
4.46.8	0.0280	22	500	XPS	50	25721.14	1.25	1.35	0.11
4.46.9	0.0280	22	600	XPS	50	25721.14	1.18	1.28	0.10
4.47.1	0.0640	19	0	XPS	50	8393.25	1.55	0.98	-0.58
4.47.2	0.0640	19	20	XPS	50	8393.25	1.46	1.02	-0.43
4.47.3	0.0640	19	60	XPS	50	8393.25	1.24	0.93	-0.31
4.47.4	0.0640	19	100	XPS	50	8393.25	0.97	0.87	-0.10
4.47.5	0.0640	19	200	XPS	50	8393.25	0.69	0.79	0.11
4.47.6	0.0640	19	300	XPS	50	8393.25	0.60	0.78	0.18
4.47.7	0.0640	19	400	XPS	50	8393.25	0.52	0.78	0.26
4.47.8	0.0640	19	500	XPS	50	8393.25	0.48	0.78	0.30
4.47.9	0.0640	19	600	XPS	50	8393.25	0.37	0.70	0.33
4.48.1	0.0760	19	0	XPS	50	7068.00	1.48	0.99	-0.49
4.48.2	0.0760	19	20	XPS	50	7068.00	1.24	0.97	-0.27
4.48.3	0.0760	19	60	XPS	50	7068.00	1.07	0.86	-0.21
4.48.4	0.0760	19	100	XPS	50	7068.00	0.94	0.89	-0.05
4.48.5	0.0760	19	200	XPS	50	7068.00	0.64	0.74	0.11

4.48.6	0.0760	19	300	XPS	50	7068.00	0.51	0.69	0.19
4.48.7	0.0760	19	400	XPS	50	7068.00	0.38	0.63	0.25
4.48.8	0.0760	19	500	XPS	50	7068.00	0.39	0.59	0.20
4.48.9	0.0760	19	600	XPS	50	7068.00	0.37	0.62	0.26

Appendix B2: Multi-Pass Form Results

Table 3: Geometric Form Data for Multi-Pass Cutting of EPS Foam

Run #	Feed (ms^{-1})	Current (A)	Distance (mm)	Blade Shape	Blade Size (mm)	Path Spacing (mm)	Rmax (mm)	Peak Spacing (mm)
7.1.1	0.052	16	0	Square	8	4	0.73	4.13
7.1.2	0.052	16	100	Square	8	4	0.70	3.92
7.1.3	0.052	16	250	Square	8	4	1.06	4.28
7.1.4	0.052	16	400	Square	8	4	0.54	3.96
7.1.5	0.052	16	600	Square	8	4	0.51	5.57
7.2.1	0.052	22	0	Square	8	4	1.33	3.91
7.2.2	0.052	22	100	Square	8	4	0.77	4.05
7.2.3	0.052	22	250	Square	8	4	0.55	4.13
7.2.4	0.052	22	400	Square	8	4	0.57	3.72
7.2.5	0.052	22	600	Square	8	4	0.71	4.21
7.3.1	0.098	22	0	Square	8	4	0.79	3.73
7.3.2	0.098	22	100	Square	8	4	0.62	3.90
7.3.3	0.098	22	250	Square	8	4	0.69	4.16
7.3.4	0.098	22	400	Square	8	4	0.77	4.83
7.3.5	0.098	22	600	Square	8	4	0.80	5.08
7.4.1	0.074	16	0	Square	8	4	0.78	3.88

7.4.2	0.074	16	100	Square	8	4	0.54	4.05
7.4.3	0.074	16	250	Square	8	4	0.65	4.09
7.4.4	0.074	16	400	Square	8	4	0.55	4.23
7.4.5	0.074	16	600	Square	8	4	0.66	5.10
7.5.1	0.074	18	0	Square	8	4	0.79	3.83
7.5.2	0.074	18	100	Square	8	4	0.59	4.22
7.5.3	0.074	18	250	Square	8	4	0.69	3.62
7.5.4	0.074	18	400	Square	8	4	0.52	3.83
7.5.5	0.074	18	600	Square	8	4	0.54	3.62
7.6.1	0.074	22	0	Square	8	8	Damaged	Damaged
7.6.2	0.074	22	100	Square	8	8	0.71	4.06
7.6.3	0.074	22	250	Square	8	8	0.62	4.18
7.6.4	0.074	22	400	Square	8	8	0.57	4.00
7.6.5	0.074	22	600	Square	8	8	0.66	4.00
7.7.1	0.052	16	0	Square	8	8	0.77	7.94
7.7.2	0.052	16	100	Square	8	8	Damaged	Damaged
7.7.3	0.052	16	250	Square	8	8	0.90	7.86
7.7.4	0.052	16	400	Square	8	8	1.26	7.56

7.7.5	0.052	16	600	Square	8	8	Damaged	Damaged
7.8.1	0.052	22	0	Square	8	8	1.43	7.92
7.8.2	0.052	22	100	Square	8	8	0.87	7.97
7.8.3	0.052	22	250	Square	8	8	0.83	7.79
7.8.4	0.052	22	400	Square	8	8	0.72	8.22
7.8.5	0.052	22	600	Square	8	8	0.92	8.09
7.9.1	0.098	22	0	Square	8	8	0.90	Damaged
7.9.2	0.098	22	100	Square	8	8	0.94	8.04
7.9.3	0.098	22	250	Square	8	8	0.88	7.75
7.9.4	0.098	22	400	Square	8	8	0.94	8.19
7.9.5	0.098	22	600	Square	8	8	Damaged	Damaged
7.10.1	0.074	16	0	Square	8	8	1.15	7.99
7.10.2	0.074	16	100	Square	8	8	0.91	7.92
7.10.3	0.074	16	250	Square	8	8	0.86	8.35
7.10.4	0.074	16	400	Square	8	8	Damaged	Damaged
7.10.5	0.074	16	600	Square	8	8	Damaged	Damaged
7.11.1	0.074	18	0	Square	8	8	0.88	7.80
7.11.2	0.074	18	100	Square	8	8	0.87	7.75

7.11.3	0.074	18	250	Square	8	8	0.63	7.90
7.11.4	0.074	18	400	Square	8	8	0.96	7.96
7.11.5	0.074	18	600	Square	8	8	1.03	8.05
7.12.1	0.074	22	0	Square	8	8	1.24	7.70
7.12.2	0.074	22	100	Square	8	8	0.73	7.83
7.12.3	0.074	22	250	Square	8	8	0.90	7.86
7.12.4	0.074	22	400	Square	8	8	0.67	8.04
7.12.5	0.074	22	600	Square	8	8	0.81	8.21
7.13.1	0.052	16	0	Square	22	10	1.04	9.58
7.13.2	0.052	16	100	Square	22	10	1.01	9.70
7.13.3	0.052	16	250	Square	22	10	1.03	8.66
7.13.4	0.052	16	400	Square	22	10	0.99	9.60
7.13.5	0.052	16	600	Square	22	10	1.39	10.08
7.14.1	0.052	22	0	Square	22	10	1.21	9.70
7.14.2	0.052	22	100	Square	22	10	1.12	10.04
7.14.3	0.052	22	250	Square	22	10	0.89	9.92
7.14.4	0.052	22	400	Square	22	10	0.87	9.66
7.14.5	0.052	22	600	Square	22	10	0.74	9.43

7.15.1	0.098	22	0	Square	22	10	Damaged	Damaged
7.15.2	0.098	22	100	Square	22	10	Damaged	Damaged
7.15.3	0.098	22	250	Square	22	10	Damaged	Damaged
7.15.4	0.098	22	400	Square	22	10	Damaged	Damaged
7.15.5	0.098	22	600	Square	22	10	Damaged	Damaged
7.16.1	0.074	16	0	Square	22	10	0.86	10.36
7.16.2	0.074	16	100	Square	22	10	0.66	9.66
7.16.3	0.074	16	250	Square	22	10	0.63	10.04
7.16.4	0.074	16	400	Square	22	10	Damaged	Damaged
7.16.5	0.074	16	600	Square	22	10	Damaged	Damaged
7.17.1	0.074	18	0	Square	22	10	1.00	9.75
7.17.2	0.074	18	100	Square	22	10	0.74	9.75
7.17.3	0.074	18	250	Square	22	10	0.88	9.98
7.17.4	0.074	18	400	Square	22	10	1.59	10.77
7.17.5	0.074	18	600	Square	22	10	1.52	10.31
7.18.1	0.074	22	0	Square	22	10	0.94	Damaged
7.18.2	0.074	22	100	Square	22	10	0.81	Damaged
7.18.3	0.074	22	250	Square	22	10	1.08	9.53

7.18.4	0.074	22	400	Square	22	10	1.09	12.11
7.18.5	0.074	22	600	Square	22	10	Damaged	Damaged
7.19.1	0.052	16	0	Square	22	15	1.43	14.11
7.19.2	0.052	16	100	Square	22	15	0.81	14.42
7.19.3	0.052	16	250	Square	22	15	Damaged	Damaged
7.19.4	0.052	16	400	Square	22	15	0.99	13.34
7.19.5	0.052	16	600	Square	22	15	1.36	15.70
7.20.1	0.052	22	0	Square	22	15	1.12	14.55
7.20.2	0.052	22	100	Square	22	15	0.62	14.62
7.20.3	0.052	22	250	Square	22	15	1.03	15.38
7.20.4	0.052	22	400	Square	22	15	0.87	15.12
7.20.5	0.052	22	600	Square	22	15	0.72	15.18
7.21.1	0.098	22	0	Square	22	15	1.34	15.32
7.21.2	0.098	22	100	Square	22	15	0.85	15.25
7.21.3	0.098	22	250	Square	22	15	0.64	15.37
7.21.4	0.098	22	400	Square	22	15	Damaged	Damaged
7.21.5	0.098	22	600	Square	22	15	Damaged	Damaged
7.22.1	0.074	16	0	Square	22	15	Damaged	Damaged

7.22.2	0.074	16	100	Square	22	15	Damaged	Damaged
7.22.3	0.074	16	250	Square	22	15	Damaged	Damaged
7.22.4	0.074	16	400	Square	22	15	Damaged	Damaged
7.22.5	0.074	16	600	Square	22	15	Damaged	Damaged
7.23.1	0.074	18	0	Square	22	15	0.63	14.89
7.23.2	0.074	18	100	Square	22	15	0.47	15.19
7.23.3	0.074	18	250	Square	22	15	0.75	15.31
7.23.4	0.074	18	400	Square	22	15	Damaged	Damaged
7.23.5	0.074	18	600	Square	22	15	1.33	15.32
7.24.1	0.074	22	0	Square	22	15	0.79	Damaged
7.24.2	0.074	22	100	Square	22	15	0.73	Damaged
7.24.3	0.074	22	250	Square	22	15	0.22	Damaged
7.24.4	0.074	22	400	Square	22	15	0.59	Damaged
7.24.5	0.074	22	600	Square	22	15	Damaged	Damaged
7.25.1	0.052	16	0	Square	22	20	0.73	19.63
7.25.2	0.052	16	100	Square	22	20	0.69	19.78
7.25.3	0.052	16	250	Square	22	20	0.60	19.39
7.25.4	0.052	16	400	Square	22	20	0.80	18.30

7.25.5	0.052	16	600	Square	22	20	1.48	20.81
7.26.1	0.052	22	0	Square	22	20	1.45	20.21
7.26.2	0.052	22	100	Square	22	20	0.72	18.24
7.26.3	0.052	22	250	Square	22	20	0.71	19.65
7.26.4	0.052	22	400	Square	22	20	0.78	19.95
7.26.5	0.052	22	600	Square	22	20	0.70	19.30
7.27.1	0.098	22	0	Square	22	20	1.16	20.59
7.27.2	0.098	22	100	Square	22	20	0.64	Damaged
7.27.3	0.098	22	250	Square	22	20	0.53	20.47
7.27.4	0.098	22	400	Square	22	20	Damaged	Damaged
7.27.5	0.098	22	600	Square	22	20	Damaged	Damaged
7.28.1	0.074	16	0	Square	22	20	1.50	17.08
7.28.2	0.074	16	100	Square	22	20	0.85	19.32
7.28.3	0.074	16	250	Square	22	20	0.69	18.40
7.28.4	0.074	16	400	Square	22	20	0.85	20.26
7.28.5	0.074	16	600	Square	22	20	0.91	20.09
7.29.1	0.074	18	0	Square	22	20	1.16	18.81
7.29.2	0.074	18	100	Square	22	20	0.64	18.59

7.29.3	0.074	18	250	Square	22	20	0.79	18.94
7.29.4	0.074	18	400	Square	22	20	0.95	17.15
7.29.5	0.074	18	600	Square	22	20	Damaged	Damaged
7.30.1	0.074	22	0	Square	22	20	1.01	20.64
7.30.2	0.074	22	100	Square	22	20	0.98	20.16
7.30.3	0.074	22	250	Square	22	20	0.82	20.04
7.30.4	0.074	22	400	Square	22	20	0.62	20.46
7.30.5	0.074	22	600	Square	22	20	1.26	21.81
7.31.1	0.052	16	0	Round	15	5	0.91	4.73
7.31.2	0.052	16	100	Round	15	5	0.68	4.77
7.31.3	0.052	16	250	Round	15	5	0.64	4.94
7.31.4	0.052	16	400	Round	15	5	0.62	4.89
7.31.5	0.052	16	600	Round	15	5	0.88	5.48
7.32.1	0.052	22	0	Round	15	5	1.01	4.40
7.32.2	0.052	22	100	Round	15	5	1.00	5.05
7.32.3	0.052	22	250	Round	15	5	0.81	5.08
7.32.4	0.052	22	400	Round	15	5	0.80	5.04
7.32.5	0.052	22	600	Round	15	5	0.74	5.04

7.33.1	0.098	22	0	Round	15	5	0.98	5.03
7.33.2	0.098	22	100	Round	15	5	0.77	4.88
7.33.3	0.098	22	250	Round	15	5	0.61	5.00
7.33.4	0.098	22	400	Round	15	5	0.84	5.08
7.33.5	0.098	22	600	Round	15	5	0.78	5.40
7.34.1	0.074	16	0	Round	15	5	0.78	4.96
7.34.2	0.074	16	100	Round	15	5	0.79	5.03
7.34.3	0.074	16	250	Round	15	5	0.67	4.94
7.34.4	0.074	16	400	Round	15	5	0.64	4.86
7.34.5	0.074	16	600	Round	15	5	0.75	5.05
7.35.1	0.074	18	0	Round	15	5	1.11	5.04
7.35.2	0.074	18	100	Round	15	5	0.74	5.16
7.35.3	0.074	18	250	Round	15	5	0.70	4.91
7.35.4	0.074	18	400	Round	15	5	0.65	4.90
7.35.5	0.074	18	600	Round	15	5	0.56	5.15
7.36.1	0.074	22	0	Round	15	5	0.88	5.07
7.36.2	0.074	22	100	Round	15	5	0.98	4.92
7.36.3	0.074	22	250	Round	15	5	0.82	4.73

7.36.4	0.074	22	400	Round	15	5	0.62	4.98
7.36.5	0.074	22	600	Round	15	5	0.69	5.23
7.37.1	0.052	16	0	Round	15	10	1.78	10.04
7.37.2	0.052	16	100	Round	15	10	1.86	9.83
7.37.3	0.052	16	250	Round	15	10	1.67	10.02
7.37.4	0.052	16	400	Round	15	10	1.66	9.79
7.37.5	0.052	16	600	Round	15	10	1.97	10.29
7.38.1	0.052	22	0	Round	15	10	1.68	10.00
7.38.2	0.052	22	100	Round	15	10	1.46	9.57
7.38.3	0.052	22	250	Round	15	10	1.57	9.91
7.38.4	0.052	22	400	Round	15	10	1.36	9.94
7.38.5	0.052	22	600	Round	15	10	1.67	9.95
7.39.1	0.098	22	0	Round	15	10	1.82	10.06
7.39.2	0.098	22	100	Round	15	10	1.78	9.83
7.39.3	0.098	22	250	Round	15	10	1.47	9.85
7.39.4	0.098	22	400	Round	15	10	1.69	9.85
7.39.5	0.098	22	600	Round	15	10	1.67	10.09
7.40.1	0.074	16	0	Round	15	10	1.92	9.78

7.40.2	0.074	16	100	Round	15	10	1.66	9.87
7.40.3	0.074	16	250	Round	15	10	1.73	9.71
7.40.4	0.074	16	400	Round	15	10	1.73	9.85
7.40.5	0.074	16	600	Round	15	10	1.62	10.23
7.41.1	0.074	18	0	Round	15	10	1.95	9.87
7.41.2	0.074	18	100	Round	15	10	1.49	9.87
7.41.3	0.074	18	250	Round	15	10	1.65	9.92
7.41.4	0.074	18	400	Round	15	10	1.73	9.82
7.41.5	0.074	18	600	Round	15	10	2.10	10.35
7.42.1	0.074	22	0	Round	15	10	1.98	9.72
7.42.2	0.074	22	100	Round	15	10	1.60	9.34
7.42.3	0.074	22	250	Round	15	10	1.53	9.78
7.42.4	0.074	22	400	Round	15	10	1.68	9.84
7.42.5	0.074	22	600	Round	15	10	1.60	10.02
7.43.1	0.052	16	0	Round	15	15	3.99	15.19
7.43.2	0.052	16	100	Round	15	15	4.47	14.88
7.43.3	0.052	16	250	Round	15	15	4.61	14.72
7.43.4	0.052	16	400	Round	15	15	5.80	15.08

7.43.5	0.052	16	600	Round	15	15	6.49	15.87
7.44.1	0.052	22	0	Round	15	15	3.79	14.87
7.44.2	0.052	22	100	Round	15	15	3.98	14.94
7.44.3	0.052	22	250	Round	15	15	3.85	14.75
7.44.4	0.052	22	400	Round	15	15	4.21	15.03
7.44.5	0.052	22	600	Round	15	15	3.80	14.89
7.45.1	0.098	22	0	Round	15	15	4.27	14.86
7.45.2	0.098	22	100	Round	15	15	4.14	15.06
7.45.3	0.098	22	250	Round	15	15	4.12	14.65
7.45.4	0.098	22	400	Round	15	15	4.51	15.00
7.45.5	0.098	22	600	Round	15	15	5.58	15.17
7.46.1	0.074	16	0	Round	15	15	4.35	14.87
7.46.2	0.074	16	100	Round	15	15	4.38	14.78
7.46.3	0.074	16	250	Round	15	15	4.52	15.02
7.46.4	0.074	16	400	Round	15	15	5.55	15.38
7.46.5	0.074	16	600	Round	15	15	6.96	15.02
7.47.1	0.074	18	0	Round	15	15	4.08	14.53
7.47.2	0.074	18	100	Round	15	15	4.48	14.71

7.47.3	0.074	18	250	Round	15	15	4.46	14.88
7.47.4	0.074	18	400	Round	15	15	4.50	14.86
7.47.5	0.074	18	600	Round	15	15	5.65	14.97
7.48.1	0.074	22	0	Round	15	15	4.07	14.65
7.48.2	0.074	22	100	Round	15	15	4.17	14.62
7.48.3	0.074	22	250	Round	15	15	4.12	14.68
7.48.4	0.074	22	400	Round	15	15	4.25	14.90
7.48.5	0.074	22	600	Round	15	15	4.85	15.04
7.49.1	0.052	16	0	Round	25	5	1.01	4.91
7.49.2	0.052	16	100	Round	25	5	0.87	4.72
7.49.3	0.052	16	250	Round	25	5	0.71	5.10
7.49.4	0.052	16	400	Round	25	5	0.88	5.13
7.49.5	0.052	16	600	Round	25	5	0.82	5.36
7.50.1	0.052	22	0	Round	25	5	Damaged	Damaged
7.50.2	0.052	22	100	Round	25	5	Damaged	Damaged
7.50.3	0.052	22	250	Round	25	5	Damaged	Damaged
7.50.4	0.052	22	400	Round	25	5	Damaged	Damaged
7.50.5	0.052	22	600	Round	25	5	Damaged	Damaged

7.51.1	0.098	22	0	Round	25	5	1.15	4.98
7.51.2	0.098	22	100	Round	25	5	0.91	4.83
7.51.3	0.098	22	250	Round	25	5	0.86	4.74
7.51.4	0.098	22	400	Round	25	5	0.80	4.94
7.51.5	0.098	22	600	Round	25	5	0.93	5.51
7.52.1	0.074	16	0	Round	25	5	1.02	4.92
7.52.2	0.074	16	100	Round	25	5	1.05	4.74
7.52.3	0.074	16	250	Round	25	5	0.65	4.84
7.52.4	0.074	16	400	Round	25	5	0.68	5.19
7.52.5	0.074	16	600	Round	25	5	Damaged	Damaged
7.53.1	0.074	18	0	Round	25	5	0.83	4.88
7.53.2	0.074	18	100	Round	25	5	0.87	5.08
7.53.3	0.074	18	250	Round	25	5	0.78	5.02
7.53.4	0.074	18	400	Round	25	5	0.82	4.96
7.53.5	0.074	18	600	Round	25	5	0.53	4.97
7.54.1	0.074	22	0	Round	25	5	1.08	4.83
7.54.2	0.074	22	100	Round	25	5	0.81	4.84
7.54.3	0.074	22	250	Round	25	5	0.94	4.98

7.54.4	0.074	22	400	Round	25	5	0.84	5.15
7.54.5	0.074	22	600	Round	25	5	0.81	4.92
7.55.1	0.052	16	0	Round	25	15	3.06	14.61
7.55.2	0.052	16	100	Round	25	15	2.80	14.74
7.55.3	0.052	16	250	Round	25	15	2.83	14.99
7.55.4	0.052	16	400	Round	25	15	3.15	15.25
7.55.5	0.052	16	600	Round	25	15	3.10	15.61
7.56.1	0.052	22	0	Round	25	15	3.12	14.80
7.56.2	0.052	22	100	Round	25	15	2.74	15.00
7.56.3	0.052	22	250	Round	25	15	3.36	14.98
7.56.4	0.052	22	400	Round	25	15	2.60	14.62
7.56.5	0.052	22	600	Round	25	15	Damaged	Damaged
7.57.1	0.098	22	0	Round	25	15	2.88	15.25
7.57.2	0.098	22	100	Round	25	15	2.76	14.87
7.57.3	0.098	22	250	Round	25	15	2.70	15.01
7.57.4	0.098	22	400	Round	25	15	3.12	13.90
7.57.5	0.098	22	600	Round	25	15	4.92	16.24
7.58.1	0.074	16	0	Round	25	15	3.45	14.68

7.58.2	0.074	16	100	Round	25	15	2.89	14.92
7.58.3	0.074	16	250	Round	25	15	3.23	14.95
7.58.4	0.074	16	400	Round	25	15	3.15	14.73
7.58.5	0.074	16	600	Round	25	15	4.03	15.25
7.59.1	0.074	18	0	Round	25	15	2.81	15.18
7.59.2	0.074	18	100	Round	25	15	3.00	14.87
7.59.3	0.074	18	250	Round	25	15	3.00	14.82
7.59.4	0.074	18	400	Round	25	15	2.94	15.02
7.59.5	0.074	18	600	Round	25	15	3.74	14.73
7.60.1	0.074	22	0	Round	25	15	2.80	14.29
7.60.2	0.074	22	100	Round	25	15	2.84	14.48
7.60.3	0.074	22	250	Round	25	15	2.84	14.55
7.60.4	0.074	22	400	Round	25	15	2.67	14.82
7.60.5	0.074	22	600	Round	25	15	2.97	14.93
7.61.1	0.052	16	0	Round	25	25	10.32	24.54
7.61.2	0.052	16	100	Round	25	25	10.56	24.73
7.61.3	0.052	16	250	Round	25	25	10.51	24.77
7.61.4	0.052	16	400	Round	25	25	9.93	25.48

7.61.5	0.052	16	600	Round	25	25	9.14	25.64
7.62.1	0.052	22	0	Round	25	25	10.13	24.50
7.62.2	0.052	22	100	Round	25	25	10.04	24.78
7.62.3	0.052	22	250	Round	25	25	10.27	24.65
7.62.4	0.052	22	400	Round	25	25	10.07	24.58
7.62.5	0.052	22	600	Round	25	25	10.63	24.79
7.63.1	0.098	22	0	Round	25	25	10.96	24.65
7.63.2	0.098	22	100	Round	25	25	10.57	24.72
7.63.3	0.098	22	250	Round	25	25	10.61	24.52
7.63.4	0.098	22	400	Round	25	25	10.05	24.90
7.63.5	0.098	22	600	Round	25	25	9.60	25.69
7.64.1	0.074	16	0	Round	25	25	10.29	24.95
7.64.2	0.074	16	100	Round	25	25	10.34	24.40
7.64.3	0.074	16	250	Round	25	25	10.13	25.09
7.64.4	0.074	16	400	Round	25	25	9.55	24.91
7.64.5	0.074	16	600	Round	25	25	9.38	24.55
7.65.1	0.074	18	0	Round	25	25	10.49	24.33
7.65.2	0.074	18	100	Round	25	25	10.79	25.41

7.65.3	0.074	18	250	Round	25	25	10.65	25.01
7.65.4	0.074	18	400	Round	25	25	9.67	25.53
7.65.4	0.074	18	600	Round	25	25	9.68	25.00
7.66.1	0.074	22	0	Round	25	25	10.17	24.73
7.66.2	0.074	22	100	Round	25	25	10.65	24.40
7.66.3	0.074	22	250	Round	25	25	10.25	24.65
7.66.4	0.074	22	400	Round	25	25	10.37	24.51
7.66.5	0.074	22	600	Round	25	25	9.68	25.23

Table 4: Geometric Form Data for Multi-Pass Cutting of XPS Foam

Run #	Feed (ms-1)	Current (A)	Distance (mm)	Blade Shape	Blade Size (mm)	Path Spacing (mm)	Rmax (mm)	Peak Spacing (mm)
8.1.1	0.0400	16	0	Square	8	4	0.66	3.73
8.1.2	0.0400	16	100	Square	8	4	0.47	3.96
8.1.3	0.0400	16	250	Square	8	4	0.75	4.25
8.1.4	0.0400	16	400	Square	8	4	0.85	4.07
8.1.5	0.0400	16	600	Square	8	4	0.50	3.84
8.2.1	0.052	16	0	Square	8	4	1.02	3.73
8.2.2	0.052	16	100	Square	8	4	0.77	3.96

8.2.3	0.052	16	250	Square	8	4	0.70	4.07
8.2.4	0.052	16	400	Square	8	4	0.64	4.03
8.2.5	0.052	16	600	Square	8	4	0.49	3.69
8.3.1	0.052	20	0	Square	8	4	1.06	3.98
8.3.2	0.052	20	100	Square	8	4	0.58	3.94
8.3.3	0.052	20	250	Square	8	4	0.82	4.09
8.3.4	0.052	20	400	Square	8	4	0.80	3.94
8.3.5	0.052	20	600	Square	8	4	0.63	4.26
8.4.1	0.076	22	0	Square	8	4	0.92	4.09
8.4.2	0.076	22	100	Square	8	4	0.63	3.96
8.4.3	0.076	22	250	Square	8	4	0.66	4.02
8.4.4	0.076	22	400	Square	8	4	0.79	4.30
8.4.5	0.076	22	600	Square	8	4	0.79	3.55
8.5.1	0.064	18	0	Square	8	4	0.75	3.88
8.5.2	0.064	18	100	Square	8	4	0.69	4.28
8.5.3	0.064	18	250	Square	8	4	0.75	4.07
8.5.4	0.064	18	400	Square	8	4	0.65	4.42
8.5.5	0.064	18	600	Square	8	4	0.48	5.33

8.6.1	0.0400	22	0	Square	8	4	1.15	3.75
8.6.2	0.0400	22	100	Square	8	4	0.81	4.11
8.6.3	0.0400	22	250	Square	8	4	0.80	4.00
8.6.4	0.0400	22	400	Square	8	4	0.85	4.32
8.6.5	0.0400	22	600	Square	8	4	0.72	4.07
8.7.1	0.0400	16	0	Square	8	8	1.25	7.88
8.7.2	0.0400	16	100	Square	8	8	0.57	7.94
8.7.3	0.0400	16	250	Square	8	8	0.71	8.15
8.7.4	0.0400	16	400	Square	8	8	0.65	7.82
8.7.5	0.0400	16	600	Square	8	8	0.53	8.09
8.8.1	0.052	16	0	Square	8	8	1.15	7.90
8.8.2	0.052	16	100	Square	8	8	0.74	7.88
8.8.3	0.052	16	250	Square	8	8	0.63	7.86
8.8.4	0.052	16	400	Square	8	8	0.76	7.85
8.8.5	0.052	16	600	Square	8	8	0.68	8.05
8.9.1	0.052	20	0	Square	8	8	1.57	8.03
8.9.2	0.052	20	100	Square	8	8	0.95	8.18
8.9.3	0.052	20	250	Square	8	8	0.90	8.11

8.9.4	0.052	20	400	Square	8	8	0.92	8.00
8.9.5	0.052	20	600	Square	8	8	0.68	8.14
8.10.1	0.076	22	0	Square	8	8	1.30	7.86
8.10.2	0.076	22	100	Square	8	8	0.71	8.05
8.10.3	0.076	22	250	Square	8	8	0.93	7.85
8.10.4	0.076	22	400	Square	8	8	0.83	8.09
8.10.5	0.076	22	600	Square	8	8	0.75	8.05
8.11.1	0.064	18	0	Square	8	8	1.43	7.77
8.11.2	0.064	18	100	Square	8	8	0.87	7.80
8.11.3	0.064	18	250	Square	8	8	0.77	7.90
8.11.4	0.064	18	400	Square	8	8	1.25	7.67
8.11.5	0.064	18	600	Square	8	8	0.69	7.88
8.12.1	0.0400	22	0	Square	8	8	1.35	7.84
8.12.2	0.0400	22	100	Square	8	8	1.05	8.26
8.12.3	0.0400	22	250	Square	8	8	1.10	7.82
8.12.4	0.0400	22	400	Square	8	8	0.95	8.15
8.12.5	0.0400	22	600	Square	8	8	0.58	7.96
8.13.1	0.0400	16	0	Square	22	10	1.13	10.01

8.13.2	0.0400	16	100	Square	22	10	0.68	9.81
8.13.3	0.0400	16	250	Square	22	10	0.65	9.75
8.13.4	0.0400	16	400	Square	22	10	1.01	9.98
8.13.5	0.0400	16	600	Square	22	10	0.60	15.21
8.14.1	0.052	16	0	Square	22	10	1.40	10.04
8.14.2	0.052	16	100	Square	22	10	1.02	9.73
8.14.3	0.052	16	250	Square	22	10	0.68	10.57
8.14.4	0.052	16	400	Square	22	10	0.84	10.49
8.14.5	0.052	16	600	Square	22	10	0.63	11.37
8.15.1	0.052	20	0	Square	22	10	1.50	10.26
8.15.2	0.052	20	100	Square	22	10	0.72	9.91
8.15.3	0.052	20	250	Square	22	10	0.70	10.54
8.15.4	0.052	20	400	Square	22	10	0.79	10.93
8.15.5	0.052	20	600	Square	22	10	1.31	7.51
8.16.1	0.076	22	0	Square	22	10	1.73	9.98
8.16.2	0.076	22	100	Square	22	10	0.71	9.98
8.16.3	0.076	22	250	Square	22	10	0.82	9.59
8.16.4	0.076	22	400	Square	22	10	0.60	9.81

8.16.5	0.076	22	600	Square	22	10	0.76	7.94
8.17.1	0.064	18	0	Square	22	10	1.40	9.80
8.17.2	0.064	18	100	Square	22	10	0.70	9.80
8.17.3	0.064	18	250	Square	22	10	0.49	9.64
8.17.4	0.064	18	400	Square	22	10	0.50	10.17
8.17.5	0.064	18	600	Square	22	10	1.02	10.61
8.18.1	0.040	22	0	Square	22	10	1.66	9.25
8.18.2	0.040	22	100	Square	22	10	0.89	9.82
8.18.3	0.040	22	250	Square	22	10	0.72	9.50
8.18.4	0.040	22	400	Square	22	10	0.62	9.57
8.18.5	0.040	22	600	Square	22	10	0.85	10.35
8.19.1	0.040	16	0	Square	22	15	1.57	14.93
8.19.2	0.040	16	100	Square	22	15	0.84	14.94
8.19.3	0.040	16	250	Square	22	15	0.74	14.48
8.19.4	0.040	16	400	Square	22	15	0.65	15.11
8.19.5	0.040	16	600	Square	22	15	0.76	18.37
8.20.1	0.052	16	0	Square	22	15	1.25	14.74
8.20.2	0.052	16	100	Square	22	15	0.76	14.74

8.20.3	0.052	16	250	Square	22	15	0.74	14.23
8.20.4	0.052	16	400	Square	22	15	0.65	14.42
8.20.5	0.052	16	600	Square	22	15	0.75	16.65
8.21.1	0.052	20	0	Square	22	15	1.89	15.00
8.21.2	0.052	20	100	Square	22	15	0.79	14.86
8.21.3	0.052	20	250	Square	22	15	0.72	14.87
8.21.4	0.052	20	400	Square	22	15	1.08	15.38
8.21.5	0.052	20	600	Square	22	15	1.09	14.23
8.22.1	0.076	22	0	Square	22	15	1.51	14.93
8.22.2	0.076	22	100	Square	22	15	0.81	14.75
8.22.3	0.076	22	250	Square	22	15	0.63	15.44
8.22.4	0.076	22	400	Square	22	15	0.55	14.68
8.22.5	0.076	22	600	Square	22	15	0.96	17.35
8.23.1	0.064	18	0	Square	22	15	1.45	14.87
8.23.2	0.064	18	100	Square	22	15	0.74	13.79
8.23.3	0.064	18	250	Square	22	15	0.69	15.00
8.23.4	0.064	18	400	Square	22	15	0.76	16.08
8.23.5	0.064	18	600	Square	22	15	1.43	20.07

8.24.1	0.040	22	0	Square	22	15	1.27	14.93
8.24.2	0.040	22	100	Square	22	15	0.77	14.73
8.24.3	0.040	22	250	Square	22	15	0.98	14.68
8.24.4	0.040	22	400	Square	22	15	0.84	14.74
8.24.5	0.040	22	600	Square	22	15	0.90	14.93
8.25.1	0.040	16	0	Square	22	20	1.09	19.94
8.25.2	0.040	16	100	Square	22	20	0.67	19.31
8.25.3	0.040	16	250	Square	22	20	0.82	19.24
8.25.4	0.040	16	400	Square	22	20	0.81	19.43
8.25.5	0.040	16	600	Square	22	20	0.69	19.89
8.26.1	0.052	16	0	Square	22	20	1.08	19.07
8.26.2	0.052	16	100	Square	22	20	0.58	20.54
8.26.3	0.052	16	250	Square	22	20	0.52	19.63
8.26.4	0.052	16	400	Square	22	20	0.61	19.32
8.26.5	0.052	16	600	Square	22	20	0.86	19.57
8.27.1	0.052	20	0	Square	22	20	1.55	18.19
8.27.2	0.052	20	100	Square	22	20	0.76	18.99
8.27.3	0.052	20	250	Square	22	20	0.56	18.23

8.27.4	0.052	20	400	Square	22	20	0.63	19.83
8.27.5	0.052	20	600	Square	22	20	0.56	20.96
8.28.1	0.076	22	0	Square	22	20	1.41	19.45
8.28.2	0.076	22	100	Square	22	20	0.87	19.64
8.28.3	0.076	22	250	Square	22	20	0.65	18.86
8.28.4	0.076	22	400	Square	22	20	0.49	19.70
8.28.5	0.076	22	600	Square	22	20	0.77	20.21
8.29.1	0.064	18	0	Square	22	20	1.40	19.71
8.29.2	0.064	18	100	Square	22	20	0.56	19.89
8.29.3	0.064	18	250	Square	22	20	0.78	19.59
8.29.4	0.064	18	400	Square	22	20	0.81	20.06
8.29.5	0.064	18	600	Square	22	20	0.53	20.63
8.30.1	0.040	22	0	Square	22	20	1.77	18.81
8.30.2	0.040	22	100	Square	22	20	1.05	19.70
8.30.3	0.040	22	250	Square	22	20	0.65	19.63
8.30.4	0.040	22	400	Square	22	20	0.56	18.94
8.30.5	0.040	22	600	Square	22	20	0.71	19.58
8.31.1	0.040	16	0	Round	15	5	1.29	4.75

8.31.2	0.040	16	100	Round	15	5	0.66	5.06
8.31.3	0.040	16	250	Round	15	5	0.92	5.12
8.31.4	0.040	16	400	Round	15	5	0.93	5.08
8.31.5	0.040	16	600	Round	15	5	0.95	5.21
8.32.1	0.052	16	0	Round	15	5	0.90	4.79
8.32.2	0.052	16	100	Round	15	5	0.78	5.11
8.32.3	0.052	16	250	Round	15	5	0.72	4.89
8.32.4	0.052	16	400	Round	15	5	0.75	5.04
8.32.5	0.052	16	600	Round	15	5	1.17	5.05
8.33.1	0.052	20	0	Round	15	5	1.20	4.70
8.33.2	0.052	20	100	Round	15	5	0.74	4.85
8.33.3	0.052	20	250	Round	15	5	0.77	4.85
8.33.4	0.052	20	400	Round	15	5	1.02	5.21
8.33.5	0.052	20	600	Round	15	5	0.83	4.93
8.34.1	0.076	22	0	Round	15	5	1.24	4.77
8.34.2	0.076	22	100	Round	15	5	0.98	5.02
8.34.3	0.076	22	250	Round	15	5	1.18	5.34
8.34.4	0.076	22	400	Round	15	5	0.91	4.78

8.34.5	0.076	22	600	Round	15	5	0.73	6.20
8.35.1	0.064	18	0	Round	15	5	1.11	5.04
8.35.2	0.064	18	100	Round	15	5	0.62	5.08
8.35.3	0.064	18	250	Round	15	5	0.75	4.96
8.35.4	0.064	18	400	Round	15	5	0.76	5.00
8.35.5	0.064	18	600	Round	15	5	0.93	5.17
8.36.1	0.040	22	0	Round	15	5	1.12	5.17
8.36.2	0.040	22	100	Round	15	5	0.89	5.15
8.36.3	0.040	22	250	Round	15	5	0.90	5.08
8.36.4	0.040	22	400	Round	15	5	1.00	5.17
8.36.5	0.040	22	600	Round	15	5	0.91	5.38
8.37.1	0.040	16	0	Round	15	10	1.66	9.94
8.37.2	0.040	16	100	Round	15	10	1.36	10.23
8.37.3	0.040	16	250	Round	15	10	1.36	9.75
8.37.4	0.040	16	400	Round	15	10	1.40	10.08
8.37.5	0.040	16	600	Round	15	10	1.73	9.97
8.38.1	0.052	16	0	Round	15	10	2.10	9.81
8.38.2	0.052	16	100	Round	15	10	1.72	10.10

8.38.3	0.052	16	250	Round	15	10	1.71	9.65
8.38.4	0.052	16	400	Round	15	10	1.73	9.66
8.38.5	0.052	16	600	Round	15	10	2.08	10.15
8.39.1	0.052	20	0	Round	15	10	1.96	9.95
8.39.2	0.052	20	100	Round	15	10	1.60	10.14
8.39.3	0.052	20	250	Round	15	10	1.57	10.05
8.39.4	0.052	20	400	Round	15	10	1.82	9.85
8.39.5	0.052	20	600	Round	15	10	1.80	10.14
8.40.1	0.076	22	0	Round	15	10	1.77	9.84
8.40.2	0.076	22	100	Round	15	10	1.63	9.88
8.40.3	0.076	22	250	Round	15	10	1.70	10.22
8.40.4	0.076	22	400	Round	15	10	1.59	9.66
8.40.5	0.076	22	600	Round	15	10	2.05	10.23
8.41.1	0.064	18	0	Round	15	10	1.99	9.57
8.41.2	0.064	18	100	Round	15	10	1.86	9.88
8.41.3	0.064	18	250	Round	15	10	1.75	9.81
8.41.4	0.064	18	400	Round	15	10	1.95	9.94
8.41.5	0.064	18	600	Round	15	10	2.02	10.46

8.42.1	0.040	22	0	Round	15	10	1.58	9.63
8.42.2	0.040	22	100	Round	15	10	1.31	10.05
8.42.3	0.040	22	250	Round	15	10	1.37	9.97
8.42.4	0.040	22	400	Round	15	10	1.40	9.88
8.42.5	0.040	22	600	Round	15	10	1.38	10.23
8.43.1	0.040	16	0	Round	15	15	4.00	15.13
8.43.2	0.040	16	100	Round	15	15	3.87	14.80
8.43.3	0.040	16	250	Round	15	15	4.26	14.74
8.43.4	0.040	16	400	Round	15	15	4.22	14.94
8.43.5	0.040	16	600	Round	15	15	3.97	14.86
8.44.1	0.052	16	0	Round	15	15	4.11	14.61
8.44.2	0.052	16	100	Round	15	15	4.42	15.00
8.44.3	0.052	16	250	Round	15	15	4.23	14.80
8.44.4	0.052	16	400	Round	15	15	3.99	15.05
8.44.5	0.052	16	600	Round	15	15	4.21	14.88
8.45.1	0.052	20	0	Round	15	15	3.60	15.31
8.45.2	0.052	20	100	Round	15	15	3.48	14.86
8.45.3	0.052	20	250	Round	15	15	3.80	14.67

8.45.4	0.052	20	400	Round	15	15	3.59	14.81
8.45.5	0.052	20	600	Round	15	15	4.21	14.55
8.46.1	0.076	22	0	Round	15	15	3.95	14.74
8.46.2	0.076	22	100	Round	15	15	4.07	14.87
8.46.3	0.076	22	250	Round	15	15	4.19	14.74
8.46.4	0.076	22	400	Round	15	15	3.77	14.55
8.46.5	0.076	22	600	Round	15	15	4.00	14.81
8.47.1	0.064	18	0	Round	15	15	3.84	14.62
8.47.2	0.064	18	100	Round	15	15	4.04	14.80
8.47.3	0.064	18	250	Round	15	15	3.97	14.81
8.47.4	0.064	18	400	Round	15	15	4.10	14.67
8.47.5	0.064	18	600	Round	15	15	4.38	15.69
8.48.1	0.040	22	0	Round	15	15	3.36	14.74
8.48.2	0.040	22	100	Round	15	15	3.23	15.00
8.48.3	0.040	22	250	Round	15	15	3.49	14.86
8.48.4	0.040	22	400	Round	15	15	3.53	14.68
8.48.5	0.040	22	600	Round	15	15	3.67	14.94
8.49.1	0.040	16	0	Round	25	5	1.11	4.83

8.49.2	0.040	16	100	Round	25	5	0.75	4.85
8.49.3	0.040	16	250	Round	25	5	0.72	4.98
8.49.4	0.040	16	400	Round	25	5	0.81	4.98
8.49.5	0.040	16	600	Round	25	5	0.57	5.21
8.50.1	0.052	16	0	Round	25	5	1.14	5.02
8.50.2	0.052	16	100	Round	25	5	0.91	5.17
8.50.3	0.052	16	250	Round	25	5	0.69	4.91
8.50.4	0.052	16	400	Round	25	5	1.24	5.23
8.50.5	0.052	16	600	Round	25	5	1.07	5.34
8.51.1	0.052	20	0	Round	25	5	0.88	4.83
8.51.2	0.052	20	100	Round	25	5	0.87	5.04
8.51.3	0.052	20	250	Round	25	5	0.60	5.08
8.51.4	0.052	20	400	Round	25	5	0.87	5.16
8.51.5	0.052	20	600	Round	25	5	0.77	4.70
8.52.1	0.076	22	0	Round	25	5	1.22	4.89
8.52.2	0.076	22	100	Round	25	5	1.14	4.91
8.52.3	0.076	22	250	Round	25	5	0.97	5.02
8.52.4	0.076	22	400	Round	25	5	0.90	5.02

8.52.5	0.076	22	600	Round	25	5	0.84	5.02
8.53.1	0.064	18	0	Round	25	5	0.88	4.96
8.53.2	0.064	18	100	Round	25	5	0.85	4.87
8.53.3	0.064	18	250	Round	25	5	0.95	5.08
8.53.4	0.064	18	400	Round	25	5	0.95	5.17
8.53.5	0.064	18	600	Round	25	5	0.65	4.81
8.54.1	0.040	22	0	Round	25	5	0.90	5.23
8.54.2	0.040	22	100	Round	25	5	0.84	5.29
8.54.3	0.040	22	250	Round	25	5	0.76	5.04
8.54.4	0.040	22	400	Round	25	5	0.84	5.29
8.54.5	0.040	22	600	Round	25	5	0.77	5.34
8.55.1	0.040	16	0	Round	25	15	3.54	15.31
8.55.2	0.040	16	100	Round	25	15	3.23	15.11
8.55.3	0.040	16	250	Round	25	15	3.17	14.68
8.55.4	0.040	16	400	Round	25	15	3.19	14.87
8.55.5	0.040	16	600	Round	25	15	3.34	14.87
8.56.1	0.052	16	0	Round	25	15	3.49	14.93
8.56.2	0.052	16	100	Round	25	15	3.19	14.87

8.56.3	0.052	16	250	Round	25	15	3.15	14.87
8.56.4	0.052	16	400	Round	25	15	3.34	15.12
8.56.5	0.052	16	600	Round	25	15	3.35	14.77
8.57.1	0.052	20	0	Round	25	15	3.45	14.80
8.57.2	0.052	20	100	Round	25	15	2.94	15.51
8.57.3	0.052	20	250	Round	25	15	3.30	14.61
8.57.4	0.052	20	400	Round	25	15	3.25	14.74
8.57.5	0.052	20	600	Round	25	15	3.25	14.73
8.58.1	0.076	22	0	Round	25	15	3.58	14.63
8.58.2	0.076	22	100	Round	25	15	3.23	15.12
8.58.3	0.076	22	250	Round	25	15	3.12	14.49
8.58.4	0.076	22	400	Round	25	15	3.46	14.55
8.58.5	0.076	22	600	Round	25	15	3.29	15.06
8.59.1	0.064	18	0	Round	25	15	3.60	15.13
8.59.2	0.064	18	100	Round	25	15	3.18	14.81
8.59.3	0.064	18	250	Round	25	15	3.02	14.74
8.59.4	0.064	18	400	Round	25	15	3.28	14.87
8.59.5	0.064	18	600	Round	25	15	3.61	14.81

8.60.1	0.040	22	0	Round	25	15	3.25	14.87
8.60.2	0.040	22	100	Round	25	15	2.71	14.74
8.60.3	0.040	22	250	Round	25	15	3.07	14.17
8.60.4	0.040	22	400	Round	25	15	2.83	14.80
8.60.5	0.040	22	600	Round	25	15	3.29	15.00
8.61.1	0.040	16	0	Round	25	25	9.99	24.70
8.61.2	0.040	16	100	Round	25	25	9.64	24.46
8.61.3	0.040	16	250	Round	25	25	9.68	24.53
8.61.4	0.040	16	400	Round	25	25	9.46	24.45
8.61.5	0.040	16	600	Round	25	25	9.23	23.81
8.62.1	0.052	16	0	Round	25	25	9.96	24.90
8.62.2	0.052	16	100	Round	25	25	9.99	25.10
8.62.3	0.052	16	250	Round	25	25	9.53	24.27
8.62.4	0.052	16	400	Round	25	25	10.09	24.54
8.62.5	0.052	16	600	Round	25	25	9.72	23.37
8.63.1	0.052	20	0	Round	25	25	10.57	24.14
8.63.2	0.052	20	100	Round	25	25	10.19	25.16
8.63.3	0.052	20	250	Round	25	25	9.82	24.57

8.63.4	0.052	20	400	Round	25	25	10.10	24.30
8.63.5	0.052	20	600	Round	25	25	10.32	23.70
8.64.1	0.076	22	0	Round	25	25	10.38	25.25
8.64.2	0.076	22	100	Round	25	25	9.98	25.02
8.64.3	0.076	22	250	Round	25	25	10.38	24.51
8.64.4	0.076	22	400	Round	25	25	10.27	24.61
8.64.5	0.076	22	600	Round	25	25	10.45	23.78
8.65.1	0.064	18	0	Round	25	25	10.39	24.52
8.65.2	0.064	18	100	Round	25	25	10.12	24.59
8.65.3	0.064	18	250	Round	25	25	9.84	24.52
8.65.4	0.064	18	400	Round	25	25	10.33	24.65
8.65.4	0.064	18	600	Round	25	25	9.99	23.73
8.66.1	0.040	22	0	Round	25	25	10.59	24.72
8.66.2	0.040	22	100	Round	25	25	10.69	24.58
8.66.3	0.040	22	250	Round	25	25	10.23	25.10
8.66.4	0.040	22	400	Round	25	25	10.80	24.46
8.66.5	0.040	22	600	Round	25	25	11.58	24.81

Appendix C: Acoustic Investigation Material

Appendix C1: Sound Analyzer Data Sheet

PRODUCT DATA

Hand-held Analyzer — Type 2250, with Sound Level Meter Software BZ-7222, Frequency Analysis Software BZ-7223, Logging Software BZ-7224, Enhanced Logging Software BZ-7225 and Sound Recording Option BZ-7226

*Type 2250 is the innovative, 4th generation, hand-held analyzer from Brüel & Kjær. The design philosophy is based on extensive research which concluded that the instrument should be **easy** and **safe** to use, while at the same time incorporating **clever** features. Type 2250 has been awarded several prizes for its combination of excellent ergonomics and attractive design.*

Type 2250 can host a number of software modules, including frequency analysis, logging (profiling) and recording of the measured signal. These are available separately at any time – or you can order a fully preconfigured instrument from the factory.

The combination of software modules and innovative hardware makes the instrument into a dedicated solution for performing high-precision measurement tasks, in environmental, occupational and industrial application areas. As a result, you get the functionality you need now, plus the option of opening up for more functionality later – and your investment is securely protected.

Uses and Features

USES

- Environmental noise assessment and monitoring
- Occupational noise evaluation
- Selection of hearing protection
- Noise reduction
- Product quality control
- Class 1 sound measurements to the latest international standards
- Real-time analysis of sound in 1/1- and 1/3-octave bands
- Analysis of time histories for broadband parameters and spectra (Logging)
- Documentation of measurements using text and voice annotations
- Documentation of measurements through recording of measured sound

FEATURES

- Large, high-resolution, touch-sensitive colour screen
- Data storage on plug-in memory-cards
- Standard USB (On-the-Go) computer interface
- Dynamic range in excess of 120 dB
- 3 Hz – 20 kHz broadband linear frequency range
- Real-time frequency analysis in 1/1- or 1/3-octave bands
- Broadband and spectral data can be logged to obtain a time history for later analysis
- Sound recording of measured signal during all or parts of a measurement
- Personal measurement, display and job setup
- PC software included for setup, archiving, export and reporting
- Automatic detection of, and correction for, windscreen
- Robust and environmentally protected (IP44)

Brüel & Kjær

Introduction

Type 2250 has generous hardware and software specifications creating an extremely flexible instrument to cover your current and future measurement and analysis needs, ranging, for example, from the traditional uses in assessing environmental and workplace noise to industrial quality control and development. Type 2250 is a technological platform for realising measurement applications in a compact and robust hand-held instrument.

This data sheet describes the suite of software applications available for Type 2250. All instruments come with the Sound Level Meter Software (BZ-7222) enabled. This makes Type 2250 into a modern Class 1 Sound Level Meter (SLM). It fulfills the requirements of the latest standard, IEC 61672–1, as well as earlier standards (see the specifications section for detailed compliance information). Even in its most basic configuration, Type 2250 is delivered with a number of pre-defined measurement and display setups tailored to suit specific requirements.

Optional Software Modules

As a platform, Type 2250 allows you to choose different combinations of software modules (applications). Additional applications can be purchased when needed and are delivered as easily installed licenses and the software can be used in any combination. In this way your investment in the Type 2250 platform is securely protected and when your need for measurements and analyses expands, Type 2250 can accommodate them. Brüel & Kjær is committed to maintaining an ever-growing range of applications on this platform.

The optional software modules described in this data sheet are:

- **Frequency Analysis Software**, providing real-time analysis of the 1/1- and 1/3-octave filter bands over a wide frequency range with a dynamic range from the noise floor in each individual band to 140 dB.
- **Logging Software**, which allows free selection of parameters to log at periods from 1 s to 24 h. Running together with the Sound Level Meter Software all broadband parameters can be logged. If Frequency Analysis Software is also enabled, spectra can be logged at the same rates. Logging (or noise profiling) is used to develop time histories for use in environmental noise as well as workplace noise assessment.
- **Enhanced Logging Software**, providing continuous monitoring and logging of Periodic Reports in addition to the features of Logging Software. Parameters like L_{dn} and L_{den} are calculated.
- **Sound Recording Option**, which provides you with a uniquely versatile facility for attaching samples of the actually measured signal to your measurements. This option works with all software modules. The recording uses the measurement transducer, while voice annotations (standard in all modules) use a separate commentary microphone.

Post-processing Software

The software modules are further enhanced by Brüel & Kjær's post-processing software suite. All Type 2250 instruments include a dedicated PC software package (Utility Software for Hand-held Analyzers BZ-5503) which handles data transfer, archiving of data, export of data, setup, remote display, and software maintenance (for example, license installation and updates). Separately available post-processing applications include 7815 Noise Explorer™ for data viewing and archiving, 7820 Evaluator™ for advanced assessment of environmental noise, and 7825 Protector™ for assessing workplace noise.

Fig. 1 *Key features of Hand-held Analyzer Type 2250*

Easy, Safe and Clever

The instrument design was inspired by the requirements of users participating in in-depth workshops around the world and the results of our research showed that besides being fun to use, the new generation of analyzer should be **easy, safe** and **clever**:

- Type 2250 is **easy** to use – its robustness, lightness and ergonomic design make it easy to grip, hold and operate single-handedly. Ingenious software ensures you can start measuring quickly. You will never feel lost in the menu structure, in every situation you are just one tap or press of a pushbutton away from where you started. The backlit pushbuttons are easy to use and the large, colour touchscreen is visible in both sunlight and in difficult lighting conditions depending on the colour-scheme chosen. Type 2250 incorporates a simple user interface that can be controlled by using the stylus or the pushbuttons. It has an easy and intuitive data storage concept and on-line guidance is included to help you get familiar with the instrument quickly.
- Type 2250 is **safe** to use – it was built for use outdoors and in difficult environmental conditions, so it is powered by rechargeable Li-Ion batteries (with high capacity) and the casing incorporates non-slip materials to ensure a safe grip. The software guides you safely through each measurement and status indicators show measurement progress, even at a distance. You can document your measurements on the spot using on-the-fly voice or text annotations. These are automatically attached to your measurement and transferred with your data to the PC. Type 2250 includes a multi-user login facility, which allows preferences, setups and data for different users – or different tasks – to be kept separate.
- Type 2250 is **clever** – it incorporates various smart features for field use, including: specially positioned backlit pushbuttons to allow vital start-stop-save actions to be done by feel and at night, single-handedly; a separate built-in commentary microphone, giving you the option of recording your personal comments while measuring and automatically attaching them to your on-going measurement; 'traffic light' indicators to give you a quick indication of your measurement's status – visible at a distance; a calibration history, allowing you to document your measurement's validity; semi-automatic calibration procedure built-in; and the presence of a windscreen is automatically detected and corrected for by built-in filters.

Using the Platform

Great care has been taken to ensure that the hardware is ergonomically optimal in field use. Similarly, the software design has focused not only on making valid measurements but also on making field use efficient, convenient and intuitive.

All user choices for setups (what to measure) and preferences (how to display it) are controlled using easy to understand lists, that can be expanded and collapsed. No more cluttered displays, choose only the parameters you want to see.

Display Options

As a user, you have several ways of tailoring the display to suit your specific needs. However, standard display elements are used to ensure commonality not only across different software modules, but also across different users, setups and preferences.

Type 2250 applies a default colour scheme for the display. This is like most examples in this data sheet. However, the instrument includes several schemes allowing you to make your own choice for outdoor use in bright sunlight (where maximum contrast is needed) and for night-time use (where no interference with night vision is wanted).

Type 2250 makes a distinction between the measurement made and how it is displayed. Generally, Type 2250 constantly measures all the available quantities in parallel, what you see on the display are the parameters you have selected to see. All the other quantities are measured simultaneously, irrespective of your display preferences.

Fig. 2
Typical display when measuring

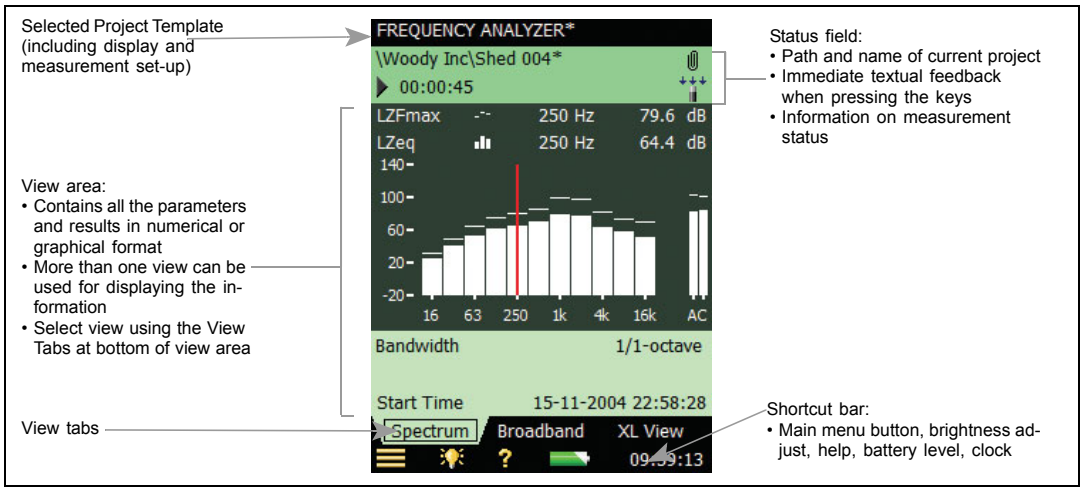

Fig. 3
Typical display when modifying/updating the measurement setup

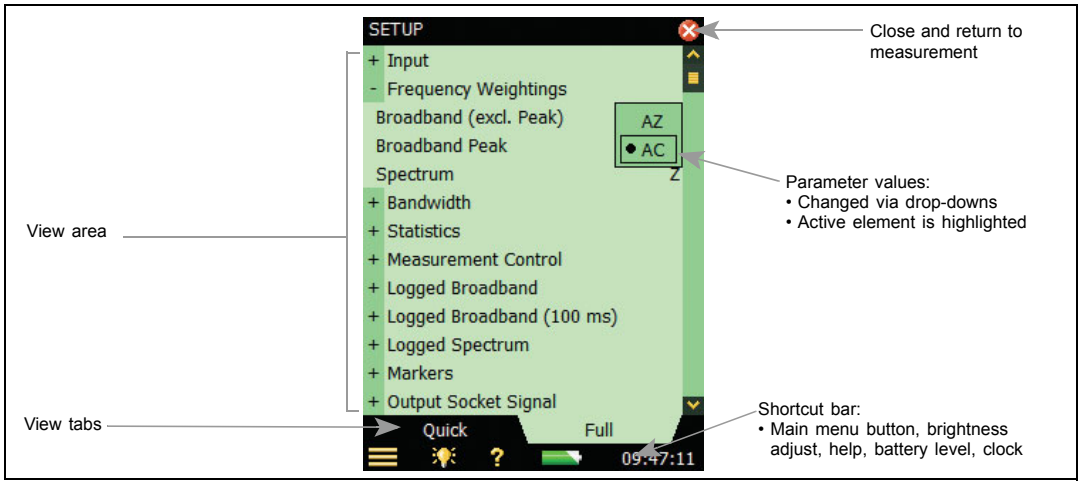

Fig. 4
Alternative display colour schemes – the left-hand display shows the maximum-contrast bright sunlight display. The right-hand display shows the night time display, which is optimised to take into account the physiology of human vision, allowing you to read the display without ruining your night vision.

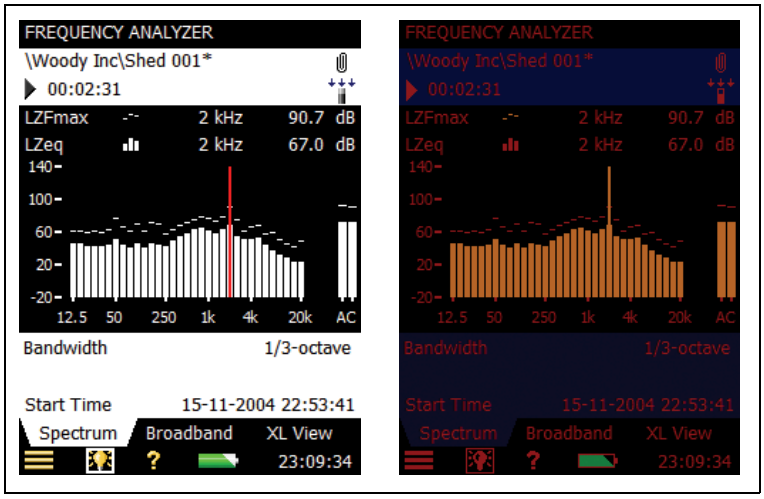

You can view any quantity being measured, either during your measurement, or at any time later. This also includes data transferred to a PC.

In all configurations, Type 2250 offers a variety of views of the same measurement. These views have no impact on the measurement, but they allow you to see exactly what you want, without interfering with any data. If, for example, you are logging broadband values as well as spectra, you can choose to observe the profile, the time history, the overall or current spectrum, or the overall or current broadband values. The choice of display has no influence on what is measured or stored.

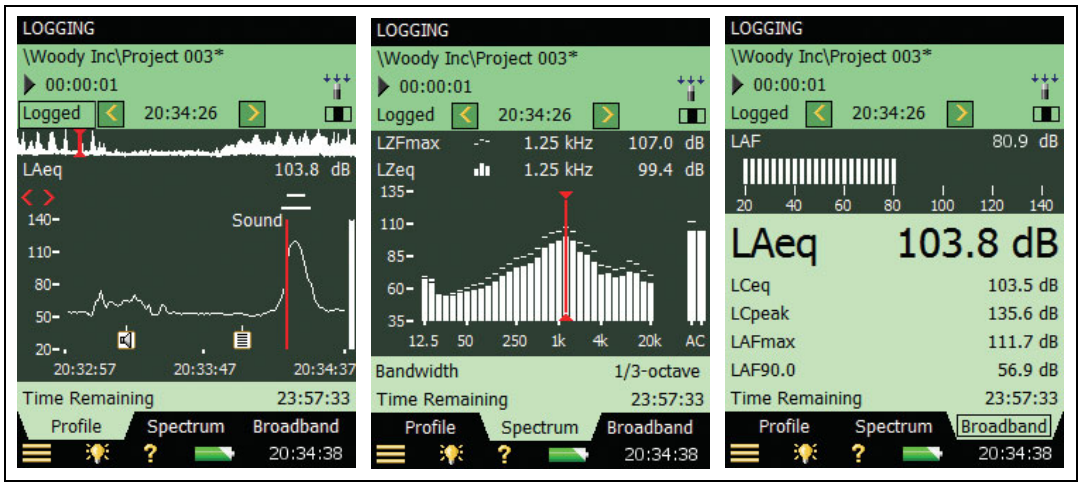

Fig. 5
Logging Software BZ-7224 displays (from left to right):
Profile with on-line sound marker, spoken commentary and note; current spectrum; and current broadband values.
Select freely between these displays at any time

Sound Level Meter Software – BZ-7222

SLM Module

All Type 2250s come with the Sound Level Meter Software enabled. This makes Type 2250 into a versatile broadband sound level meter; it complies with the latest international standard (IEC 61672–1) as well as previous international and national standards.

All quantities are measured at the same time. For example, A and C frequency weighted levels are measured simultaneously, and at the same time F, S and I time weightings are applied in parallel. In addition, Peak levels are measured. Full statistics are also computed on-the-fly. Combine this with the dynamic range exceeding 120 dB and you will never miss a beat! You get all the parameters in one attempt, under-range is non-existent and you will have difficulties provoking an overload. The detailed list of available parameters can be found in the specifications section. You choose what you want on the display, but, at any time – during or after the measurement – all other parameters can be inspected and reported.

The standard package allows you to document your measurements with written notes and voice annotations. Notes are added using a virtual keyboard on the touch screen.

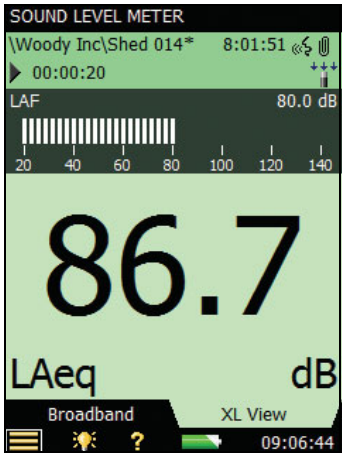

Fig. 6
Example of a typical SLM display, including the icon for recording annotations, visible in the upper right hand corner (see another example in the right hand display of Fig. 5)

Voice annotations are recorded using a separate commentary microphone when the commentary pushbutton is pushed and held. Voice annotations and notes can be attached before, during and after the measurement. Spoken comments during the measurement should, of course, be made during a pause or with the microphone placed at a distance using an extension cable. These unique features allows you to document your measurement (where, when, how, etc.,) and always have this information attached to the measurement. Notes and voice annotations can be reviewed on the instrument itself or after the data has been transferred to a PC.

If Sound Recording Option BZ-7226 (see page 9) is also enabled, you can record all or part of the measured signal. This recording is safely stored with the measurement. Thus it is easy to document that measured levels are indeed related to a particular noise source under investigation.

Frequency Analysis Software – BZ-7223

Frequency Analysis Software for Type 2250

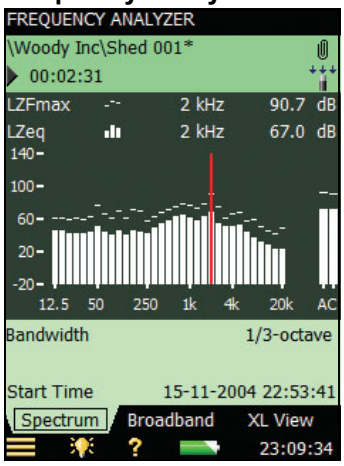

Fig. 7
Example of 1/3-octave frequency analysis. Note that two spectra are displayed simultaneously

Frequency Analysis Software BZ-7223 is an optional software module. It allows you to make real-time measurements in 1/1- and 1/3-octave bands over a wide frequency range. This makes it a simple matter to obtain spectra in order to, for example, select hearing protection, qualify heat and ventilation systems, and assess tonality.

The following frequency ranges are available:

- 1/1-octave spectra (centre frequencies 8 Hz to 16 kHz)
- 1/3-octave spectra (centre frequencies 6.3 Hz to 20 kHz)

In each band you have a full and unrivalled dynamic range from the noise floor in that particular band to 140 dB. That is, a dynamic range generally in excess of 135 dB.

Spectra can be A-, B-, C- or Z-weighted. Five spectra and full spectral statistics are measured and stored and, in addition, seven different L_N spectra and instantaneous values are available for display. Two spectra, for example, a minimum and maximum spectrum, can be superimposed on the display. As a matter of course, all the broadband quantities measured by Sound Level Meter Software BZ-7222 are computed in parallel with the frequency analysis. Spectral analyses can be documented using notes and voice annotations.

Logging Software – BZ-7224

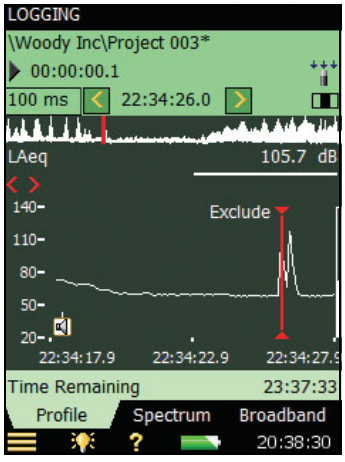

Fig. 8
Display showing part of profile with 100 ms resolution

With the optional Logging Software enabled, Type 2250 becomes a versatile instrument for obtaining time histories. The Logging Software allows you to select freely among the broadband parameters and log them at intervals from 1 s to 24 h. At the same time L_{Aeq} and/or L_{AF} can be logged at 100 ms intervals.

If Frequency Analysis Software BZ-7223 is enabled, the Logging Software additionally lets you log spectra at the same 1 s to 24 h periods.

Logging Software BZ-7224 incorporates a number of features designed to make difficult field work as manageable as possible.

Among the most salient of these features are the following:

- Five user-definable markers can be set on-the-fly in the profile. Use these, for example, to clearly indicate specific noise sources
- Markers can be set directly on the profile display using the stylus and the touch screen. Simply ‘tap and drag’ on the part of the profile you want to mark and select a marker from the drop-down list
- Markers can even be set ‘after the fact’. The display covers the latest 100 samples (that is, 100 s of profile when logging at 1 s intervals, otherwise more) meaning that in most cases you can wait for the event (or disturbance) to stop before placing your marker. Alternatively, scroll back in the profile and set your marker
- Lets you browse easily between markers (like sound recordings)

- The profile display can be ‘frozen’ at any time (this happens automatically when you tap the screen), allowing you to work at ease
- Voice annotations, using the commentary microphone, are attached to the exact point on the profile where the annotation is made. With the microphone on an extension cable, comments can be associated with particular parts of the profile without interfering with the measurement

All markers and annotations are saved with the measurement, see Fig. 8 and Fig. 9. No further bookkeeping is required. When exporting data to, for example, 7820 Evaluator software for further analyses, markers, as well as annotations, are directly accessible on the profile.

Data is stored directly on SD or CF cards. BZ-7224 includes a suitable SD card. Data can be directly read from the SD card by the included PC software BZ-5503 (see page 11). This means that even large amounts of data can be quickly transferred to a PC.

In order to give an indication of the amount of memory required, some examples have been listed below. Values should be compared to the standard size of the SD cards used, which start at 128 Mbyte.

For convenience, values for 1 s logging periods during 24 h are given. Other values easily compute from these:
- Five broadband parameters, no statistics: 1 Mbyte
- All broadband parameters, one 100 ms parameter: 3 Mbyte
- All broadband parameters, no statistics: 4 Mbyte
- All broadband parameters, one 100 ms parameter, all 1/3-octave spectra: 30 Mbyte
- All broadband parameters with full statistics: 58 Mbyte
- All broadband parameters, one 100 ms parameter, all 1/3-octave spectra, full statistics: 86 Mbyte

Space needed for annotations and recordings must, of course be added to this. As a guideline, 10 s of voice annotation requires approximately 312 kB.

Enhanced Logging Software – BZ-7225

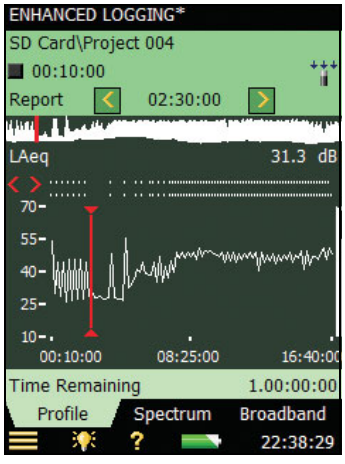

Fig. 9
Display showing part of a report profile with 10 min resolution

With the optional Enhanced Logging Software enabled, Type 2250 is optimised for long-term monitoring. It has the functionality of both Logging and Frequency Analysis software, but in addition it will:
- Measure continuously, limited only by data memory and power supply
- Reboot automatically and resume operation in case of power failure
- Save data in manageable portions (every 24 hours), selectable for download
- Make periodic reports, i.e., log all measurement data at a preset report period
- Measure L_{dn}, L_{den}, L_{day}, $L_{evening}$ and L_{night}

A periodic report is similar to the *Measurement Total* of the Logging software, except it is made periodically. It is useful for analysing sound levels over days or weeks. If you combine periodic reports with level triggered event markers and Sound Recording (option) you have an overview as well as a focus on essential details.

L_{dn} and L_{den} are 24 hour, A-weighted equivalent levels specified by the EPA (USA) and the European Union respectively.

L_{dn} applies a 10 dB penalty for nighttime levels, while L_{den} in addition has a 5 dB penalty for evening levels.

A typical setup for 24 hours of unattended monitoring might be:
- Continuous measurement
- Hourly periodic reports
- Level triggered marker for events above L_{AF} = 60 dB(A)
- Sound Recording of events (please refer to the Sound Recording Option)
- Logging of other parameters as required (please refer to the Logging Software)

After the measurement, you can check L_{dn} or L_{den}, the Total and the periodic reports, and then browse the events and sound recordings to verify the quality of your measurements.

Sound Recording Option – BZ-7226

Sound Recording BZ-7226 is an option that works with all other software modules. In all cases it allows you to make recordings of the actual measured signal, that is, the microphone signal used for measurements (this must not be confused with recorded voice annotations, which uses the commentary microphone). However, its detailed working is dependent upon which other software module is enabled and running. In any case, recordings are automatically attached to the measurement and kept with it, even after transfer of the data to a PC.

The purpose of the Sound Recording Option is to let you record the measurement signal in order to identify and document sound sources, for example:
- The measured L_{Aeq} at 57 dB, did it actually stem from the rather distant compressor, or from other sources such as nearby birds or traffic? Not necessarily easy to evaluate on-site, very difficult to document convincingly later. If the signal is recorded: No discussion
- Is it really true that this noise is impulsive and should be penalised accordingly? If the signal is recorded: There may still be an argument, but it is based on facts
- Exceedances were identified while no operator was present. Did they originate from the plant under investigation or from another source. If the signal is recorded: No discussion

With Sound Level Meter Software BZ-7222 and Frequency Analysis Software BZ-7223, the Sound Recording Option BZ-7226 basically lets you do the following:
- Record all or parts of the measured signal giving rise to specific results, levels and spectra
- Set up your instrument so that recording can be set to start automatically when the measurement is started, or you can initiate recordings manually

With Logging Software BZ-7224 and Enhanced Logging Software BZ-7225, additional options are available:
- Recording of sound can be associated with the Event Marker. Use the Event key or set an Event marker on the profile display: The sound during the event is recorded and attached to the appropriate part of the profile
- Automatic detection of events – based on level exceedance is also possible, meaning that recordings can also be initiated when no operator is present

In all of the above cases the maximum duration of recordings can be set (Type 2250 is only limited by available storage on the memory card currently in use). Recording sound obviously requires large amounts of storage, therefore Sound Recording Option BZ-7226 allows you to decide on the trade-off between storage needed and recording quality (sampling rate).

Overview of Type 2250 Software Features

The table below presents a summary of the features of each of the software modules available with Type 2250. See Specifications for details.

Feature	SLM Software	Frequency Analysis Software	Logging Software	Enhanced Logging Software
120+ dB Dynamic Range – no need for range switching	●	●	●	●
Sound levels up to 140 dB with supplied Microphone Type 4189	●	●	●	●
Sound levels up to 152 dB using Microphone Type 4191	●	●	●	●
IEC/ANSI SLM standards Type/Class 1	●	●	●	●
Frequency weightings A, B, C, Z (linear) and time weightings F, S, I	●	●	●	●
Free-field/diffuse-field correction	●	●	●	●
Automatic windscreen detection and correction	●	●	●	●
Pre-set time start/stop	●	●	●	●
Back-erase – last 5 seconds of measurement data	●	●		
Multi-language user interface	●	●	●	●
Context-sensitive help	●	●	●	●
Voice and text annotation of measurements	●	●	●	●
Display colour-schemes optimised for day, night, indoor and outdoor use	●	●	●	●
Personal login – protects your personal setups from other users	●	●	●	●
Broadband statistics based on L_{Aeq}, L_{AF} or L_{AS}	●	●	●	●
Broadband frequency range: 3 Hz – 20 kHz	●	●	●	●
Remote control using Analogue or GSM modem	●	●	●	●
Transfer of data files while measuring (USB or modem)	●	●	●	●
Recording of measured signal during measurement	●[a]	●[a]	●[a]	●[a]
1/1-octave spectra (centre frequencies 8 Hz to 16 kHz)		●	●[b]	●[b]
1/3-octave spectra (centre frequencies 6.3 Hz to 20 kHz)		●	●[b]	●[b]
Spectral statistics based on L_{AF} or L_{AS}		●	●[b]	●[b]
Periodic reports of all measured data				●
Report period 1 min to 24 h				●
L_{dn}, L_{den}, L_{day}, $L_{evening}$, L_{night}				●
Logging of all or selected broadband parameters and spectra			●	●
Logging period 1 s to 24 h			●	●
L_{Aeq} and/or L_{AF} logged every 100 ms			●	●
Profile display			●	●
Profile overview of entire measurement			●	●
Continuous measurement				●
Markers on profile display			●	●
Recording of sound during noise events			●[a]	●[a]

a. If Sound Recording Option is enabled
b. If Frequency Analysis Software is enabled

Type 2250 PC Software – Utility Software for Hand-held Analyzers BZ-5503

Utility Software for Hand-held Analyzers BZ-5503 is an archiving tool for Type 2250 data and setups, and functions as the link between Type 2250 and post-processing or reporting software on a PC. It enables you to do the following:

Control Type 2250 from a PC

- Create users on Type 2250
- Manage data on Type 2250
- Transfer data to Type 2250
- Create, edit and transfer setups to Type 2250
- Control the instrument 'on-line' for demonstration purposes, or if you need a very large display

Manage and archive data on a PC

- Transfer data and setups from Type 2250 to an archive on the PC
- Transfer data between SD- or CF-Cards and the archives
- Keep data in archives, organised in job folders, per user – in the same way you have organised the data in Type 2250
- View data or annotations
- Export data to Type 7815, 7820 or 7825 for postprocessing and reporting
- Export data to Microsoft® Excel

Keep your Type 2250 software up to date

- Update software on Type 2250
- Install licenses for Type 2250 software

Recommended Application Software – For Use on PC

For comprehensive data management and post-process reporting, consider using Type 2250 data together with one of following well-known PC-software packages:

- Type 7815 Noise Explorer – Data Viewing software
- Type 7820 Evaluator – Environmental Noise software
- Type 7825 Protector – Noise at Work software

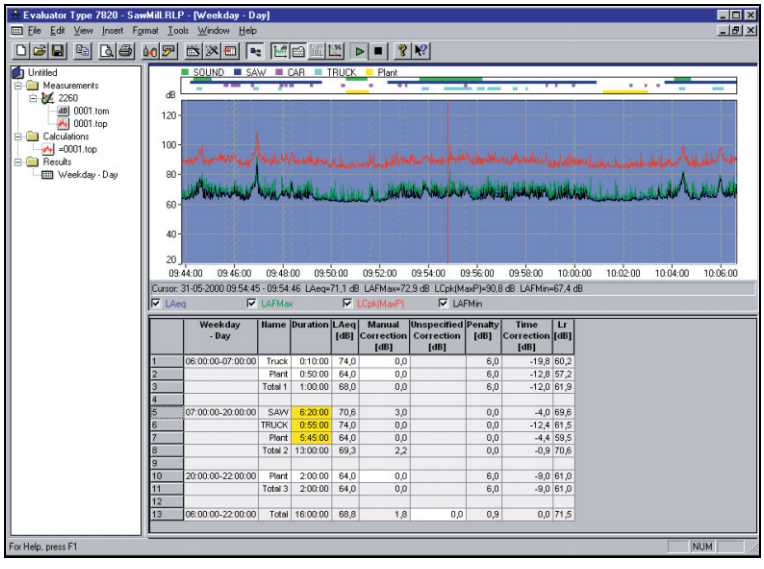

Fig. 10
A typical Evaluator display. The table shows Rating Level calculation results based on marked parts of the measured profile

Noise Explorer, Evaluator and Protector all support a wide range of user-definable graphic and tabular displays. Graphs and tables can be imported into standard Windows® applications such as word processors and spreadsheets.

Evaluator Type 7820 has built-in calculation algorithms that allow you to produce compound sound level figures from several contributions (see Fig. 10).

Some may have impulse or pure tone penalties, depending on which measurement standard you choose, for example, ISO 1996, DIN 45 645, TA Lärm, NF S 31-010, or BS 4142. (See Product Data BP 1752.)

Protector Type 7825 calculates noise exposure according to ISO 9612.2. For situations where only workpoint noise measurements are available, Protector can combine these measurements with a profile of a person's movements, simulating their personal noise exposure. (See Product Data BP 1717.)

Compliance with Standards

CE, C-Tick	CE-mark indicates compliance with the EMC Directive and Low Voltage Directive. C-Tick mark indicates compliance with the EMC requirements of Australia and New Zealand.
Safety	EN/IEC 61010–1: Safety requirements for electrical equipment for measurement, control and laboratory use. UL 61010B–1: Standard for Safety – Electrical measuring and test equipment.
EMC Emission	EN/IEC 61000–6–3: Generic emission standard for residential, commercial and light industrial environments. CISPR 22: Radio disturbance characteristics of information technology equipment. Class B Limits. FCC Rules, Part 15: Complies with the limits for a Class B digital device. IEC 61672–1, IEC 61260, IEC 60651 and IEC 60804: Instrumentation standards
EMC Immunity	EN/IEC 61000–6–2: Generic standard – Immunity for industrial environments. EN/IEC 61326: Electrical equipment for measurement, control and laboratory use – EMC requirements. IEC 61672–1, IEC 61260, IEC 60651 and IEC 60804: Instrumentation standards

Specifications – Type 2250 Platform

Specifications apply to Type 2250 fitted with Microphone Type 4189 and Microphone Preamplifier ZC-0032

SUPPLIED MICROPHONE
Type 4189: Prepolarized Free-field ½″ Microphone
Nominal Open-circuit Sensitivity: 50 mV/Pa (corresponding to −26 dB re 1 V/Pa) ± 1.5 dB
Capacitance: 14 pF (at 250 Hz)

MICROPHONE PREAMPLIFIER ZC-0032
Nominal Preamplifier Attenuation: 0.25 dB
Connector: 10-pin LEMO
Extension Cables: Up to 100 m in length between the microphone preamplifier and Type 2250, without degradation of the specifications
Accessory Detection: Windscreen UA-1650 can be automatically detected when fitted over ZC-0032

MICROPHONE POLARIZATION VOLTAGE
Selectable between 0 V and 200 V

SELF-GENERATED NOISE LEVEL
Typical values at 23°C for nominal microphone open-circuit sensitivity:

Weighting	Microphone	Electrical	Total
"A"	14.6 dB	12.4 dB	16.6 dB
"B"	13.4 dB	11.5 dB	15.6 dB
"C"	13.5 dB	12.9 dB	16.2 dB
"Z" 5 Hz–20 kHz	15.3 dB	18.3 dB	20.1 dB
"Z" 3 Hz–20 kHz	15.3 dB	25.5 dB	25.9 dB

KEYBOARD
Pushbuttons: 11 keys with backlight, optimised for measurement control and screen navigation

ON-OFF BUTTON
Function: Press 1 s to turn on; press 1 s to enter standby; press for more than 5 s to switch off

STATUS INDICATORS
LEDs: Red, amber and green

DISPLAY
Type: Transflective back-lit colour touch screen 240 × 320 dot matrix
Colour Schemes: Five different – optimised for different usage scenarios (day, night, etc.)
Backlight: Adjustable level and on-time

USER INTERFACE
Measurement Control: Using pushbuttons on keyboard
Setup and Display of Results: Using stylus on touch screen or pushbuttons on keyboard
Lock: Keyboard and touch screen can be locked and unlocked

USB INTERFACE
USB 1.1 OTG Mini B socket

MODEM INTERFACE
Hayes compatible GSM or standard analogue modems connected through the Compact Flash slot

INPUT SOCKET
Connector: Triaxial LEMO
Input Impedance: ≥ 1 MΩ
Direct Input: Max. input voltage: ± 14.14 V_{peak}
CCLD Input: Max. input voltage: ± 7.07 V_{peak}
CCLD Current/voltage: 4 mA/25 V

TRIGGER SOCKET
Connector: Triaxial LEMO
Max. Input Voltage: ± 20 V_{peak}
Input Impedance: > 47 kΩ

OUTPUT SOCKET
Connector: Triaxial LEMO
Max. Peak Output Level: ± 4.46 V
Output Impedance: 50 Ω

HEADPHONE SOCKET
Connector: 3.5 mm Minijack stereo socket
Max. Peak Output Level: ± 1.4 V
Output Impedance: 32 Ω in each channel

MICROPHONE FOR COMMENTARY
Microphone, which utilises Automatic Gain Control (AGC), is incorporated in underside of instrument. Used to create voice annotations for attaching to measurements

EXTERNAL DC POWER SUPPLY REQUIREMENTS
Used to charge the battery pack in the instrument

Voltage: 8 – 24 V DC, ripple voltage < 20 mV
Current Requirement: min. 1.5 A
Power Consumption: < 2.5 W, without battery charging, < 10 W when charging
Cable Connector: LEMO Type FFA.00, positive at centre pin

BATTERY PACK
Type: Li-Ion rechargeable
Typical Operating Time: > 8 hours

STORAGE SYSTEM
Internal Flash-RAM (non-volatile): 20 Mbyte for user setups and measurement data
External Secure Digital Memory Card (SD-card): For store/recall of measurement data
External Compact Flash Memory Card (CF-card): For store/recall of measurement data

CLOCK
Back-up battery powered clock. Drift < 0.45 s per 24 hour period

WARM-UP TIME
From Power Off: < 2 minutes
From Standby: < 10 seconds for prepolarized microphones

TEMPERATURE
IEC 60068–2–1 & IEC 60068–2–2: Environmental Testing. Cold and Dry Heat.
Operating Temperature: –10 to + 50°C (14 to 122°F), < 0.1 dB
Storage Temperature: –25 to +70°C (–13 to +158°F)

HUMIDITY
IEC 60068–2–78: Damp Heat: 90% RH (non-condensing at 40°C (104°F)).
Effect of Humidity: < 0.1 dB for 0% < RH < 90% (at 40°C (104°F) and 1 kHz)

MECHANICAL
Environmental Protection: IP44
Non-operating:
IEC 60068–2–6: Vibration: 0.3 mm, 20 m/s^2, 10 – 500 Hz
IEC 60068–2–27: Shock: 1000 m/s^2
IEC 60068–2–29: Bump: 4000 bumps at 400 m/s^2

WEIGHT AND DIMENSIONS
650 g (23 oz.) including rechargeable battery
300 × 93 × 50 mm (11.8 × 3.7 × 1.9″) including preamplifier and microphone

LANGUAGE
User Interface in Catalan, Croatian, Czech, Danish, English, Flemish, French, German, Hungarian, Japanese, Italian, Polish, Portuguese, Romanian, Serbian, Slovenian, Spanish and Swedish

HELP
Concise context-sensitive help in Catalan, English, French, German, Italian, Japanese, Polish, Portuguese, Romanian, Serbian, Slovenian and Spanish

Software Specifications – 2250 Sound Level Meter Software BZ-7222

Conforms with the following National and International Standards:
- IEC 61672 – 1 (2002 – 05) Class 1
- IEC 60651 (1979) plus Amendment 1 (1993–02) and Amendment 2 (2000–10), Type 1
- IEC 60804 (2000–10), Type 1
- DIN 45657 (1997–07)
- ANSI S1.4 – 1983 plus ANSI S1.4A – 1985 Amendment, Type 1
- ANSI S1.43 – 1997, Type 1

Note: The International IEC Standards are adopted as European standards by CENELEC. When this happens, the letters IEC are replaced with EN and the number is retained. Type 2250 also conforms to these EN Standards

TRANSDUCERS
Transducers are described in a transducer database with information on Serial Number, Nominal Sensitivity, Polarization Voltage, Free-field Type, CCLD required, Capacitance and additional information. The analogue hardware is set up automatically in accordance with the selected transducer

CORRECTION FILTERS
For microphone Types 4189, 4191, 4193 and 4952, BZ-7222 is able to correct the frequency response to compensate for sound field and accessories:
Sound Field: Free-field or Diffuse-field (for Type 4952 only: 0° (Top) reference direction and 90° (Side) reference direction)
Accessories (Type 4189 only): None, Windscreen UA-1650 or Outdoor Microphone Kit UA-1404
Accessories (Types 4191 and 4193 only): None or Windscreen UA-1650

DETECTORS
Parallel Detectors on every measurement:
A- or B-weighted (switchable) broadband detector channel with three exponential time weightings (Fast, Slow, Impulse), one linearly averaging detector and one peak detector
C- or Z-weighted (switchable) as for A- or B-weighted
Overload Detector: Monitors the overload outputs of all the frequency weighted channels

MEASUREMENTS
X = frequency weightings A or B
Y = frequency weightings C or Z
V = frequency weightings A, B, C or Z
U = time weightings F or S
N = number between 0.1 and 99.9
For Storage
Full statistics
For Display and Storage

Start Time	Stop Time	Overload %
Elapsed Time	L_{Xeq}	L_{Yeq}
L_{AE}	L_{Ceq}-L_{Aeq}	L_{Vpeak}
L_{XSmax}	L_{XFmax}	L_{XImax}
L_{YSmax}	L_{YFmax}	L_{YImax}
L_{XSmin}	L_{XFmin}	L_{XImin}
L_{YSmin}	L_{YFmin}	L_{YImin}
L_{XIeq}	L_{YIeq}	L_{AIeq}-L_{Aeq}
L_{AFTeq}	L_{AFTeq}-L_{Aeq}	Time Remaining

Only for Display as Numbers or Quasi-analogue Bars

L_{XS}	L_{XF}	L_{XI}
L_{YS}	L_{YF}	L_{YI}
$L_{XS(SPL)}$	$L_{XF(SPL)}$	$L_{XI(SPL)}$
$L_{YS(SPL)}$	$L_{YF(SPL)}$	$L_{YI(SPL)}$
L_{XN1} or L_{XUN1}	L_{XN2} or L_{XUN2}	L_{XN3} or L_{XUN3}
L_{XN4} or L_{XUN4}	L_{XN5} or L_{XUN5}	L_{XN6} or L_{XUN6}
L_{XN7} or L_{XUN7}		

MEASURING RANGES
When using Microphone Type 4189:
Dynamic Range: From typical noise floor to max. level for a 1 kHz pure tone signal, A-weighted: 16.6 to 140 dB
Primary Indicator Range: In accordance with IEC 60651, A-weighted: 23.5 dB to 123 dB
Linearity Range: In accordance with IEC 60804, A-weighted: 21.4 dB to 140 dB
Linear Operating Range: In accordance with IEC 61672, A-weighted: 1 kHz: 24.8 dB to 140 dB
Peak C Range: In accordance with IEC 61672: 29.5 dB to 143 dB

SAMPLING FOR STATISTICS
The Statistics can be based on either L_{XF}, L_{XS} or L_{Xeq}:
- Statistics L_{XFN1-7} or L_{XSN1-7} are based on sampling L_{XF} or L_{XS}, resp., every 10 ms into 0.2 dB wide classes over 130 dB
- Statistics L_{XN1-7} are based on sampling L_{Xeq} every second into 0.2 dB wide classes over 130 dB

Full distribution saved with measurement

MEASUREMENT DISPLAYS
SLM: Measurement data displayed as numbers of various sizes and one quasi-analogue bar
Measured data are displayed as dB values, housekeeping data as numbers in relevant format.
Instantaneous measurement L_{XF} is displayed as a quasi-analogue bar

MEASUREMENT CONTROL
Manual: Manually controlled single measurement
Automatic: Pre-set measurement time from 1 s to 24 hours in 1 s steps
Manual Controls: Reset, Start, Pause, Back-erase, Continue and Store the measurement manually

BACK-ERASE
The last 5 s of data can be erased without resetting the measurement

MEASUREMENT STATUS
On Screen: Information such as overload and running/paused are displayed on screen as icons
Traffic Lights: Red, yellow and green LEDs show measurement status and instantaneous overload as follows:
- Yellow LED flash every 5 s = stopped, ready to measure
- Green LED flashing slowly = awaiting calibration signal
- Green LED on constantly = measuring
- Yellow LED flashing slowly = paused, measurement not stored
- Red LED flashing quickly = intermittent overload, calibration failed

CALIBRATION
Initial calibration is stored for comparison with later calibrations
Acoustic: Using Sound Calibrator Type 4231 or custom calibrator. The calibration process automatically detects the calibration level when Sound Calibrator Type 4231 is used
Electrical: Uses internally generated electrical signal combined with a typed-in value of microphone sensitivity
Calibration History: Up to 20 of the last calibrations made are listed and can be viewed on the instrument

SIGNAL MONITORING
The input signal can be monitored using an earphone/headphones connected to the headphone socket, or it can be fed to the output socket
Output Signal: Input conditioned; A-, B-, C- or Z-weighted
Gain Adjustment: –60 dB to 60 dB
L_{XF} output (every ms) as a DC voltage between 0 V and 4 V
DC output for calibration purposes: 0 dB ~ 0 V and 200 dB ~ 4 V
Headphone Signal: Input signal can be monitored using this socket with headphones/earphones
Gain Adjustment: –60 dB to 60 dB

VOICE ANNOTATIONS
Voice annotations can be attached to measurements so that verbal comments can be stored together with the measurement
Playback: Playback of voice annotations can be listened to using an earphone/headphones connected to the headphone socket
Gain Adjustment: –60 dB to 0 dB

TEXT ANNOTATIONS
Text annotations can be attached to measurements so that written comments can be stored with the measurement

DATA MANAGEMENT
Project Template: Defines the display and measurement setups
Project: Measurement data stored with the Project Template
Job: Projects are organised in Jobs
Explorer facilities for easy management of data (copy, cut, paste, delete, rename, view data, open project, create job, set default project name)

USERS
Multi-user concept with login. Users can have their own settings with jobs and projects totally independent of other users

PREFERENCES
Date, Time and Number formats can be specified per user

Software Specifications – 2250 Frequency Analysis Software BZ-7223

The specifications for BZ-7223 include the specifications for 2250 Sound Level Meter Software BZ-7222. BZ-7223 adds:

STANDARDS
Conforms with the following National and International Standards:
- IEC 61260 (1995–07) plus Amendment 1 (2001–09), 1/1-octave Bands and 1/3-octave Bands, Class 0
- ANSI S1.11–1986, 1/1-octave Bands and 1/3-octave Bands, Order 3, Type 0–C
- ANSI S1.11–2004, 1/1-octave Bands and 1/3-octave Bands, Class 0

CENTRE FREQUENCIES
1/1-octave Band Centre Frequencies: 8 Hz to 16 kHz
1/3-octave Band Centre Frequencies: 6.3 Hz to 20 kHz

MEASUREMENTS
X = frequency weightings A, B, C or Z , Y = time weightings F or S
Data for Storage
Full Spectral Statistics
Spectra for Display and Storage

L_{Xeq}	L_{XSmax}	L_{XFmax}
L_{XSmin}	L_{XFmin}	

Spectra for Display Only

L_{XS}	L_{XF}	L_{XYN1}
L_{XYN2}	L_{XYN3}	L_{XYN4}
L_{XYN5}	L_{XYN6}	L_{XYN7}

Single Values

SIL	PSIL	SIL3
$L_{Aeq\ (20\text{-}200\ Hz)}$		

MEASURING RANGES
When using Microphone Type 4189:
Dynamic Range: From typical noise floor to max. level for a pure tone signal at 1 kHz 1/3-octave: 1.7 to 140 dB
Linear Operating Range: In accordance with IEC 61260: ≤ 20.5 dB to 140 dB

SAMPLING FOR OCTAVE OR 1/3-OCTAVE STATISTICS
X = frequency weightings A or B
The Statistics can be based on either L_{XF} or L_{XS}:
- Statistics L_{XFN1-7} or L_{XSN1-7} are based on sampling L_{XF} or L_{XS}, respectively, every T ms into 1 dB wide classes over 150 dB;

T = 100 for frequency range set to 12.5 – 20 kHz
T = 200 for frequency range set to 6.3 – 20 kHz
Full distribution can be saved with measurement

MEASUREMENT DISPLAYS
Spectrum: One or two spectra superimposed + A/B and C/Z broadband bars
Y-axis: Range: 5, 10, 20, 40, 60, 80, 100, 120, 140 or 160 dB. Auto zoom or auto scale available
Cursor: Readout of selected band

Software Specifications – 2250 Logging Software BZ-7224

The specifications for BZ-7224 include the specifications for 2250 Sound Level Meter Software BZ-7222. BZ-7224 adds:

MEASUREMENTS
Logging: Measurement data logged at pre-set periods into files on external SD- or CF-cards
Logging Period: From 1 s to 24 hours with 1 s resolution
Fast Logging: L_{AF} and L_{Aeq} can be logged every 100 ms, irrespective of logging period
Broadband Data Stored at each Logging Interval: All, or up to 10 selectable broadband data

Broadband Statistics Stored at each Logging Interval: Full distribution, or none
Spectrum Data Stored at each Logging Interval: All, or up to 3 selectable spectra (license for BZ-7223 required)
Spectral Statistics Stored at each Logging Interval: Full distribution, or none (license for BZ-7223 required)
Logging Time: From 1 second to 31 days with 1 s resolution
Measurement Total: For the logging time, in parallel with logging: All broadband data, statistics and spectra (license for BZ-7223 required)

MARKERS
One data exclusion marker and four user-definable markers for on-line marking of sound categories heard during the measurement Events can be set manually

TRIGGERS
Markers can be set when a broadband level is above or below a specified level

ANNOTATIONS
On-line annotations with spoken comments or written notes

MEASUREMENT DISPLAYS
Profile: Graphical display of selectable measurement data versus time. Fast display of next or previous marker, Profile Overview of entire measurement
Y-axis: Range: 5, 10, 20, 40, 60, 80, 100, 120, 140 or 160 dB. Auto zoom or auto scale available
X-axis: Scroll facilities
Cursor: Readout of measurement data at selected time

Software Specifications – 2250 Enhanced Logging Software BZ-7225

The specifications for BZ-7225 include the specifications for 2250 Logging Software BZ-7224 and for 2250 Frequency Analysis Software BZ-7223. Licenses for BZ-7223 and BZ-7225 are required to run BZ-7225. BZ-7225 adds:

MEASUREMENTS
For Display and Storage
L_{dn}, L_{den}, L_{day}, $L_{evening}$ and L_{night}
Selectable Day, Evening and Night periods and penalties
Periodic Reports: Measurement data logged at a pre-set report period into files on external SD- or CF-cards
Report Period: From 1 min to 24 hours with 1 min resolution
Broadband Data and Statistics Stored at each Reporting Interval: All
Spectrum Data Stored at each Reporting Interval: All
Spectral Statistics Stored at each Reporting Interval: Full distribution, or none
Logging Time: From 1 second to 31 days with 1 s resolution or Continuous
Data are saved in separate projects for every 24 hrs of logging
Automatic reboot and resume of operation in case of power failure

Software Specifications – Sound Recording Option BZ-7226

Sound Recording Option BZ-7226 is enabled with a separate license. It works with all the software for Type 2250: Sound Level Meter, Frequency Analysis, Logging Software and Enhanced Logging Software
Sound Recording requires a CF- or SD-Card for data storage

RECORDED SIGNAL
A-, B-, C- or Z-weighted signal from the measurement transducer

AUTOMATIC GAIN CONTROL
The average level of the signal is kept within a 40 dB range, or the gain can be fixed

SAMPLING RATE AND PRE-RECORDING
Sound is buffered for the pre-recording of sound. This allows the beginning of events to be recorded even if they are only detected later.

Sampling Rate (kHz)	Maximum Pre-recording (s)	Sound Quality	Memory (KB/s)
8	100	Low	16
16	50	Fair	32
24	30	Medium	48
48	10	High	96

FUNCTIONS WITH BZ-7222 AND BZ-7223
Manual Control of Recording: Recording can be manually started and stopped during a measurement using a pushbutton or an external signal
Automatic Control of Recording: Start of recording when measurement is started. Minimum and Maximum recording time can be preset

FUNCTIONS WITH BZ-7224
Manual Control of Recording (using Manual Event or Back-erase pushbutton, or an external signal): Recording during all of the event, or for preset minimum and maximum duration. A Sound marker is set while recording. Selectable pre- and post-recording time
Manual Control of Recording (using touch screen): Recording for the selected time period (subject to the limitations of the pre-recording buffer). A Sound marker is set for the selected time period
Automatic Control of Recording: An event can be triggered when a broadband level is above or below a specified level. Recording during all of the event or for preset minimum and maximum duration. Selectable pre- and post-recording time

PLAYBACK
Playback of sound recordings can be listened to using the earphone/ headphones connected to the headphone socket

RECORDING FORMAT
The recording format is 16-bit wave files (extension .wav) attached to the data in the project, easily played-back afterwards on a PC using Type 7815, 7820 or 7825. Calibration information is stored in the wav file, allowing PULSE to analyse the recordings

Software Specifications – Utility Software for Hand-held Analyzers BZ-5503

BZ-5503 is included with Type 2250 for easy synchronisation of setups and data between PC and Type 2250. BZ-5503 is supplied on CD-ROM BZ-5298

ON-LINE DISPLAY OF TYPE 2250 DATA
Measurements on Type 2250 can be controlled from the PC and displayed on-line with the PC, using the same user interface on the PC as on Type 2250

DATA MANAGEMENT
Explorer: Facilities for easy management of Instruments, Users, Jobs, Projects and Project Templates (copy, cut, paste, delete, rename, create)
Data Viewer: View measurement data (content of projects)
Template Editor: Editor for changing setups in Project Templates
Synchronisation: Project Templates and Projects for a specific user can be synchronised between PC and Type 2250

USERS
Users of Type 2250 can be created or deleted

EXPORT FACILITIES
Excel: Projects (or user specified parts) can be exported to Microsoft® Excel
Type 7810/12/15/16/20/25: Projects can be exported to Predictor Type 7810, Lima Type 7812, Noise Explorer Type 7815, Acoustic Determinator Type 7816, Evaluator Type 7820 or Protector Type 7825

TYPE 2250 SOFTWARE UPGRADES AND LICENSES
The utility software controls Type 2250 software upgrades and licensing of the Type 2250 applications

INTERFACE TO TYPE 2250
USB ver. 1.1 or Hayes compatible GSM or standard analogue modem

PC REQUIREMENT
Operating System: Windows® 2000/Windows® XP, Microsoft®.NET
Recommended PC: Pentium® III (or equivalent) processor, 128 Mbyte RAM, SVGA graphics display/adaptor, sound card, CD ROM drive, mouse, USB, Windows® XP

Ordering Information

PACKAGES

Type 2250 A	Hand-held Analyzer with Sound Level Meter Software
Type 2250 B	Hand-held Analyzer with Sound Level Meter and Frequency Analysis Software
Type 2250 C	Hand-held Analyzer with Sound Level Meter and Logging Software
Type 2250 D	Hand-held Analyzer with Sound Level Meter, Frequency Analysis and Logging Software
Type 2250 E	Hand-held Analyzer with Sound Level Meter, Frequency Analysis, Enhanced Logging Software and Sound Recording Software

SOFTWARE MODULES AVAILABLE SEPARATELY

BZ-7223	2250 Frequency Analysis Software
BZ-7224	2250 Logging Software
BZ-7225	2250 Enhanced Logging Software
BZ-7225-UPG	Upgrade from 2250 Logging Software BZ-7224 to 2250 Enhanced Logging Software BZ-7225 (does not include memory card)
BZ-7226	2250 Sound Recording Option

COMPONENTS INCLUDED WITH TYPE 2250 HAND-HELD ANALYZER

Type 4189	Prepolarized Free-field 1/2″ Microphone
ZC-0032	Microphone Preamplifier
AO-1476	USB Standard A to USB Mini B Interface Cable, 1.8 m (6 ft)
BZ-5298	Environmental Software, including BZ-5503 Utility Software for Hand-held Analyzers
UA-1650	90 mm dia. Windscreen with AutoDetect
UA-1651	Tripod Extension for Hand-held Analyzer
UA-1673	Adaptor for Standard Tripod Mount
DH-0696	Wrist Strap
KE-0440	Travel Bag
KE-0441	Protective Cover for Type 2250
FB-0679	Hinged Cover for Hand-held Analyzer
HT-0015	Earphones
UA-1654	5 Extra Styli
QB-0061	Battery Pack
ZG-0426	Mains Power Supply

COMPONENTS INCLUDED WITH 2250 LOGGING SOFTWARE BZ-7224 AND ENHANCED LOGGING SOFTWARE BZ-7225

Memory Card for Hand-held Analyzers **Note:** the upgrade from Logging Software BZ-7224 to Enhanced Logging Software BZ-7225 (BZ-7225-UPG) does not include memory card

ACCESSORIES AND COMPONENTS AVAILABLE SEPARATELY

ANALYZER

ZG-0444	Charger for QB-0061 Battery Pack

CALIBRATION

Type 4231	Sound Calibrator (fits in KE-0440)
Type 4226	Multifunction Acoustic Calibrator
Type 4228	Pistonphone
2250 CAI	Accredited Initial Calibration of Type 2250
2250 CAF	Accredited Calibration of Type 2250
2250 CTF	Traceable Calibration of Type 2250
2250 TCF	Conformance Test of Type 2250, with certificate

MEASURING

Type 3592	Outdoor Measuring Gear (see Product Data BP 1744)
AO-0440-D-015	Signal cable, LEMO to BNC, 1.5 m (5 ft)
AO-0646	Sound Cable, LEMO to Minijack, 1.5 m (5 ft)
AO-0441-D-030	Microphone Extension Cable, 10-pin LEMO, 3 m (10 ft)
AO-0441-D-100	Microphone Extension Cable, 10-pin LEMO, 10 m (33 ft)
UA-0587	Tripod
UA-0801	Small Tripod
UA-1317	Microphone Holder
UA-1404	Outdoor Microphone Kit
UA-1672	AutoDetect Insert for UA-1650
UL-1009	SD Memory Card for Hand-held Analyzers
UL-1013	CF Memory Card for Hand-held Analyzers

INTERFACING

Type 7815	Noise Explorer – data viewing software
Type 7820	Evaluator – data viewing and calculation software
Type 7825	Protector – software for calculation of Personal Noise Exposure

SERVICE PRODUCTS

2250-EW1	Extended Warranty, one year extension
2250-MW1	5 Years Warranty including yearly Accredited Calibration – annual payment
2250-MW5	5 Years Warranty including yearly Accredited Calibration

HEADQUARTERS: DK-2850 Nærum · Denmark · Telephone: +45 4580 0500
Fax: +45 4580 1405 · www.bksv.com · info@bksv.com

Australia (+61) 2 9889-8888 · Austria (+43) 1 865 74 00 · Brazil (+55) 11 5188-8161
Canada (+1) 514 695-8225 · China (+86) 10 680 29906 · Czech Republic (+420) 2 6702 1100
Finland (+358) 9-755 950 · France (+33) 1 69 90 71 00 · Germany (+49) 421 17 87 0
Hong Kong (+852) 2548 7486 · Hungary (+36) 1 215 83 05 · Ireland (+353) 1 807 4083
Italy (+39) 0257 68061 · Japan (+81) 3 5715 1612 · Republic of Korea (+82) 2 3473 0605
Netherlands (+31) 318 55 9290 · Norway (+47) 66 77 11 55 · Poland (+48) 22 816 75 56
Portugal (+351) 21 4169 040 · Singapore (+65) 377 4512 · Slovak Republic (+421) 2 5443 0701
Spain (+34) 91 659 0820 · Sweden (+46) 33 225 622 · Switzerland (+41) 44 8807 035
Taiwan (+886) 2 2502 7255 · United Kingdom (+44) 14 38 739 000 · USA (+1) 800 332 2040

Local representatives and service organisations worldwide

Brüel & Kjær

BP 2025 – 16 06/06 Rosendahls Bogtrykkeri

Appendix C2: Published Material

NZ RAPID PRODUCT DEVELOPMENT CONFERENCE 2011
FEBRUARY 7-8, AUCKLAND UNIVERSITY OF TECHNOLOGY, AUCKLAND, NEW ZEALAND

Acoustic-Feedback Current Control for Thermomechanical Cutting of Polystyrene Foam

Bain, Joseph[1]; Aitchison, David[1]; Kato, Fumi[1]; Pearse, John[1]; Pons, Dirk[1]
[1]Department of Mechanical Engineering, University of Canterbury, Christchurch, New Zealand

KEYWORDS:

Foam cutting, thermomechanical cutting, cutting force, acoustic output, rapid manufacturing, current control.

ABSTRACT

Robotic Foam Sculpting (RFS) is a new subtractive rapid manufacturing system under development at the University of Canterbury. The system uses an industrial robot with electrically-heated tools (wires or blades) to thermomechanically cut polystyrene foam, to produce large-volume prototypes or patterns at relatively low cost. A major focus of this research is developing an understanding of the cutting mechanics and cutting strategy required to achieve high surface qualities, and the development of control systems for the heated tools, so that high-quality surfaces can be cut automatically with a high degree of confidence. A method of controlling the temperature of the tool based on measurements of cutting force has previously been developed, but this suffers from a number of drawbacks including the need to have a loadcell on the cutting tool, which limits the range of possible tool and robot configurations.

This paper presents the results of a study undertaken to assess whether the acoustic output of thermomechanical cutting can be used as a control input for heated tools. This study found that the thermomechanical cutting process generated a distinctive and measurable acoustic output, especially at frequencies above 1 kHz. It was also found that the output was repeatable and consistent for a given set of cutting conditions, subject to some variation resulting from the inherently unpredictable nature of thermomechanical cutting of foam materials. Finally, it was found that the acoustic output can be related to the cutting force and cutting conditions such as tool feedrate and supplied current.

Based on these findings, a new method of controlling the energy supplied to the heated tool based on acoustic measurements is proposed, which should overcome the drawbacks of the current force-feedback control system and allow in-process control of the tool temperature, to improve the surface quality and reduce energy consumption.

INTRODUCTION

Robotic Foam Sculpting (RFS) is a new rapid manufacturing system under development at the University of Canterbury, using a six-axis industrial robot equipped with hot-wire and hot-blade tools to subtractively sculpt 3D objects from blocks of polystyrene foam, using a combination of single-pass and multi-pass cutting depending on the geometry of the part to be sculpted. Most of the work carried out on the RFS system to date has been concerned with understanding the cutting mechanics, cutting force and the effect of these parameters on outputs like surface roughness and kerfwidth (Aitchison et al., 2009, Aitchison et al., 2006, Aitchison et al., 2005). Despite the merits of polystyrene foam as a material for rapid prototyping, including its low cost, the smooth achievable surface finish and the low forces associated with cutting, relatively little work has been published on the development of foam-based RP systems. The authors are aware of only two other fully-developed systems: Variable Lamination Manufacturing developed by the Korea Advanced Institute of Science and Technology (Ahn et al., 2002, Ahn et al., 2003) and Free-Form Thick Layer Object Manufacturing developed by the Delft University of Technology (De Smit et al., 2000, De Smit et al., 1999). These systems are both hybrids of subtractive and additive cutting strategies, where hot-tool cutting is used to shape foam layers which are then assembled into 3D models: as such, they are fundamentally different from RFS, which uses an entirely-subtractive cutting strategy to shape a foam workpart into the final desired shape. No work concerned with active control of the tool temperature appears to have been published by either of these projects.

As part of the development of the RFS system, a current-control system has been developed that uses a real-time measure of the cutting force to apply a step increase to the applied current (Brooks and Aitchison). This control system has a significant disadvantage: since a cutting force reading is necessary, a loadcell must be incorporated into the system. This means that the system has to be configured with the robot moving the foam workpart and the tool (with loadcell) mounted on a fixed base, since if the loadcell and tool are on the robot then every robot movement results in force readings that would result in activation of the current control system. Mounting the tool on the robot is desirable since it is easier to move a small tool through complex toolpaths than it is to move a large foam block around a fixed tool.

Apart from this major drawback, the adaptive current-control system developed for the RFS system is a very useful tool that stabilizes the kerfwidth along the length of the cut, so it is desirable to find another input that can be used to trigger the step-change in current without needing a cutting force reading. Whatever metric is used, it should be proportional to the cutting force, measureable and repeatable.

Based on these requirements, and qualitative observation of a wide range of cuts, it was hypothesised that the acoustic output of the cutting process was related to the cutting force

and could be used as a control metric. This paper will present a summary of the hot-tool cutting process and the force-feedback current control system, and presents the results of an investigation into the acoustic output of hot-tool cutting of foam.

I. Thermomechanical Foam Cutting

When a hot-wire or hot-blade cut is made in polystyrene foam with a constant applied current, characteristic cutting force and centre-temperature profiles become apparent. At the beginning of the cut, the wire is at its free-air temperature, which is proportional to the applied current. When the wire enters the foam, it is initially much hotter than the melting temperature of the foam, so it travels through the foam within a thermal field that vapourises the foam without any contact between the foam and the wire. This cutting mode is referred to as vapourised cutting and is associated with near-zero cutting force. As the wire passes through the foam it begins to cool, especially at the centre of the engaged length, and the thermal field around the wire gets progressively smaller until there is physical contact between the wire and the foam. During this transition the centre temperature reduces and the cutting force increases. Eventually the tool reaches a steady state with stable centre-cut temperatures and cutting forces. This is referred to as steady-state cutting. When a cut is in the steady-state, the foam is being cut by a combination of thermal and mechanical means. Characteristic cutting force and centre-temperature profiles are shown in Fig. 1.

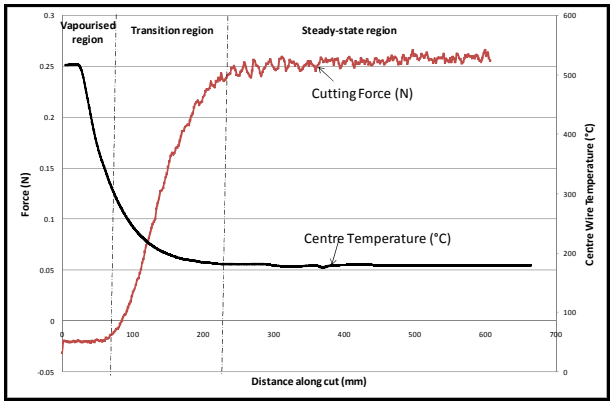

Fig. 1. Characteristic cutting force and temperature profiles along a constant-current hot wire cut (30mm, 7A, 0.0183ms^{-1})

These characteristic centre-temperature and cutting force profiles occur with all cuts of sufficient length, but the exact shape varies as a function of the applied current and the tool feedrate. Short cuts follow the same pattern but may not be long enough to achieve steady-state conditions. Higher currents or lower feedrates result in a cut that takes longer to reach steady-state conditions: for two cuts made with the same applied current but different feedrates, the cut made with the higher feedrate will reach steady-state conditions sooner than the cut made with the lower feedrate. The high-feed cut will also have generally higher cutting force in steady state conditions.

The transient nature of the cutting conditions before steady-state cutting is achieved presents a problem for the dimensional accuracy and surface texture of parts being sculpted by RFS. During vapourised cutting, the kerf of the cut (the volume of material lost as a result of the cutting process) is much larger than it is in steady-state cutting, while the surface texture of the cut foam is much more predictable if the surface is produced by vapourised cutting than if it is produced by thermomechanical cutting (although smoother surfaces can be produced with thermomechanical cutting, the smeared nature of these surfaces means they are difficult to produce in a reliable and repeatable manner). While the effect of kerf on the dimensional accuracy of parts can be corrected by applying an offset, this is much more difficult when the kerfwidth is varying along the length of the cut.

II. Force – Feedback Current Control

In order to improve the dimensional accuracy of hot-tool foam cutting, a current control system has been developed that uses a real-time measure of the cutting force to determine when the vapourised cutting phase has ended (by detecting a non-zero cutting force), and to increase the current at this point. This increased current compensates for the cooling of the wire to be expected in an uncontrolled cut, so that the wire temperature in the cut is kept close to the value of free-air wire temperature. Fig. 2 shows the temperature of the tool in the centre of the cut for a feedrate of 0.0183ms^{-1}, for both a constant 7A current and the controlled-current case where the current has been stepped from 3A to 7A at the end of the vapourised cutting phase. As is clear, the temperature in the controlled-current case is much more stable along the cut than in uncontrolled cutting.

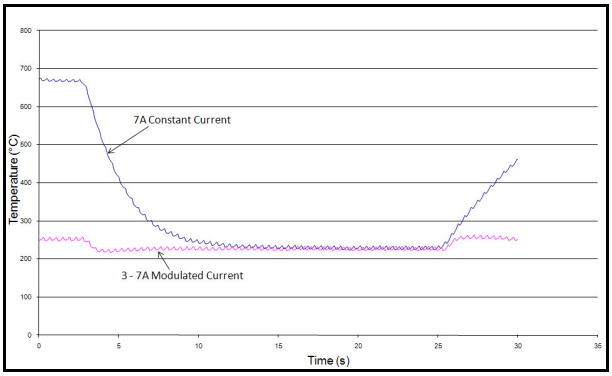

Fig. 2. Temperature at the centre of the tool engaged length with and without force-feedback temperature control (Wire tool, 30mm, 0.0183ms^{-1})

As a result of the stable tool temperature resulting from active current control, the kerfwidth is also more stable along the cut, as shown in Fig. 3: when current control is implemented the kerfwidth along the cut becomes effectively constant. This stands in stark contrast with the uncontrolled case where the kerfwidth at the start of the cut is approximately 2.6mm and falls to 1mm when steady-state cutting is achieved. In effect, force-feedback current control makes steady-state thermomechanical cutting conditions occur earlier in the cut.

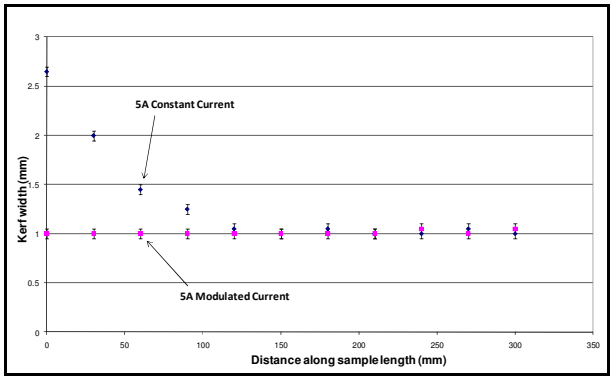

Fig. 3. Kerf width along the cut with and without force-feedback temperature control (Wire tool, XPS, 0.0150ms^{-1})

Force-feedback current control has been proven as a useful tool for controlling the dimensional accuracy of the cut surface, and also saves energy by reducing the tool temperature when cutting is not taking place, but there are some significant drawbacks. Most importantly, the system requires a loadcell to measure the cutting force. This means that the cutting tool has to be mounted on a loadcell on a worktable and the robot has to move the foam workpart, since if the tool and loadcell are on the robot spurious force readings are recorded during robot movement and can impair the function of the current control system. This arrangement is less than ideal, since it is more difficult to achieve a desired toolpath without violating the robot joint limits when the robot is moving a large block of foam than it would be if the robot were only moving the tool. As a result of this major drawback, current control has only been implemented for hot-wire tools and for a limited range of cutting conditions to date.

Since cutting force-based current control has such a major drawback, but since current-control presents such significant advantages for the RFS system, there is a need to determine a new metric to use to trigger the current step. This metric needs to be repeatable and predictable, it needs to be easily implemented when the cutting tool is mounted on the robot and it needs to be applicable to both hot-wire and hot-blade tools.

During cutting trials undertaken to assess the surface form and surface texture accuracy of thermomechanical cutting, it was noticed (by aural observation) that the cutting process made a sound that seemed to be consistent and seemed to change along the length of the cut in a manner related to the thermomechanical balance of the cut, and was therefore thought to be related to the cutting force. This presented the possibility that the acoustic output could be used as a control metric for a current-control system, so an investigation was undertaken to assess the usefulness of the acoustic output for this purpose. If the acoustic output is consistent, repeatable and related to the input cutting conditions, then it should be possible to use this to identify when cutting is taking place and to trigger a current step based on this.

III. Acoustic Output Of Thermomechanical Foam Cutting

A. Acoustic Output Scoping Investigation

Before carrying out a detailed investigation of the acoustic output of thermomechanical foam cutting, a brief scoping exercise was conducted to verify that the acoustic output could be used to determine when cutting was taking place. To do this, acoustic data was gathered (using a Bruel and Kjaer Type 2250 acoustic data analyser) for a number of sets of cutting conditions both with and without cutting foam. The data gathered covered the full length of the cut. For each combination of feedrate and current, acoustic data was gathered for a cut and for the same situation without cutting. As a result, the non-cutting acoustic data includes all non-cutting sounds, such as background noise and robot movement noise. The non-cutting acoustic data can be compared with the acoustic data to determine if there is an identifiable difference in the acoustic output, and therefore if the acoustic output is measureable and useful for current control.

Fig. 4 shows the acoustic output without cutting, where the robot moves the foam through the same path as for cutting at a feedrate of 0.0217ms^{-1}, and Fig. 5 shows the acoustic output when hot-wire cutting takes place with a constant current of 7A and a feedrate of 0.0217ms^{-1}.

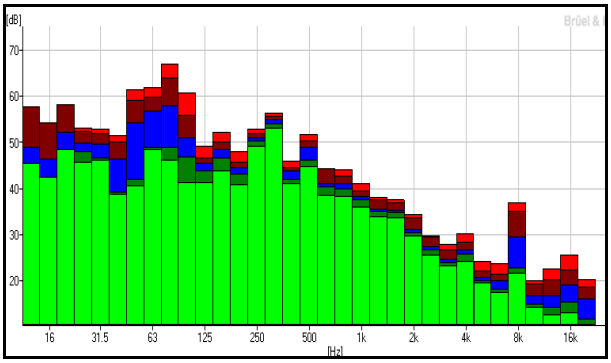

Fig. 4. Acoustic output without thermomechanical cutting

Comparing these two plots, the acoustic output resulting from thermomechanical cutting is evident. The sound of the hot-wire cut is clearly visible across all of the frequency ranges tested, but is most pronounced at frequencies higher than 1 kHz. This basic pattern of overall acoustic output was present for all of the sets of cutting conditions tested in the scoping investigation.

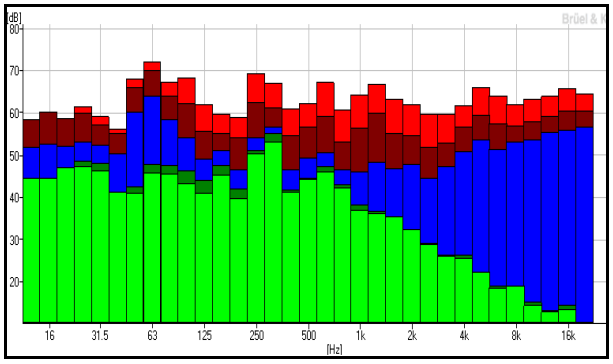

Fig. 5. Acoustic output with thermomechanical cutting

Based on this scoping exercise, it was apparent that the acoustic output of foam cutting was both present and measureable, and that there was a clear difference between times when no cutting takes place and times when cutting occurs. This indicated that acoustic output was a promising potential metric for a current control system and that a more comprehensive investigation of the acoustic output was warranted.

B. Empirical Investigation of Acoustic Output

In order to characterise the acoustic output across a full range of cutting conditions, a detailed experimental investigation was conducted. This experiment used extruded polystyrene foam (XPS, sold under the brand name 'Goldfoam'), two foam thicknesses (30 and 50mm), two tool types (ø0.6mm hot-wire and 1/8" by 0.018in. rectangular-section hot-blade tools) and a full range of cutting conditions as shown in Tables 1 and 2. Since this experimental work was based on single-pass cutting, the foam thickness was also the engaged length of the cutting tool.

Table 1: Cutting conditions for investigation of acoustic output for hot-wire cutting of XPS

Current	Tool Feedrate (ms^{-1})					
(A)	.0133	.0167	.0183	.0187	.0200	.0217
5	+	+			+	
6	+	+			+	
7	+	+	X	+	+	+

Table 2: Cutting conditions for investigation of acoustic output for hot-blade cutting of XPS

Current	Tool Feedrate (ms^{-1})				
(A)	0.028	0.040	0.052	0.064	0.076
16	+		+		
19	+	+	X	+	+
22	+		+		+

Cutting conditions marked by a '+' were carried out once for each foam type, while conditions marked by an 'X' were repeated six times for 30mm foam to provide a measure of the repeatability of the acoustic output. These cutting conditions were established based on previous cutting trials: blade cutting uses much higher currents than wire cutting because a higher current is required to achieve appropriate cutting temperatures, and higher feedrates because the rectangular section of the blade is more resistant to bending, and so can be used to cut much faster. The acoustic output for these cuts was recorded for the whole length of the cut, sampling every 0.1s, in frequency bands of 1 – 4 kHz, 4 – 8 kHz, 8 – 12 kHz and 12 – 16 kHz. The total cut length was at least 650mm, which resulted in many thousands of acoustic data points being captured for analysis.

C. Acoustic Output Characterisation

The captured acoustic data was compared to the cutting force along the length of the cut, since a relationship between the acoustic data and the cutting force is desirable so that acoustic output can replace cutting force as a trigger for current control. The cutting force and the acoustic output for each frequency band can be seen in Fig. 6 through Fig. 9, plotted along the length of the cut, for the case of 30mm XPS cut by a hot-wire with applied current of 7A and a feedrate of $0.0183ms^{-1}$. The units used for the acoustic magnitude are a proprietary dimensionless unit built into the analysis software provided with the acoustic data analyser, and are analogous to dB. These figures have been selected as representative of the acoustic output of all cuts, since space constraints prevent the presentation of all of the available data.

A number of key features of the acoustic output became apparent. The first was that the acoustic output in all four of the frequency bands investigated was proportional to the cutting force. This proportionality also applied to the variability of the acoustic output: the higher the cutting force, the more the acoustic signal would oscillate during the cut. One result of this is that the magnitude of the acoustic output during thermomechanical cutting was greater for an engaged length of 50mm than for an engaged length of 30mm, because the cutting force is greater for longer engaged lengths. The same acoustic trends and patterns are exhibited regardless of the tool engaged length, but the magnitudes vary depending on engaged length.

The second key trend was that the acoustic signals between 1 kHz and 12 kHz all exhibited consistent and regular behavior in the vapourised region. Every acoustic measurement, irrespective of tool type or engaged length, had a stable value of 0.00020 in the vapourised region in the 1 – 4 kHz band, while all the measurements in the 4 – 8 kHz and 8 – 12 kHz bands had a value of 0.00000 in the vapourised region. In all three of these frequency bands the beginning of the transition region (i.e. where cutting force began to increase) was denoted by a marked increase in the magnitude of the acoustic output, and this increase in magnitude was greater for the 4 – 8 kHz and 8 – 12 kHz bands than for the 1 – 4 kHz band.

These patterns are clearly demonstrated by Fig. 6 through Fig. 8, where the increase in acoustic magnitude happens at the beginning of the transition region. These are very useful characteristics of the acoustic output, since the magnitude of the results is completely independent of the type of tool and the engaged length of the tool. This means that a control system based on these results could be much simpler than a system based on other frequency bands, since the same trigger signal could be used in all cases.

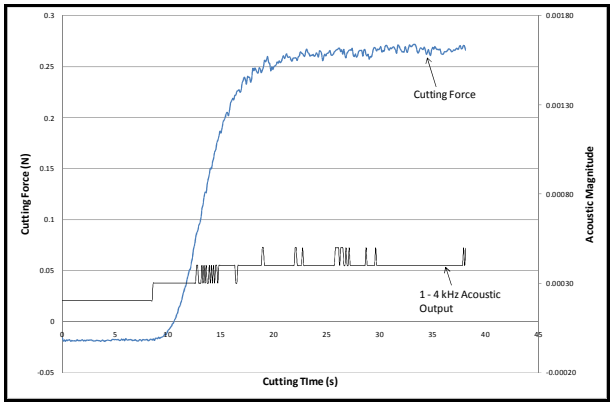

Fig. 6. Cutting force and 1 - 4 kHz acoustic output for 30mm XPS, 7A, 0.0183ms^{-1}

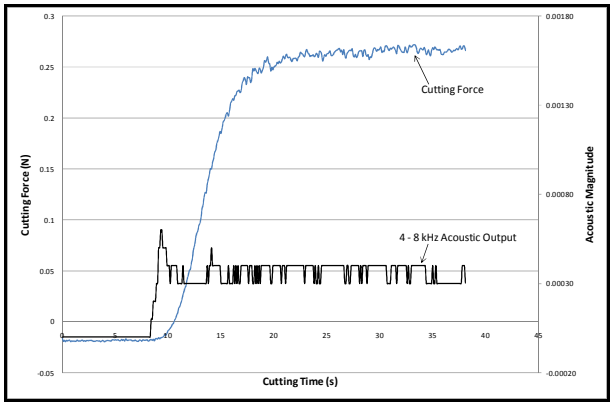

Fig. 7. Cutting force and 4 - 8 kHz acoustic output for 30mm XPS, 7A, 0.0183ms^{-1}

It is also clear that the acoustic output for the 4 – 8 kHz band and the 8 – 12 kHz band are the same. In the case presented here in Fig. 7 and Fig. 8 the acoustic output is exactly the same, and this is true for all of the cuts carried out in this investigation. Some small discrepancies were observed between the acoustic outputs for these two frequency bands, but these discrepancies are limited to the occasional data point which can be regarded as random error. The largest number of differing data points found was 3 in a 35s cut, or 3 data points out of 350, and less than 5% of the samples cut exhibited any discrepancy. This result means that an acoustic-feedback current control system could be implemented based on the 8 kHz-wide band from 4 – 12 kHz: since this band is wider than the 4 kHz bands investigated in this study, it would be easier to measure and such a current control system would be somewhat more robust.

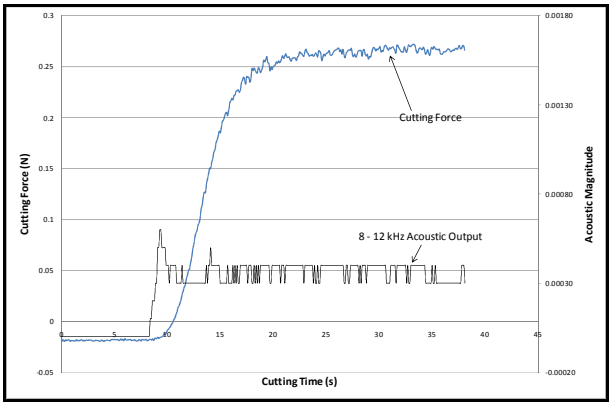

Fig. 8. Cutting force and 8 - 12 kHz acoustic output for 30mm XPS, 7A, 0.0183ms^{-1}

As noted above, the magnitude of the acoustic output was proportional to the cutting force. It is also true that, for a given cut, the mean and peak acoustic magnitudes were larger for higher frequency bands. This suggests that the acoustic output measured in the higher frequency bands is mostly a result of the mechanical component of thermomechanical cutting, while the acoustic output resulting from the thermal component is mostly (but not entirely) present in the lower frequency bands examined. This can be confirmed by comparing Fig. 6 with Fig. 9. These are both charts of the same cut, but show different frequency bands. The change in the 1 – 4 kHz band as the cutting force increases is a relatively small 0.00040, while the 12 – 16 kHz band has a maximum change of 0.00170.

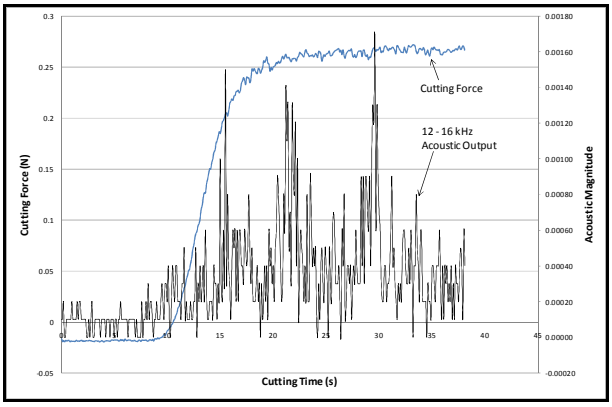

Fig. 9. Cutting force and 12 - 16 kHz acoustic output for 30mm XPS, 7A, 0.0183ms^{-1}

From a practical point of view, to implement an acoustic-feedback current control system for RFS it is only necessary to be able to identify when thermomechanical cutting is taking place from the acoustic output, or in other words to identify the point at which the cutting force begins to increase at the end of the vapourised region. This work has established that the acoustic output is definitely related to the cutting force, and there are a number of ways in which an acoustic-feedback control system could be implemented. Any or all of the frequency bands examined here could serve as a trigger signal for adaptive current control, but some are more suitable than others and the exact trigger signal used in practice will

depend on the nature of the control system and sensors available. The 12 – 16 kHz band has the greatest magnitude of acoustic output, and therefore may be the easiest frequency band to measure. However, the very variable nature of the acoustic signal in this band at all stages of cutting will probably substantially increase the complexity of the control rule required to differentiate the separate cutting stages, because there are no clear and stable acoustic signals associated with the vapourised and thermomechanical cutting stages across all cutting conditions and tool types.

In the lower frequency bands, there are stable and reliable acoustic characteristics of this type. As noted above, the 1 – 4 kHz band has a value of 0.00020 when in the vapourised cutting zone, for all sets of cutting conditions, all engaged lengths, and all tool types. The 4 – 8 kHz and 8 – 12 kHz bands also have a stable level during vapourised cutting regardless of conditions, engaged length and tool type: there is no acoustic output in these frequency bands during vapourised cutting. These three frequency bands also exhibit substantially lower levels of variability during thermomechanical cutting than the 12 – 16 kHz band.

Based on the characteristic patterns of acoustic output that have been observed, it seems likely that the best trigger signal for acoustic-feedback current control will be the acoustic output in the 4 – 12 kHz band. The 1 – 4 kHz band would be suitable, with the current step being triggered whenever the acoustic reading is greater than 0.00020. However, in this band the relative size of the increase in acoustic output is relatively small in this frequency band. In the 4 – 12 kHz band (made up of the examined 4 – 8 kHz and 8 – 12 kHz bands, which exhibited the same behavior), the higher current level would be triggered whenever the acoustic output magnitude in this frequency band was greater than zero. Additionally, using the 4 – 12 kHz frequency band as the trigger signal means that a wider input range can be used which should also simplify the acoustic-feedback current control system.

D. Repeatability of Acoustic Output

Acoustic data gathered was collected for two different sets of conditions six times so that the repeatability of the output could be verified. The acoustic output undergoes considerable variation along a cut, which is an inevitable consequence of the thermomechanical cutting process itself (being related to local variations in cutting force along the cut as the amount of actual plastic engaged with the tool varies), so it was not expected that cuts with the same cutting conditions would present exactly the same acoustic output profiles. In order to assess how repeatable the acoustic output was despite this unpredictability, comparisons were made between the range, mean and standard deviation of the data in each frequency band.

When these data-set statistics were compared, it was found that the acoustic output was highly consistent for a given set of cutting conditions. Due to space constraints the details of the repeatability analysis cannot be presented here, but the maximum variation of the means for these data sets was 0.00060, and the larger variations occurred for the 12 – 16 kHz band. In the 1 – 4, 4 – 8 and 8 – 12 kHz bands the range, mean and standard deviation of the acoustic magnitude for each run were identical.

IV. CONCLUSIONS

This study has established that the acoustic output resulting from thermomechanical cutting of polystyrene foam would be a suitable trigger metric for adaptive current control in the RFS system, since it is measureable, repeatable and a result of the cutting process. At frequencies between 1 kHz and 16 kHz the measured acoustic signal is predominantly due to the cutting process, and the magnitude of the acoustic output is related to the cutting forces and the thermomechanical balance.

The most promising frequency band for in-process measurement of the acoustic output is between 4 and 12 kHz, which has no acoustic output during vapourised cutting and a magnitude greater than zero when thermomechanical cutting is taking place. This means that the step-change to the current can be applied as soon as the acoustic magnitude in this frequency band is greater than zero and the benefits of adaptive current control will be achievable using a sensor that can be mounted on the robot adjacent to the cutting tool.

REFERENCES

AHN, D. G., LEE, H. S. & YANG, D. Y. (2002) Investigation into development of progressive-type variable lamination manfacturing using expandable polystyrene foam and its apparatus. *Proceedings of the I MECH E Part B Journal of Engineering Manufacture,* 216**,** 1239 - 1252.

AHN, D. G., LEE, H. S. & YANG, D. Y. (2003) Development of transfer-type variable lamination manufacturing (VLM-) process. *International Journal of Machine Tools and Manufacture,* 43**,** 1447 - 1464.

AITCHISON, D., BROOKS, H., BAIN, J. & PONS, D. (2009) An investigation into the prediction of optimal machining conditions for polystyrene foam cut with a taut hot-wire. *International Conference New Technologies in Manufacturing*. Galati, Romania.

AITCHISON, D., BROOKS, H., KANDULA, R., KRAUS, B. & TAYLOR, M. (2006) Feed-rate, temperature and feed-force relationships for foam plastics cut by a taut hot-wire. *ICOMAST2006: International Conference on Manufacturing Science and Technology.* Melaka, Malaysia.

AITCHISON, D. R., GERMANN, T. S. & TAYLOR, M. (2005) Sculpting of Expanded Foam Plastics for Rapid Prototyping Applications. IN BARTOLO, P. (Ed.) *Virtual Modelling and Rapid Manufacturing.* Leiria, Portugal.

BROOKS, H. L. & AITCHISON, D. R. Force feedback temperature control for hot-tool plastic foam cutting. *Proceedings of the Institution of Mechanical Engineers, Part B: Journal of Engineering Manufacture,* 224**,** 709-719.

DE SMIT, B., BROEK, J. & HORVATH, I. (1999) Experimental Investigation Of Factors Influential For The Flexible Blade Based Prototyping Process. IN ASME (Ed.) *The 1999 ASME Design Engineering Technical Conference.* Las Vegas, Nevada, USA, ASME.

DE SMIT, B., BROEK, J., HORVATH, I. & LENNINGS, L. (2000) Implementation of the freeform thick layered object manufacturing technology (FF-TLOM), a status review. *Proceedings of the Ninth European Conference on Rapid prototyping and manufacturing.*